# *Towards the Development of Photoresponsive Molecular Assemblies*

Matthew James Cunningham (639356)

The Queen's College

University of Oxford




A thesis submitted for the degree of

*Doctor of Philosophy*

Trinity Term 2016

*In Memory of Mr. and Mrs. Harry Cunningham*

# Acknowledgments

Firstly, I would like to thank my supervisory team of Professors Paul Beer, Jason Davis and Stephen Faulkner for allowing me to undertake research within such an interesting and challenging area of Chemistry at the University of Oxford. Thanks must also be extended to Drs Asha Brown, Ashley Shephard, Robert Jacobs and Joshua Lehr for their continued help and guidance in regards to the synthesis of utilised molecular components and / or with the intricacies of surface analysis, respectively.

Aside from those already mentioned, I would like to thank all current (hang in there, Justin!), and past members of the Davis Group for their help and guidance over the course of my PhD, but special thanks must be reserved for Ms. Rachel Kelly and Drs. Daniel Trawny and Flavio Bedatty, for whom I possess the utmost respect for. Daniel, together we walked the coast of Normandy, spent many a good day in Berlin, managed to somehow flood Iris's lab, and purified complex mixtures that other groups couldn't! We share the same sense of humour, appreciate the value of possessing good morals, and it was a true shame that your stint in the Davis group was not longer. However, children (Mini T) must be had, so all the best with that! Flavio, aka Mr Brazil, we shared some special moments together with Pembroke MCR's football team, as well as many wonderful dishes in my kitchen at SAH (+ BOPE); I scored THAT goal for you, and you only. Finally, Rachel, what can I say, other than that you're a bad influence, give terrible banter, but somehow made the office a very enjoyable place; it hasn't been the same since, but I am glad that you managed to escape unscathed. Thanks must also be extended to Paul, Martin and Levi of the PTCL, who keep things running smoothly and of whom I have also got the utmost respect for. You all made coming to work much more bearable, had a laugh and a joke with me on almost a daily basis, and all understood the political struggles faced by a DPhil student at the University of Oxford. I appreciated your help and / or advice greatly, and I wish you all the very best from here on in; the department would be a much darker place without you all! Furthermore, special mention must go to Andrew Baxter, of whom I had the pleasure of supervising throughout my second year; your work ethic could not be faulted, your banter was always on point, although your left foot left me baffled, for all the wrong reasons, on many an occasion, as has your decision to introduce me to ChCh's ex-JCR president, the one and only Mr Christopher Hutchinson (MChem ONLY, PhDropout). Having originally regretted my decision to move in with this guy (Stud and / or Mr Unemployed), I will forever look fondly back on my time living alongside him, Thomas Lewin (Varsity Duathlon and Triathlon Champion 2016) and Sophia Saller (Winner of the GBBO 2018 and an amateur triathlete) at 26 Marston Street. Chris, you p**s me off in all the right ways, make an awful cup of tea, use no soap when washing the dishes, yet I still consider you to be one of the finest gentlemen around, so keep preparing that speech (I promise you that the time WILL come). Tom, a fellow tortellini (+ sauce) enthusiast of whom has great arms, you're one of a kind, possessing niche banter, great music taste and the ability to not let your anger

surface when a certain individual frequently disturbs you when bored of an evening. Sophia, what can I say, apart from that I think that you need to spend less time in bed, more time on the turbo and allow the tea bag to steep for much longer than a few seconds. On a lighter note, thanks for developing into the motherly figure within the house, keeping us three unruly lads in check, and for telling us to tone it down on numerous occasions; for this you deserve a medal (Olympic). Overall, the three of you have made my final year in Oxford much less stressful than it should have been, so I thank you from the bottom of my heart. However, I would have been done by now if it wasn't for you and all those episodes of First Dates on a Thursday evening. When not confined within the 'Madhouse', I found myself gracing either the gym with one Dr Jack Routledge, aka 'The Beast', or a football pitch alongside Jumbo, aka Dr James Dowthwaite, who I recently bought Gdansk with. The both of you have been friends of mine since Day 1, so thank you for putting up with me for so long, resolving the trouble that I inevitably caused along the way (rampage Thursdays), and bringing a smile, and the odd beverage, to me at times of distress.

When back in Bere Alston and / or away from Oxford on rest bite, I could always count on the company of Mike Gentle (Ox), Mike Brown (Grin), Ryan Greep (Zoro) and Matthew Ash (Snout) to cheer me up, whether that involved being dragged out for a night out in Plymouth, which would inevitably end up in North Hill, or a night in playing Fifa (that was when the controllers contained full batteries). I cherish your years of friendship dearly and I am extremely pleased that you have all gone on to achieve so much. We village boys did not do too badly, did we!?

Talking about Bere Alston...

I would now like to take this opportunity to thank my family who have stuck by me every step of the way. You gave me the confidence to pursue this pathway, installed in me an attitude of not to quit, whatever the situation, and have still resisted the temptation to turn my room into another guest suite. I can't stress enough how much sending me away with multiple cheese sandwiches and copious packets of crisps, the flavours of which you all dislike (Mum), money for a coffee on the train (Nan and Granddad), and emails containing every fixture that I could possibly watch on BT Sport in the coming week (Dad), helps. I'd also like to take this opportunity to state that I am dedicating this thesis to the memory of Mr. and Mrs Harry Cunningham, who invested huge amounts of time in Megan, my sister and best friend, and I from a young age. Unfortunately, you were both taken too soon, but your memory lives strong and will continue to drive us both onto bigger and better things, I can assure you. 'You could have left a note', but until we meet again, thanks.

**I will always call '8 West View Road' home and all of this would not have been possible without EVERY single one of you, so thank you. I DID IT!**

# Towards the Development of Photoresponsive Molecular Assemblies

A thesis submitted for the degree of Doctor of Philosophy

Matthew James Cunningham, The Queen's College, University of Oxford

Trinity Term 2016

## Abstract

The emergence of complex, carefully designed, molecular architectures incorporating either a lanthanide ion or the porphyrinic macrocycle have stimulated significant interest of late, particularly in the fields of molecular switches, molecular machines and data storage systems. The integration of these emissive species has been shown to permit the analysis of conformational, coordinative, or electronic change, and employed, in the case of the porphyrinic macrocycle, to acquire a deeper understanding of the natural process of photosynthesis, thus opening up the possibility of developing more efficient and inexpensive photovoltaic cells.

This thesis begins by providing insight into the generation of cathodic photocurrent density within both monophasic and biphasic self-assembled monolayers, before documenting how the magnitude of such photoelectochemical output can be gated upon the integration of an electron relay moiety, both at the interface and into solution. The introduction of an electron relay moiety into solution has been shown to bring about increases of up to 283 % in the magnitude of the cathodic photocurrent density acquired, whilst optimisation of the distances between the metallic interface, the electron relay moiety and the porphyrinic macrocycle has also proven beneficial. Greatest photoelectrochemical output ($5.1 \times 10^{14}$ nA $mol^{-1}$ $cm^{-2}$) is realised when the porphyrinic macrocycle is covalently tethered at a distance of 4.6 nm from the quenching, metallic interface, and the relay moiety integrated at a distance of 1.7 nm from the interface and 2.9 nm from the porphyrinic macrocycle, respectively. However, greatest variation (94 %) in the magnitude of the cathodic photocurrent densities acquired is observed when the distance between the porphyrinic macrocycle and the gold surface is kept at 3.3 nm, and the relay moiety situated at either 1.2 nm or 1.7 nm from the interface, respectively. Research then moved towards trying to integrate this established conformational ruler within a porphyrin-appended, bistable [2]rotaxane. Its implementation served to try to ensure that photoelectrochemical differentiation of the ground state co-conformation (GSCC) and the metastable state co-conformations (MSCC) was viable, thus enabling the efficient resolution of anion-induced molecular motion within a dynamic supramolecular architecture by means of a novel approach.

The focus of this thesis then shifts to the assembly of novel, optically switchable, ternary complexes exhibiting charge-transfer based on the donor-acceptor interaction between an electron-rich naphthalene derivative (EuNap) and $MV^{2+}$, an electron-poor, redox-addressable moiety. Prior to the deposition of (MV, EuNap)-CB[8] at the interface, the homoternary analogue ($(MV^{+\cdot})_2$-CB[8]) was acquired upon

one electron reduction of (MV, EuNap)-CB[8] in the presence of excess $MV^{2+}$. This process was revealed to be reversible upon the application of a stream of oxygen, and the relative concentration of each complex present in solution quantified upon mathematical manipulation of the biexponential decay curve acquired; upon the addition of sodium thiosulfate ($Na_2S_2O_3$), the percentage of uncomplexed EuNap ($\tau$ = 0.60 ms *cf.* $\tau$ = 0.1 ms (MV, EuNap)-CB[8]) present in solution increased in accordance with the generation of $((MV^{+\cdot})_2$-CB[8]) and loss of the charge-transfer interaction ($\lambda_{max}$ = 390, 490 nm), of which has been shown to quench lanthanide luminescence ($Eu^{3+}$, $Yb^{3+}$, $Nd^{3+}$). Thus, the assembly of a molecular switch is documented which may be followed qualitatively at higher concentration by a visible colour change, and at low concentrations quantitatively by virtue of luminescence spectroscopy. No optical output ($\lambda_{ex}$ = 227 nm, $\lambda_{em}$ = 616 nm) was acquired upon the deposition of (MV, EuNap)-CB[8]) due to the occurrence of surface energy transfer (SET). As a result, 1-(10-mercaptodecyl)-1'-methyl-[4,4'-bipyridine]-diium bromide and 1-methyl-1'-(10-(naphthalen-2yloxy)decyl)-[4,4'-bipyridine]-1,1'-diium bromide iodide were synthesised and the assembly of a molecular film envisaged in which the molecular recognition properties of CB[*n*] were maintained and significant optical output from the lanthanide ion ($Eu^{3+}$, $\lambda_{em}$ 616 nm) detected; the assembly of such a film centred on the formation of 1:2 *inter*molecular heteroternary complexes and the recruitment of EuNap at a distance ≥ 3.2 nm from the gold substrate. It was envisaged that the modulation of any emissive output would be brought about upon manipulating the oxidation state of a surface-confined metallocene.

This thesis ends by summarising the research conducted and assessing how the inclusion chemistry of cucurbit[8]uril and the photophysical properties of the porphyrinic macrocycle can be combined in order to fabricate a dynamic, photoresponsive molecular assembly. The electrical energy generated from the efficient harvesting of light energy could be used in a multitude of applications, most notably as a nanoscale power supply to drive and control molecular and supramolecular actuations.

## List of Publications

**Neutral redox-active hydrogen- and halogen-bonding [2]rotaxanes for the electrochemical sensing of chloride**. Jason Y. C. Lim, Matthew J. Cunningham, Jason J. Davis and Paul D. Beer.

*Dalton Trans*., **2014**, 43, 17274–17282.

**Halogen bonding-enhanced electrochemical halide anion sensing by redox-active ferrocene receptors.** Jason Y. C. Lim, Matthew J. Cunningham, Jason J. Davis and Paul D. Beer.

*Chem. Commun.*, **2015**, 51, 14640–14643.

**Acyclic halogen and hydrogen bonding diquat-containing receptors for the electrochemical sensing of anions**. Benjamin R. Mullaney, Matthew J. Cunningham, Jason J. Davis and Paul D. Beer.

*Polyhedron*, **2016**, 116, 20–25.

## Nomenclature

% – Percentage

(g) – Gas phase

° - Degrees

°C – Degrees Celsius

µ – Micron

µM – Micromolar

$^{13}$C NMR – Carbon-13 Nuclear Magnetic Resonance

$^{1}E_{u}$ – Porphyrin-centred singlet excited state

$^{1}$H NMR – Proton Nuclear Magnetic Resonance

2,6-Np – 2,6-dihydroxynaphthalene

Å – Angstroms

A – Electrode Area

A – Empirical background noise factor

a.u. – Arbitrary Units

$a_{1u}$ – Porphyrin-Centred Molecular Orbital (LUMO)

$a_{2u}$ – Porphyrin-Centred Molecular Orbital (LUMO)

AB – Azobenzene

AcN – Acetonitrile

AdHCl – Adamantane Hydrochloride

AFM – Atomic-Force Microscopy

Ag / AgCl – Silver / Silver Chloride Reference Electrode

Ag / $AgNO_3$ – Silver / Silver Nitrate Reference Electrode

$Ag^{II}$ – Silver (II)

apo-GOx – Reconstituted Glucose Oxidase

APTES – (3-aminopropyl)triethoxysilane

aq. – Aqueous

AsA – Ascorbic Acid

atm – Atmospheres

Au – Gold

AuNPs – Gold Nanoparticles

$B_1$ – Empirical amplitude scaling factor (Emissive Species 1)

$B_2$ – Empirical amplitude scaling factor (Emissive Species 2)

BET – Back Election Transfer

BHEEN – 1,5-bis[(2-hydroxyethoxy)ethoxy]naphthalene

$Br(CH_2)_{10}Br$ – 1,10-Dibromodecane

C – Concentration

$C_{60}$ – Buckminsterfullerene

CB[*n*] – Cucurbit[*n*]uril, *n* = 5 – 11

$CBPQT^{4+}$ – Cyclobis(paraquat-*p*-phenylene)

CD – Cyclodextrin

$CD_2Cl_2$ – Dichloromethane-d2

$Cd^{II}$ – Cadmium (II)

$CH_2Cl_2$ – Dichloromethane

$cm^{-2}$ – per centimetre$^2$

$Cu^{II}$ – Copper (II)

$CuSO_4.5H_2O$ – Copper(II) sulphate pentahydrate

CV – Cyclic Voltammetry

D – Diffusion coefficient

d – Distance

$D_2O$ – Deuterium oxide

Da – Dalton

D-A – Donor-Acceptor dyad

DCM – Dichloromethane

$D_{EnT}$ – The distance associated with energy transfer

DMF – Dimethylformamide

$d^n$ – $d^n$ configuration

DNA – Deoxyribonucleic Acid

DO3A – Macrocyclic chelator

DOTA – 1,4,7,10-tetraazacyclododecane-1,4,7,10-tetraacetic acid

$d\pi$ ($d_{xz}$, $d_{yz}$) – Metal-centred orbitals

$e^-$ – Electron

$E_{1/2}$ – Half-way potential

$E_{Aff}$ – Electron Affinity

$E_{ap}$ – Applied Potential

$E_{CT}$ – Energy of Charge Transfer

EDC – 1-Ethyl-3-(3-dimethylaminopropyl)carbodiimide

$e_g$ – Porphyrin-centred molecular orbital

$E_{HOMO}$ – Energy of Highest Occupied Molecular Orbital

$E_{ION}$ – Ionisation Energy

$E_{LUMO}$ – Energy of Lowest Unoccupied Molecular Orbital

ER – Electron Relay

ESI-MS – Electrospray Ionisation Mass Spectrometry

ET – Electron Transfer

*et al* – and others

$Et_3N$ – Triethylamine

EtOH – Ethanol

Eu.2 – Europium-ferrocene dyad

$Eu^{3+}$ – Europium (III)

EuNap – Europium-Naphthalene Species

eV – Electron Volts

ε – Extinction coefficient

F – Faraday's constant

FAD – Flavin Adenine Dinucleotide

Fc – Ferrocene

$Fc^+$ – Ferrocenium

Fc11 – 11-(ferrocenyl)undecanethiol

Fc6 – 6-(ferrocenyl)hexanethiol

$FcC_{11}SH$ – 11-(ferrocenyl)undecanethiol

$FcC_6SH$ – 6-(ferrocenyl)hexanethiol

FcD – Ferrocenylmethyltrimethylammonium

FcMeOH – Ferrocenemethanol

$FcNMe_3^+$ – Ferrocenylmethyltrimethylammonium

$Fe^{II}$ – Iron(II)

FRET – Förster Resonance Energy Transfer

FTIR – Fourier Transform Infrared spectroscopy

g – Grams

$GO_x$ – Glucose Oxidase

GSCC – Ground-State Co-Conformation

h – Hours

$H_2O$ – Water

$H_2Q$ – Hydroquinone

$H_2SO_4$ – Sulphuric acid

Hg / $Hg_2SO_4$ – Mercury / mercury sulphate reference rlectrode

HOMO – Highest Occupied Molecular Orbital

*hv* – Irradiation with light

IC – Internal Conversion

$i_p$ – Current

ISC – Intersystem Crossing

ITC – Isothermal Titration Calorimetry

ITO – Indium Tin Oxide

*J* – Reorganisation energy

JL241 – Ferrocene-appended macrocycle

K – Kelvin

$K_2CO_3$ – Potassium carbonate

$K_2S_2O_8$ – Potassium persulfate

$K_3[Fe(CN)_6]$ – Potassium ferricyanide

$K_a$ – Association constant

$k_B$ – Boltzmann constant

$k_{el}$ – Electron transmission coefficients

$K_{EnT}$ – Rate of Energy Transfer

$k_{ET}$ – Rate of Electron Transfer

KOH – Potassium hydroxide

KSAc – Potassium thioacetate

LMCT – Ligand-to-Metal Charge-Transfer

Ln – Lanthanide

logK – Binding constant

LUMO – Lowest Unoccupied Molecular Orbital

M – Molar

m / z – Mass-to-charge Ratio

MALDI-TOF – Matrix Assisted Laser Desorption/Ionization-Time of Flight

MeCN – Acetonitrile

MeI – Methyl Iodide

MeOH – Methanol

mg – Milligram

MHDA – 16-mercaptohexadecanoic Acid

MHz - Megahertz

MLCT – Metal-to-Ligand Charge-Transfer

mM – Millimolar

MO – Molecular Orbital

$mol^{-1}$ – Per mole

ms – Milliseconds

MSCC – Metastable-State Co-Conformation

MUA – 11-mercaptoundecanoic Acid

mV – Millivolts

$MV^{2+}$ – Methyl Viologen

$MV^{2+}$-SH – 1-(10-mercaptodecyl)-1'-methyl-[4,4'-bipyridine]-diium bromide

MVFc – Ferrocenyl Viologen Derivative

$MVN_3^+$ - 1-(3-azidopropyl)-1'-methyl-[4,4'-bipyridine]-1,1'-diium

$MVNH_3^+$ - 1-(3-aminopropyl)-1'-methyl-[4,4'-bipyridine]-1,1'-diium

n – Number of electrons

nA – Nanoamps

$Na_2S_2O_4$ – Disodium dithionite

NaCl – Sodium Chloride

$NaClO_4$ – Sodium perchlorate

NAMV – Non-Aromatic Methyl Viologen Derivative

NaOD – Sodium deuteroxide

NaOH – Sodium hydroxide

$Nd^{3+}$ – Neodymium (III)

NdNap – Neodymium-Naphthalene Species

NHS – N-Hydroxysuccinimide

$Ni^{II}$ – Nickel (II)

nm – Nanometres

$O_2$ – Oxygen

OCP – Open Circuit Potential

OEG – $HS\text{-}(CH_2)_{10}\text{-}EG_3\text{-}OCH_2\text{-}COOH$

$P^*$ - Excited State of Porphyrinic Macrocycle

Pd/C – Palladium on Carbon

$Pd^{II}$ – Palladium (II)

PET – Photoinduced Electron Transfer

pH – Potential Hydrogen

pKa – Acid Dissociation Constant

PMT – Photomultiplier Tube

Por – Porphyrin

$Por^{*}$ - Excited State of Porphyrinic Macrocycle

ppm – Parts Per Million

PSYN – Photosynthesis

Pt – Platinum

$Q_x$, $Q_y$ – Q-bands of porphyrinic macrocycle

$QY_x$ – Quantum Yield

ROESY – Rotating-frame Overhauser Effect

RT – Room Temperature

$s^{-1}$ – Per second

SAM – Self-Assembled Monolayer

SCE – Saturated Calomel Electrode

SET – Surface Energy Transfer

Si – Silicon

T – Temperature

TBACl – Tetrabutylammonium Chloride

$TBAPF_6$ – Tetrabutylammonium hexafluorophosphate

TEOA – Triethanolamine

THF – Tetrahydrofuran

$TiO_2$ – Titanium dioxide

TPAPP – 5,10,15,20-Tetrakis(4-aminophenyl)porphyrin

$TPP^{*}$ - Excited State of porphyrin derivative (TPP)

TTF – Tetrathiafulvalene

UV-Vis – Ultraviolet–Visible

$\nu$ – Scare rate

V – Volts

VR – Vibrational Relaxation

W - Watts

XPS – X-ray Photoelectron Spectroscopy

$Yb^{3+}$ - Ytterbium (III)

$Zn^{2+}$ - Zinc (II)

α-CD – Alpha Cyclodextrin

β – Constant (Scaling Distance Dependence)

ΔE – Change in Energy

$\Delta E_{CT}$ – Energy change of Charge Transfer

$\Delta G^0$ – Change in Gibbs Free Energy

$\Delta_{ml}$ – Laporte selection rule

λ – Wavelength

$\lambda_{em}$ – Emission wavelength

$\lambda_{ex}$ – Excitation wavelength

$\lambda_{irr}$ – Wavelength of irradiation

$\lambda_{max}$ – Wavelength of maximum absorption

$\pi^*$ – Porphyrin-centred molecular orbital

τ – Luminescence lifetime

# Table of Contents

**Acknowledgments** ..... **I**

**Abstract** ..... **IV**

**List of Publications** ..... **VI**

**Nomenclature** ..... **VII**

**1. Supramolecular Chemistry and the Development of Dynamic, Interlocked Molecular Architectures**

**1 – An Introduction to Supramolecular Chemistry.** ..... **1**

**1.1 – The Development and Formation of Functional, Bistable [2]Rotaxanes.** ..... **1**

**1.2 – The Templated Assembly of Molecular Architectures.** ..... **3**

***1.2.1 – Anion-Templated Synthesis.*** ..... ***3***

***1.2.2 – Metal-Templated Synthesis.*** ..... ***4***

**1.3 – Stimuli-Responsive Molecular Architectures.** ..... **4**

**1.4 – The Surface-Assembly of Stimuli-Responsive Molecular Architectures.** ..... **8**

**1.5 – Summary** ..... **11**

**1.6 – Research Aim(s).** ..... **14**

**The Porphyrinic Macrocycle and the Generation of Cathodic Photocurrent**

**1.7 – An Introduction to the Porphyrinic Macrocyclic Arrangement** ..... **16**

**1.8 – An Introduction to Artificial Photosynthesis and the Self-Assembly of Efficient Photoconversion Devices.** ..... **19**

**1.9 – PET Indution at the Interface.** ..... **24**

***1.9.1 – Electrochemically Modulating the Magnitude of the Cathodic Photocurrent Density Generated via the Integration of a Redox Mediator.*** ..... ***25***

***1.9.2 – Further Modulation of the Magnitude of the Cathodic Photocurrent Density Generated.*** ..... ***28***

**1.10 – Summary and Objective(s).** ..... **29**

**Cucurbituril and the Development of Switchable Ternary Complexes**

**1.11 – An Introduction to the Cucurbit[n]uril, CB[n], Family.** ..... **30**

**1.12 – Inclusion within CB[n] and Applications of Host-Guest Chemistry. ..... 31**

**1.13 – Inclusion within CB[8] – Ternary Complex Formation. ..... 33**

**1.14 – Incorporating Lanthanide Ions into Supramolecular Assemblies ..... 35**

***1.14.1 – Electronic Properties of Europium ($Eu^{3+}$). ..... 35***

***1.14.2* – Sensitised Luminescence via the Integration of Molecular Antenna. ..... *36***

***1.14.3* – Energy Transfer Mechanisms in Luminescence Sensitisation. ..... *37***

***1.14.4* – The Effect of Complexation on Lanthanide Luminescence. ..... *38***

**1.15 – The Impact of Redox-Active Species on Lanthanide Luminescence. ..... 38**

**1.16 – Aim(s) of Project. ..... 39**

**2. Photoinduced Electron Transfer within Porphyrin-Appended Self-Assembled Monolayers. ..... 61**

**2.1 – Exploiting the Distance Dependence of Photoinduced Electron Transfer to Construct a Conformational 'Ruler'. ..... 62**

**2.2 – Establishing a Conformational 'Ruler' within Monophasic, Porphyrin-Appended SAMs 68**

***2.2.1 – Formation and Characterisation of Monophasic, Porphyrin-Appended SAMs. ..... 69***

***2.2.2 – Investigating the Generation of Cathodic Photocurrent within Monophasic, Porphyrin-Appended SAMs. ..... 77***

***2.2.3 – Modulating the Magnitude of Photoelectrochemical Output. ..... 78***

**2.3 – Establishing a Conformational 'Ruler' within Biphasic, Porphyrin-Appended SAMs. ..... 82**

**2.4 – Concluding Remarks and Moving Forwards ..... 90**

**3. Towards Photoelectrochemically 'Mapping' the Position of Redox-Active Macrocycles within Dynamic Supramolecular Architectures. ..... 99**

**3.1 – Confirming Solution Phase Pseudorotaxane Assembly. ..... 99**

**3.2 – Tethering AB-14-172-JL241 to an Underlying, Thiolated Interface Deposited at Au ..... 103**

***3.2.1 – Covalent Attachment of AB-14-172-JL241 to a SAM of MUA. ..... 103***

***3.2.2 – Generation of Cathodic Photocurrent at Rotaxanated Interfaces ..... 107***

**3.3 – Utilising Thioctic Acid-Appended Axle Components in the Assembly of Interlocked Molecular Films. ..... 109**

***3.3.1 – Direct Deposition of Interlocked Architectures at the Interface. ..... 109***

*3.3.2 – Role of Coordinated Metal Ions and the Triazolium Motif in the Generation of Cathodic Photocurrent.....120*

**3.4 – Concluding Remarks and Moving Forwards. .....122**

**4. Host-Guest Recognition & the Generation of Ternary Complexes in Solution. .....129**

**4.1 – Ternary Complex Formation. .....130**

**4.2 – Formation of the Model Homoternary Dimer Complex, $(MV^{+\bullet})_2$-CB[8]. .....132**

**4.3 – Elucidating the Effect of Charge Transfer on the Sensitised Radiative Output Acquired from a Lanthanide Centre, Confined within a Ternary Complex.....134**

**4.4 – Formation of the Desired Ternary Complex, (FcMV, EuNap)-CB[8]: a Sterically and Kinetically Impeded Process. .....140**

**4.5 – Quenching Effect of Charge-Transfer by Reducing Conjugation.....143**

**4.6 – Negating the Quenching Effect of Charge Transfer at the Interface.....149**

**4.7 – Utilising Ternary Complex Formation in the Stepwise Growth of an Emissive Interface. .....154**

**4.8 – Ensuring that the Stepwise Growth of an Emissive Interface is Viable.....157**

**5. The Surface Assembly of Molecular Switches.....165**

**5.1 – Recruiting Redox-Active Derivatives to CB[*n*]-Functionalised Surfaces. .....165**

*5.1.1 – Exploiting Multivalent Interactions in the Assembly of CB[n]-Functionalised Interfaces.165*

*5.1.2 – Electrostatic Recruitment of CB[7] at Non-Quenching Substrates. .....170*

*5.1.3 – Recruiting $MV^{2+}$ and FeMeOH at CB[7]-Functionalised Monolayers Deposited at Non-Quenching Surfaces.....174*

*5.1.4 – Elucidating the Mechanism of Assembly of a SAM of CB[7] at APTES-Modified Substrates. .....179*

*5.1.5 – Maintaining the Recognition Properties of CB[7] at the Interface.....186*

**5.2 – Utilising Charge-Transfer in the Surface Assembly of Switchable, Lanthanide-Appended Molecular Systems. .....188**

*5.2.1 – Formation and Characterisation of $MV^{2+}$-Functionalised Monolayers. .....188*

*5.2.2 – Towards the Stepwise Growth of Lanthanide-Appended Interfaces. .....194*

*5.2.3 – Formation of the 1:1 Intramolecular Heteroternary Charge-Transfer Complex and Subsequent Disassembly of the Supramolecular Architecture. .....197*

*5.2.4 – Assembling Intermolecular Charge-Transfer Complexes from their Intramolecular Analogues.* ..... *201*

*5.2.5 – Modelling Migration of the Macrocyclic Host from the Periphery of the Interface.* ..... *204*

**5.3 – Moving Forwards.** ..... **207**

**6. Summary and Outlook.** ..... **217**

**7. Experimental.** ..... **221**

**7.1 – Material and Reagents.** ..... **221**

**7.2 – Electrochemistry.** ..... **221**

*7.2.1 – Electrode Preparation.* ..... *221*

*7.2.2 – Calculating the Surface Coverage.* ..... *222*

*7.2.3 – Calculating the Cathodic Photocurrent Density.* ..... *224*

*7.2.4 – Electrochemical Parameters.* ..... *226*

**7.3 – The Formation of Self-Assembled Monolayers (SAMs)** ..... **227**

*7.3.1 – The Formation of SAMs of CB[7] at Gold.* ..... *227*

*7.3.2 – The Formation of Thiolated SAMs.* ..... *227*

*7.3.3 – Carbodiimide Coupling.* ..... *227*

*7.3.4 – Azide-Alkyne Huisgen Cycloaddition.* ..... *228*

*7.3.5 – CB[7]-Functionalised Silicon.* ..... *228*

*7.3.6 – Towards The Covalent Immobilisation of CB[7] on Silicon.* ..... *228*

**7.4 – Ellipsometry** ..... **228**

**7.5 – UV-Vis and Transmissive UV-Vis Spectroscopy.** ..... **229**

**7.6 – X-Ray Photoelectron Spectroscopy (XPS).** ..... **229**

**7.7 – NMR and Mass Spectroscopy.** ..... **229**

**7.8 – Luminescence Spectroscopy.** ..... **229**

**7.9 – Contact Angle Measurements.** ..... **230**

**7.10 – Ternary Complex Formation.** ..... **230**

**7.11 – Hydrogenation Reaction.** ..... **230**

**7.12 – Synthesis of naphthalene-appended lanthanide DO3A (1,4,7,10-tetraazacyclododecane-1,4,7,10-tetraacetic acid) complexes, LnNap. ..... 231**

**7.13 – Synthesis of the ferrocene functionalised viologen, FcMV. ..... 238**

**7.14 – Synthesis of functionalised viologen derivatives $MVNH_3$ and $MVN_3$. ..... 242**

**7.15 – Synthesis of 1-(10-mercaptodecyl)-1'-methyl-[4,4'-bipyridine]-diium bromide, D. ..... 245**

**7.16 – Synthesis of 1-methyl-1'-(10-(naphthalen-2-yloxy)decyl)-[4,4'-bipyridine]-1,1'-diium bromide iodide, F. ..... 251**

**7.17 – Synthesis of PerhydroxyCB[6], 1. ..... 254**

**8. Appendix. ..... 260**

**8.1 – The Characterisation of Porphyrin-Appended SAMs. ..... 260**

***8.1.1 – Solution Phase Characterisation of AB-14-172 ..... 260***

***8.1.2 – Characterisation of Monophasic, Porphyrin-Appended SAMs ..... 261***

***8.1.3 – Characterisation of Biphasic, Porphyrin-Appended SAMs ..... 261***

**8.2 – Characterisation of Porphyrin-Appended SAMs by XPS ..... 264**

**8.3 – Photocurrent Density Measurements at Porphyrin-Appended SAMs ..... 273**

***8.3.1 – Photoelectrochemical Analysis of Monophasic, Porphyrin-Appended SAMs ..... 273***

***8.3.2 – Photoelectrochemical Analysis of Biphasic, Porphyrin-Appended SAMs ..... 280***

**8.4 – Comparison of the Photocurrent Densities Acquired at Monophasic and Biphasic, Porphyrin-Appended SAMs ..... 285**

**8.5 – Characterisation of Rotaxanated Interfaces by XPS ..... 287**

***8.5.1 – AB-14-172–OEG ..... 287***

***8.5.2 – (AB-14-172-JL241)–OEG. ..... 288***

***8.5.3 – AB-19-144 ..... 291***

**8.6 – Cathodic Photocurrent Density Measurements at Rotaxanated Interfaces ..... 293**

***8.6.1 – AB-14-172–OEG, AB-14-172–OEG–Fc11, (AB-14-172-JL241)–OEG ..... 293***

***8.6.2 – AB-18-088, AB-18-088–Fc11. ..... 294***

***8.6.3 – AB-19-144, AB-19-144 + 1 mM FcMeOH ..... 294***

**8.7 – Absorption Spectra of Free Base and Metal-Containing Porphyrin Derivatives ..... 295**

**8.8 – Spectroscopic Characterisation of EuNap, ($MV^{2+}$, EuNap) and ($MV^{2+}$, EuNap)-CB[8] ... 296**

*8.8.1 – EuNap* ..... *296*

*8.8.2 – ($MV^{2+}$, EuNap)* ..... *297*

*8.8.3 – ($MV^{2+}$, EuNap)-CB[8].* ..... *297*

**8.9 – Monitoring the Formation of ($MV^{+\cdot}$)$_2$-CB[8] Upon Addition of $Na_2S_2O_4$ to a Solution of ($MV^{2+}$, EuNap)-CB[8]** ..... **299**

**8.10 – Estimating the Efficacy of Generating ($MV^{+\cdot}$)$_2$-CB[8] in Solution** ..... **300**

**8.11 – Characterisation of Heteroternary Complexes Formed from the Non-Aromatic Derivatives Acquired *via* Hydrogenation** ..... **301**

**8.12 – Investigating the Quenching Effect of Incorporating Yd and Nd into the Hydrophobic Cavity of CB[8]** ..... **303**

*8.12.1 – ($MV^{2+}$, YdNap)-CB[8]* ..... *303*

*8.12.2 – ($MV^{2+}$, NdNap)-CB[8]* ..... *305*

**8.13 – Investigating the Effect of Chromophore Confinement and the Presence of Oxygen on the Emissive Output from NdNap** ..... **306**

**8.14 – Characterisation of Heteroternary Charge Transfer Complexes by UV-Vis Spectroscopy** ..... **309**

**8.15 – Characterisation of (FcMV, EuNap)-CB[8]** ..... **311**

**8.16 – Recruitment of Fc-Appended Derivatives at CB[7]-Modified Au Electrodes** ..... **311**

**8.17 – Quantifying the Level of Non-Specific Adsorption of Eu.2 and $FcCH_2NH_2$ at Bare Au** ..... **312**

**8.18 – Spectroscopic Characterisation of Eu.2** ..... **313**

**8.19 – Spectroscopic Characterisation of Eu.2-CB[7] at Au** ..... **315**

## 1 – An Introduction to Supramolecular Chemistry

Supramolecular chemistry is defined as 'the chemistry of the intermolecular bond, covering the structures and functions of the entities formed by the association of two or more chemical species'.[1]

Cooperativity is central to understanding molecular recognition and supramolecular self-assembly, and arises from the combination of two or more non-covalent interactions (electrostatic, hydrogen bonding, halogen bonding, aromatic donor-acceptor, cation- and anion- π, and solvatophobic). Thus, the system behaves differently from expectations based on the properties of the individual interactions acting independently.[2]

Numerous molecular receptors capable of selectively binding specific substrates *via* non-covalent interactions have been developed. The level of control supplementary to the recognition processes facilitates the development of functional molecular and supramolecular devices, structurally organised and functional systems built from suitably designed molecular components performing a given action.[3]

The increase in understanding of intermolecular interactions and molecular recognition has culminated in increased control over molecular self-assembly and the synthesis of multimolecular architectures varying in shape, size, and composition, both in solution and the solid state.[4]

In vivo, the self-assembly of supramolecular systems (haemoglobin, myoglobin, microtubules) is common place, but replicating the precise positioning of many non-covalent interactions remains a serious challenge in the design of a new class of material and devices for future technologies.[5]

### 1.1 – The Development and Formation of Functional, Bistable [2]Rotaxanes

Inspired by the increasing complexity of studies centred on such systems, a huge variety of templated molecular architectures have been synthesised in recent years[6,7,8]. The binding of both sulphate and phosphate anions, in a strong and highly selective manner, is achieved in nature by virtue of a network of hydrogen bonds buried deep inside specific proteins[9-14,15-18]. In order to replicate this high degree of selectively in the encapsulation of anions, elaborate three-dimensional receptors must be constructed[6-8,12-15,19]. However, the fact that anions are less charge dense than comparable isoelectronic cations, display no exploitable ligand-field effects, are pH dependent, and exhibit high hydration energies, makes the design and synthesis of such receptors somewhat challenging[7,9,14,19].

An innovative approach to the design of such receptors rests on the threading of a one-dimensional, acyclic receptor through the annulus of a two-dimensional, macrocyclic receptor, thus generating a three-dimensional cavity in which anions can be encapsulated[6,12,13]. This approach is advantageous in the sense that it permits two binding motifs to be orthogonally dispositioned, something which is difficult to achieve by means of other methods, and the induced reduction in rigidity lowers the risk

of slow exchange[14]. Various molecular topologies, many of which cannot be generated *via* traditional synthetic methodologies, can also be acquired using ionic and molecular templates of varying shape, size and charge by virtue of manipulating the intermolecular forces holding the components of the interlocked structure together[6]. In addition, numerous methods of signal transduction exist that can be exploited in order to monitor guest-induced changes in co-conformation, and fluctuation in mutual interaction between the interlocked components upon sensing of the desired analyte; NMR spectroscopy and solution-phase voltammetry have been central[6-9,19].

The formation of rotaxanes, mechanically interlocked, kinetically trapped, assemblies of macrocycles and dumbbell-shaped axles, **Figure 1**, is driven by a combination of π-electron donor-acceptor interactions, hydrogen bonding interactions, and by either cation[13] or anion[6-8,13,14] templation. Pseudorotaxanes are afforded in the absence of sterically bulky end groups, or stoppers, at either end of the thread or axle component, and their formation is reversible due to the fact that the components are not mechanically interlocked[6].

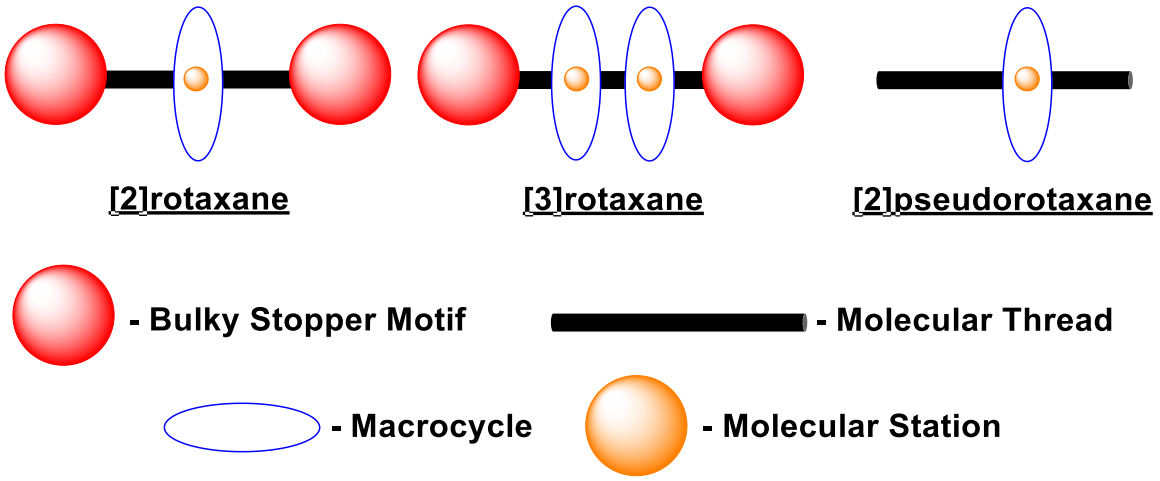


**Figure 1.** A schematic representation of a [2]rotaxane, a [3]rotaxane, and a [2]pseudorotaxane. Figure reproduced with permission from reference [6].

Rotaxanes can be formed in a variety of ways, and are most commonly generated upon the cyclisation of a macrocycle around an axle component possessing stopper groups, a method commonly referred to as '*clipping*'.[20-22] Another method of choice centres on the tethering of stopper motifs to the termini of a pseudorotaxane assembly ('*stoppering*')[23-25], thereby presenting a kinetic barrier to dissociation. A surface that is able to bind the molecular thread is also able to act as a stoppering unit. In addition, thermal excitation of the individual components can afford rotaxanes as the thermodynamic product ('*slippage*')[26-29], whilst an alternative '*snapping*' approach involves the covalent linkage of two half-stoppered axle fragments, at least one of which is anchored within the cavity of a macrocycle[30,31]. Finally, the '*swelling*' method of rotaxane formation involves the

terminal groups undergoing a dilating rearrangement through thermal or photochemical treatment[32,33].

In order to ensure that these interlocked architectures are suitable for the selective sensing of anions, and thus are able to act as sophisticated molecular switches, sensors and machines, their unique bistability, brought about by the incorporation of differing recognition sites or molecular stations, into their molecular architecture, must be exploited[7,34]. In order to do so, and thus observe translational motion upon the application of an external stimulus, such as heat[35], photoirradiation[19] or fluctuations in pH[36,37], brought about *via* the addition of an acid or a base, a large difference in the binding affinities for the ring by the two different recognition sites within the axle component is a prerequisite[34,38]. Functionalisation of either the periphery of the macrocyclic host, or the termini of the axle component, with suitable optical[39-42] or electrochemical reporter groups[43,44], such as a rhenium(I)-bipyridyl lumiphore, an osmium(II) bipyridyl motif[45], ferrocene[43], or a DO3A-lanthanide complex[46], allows such form of motion to be effectively transduced, **Figure 2**.[19]

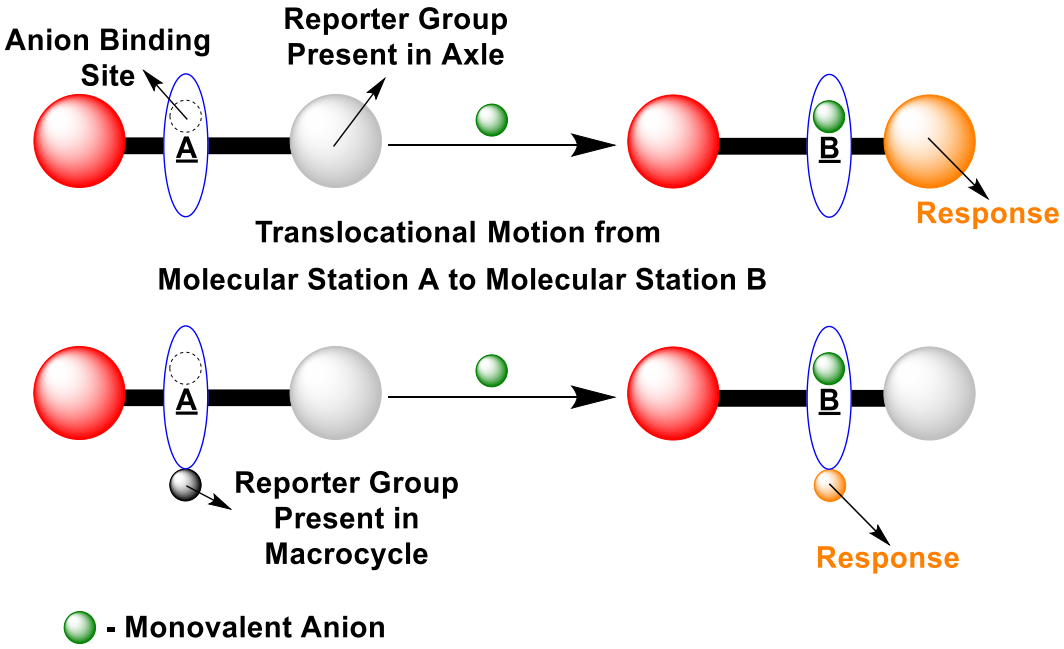


**Figure 2.** Mapping anion-induced molecular motion (translocation) *via* functionalisation of either the thread component (**Top**) or the macrocyclic motif (**Bottom**). Figure reproduced with permission from reference [38].

## 1.2 – The Templated Assembly of Molecular Architectures

### 1.2.1 – Anion-Templated Synthesis

Over the past few years, the research group of Professor Paul Beer have developed a general anion templation methodology for the synthesis of various interpenetrated molecular structures. Their approach hinges on the fact that the coordination sphere of the templating, chloride anion remains unsaturated, subsequent to it becoming strongly associated with a cationic, pyridinium station

integrated into a threading component. This permits anion binding by an isophthalamide-based macrocyclic ligand, which in turn results in the interpenetration of an ion-paired threading component through the annulus of the macrocycle. This process is enhanced by the presence of complementary, supramolecular interactions (π-π stacking, CH-O hydrogen bonds) between the macrocyclic and axle motifs, induced upon the formation of the interlocked architecture[14,6-9,14,38,43,47-52]

### 1.2.2 – Metal-Templated Synthesis

Mechanically interlocked molecular architectures can also be acquired *via* the use of a metal template, whereby the metal ion acts in either a 'passive' or 'active' manner. The 'passive' metal template approach, first reported by Sauvage *et al*. in 1983[53], centres on the coordination of ligands to a metal ion, and the subsequent formation of a covalent bond between the constituent components, brought into close proximity to one another[54]. The presence of the metal ion ensures that the ligands are orientated as to direct interlocking, and a stoichiometric amount of the template and permanent coordination sites on each component must be present in order to facilitate the assembly of the desired species[54].

This passive methodology is not designed to utilise the chemistry of the metal ion, unlike the analogous 'active' metal template approach introduced by Walker *et al*. in 2006[55], whereby the metal ion serves to both direct the assembly process, and mediate covalent bond formation between the two species[54]. This approach relies on the use of a macrocycle which is able to bind a metal ion endotopically within its cavity, and is advantageous in the sense that permanent recognition sites are not required on each component of the interlocked product, thus rendering its formation 'traceless'.[54] In addition, sub-stoichiometric quantities of the active template may only be required, the approach is applicable to many different types of well-known transition metal-catalysed reactions, and has been able to provide mechanistic insight into the reactions themselves[56-63].

## 1.3 – Stimuli-Responsive Molecular Architectures

Mechanically interlocked molecules are considered suitable candidates for the construction of molecular switches, data storage devices, and platforms for the sensing of anions of environmental importance[14,34,35,45,64-66]. This assumption is made based on the fact that they are known to possess the ability to undergo controllable and reversible motion (of one component relative to the other), without any damage being caused to the mechanically interlocked architecture itself. Such motion is triggered by three types of external stimuli, that is chemical[67,68], photochemical[67,68], and electrochemical[34,69], whilst several spectroscopic and electrochemical[70] techniques have been exploited in order to monitor this induced process in solution, **Figure 2**, and distinguish it from the perpetual Brownian motion of the consistent moieties at ambient temperature[34].

A free energy difference of 1.2 kcal $mol^{-1}$ between the two translational isomers ensures that at room temperature, 90 % of the macrocyclic component resides at one of the two recognition sites, or molecular stations, incorporated within the axle component[34]. This state, where the macrocycle is positioned at one recognition site in preference to the other, is known as the highly preferred, ground state co-conformation (GSCC)[34]. Upon the application of an external stimulus, such as an applied potential, an anion, or thermal energy, the interactions stabilising the GSCC begin to weaken, triggering translation of the macrocyclic moiety towards the alternative recognition site, thus generating the metastable state co-conformation (MSCC)[34], **Figure 3**. Relaxation of this state, to the GSCC, is most commonly induced by the addition of a competitive anion into solution, or upon the application of a reductive potential[34]. This completes the translational cycle, and highlights the potential of bistable [2]rotaxanes to function as efficient molecular machines[34].

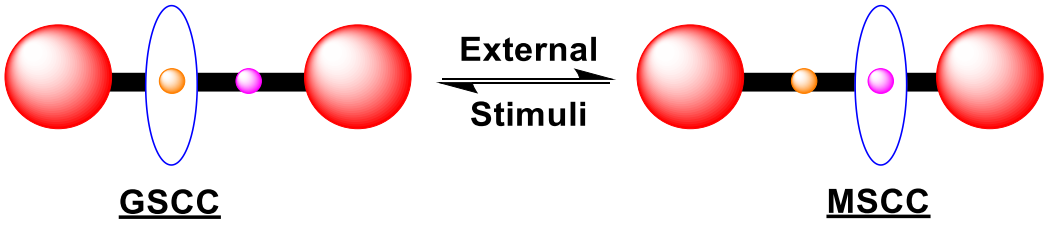


**Figure 3.** A schematic representation highlighting translocation of the ring component, from molecular station A (**Orange**) to molecular station B (**Pink**), in order to bring about the formation of the metastable state co-conformation (MSCC) from the ground state co-conformation (GSCC).

This potential was primarily highlighted by Sauvage and co-workers who were able to modulate the position of a 2,9-diphenyl-1,10-phenanthroline-containing 30-membered ring within an axle component incorporating two different coordination sites, 2,9-disubstituted-1,10-phenanthroline and a 5,5″-disubstituted-2,2′:6′,2″-terpyridine unit[71]. Large, reversible molecular motion was induced upon altering the oxidation state of the templating cation[71], **Figure 4**.

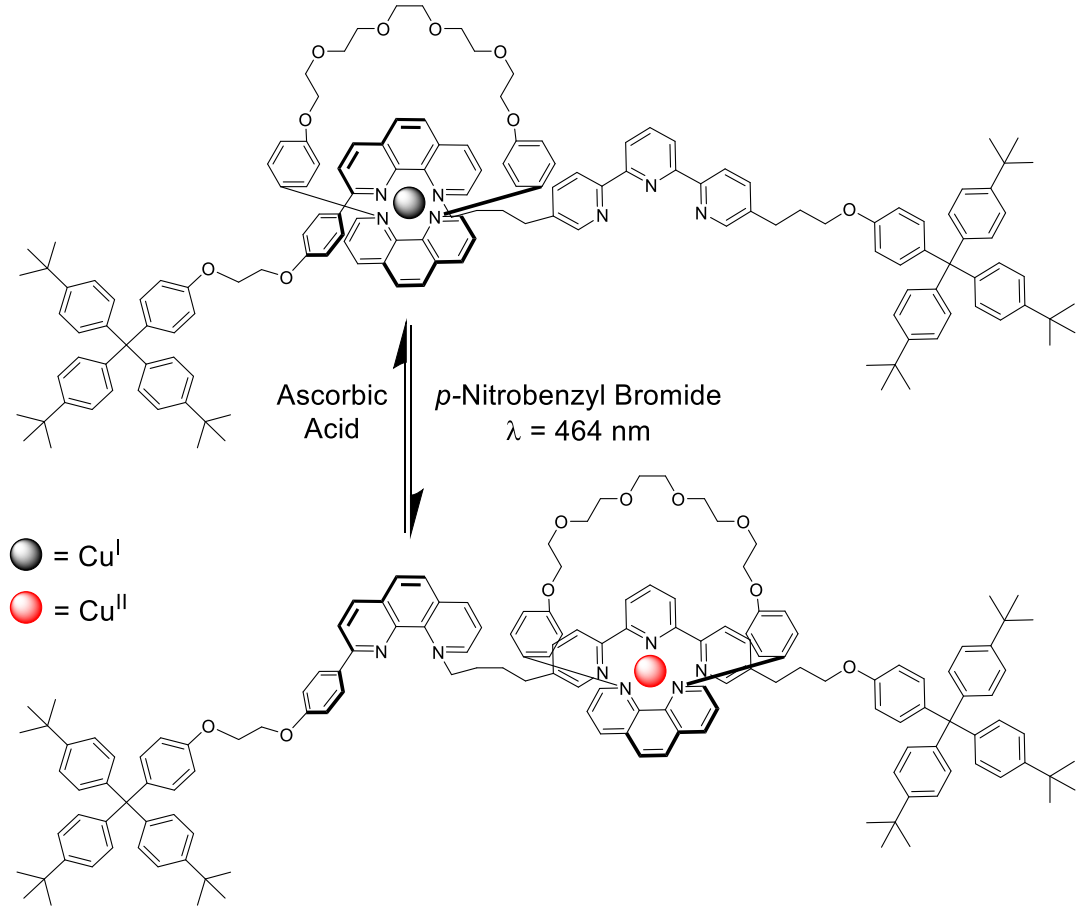


**Figure 4.** Photochemically induced switching within a bistable, [2]rotaxane. Photo-induced oxidation of the Cu(I) centre, to Cu(II), brings about translocation of the macrocyclic motif from the bidentate phen binding unit (GSCC), to the terdentate terpy binding unit (MSCC). This process is reversed upon chemical reduction of the Cu(II) centre. Figure reproduced with permission from reference [71].

In contrast, Nakashima *et al.* have been able to demonstrate that it is possible to photochemically induce the molecular motion of alpha-cyclodextrin (α-CD) within a rotaxanated system incorporating the photoisomerisable azobenzene unit[72], **Figure 5**. Anion-induced molecular shuttling on the other hand has been exploited by the groups of Smith[73,74], **Figure 6**, and Beer[75-77], **Figure 7**, respectively.

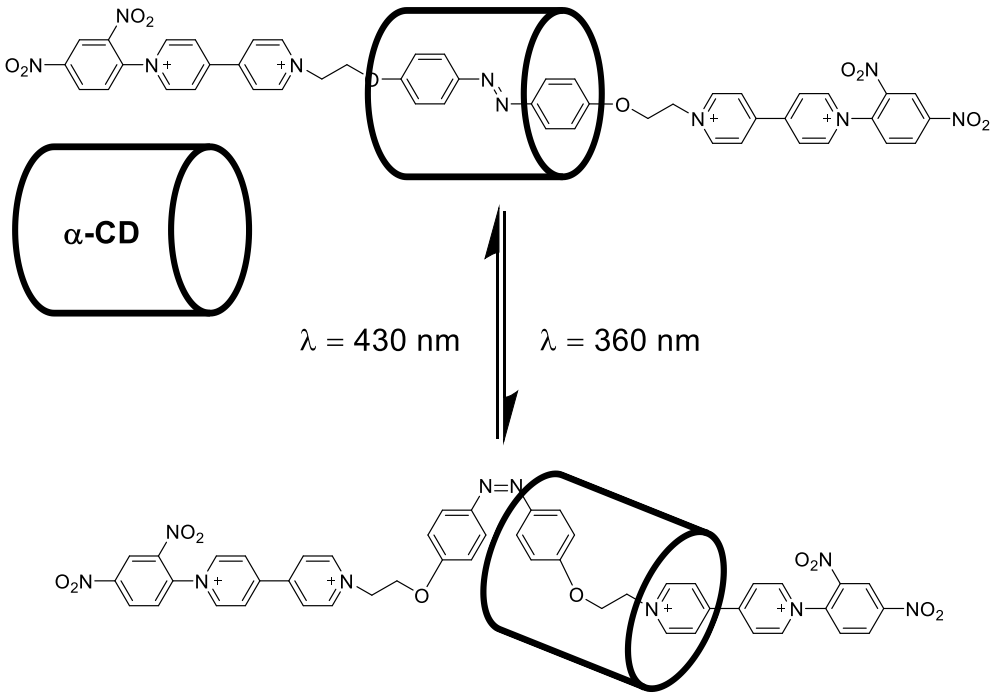


**Figure 5.** Photochemically inducing the translocation of α-CD within an azobenzene-containing rotaxane. λ denotes wavelength of irradiation. Figure reproduced with permission from reference [72].

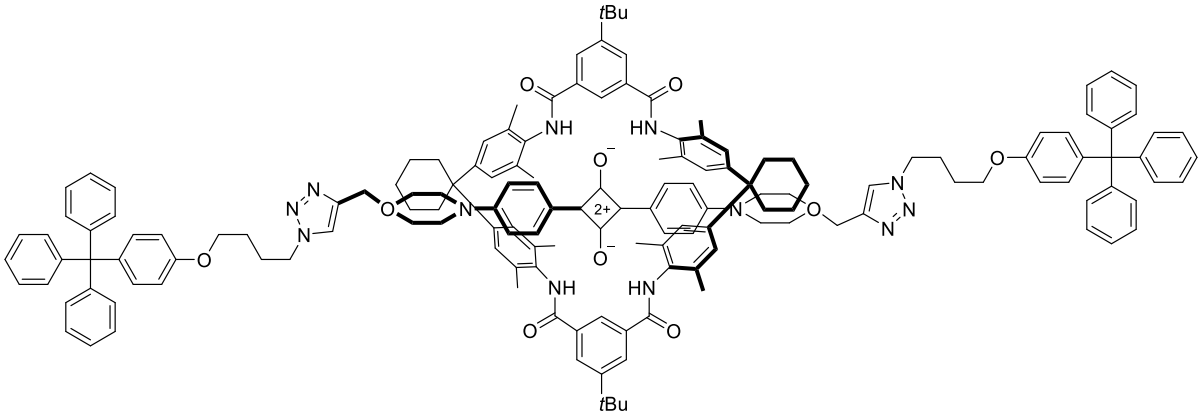

**Figure 6.** Smith's reversible optical chloride sensor. Upon the addition of chloride, the squaraine dye is displaced and / or the tetralactam macrocycle translocates to either of the triazole units present within the axle component. As a result, the fluorescence intensity of the dye recovers; the non-covalent encapsulation of squaraine dyes, within the cavity of tetralactam macrocycles, has been shown to bring about a three-fold decrease in quantum yield. Figure reproduced with permission from references [73] and [74].

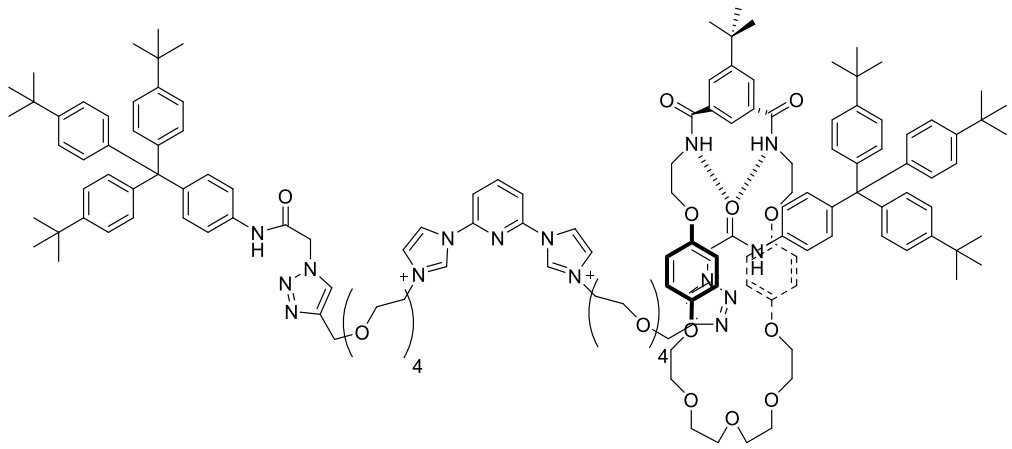

**Figure 7.** Anion-induced molecular shuttling within a [2]rotaxane synthesised by the group of Professor Paul Beer. Upon the addition of chloride, the macrocycle was observed to migrate to the axle's bis-imidazolium molecular station. Figure reproduced with permission from reference [75].

Molecular motion can also be driven electrochemically; Stoddart *et al*. have been able to control the position of a cyclobis(paraquat-*p*-phenylene) macrocycle within an acyclic polyether incorporating the tetrathiafulvalene electron donor unit[78-80]. Molecular motion is controlled by way of modulating the redox state of either the tetrathiafulvalene or bipyridinium units, or by adding a secondary guest species into solution[78,79].

In order to integrate these forms of switchable, molecular assembly into sensory, electronic, data storage, and macroscopic platforms, their deposition at electroactive or optically transparent, solid surfaces must be well understood, and the chemistry used to tether them to the interface robust. To date, only a handful of examples exist[45,66], which is in part down to the fact that the dynamics of such molecular motions are difficult to resolve at the interface, by means of the aforementioned methods of signal transduction. Furthermore, the deposition of such systems often leads to the generation of monolayers that are either not crystalline, are disordered, or in which the required system has been deposited at the interface at too low a concentration, as to permit the detection of a quantifiable output[14,64,66].

## 1.4 – The Surface-Assembly of Stimuli-Responsive Molecular Architectures

Surface-confined, interlocked molecular architectures are most effectively characterised by voltammetry, Fourier transform infrared (FTIR) spectroscopy, atomic-force microscopy (AFM), and x-ray photoelectron spectroscopy (XPS),[66] whilst the molecular system is ordinarily preassembled in solution before being subsequently chemisorbed at the interface through standard silane or thiolate chemistry.[81-87,] Additionally, examples do exist whereby the molecular system has been systematically assembled at modified gold or oxide surfaces by way of a self-assembly approach[88].

Developing and employing methods to 'map' macrocyclic motion, within surface-confined, bistable [2]rotaxanes, is demanding in itself. Currently, such motion is typically resolved by means of electrochemistry, as pioneered by the group of Willner in 2004[87], who investigated the effect of electrochemically driven, mechanical cyclophane translation on the rate of electron transfer within a bistable, [2]rotaxane, **Figure 8**. Upon reduction of the macrocyclic motif, and generation of the biradical-cation, electrostatically driven, translocation of the cyclophane unit, away from the π-donor diiminobenzene unit, and towards the electrode surface, was induced, bringing about an increase in both the rate of electron transfer ($K_{et}$) and surface capacitance[87].

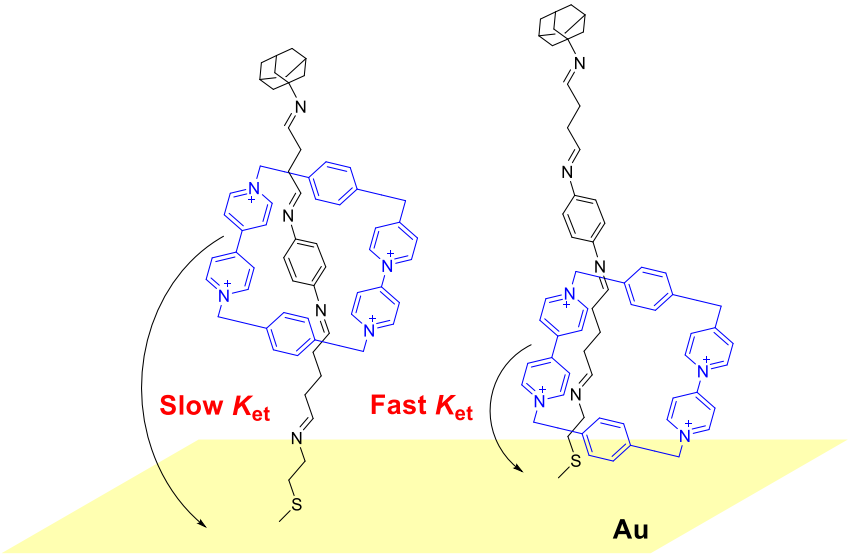


**Figure 8.** Electrochemically-induced translocation of a redox-active, cyclophane motif within a surface-tethered molecular architecture. The rate of interfacial electron transfer ($K_{et}$) could be used to gauge in which state (GSCC or MSCC) the system was residing. Figure reproduced with permission from reference [87].

Upon substitution of the adamantane stopper, with a bulky flavin adenine dinucleotide (FAD) unit, Willner and co-workers were able to utilise this concept in the fabrication of a new supramolecular configuration for the bioelectrocatalysed activation of enzymes[89], **Figure 9**.

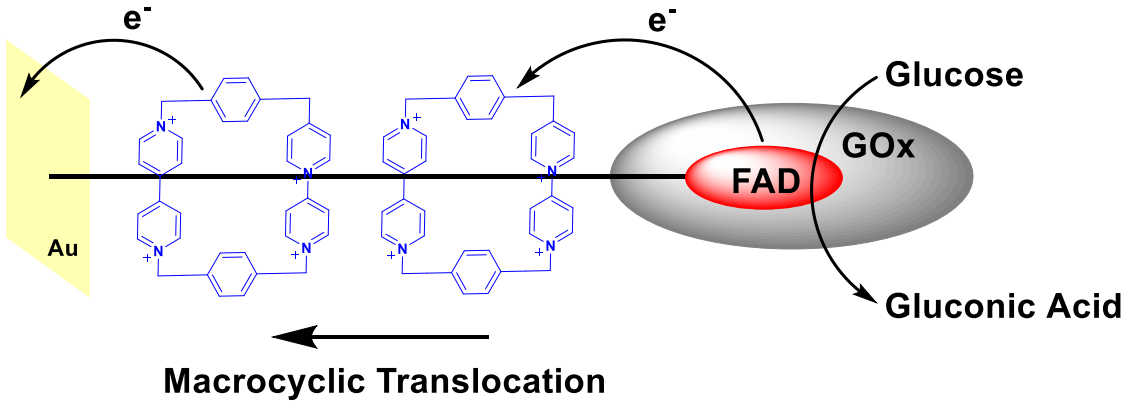


**Figure 9.** Utilising the translocation of a $CBPQT^{4+}$ ring to mediate the electron transfer process within a novel supramolecular configuration for the bioelectrocatalysed activation of enzymes, thereby reducing the overpotential required for the electrocatalytic oxidation of glucose. **e**$^-$ denotes the movement of an electron. Figure reproduced with permission from reference [89].

Reconstituted glucose oxidase (apo-GOx) was brought into electrical contact with the electrode *via* its association with the redox-active, FAD-'capped' rotaxane, which served as an electron-transfer mediator in the effective bioelectrocatalytic oxidation of glucose, at – 400 mV *vs.* SCE. Vectorial electron transfer is mediated by the rotaxane, provided the FAD unit remains in its biocatalytically reduced state. Electrocatalytic anodic currents, corresponding to the oxidation of glucose, are acquired at open circuit potential (OCP). The oxidation of glucose leads to the reduction of the rotaxane, in which the cyclophane unit is shown to primarily reside at the π-donor site. As a result of intramolecular reduction, displacement of the biradical cation occurs, as it did in the adamantane-stoppered analogue, and an electrocatalytic anodic current is generated, the cycle of which is completed upon oxidative recycling of the electrocatalytic system.[89]

In a further example, Stoddart and co-workers have been able to validate the viability of utilising plasmonic properties in reversibly mapping the position of a macrocycle within a bistable, redox-controllable [2]rotaxane[90] Upon deposition of the 'Stoddart' rotaxane, at a gold nanodisk array, the group were able to demonstrate that the extinction properties of the interlocked, molecular architecture could be chemically modulated by virtue of adding either a chemical reductant or a chemical oxidant into the electrochemical cell. Upon oxidation of the integrated tetrathiafulvalene (TTF) unit, and the subsequent change in refractive index, a red shift of the localized surface plasmon resonance arose, 690.4 ± 0.2 to 699.9 ± 0.2 nm. This was reversed (blue shift) upon reduction of the aforementioned redox-addressable motif.[90]

From a chemical assembly point of view, the deposition of such systems should also be possible on the highly curved surface of a nanoparticle; in 2003, Fitzmaurice *et al.* successfully assembled an electronically switchable, tripodal rotaxane on the surface of a titanium dioxide ($TiO_2$) nanoparticle[91], **Figure 10**.

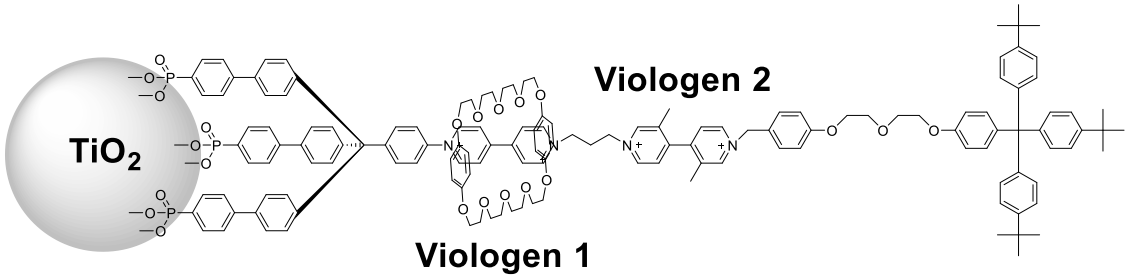


**Figure 10.** The immobilisation of a tripodal [2]rotaxane on the surface of a titanium dioxide nanoparticle. Figure reproduced with permission from reference [91].

In its GSCC, the crown ether motif was seen to encapsulate viologen 1, and continued to do so, even upon one-electron reduction of the aforementioned molecular station. However, macrocyclic translocation, to viologen 2, was brought about upon further reduction of the radical cation. Yet, upon either one-electron or two-electron reduction of viologen 2, the macrocycle was no longer positionally localised at this station; it was assumed that the macrocycle was in motion along the entire length of the molecular thread, and in fact a conformational change was observed in which it was thought that the fully reduced [2]rotaxane had folded in on itself, thereby initiating stacking of the diradical cations. Subsequent transformation back to the GSCC, was instigated upon the removal of electrons from the molecular system.[91]

## 1.5 – Summary

The assembly of mechanically interlocked, molecular architectures, at electrochemically and optically addressable substrates, is of importance and interest to those working within a variety of fields. Their potential application in the fabrication of nanoscale motors, energy/data storage devices and sensory platforms, outweighs the issues associated with trying to control, and subsequently follow, their stimuli-responsive, interfacial molecular motion. To date, such reversible motion is most effectively resolved by means of cyclic voltammetry[44,66,69,87,89,91]. Currently, to the best of our knowledge, macrocyclic motion is yet to be photoelectrochemically 'mapped' within a dynamic system, such as a bistable [2]rotaxane, by virtue of comparing the magnitude of cathodic photocurrent density acquired at each molecular station. The closest example of such a system reported to date is the molecular triad assembled by Stoddart *et al.* in 2005[78,79], **Figure 11**, which was shown to perform efficient photo-to-electrical energy conversion upon excitation of its porphyrin stopper.

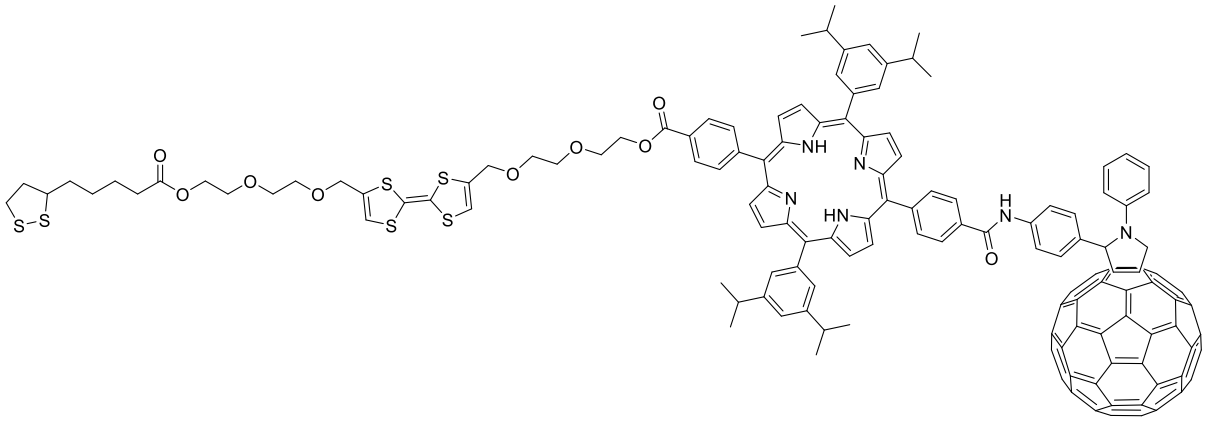

**Figure 11.** Stoddart's photoactive, molecular triad, consisting of a disulphide tether, an electron-accepting buckminsterfullerene ($C_{60}$) unit, a chromophoric porphyrin unit, and an electron-donating TTF unit. Figure reproduced with permission from reference [78].

The incorporation of a relay moiety, in the form of TTF, enabled the formation of a relatively stable, charge-separated intermediate ($TTF^{+\cdot}$-P-$C_{60}^{-\cdot}$), permitting efficient vectorial electron transfer and the generation of electrical energy which could be used to drive the solution-phase dethreading of a pseudorotaxane, formed between the $CBPQT^{4+}$ cyclophane and 1,5-bis[(2-hydroxyethoxy) ethoxy]naphthalene (BHEEN), an electron-rich, highly fluorescent thread component, **Figure 12**.[74] That is, unlike in the work reported by the groups of Uosaki[92-101] and Imahori[102-104], respectively, Stoddart *et al*. utilised the electrical energy generated, upon the irradiation of a porphyrin-terminated molecular assembly, of which had been deposited at gold (Au), to drive supramolecular motion[79].

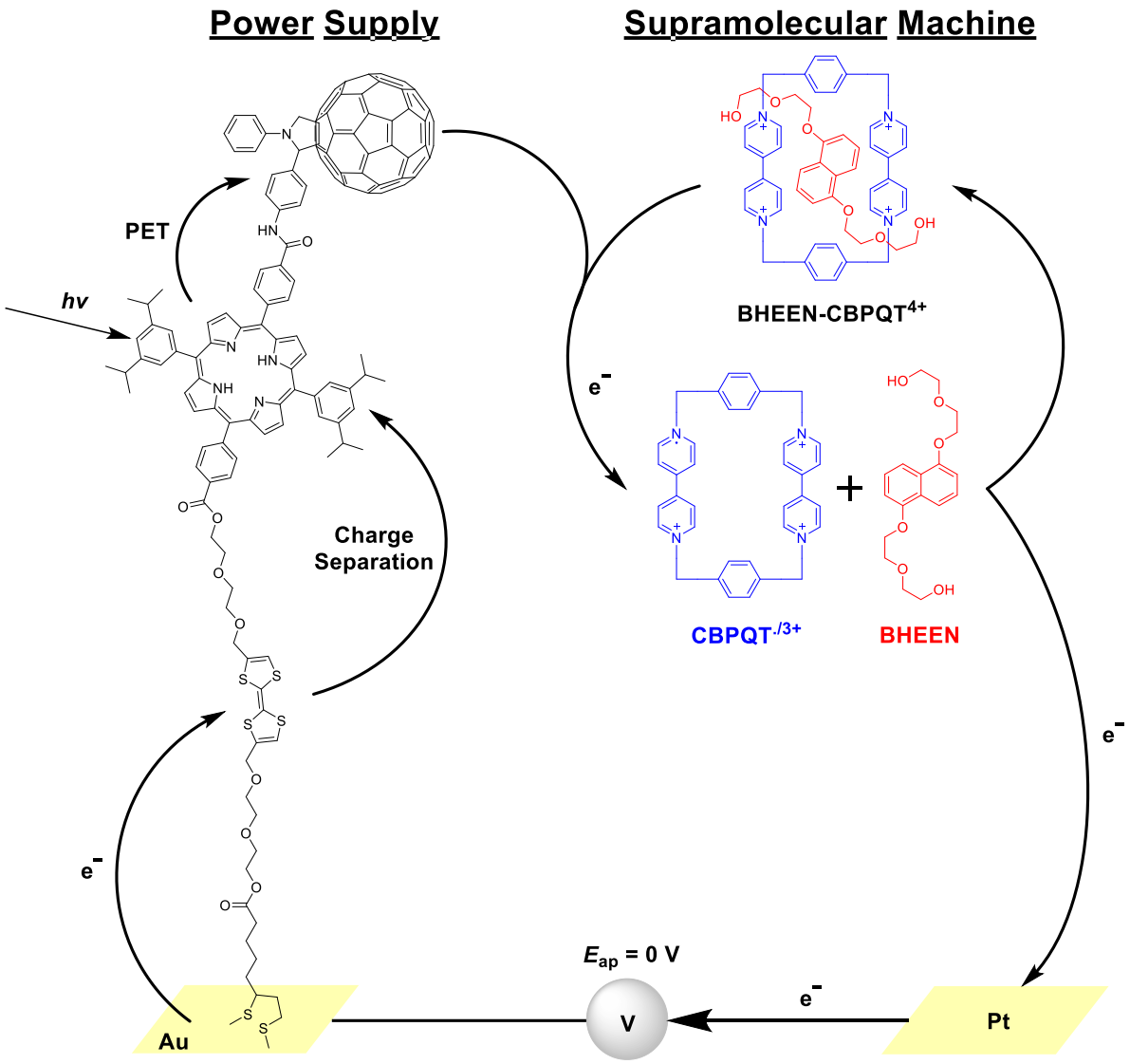


**Figure 12.** A schematic representation highlighting how the group of Stoddart utilised the electrical energy generated, from a molecular triad, to drive the dethreading of [2]pseudorotaxane present in solution. The [2]pseudorotaxane was formed upon the encapsulation of BHEEN within the cavity of a $CBPQT^{4+}$ cyclophane. Upon photo-excitation of the porphyrin unit (413 nm), photoinduced, vectorial electron transfer (PET) to the $C_{60}$ stopper was induced, resulting in a charge shift to the TTF component. Charge neutralisation then followed, prior to the electron being transferred to the [2]pseudorotaxane, which in turn led to the dethreading of the reduced $CBPQT^{3.+}$ cyclophane. The electron was then transferred to the Pt counter electrode. $\mathbf{E_{ap}}$ denotes applied potential (V), $\mathbf{e^-}$ the movement of an electron, and ***hv*** photoirradiation of the system. Figure reproduced with permission from reference [79].

The degree of dethreading was gauged by monitoring the total change in the fluorescence intensity of the electrolytic solution. Following dethreading, or photoinduced reduction of the cyclophane ($CBPQT^{4+} \rightarrow CBPQT^{3+}$), an increase (3.36 %) in solution-phase fluorescence (BHEEN ($\lambda_{irr}$ 257 nm)) was observed, consistent with the release of the threading component from within the quenching, macrocyclic cavity.[79]

## 1.6 – Research Aim(s)

The aim of this project is to assemble a novel, bistable [2]rotaxane, where the magnitude of cathodic photocurrent density generated can be used to verify the position of an interlocked ferrocene-appended, bis-isophthalamide macrocycle, **Figure 13**. As within the systems reported by the groups of Uosaki[92-101] and Stoddart[78,79], respectively, vectorial electron transfer was expected to proceed *via* the integrated, macrocyclic relay component upon photoexcitation of the porphyrin stopper.

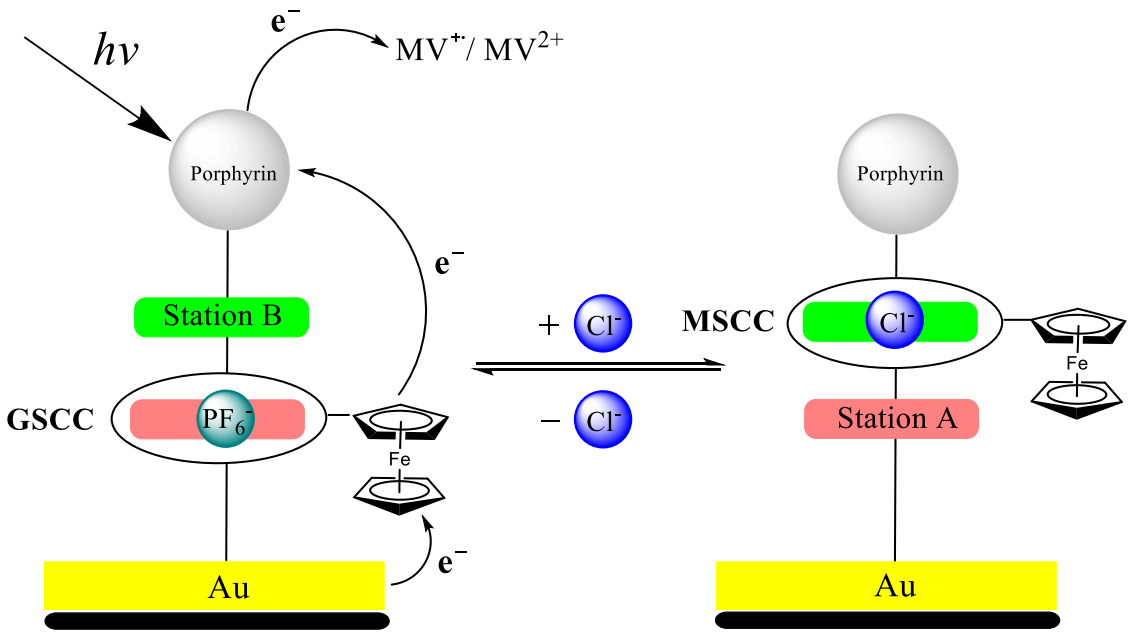


**Figure 13.** A schematic representation of the envisaged artificial, photosynthetic molecular machine, constructed on Au. The magnitude of the cathodic photocurrent density generated at each molecular station, upon photoexcitation of the porphyrin stopper, should vary (Section 1.9). The generation of cathodic photocurrent density is likely to be most efficient at molecular station A, due to the fact that the rate of back electron transfer, from the excited state of the porphyrinic macrocycle (P*) to ferrocenium ($Fc^+$) and Au, will be reduced to a greater extent than the forward rate of electron transfer, from ferrocene (Fc) to P*.[92-101] **$MV^{2+}$**: Methyl Viologen. ***hv:*** Photoirradiation. **$e^-$**: Electron.

It was envisaged, that in its GSCC, the macrocycle would primarily encircle an amide functionality integrated into the molecular thread, whilst upon anion exchange, for the chloride anion, the macrocyclic relay motif would translocate in order to encapsulate a triazolium motif, generating the MSCC and gating the magnitude of the photoelectrochemical response in the process. The induced interaction between the chloride anion and the neutral amide cleft of the macrocycle was expected to drive molecular motion, a process that could be reversed upon precipitation of the chloride anion out of solution with silver hexafluorophosphate.

Fundamental research was to be undertaken, building on the work reported by the groups of Uosaki[92-101] and Imahori[102-104], respectively, within both porphyrin-appended, biphasic self-assembled monolayers, and static, interlocked molecular architectures. It was anticipated that a conformational ruler would be devised, and subsequently applied in the design of a novel, bistable [2]rotaxane, thus

ensuring that the magnitude of the cathodic photocurrent density generated at each molecular station, upon the threading of a redox-active macrocycle, could be differentiated, which in turn would allow the two states, GSCC and MSCC, to be photoelectrochemically resolved; variation in the forward and backwards rates of both electron and energy transfer within the two isomers, **Section 1.9**, was expected to facilitate the application of this novel method of signal transduction within dynamic, supramolecular architectures, in a bid to resolve molecular motion.

Porphyrins, a large class of deeply coloured pigments found in various biological compounds of interest, such as haemoglobin and chlorophyll, are an important type of macrocyclic compound[106,107,108], and metalloporphyrins are fundamental to the existence of life, and major biochemical, enzymatic, and photochemical functions depend on the spectral properties of the tetrapyrollic macrocycle[105]. Thus, acquiring a thorough understanding of the porphyrinic macrocycle and its excited states is essential in enhancing our understanding of oxygen binding, electron transfer, catalysis, and the initial photochemical step of photosynthesis (PSYN).[106,107,108] Such research has also led to the discovery of new applications of these systems in photodynamic therapy, information storage devices or photoelectrical devices that transform energy in both directions (photocells and light-emitting diodes)[105].

## 1.7 – An Introduction to the Porphyrinic Macrocyclic Arrangement

The porphyrinic macrocycle, **Figure 14**, contains 18 delocalised π-electrons, and its structure, of which consists of four pyrrole rings, linked by four methine bridges, supports a highly stable configuration of both single and double bonds.[106,107,108,109] Many reports exist documenting the synthesis of porphyrins, with the most renowned being the one developed in 1935 by Rothemund[110]; tetraphenyl porphyrins were synthesised by virtue of a one-step, monopyrrole polymerisation route[110-115], **Figure 14**.

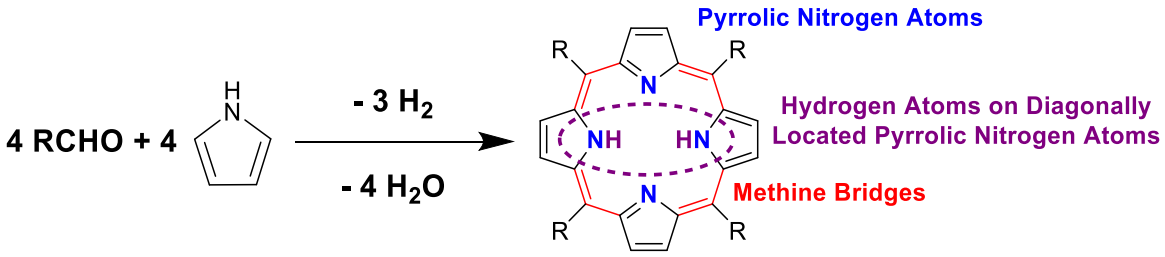


**Figure 14.** The Rothemund Condensation; the thermal condensation of aldehydes with pyrroles. Porphine (**Right**), the fundamental ring structure of four covalently-linked pyrrole nuclei around which porphyrins are built.

The reaction, between pyrrole and benzaldehyde, was performed in pyridine, at 150 °C, for 24 h, but the substituted porphyrin was acquired in low yield[110]. A low yield was obtained due to the fact that the experimental conditions favoured the formation of the *meso*substituted chlorin[110,116]. Following modification of the procedure by Adler *et al*. in 1967[117,118], who developed an alternative approach based on an acid catalysed, pyrrole aldehyde condensation reaction, the method of porphyrin synthesis was optimised by Lindsey's group in 1987[116]; their two-step, room temperature method of synthesis involves sequential condensation and oxidative reaction steps, **Figure 15**. The fact that the reaction is performed at room temperature ensures that equilibrium is reached during the condensation phase, thus preventing the occurrence of side reactions at any stage of the process.[119-124]

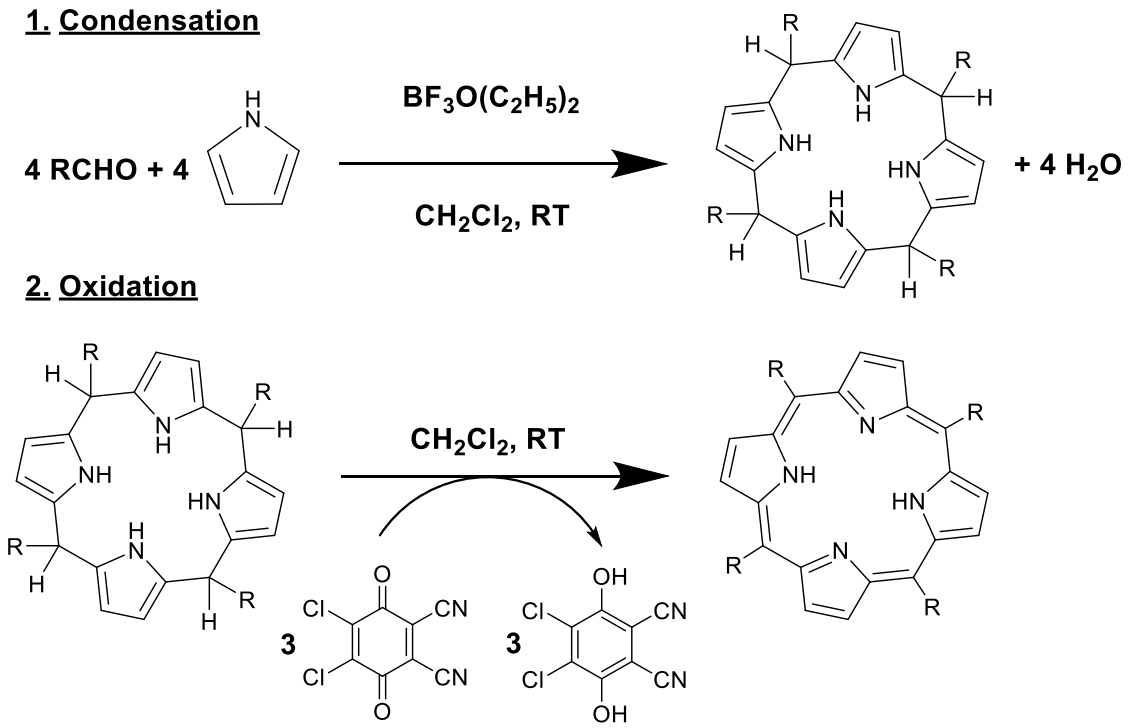


**Figure 15.** Lindsey's method of porphyrin synthesis whereby the condensation and oxidation processes are carried out sequentially at room temperature. The reaction(s) is very sensitive to changes in the concentration of both the reactants and the catalyst ($BF_3O(C_2H_5)_2$, boron trifluoride ethyl etherate), and yields of up to 50 % have been reported.[116]

Both free base porphyrins and metalloporphyrins, porphyrins in which a metal ion occupies the centre of the macrocyclic cavity, at the expense of the two hydrogen atoms located on the diagonally positioned pyrrolic nitrogen atoms, **Figure 14**, absorb visible light, in the range 350 – 700 nm, in the singlet manifold and transform it into the triplet state.[106,107,125-129] Their electron-rich, molecular conformation, **Figure 14**, gives rise to their unique optical properties, and the absorption spectrum of porphyrins is best understood by considering the models devised, by Martin Gouterman in 1959[130] and 1961[131], which are built on the importance of charge localisation in the prediction of electronic spectroscopic properties. The four-orbital model considers the two highest occupied molecular orbitals (HOMO) and the lowest unoccupied molecular orbitals (LUMO) of the porphyrin moiety, and accounts for all possible electronic interactions between them[132]. Configuration interaction theory has been used to do so, and the identity of the metal centre[133,134] and the substituents[130] on the porphyrinic macrocycle affect the relevant energies of all the possible transitions. The associated absorption bands in their UV-Vis spectra are ascribed to $\pi - \pi^*$ transitions, and the degenerate pair of $e_g$ orbitals assigned to the LUMO, whilst the $a_{1u}$ and $a_{2u}$ orbitals are assigned to the HOMOs, respectively, **Figure 16**.[135-140]

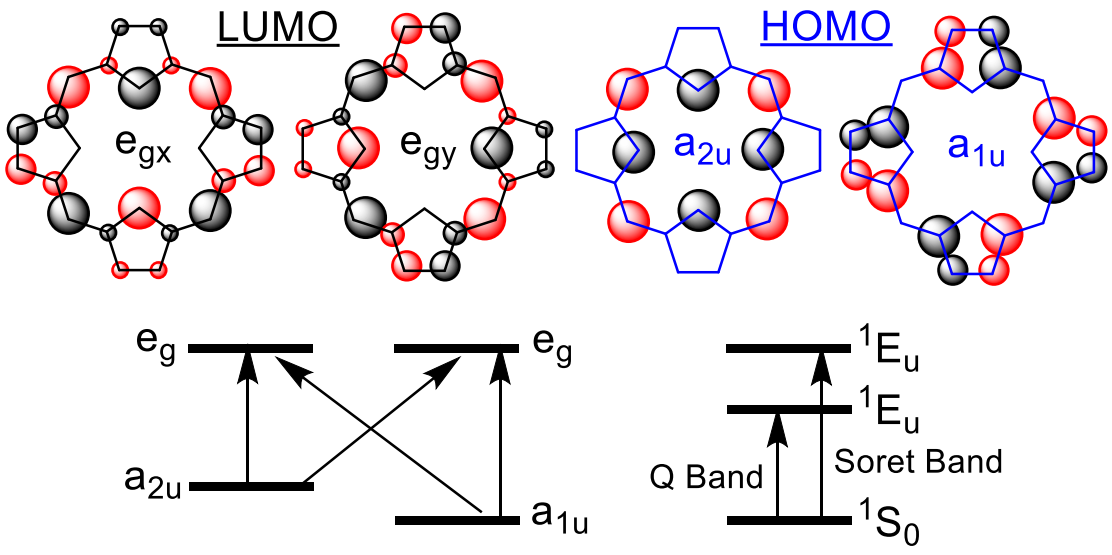


**Figure 16.** Gouterman's four-orbital model (**Top**) and a simplified representation of the one electron transitions from the HOMO to the LUMO of the porphyrinic macrocycle (**Bottom**).[140]

One electron transitions between these molecular orbitals (MOs), $e_g$, $a_{1u}$ and $a_{2u}$, gives rise to two excited singlet states of $^1E_u$ character, **Figure 16** (**Bottom**). Orbital mixing of these two singlet $^1E_u$ states creates a state of higher energy with greater oscillator strength, and a state of lower energy and less oscillator strength. An electronic transition, of the type $a_{1u} \rightarrow e_g$, from the ground state to the higher energy $^1E_u$ state gives rise to the Soret band, whilst an electronic transition, of the type $a_{2u} \rightarrow e_g$, from the ground state to the lower energy $^1E_u$ state is conveyed by the appearance of the *Q* band, **Figure 18**.[106,107,130-133]

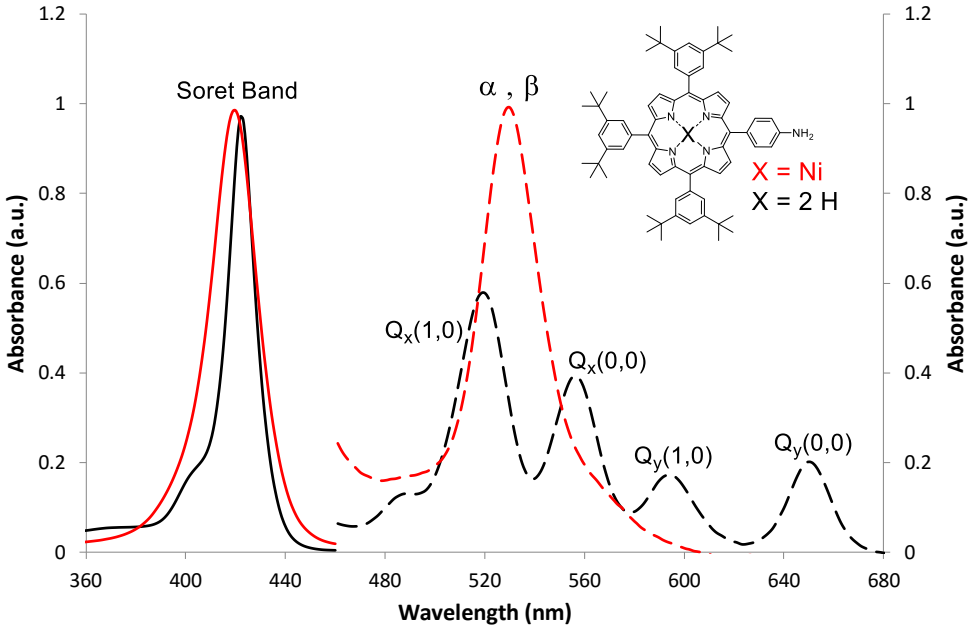


**Figure 17.** A UV-Vis spectrum highlighting the difference in electronic structure between a free base porphyrin (**Black Trace**), and a metalloporphyrin (**Red Trace**). Both UV-Vis spectra were recorded in anhydrous $CH_2Cl_2$, at room temperature, and the porphyrin moiety was present at a concentration of 20 μM in each case. The Q band (490 – 680 nm) region has been enlarged and plotted on a secondary *y*-axis in order to aid clarification.

Four *Q* bands appear in the spectra of free base porphyrins, **Figure 17**, **Black Trace**, due to the fact that the *Q* band is split as the result of vibrational excitation and a break in symmetry[130,139]. The break in symmetry is brought about by the presence of the pyrrolic nitrogen protons in the centre of the macrocyclic moiety, **Figure 14**. Hence, the *x* and *y* components are no longer degenerate, and the *Q* band, *Q* (0,0), is split into $Q_x$ (0,0) and $Q_y$ (0,0), with each band having a vibronic overtone, $Q_x$ (1,0) and $Q_y$ (1,0), respectively[106,107,140]. The intensity of the Soret band is greater than that of the Q bands due to the fact that the former transition (Soret, $S_0 \rightarrow S_2$) is allowed ($\Delta m_l = \pm 1$), while the latter, lower energy transitions ($S_0 \rightarrow S_1$) are not[132]. The weakness of the Q band is not due to the degeneracy of orbitals but is due to the alternancy symmetry. The transitions which give rise to the lower component of the Q band mix with a different sign. These transition dipole moment vectors are almost the same in magnitude and parallel in their orientation, leading to the cancelation of their intensities. A similar cancelation also occurs in the upper component. The Q band is weak because the transitions are psuedoparity-forbidden as a result of the alternancy symmetry.[132]

However, upon metalation of the porphyrinic core, an increase in symmetry is observed ($D_{2h} \rightarrow D_{4h}$), meaning the axes defined by the pyrrolic nitrogen atoms are no longer equivalent[127,128]. As a result, the $Q_x$ and $Q_y$ excitation pair is degenerate, and additional splitting of the transitions is not witnessed, like it is in the case of their free-base analogues[106,107,130,131,132]. The *Q* bands which remain are commonly labelled α and β, **Figure 17**, **Red Trace**, and the stability of the resultant complex correlates with the relative intensity of both. When α is more intense than β, a stable, square-planar complex arises, whereas when β is more intense, it is likely that the metal ion will be displaced upon protonation of the core. The latter is commonly observed for complexes of $Ni^{II}$, $Pd^{II}$ and $Cd^{II}$.[131,132,133] In addition to this change, the Soret band is also liable to shift, depending on the $d^n$ configuration of the metal ion inserted. *Regular* metalloporphyrins are acquired upon the insertion of a closed-shell metal ion ($d^0$ or $d^{10}$), in which the $d\pi$ ($d_{xz}$, $d_{yz}$) metal-based orbitals are relatively low in energy[132,134]. These metal ions, such as $Zn^{II}$, have very little effect on the porphyrin energy gap (π to π*), unlike $Fe^{II}$ ($d^6$) and $Ni^{II}$ ($d^8$) which bring about hypsochromic (blue) shifts of the Soret band[106,107,132]. The shift of the Soret transition to lower wavelength is the result of an increased porphyrin energy gap, brought about by the fact that there is now considerable interaction between the metal-centred $d\pi$ and porphyrin π* orbitals[140]. This becomes important when trying to induce and optimise the flow of anodic or cathodic current within artificial photosynthetic devices, assembled on electronically-addressable interfaces.

## 1.8 – An Introduction to Artificial Photosynthesis and the Self-Assembly of Efficient Photoconversion Devices

Photosynthesis, the fundamental basis for the life of all organisms present on earth, is centred on the conversion of solar energy into useful forms of chemical energy[141,142,143]. This process is driven by

both photoinduced energy and electron-transfer reactions, and occurs within a highly complex, photosynthetic membrane system. The membrane itself contains various pigments, with chlorophyll being one. These organic pigments capture incident light, before the resulting excitation energy is transduced to the reaction centre. This centre contains a series of preorganised electron donor and electron acceptor moieties, where a charge-separation process occurs, which in turn generates a redox potential energy that is used to drive the chemical reactions needed to keep organisms alive. This multistep, electron transfer process proceeds extremely quickly in a unidirectional fashion, and the charge separated state is generated across the membrane with a quantum efficiency of nearly 100 %.[144-151]

Numerous reports exist in which chemists have attempted to mimic this level of efficiency within carefully constructed molecular assemblies, by virtue of uniformly incorporating donor and acceptor moieties into well-ordered arrays, both in solution and at a variety of interfaces[144]. Porphyrinic pigments are often used as the electron donors within these types of artificial photosynthetic model systems due to the fact that they are structurally similar to chlorophyll, and possess attractive photophysical properties, as was highlighted previously (**Section 1.7**).

Not only does this approach offer a way of trying to acquire a deeper understanding of the natural process of converting light into chemical energy, by permitting systematic investigations into the effects of molecular topology on the thermodynamic and kinetic parameters of the electron and energy transfer processes involved, it also provides chemists with the opportunity to utilise the concept of PET within mechanically interlocked architectures and / or sensory platforms. Thus, the possibility of developing more efficient and inexpensive photovoltaic cells that convert light into electricity is opened up.

In order to ensure that the electron donor and electron acceptor moieties are uniformly incorporated into molecular arrays, in a bid to prolong the lifetime of the photoinduced, charge separated state, and thus attempt to replicate the level of efficiency portrayed by nature in converting light into electrical current, a self-assembly technique is often adopted; ordered monolayers are formed at the interface upon spontaneous adsorption of the molecular entities at the surface, **Figure 18**. The resultant films are often robust and highly ordered, making them ideal candidates at which to investigate and / or utilise unidirectional, photoinduced, vectorial electron transfer.[144,152]

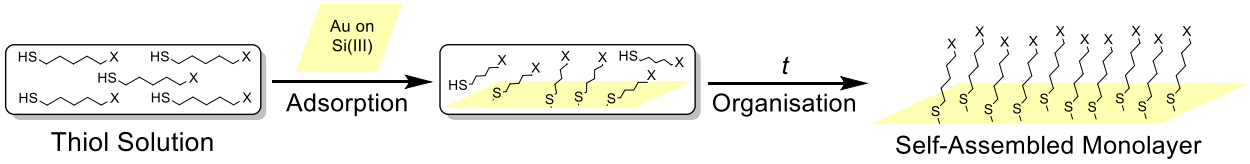


**Figure 18.** The formation of self-assembled monolayers (SAMs). SAMs form spontaneously upon the exposure of a substrate to a solution of the surface-active material. The spontaneous deposition and ordering of the monolayer is driven by both chemical bond formation and intermolecular interaction(s). *t* denotes time, whilst *x* signifies the presence of the porphyrinic macrocycle.

As this approach permits control over the orientation of the chromophores within the system, by taking advantage of H-bonding, metal coordination and π-π interactions, photoinduced, intramolecular electron transfer can be modulated with much more control[142,144]. Thus, photoinduced charge separation is accelerated, and charge recombination decelerated, to a greater extent than it is within systems where efficient light energy conversion is impeded by the poor control and ordering of covalently linked donor-acceptor dyads.[152] A well-defined energy gradient is also more likely to be acquired *via* a self-assembly approach, in comparison to arrays constructed systematically, layer-by-layer, or *via* the deposition of a mixed monolayer. The former method is known to bring about the growth of clusters and defects in the donor-acceptor architecture, whilst the latter approach is reported to give rise to films in which both the donor and acceptor moieties are unevenly distributed, that is they are phase segregated.

When the electron donor and electron acceptor moieties are covalently connected, **Figure 19**, and a definitive energy gradient established, PET ordinarily proceeds *via* singlet excited states[146]. However, when the distance between the two is short, and energy transfer is favoured, it occurs *via* the triplet state, formed as the result of fast intersystem crossing[146]. Such behaviour has been witnessed in the case of molecular dyads when the energy level of the radical ion pair is similar to the triplet states of both the donor and acceptor moieties[146]. Thus, the lifetime of the charge separated state is extended due to the fact that the radical ion pair gains triplet-spin character, which in turn permits energy transfer with greater efficiency[146,153,154].

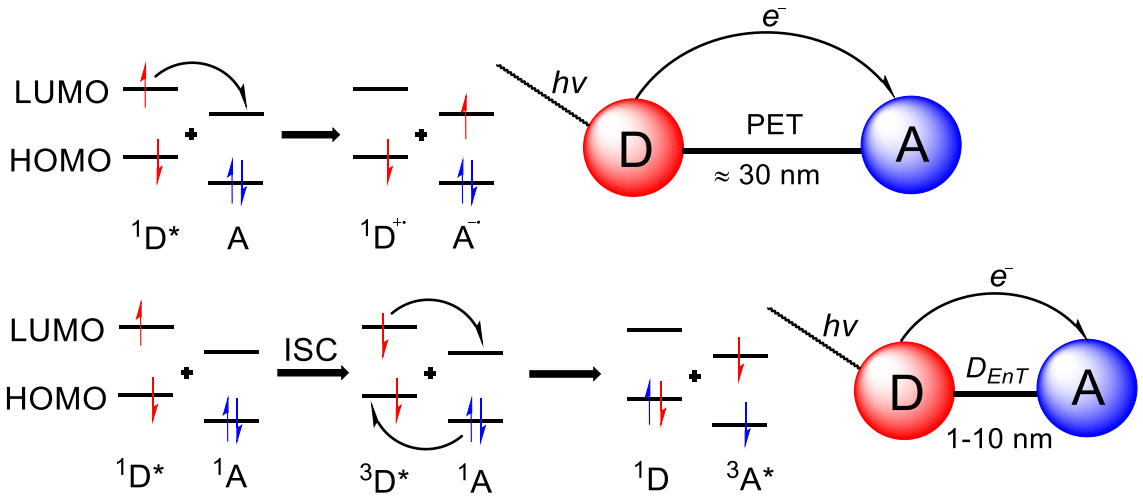


**Figure 19.** PET within covalently linked donor-acceptor (D-A) architectures. When the distance between the two moieties is large (**Top**), the PET process usually proceeds *via* the singlet excited state. However, when the distance is much shorter and thus energy transfer (EnT) is favoured (**Bottom**), PET proceeds *via* the triplet excited state; this state is generated as the result of relatively fast intersystem crossing (ISC).

The anchoring of donor-acceptor dyad-like systems to both metallic and semi-conductive materials, in an attempt to fabricate donor-acceptor architectures, permits the transfer of an electron across the interface, in a direction determined by the energy states of both the interface itself and the molecular architecture deposited.

Whilst the immobilisation of such architectures is widely reported at gold, by virtue of thiolate chemistry, **Figure 18**, research appears to be migrating towards the functionalisation of indium tin oxide (ITO), a material that possesses both high optical transparency (> 90 %) and electrical conductivity ($\approx 10\ \Omega\ cm^{-1}$)[155,157,158]. Strong energy transfer from the excited state of the chromophore, to the gold surface, has thus far prohibited chemists from acquiring a high quantum yield for charge separation at the interface, as is seen in photosynthesis[155,156]. Although ITO is known to suppress the quenching of the excited states of dyes adsorbed onto the surface, its use has thus far been limited by the fact that its chemical modification requires carefully controlled conditions, of which are difficult to achieve, and its surface is inherently rough in comparison to that of golds[155].

The immobilisation of donor-acceptor-like dyads (D-A) incorporating both $C_{60}$, or buckminsterfullerene, a spherical fullerene molecule containing a large number of π-electrons, and the porphyrinic macrocycle, has led to the fabrication of supramolecular assemblies from which valuable insight into the development of artificial photosynthetic devices can be acquired[141,142,155,156]. The incorporation of $C_{60}$, a well-known acceptor moiety possessing small reorganisation energies, brings about the acceleration of both photoinduced charge separation and charge shift, but a retardation of charge recombination. Fullerenes have small reorganisation energies due to the fact the delocalisation of an electron in $C_{60}^-$ occurs over all carbon atoms, meaning that only a small electron density is centred at each one at any given time. Consequently, only a small reorganisation

of the solvent molecules is required to bring about this transformation. In addition, $C_{60}$ is rigid enough to prevent this transformation from bringing about a large structural change. The use of porphyrins as electron donors is also driven by the fact that they too are known to exhibit small reorganization energies.[155-161]

Marcus theory states that in order for electron transfer to proceed, from the HOMO of D-A, to the LUMO of $D^+A^-$, the reactant state must distort from its equilibrium energy, reaching a transition state which also exists as a distorted form of the product state. Electron transfer occurs at the point along the reaction coordinate when the transition state has a 50 % chance of producing the $D^+A^-$ product state. The change in Gibbs energy, if the reactant state (D-A) were to distort to the equilibrium conformation of the product state ($D^+A^-$), without the transfer of an electron, is defined as the reorganisation energy, λ. The classical Marcus equation, **Equation 1**, implies that for moderately exergonic reactions, that are reactions in which energy is released, $\Delta G^{\ddagger}$ decreases, whilst the rate of electron transfer, $K_{ET}$, increases, as $\Delta G^0$ becomes more negative.[162-167, 168-173]

$$k_{ET} = k_{el} \nu_n \exp\left(\frac{-(\lambda + \Delta G^{\circ})^2}{4\lambda\, k_B\, T}\right)$$

**Equation 1.** The Marcus equation, where $k_{ET}$ is the rate of electron transfer, $k_{el}$ the electron transmission coefficient (≈ 1), $\nu_n$ the vibrational frequency of the transition state (≈ $10^{13}$ $s^{-1}$), $k_B$ the Boltzmann constant, $T$ (K) the temperature, $\lambda$ the reorganisation energy, and $\Delta G^0$ the free energy change between the reactant state and the product state. $\Delta G^{\ddagger} = (((\lambda + \Delta G^0)^2) / (4\,\lambda))$.[160-166, 173]

However, as $-\Delta G^0$ becomes increasingly negative, the point at which the potential energy surfaces of the reactant and product coordinates intersect, moves to the left, *i.e.* to within the 'inverted region'.[57-62] This shift brings about an increase in $\Delta G^{\ddagger}$, signifying that $K_{ET}$ will eventually begin to decrease as more energy is released. Essentially, electron transfer will occur quickest when less reorganisation energy is required to conform the system to equal energy in order for the aforementioned process to proceed; this is aided when the starting and product ions are greater in similarity[162-167]. As a result, a long-lived, charge-separated state, with a high quantum yield, is generated, and a photochemical output of greater magnitude acquired upon irradiation of the molecular film[141-143,145].

In nature, photosynthetic reaction centres have evolved so that their interiors are non-polar ($\lambda \leq 1$ eV), the forward electron transfer reactions are activationless ($|\Delta G^0| = \lambda$), and the reverse electron transfer reactions appear within the 'inverted' Marcus region ($|\Delta G^0| > \lambda$); their non-polar interior is advantageous due to the fact that it enables higher electronic states to become involved within the electron transfer process at $\Delta G$'s >> $-\lambda$[164, 171]. Hence, an optimised cascade of photoinduced energy transfer and electron transfer processes is initiated between donor and acceptor moieties embedded in the antenna complexes and photosynthetic reaction centres[106-108, 146-151]; it is the mimicking of this level of complexity and / or efficiency that has engaged a variety of researchers, including chemists, biologists, physicists, and materials scientists, for years.

## 1.9 – PET Induction at the Interface

Upon the irradiation ($\lambda_{irr}$ 380 – 450 nm) of a gold electrode, modified with a SAM incorporating the photoactive, porphyrin moiety, a stable, photoelectrochemical response should be acquired in the presence of either a suitable electron acceptor, such as methyl viologen ($MV^{2+}$)[174-187] or oxygen ($O_2$)[188-190], or a sacrificial electron donor[191-196], such as triethanolamine (TEOA)[191,195]. The photoinduced electrochemical response should flow until the illumination source is turned off, and the direction in which the current flows is dependent on both the Fermi level of the gold surface, and the redox potential of both the donor and acceptor moieties present within both the monolayer and the electrolytic solution[174,175,177-179,190-196], **Figure 20**.

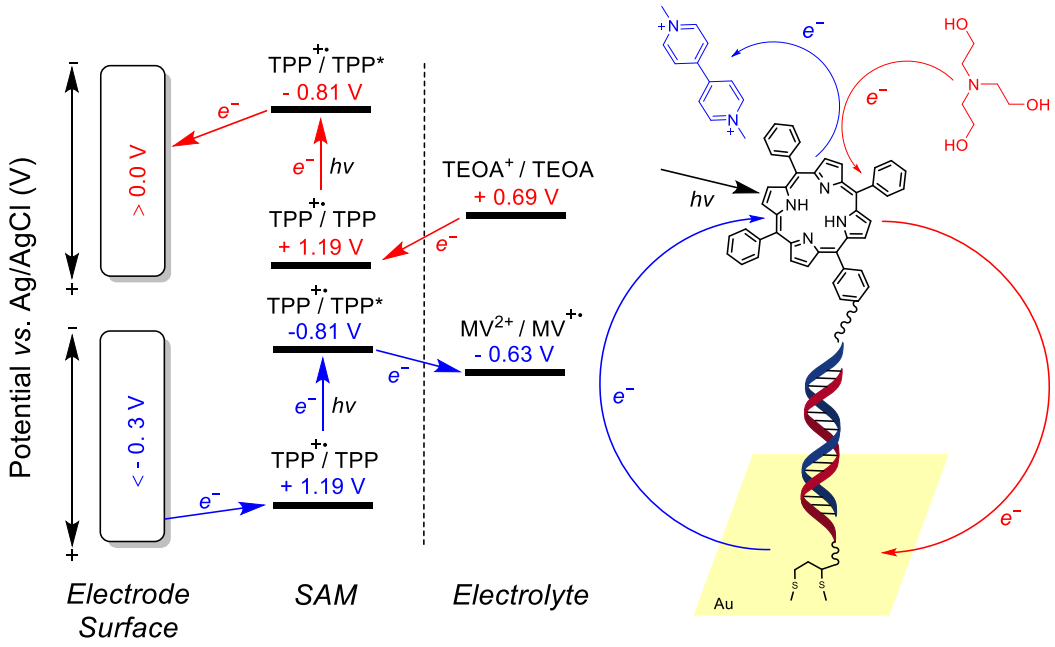


**Figure 20.** A schematic illustration of the generation of both **anodic** and **cathodic** photocurrent within a SAM of a porphyrin-terminated, helical peptide. All photoelectrochemical experiments were undertaken, by Uji *et al.*, within a 0.1 M $Na_2SO_4$ solution (aqueous), and either an electron acceptor ($MV^{2+}$) or a sacrificial electron donor (TEOA) present at a concentration of 0.05 M. All redox and applied potentials quoted are reported with respect to a Ag / AgCl reference electrode, and photoelectrochemical output was acquired upon illumination of the monolayer with light of wavelength 430 nm. Figure reproduced with permission from references [191] and [195].

Cathodic photocurrent flows following photoirradiation of the interface, in the presence of an electron donor, and upon the application of a bias / local surface potential of lower magnitude than that of the reduction potential of the porphyrin cation radical[174-177]. Upon photoexcitation of the porphyrin moiety, electron transfer occurs, from either its singlet or triplet excited state, to the electron acceptor, commonly $MV^{2+}$, present in the electrolytic solution[174-177]. The reduced form of $MV^{2+}$ then diffuses to the surface of the auxiliary electrode (Pt wire) in order to release an electron, whilst the porphyrin cation radical captures an electron from the gold surface, thus generating the ground state and initiating the flow of cathodic current[174-177], **Figure 20**, **Blue Electron Flow**. The singlet ($^1P^*/P^{\cdot+}$, - 800 mV *vs.* Ag / AgCl) and triplet ($^3P^*/P^{\cdot+}$, - 340 mV *vs.* Ag / AgCl) excited states

of the porphyrinic macrocycle have been shown to be equivalent in solution and at the interface, but only the singlet excited state is able to participate in PET to the $MV^{2+}$ electron carrier[175]. The redox potential of $MV^{2+}/MV^{\cdot+}$ (- 620 mV *vs.* Ag / AgCl) is located between the two aforementioned potentials, hence why the diffusive species can only accept an electron from the singlet excited state, and not from the triplet excited state[175].

In comparison, anodic photocurrent is generated when upon photoexcitation of the porphyrin moiety, the sacrificial electron donor, commonly TEOA, donates an electron to the hole of the HOMO of the excited state of the porphyrin moiety, $TPP^*$, thereby generating an anion radical[191-195]. An electron is then transferred from the LUMO of $TPP^*$ to the gold Fermi level, thus bringing about the flow of anodic current[191-195], **Figure 20**, **Red Electron Flow**. In order for this process to proceed, a bias potential more positive than the oxidative potential of $TPP/TPP^-$, and clear of any zero-photocurrent potential, must be applied[191]. Zero-photocurrent potentials are potentials at which the anodic and cathodic photocurrents cancel one another out[191]. For example, here (**Figure 20**), a bias potential of 0.19 V (vs. Ag / AgCl) will bring about this effect by placing the gold Fermi level at the centre of the $TPP^+/TPP$ and $TPP/TPP^-$ redox couples[191].

### 1.9.1 – Electrochemically Modulating the Magnitude of the Cathodic Photocurrent Density Generated *via* the Integration of a Redox Mediator

The efficiency of PET at gold electrodes, modified with SAMs of molecules incorporating the porphyrinic macrocycle, is adversely affected by the occurrence of competing energy transfer and electron transfer processes, all of which have been shown to be highly dependent on the distance between the photon absorber (porphyrin) and the electrode surface (Au)[174,175,176,179], **Figure 21**.

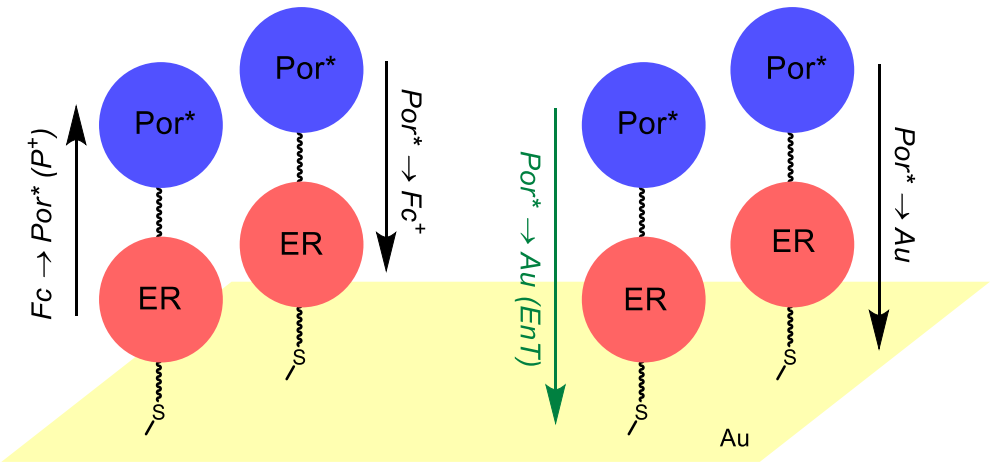


**Figure 21.** A schematic representation highlighting the four processes that need to be considered when trying to optimise the lifetime of the excited state of the porphyrinic macrocycle ($Por^*$), and thus enhance the efficiency of photocurrent generation. The four processes are as follows, 1) the rate of forward electron transfer from an embedded electron relay (ER) group to $Por^*$, 2) the backward rate of electron transfer from $Por^*$ to the oxidised form of the ER group, 3) the backward rate of electron transfer from Por* to the metallic surface (Au), and 4) energy transfer $Por^*$ to the metallic surface (Au).

The rate of electron transfer, $K_{et}$, is generally taken to decrease exponentially with distance, d, $K_{et} \propto \exp(-\beta d)$, where β is a constant, scaling distance dependence[179]. Thus, in theory, when the distance between the porphyrinic macrocycle and the gold surface is shortened, the rate of electron transfer, and hence the efficiency of photocurrent generation, should increase, *i.e.* a cathodic photocurrent density of increased magnitude should be acquired[179]. If this is the case, then it can be concluded that the rate of electron transfer, between the electrode surface and the porphyrinic macrocycle, plays a key role in determining the efficiency of photocurrent generation[179]. However, both Imahori[175,176] and Uosaki[174,179] *et al.*, have shown this not to be the case, that is upon increasing the distance between the two, up until the point at which they start to become electronically decoupled from one another, the efficiency of PET is enhanced, suggesting that the inhibition of reverse electron transfer and / or energy transfer from the excited state of the porphyrin moiety, to the gold electrode, is more important in enhancing the efficiency of photocurrent generation[179].

In order to counteract the reduction in the rate of forward electron transfer, whilst still setting out to minimise quenching of the porphyrinic excited state ($P^*$), *via* both electron and energy transfer to the Au surface, Uosaki *et al*. incorporated an electron relay (ER) group, in the form of ferrocene (Fc), into a porphyrin-terminated SAM[178,179,197], **Figure 22**; Fc was selected as the ER group due to fact that the rate of electron transfer from gold to the metallocene is reported to be very fast[198].

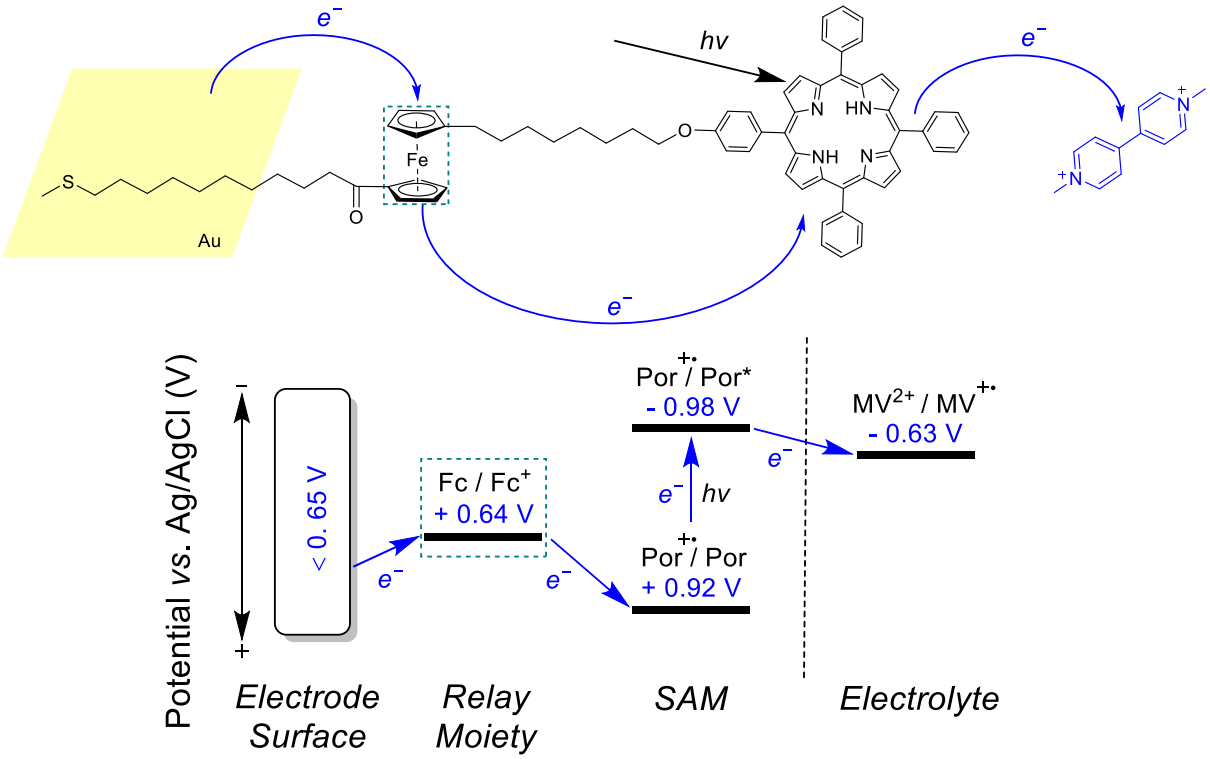


**Figure 22.** **Top.** The molecular structure of the porphyrin-terminated SAM deposited at Au by the group of Uosaki. **Bottom.** An energy diagram demonstrating photoinduced cathodic upconversion within the aforementioned SAM. Por = Porphyrin, Fc = Ferrocene, and $MV^{2+}$ = Methyl Viologen. Figure reproduced with permission from references [178] and [179].

A stable cathodic photocurrent was acquired upon illumination of the molecular film (**Figure 22**), but fell instantly when the illumination source was either turned off or the bias potential was set less positive than + 650 mV (*vs*. Ag / AgCl)[178,179]. This coincides with the redox potential of the incorporated Fc moiety, thus demonstrating that PET proceeds *via* the ER group[178,179], as was expected.

However, the increase in both quantum and energy conversion efficiency, brought about upon the incorporation of an ER group, is also dependent upon the spatial separation between the functionalities present within the SAM[179], **Figure 21**. It has been shown that upon extending the length of the alkyl chain linker, between the ER group and the porphyrinic sensitizer, the rates of both forward electron transfer, from the metallocene to $P^*$ ($P^+$), and backward electron transfer, from $P^*$ to both the gold surface and $Fc^+$, fall[179]. β is known to be inversely proportional to activation energy, which is the energy difference between the energy level of the donor and the energy level barrier of the alkyl chain linker[179]. Since β is larger when the activation energy is small, the backward rate of electron transfer, whereby $P^*$ serves as the electron donor, is reduced more than the forward rate of electron transfer from $Fc^+$ to $P^*$ ($P^+$)[179]. Upon increasing the length of the alkyl chain linker, the rate of energy transfer also decreases in accordance with the following equation, $K_{en} \propto (d_0/d)^4$, whereby $d_0$ is the critical distance, and is dependent on the efficiency of overlap between the donor's fluorescent and the acceptor's absorption properties[179].

In addition, Uosaki *et al*. have been able to demonstrate this phenomenon within a system that predominantly generates anodic photocurrent; a novel porphyrin-mercaptoquinone derivative was deposited onto a mechanically polished, polycrystalline gold electrode, and the involvement of the quinone moiety inferred by the fact that the photoelectrochemical properties of the SAM were shown to be both pH and potential dependent[193,194], **Figure 23**.

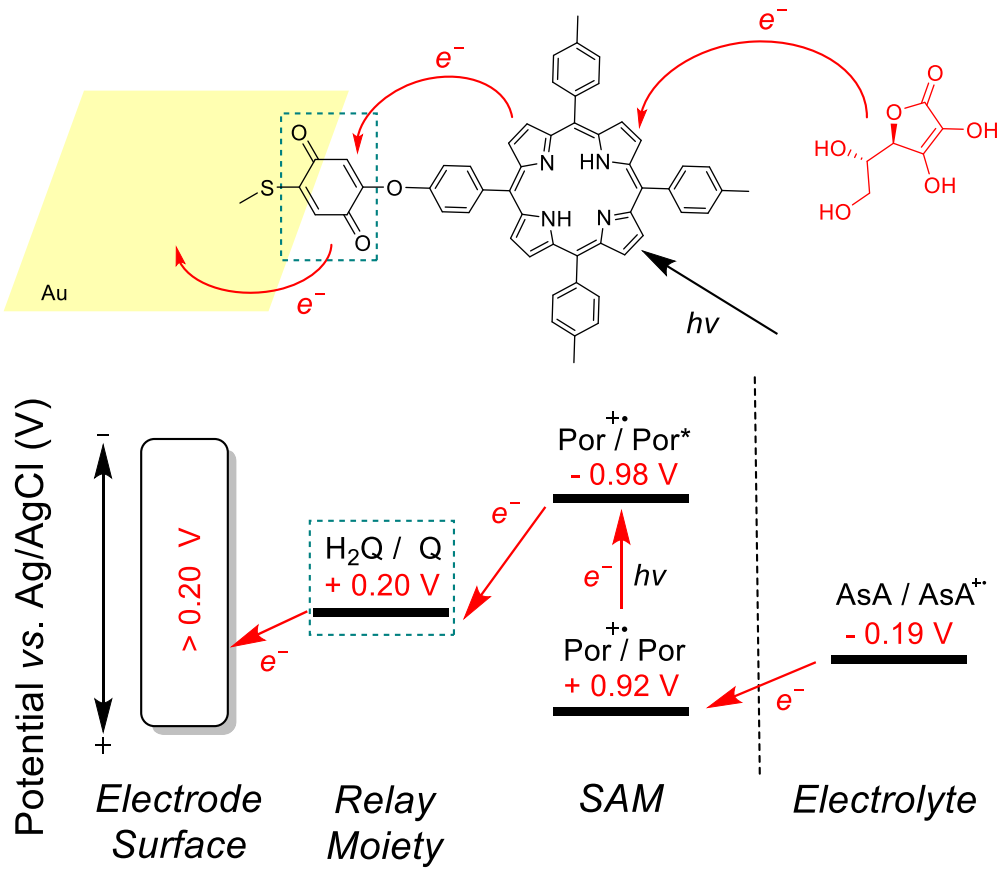


**Figure 23.** **Top.** The molecular structure of the porphyrin-terminated SAM deposited at Au by the group of Uosaki. **Bottom.** An energy diagram depicting the generation of anodic photocurrent within the aforementioned SAM. Por = Porphyrin, $H_2Q$ = Quinone, and AsA = Ascorbic Acid. Figure reproduced with permission from references [193] and [194].

Upon altering the pH of the electrolytic solution, the redox couple of the quinone moiety shifted[194]. That is, with increasing pH, the hydroquinone-centred redox couple shifted cathodically by approximately 60 mV / pH unit[194]. Consequently, as the pH of the solution was increased, the potential dependence of photocurrent generation was shifted in the negative direction[194].

In summary, the incorporation of an ER group allows for the generation of both anodic and cathodic photocurrents with greater quantum efficiency. Their integration ensures that the forward rate of electron transfer within the system is not adversely affected following optimisation of the spatial separation between the moieties (ER group, photoactive group, metallic substrate) present within the deposited monolayer; optimisation is required in order to reduce the backward rates of both energy and electron transfer.

### 1.9.2 – Further Modulation of the Magnitude of the Cathodic Photocurrent Density Generated

Although the incorporation of an ER group has been shown to bring about an enhancement in the magnitude of the photocurrent generated, the incident photon-to-current efficiency (IPCE) still remains low as the result of limited photon absorption[180-183]. Unfortunately, the synthesis of entire photosynthetic systems incorporating antennae complexes, in order to ensure that this is not an issue,

has thus far proven too difficult. Further enhancement of the efficiency of photoenergy conversion can be brought about *via* the systematic incorporation of photon-absorbing antennae, something Uosaki *et al*. sought to investigate upon the deposition of hexanethiol-functionalised gold nanoparticles (AuNPs) at the periphery of a SAM of (5-(4-(8-(10-mercaptoundecanoyl)-ferrocenyloctane)oxy-phenyl)-10,15,20-triphenylporphyrin[181]. It was shown that upon exciting the highly localised field induced within the nanogap between the metallic substrate (Au) and the nanosphere (AuNPs), incident photon energy is captured and delivered to the photofunctional monolayer by virtue of increased plasmon coupling[181-183]. As a result, the population of excited molecules increased, as did the magnitude of the cathodic photocurrent density acquired[181-183].

Surface morphology and porphyrin-porphyrin interaction within the SAM are also of importance in the generation of cathodic photocurrent density, hence need to be optimised in order to ensure that maximum photoelectrochemical output is realised upon photoirradiation of the molecular film. By preparing a systematic series of mixed SAMs of porphyrin and alkanethiol, Imahori *et al*. have been able to show, by virtue of time-resolved, single-photon counting fluorescence measurements, that porphyrin-porphyrin interaction is not a critical factor in controlling the efficiency of photocurrent generation[177], unlike the interaction between the porphyrinic macrocycle and the Au surface[174-176,179], and the morphology of the underlying substrate[184]. Uosaki *et al*. have been able to show that the efficiency of photocurrent generation is higher at substrates of lower surface roughness, owing to the decreased number of molecular domains and thus the formation of a more ordered SAM[184].

## 1.10 – Summary and Objective(s).

In short, due to their structure resembling that of chlorophyll[106,107,108], and the fact that they possess a small reorganisation energy, as well as other attractive photophysical properties, porphyrins are considered ideal candidates for incorporation within artificial photosynthetic devices[155-161]. Their incorporation permits a deeper understanding of both the electron and energy transfer processes driving photosynthesis to be acquired, which in turn should pave the way for the development of more efficient and inexpensive photovoltaic cells. The quantum efficiencies reported for such systems are low ($\leq$ 11 %)[178, 199-204] in comparison to that of the natural system ($\approx$ 100 %). However, it has proven possible to modulate both the direction of PET, and the magnitude of the resultant photoelectrochemical response acquired, within porphyrin-functionalised molecular films, of which have been deposited at electronically-addressable interfaces (Au). Whilst the direction of PET is dependent upon both the Fermi level of the gold surface, and the redox potential of the electron donor and electron acceptor moieties present, the magnitude of the photoelectrochemical response realised can be enhanced by covalently integrating an ER group into the system[178,179,197], and subsequently gating the rates of electron transfer concerned in the generation of either cathodic or anodic

photocurrent[174,175-179,190-195]. In addition, it is important to ensure that the surface on which the monolayers are deposited are atomically flat[184].

Although this principle has been exploited within molecular assemblies deposited at gold, it has not yet been employed within the area of supramolecular chemistry in order to monitor molecular motion within surface-mounted, porphyrin-terminated rotaxanes. This project aims to culminate in the assembly of a bistable [2]rotaxane in which this is possible (**Section 1.6**)

One of the greatest challenges to those working within the field of supramolecular chemistry lies in the synthesis of receptors that have both a high affinity and a high selectivity for the binding of guest species in water. The host molecule needs to be soluble in water, overcome the competitive influence of water, and facilitate the study of molecular interactions, including charge-transfer, within a confined space.[205] Thus, cucurbituril is an ideal candidate for use in the development of water-soluble, supramolecular architectures.

## 1.11 – An Introduction to the Cucurbit[*n*]uril, CB[*n*], Family

The cucurbit[*n*]urils, CB[*n*], are a family of macrocyclic cavitand, whose name is derived from the Latin *cucurbita*, meaning pumpkin, in reference to their distinctive shape[206]. Synthesised by way of a condensation reaction between *n* glycoluril units and formaldehyde[207], the resultant cyclic oligomeric species possess hydrophobic cavities that are accessible through two identical carbonyl-fringed portals[208]. It is this structural feature that has attracted interest from all those working within the field of supramolecular chemistry, and that has permitted the diversity of chemistry available to the series. Synthesis of the parent compound, CB[6], was first reported in 1905[209,210], but its chemical nature and structural framework remained unknown until 1981[206]. Since then, the homologues CB[5]-CB[11] have been isolated and characterised[207], with much of the focus remaining on the species CB[6]-CB[8][211,212], **Figure 24**[213].

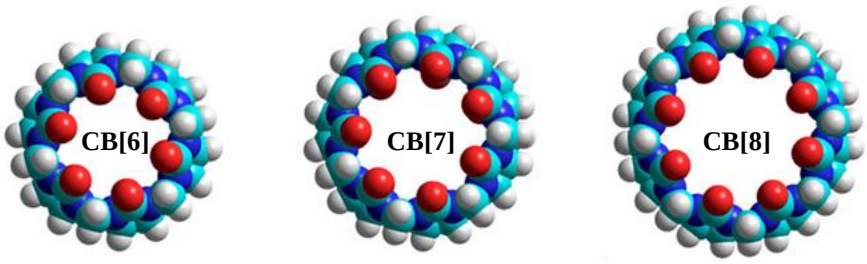


**Figure 24.** Space filling models of CB[*n*], for [*n*] = 6, 7 and 8. Elemental Key: Carbon – Light Blue; Nitrogen – **Dark Blue**; Oxygen – **Red**; Hydrogen – Grey. Reprinted with permission from reference [213].

The mean diameter of the internal cavity increases progressively from 5.8 (CB[6]) to 8.8 Å (CB[8]), whilst the height of the macrocyclic cavitand remains 9.0 Å.[211] In addition to the increase in cavity volume, the annular width, of which is dictated by the protruding carbonyl portals, also increases.[211,214] Furthermore, the solubility of the derivatives, in aqueous media, is governed by the number of glycoluril units present, **Figure 25**.[211,215,216] It is enhanced in concentrated aqueous acid, with CB[6] and CB[8] reported to be inherently less soluble than CB[5] and CB[7], respectively.[211,217,218]

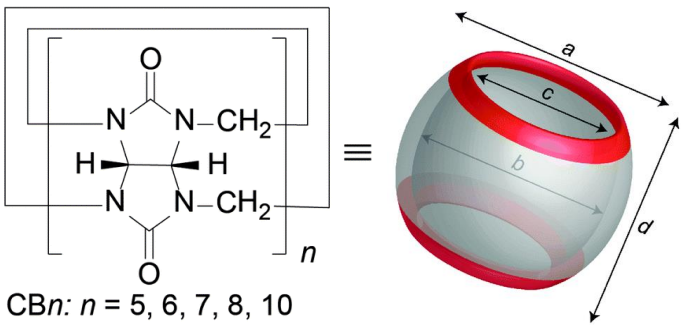


| | Outer Diameter (Å) (**a**) | Annular Width (Å) (**b**) | Cavity Diameter (Å) (**c**) | Cavity Volume (Å$^3$) | Solubility (mM) |
|---|---|---|---|---|---|
| CB[6] | 14.4 | 2.9 | 5.8 | 164 | 0.018[11] |
| CB[7] | 16.0 | 5.4 | 7.3 | 279 | 20 – 30 |
| CB[8] | 17.5 | 6.9 | 8.8 | 479 | < 0.01 |

**Figure 25.** Dimensions (**Top**) and selected properties (**Bottom**) of CB[*n*] for [*n*] = 6, 7 and 8. Solubility refers to aqueous solubility at 298 K. All data and image reproduced with permission from references [211] and [215], respectively.

Whilst their aqueous solubility limits their use, it is the combination of the polar carbonyl groups and the apolar hydrophobic cavity that leads to their remarkable, differing molecular recognition properties.[211] This falls within the field of supramolecular chemistry, whereby reversible association of two or more species is facilitated by non-covalent interactions, and is a trait that has seen the CB[*n*] family become an attractive building block for use in the construction of functional supramolecular architectures[211].

## 1.12 – Inclusion within CB[*n*] and Applications of Host-Guest Chemistry

Interest in this class of macrocyclic compound stems from their ability to include guest species within their molecular cavity, a process facilitated by non-covalent interactions, the most prominent being electrostatics, solvophobic effects, and π-π interactions.[219,220]

CB[6] is known to form stable host-guest complexes with alkyl ammonium ions (spermidine[213,221], $K_a$ = 6.6 x $10^5$ $M^{-1}$)[221-228], whilst larger guest molecules that are not encapsulated by the aforementioned homologue, such as ferrocenemethanol[8] ($K_a$ = 3.0 x $10^9$ $M^{-1}$)[229-231], are encapsulated by CB[7]. The cavity of CB[8] on the other hand, is large enough to encapsulate two guest molecules (CB[8]-methyl viologen-2,6-dihydroxynapthalene, $K_a$ = 5.1 x $10^{11}$ $M^{-2}$)[225], facilitating the formation of 1:2, 1:1 and 2:2 host-guest, ternary complexes of which are stabilised by charge-transfer interactions[232-240], **Figure 26**.

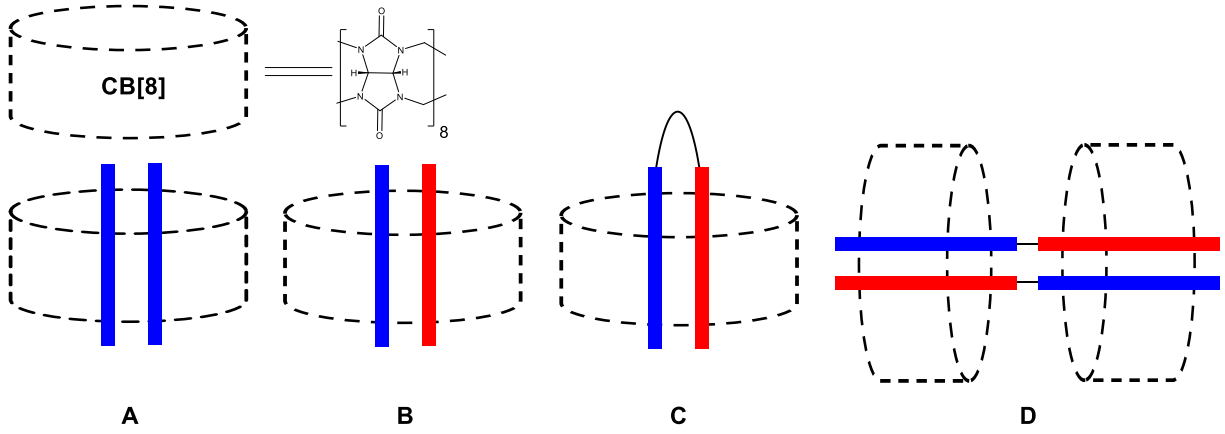


**Figure 26.** A schematic representation depicting the co-inclusion of guest species within the molecular cavity of CB[8], in order to form 1:1 homoternary (**A**), 1:1 *intermolecular* heteroternary (**B**), 1:1 *intramolecular* heteroternary (**C**), and 2:2 *intramolecular* heteroternary (**D**) complexes. All are stabilised upon the induction of charge-transfer between an electron-rich and an electron-deficient moiety.

The inclusion of neutral guest species is driven by the hydrophobic effect[241], whereby the loss of solvent ordering around the species drives the association of moieties that are poorly solvated in aqueous solution. The increase in permutations of hydrogen bonding upon restoration of the fluxional solvent structure, following complexation, leads to a favourable increase in entropy of the system[242]. An enhancement in the binding constant of complexation is further afforded as the result of CB[*n*]'s rigid structure; upon inclusion of the guest species, the host's conformational flexibility is not reduced to the same extent as it is upon the inclusion of an acyclic analogue. This preorganization is central to the macrocyclic effect[243] and in part explains the high stability of association characteristically observed in supramolecular complexes[244]. This, in conjunction with size complementarity of the host and guest species, contributes significantly to complex stability; restricted solvent penetration upon binding augments the hydrophobic contribution to inclusion, and is of importance in the encapsulation of positively charged guest species. The optimisation of molecular geometry enhances electrostatic interaction between cationic guest molecules and the negatively charged electrostatic potential surface of the CB[*n*] nanocavity[245], **Figure 27**.

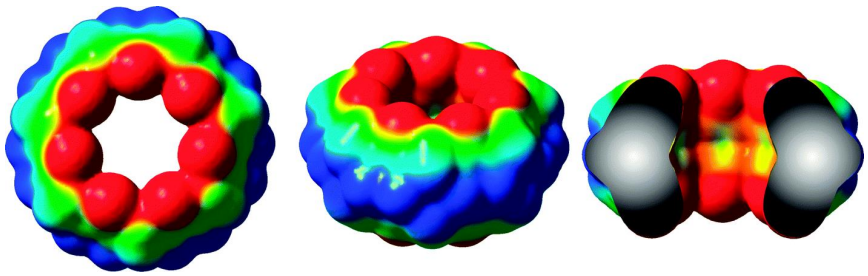

**Figure 27.** An electrostatic potential map of CB[7], highlighting the negatively charged carbonyl portals (**Red**). Reprinted with permission from reference [215].

It is the recognition of cationic guest species which generated interest in the CB[*n*] series at the expense of the cyclodextrin (CD) family, a class of macrocyclic compound with cavities of similar

shape and volume to the analogous CB[*n*] homologue[220,243], but whose electrostatic surface potential favours the binding of anionic guest molecules[246].

The inclusion of certain guest species within the cavity of CB[*n*] has been reported to bring about modulation of the guest's spectral output[247], including fluorescent enhancement upon isolation from quenching species present in solution[248], and following interaction with the macrocyclic motif's weakly basic carbonyl groups[249]. The latter alters the protonation state of the guest species, which in turn modulates its absorption profile. These changes may often be reversed by introducing a more competitive guest species into solution, thereby displacing the original guest species from the host's macrocyclic cavity. The ability to reverse such spectral changes permits the integration of intricate CB[*n*]-centred systems into sensory architectures. Numerous molecular machines, including propellers, turnstiles and rotaxane shuttles[249,251], have been fabricated in which complexes of CB[*n*] are incorporated; alterations in pH[252] and of the redox state[253] of the included guest moieties have been used to induce reversible translocation by virtue of reversibly altering the affinity of the incorporated binding sites for inclusion[254]. Such inclusion chemistry has also been employed in order to template the photodimerisation of t*rans*-1,2-bis*(*n-pyridyl*)*ethylenes and stilbazoles within aqueous media[*255*]. Confinement within the apolar cavity of the host ensures that the reactants are orientated relative to one another in order to ensure and drive formation of the *syn*-dimer, **Figure 28**; such a reaction is not permitted in solution.[256]

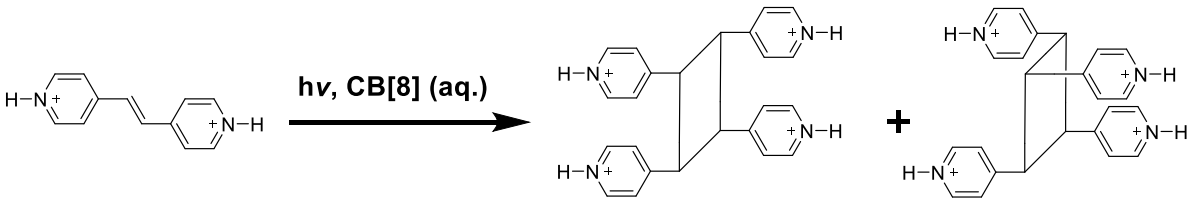


**Figure 28.** Stereochemical control of photoinduced dimerization within the cavity of CB[8].

## 1.13 – Inclusion within CB[8] – Ternary Complex Formation

The cavity size of CB[8] permits the encapsulation of a pair of electron-rich and electron-deficient guest molecules, and thus facilitates the formation of stable 1:1:1 ternary complexes. The formation of such complexes is driven by the remarkable enhancement in charge-transfer interaction that arises following close confinement and / or face-to-face, π-π stacking of the two guest molecules within the apolar cavity of the macrocyclic host[236]. Their successful formation is inferred upon the appearance of a characteristic absorption peak in the visible region of the electromagnetic spectrum[232,234,235,257], and can also be deduced by virtue of $^{1}$H NMR spectroscopy[236,237,238], cyclic voltammetry (CV)[235], providing the complex incorporates a redox-active motif, electrospray ionisation mass spectrometry (ESI-MS)[258,259,260,261], X-ray crystallography[232,236,239], circular dichroism[239] and isothermal titration calorimetry (ITC)[260].

The charge-transfer band results from energetic transfer between the highest occupied molecular orbital (HOMO) of the electron-rich moiety, and the lowest unoccupied molecular orbital (LUMO) of the conjugated electron-deficient species[236]. $\lambda_{max}$, that is the wavelength at which absorbance is highest, is strongly red shifted upon complexation, indicating a decrease in energy absorbed in accordance with the relationship, $\Delta E = \frac{hc}{\lambda}$, and in agreement with the Mulliken model, which models the energy of charge-transfer as, $E_{CT} = E_{Ion} - E_{Aff} + J$, where $E_{Aff}$ is the electron affinity of the acceptor species ($E_{LUMO}$ of electron-deficient species), $E_{Ion}$ the ionisation energy of the donor species ($E_{HOMO}$ of electron-rich species), and $J$ the electronic reorganisation energy associated with the complexation process[262]. Upon complexation, the negative electrostatic potential of CB[8]'s apolar cavity brings about an increase in the $E_{HOMO}$ of the electron-rich species, whilst $J$ is dominated by stabilisation of the excited state of the donor-acceptor complex for a similar reason; both have partial positive charge following the onset of charge-transfer, and the summation of these two effects is a red shift of the charge-transfer band.[234]

One advantage of such a complex is the ability to address a set of 'on' and 'off' states on demand following the encapsulation of both redox- and light-responsive guests by the single, supramolecular entity. Their response, in a controlled and reversible manner, to orthogonal stimuli permits the generation of multifunctional switches and could provide a working principle for electro- and photochemically controllable molecular machines. For example, it is possible to reversibly generate both the homoternary complex (1:2) and the corresponding binary complex (1:1), from the 'closed' heteroternary complex (1:1:1), through light-driven isomerization and redox-driven dimerization, respectively, **Figure 29**.[240]

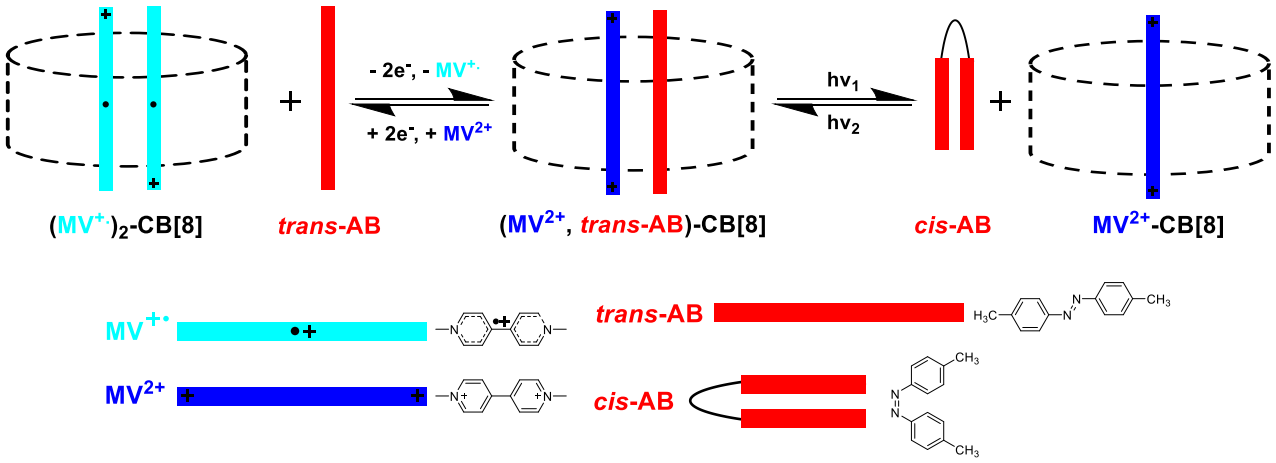


**Figure 29.** A schematic representation depicting the orthogonal switching of a heteroternary complex containing both redox- and photochemically addressable guest species, ((**MV²⁺, *trans*-AB**)-**CB[8]**). The homoternary complex ((**MV⁺·**)₂-**CB[8]**) is afforded upon two electron reduction of the heteroternary complex, in the presence of excess methyl viologen ($MV^{2+}$), whilst formation of the binary inclusion complex (**MV²⁺-CB[8]**) is induced upon *trans-cis* isomerisation ($\lambda_{irr}$:342 nm) of the included azobenzene (**AB**) derivative. The heteroternary complex is regenerated upon either oxidation of the homoternary complex, or by virtue of the *cis-trans* isomerism (420 nm) of the included AB derivative.[240]

Charge-transfer is easily identifiable on account of its characteristic features in electronic spectra, and its energetic contribution to complex formation is often easily detectable. This, in accordance with the ability to reversibly modulate complexation stoichiometry, **Figure 29**, has permitted the use of ternary complex formation in the generation of solution-phase supramolecular switches[234,240,263], nanoparticle-centred delivery systems[264-271], and facilitated the selective, fluorescent–based detection of both aromatic compounds[272-275] and peptide sequences[276-279]. In addition, such chemistry has been integrated into molecular films, thereby permitting the fabrication of both CB[8]-based rotaxanes[280,281,282] which function to selectively detect nitrated explosives[283,284], and surface immobilised micelles which release their cargo upon exposure to organic solvents[285]. Furthermore, this branch of interfacial, host-guest chemistry has allowed for the development of ultrathin films able to act as nanocarriers for DNA[286], permitted the selective separation of peptides bearing the *N*-terminal tryptophan residue[287], and allowed for the development of a photoresponsive platform capable of mediating the adhesion of bacteria on supported lipid bilayers[288-291].[228]

## 1.14 – Incorporating Lanthanide Ions into Supramolecular Assemblies

'Owing to their unique photophysical and coordination properties, lanthanides have become important players in the field of supramolecular chemistry'. When complexed, lanthanide ions often reside in their + 3 oxidation state, with the trivalent cations portraying well-defined and characteristic luminescent emission[292]. Although this property has seen them employed within the fields of advanced optical materials, communications[293,294], medical imaging[295], and as effective reporter groups within molecular switching applications[296,297], focus has now shifted towards developing bimetallic systems in which the photophysical and magnetic properties of the lanthanide centre are dependent on the proximity of a secondary metal centre.

### 1.14.1 – Electronic Properties of Europium ($Eu^{3+}$)

$Eu^{3+}$ has the electronic configuration $[Xe]4f^6$, whilst its ground ($^7F$) and excited ($^5D$) states are split by interelectronic repulsion and ordered in accordance with Hund's rules. Additionally, interconversion between the ground and excited states is forbidden by the spin selection rule, but does not hold as the result of spin-orbit coupling. The coupling constant is proportional to nuclear charge ($\zeta \propto Z^4$), and spin-orbit coupling is further enhanced by the contracted nature of the 4*f* orbitals, so has a significant effect on the behaviour of the lanthanides. $^7D_0$ manifests itself as the emissive state of excited $Eu^{3+}$, minimising non-radiative decay processes as it does so; this state is furthest from the next lowest energetic state. From this, decay to all $^7F_J$ states occurs, from which the electronic ground state ($^7F_0$) is subsequently yielded by way of vibrational relaxation. Traceable optical switching is permitted due to the fact that the magnitude of the energy lost corresponds to the emission of light of a wavelength within the visible region of the electromagnetic spectrum[298].

Although their sharp emissive output is easily detectable, lanthanide complexes have low extinction coefficients (0.3 – 3 $M^{-1}$ $cm^{-1}$)[299], and thus direct excitation has proven challenging. Electric dipole transitions between *f*-orbitals is formally forbidden (Laporte selection rule), and thus the absorption of a quanta of energy corresponding to an *f-f* transition will rarely induce efficient excitation[300]. For the same reason, luminescent decay of the excited state is associated with a long lifetime, and both effects are surmountable through indirect excitation.

### 1.14.2 – Sensitised Luminescence *via* the Integration of Molecular Antenna

The use of molecular antenna to mediate lanthanide luminescence is well established[301], whereby the excited state of the lanthanide species is generated *via* energy transfer from a species with a high absorption extinction coefficient[302, 303], **Figure 30**.

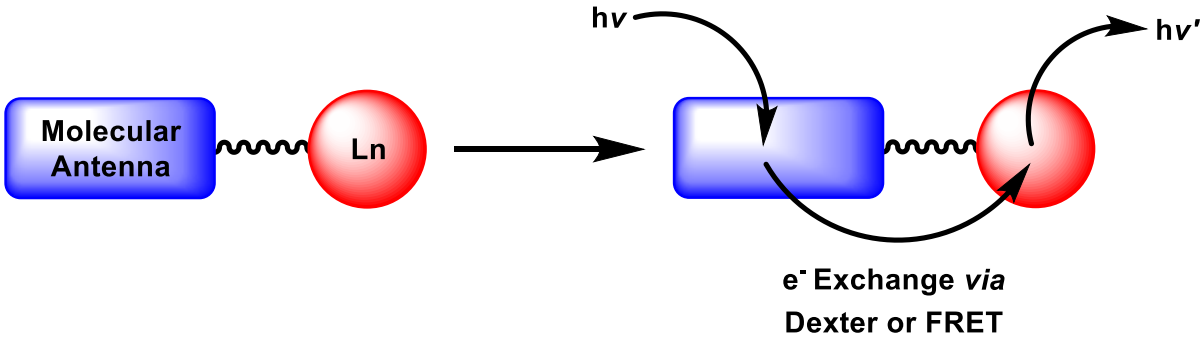


**Figure 30.** A schematic representation highlighting the energy transfer processes involved in sensitised lanthanide luminescence. Energy transfer from the excited state of the molecular antenna to the ground state of the lanthanide ion (Ln) proceeds **via** either Dexter or Förster resonance energy transfer (FRET).

Aromatic species, such as 2,6-dihydroxynapthalene (2,6-Np), often make good molecular antenna, and singlet excitation proceeds intersystem crossing (ISC) to give an excited triplet state ($T_1$). Energy transfer to the lanthanide centre, followed by vibrational relaxation, harvests the emissive state of the lanthanide from which long-lived luminescent emission can occur, **Figure 31**.

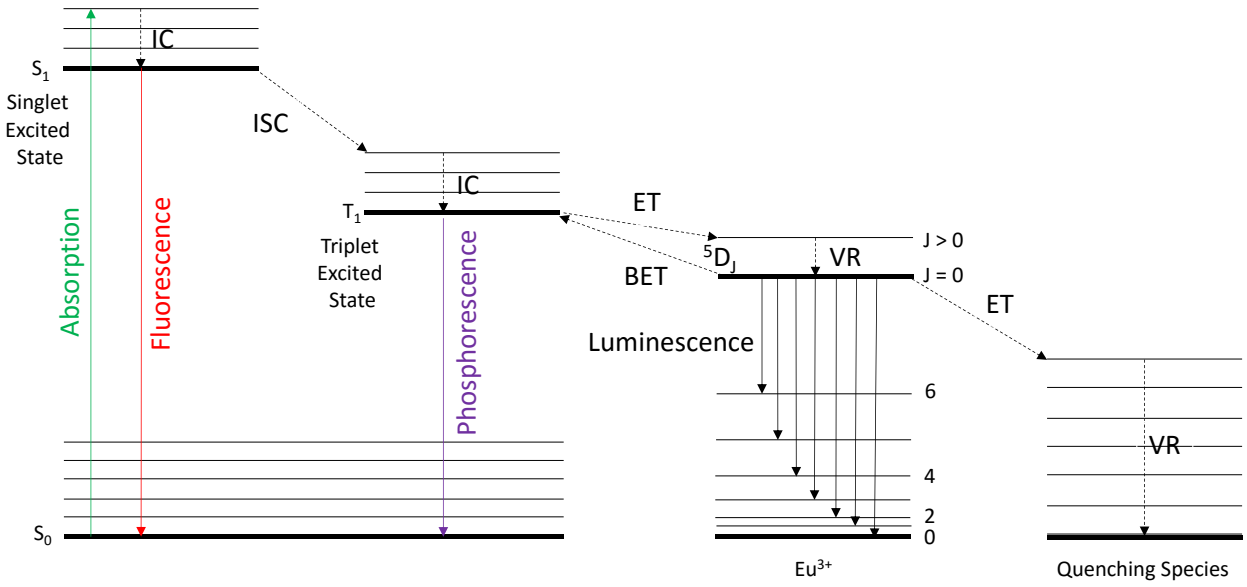


**Figure 31.** A Jablonski diagram highlighting the energetic processes available upon excitation of a molecular antenna species, including internal conversion (IC), intersystem crossing (ISC), vibrational relaxation (VR), electron and / or energy transfer (ET) and back electron transfer (BET).

$T_1$ must be sufficiently higher in energy than the lanthanide excited state in order for sensitisation to occur. However, the two states must remain close enough energetically to ensure that efficient energy transfer does arise, but are not too close as to induce back energy transfer (BET) and / or deactivation of the excited state.

### 1.14.3 – Energy Transfer Mechanisms in Luminescence Sensitisation

Energy transfer from the excited state of the molecular antenna to the ground state of the lanthanide ion proceeds *via* either Dexter or Förster resonance energy transfer (FRET), and is associated with a large Stokes shift, making it possible to discriminate the spectral peaks of emission from the excitation wavelength.

Dexter energy transfer, an electron exchange process which normally occurs on the ångström scale, is governed by spectral overlap of the donor and acceptor orbitals of the species involved[304]. The exchange process has a distance dependence proportional to $e^{-r}$,[305] hence the two species must be in close proximity for electron exchange to occur, unless the molecular antenna and emitting species are integrated within a conjugated system, whereby electron transfer is permitted by super exchange. FRET on the other hand, occurs at distances of up to 10 nm, and involves concomitant dipole-dipole interactions between the donor and acceptor species. A distance dependence of $r^{-6}$ is witnessed in this case, owing to its relation to the electric fields generated by the transition dipole moments of the species involved.[306]

### 1.14.4 – The Effect of Complexation on Lanthanide Luminescence

Efficient Dexter energy transfer is commonly induced upon appending a suitable molecular antenna species to a lanthanide complex in the absence of an insulating spacer moiety[307]. Complexation of the lanthanide ion, to yield a kinetically inert species, requires the presence of strong electrostatic interactions and a high degree of preorganization in order to ensure that their 'hard' Lewis acidic cationic nature is satisfied. The macrocyclic 1,4,7,10-tetraazacyclododecane-1,4,7,10-tetraacetic acid (DOTA) host species is a good candidate in the provision of such complexes because it is reported to have high affinity for lanthanide ions, including $Eu^{3+}$, and can be functionalised accordingly[308,309]. Functionalisation of the host with a suitable sensitizer, such as 2,6-Np, serves to reduce the symmetricity of the lanthanide environment, which consequently increases the extinction coefficient of *f-f* electronic transitions. In addition, the sensitisation pathway is further enhanced by the fact that the host's polydenticity reduces the number of bound water molecules that would otherwise be bound at the lanthanide centre and / or able to act as vibrational oscillators, thus quenching the emissive output of the lanthanide ion; bound water molecules are known to promote energy transfer from the excited state of the lanthanide ion to the fourth vibrational overtone[310]. Finally, the presence of the 'heavy' lanthanide ion serves to increase the efficiency of the formally forbidden formation of the antenna excited triplet state, *via* ISC from the excited singlet state, **Figure 31**. Mixing of the spin and orbital angular momentum through spin-orbit coupling drives this process[311].

## 1.15 – The Impact of Redox-Active Species on Lanthanide Luminescence

Ferrocene has been shown to effectively sensitise lanthanide-containing complexes[312]. Its low-lying excited triplet states are of a suitable energy as to permit Dexter energy transfer to lanthanide ions held in close proximity[313]. Sensitisation may however occur by means of an alternative mechanism involving ligand-to-metal charge-transfer (LMCT), whereby the excited state of the antenna species reduces the lanthanide ion[314]. Subsequent metal-to-ligand charge-transfer (MLCT) affords the lanthanide ion in its emissive state. The LMCT transition is highly sensitive to the metal redox state, and upon oxidation of the metallocene, to ferrocenium, quenching of the lanthanide species is prompted. Therefore, electrochemistry can, and has[315,316], been exploited as an emission switch within such systems, both in solution and at electronically addressable interfaces, **Figure 32**.

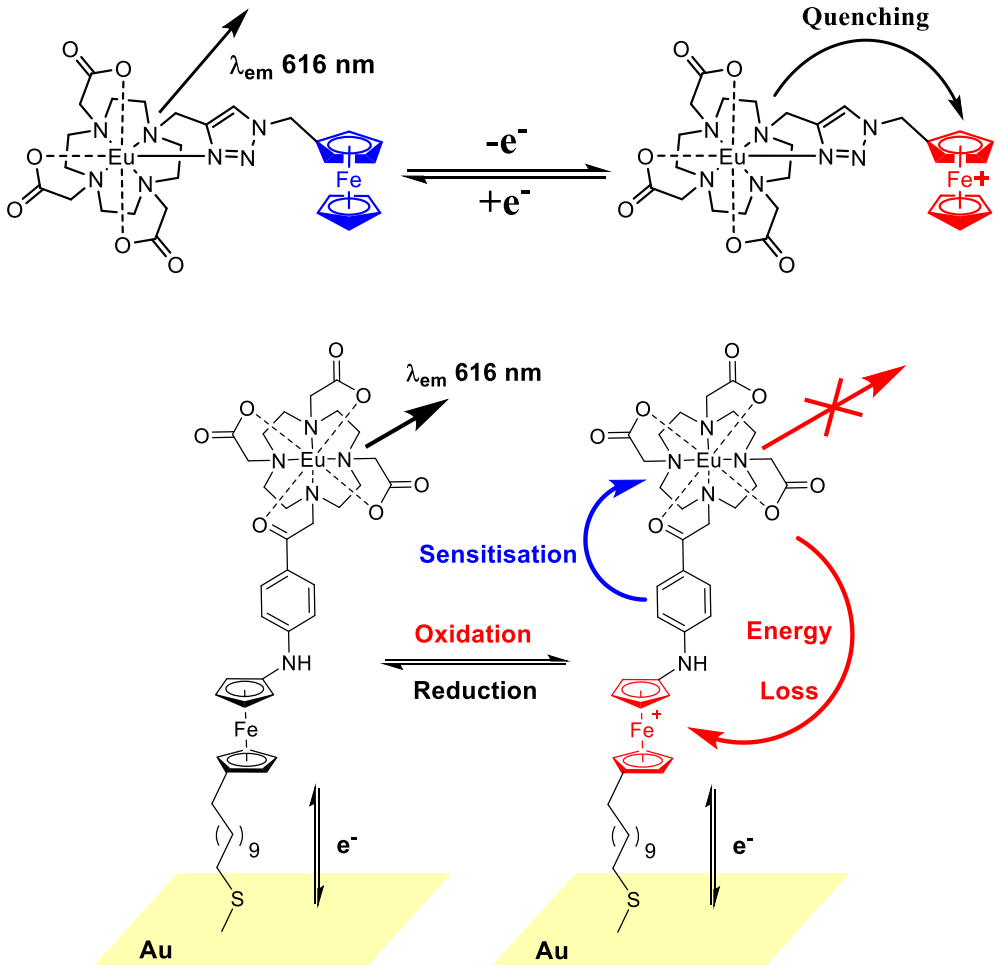


**Figure 32.** Reversibly modulating the photophysical properties of diffusive (**Top**) and interfacially assembled (**Bottom**) *d-f* dyads, by virtue of varying the oxidation state of the ferrocene chromophore, *i.e.* by inducing the formation of the quenching ferrocenium species.[316]

## 1.16 – Aim(s) of Project

This project aimed to culminate in the synthesis of a novel, optically switchable, ternary complex exhibiting charge-transfer based on the donor-acceptor interaction between an electron-rich naphthalene derivative (**EuNap**) and an electron-poor, redox-addressable, $MV^{2+}$ derivative (**MVFc**), **Figure 33**. It was envisaged, in line with what has been reported to date[300,312-316], that electrochemically switching the oxidation state of the metallocene would bring about reversible modulation of the lanthanide centre's sensitised emissive output, ascribed to the reversible generation of the quenching ferrocenium species. It was intended for the derivatives, and complexes thereof, to be characterised in as full a manner as possible in order to glean insight into the nature of the association, and to understand differential behaviour patterns in comparison with a model ternary complex (**Figure 33, Complex B**), upon incorporation of the ferrocene-appended paraquat derivative, **MVFc**.

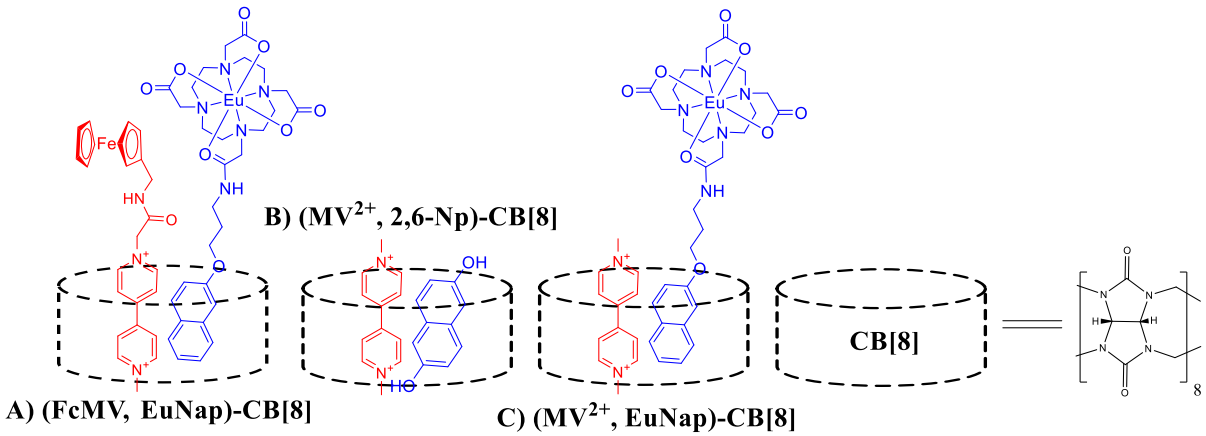


**Figure 33.** The ternary complexes conceived for attempted synthesis and full characterisation.

If successful, this concept was to be integrated within a molecular film, in a bid to translate the switchable behaviour observed in solution, to detectable output on a macroscopic level, **Figure 34**. It was planned for the metallocene to be incorporated in the form of 11-(ferrocenyl)undecanethiol, and for the binary complex to be assembled at the interface by virtue of the deposition of a thiolated paraquat derivative. Although both entities (ferrocene and Eu) would not be confined within a charge-transfer environment, like in solution (**Figure 33**), the electrochemical approach envisaged to modulate lanthanide emission at the interface, would still prove novel. This approach is likely to be more robust than an approach in which the (**FcMV, EuNap**)**-CB[8]** complex is directly deposited at the interface. It was envisaged that the emissive output from the lanthanide ion could be electrochemically modulated *via* the formation of both ferrocenium[315,316] (**Figure 34, Top**) and the homoternary complex[240] (**Figure 34, Bottom**). As shown by the group of Sherman, **Figure 29**, the homoternary complex ((**MV**$^{+\cdot}$)$_2$**-CB[8]**) is afforded upon one electron reduction of the heteroternary complex ((**FcMV, EuNap**)**-CB[8]**) in the presence of excess $MV^{2+}$.[208]

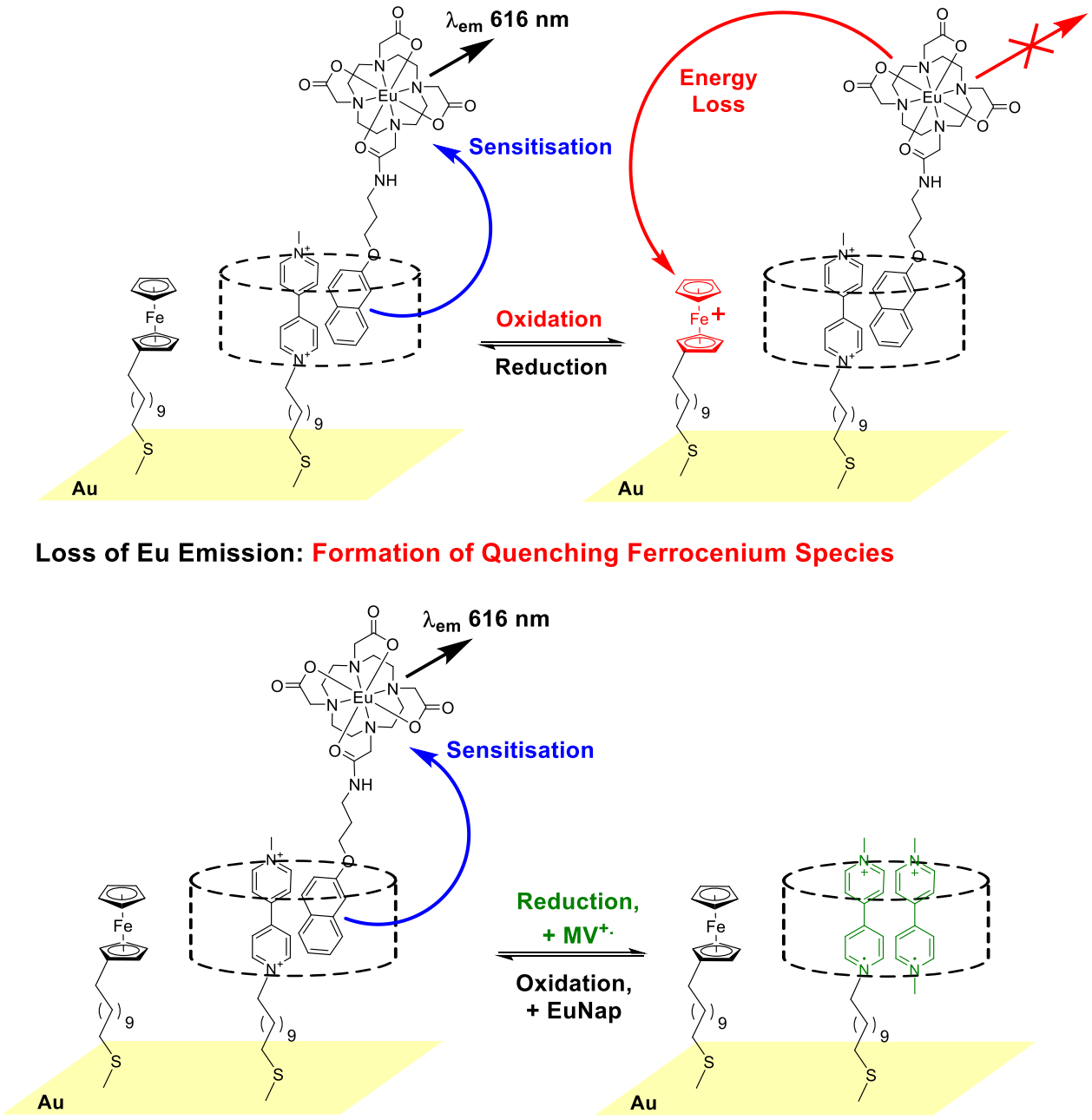


**Figure 34.** Utilising the formation of charge-transfer complexes in the generation of optically switchable, lanthanide-appended molecular films at electrochemically addressable surfaces. It was envisaged that the emissive output from the lanthanide ion could be electrochemically modulated *via* the formation of both ferrocenium (**Top**) and the homoternary complex (**Bottom**).

## List of References


1. Prof. Jean-Marie Lehn, *Angew. Chem. Int. Ed. Engl*., **1988**, 27, 89–112.
2. Christopher A. Hunter Prof., Harry L. Anderson Prof., *Angew. Chem. Int. Ed.*, **2009**, 48, 7488–7499.
3. Jean-Marie Lehn, *Chem. Soc. Rev*., **2007**, 36, 151–160.
4. Dana A. Uhlenheuer, Katja Petkau, Luc Brunsveld, *Chem. Soc. Rev*., **2010**, 39, 2817–2826.
5. David S. Lawrence, Tao. Jiang, Michael. Levett, *Chem. Rev*., **1995**, 95, 2229–2260.
6. Matthew S. Vickers, Paul D. Beer, *Chem. Soc. Rev*., **2007**, 36, 211–225.
7. Antonio Caballero, Fabiola Zapata, Paul D. Beer, *Coord. Chem. Rev*., **2013**, 257, 2434–2455.
8. Paul D. Beer, Mark R. Sambrook, David Curiel, *Chem. Commun*., **2006**, 20, 2105–2117.
9. Paul D. Beer Prof., Philip A. Gale Dr., *Angew. Chem. Int. Ed*., **2001**, 40, 486–516.
10. Prof. Jean-Marie Lehn, *Angew. Chem. Int. Ed*., **1988**, 27, 89 –112.
11. Christoph A. Schalley, Kaweh Beizai, Fritz Vögtle, *Acc. Chem. Res.*, **2001**, 34, 465–476.
12. Gloria A Breault, Christopher A Hunter, Paul C Mayers, *Tetrahedron*, **1999**, 55, 5265–5293.
13. Timothy J. Hubin, Daryle H. Busch, *Coord. Chem. Rev*., **2000**, 200, 5–52.
14. Michał J. Chmielewski, Jason J. Davis, Paul D. Beer, *Org. Biomol. Chem*., **2009**, 7, 415–424.
15. J. W. Pflugrath, F. A. Quiocho, *Nature*, **1985**, 314, 257–260.
16. Hartmut Luecke, Florante A. Quiocho, *Nature*, **1990**, 347, 402–406.
17. J. J. He, F. A. Quiocho, *Science*, **1991**, 251, 1479–1481.
18. Z. F. Kanyo, D. W. Christianson, *J. Biol. Chem.*, **1991**, 266, 4264–4268.
19. Sundus Erbas-Cakmak, David A. Leigh, Charlie T. McTernan, Alina L. Nussbaumer, *Chem Rev*., **2015**, 115, 10081–10206.
20. Sune Nygaard, Bo W. Laursen Professor, Thomas S. Hansen, Andrew D. Bond Dr., Amar H. Flood Professor, Jan O. Jeppesen Professor, *Angew. Chem. Int. Ed*., **2007**, 46, 6093–6097.
21. Christian Seel Dr., Fritz Vögtle Prof. Dr., *Chem. Eur. J*., **2000**, 6, 21–24.
22. Francesco G. Gatti, David A. Leigh, Sergey A. Nepogodiev, Alexandra M. Z. Slawin, Simon J. Teat, Jenny K. Y. Wong, *J. Am. Chem. Soc*., **2001**, 123, 5983–5989.
23. Christopher A. Hunter Prof., Caroline M. R. Low Dr., Martin J. Packer Dr., Sharon E. Spey, Jeremy G. Vinter Dr., Myroslav O. Vysotsky Dr., Cristiano Zonta, *Angew. Chem. Int. Ed*., **2001**, 40, 2678–2682.

24. Diego J. Cárdenas, Pablo Gaviña, Jean-Pierre Sauvage, *J. Am. Chem. Soc*., **1997**, 119, 2656–2664.
25. Brenda Long, Kirill Nikitin, Donald Fitzmaurice, *J. Am. Chem. Soc*., **2003**, 125, 15490–15498.
26. Hsian-Rong Tseng Dr., Scott A. Vignon, Paul C. Celestre, Julie Perkins Dr., Jan O. Jeppesen Dr., Alberto Di Fabio, Roberto Ballardini Dr., M. Teresa Gandolfi Prof., Margherita Venturi Prof., Vincenzo Balzani Prof., J. Fraser Stoddart Prof. Dr., *Chem. Eur. J*., **2004**, 10, 155–172.
27. F. M. Raymo, J. F. Stoddart, *Pure Appl. Chem*., **1997**, 69, 1987–1997.
28. Peter R. Ashton, Roberto Ballardini, Vincenzo Balzani, Ian Baxter, Alberto Credi, Matthew C. T. Fyfe, Maria Teresa Gandolfi, Marcos Gómez-López, M.-Victoria Martínez-Díaz, Arianna Piersanti, Neil Spencer, J. Fraser Stoddart, Margherita Venturi, Andrew J. P. White, David J. Williams, *J. Am. Chem. Soc*., **1998**, 120, 11932–11942.
29. P. Linnartz, S. Bitter, C. A. Schalley, *Eur. J. Org. Chem*., **2003**, 4819–4829.
30. Scott A. Vignon, Thibaut Jarrosson, Takahiro Iijima, Hsian-Rong Tseng, Jeremy K. M. Sanders, J. Fraser Stoddart, *J. Am. Chem. Soc*., **2004**, 126, 9884–9885.
31. Vincent Aucagne, Kevin D. Hänni, David A. Leigh, Paul J. Lusby, D. Barney Walker, *J. Am. Chem. Soc*., **2006**, 128, 2186–2187.
32. Gosia M. Hübner, Jens Gläser, Christian Seel, Fritz Vögtle, *Angew. Chem. Int. Ed*., **1999**, 38, 383–386.
33. Ching-Wei Chiu, Chien-Chen Lai, Sheng-Hsien Chiu, *J. Am. Chem. Soc*., **2007**, 129, 3500–3501.
34. Sourav Saha, J. Fraser Stoddart, *Chem. Soc. Rev*., **2007**, 36, 77–92.
35. Isurika R. Fernando, Semere G. Bairu, Guda Ramakrishna, Gellert Mezei, *New J. Chem*., **2010**, 34, 2097–2100.
36. Reguram Arumugaperumal, Venkatesan Srinivasadesikan, Mandapati V. Ramakrishnam Raju, Ming-Chang Lin, Tarun Shukla, Ravinder Singh, Hong-Cheu Lin, *ACS Appl. Mater. Interfaces*, **2015**, 7, 26491–26503.
37. Ken Cham-Fai Leung Prof., Chun-Pong Chak, Chui-Man Lo Dr., Wing-Yan Wong, Shouhu Xuan Dr., Christopher H. K. Cheng Prof., *Chem. Asian J*., **2009**, 4, 364–381.
38. Matthew J. Langton, Paul D. Beer, *Acc. Chem. Res*., **2014**, 47, 1935–1949.
39. D. I. Schuster, K. Li, D. Guldi, *C. R. Chimie*, **2006**, 9, 892–908.
40. Jean-Claude Chambron, Jean-Paul Collin, Jean-Olivier Dalbavie, Christiane O. Dietrich-Buchecker, Valérie Heitz, Fabrice Odobel, Nathalie Solladié, Jean-Pierre Sauvage, *Coord. Chem. Rev*., **1998**, 178, 1299–1312.
41. Jonathan A. Faiz, Valérie Heitz, Jean-Pierre Sauvage, *Chem. Soc. Rev*., **2009**, 38, 422–442.

42. Xiang Ma, He Tian, *Chem. Soc. Rev*., **2010**, 39, 70–80.
43. Nicholas H. Evans, Paul D. Beer, *Org. Biomol. Chem*., **2011**, 9, 92–100.
44. Christian A. Nijhuis, Bart Jan Ravoo, Jurriaan Huskens, David N. Reinhoudt, *Coord. Chem. Rev*., **2007**, 251, 1761–1780.
45. Dr. Joshua Lehr, Dr. Thomas Lang, Dr. Octavia A. Blackburn, Timothy A. Barendt, Prof. Stephen Faulkner, Dr. Jason J. Davis, Prof. Paul D. Beer, *Chem. Eur. J*., **2013**, 19, 15898–15906.
46. Matthew J. Langton, Dr. Octavia A. Blackburn, Dr. Thomas Lang, Prof. Stephen Faulkner, Prof. Paul D. Beer, *Angew. Chem. Int. Ed*., **2014**, 53, 11463–11466.
47. Mark R. Sambrook, Paul D. Beer, Michael D. Lankshear, R. Frederick Ludlow, James A. Wisner, *Org. Biomol. Chem*., **2006**, 4, 1529–1538.
48. Mark R. Sambrook, Paul D. Beer, James A. Wisner, Rowena L. Paul, Andrew R. Cowley, Fridrich Szemes, Michael G. B. Drew, *J. Am. Chem. Soc*., **2005**, 127, 2292 –2302.
49. Nathan L. Kilah, Matthew D. Wise, Christopher J. Serpell, Amber L. Thompson, Nicholas G. White, Kirsten E. Christensen, Paul D. Beer, *J. Am. Chem. Soc*., **2010**, 132, 11893–11895.
50. James A. Wisner, Paul D. Beer, Michael G. B. Drew, Mark R. Sambrook, *J. Am. Chem. Soc*., **2002**, 124, 12469–12467.
51. Kathleen M. Mullen, Paul D. Beer, *Chem. Soc. Rev*., **2009**, 38, 1701–1713.
52. Michael D. Lankshear, Paul D. Beer, *Acc. Chem. Res*., **2007**, 40, 657–668.
53. C. O. Dietrich-Buchecker, J. P. Sauvage, J. P. Kintzinger, *Tetrahedron Lett*., **1983**, 24, 5095–5098.
54. James D. Crowley, Stephen M. Goldup, Ai-Lan Lee, David A. Leigh, Roy T. McBurney, *Chem. Soc. Rev*., **2009**, 38, 1530–1541.
55. Vincent Aucagne, Kevin D. Hänni, David A. Leigh, Paul J. Lusby, D. Barney Walker, *J. Am. Chem. Soc*., **2006**, 128, 2186–2187.
56. Kevin D. Hänni, David A. Leigh, *Chem. Soc. Rev*., **2010**, 39, 1240–1251.
57. Levon D. Movsisyan, Michael Franz, Frank Hampel, Amber L. Thompson, Rik R. Tykwinski, Harry L. Anderson, *J. Am. Chem. Soc*., **2016**, 138, 1366–1376.
58. Steven Hoekman, Matthew O. Kitching, David A. Leigh, Marcus Papmeyer, Diederik Roke, *J. Am. Chem. Soc*., **2015**, 137, 7656–7659.
59. Asif Noor, Stephen C. Moratti, James D. Crowley, *Chem. Sci*., **2014**, 5, 4283–4290.
60. Ryuto Hayashi, Petr Slavík, Yuichiro Mutoh, Takeshi Kasama, Shinichi Saito, *J. Org. Chem*., **2016**, 81, 1175–1184.
61. Ryuto Hayashi, Yuichiro Mutoh, Takeshi Kasama, Shinichi Saito, *J. Org. Chem*., **2015**, 80, 7536–7546.

62. Alexander I. Prikhod′ko, Jean-Pierre Sauvage, *J. Am. Chem. Soc*., **2009**, 131, 6794–6807.
63. Dr. Matthew J. Langton, Yaoyao Xiong, Prof. Paul D. Beer, *Chem. Eur. J*., **2015**, 21, 18910–18914.
64. Eugenio Coronado, Pablo Gaviña, Sergio Tatay, *Chem. Soc. Rev*., **2009**, 38, 1674–1689.
65. Ying-Wei Yang, Yu-Long Sun, Nan Song, *Acc. Chem. Res*., **2014**, 47, 1950–1960.
66. Jason J. Davis, Grzegorz A. Orlowski, Habibur Rahman, Paul D. Beer, *Chem. Commun*., **2010**, 46, 54–63.
67. Vito Fasano, Massimo Baroncini, Maria Moffa, Donata Iandolo, Andrea Camposeo, Alberto Credi, Dario Pisignano, *J. Am. Chem. Soc*., **2014**, 136, 14245–14254.
68. Zhan-Qi Cao, Qi Miao, Qi Zhang, Hong Li, Da-Hui Qu, He Tian, *Chem Commun*., **2015**, 51, 4973–4976.
69. Giulia Fioravanti, Natalia Haraszkiewicz, Euan R. Kay, Sandra M. Mendoza, Carlo Bruno, Massimo Marcaccio, Piet G. Wiering, Francesco Paolucci, Petra Rudolf, Albert M. Brouwer, David A. Leigh, *J. Am. Chem. Soc*., **2008**, 130, 2593–2601.
70. Nai-Chia Chen, Po-Yi Huang, Chien-Chen Lai, Yi-Hung Liu, Yu Wang, Shie-Ming Peng, Sheng-Hsien Chiu, *Chem. Commun*., **2007**, 40, 4122–4124.
71. Nicola Armaroli, Vincenzo Balzani, Jean-Paul Collin, Pablo Gaviña, Jean-Pierre Sauvage, Barbara Ventura, *J. Am. Chem. Soc*., **1999**, 121, 4397–4408.
72. Hiroto Murakami, Atsushi Kawabuchi, Rika Matsumoto, Takeshi Ido, Naotoshi Nakashima, *J. Am. Chem. Soc*., **2005**, 127, 15891–15899.
73. Carleton G. Collins, Evan M. Peck, Patrick J. Kramer, Bradley D. Smith, *Chem. Sci*., **2013**, 4, 2557–2563.
74. Jeremiah J. Gassensmith Dr., Sarah Matthys, Jung-Jae Lee Dr., Aleksandra Wojcik Dr., Prashant V. Kamat Prof. Dr., Bradley D. Smith Prof. Dr., *Chem. Eur. J*., **2010**, 16, 2916–2921.
75. C. J. Serpell, R. Chall, A. L. Thompson, P. D. Beer, *Dalton Trans*., **2011**, 40, 12052–12055.
76. Graeme T. Spence, Dr. Mateusz B. Pitak, Prof. Paul D. Beer, *Chem. Eur. J*., **2012**, 18, 7100–7108.
77. Timothy A. Barendt, Sean W. Robinson, Paul D. Beer, *Chem Sci*., **2016**, 7, 5171–5180.
78. Sourav Saha, L. Erik Johansson, Amar H. Flood Dr., Hsian-Rong Tseng Dr., Jeffrey I. Zink Prof., J. Fraser Stoddart Prof., *Small*, **2005**, 1, 87–90.
79. Sourav Saha, Erik Johansson, Amar H. Flood Dr., Hsian-Rong Tseng Dr., Jeffrey I. Zink Prof., J. Fraser Stoddart Prof., *Chem. Eur. J*., **2005**, 11, 6846–6858.
80. Yun Hee Jang, William A. Goddard III, *J. Phys. Chem. C*, **2010**, 114, 4611–4616.

81. Vincenzo Balzani Prof., Alberto Credi Prof., Margherita Venturi Prof., *ChemPhysChem*., **2008**, 9, 202–220.
82. Shinye Chia, Jianguo Cao, J. Fraser Stoddart Prof., Jeffrey I. Zink Prof., *Angew. Chem. Int. Ed*., **2001**, 40, 2447–2451.
83. Francesca Cecchet, Petra Rudolf, *J. Phys. Chem. B*, **2004**, 108, 15192–15199.
84. Laurence Raehm, Jean-Marc Kern Prof., Jean-Pierre Sauvage Dr., Christine Hamann, Serge Palacin Dr., Jean-Philippe Bourgoin, *Chem. Eur. J*., **2002**, 8, 2153–2162.
85. Weber *et al*., *Inorg. Chem*., **2003**, 42, 6780–6792.
86. Shinye Chia, Jianguo Cao, J. Fraser Stoddart Prof., Jeffrey I. Zink Prof., *Angew. Chem. Int. Ed*., **2003**, 42, 2293–2296.
87. Eugenii Katz, Oleg Lioubashevsky, Itamar Willner, *J. Am. Chem. Soc*., **2004**, 126, 15520–15532.
88. Simon R. Bayly, Thomas M. Gray, Michał J. Chmielewski, Jason J. Davis, Paul D. Beer, *Chem Commun.*, **2007**, 2234–2236.
89. Eugenii Katz Dr., Laila Sheeney-Haj-Ichia, Itamar Willner Prof., *Angew. Chem. Int. Ed*., **2004**, 43, 3292–3300.
90. Yue Bing Zheng, Ying-Wei Yang, Lasse Jensen, Lei Fang, Bala Krishna Juluri, Amar H. Flood, Paul S. Weiss, J. Fraser Stoddart, Tony Jun Huang, *Nano Lett*., **2009**, 9, 819–825.
91. Brenda Long, Kirill Nikitin, Donald Fitzmaurice, *J. Am. Chem. Soc*., **2003**, 125, 15490–15498.
92. New Challenges in Organic Electrochemistry; Tetsuo Osa *et al*., Ed.; Gordon and Breach Science Publishers, **1998**, Chapter 1.5, 99-111.
93. Kohei Uosaki, Toshihiro Kondo, Xue-Qun Zhang, Masatoshi Yanagida, *J. Am. Chem. Soc*., **1997**, 119, 8367–8368.
94. . Kondo, T. Kanai, K. Iso-o, K. Uosaki, *Z. Phys. Chem.*, **1999**, 212, 23–30.
95. Katsuyoshi Ikeda, Kenji Takahashi, Takuya Masuda, Hiromu Kobori, Masayuki Kanehara, Toshiharu Teranishi, Kohei Uosaki, *J. Phys. Chem. C*, **2012**, 116, 20806–20811.
96. Ikeda, *J. Electroanal. Chem*., **2013**, 112, 864–867.
97. T. Kondo, M. Yanagida, X.-Q. Zhang, K. Uosaki, *Chem. Lett*., **2000**, 29, 964–965.
98. Dr. Katsuyoshi Ikeda, Kenji Takahashi, Dr. Takuya Masuda, Prof. Kohei Uosaki, *Angew. Chem. Int. Ed*., **2011**, 50, 1280 –1284.
99. Toshihiro Kondo, Takashi Ito, Shu-ichi Nomura, Kohei Uosaki, Thin Solid Films, 1996, 284, 652–655.
100. Toshihiro Kondo, Masatoshi Yanagida, Shu-ichi Nomura, Takashi Ito, Kohei Uosaki, *J. Electroanal. Chem*., **1997**, 438, 121–126.

101. M. Yanagida, T. Kanai, X.-Q. Zhang, T. Kondo, K. Uosaki, *Bull. Chem. Soc. Jpn*., **1998**, 71, 2555–2559.
102. Hiroshi Imahori, Hiroko Yamada, Shinichiro Ozawa, Yoshiteru Sakata, Kiminori Ushida, *Chem. Commun*., **1999**, 1165–1166.
103. Hiroshi Imahori, Hiroyuki Norieda, Yoshinobu Nishimura, Iwao Yamazaki, Kazuo Higuchi, Naohiko Kato, Tomoyoshi Motohiro, Hiroko Yamada, Koichi Tamaki, Masatoshi Arimura, Yoshiteru Sakata, *J. Phys. Chem. B*, **2000**, 104, 1253–1260.
104. Hiroshi Imahori, Hiroyuki Norieda, Shinichiro Ozawa, Kiminori Ushida, Hiroko Yamada, Takayuki Azuma, Koichi Tamaki, Yoshiteru Sakata, *Langmuir*, **1998**, 14, 5335–5338.
105. Irina Beletskaya, Vladimir S. Tyurin, Aslan Yu. Tsivadze, Roger Guilard, Christine Stern, *Chem. Rev*., **2009**, 109, 1659–1713.
106. The Porphyrins; Dolphin, D., Ed.; Academic Press: New York, NY, USA, **1978**; Volume III.
107. The Porphyrins; Dolphin, D., Ed.; Academic Press: New York, NY, USA, **1978**; Volume V.
108. Organised Monolayers and Assemblies: Structure, Processes, and Function; Möbius, D. and Miller, R., Ed.; Elsevier: Amsterdam, **2002**.
109. Timothy D. Lash, *Eur. J. Org. Chem*., **2007**, 33, 5461–5481.
110. Rothemund, *J. Am. Chem. Soc*., **1935**, 57, 2010–2011.
111. Dr. Piotr J. Chmielewski, Prof. Dr. Lechoslaw Latos-Grażyński, Dr. Krystyna Rachlewicz, *Chem. Eur. J*., **1995**, 1, 68–73.
112. Russell H. Ball, G. D. Dorough, M. Calvin, *J. Am. Chem. Soc*., **1946**, 68, 2278–2281.
113. Roberto Paolesse, Sara Nardis, Francesco Sagone, Richard G. Khoury, *J. Org. Chem*., **2001**, 66, 550–556.
114. A. M. D'A. Rocha Gonsalves, Mariette M. Pereira, *J. Heterocyclic Chem*., **1985**, 22, 931–933.
115. R. C. Haushalter, W. M. Butler, R. W. Rudolph, *J. Am. Chem. Soc*., **1981**, 103, 2620–2627.
116. Jonathan S. Lindsey, Irwin C. Schreiman, Henry C. Hsu, Patrick C. Kearney, Anne M. Marguerettaz, *J. Org. Chem*., **1987**, 52, 827–836.
117. Alan D. Adler, Frederick R. Longo, William. Shergalis, *J. Am. Chem. Soc*., **1964**, 86, 3145–3149.
118. A. D. Alder *et al*., *J. Org. Chem*., **1967**, 32, 476.
119. Jonathan S. Lindsey, Henry C. Hsu, Irwin C. Schreiman, *Tetrahedron Lett*., **1986**, 27, 4969–4970.

120. Benjamin J. Littler, Yangzhen Ciringh, Jonathan S. Lindsey, *J. Org. Chem*., **1999**, 64, 2864–2872.
121. G. Richard Geier, Jennifer A. Riggs, Jonathan S. Lindsey, *JPP*, **2001**, 5, 681.
122. Joydev K. Laha, Savithri Dhanalekshmi, Masahiko Taniguchi, Arounaguiry Ambroise, Jonathan S. Lindsey, *Org. Process Res. Dev*., **2003**, 7, 799–812.
123. C. C. Leznoff, P. I. Svirskaya, *Angew. Chem. In. Ed*., **1978**, 12, 947.
124. Charles M. Drain, Xianchang Gong, *Chem. Commun*., **1997**, 2117–2118.
125. The Colours of Life: An Introduction to the Chemistry of the Porphyrins and Related Compounds; Milgrom, R. L., Ed.; Oxford University Press: Oxford, **1997**
126. A. Blank, T. Galili, H. Levanon, *J. Porphyrins and Phthalocyanines*, **2001**, 5, 58-66.
127. Diane Marsh, Larry Mink, *J. Chem. Educ*., **1996**, 73, 1188.
128. Alsoph H. Corwin, Arthur B. Chivvis, Robert W. Poor, David G. Whitten, Earl Wayne Baker, *J. Am. Chem. Soc*., **1968**, 90, 6577–6583.
129. Yves Le Mest, Maurice L'Her, Neil H. Hendricks, Kimoon Kim, James P. Collman, *Inorg. Chem*., **1992**, 31, 835–847.
130. M. Gouterman, *J. Chem. Phys*., **1959**, 30, 1139–1161.
131. Martin Goutermam, *J. Mol. Spectrosc*., **1961**, 6, 138–163.
132. The Porphyrins; Dolphin, D., Ed.; Academic Press: New York, NY, USA, **1978**; Volume III, 1–165.
133. P. J. Spellane, M. Gouterman, A. Antipas, S. Kim, Y. C. Liu, *Inorg. Chem*., **1980**, 19, 386 –391.
134. A. Ceulemans, W. Oldenhof, C. Gorller-Walrand, L. G. Vanquickenborne, *J. Am. Chem. Soc*., **1986**, 108, 1155–1163.
135. Martin Gouterman, Georges H. Wagnière, Lawrence C. Snyder, *J. Mol. Spectrosc*., **1963**, 11, 108–127.
136. Charles Weiss, Hiroshi Kobayashi, Martin Gouterman, *J. Mol. Spectrosc*., **1965**, 16, 415–450.
137. S. C. Mathur, J. Singh, H. Kumar, *Phys. Status Solidi B*, **1971**, 48, 843–849.
138. E. J. Baerends, G. Ricciardi, A Rosa, S. J. A. van Gisbergen, *Coord. Chem. Rev*., **2002**, 230, 5–27.
139. Mathias O. Senge, Aoife A. Ryan, Kristie A. Letchford, Stuart A. MacGowan, Tamara Mielke, *Symmetry*, **2014**, 6, 781–843.
140. Jordan A. Greco, Sumie Shima, Nicole L. Wagner, Jason R. McCarthy, Karissa Atticks, Christian Brückner, Robert R. Birge, *J. Phys. Chem. C*., **2015**, 119, 3711–3724.

141. Y. Sakata, H. Imahori, H. Tsue, Suguru Higashida, T. Akiyama, Eiichi Yoshizawa, Masanori Aoki, Koji Yamada, Kiyoshi Hagiwara, S. Taniguchi and T. Okada, *Pure & Appl. Chem.*, **1997**, 69, 1951–1956.
142. Yoshiteru Sakata, Hiroshi Imahori, Ken-Ichi Sugiura, *J. Incl. Phenom. Macrocycl. Chem*., **2001**, 41, 31–36.
143. J. Deisenhofer, O. Epp, K. Miki, R. Huber, H. Michel, *J. Mol. Biol*., **1994**, 180, 385–398.
144. Hiroshi Imahori, Shinichiro Ozawa, Kiminori Ushida, Masao Takahashi, Takayuki Azuma, Anawat Ajavakom, Tsuyoshi Akiyama, Masato Hasegawa, Seiji Taniguchi, Tadashi Okada, Yoshiteru Sakata, *Bull. Chem. Soc. Jpn*., **1999**, 72, 485–505.
145. N. E. Geacintov, J. Breton, *Crit. Rev. Plant Sci*., **1987**, 5, 1–44.
146. Atula S.D. Sandanayaka, Hisahiro Sasabe, Toshikazu Takata, Osamu Ito, *J. Photochem. Photobiol. C: Photochem. Rev*., **2010**, 11, 73–92.
147. J. Deisenhofer *et al.*, The Photosynthetic Reaction Centre, Academic Press, San Diego, **1993**.
148. Blankenshi *et al.*, Anoxygenic Photosynthetic Bacteria, Kluwer Academic Publishing, Dordrecht, **1995**.
149. G. McDermott, S. M. Prince, A. A. Freer, A. M. Hawthornthwaite-Lawless, M. Z. Papiz, R. J. Cogdel, N. W. Isaacs, *Nature*, **1995**, 374, 517–521.
150. John M. Olson, *Photochem. Photobiol*., **1998**, 67, 61–75.
151. A. Zouni, H. T. Witt, P. Fromme, N. Krauss, W. Saenger, P. Orth, *Nature*, **2001**, 409, 739–743.
152. Hiroshi Imahori Prof. Dr., Makoto Kimura, Kohei Hosomizu, Tomoo Sato Dr., Tae Kyu Ahn, Seong Keun Kim Prof. Dr., Dongho Kim Prof. Dr., Yoshinobu Nishimura Dr., Iwao Yamazaki Prof. Dr., Yasuyuki Araki Dr., Osamu Ito Prof. Dr., Shunichi Fukuzumi Prof. Dr., *Chem. Eur. J*., **2004**, 10, 5111–5122.
153. Hiroshi Imahori, Mohamed E. El-Khouly, Mamoru Fujitsuka, Osamu Ito, Yoshiteru Sakata, Shunichi Fukuzumi, *J. Phys. Chem. A*, **2001**, 105, 325–332.
154. Mohamed E. El-Khouly, Osamu Ito, Phillip M. Smith, Francis D'Souza, *J. Photochem. Photobiol. C: Photochem. Rev*., **2004**, 5, 79–104.
155. Hiroko Yamada, Hiroshi Imahori, Yoshinobu Nishimura, Iwao Yamazaki, Tae Kyu Ahn, Seong Keun Kim, Dongho Kim, Shunichi Fukuzumi, *J. Am. Chem. Soc*., **2003**, 125, 9129–9139.
156. Hiroshi Imahori, Yukiyasu Kashiwagi, Taku Hasobe, Makoto Kimura, Takeshi Hanada, Yoshinobu Nishimura, Iwao Yamazaki, Yasuyuki Araki, Osamu Ito, Shunichi Fukuzumi, *Thin Solid Films*, **2004**, 451, 580–588.

157. Mitsuhiko Morisue, Dipak Kalita, Noriko Haruta, Yoshiaki Kobuke, *Chem. Commun*., **2007**, 2348–2350.
158. Deisenhofer, O. Epp, K. Miki, R. Huber, H. Michel, *J. Mol. Biol*., **1984**, 180, 385–398.
159. Lee, *J. Organomet. Chem*., **2014**, 261, 20–27.
160. Imahori Hiroshi, Hagiwara Kiyoshi, Akiyama Tsuyoshi, Aoki Masanori, Taniguchi Seiji, Okada Tadashi, Shirakawa Masahiro, Sakata Yoshiteru, *Chem. Phys. Lett*., **1996**, 263, 545.
161. Shunsuke Sakai, Tomoyasu Noji, Masaharu Kondo, Toshihisa Mizuno, Takehisa Dewa, Tsuyoshi Ochiai, Hisanori Yamakawa, Shigeru Itoh, Hideki Hashimoto, Mamoru Nango, *Langmuir*, **2013**, 29, 5104–5109.
162. Rudolph A. Marcus, *J. Chem. Phys*., **1956**, 24, 966–978.
163. Rudolph A. Marcus, Norman Sutin, *Biochim. Biophys. Acta*, **1985**, 811, 265–322.
164. Prof. Dr. Rudolph A. Marcus, *Angew. Chem. Int. Ed*., **1993**, 32, 1111–1121.
165. Rudolph A. Marcus, *J. Phys. Chem*., **1968**, 72, 891–899.
166. Rudolph A. Marcus, *Rev. Mod. Phys*., **1993**, 65, 599–610.
167. Electron Transfer Theories in Solar Energy Conversion: Chemical Aspects; Likhtenshtein, Ed.; Wiley-VCH Verlag GmbH & Co. KGaA, Weinheim, Germany, **2012**.
168. Gamov *et al*., *Quanum Theo. Atoms Phys*., **1926**, 51, 204–212.
169. N. S. Hush, *J. Chem. Phys*., **1958**, 28, 962–972.
170. Prof. Dr. Henry Taube, *Angew. Chem. Int. Ed*., **1984**, 23, 329–339.
171. Prof. Dr. Robert Huber, *Angew. Chem. Int. Ed*., **1989**, 28, 848–869.
172. Prof. Dr. Johann Deisenhofer, Prof. Dr. Hartmut Michel, *Angew. Chem. Int. Ed*., **1989**, 28, 829–847.
173. Physical Chemistry; Atkins *et al*., Ed.; W.H. Freeman and Company, New York, NY, **2001**; 7th Edition, 1015–1018.
174. New Challenges in Organic Electrochemistry; Tetsuo Osa *et al.*, Ed.; Gordon and Breach Science Publishers, **1998**, Chapter 1.5, 99-111.
175. Hiroshi Imahori, Hiroyuki Norieda, Yoshinobu Nishimura, Iwao Yamazaki, Kazuo Higuchi, Naohiko Kato, Tomoyoshi Motohiro, Hiroko Yamada, Koichi Tamaki, Masatoshi Arimura, Yoshiteru Sakata, *J. Phys. Chem. B*, **2000**, 104, 1253–1260.
176. Hiroshi Imahori, Hiroyuki Norieda, Shinichiro Ozawa, Kiminori Ushida, Hiroko Yamada, Takayuki Azuma, Koichi Tamaki, Yoshiteru Sakata, *Langmuir*, **1998**, 14, 5335–5338.
177. Hiroshi Imahori, Taku Hasobe, Hiroko Yamada, Yoshinobu Nishimura, Iwao Yamazaki, Shunichi Fukuzumi, *Langmuir*, **2001**, 17, 4925–4931.

178. Kohei Uosaki, Toshihiro Kondo, Xue-Qun Zhang, Masatoshi Yanagida, *J. Am. Chem. Soc*., **1997**, 119, 8367–8368.
179. T. Kondo, T. Kanai, K. Isoo, K. Uosaki, *Z. Phys. Chem.*, **1999**, 212, 23-30.
180. Katsuyoshi Ikeda, Kenji Takahashi, Takuya Masuda, Hiromu Kobori, Masayuki Kanehara, Toshiharu Teranishi, Kohei Uosaki, *J. Phys. Chem. C*, **2012**, 116, 20806–20811.
181. Ikeda, *J. Electroanal. Chem*., **2013**, 112, 864–867.
182. Tzuriel Simcha Metzger, Ran Tel-Vered, Hendrik Bauke Albada, Itamar Willner, *Adv. Funct. Mater*., **2015**, 25, 6470–6477.
183. Dr. Katsuyoshi Ikeda, Kenji Takahashi, Dr. Takuya Masuda, Prof. Kohei Uosaki, *Angew. Chem. Int. Ed*., **2011**, 50, 1280 –1284.
184. T. Kondo, M. Yanagida, X.-Q. Zhang, K. Uosaki, *Chem. Lett*., **2000**, 29, 964–965.
185. Hiroshi Imahori, Hiroyuki Norieda, Hiroko Yamada, Yoshinobu Nishimura, Iwao Yamazaki, Yoshiteru Sakata, Shunichi Fukuzumi, *J. Am. Chem. Soc*., **2001**, 123, 100–110.
186. Lucia Flamigni, *J. Photochem. Photobiol. C: Photochem. Re*v., **2007**, 8, 191–210.
187. Tzuriel S. Metzger, Ran Tel-Vered, Itamar Willner, *Small*, **2016**, 12, 1605–1614.
188. Benjamin Vonhoeren, Simon Dalgleish, Laigui Hu, Michio M. Matsushita, Kunio Awaga, Bart Jan Ravoo, *ACS Appl. Mater. Interfaces*, **2015**, 7, 7049−7053.
189. Dr. Andrea Vecchi, Nathan R. Erickson, Jared R. Sabin, Prof. Barbara Floris, Prof. Valeria Conte, Prof. Mariano Venanzi, Dr. Pierluca Galloni, Prof. Victor N. Nemykin, *Chem. Eur. J*., **2015**, 21, 269–279.
190. Hiroshi Imahori, Hiroko Yamada, Shinichiro Ozawa, Yoshiteru Sakata, Kiminori Ushida, *Chem. Commun*., **1999**, 1165–1166.
191. Hirotaka Uji, Yuji Yatsunami, Shunsaku Kimura, *J. Phys. Chem. C*, **2015**, 119, 8054–8061.
192. Hiroko Yamada, Hiroshi Imahori, Shunichi Fukuzumi, *J. Mater. Chem*., **2002**, 12, 2034–2040.
193. Toshihiro Kondo, Takashi Ito, Shu-ichi Nomura, Kohei Uosaki, *Thin Solid Films*, **1996**, 284, 652–655.
194. Toshihiro Kondo, Masatoshi Yanagida, Shu-ichi Nomura, Takashi Ito, Kohei Uosaki, *J. Electroanal. Chem*., **1997**, 438, 121–126.
195. Hirotaka Uji, Kazuyoshi Tanaka, Shunsaku Kimura, *J. Phys. Chem. C*, **201**6, 120, 3684–3689.
196. Dr. Alexander S. Konev, Prof. Alexander F. Khlebnikov, Dr. Oleg V. Levin, Daniil A. Lukyanov, Dr. Ivan M. Zorin, *ChemSusChem*, **2016**, 9, 676 –686.

197. Masatoshi Yanagida, Toshihito Kanai, Xue-Qun Zhang, Toshihiro Kondo, Kohei Uosaki, *Bull. Chem. Soc. Jpn*., **1998**, 71, 2555–2559.
198. Christopher E. D. Chidsey, *Science*, **1991**, 251, 919–922.
199. P. Seta, E. Bienvenue, A. L. Moore, P. Mathis, R. V. Bensasson, P. Liddel, P. J. Pessiki, A. Joy, T. A. Moore, D. Gust, *Nature*, **1985**, 316, 653–655.
200. Sakata, *Chem. Lett.*, **1988**, 1625–1628.
201. Masamichi Fujihira, *Mol. Cryst. Liq. Cryst.*, **1990**, 183, 59–69.
202. M. Fujihira, K. Nishiyama, H. Yamada, *Thin Solid Films*, **1985**, 132, 77–82.
203. M. Fujihira, H. Yamada, *Thin Solid Films* **1988**, 160, 125–132.
204. G. Steinberg-Yfrach, R. L. Rigaud, E. N. Durantini, A. L. Moore, D. Gust, T. A. Moore, *Nature*, **1998**, 392, 479–482.
205. Gennady V. Oshovsky Dr. Dr., David N. Reinhoudt Prof. Dr. Ir., Willem Verboom Dr., *Angew. Chem. Int. Ed.*, **2007**, 46, 2366–2393.
206. W. A. Freeman, W. L. Mock, N. Y. Shih, *J. Am. Chem. Soc*., **1981**, 103, 7367-7368.
207. Jaheon Kim, In-Sun Jung, Soo-Young Kim, Eunsung Lee, Jin-Koo Kang, Shigeru Sakamoto, Kentaro Yamaguchi, Kimoon Kim, *J. Am. Chem. Soc*., **2000**, 122, 540-541.
208. F. Pichierri, *Chem. Phys. Lett.*, **2004**, 390, 214-219.
209. Kimoon Kim, Narayanan Selvapalam, Young Ho Ko, Kyeng Min Park, Dongwoo Kim, Jeeyeon Kim, *Chem. Soc. Rev*., **2007**, 36, 267-279.
210. R. Behrend, E. Meyer, F. Rusche, *Justus Liebigs Ann. Chem*., **1905**, 339, 1–37.
211. Jae Wook Lee, S. Samal, N. Selvapalam, Hee-Joon Kim, Kimoon Kim, *Acc. Chem. Res*., **2003**, 36, 621-630.
212. Jason Lagona, Pritam Mukhopadhyay Dr., Sriparna Chakrabarti Dr., Lyle Isaacs Prof. Dr., *Angew. Chem. Int. Ed*, **2005**, 44, 4844-4870.
213. Steven J. Barrow, Setu Kasera, Matthew J. Rowland, Jesús del Barrio, Oren A. Scherman, *Chem. Rev*., **2015**, 115, 12320-12406.
214. Sharon Hannah, Vincent M. Lynch, Nikolay Gerasimchuk, Darren Magda, Jonathan L. Sessler, *Org. Lett*., **2003**, 3, 3911-3914.
215. Khaleel I. Assaf, Werner M. Nau, *Chem. Soc. Rev*., **2015**, 44, 394-418.
216. Hans-Jürgen Buschmann, Ernst Cleve, Klaus Jansen, Andreas Wego, Eckhard Schollmeyer, *Mater. Sci. Eng., C*, **2001**, 14, 35-39.
217. H.-J. Buschmann, K. Jansen, C. Meschke, E. Schollmeyer, *J. Solution Chem.*, **1998**, 27, 135-140.
218. K. Jansen, H.-J. Buschmann, A. Wego, D. Döpp, C. Mayer, H.-J. Drexler, H.-J. Holdt, E. Schollmeyer, *J. Incl. Phenom. Macrocycl. Chem.*, **2001**, 39, 357-363.
219. Galit Parvari, Ofer Reany, Ehud Keinan, *Isr. J. Chem.*, **2011**, 51, 646-663.

220. Prof. Jean-Marie Lehn, *Angew. Chem. Int. Ed.*, **1988**, 27, 89-112.

221. H. J. Buschmann, L. Mutihac, E. Schollmeyer, *J. Incl. Phenom. Macrocycl. Chem*., **2005**, 53, 85–88.

222. Mikhail V. Rekharsky, Young Ho Ko, N. Selvapalam, Kimoon Kim, Yoshihisa Inoue, *Supramol. Chem*., **2007**, 19, 39–46.

223. Hyung-Kun Lee, Kyeng Min Park, Young Jin Jeon, Dongwoo Kim, Dong Hyun Oh, Hyung Seok Kim, Chan Kyung Park, Kimoon Kim, *J. Am Chem. Soc*., **2005**, 127, 5006-5007.

224. Mikhail V. Rekharsky, Hatsuo Yamamura, Masao Kawai, Issey Osaka, Ryuichi Arakawa, Akihiro Sato, Young Ho Ko, N. Selvapalam, Kimoon Kim, Yoshihisa Inoue, *Org. Lett*., **2006**, 8, 815-818.

225. You-Moon Jeon, Dongmok Whang, Jaheon Kim, Kimoon Kim, *Chem. Lett*., **1996**, 25, 503-504.

226. Kyungpil Kim, Woo Sung Jeon, Jin-Koo Kang, Jae Wook Lee Dr., Sang Yong Jon Dr., Taisun Kim Prof. Dr., Kimoon Kim Prof. Dr., *Angew. Chem. Int. Ed*., **2003**, 42, 2293-2296.

227. Jeonghan Kim, Youngkook Kim, Kangkyun Baek, Young Ho Ko, Dongwoo Kim, Kimoon Kim, *Tetrahedron*, **2008**, 64, 8389-8393.

228. Kimoon Kim, *Chem. Soc. Rev*., **2002**, 31, 96-107.

229. Woo Sung Jeon, Kwangyul Moon, Sang Hyun Park, Hyungpil Chun, Young Ho Ko, Jin Yong Lee, Eun Sung Lee, S. Samal, N. Selvapalam, Mikhail V. Rekharsky, Vladimir Sindelar, David Sobransingh, Yoshihisa Inoue, Angel E. Kaifer, Kimoon Kim, *J. Am. Chem. Soc*., **2005**, 127, 12984-12989.

230. Lu Cui, Suresh Gadde, Wei Li, Angel E. Kaifer, *Langmuir*, **2009**, 25, 13763-13769.

231. Wei Wang, Angel E. Kaifer, *Supramol. Chem.*, **2010**, 22, 710-716.

232. Jae Wook Lee, S. Samal, N. Selvapalam, Hee-Joon Kim, Kimoon Kim, *Acc. Chem. Res*., **2003**, 36, 621-630.

233. Kimoon Kim, N. Selvapalam, Dong Hyun Oh, *J. Incl. Phenom. Macrocycl. Chem.*, **2004**, 50, 31-36.

234. Frank Biedermann, Oren A. Scherman, *J. Phys. Chem. B.*, **2012**, 116, 2842-2849.

235. Woo Sung Jeon, Hee-Joon Kim, Chongmok Lee, Kimoon Kim, *Chem. Commun.*, **2002**, 38, 1828-1829.

236. Hee-Joon Kim Dr., Jungseok Heo, Woo Sung Jeon, Eunsung Lee, Jaheon Kim Dr., Shigeru Sakamoto, Kentaro Yamaguchi Prof. Dr., Kimoon Kim Prof. Dr., *Angew. Chem. Int. Ed*., **2001**, 40, 1526-1529.

237. Young Ho Ko, Kyungpil Kim, Jin-Koo Kang, Hyungphil Chun, Jae Wook Lee, Shigeru Sakamoto, Kentaro Yamaguchi, James C. Fettinger, Kimoon Kim, *J. Am. Chem. Soc*., **2004**, 126, 1932-1933.

238. Young Ho Ko, Kyungpil Kim, Eunju Kim, Kimoon Kim, *Supramol. Chem.*, **2007**, 19, 287-293.

239. Tadashi Mori, Young Ho Ko, Kimoon Kim, Yoshihisa Inoue, *J. Org. Chem*., **2006**, 71, 3232-3247.

240. Tian *et al*., *Nat. Commun*., **2012**, 3, 1-8.

241. Werner M. Nau, Mara Florea, Khaleel I. Assaf, *Isr. J. Chem.*, **2011**, 51, 559-577.

242. Todd P. Silverstein, *J. Chem. Educ*., **1998**, 75, 116.

243. Prof. Donald J. Cram, *Angew. Chem. Int. Ed.*, **1988**, 27, 1009-1020.

244. Dale K. Cabbiness, Dale W. Margerum, *J. Am. Chem. Soc.*, **1969**, 91, 6540-6541.

245. Eric Masson, Xiaoxi Ling, Roymon Joseph, Lawrence Kyeremeh-Mensah, Xiaoyong Lu, *RSC Adv*., **2012**, 2, 1213-1247.

246. K. N. Houk Prof. Dr., Andrew G. Leach Dr., Susanna P. Kim, Xiyun Zhang, *Angew. Chem. Int. Ed.*, **2003**, 42, 4872-4897.

247. László Biczók, Véronique Wintgens, Zsombor Miskolczy, Mónika Megyesi, *Isr. J. Chem.*, **2011**, 51, 625-633.

248. Mónika Megyesi, László Biczók, István Jablonkai, *J. Phys. Chem. C*, **2008**, 112, 3410-3416.

249. Saleh *et al*., *J. FLUORESC.*, **2006**, 16, 487-493.

250. William L. Mock, John Pierpont, *J. Chem. Soc. Chem. Comm.*, **1990**, 1509-1511.

251. Sarah Angelos, Niveen M. Khashab, Ying-Wei Yang, Ali Trabolsi, Hussam A. Khatib, J. Fraser Stoddart, Jeffrey I. Zink, *J. Am. Chem. Soc.*, **2009**, 131, 12912-12914.

252. Vladimir Sindelar, Serena Silvi, Angel E. Kaifer, *Chem. Commun.*, **2006**, 2185-2187.

253. V. Sindelar, S. Silvi, S. E. Parker, D. Sobransingh, A. E. Kaifer, *Adv. Funct. Mater*., **2007**, 17, 694-701.

254. Mona A. Gamal-Eldin, Donal H. Macartney, *Org. Biomol. Chem*., **2013**, 11, 1234-1241.

255. Kimoon Kim, Narayanan Selvapalam, Young Ho Ko, Kyeng Min Park, Dongwoo Kim, Jeeyeon Kim, *Chem. Soc. Rev.*, **2007**, 36, 267-279.

256. Mahesh Pattabiraman, Arunkumar Natarajan, Raja Kaliappan, Joel T. Mague, V. Ramamurthy, *Chem. Commun.*, **2005**, 4542-4544.

257. Liulin Yang, Hui Yang, Fei Li, Xi Zhang, *Langmuir*, **2013**, 29, 12375-12379.

258. Sanem Senler, Lu Cui, Ana Michelle Broomes, Erika L. Smith, James N. Wilson, Angel E. Kaifer, *J. Phys. Org. Chem*., **2012**, 25, 592–596.

259. Vladimir Sindelar Dr., Mabel A. Cejas Dr., Françisco M. Raymo Prof., Weizhong Chen, Samantha E. Parker, Angel E. Kaifer Prof., *Chem. Eur. J*., **2005**, 11, 7054-7059.

260. Urs Rauwald, Frank Biedermann, Stéphanie Deroo, Carol V. Robinson, Oren A. Scherman, *J. Phys. Chem. B*, **2010**, 114, 8606–8615.

261. Issey Osaka, Masanobu Kondou, Narayanan Selvapalam, Shashadhar Samal, Kimoon Kim, Mikhail V. Rekharsky, Yoshihisa Inoue, Ryuichi Arakawa, *J. Mass Spectrum*, **2006**, 41, 202-207.

262. Robert S. Mulliken, *J. Am. Chem. Soc.*, **1950**, 72, 600-608.

263. Sung Im Jun, Jae Wook Lee, Shigeru Sakamoto, Kentaro Yamaguchi, Kimoon Kim, *Tetrahedron Lett*., **2000**, 41, 471-475.

264. Sarah Angelos, Ying-Wei Yang, Niveen M. Khashab, J. Fraser Stoddart, Jeffrey I. Zink, *J. Am. Chem. Soc*., **2009**, 131, 11344-11346.

265. Ning Ma, Wen-Jing Wang, Si Chen, Xiao-Shuang Wang, Xiao-Qiang Wang, Shi-Bo Wang, Jing-Yi Zhu, Si-Xue Cheng, Xian-Zheng Zhang, *Chem. Commun*., **2015**, 51, 12970-12973.

266. Kyeng Min Park, Kyungwon Suh, Hyuntae Jung, Don-Wook Lee, Youngjoo Ahn, Jeeyeon Kim, Kangkyun Baek, Kimoon Kim, *Chem. Commun*., **2009**, 71-73.

267. Carmen Stoffelen, Dr. Jens Voskuhl, Prof. Dr. Pascal Jonkheijm, Prof. Dr. Jurriaan Huskens, *Angew. Chem. Int. Ed*., **2014**, 53, 3400-3404.

268. Yang Lan, Yuchao Wu, Dr. Athan Karas, Prof. Oren A. Scherman, *Angew. Chem. Int. Ed*., **2014**, 53, 2166-2169.

269. Sarah Angelos, Niveen M. Khashab, Ying-Wei Yang, Ali Trabolsi, Hussam A. Khatib, J. Fraser Stoddart, Jeffrey I. Zink, *J. Am. Chem. Soc*., **2009**, 131, 12912-12914.

270. Samuel T. Jones, Jameel M. Zayed, Oren A. Scherman, *Nanoscale*, **2013**, 5, 5299-5302.

271. Carmen Stoffelen, Jurriaan Huskens, *Chem. Commun*., **2013**, 49, 6740-6742.

272. María del Pozo, Pedro Hernández, Lucas Hernández, Carmen Quintana, *J. Mater. Chem*., **2011**, 21, 13657-13663.

273. Frank Biedermann, Urs Rauwald, Dr. Monika Cziferszky, Dr. Kyle A. Williams, Lauren D. Gann, Bi Y. Guo, Prof. Adam R. Urbach, Prof. Christopher W. Bielawski, Dr. Oren A. Scherman, *Chem. Eur. J*., **2010**, 16, 13716-13722.

274. Matthew A. Rankin, Brian D. Wagner, *Supramol. Chem.*, **2004**, 16, 513-519.

275. Yonghua Ling, Wei Wang, Angel E. Kaifer, *Chem. Commun*., **2007**, 610-612.

276. Omar A. Ali, Eric M. Olson, Adam R. Urbach, *Supramol. Chem.*, **2013**, 25, 863-868.

277. Shrikrishnan Sankaran, Mark de Ruiter, Jeroen J. L. M. Cornelissen, Pascal Jonkheijm, *Bioconjugate Chem*., **2015**, 26, 1972-1980.

278. Arántzazu González-Campo, Melanie Brasch, Dana A. Uhlenheuer, Alberto Gómez-Casado, Lanti Yang, Luc Brunsveld, Jurriaan Huskens, Pascal Jonkheijm, *Langmuir*, **2012**, 28, 16364-16371.

279. Jin Geng, Frank Biedermann, Jameel M. Zayed, Feng Tian, Oren A. Scherman, *Macromolecules*, **2011**, 44, 4276-4281.

280. Chi Hu, Yang Lan, Feng Tian, Kevin R. West, Oren A. Scherman, *Langmuir*, **2014**, 30, 10926-10932.

281. Chi Hu, Feng Tian, Yu Zheng, Cindy Soo Yun Tan, Kevin R. West, Oren A. Scherman, *Chem. Sci*., **2015**, 6, 5303-5310.

282. Chi Hu, Yang Lan, Kevin R. West, Oren A. Scherman, *Adv. Mater*., **2015**, 27, 7957-7962.

283. Wei Zhu, Chen Wang, Weina Li, Cheng-an Tao, Jiecheng Cui, Haowei Yang, Yin Jiang, Guangtao Li, *J. Mater. Chem. A*, **2013**, 1, 11741-11747.

284. Wei Zhu, Weina Li, Chen Wang, Jiecheng Cui, Haowei Yang, Yin Jiang, Guangtao Li, *Chem. Sci*., **2013**, 4, 3583-3590.

285. Chi Hu, Yu Zheng, Ziyi Yu, Chris Abell, Oren A. Scherman, *Chem. Commun*., **2015**, 51, 4858-5860.

286. Dan-dan Li, Ke-feng Ren, Hao Chang, Hai-bo Wang, Jin-lei Wang, Chao-jian Chen, Jian Ji, *Langmuir*, **2013**, 29, 14101-14107.

287. Feng Tian, Monika Cziferszky, Dezhi Jiao, Karolina Wahlström, Jin Geng, Oren A. Scherman, *Langmuir*, **2011**, 27, 1387-1390.

288. Shrikrishnan Sankaran, Jasper van Weerd, Jens Voskuhl, Marcel Karperien, Pascal Jonkheijm, *Small*, **2015**, 11, 6187-6196.

289. Debapratim Das, Oren A. Scherman, *Isr. J. Chem*., **2011**, 51, 537-550.

290. Hui Yang, Bin Yuan, Xi Zhang, *Acc. Chem. Res*., **2014**, 47, 2106-2115.

291. You-Moon Jeon, Jaheon Kim, Dongmok Whang, Kimoon Kim, *J. Am. Chem. Soc*., **1996**, 118, 9790-9791.

292. Henri B. Kagan, *Chem. Rev.*, **2002**, 102, 1805-1806.

293. A. Thibonn, V. C. Pierre, *Anal. Bioanal. Chem.*, **2009**, 394, 107-120.

294. R. Weissleder, V. Ntziachristos, *Nat Med*, **2003**, 9, 123-128.

295. Robert Pal, David Parker, Leslie C. Costello, *Org. Biomol. Chem.*, **2009**, 7, 1525-1528.

296. C. P. Collier, E. W. Wong, M. Belohradsky, F. M. Raymo, J. F. Stoddart, P. J. Kuekes, R. S. Williams, J. R. Heath, *Science*, **1999**, 285, 391-394.

297. A. H. Flood, J. F. Stoddart, D. W. Steuerman, J. R. Heath, *Science*, **2004**, 306, 2055-2056.

298. J. L. Kropp, M. W. Windsor, *J. Chem. Phys.*, **1965**, 42, 1599-1608.

299. David Parker, Rachel S. Dickins, Horst Puschmann, Clare Crossland, Judith A. K. Howard, *Chem. Rev.*, **2002**, 102, 1977-2010.

300. Joshua Lehr, Paul D. Beer, Stephen Faulkner, Jason J. Davis, *Chem. Commun.*, **2014**, 50, 5678-5687.

301. S. I. Weissman, *J. Chem. Phys*., **1942**, 10, 214-217.

302. A. Thibonn, V. C. Pierre, *Anal. Bioanal. Chem.*, **2009**, 394, 107-120.

303. Niamh S. Murray, Suzi P. Jarvis, Thorfinnur Gunnlaugsson, *Chem. Commun*., **2009**, 4959-4961.
304. D.L Dexter, *J. Chem. Phys*., **1953**, 21, 836–850.
305. Turro *et al*., Principles of Molecular Photochemistry, University Science Books, **2009**.
306. T. Förster, *Radiation Research Supplement*, **1960**, 2, 326-339.
307. Theodore Lazarides Dr., Daniel Sykes Dr., Stephen Faulkner Prof., Andrea Barbieri Dr., Michael D. Ward Prof., *Chem. Eur. J*, **2008**, 14, 9389-9399.
308. M. F. Loncin, J. F. Desreux, E. Merciny, *J. Inorg. Chem*., **1986**, 25, 2646-2648.
309. W. P. Cacheris, S. K. Nickle, A. D. Sherry, *J. Inorg. Chem*., **1987**, 26, 958-960.
310. J. L. Kropp, M. W. Windsor, *J. Chem. Phys*., **1963**, 39, 2769-2770.
311. G. P. Gurinovich, A. N. Sevchenko, K. N. Solov'ev, *Phys. Usp*., **2005**, 48, 231-253.
312. Yao-Feng Yuan, Thomas Cardinaels, Kyra Lunstroot, Kristof Van Hecke, Luc Van Meervelt, Christiane Görller-Walrand, Koen Binnemans, Peter Nockemann, *J. Inorg. Chem*., **2007**, 46, 5302-5309.
313. Stephen I. Klink, Henk Keizer, Hans W. Hofstraat, Frank C.J.M. van Veggel, *Synt. Met*., **2002**, 127, 213-216.
314. Andrew Beeby, Stephen Faulkner, J. A. Gareth Williams, *J. Chem. Soc., Dalton Trans*., **2002**, 1918-1922.
315. Manuel Tropiano, Nathan L. Kilah, Michael Morten, Habibur Rahman, Jason J. Davis, Paul D. Beer, Stephen Faulkner, *J. Am. Chem. Soc*., **2011**, 133, 11847-11849.
316. Joshua Lehr, Manuel Tropiano, Paul D. Beer, Stephen Faulkner, Jason J. Davis, *Chem. Commun*., **2015**, 51, 6515-6517.

## List of Figures

**Figure 1.** A schematic representation of a [2]rotaxane, a [3]rotaxane, and a [2]pseudorotaxane. Figure reproduced with permission from reference [1].

**Figure 2.** Mapping anion-induced molecular motion (translocation) *via* functionalisation of either the thread component (**Top**) or the macrocyclic motif (**Bottom**). Figure reproduced with permission from reference [33].

**Figure 3.** A schematic representation highlighting translocation of the ring component, from molecular station A (**Orange**) to molecular station B (**Pink**), in order to bring about the formation of the metastable state co-conformation (MSCC) from the ground state co-conformation (GSCC).

**Figure 4.** Photochemically induced switching within a bistable, [2]rotaxane. Photo-induced oxidation of the Cu(I) centre, to Cu(II), brings about translocation of the macrocyclic motif from the bidentate phen binding unit (GSCC), to the terdentate terpy binding unit (MSCC). This process is reversed upon chemical reduction of the Cu(II) centre. Figure reproduced with permission from reference [66].

**Figure 5.** Photochemically inducing the translocation of α-CD within an azobenzene-containing rotaxane. λ denotes wavelength of irradiation. Figure reproduced with permission from reference [67].

**Figure 6.** Smith's reversible optical chloride sensor. Upon the addition of chloride, the squaraine dye is displaced and / or the tetralactam macrocycle translocates to either of the triazole units present within the axle component. As a result, the fluorescence intensity of the dye

recovers; the non-covalent encapsulation of squaraine dyes, within the cavity of tetralactam macrocycles, has been shown to bring about a three-fold decrease in quantum yield. Figure reproduced with permission from references [68] and [69].

**Figure 7.** Anion-induced molecular shuttling within a [2]rotaxane synthesised by the group of Professor Paul Beer. Upon the addition of chloride, the macrocycle was observed to migrate to the axle's bis-imidazolium molecular station. Figure reproduced with permission from reference [70].

**Figure 8.** Electrochemically-induced translocation of a redox-active, cyclophane motif within a surface-tethered molecular architecture. The rate of interfacial electron transfer ($K_{et}$) could be used to gauge in which state (GSCC or MSCC) the system was residing. Figure reproduced with permission from reference [82].

**Figure 9.** Utilising the translocation of a $CBPQT^{4+}$ ring to mediate the electron transfer process within a novel supramolecular configuration for the bioelectrocatalysed activation of enzymes, thereby reducing the overpotential required for the electrocatalytic oxidation of glucose. $\mathbf{e}^-$ denotes the movement of an electron. Figure reproduced with permission from reference [84].

**Figure 10.** The immobilisation of a tripodal [2]rotaxane on the surface of a titanium dioxide nanoparticle. Figure reproduced with permission from reference [86].

**Figure 11.** Stoddart's photoactive, molecular triad, consisting of a disulphide tether, an electron-accepting buckminsterfullerene ($C_{60}$) unit, a chromophoric porphyrin unit, and an electron-donating TTF unit. Figure reproduced with permission from reference [73].

**Figure 12.** A schematic representation highlighting how the group of Stoddart utilised the electrical energy generated, from a molecular triad, to drive the dethreading of [2]pseudorotaxane present in solution. The [2]pseudorotaxane was formed upon the encapsulation of BHEEN within the cavity of a $CBPQT^{4+}$ cyclophane. Upon photo-excitation of the porphyrin unit (413 nm), photoinduced, vectorial electron transfer (PET) to the $C_{60}$ stopper was induced, resulting in a charge shift to the TTF component. Charge neutralisation then followed, prior to the electron being transferred to the [2]pseudorotaxane, which in turn led to the dethreading of the reduced $CBPQT^{3.+}$ cyclophane. The electron was then transferred to the Pt counter electrode. $\mathbf{E_{ap}}$ denotes applied potential (V), $\mathbf{e}^-$ the movement of an electron, and ***hv*** photoirradiation of the system. Figure reproduced with permission from reference [74].

**Figure 13.** A schematic representation of the envisaged artificial, photosynthetic molecular machine, constructed on Au. The magnitude of the cathodic photocurrent density generated at each molecular station, upon photoexcitation of the porphyrin stopper, should vary (Section 1.9). The generation of cathodic photocurrent density is likely to be most efficient at molecular station A, due to the fact that the rate of back electron transfer, from the excited state of the porphyrinic macrocycle (P*) to ferrocenium ($Fc^+$) and Au, will be reduced to a greater extent than the forward rate of electron transfer, from ferrocene (Fc) to P*.[87-96] $\mathbf{MV^{2+}}$: Methyl Viologen. ***hv***: Photoirradiation. $\mathbf{e}^-$: Electron.

**Figure 14.** The Rothemund Condensation; the thermal condensation of aldehydes with pyrroles. Porphine (**Right**), the fundamental ring structure of four covalently-linked pyrrole nuclei around which porphyrins are built.

**Figure 15.** Lindsey's method of porphyrin synthesis whereby the condensation and oxidation processes are carried out sequentially at room temperature. The reaction(s) is very sensitive to changes in the concentration of both the reactants and the catalyst ($BF_3O(C_2H_5)_2$, boron trifluoride ethyl etherate), and yields of up to 50 % have been reported.[11]

**Figure 16.** Gouterman's four-orbital model (**Top**) and a simplified representation of the one electron transitions from the HOMO to the LUMO of the porphyrinic macrocycle (**Bottom**).[35]

**Figure 17.** A UV-Vis spectrum highlighting the difference in electronic structure between a free base porphyrin (**Black Trace**), and a metalloporphyrin (**Red Trace**). Both UV-Vis spectra were recorded in anhydrous $CH_2Cl_2$, at room temperature, and the porphyrin moiety was present at a concentration of 20 μM in each case. The Q band (490 – 680 nm) region has been enlarged and plotted on a secondary *y*-axis in order to aid clarification.

**Figure 18.** The formation of self-assembled monolayers (SAMs). SAMs form spontaneously upon the exposure of a substrate to a solution of the surface-active material. The spontaneous deposition and ordering of the monolayer is driven by both chemical bond formation and intermolecular interaction(s). *t* denotes time, whilst *x* signifies the presence of the porphyrinic macrocycle.

**Figure 19.** PET within covalently linked donor-acceptor (D-A) architectures. When the distance between the two moieties is large (**Top**), the PET process usually proceeds *via* the singlet excited state. However, when the distance is much shorter and thus energy transfer (EnT)

is favoured (**Bottom**), PET proceeds *via* the triplet excited state; this state is generated as the result of relatively fast intersystem crossing (ISC).

**Figure 20.** A schematic illustration of the generation of both **anodic** and **cathodic** photocurrent within a SAM of a porphyrin-terminated, helical peptide. All photoelectrochemical experiments were undertaken, by Uji *et al.*, within a 0.1 M $Na_2SO_4$ solution (aqueous), and either an electron acceptor ($MV^{2+}$) or a sacrificial electron donor (TEOA) present at a concentration of 0.05 M. All redox and applied potentials quoted are reported with respect to a Ag / AgCl reference electrode, and photoelectrochemical output was acquired upon illumination of the monolayer with light of wavelength 430 nm. Figure reproduced with permission from references [86] and [90].

**Figure 21.** A schematic representation highlighting the four processes that need to be considered when trying to optimise the lifetime of the excited state of the porphyrinic macrocycle ($Por^*$), and thus enhance the efficiency of photocurrent generation. The four processes are as follows, 1) the rate of forward electron transfer from an embedded electron relay (ER) group to $Por^*$, 2) the backward rate of electron transfer from $Por^*$ to the oxidised form of the ER group, 3) the backward rate of electron transfer from Por* to the metallic surface (Au), and 4) energy transfer $Por^*$ to the metallic surface (Au).

**Figure 22. Top.** The molecular structure of the porphyrin-terminated SAM deposited at Au by the group of Uosaki. **Bottom.** An energy diagram demonstrating photoinduced cathodic upconversion within the aforementioned SAM. Por = Porphyrin, Fc = Ferrocene, and $MV^{2+}$ = Methyl Viologen. Figure reproduced with permission from references [73] and [74].

**Figure 23. Top.** The molecular structure of the porphyrin-terminated SAM deposited at Au by the group of Uosaki. **Bottom.** An energy diagram depicting the generation of anodic photocurrent within the aforementioned SAM. Por = Porphyrin, $H_2Q$ = Quinone, and AsA = Ascorbic Acid. Figure reproduced with permission from references [88] and [89].

**Figure 24.** Space filling models of CB[*n*], for [*n*] = 6, 7 and 8. Elemental Key: Carbon – **Light Blue**; Nitrogen – **Dark Blue**; Oxygen – **Red**; Hydrogen – **Grey**. Reprinted with permission from reference [8].

**Figure 25.** Dimensions (**Top**) and selected properties (**Bottom**) of CB[*n*] for [*n*] = 6, 7 and 8. Solubility refers to aqueous solubility at 298 K. All data and image reproduced with permission from references [6] and [10], respectively.

**Figure 26.** A schematic representation depicting the co-inclusion of guest species within the molecular cavity of CB[8], in order to form 1:1 homoternary (**A**), 1:1 *intermolecular* heteroternary (**B**), 1:1 *intramolecular* heteroternary (**C**), and 2:2 *intramolecular* heteroternary (**D**) complexes. All are stabilised upon the induction of charge-transfer between an electron-rich and an electron-deficient moiety.

**Figure 27.** An electrostatic potential map of CB[7], highlighting the negatively charged carbonyl portals (**Red**). Reprinted with permission from reference X.

**Figure 28.** Stereochemical control of photoinduced dimerization within the cavity of CB[8].

**Figure 29.** A schematic representation depicting the orthogonal switching of a heteroternary complex containing both redox- and photochemically addressable guest species, (**($MV^{2+}$, *trans*-AB)-CB[8]**). The homoternary complex (**($MV^{+\cdot}$)$_2$-CB[8]**) is afforded upon two electron reduction of the heteroternary complex, in the presence of excess methyl viologen ($MV^{2+}$), whilst formation of the binary inclusion complex (**$MV^{2+}$-CB[8]**) is induced upon *trans*-*cis* isomerisation ($\lambda_{irr}$:342 nm) of the included azobenzene (**AB**) derivative. The heteroternary complex is regenerated upon either oxidation of the homoternary complex, or by virtue of the *cis*-*trans* isomerism (420 nm) of the included AB derivative.[35]

**Figure 30.** A schematic representation highlighting the energy transfer processes involved in sensitised lanthanide luminescence. Energy transfer from the excited state of the molecular antenna to the ground state of the lanthanide ion (Ln) proceeds **via** either Dexter or Förster resonance energy transfer (FRET).

**Figure 31.** A Jablonski diagram highlighting the energetic processes available upon excitation of a molecular antenna species, including internal conversion (IC), intersystem crossing (ISC), vibrational relaxation (VR), electron and / or energy transfer (ET) and back electron transfer (BET).

**Figure 32.** Reversibly modulating the photophysical properties of diffusive (**Top**) and interfacially assembled (**Bottom**) *d*-*f* dyads, by virtue of varying the oxidation state of the ferrocene chromophore, *i.e.* by inducing the formation of the quenching ferrocenium species.[111]

**Figure 33.** The ternary complexes conceived for attempted synthesis and full characterisation.

**Figure 34.** Utilising the formation of charge-transfer complexes in the generation of optically switchable, lanthanide-appended molecular films at electrochemically addressable surfaces. It was envisaged that the emissive output from the lanthanide ion could be electrochemically modulated *via* the formation of both ferrocenium (**Top**) and the homoternary complex (**Bottom**).

## List of Equations

**Equation 1.** The Marcus equation, where $k_{ET}$ is the rate of electron transfer, $k_{el}$ the electron transmission coefficient ($\approx 1$), $\nu_n$ the vibrational frequency of the transition state ($\approx 10^{13}$ $s^{-1}$), $k_B$ the Boltzmann constant, $T$ (K) the temperature, $\lambda$ the reorganisation energy, and $\Delta G^0$ the free energy change between the reactant state and the product state. $\Delta G^{\ddagger} = (((\lambda + \Delta G^0)^2) / (4 \lambda))$.[55-61, 68]

## 2. Photoinduced Electron Transfer within Porphyrin-Appended Self-Assembled Monolayers

In order to permit the photoelectrochemical differentiation of the ground state co-conformation (GSCC) and the metastable state co-conformation (MSCC), within dynamic, interlocked molecular architectures, a conformational ruler first needed to be established within static, biphasic systems[1,2,3,4,5]. Biphasic systems are systems in which both the photoactive moiety and the relay group are covalently tethered to an underlying, electroactive interface, as opposed to being covalently integrated within either a molecular dyad configuration, such as those reported by the research group of Uosaki[6,7,8,9], or a bistable [2]rotaxane, such as the one depicted in **Figure 1**.

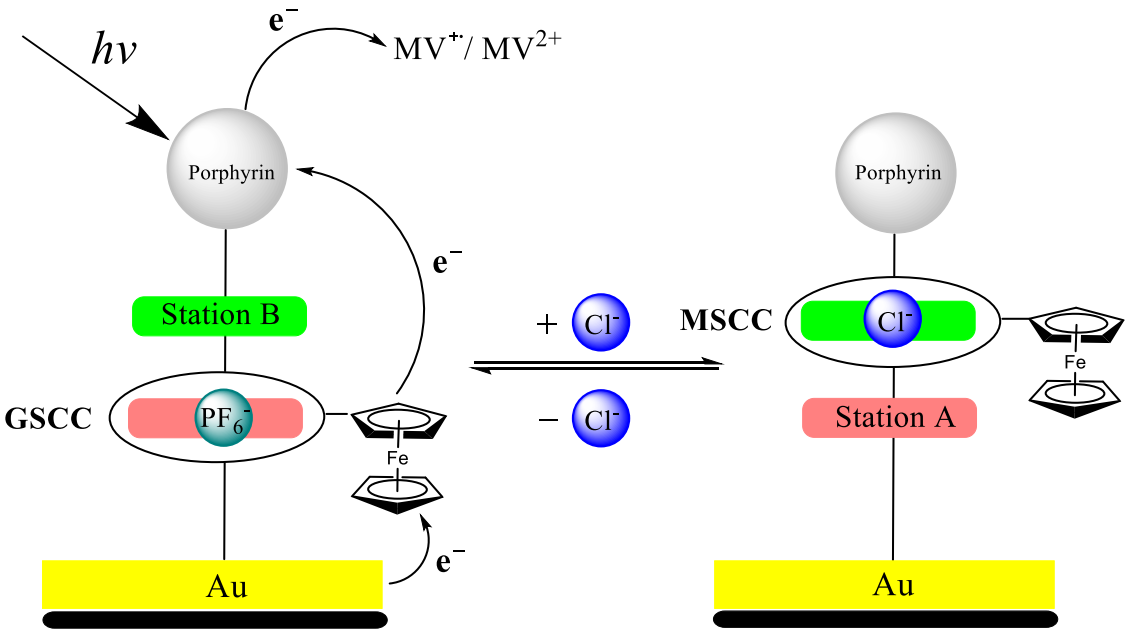


**Figure 1.** Anion-induced translocation of a redox-active macrocycle within a photoelectrochemically active, bistable [2]rotaxane; formation of the MSCC is brought about upon addition of the chloride anion. $MV^{2+}$: Methyl Viologen. *hv:* Photoirradiation. $\mathbf{e}^-$: Electron.

It was expected that the application of a conformational ruler would aid in the molecular design of the porphyrin-appended, bistable [2]rotaxane sought, **Figure 1**, by way of ensuring that the magnitude of the cathodic photocurrent density generated at each molecular station, upon illumination of the system with visible light, varied significantly. This would allow for the anion-induced, translational motion of a ferrocene-appended macrocycle to be 'mapped' effectively by a novel approach, **Figure 1**.

## 2.1 – Exploiting the Distance Dependence of Photoinduced Electron Transfer to Construct a Conformational 'Ruler'

To mechanistically elucidate the role of each molecular component, in regards to the role it plays in the generation of cathodic photocurrent density within monophasic, porphyrin-appended systems, carboxy-functionalised thiols, of varying chain length, were to be initially deposited at gold (Au). A variety of amine-functionalised porphyrin derivatives were to then be covalently tethered to the subsequently activated interfaces, affording porphyrin-appended monolayers in which the spatial separation between the photoactive moiety (porphyrinic macrocycle (Por)) and the metallic surface (Au) varied, **Figure 2**. It was at these molecular films that PET would be induced, and shown to be distance dependent. It was believed that these molecular systems, the monophasic analogues of the envisaged biphasic monolayers (**Figure 3**), would serve as a good starting point in the construction of a conformational ruler.

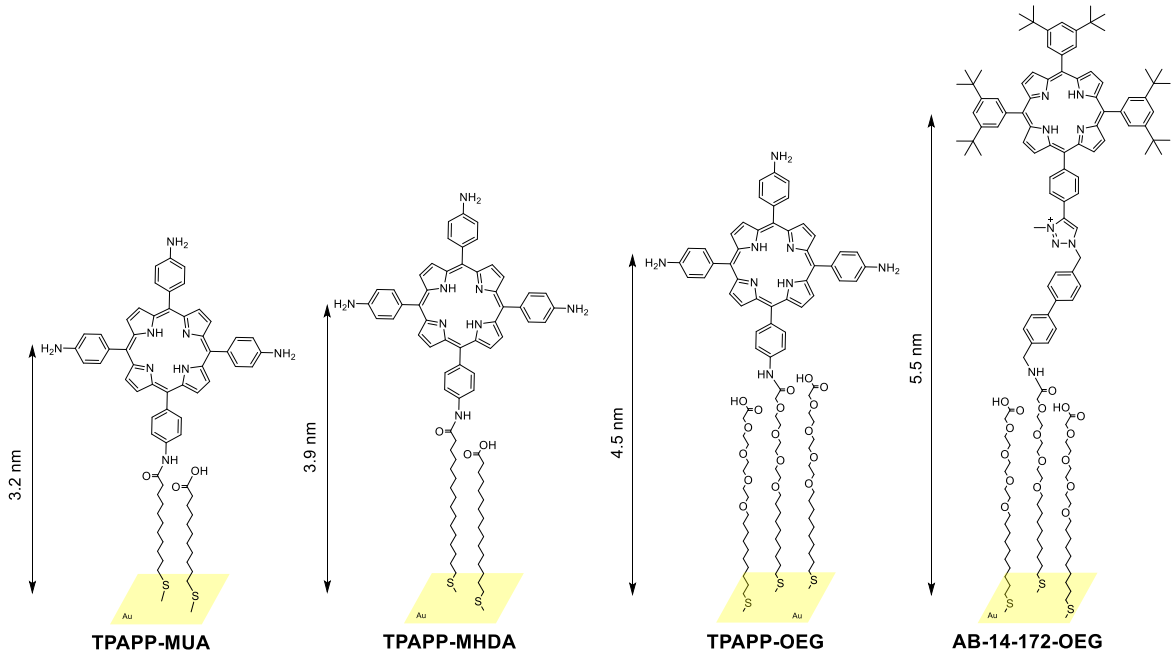


**Figure 2.** Varying the distance between the porphyrin 'stopper' and the Au surface. **MUA**: 11-Mercaptoundecanoic acid. **MHDA**: 16-Mercaptohexadecanoic acid. **OEG**: HS-$(CH_2)_{10}$-$EG_3$-$OCH_2$-COOH. **TPAPP**: Tetra(4-aminophenyl)porphyrin. **AB-14-172**: a porphyrin-appended axle component synthesised by Dr Asha Brown of the Paul Beer Group (University of Oxford). All quoted distances were estimated by a minimisation approach (MM2) performed in Chem3D 15.0.

It was then expected that the effect of incorporating a relay group on the magnitude of the cathodic photocurrent density acquired could be elucidated by integrating a metallocene, in the form of varying chain length ferrocenethiols, thus allowing the spatial separation between the various functionalities (Au surface, relay moiety and photoactive site) present within the molecular system to be modulated, **Figure 3**. It was expected that the findings could then be applied within more complex and / or dynamic systems such as interpenetrated molecular architectures, to ensure that the

magnitude of the cathodic photocurrent density generated at each molecular station, upon illumination of the system with visible light, varied significantly. This would permit the photoelectrochemical transduction of macrocyclic motion, **Figure 1**.

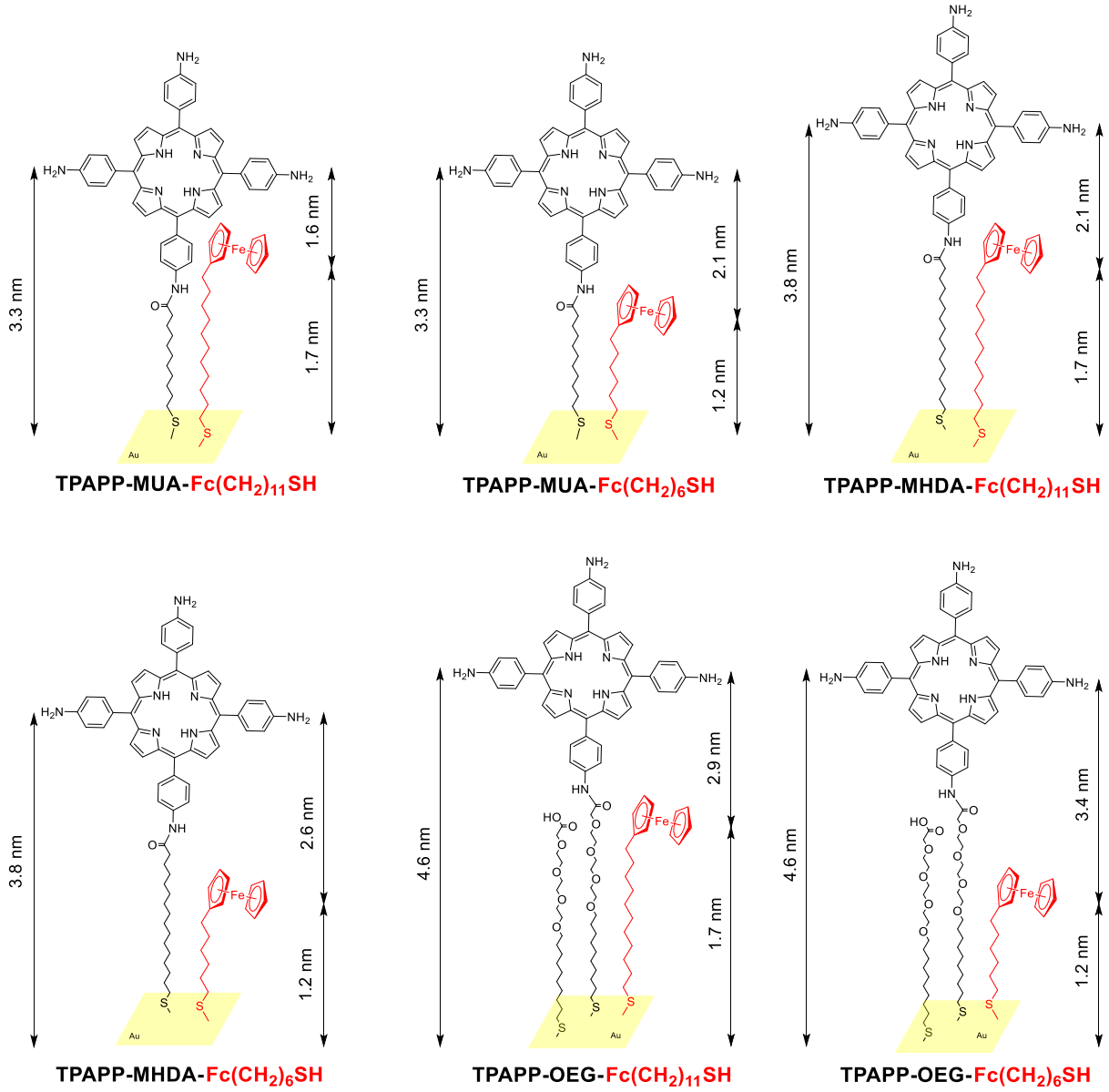

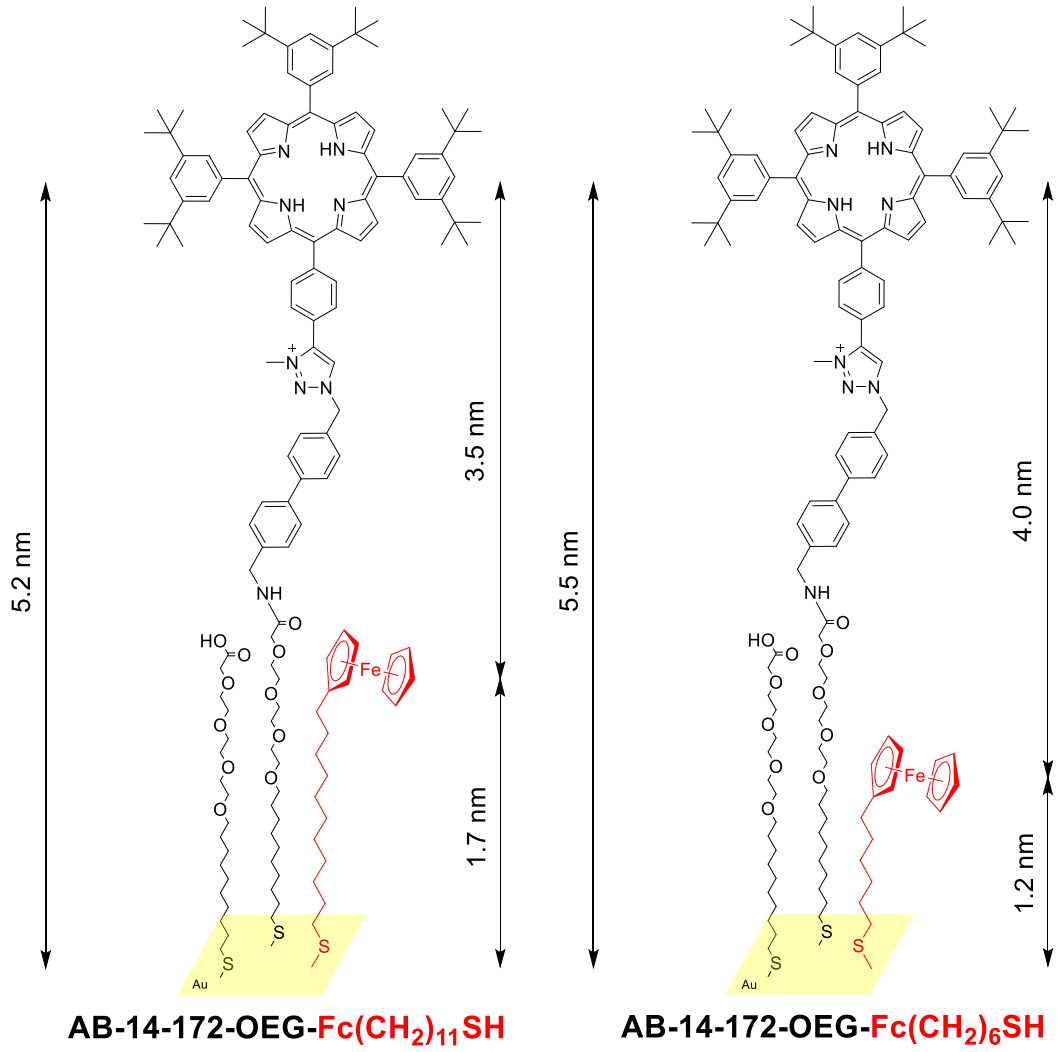


**Figure 3.** Varying the distances between the porphyrin 'stopper', the relay moiety and the Au surface. Varying chain length carboxy-terminated (MUA, MHDA, OEG) and ferrocene-functionalised (6-(ferrocenyl)hexanethiol ($Fc(CH_2)_6SH$) or 11-(ferrocenyl)undecanethiol ($Fc(CH_2)_{11}SH$)) thiols were deposited. **AB-14-172**: a porphyrin-appended axle component synthesised by Dr Asha Brown of the Paul Beer Group (University of Oxford). All quoted distances were estimated by a minimisation approach (MM2) performed in Chem3D 15.0.

*Hence, this series of experiments set out to establish the distance at which the two molecular stations should be set apart, for cathodic photocurrent density of varying magnitude to be acquired at each, as to permit the effective transduction of the translocation of redox-active macrocycles within dynamic, rotaxanated systems*, **Figure 1.**

It was expected, in line with what has been previously reported by the research groups of both Uosaki[8,9] and Imahori[10], and the mechanism of cathodic photocurrent generation highlighted previously (**Introduction, Section 2.3**), that upon increasing the distance between the metallic substrate and the porphyrin moiety, up until an unknown point (**X**), the efficiency of PET, and therefore the magnitude of cathodic photocurrent density acquired, should increase. That is, upon increasing the length of the thiolate linker to which the aminated porphyrin derivatives are covalently

tethered, from 1.4 (11-mercaptoundecanoic acid (MUA)) through to 2.7 nm ($(CH_2)_{10}$-$EG_3$-$OCH_2$-COOH (OEG)), **Figure 2**, the magnitude of cathodic photocurrent density acquired should increase. An increase is expected in line with a greater reduction in the rates of both backward electron and backward energy transfer, from the excited state of the porphyrinic macrocycle ($P^*$) to the gold surface, *cf.* the forward rate of electron transfer between the two[6,7,8,9,10,11]. However, beyond this point, **X**, the magnitude of photoelectrochemical output is likely to diminish due to a further reduction in the rate of forward electron transfer. Hence, it was to be expected that a greater cathodic photocurrent density would be acquired upon covalently tethering the amine-functionalised porphyrin derivatives to the OEGylated interface, as opposed to the MHDA and MUA-functionalised substrates, respectively. However, it was not known at what distance from the interface the porphyrinic macrocycle would begin to become electrochemically decoupled from the metallic substrate, necessitating the integration of a relay moiety in order to combat this effect, whilst maintaining a reduction in the rates of both backward electron and backward energy transfer from P* to the Au surface[6,7,8,9,10,11]. Therefore, it is reasonable to believe that the use of a OEGylated thiol linker could bring about a decrease in the rate of forward electron transfer, thus reducing the magnitude of the cathodic photocurrent density acquired. That is, upon covalently tethering the porphyrinic macrocycle (TPAPP) to a SAM of the OEGylated thiol, it is likely to become electrochemically decoupled from the redox addressable substrate; in theory, the distance between the metallic interface and the porphyrin moiety could be as great as 4.5 nm (**Figure 2**). Essentially, it was hoped that the incorporation of a relay group would move **X** further from the surface (**X'**). **Figure 4** depicts and compares these two regimes.

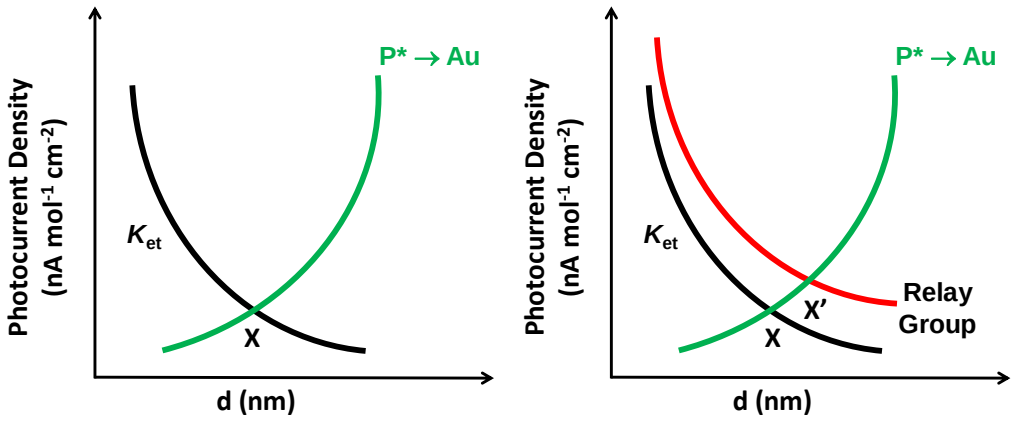


**Figure 4.** The electron (et) and energy transfer (**P*→Au**) processes governing the magnitude of cathodic photocurrent density deposited at the interface. In the absence of an electron relay group (**Left**), the magnitude of cathodic photocurrent density is limited by the rate of forward electron transfer ($K_{et}$), an effect more dominant upon increasing the spatial separation, d, between the Au interface and the porphyrinic macrocycle, as to limit the rates of both backward electron and backward energy transfer from the excited state of the porphyrinic macrocycle ($P^*$) to the Au surface. Thus, upon increasing d, the magnitude of cathodic photocurrent density should increase in accordance with a drop in the rates of both backward electron and backward energy transfer from $P^*$ to the Au surface, as implied by

the **green line**. These otherwise act to reduce the magnitude of photoelectrochemical output. Upon integrating a relay group (**Right**), this effect is reduced, that is the drop in $K_{et}$ is not as dominant, and **X** is moved further away from the interface (**X'**).[6,7,8,9,10,11]

This concept was first investigated by the group of Uosaki[8], who were able to show that upon increasing the distance between an integrated ferrocene (Fc) unit, and the porphyrin stopper of an interfacially deposited molecular dyad, **Figure 5**, larger cathodic photocurrent densities were acquired, owing to a reduction in the rates of both back energy and back electron transfer from $P^*$ to the oxidised metallocene ($Fc^+$).[8]

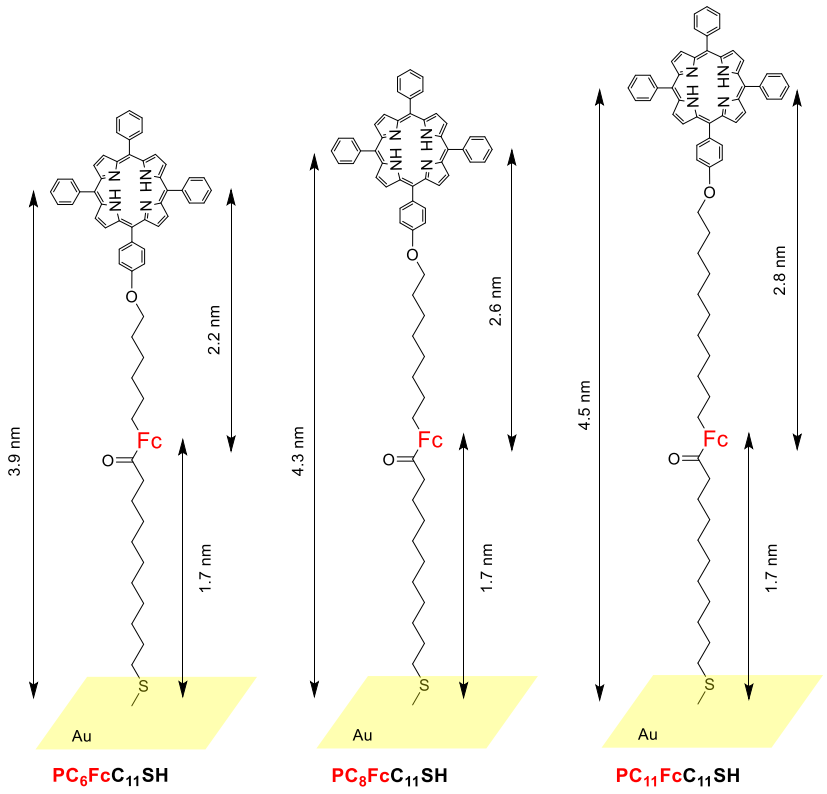


**Figure 5.** The molecular dyads deposited at Au by the group of Uosaki[6,7,8,9]. Fc = ferrocene. All quoted distances were estimated by a minimisation approach (MM2) performed in Chem3D 15.0.

Consequently, it was to be expected that a systematic increase in the magnitude of cathodic photocurrent density acquired would be witnessed upon increasing the spatial separation between the relay ($Fc(CH_2)_6SH$ or $Fc(CH_2)_{11}SH$) and photoactive moieties (TPAPP or AB-14-172) present within the biphasic systems highlighted in **Figure 3**. Spatial separation spanning a 2.8 nm (1.5 → 4.3 nm) range was to be achieved by simultaneously depositing varying chain length carboxy, to which aminated porphyrin derivatives could be covalently coupled to, and ferrocene-terminated thiols, **Figure 3**.

Upon analysis of the data acquired, the synthesis of and generation of cathodic photocurrent density within both static and dynamic interpenetrated molecular architectures was to be probed; this body of work forms the basis of **Chapter 3**. To summarise, the knowledge acquired upon the

photoelectrochemical analysis of the biphasic systems, **Figure 3**, was to be utilised in the construction of a bistable [2]rotaxane in which the anion-induced, translocation of a ferrocene-appended macrocycle could be reversibly monitored by considering the magnitude of the cathodic photocurrent density acquired at each molecular station. In addition, the recognition motifs were to be synthetically integrated into the molecular architecture, or axle component, at an experimentally determined distance relative to one another, as to ensure that this novel transduction process was easily resolvable, that is the magnitude of cathodic photocurrent density acquired at each could be differentiated and was not limited by the error associated with the photochemical measurement itself.

In the absence of the ferrocene-appended macrocycle, the magnitude of the cathodic photocurrent density acquired was expected to be negligible, whilst an increase in magnitude would be brought about upon prior threading of the relay construct. Furthermore, it was envisaged that, upon anion exchange, or selective detection of the chloride anion, the macrocyclic component would translocate, thereby bringing about a clear reduction in the magnitude of the photoelectrochemical output observed. This scenario is depicted in **Figure 6** along with a brief scientific explanation[6,7,8,9,10,11] as to why the magnitude of cathodic photocurrent density generated at each molecular station should vary.

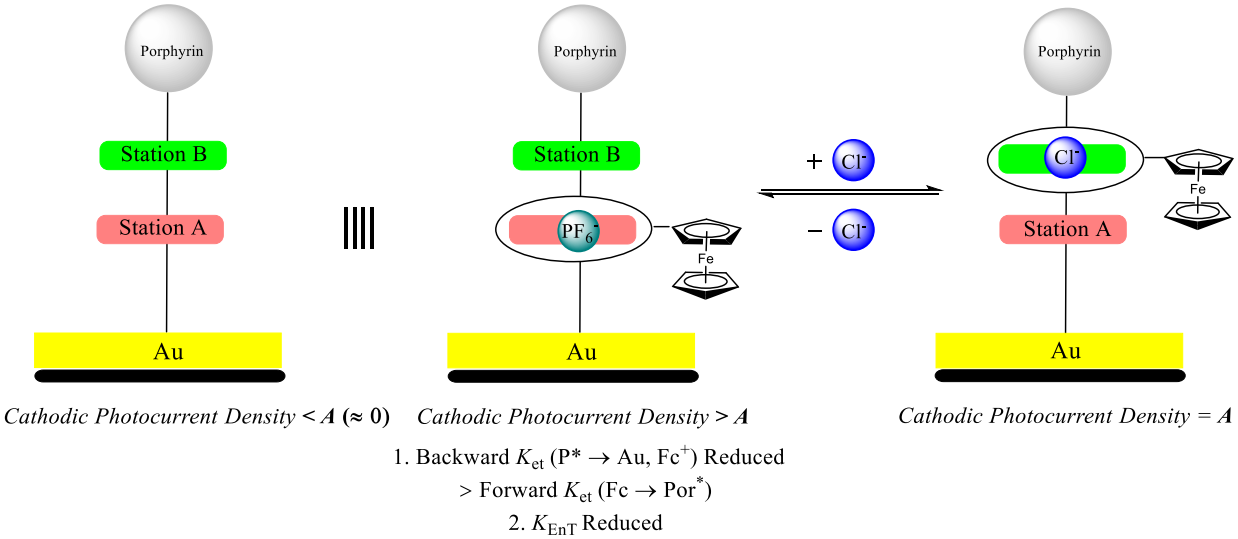


**Figure 6.** Photoelectrochemically 'mapping' the translocation of a ferrocene-appended macrocycle within a bistable [2]rotaxane deposited at Au.

The magnitude of the cathodic photocurrent density acquired, upon illumination (430 ± 5 nm, **Experimental, 7.2.3**) of each molecular film, was to be calculated by way of determining the difference in magnitude of cathodic current acquired in the presence and absence of light, **Figure 7**. The value would then be normalised for the concentration of porphyrin present at the interface, as determined by cyclic voltammetry (**Experimental, 7.2.2**), thereby generating a representative cathodic photocurrent density (nA $mol^{-1}$ $cm^{-2}$) in the process.

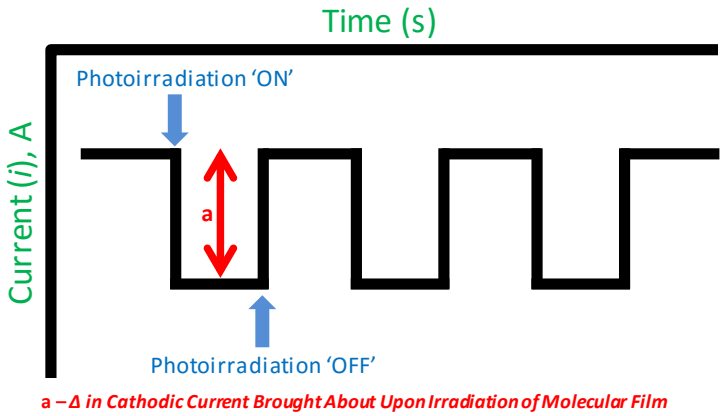


**Figure 7.** Current *vs.* time profile showing how the magnitude of cathodic photocurrent density is calculated. Δ denotes change.

## 2.2 – Establishing a Conformational 'Ruler' within Monophasic, Porphyrin-Appended SAMs

Prior to investigating the effect that integrating an electron relay group into the molecular architecture has on the magnitude of the cathodic photocurrent density acquired, in a bid to gauge the distance at which the two molecular stations should be set apart, PET was investigated at the monophasic molecular films (**Figure 2**). The molecular films were prepared by covalently coupling aminated porphyrin derivatives to underlying SAMs of carboxy-functionalised, alkylated thiols, **Figure 8**; **Experimental, 7.3.2** and **7.3.3**.

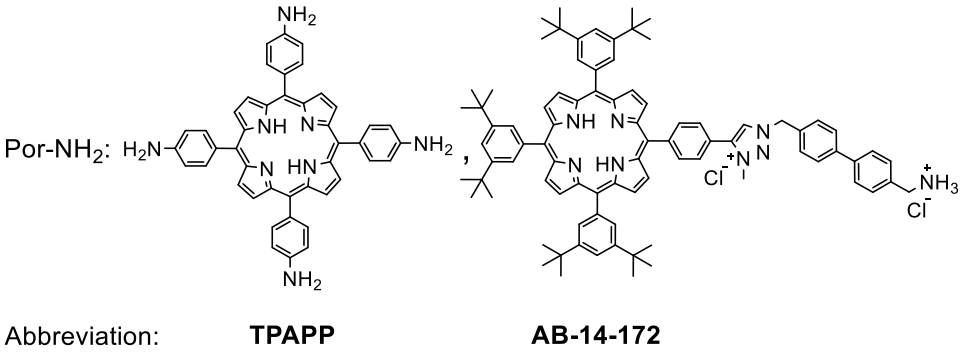


**Figure 8.** Covalent attachment of TPAPP and AB-14-172 to SAMs of carboxy-functionalised, alkylated thiols deposited at Au.

The carboxy-functionalised, alkylated thiols used, of which all are commercially available, were of varying chain length, **Figure 9**, as to permit the fabrication of porphyrin-appended, monophasic molecular films in which the porphyrin-gold distance differed, **Figure 2**, thereby allowing its effect on the magnitude of the cathodic photocurrent density generated to be elucidated.

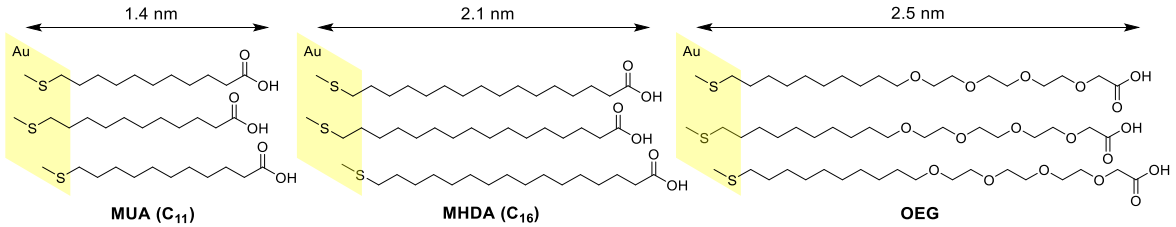


**Figure 9.** SAMs of MUA (**Left**, 1.4 nm), MHDA (**Centre**, 2.1 nm) and OEG (**Right**, 2.5 nm) deposited at Au. All quoted distances were estimated by a minimisation approach (MM2) performed in Chem3D 15.0.

To reiterate, it was expected that the magnitude of cathodic photocurrent density would increase upon increasing the distance between the photoactive moiety (Por) and the quenching metallic interface, Au[6,7,8,9,10,11]. That is, as the distance between the two is increased, **Figure 2**, **Left → Right**, from 3.2 to 5.5 nm, a reduction in the rates of both backward electron and backward energy transfer, from $P^*$ to the Au surface, should arise[6,7,8,9,10,11]. This reduction should permit the generation of cathodic photocurrent density with increased efficiency, and therefore an output of greater magnitude should be acquired. However, it was expected for this principle to only hold up until a certain distance from the interface, after which a decline in the magnitude of cathodic photocurrent density was expected in line with a decrease in the rate of forward electron transfer from the metallic surface to $P^*$.[6,7,8,9,10,11]

### 2.2.1 – Formation and Characterisation of Monophasic, Porphyrin-Appended SAMs

Prior to covalently tethering the aminated porphyrin derivatives to the thiolated interfaces, the precursor molecular films (MUA, MHDA, OEG (**Figure 9**)) were characterised in a bid to ensure that the gold surface was passivated, and that the SAMs formed were uniform in structure. It was important to ensure that uniformity was achieved in each case because if the monolayers had not aligned themselves normal to the interface, it is likely that their deposition would yield surface coverages of the carboxy-functionalised derivatives that were significantly lower than that expected and / or reported. This would have limited the amount of porphyrin present at the interface, which in turn would have supressed the photochemical output acquired upon wavelength selective irradiation of the modified interfaces. In addition, it is likely to have increased the degree of porphyrin aggregation observed at the interface as the result of macrocyclic π-stacking[10,12,13]. The deposition of each thiol derivative was confirmed, prior to the covalent coupling of the aminated porphyrin derivatives, by means of cyclic voltammetry (CV, **Experimental, 7.2.2** and **7.2.4**, **Appendix, 8.1.2**) and ellipsometry (**Experimental, 7.4**).

Upon the deposition of each carboxy-functionalised thiol derivative at Au, **Figure 9**, film thickness measurements were acquired by means of ellipsometry, **Table 1**, and the degree of surface

passivation assessed, **Figure 10**, by recording cyclic voltammograms in the presence of a diffusive redox probe (potassium ferrocyanide, $K_3[Fe(CN)_6]$), **Experimental, 7.2.4**.

| Deposited Thiol | *Estimated | **Reported[14,15,16,17] (± 0.3 nm) | ***Experimentally Determined (± 0.2 nm) |
|---|---|---|---|
| MUA | 1.4 | 1.5 | 1.4 |
| MHDA | 2.1 | 1.9 | 2.0 |
| OEG | 2.7 | - | 2.6 |

**Table 1.** Ellipsometric film thicknesses for SAMs of MUA, MHDA and OEG deposited at Au. *Estimated by means of minimisation (MM2) in Chem3D 15.0. ** Calculated by either attenuation of the Au 4*f* x-ray photoelectron spectroscopy signature[15] or ellipsometry[14,16,17]. *** Experimentally determined by ellipsometry. Reported film thicknesses are those determined from, and averaged over, four separately prepared samples, with two measurements per sample.

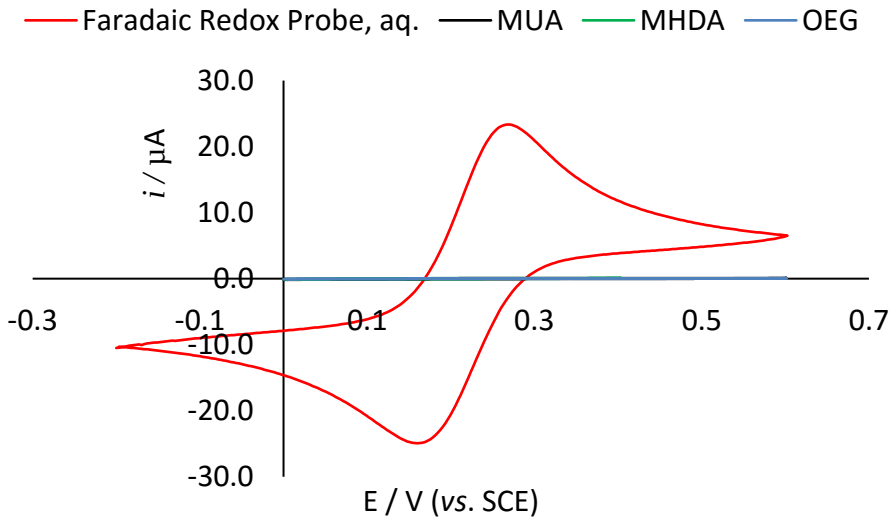


**Figure 10.** Cyclic voltammograms of a 1 mM solution (aqueous) of $K_3[Fe(CN_6)]$ recorded at a bare Au electrode (**Red**), and those modified with SAMs of MUA (**Black**), MHDA (**Green**) and OEG (**Blue**), **Figure 9**. Electrochemical Setup: *Working Electrode*: SAM. *Reference Electrode*: SCE. *Auxiliary Electrode*: Pt wire. *Electrolytic Solution*: 0.1 M $NaClO_4$, aq. *Scan Rate:* 100 mV / s.

In addition, the surface coverage of each thiol deposited was calculated, and compared to the theoretical maximum, by considering the area of the reductive stripping peaks acquired upon repeatedly sweeping the potential of the modified substrates between – 0.5 and – 1.5 V, in a degassed 0.5 M solution (50:50, EtOH: $H_2O$) of KOH, **Figure 11**.[18,19,20,21]

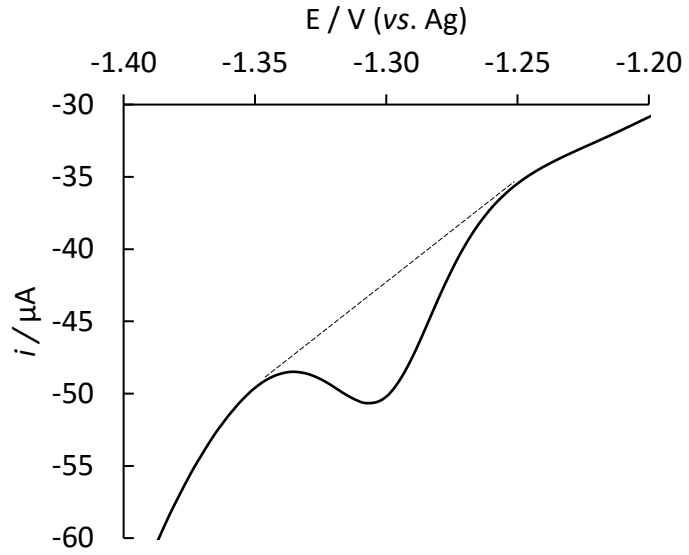


**Figure 11.** The characteristic peak acquired upon reductively 'stripping' thiols from Au interfaces. Above example acquired upon repeatedly sweeping (100 mV / s) the potential of a MHDA-modified Au electrode between – 0.5 and – 1.5 V (*vs.* Ag wire) in a 0.5 M solution (50:50, EtOH: $H_2O$, degassed) of KOH.

Surface concentrations close to those reported ($8.8 \pm 0.6 \times 10^{-10}$ mol $cm^{-2}$)[21] for the deposition of SAMs of *n*-alkanethiols at Au were acquired, thus inferring that closely-packed monolayers of MUA ($7.8 \pm 0.4 \times 10^{-10}$ mol $cm^{-2}$), MHDA ($8.4 \pm 0.6 \times 10^{-10}$ mol $cm^{-2}$) and of the OEGylated thiol ($5.6 \pm 0.5 \times 10^{-10}$ mol $cm^{-2}$) were consistently deposited; the error bars have been calculated based on the differences in the concentration of each thiol deposited across five separately prepared electrodes, with the error bars being 3SD (standard deviations). This, in conjunction with the close to ideal ellipsometric film thickness values obtained, **Table 1**, and the fact that all three of the SAMs fabricated (**Figure 2**) appeared to ensure that only a negligible faradaic response to $K_3[Fe(CN_6)]$ was observed, *cf*. bare Au, **Figure 11**, suggested that all three monolayers had formed with a high degree of uniformity. Furthermore, formation of the sulphur-gold bond was confirmed in each case by XPS (**Experimental, 7.6**, **Appendix, 8.2** (**Figure 9**)); a peak in the $S_{2p}$ region of the spectrum was observed at a binding energy of 163.0 eV ($S_{2p1/2}$)[7,22,23,24,25,26,27], **Figure 12**. Thus, the covalent coupling of the aminated porphyrin derivatives (TPAPP or AB-14-172) to the carboxy-terminus of each (MUA, MHDA or OEG) could proceed, **Figure 8**, in a bid to generate the monophasic monolayers at which PET could be investigated, **Figure 2**.

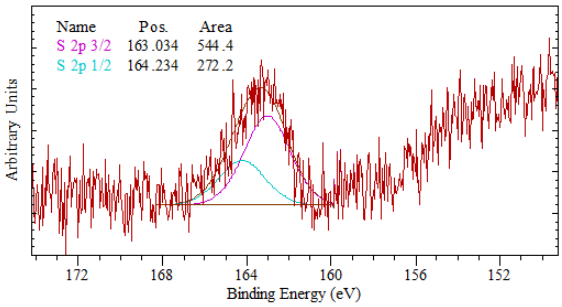


**Figure 12.** Narrow scan (S 2p) XPS spectra of SAMs of MUA, MHDA and OEG deposited at Au.

Upon immersion of the characterised substrates (MUA-Au, MHDA-Au, OEG-Au) into a solution of the respective aminated porphyrin derivative, following activation of the carboxy-termini, XPS (**Appendix, 8.2**), CV (**Experimental, 7.2.4, Appendix, 8.1.2**) and ellipsometry were used to confirm that the porphyrin derivative had become covalently tethered to the underlying monolayers, **Figure 2**. X-ray irradiation of the molecular films revealed peaks at binding energies of approximately 400 and 532 eV in the x-ray photoelectron spectrum of each, **Figure 13** (**Appendix, 8.2**). The peak at approximately 400 eV confirmed the presence of the –N= functionalities of the porphyrinic macrocycle at the interface[7], whilst the peak at approximately 532 eV corresponds to the presence of a carbonyl group of an amide bond[7], thus suggesting that the coupling reaction was successful in each case, and the porphyrin derivatives had become covalently tethered to the underlying monolayers, as was expected.

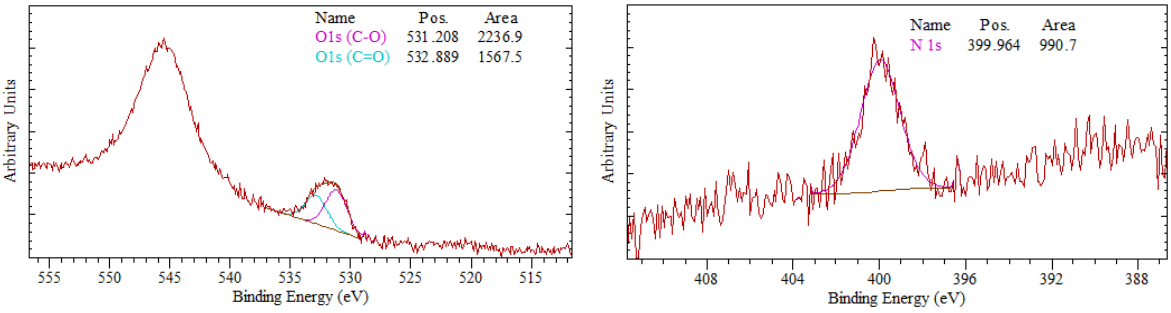


**Figure 13.** Narrow scan (O 1s (**Left**), N 1s (**Right**)) XPS spectra of a SAM of MUA-TPAPP deposited at Au.

This observation was further highlighted by the associated increases in film thickness attained, **Table 2**, and by the fact that the porphyrin redox couple ($P^0$ / $P^{+1}$) was observed upon utilising the coupling reagents, **Figure 14** (**Appendix, 8.1.2**).

| **Precursor Interface** | **Aminated Porphyrin Derivative** | **Experimentally Determined Increase** (± 0.2 nm) | **Film Thickness** (± 0.2 nm) (*Modelled Film Thickness) |
|---|---|---|---|
| MUA | TPAPP | 1.9 | 3.3 (**3.2**) |
| MHDA | TPAPP | 1.8 | 3.8 (**3.9**) |
| OEG | TPAPP | 2.0 | 4.6 (**4.5**) |
| OEG | AB-14-172 | 2.6 | 5.2 (**5.5**) |

**Table 2.** Ellipsometric film thickness increases following the covalent attachment of TPAPP or AB-14-172 to SAMs of MUA, MHDA and OEG deposited at Au. Reported film thicknesses are those determined from, and averaged over, four separately prepared samples, with two measurements per sample. *Estimated by minimisation (MM2) in Chem3D 15.0.

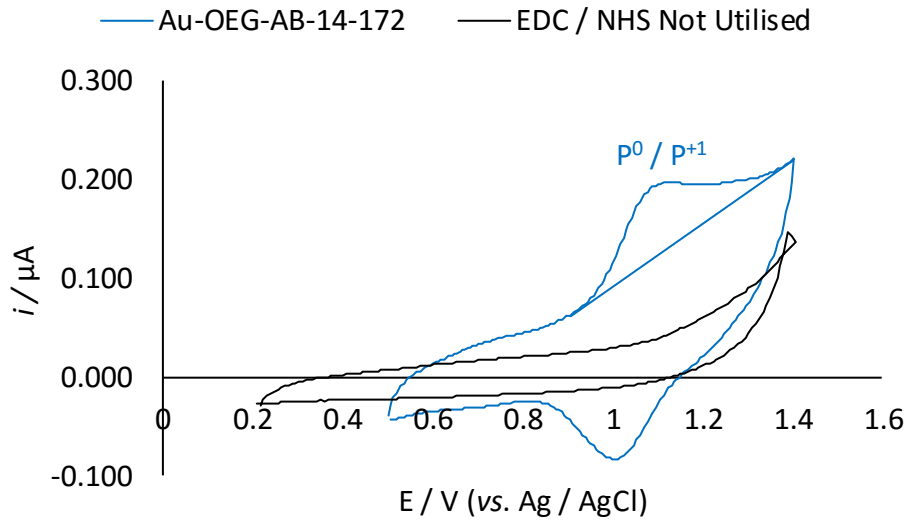


**Figure 14.** Cyclic voltammograms of a SAM of OEG following exposure to AB-14-172 in the presence (**Blue**) and absence (**Black**) of EDC / NHS. Electrochemical Setup: *Working Electrode*: SAM. *Reference Electrode*: Ag / AgCl. *Auxiliary Electrode*: Pt wire. *Electrolytic Solution*: 0.1 M $TBAPF_6$, anhydrous $CH_2Cl_2$. *Scan Rate:* 1000 mV / s. **Note.** Prior to immersion of the substrate, diffusive voltammograms of a solution of AB-14-172 were recorded at glassy carbon and Au (**Appendix, 8.1.1**); **Experimental, 7.2.4**.

**Table 2** demonstrates that the film thickness values acquired were as expected, that is an increase of between 1.8 and 2.0 nm was observed upon exposure of the activated self-assembled monolayers to TPAPP, and an increase of 2.6 nm was acquired upon exposure of the activated OEGylated thiol interface to AB-14-172; both values are in good agreement with those estimated by way of a minimisation approach (MM2) performed in Chem3D 15.0 to calculate the length of an extended conformation of the surface modification. Thus, the desired variation in vertical spatial separation

between the metallic interface and the photoactive porphyrin moiety was achieved, and the magnitude of cathodic photocurrent density was measured at each upon irradiation (430 ± 5 nm) of the molecular film. This wavelength of light was chosen because an 8 nm red shift (428 → 436 nm) in the position of the porphyrinic macrocycle's (TPAPP) Soret band arose as the result of the formation of *J*-aggregates upon the derivative becoming tethered to the interface[10,28,29,30,31], **Figure 15**; **Experimental, 7.5**. This shift (418 → 426 nm) in the position of the Soret Band was also witnessed upon tethering AB-14-172 to the interface; thus, the same wavelength of irradiation could be used to induce the flow of cathodic current within such systems.

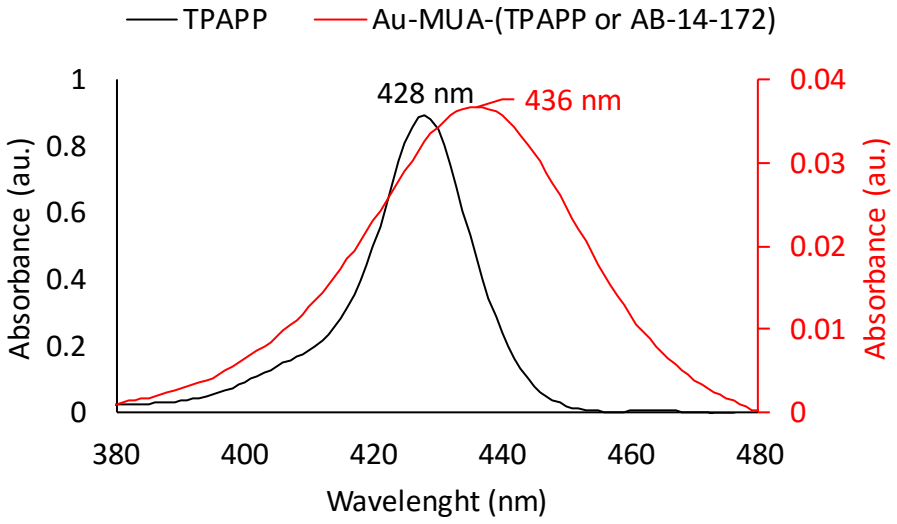


**Figure 15.** UV-Vis spectra of a solution (25 μM, anhydrous $CH_2Cl_2$) of TPAPP (**Green**, primary y-axis), and of SAMs of MUA-TPAPP/AB-14-172 (**Red**, secondary y-axis) deposited at Au.

The magnitude of the photochemical output observed was normalised for the concentration of porphyrin present at the interface. This allowed representative cathodic photocurrent densities (nA $mol^{-1}$ $cm^{-2}$) to be calculated, which could be directly compared with one another. The concentration of porphyrin present at the interface was calculated by integrating the area under the oxidative peak ($P^0$ / $P^{+1}$), **Figure 14**, and normalising it for the geometric surface area of the electrode on which the monolayers were deposited. The geometric area of each electrode was established prior to use by integrating the peak associated with the reduction of the Au/α gold oxide layer (+ 750 to + 1000 mV, *vs* SCE) revealed upon sweeping (sweep rate: 100 mV $s^{-1}$) the potential of the electrode in a 100 mM aqueous solution of $H_2SO_4$[32], **Experimental, 7.2.1**. Surface concentrations within the range 4.3 – 8.2 x $10^{-10}$ mol $cm^{-2}$ were acquired for the TPAPP-appended monolayers (≈ 670 % of the theoretical value calculated (9.4 x $10^{-11}$ mol $cm^{-2}$) based on the size of the porphyrin moiety), whilst surface concentrations within the range 3.5 – 5.4 x $10^{-11}$ mol $cm^{-2}$ were attained following the coupling of AB-14-172 to the activated, OEGylated thiol interface (≈ 69 % of the theoretical value calculated

(6.5 x $10^{-11}$ mol $cm^{-2}$) based on the size of the porphyrin moiety). All the surface coverages quoted are either significantly higher (TPAPP) or much lower (AB-14-172) than those reported by the groups of both Uosaki (2.3 x $10^{-10}$ mol $cm^{-2}$)[6,7,8,9] and Imahori (7.7 – 15.0 x $10^{-11}$ mol $cm^{-2}$)[10,11], although this is not surprising because their work centres on the direct deposition of porphyrin-appended thiols, as opposed to utilising a self-assembly approach in a bid to fabricate the desired monolayers. The direct deposition of thiolated derivatives is unlikely to be associated with the same level of steric impedance and / or unwanted association presumed to occur when attempting to covalently couple aminated porphyrin derivatives to activated monolayers *via* the use of EDC and NHS. In the absence of the coupling reagents (EDC / NHS), the porphyrinic redox couple ($P^0$ / $P^{+1}$) of TPAPP was still apparent upon voltammetric analysis of the interface(s), **Figure 16**. This suggests that the aminated porphyrin derivative intercalates and / or adheres to the unactivated SAM (MUA and MHDA). The redox signature ($P^0$ / $P^{+1}$) was, however, not stable, that is the peak current declined rapidly (within five potential sweeps), suggesting that the derivative migrates from the interface over time, **Figure 16**. This was also observed when utilising the coupling reagents, to bring about the formation of an amide bond, but not to the same extent. In the presence of the coupling reagents, the surface coverage of the porphyrinic macrocycle declined by 30 ± 4 %, as opposed to 70 ± 6 % in their absence, **Figure 16**. Hence, the above determination of surface coverage is expected because TPAPP can variably adhere to the monolayer, irrespective of whether the latter has been activated.

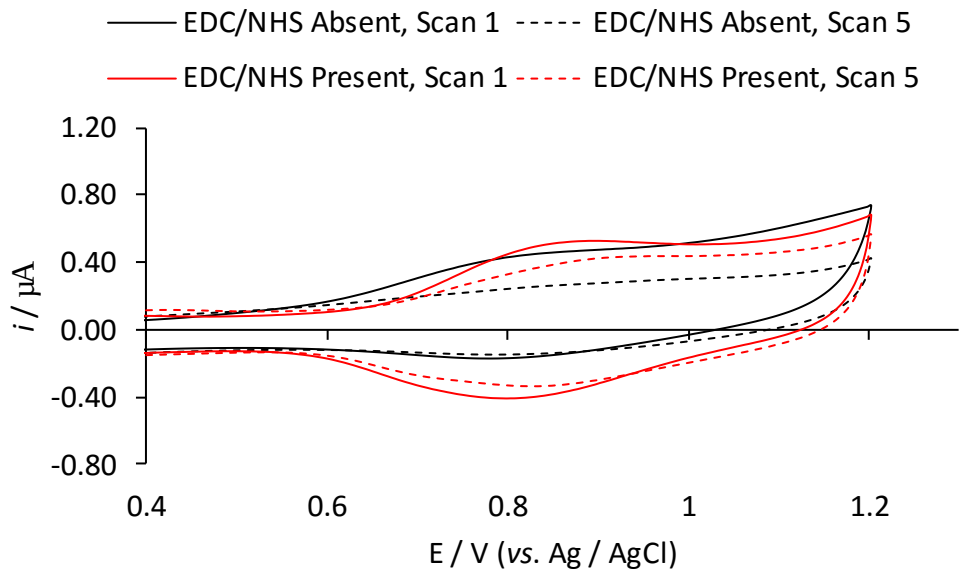


**Figure 16.** Cyclic voltammograms of activated (**Red**) and unactivated (**Black**) SAMs of MUA following exposure to a solution (50 µM, anhydrous $CH_2Cl_2$) of TPAPP. Electrochemical Setup: *Working Electrode*: SAM. *Reference Electrode*: Ag / AgCl. *Auxiliary Electrode*: Pt wire. *Electrolytic Solution*: 0.1 M $TBAPF_6$, anhydrous $CH_2Cl_2$. *Scan Rate:* 1000 mV / s.

This observation was also highlighted by XPS (**Appendix, 8.2**). The C/N ratio for self-assembled monolayers of TPAPP-MUA (**Appendix, 8.2** (**Figure 10**)) and AB-14-172-OEG (**Appendix, 8.2** (**Figures 11 and 12**)) was calculated from the relative peak intensities of C and N, respectively, and the values compared to those theoretically determined in ChemDraw 15.0 upon consideration of their envisaged molecular structures, **Table 3**.

| SAM | Theoretical C/N Ratio | | Measured C/N Ratio | |
|---|---|---|---|---|
| TPAPP-MUA | 1 | 6.9 | 1 | 16.0 |
| AB-14-172-OEG (1) | 1 | 12.9 | 1 | 26.4 |
| AB-14-172-OEG (2) | 1 | 12.9 | 1 | 22.1 |

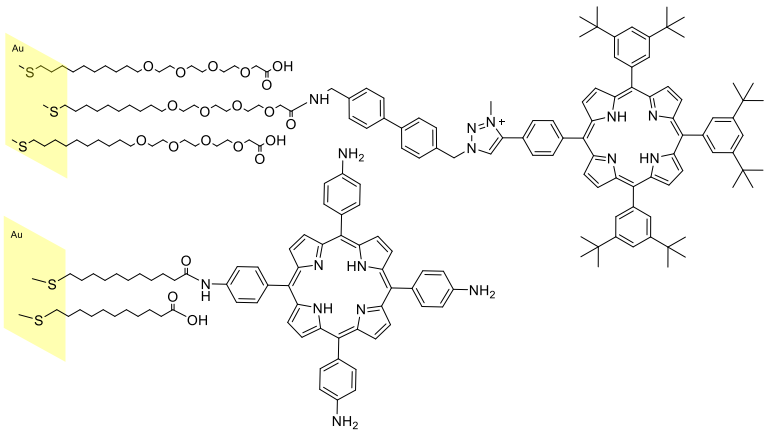


**Table 3.** C/N ratio for SAMs of TPAPP-MUA (Bottom) and AB-14-172-OEG (Top) deposited at Au.

In each case, the measured C/N ratio is greater than its theoretical value. This observation suggests that the porphyrin derivatives intercalate into the respective self-assembled monolayers formed at Au (MUA, OEG), or that the crosslinking reaction is not very efficient; that is, a high proportion of the thiolated interface remains unreacted following activation and subsequent exposure to the respective porphyrin solution (TPAPP, AB-14-172).

Both pathways serve to increase the concentration of C (relative to N) at the interface (porphyrin being the sole source of N and comprised mainly of C), and it is likely that both occur concomitantly, especially in the case of TPAPP; the intercalation of AB-14-172 into a SAM of OEG was dismissed by cyclic voltammetry (**Figure 14**) and XPS (**Appendix, 8.2** (**Figure 13**)), *cf.* TPAPP (**Figure 16**).

This, in addition to the fact that AB-14-172 possess more steric bulk than TPAPP, and the coupling reaction was performed in aqueous media explains why a diminished concentration of AB-14-172 was observed at the interface upon covalent attachment to OEG. In aqueous media, hydrolysis of the unstable, reactive *o*-acylisourea intermediate is likely.

### 2.2.2 – Investigating the Generation of Cathodic Photocurrent within Monophasic, Porphyrin-Appended SAMs

Upon irradiation of the fabricated monolayers, **Figure 2**, in the presence of methyl viologen ($MV^{2+}$), the effect of varying the vertical spatial separation between the metallic interface and the photoactive moiety, on the magnitude of cathodic photocurrent density generated, was elucidated, **Figure 17** (**Appendix, 8.3.1**).

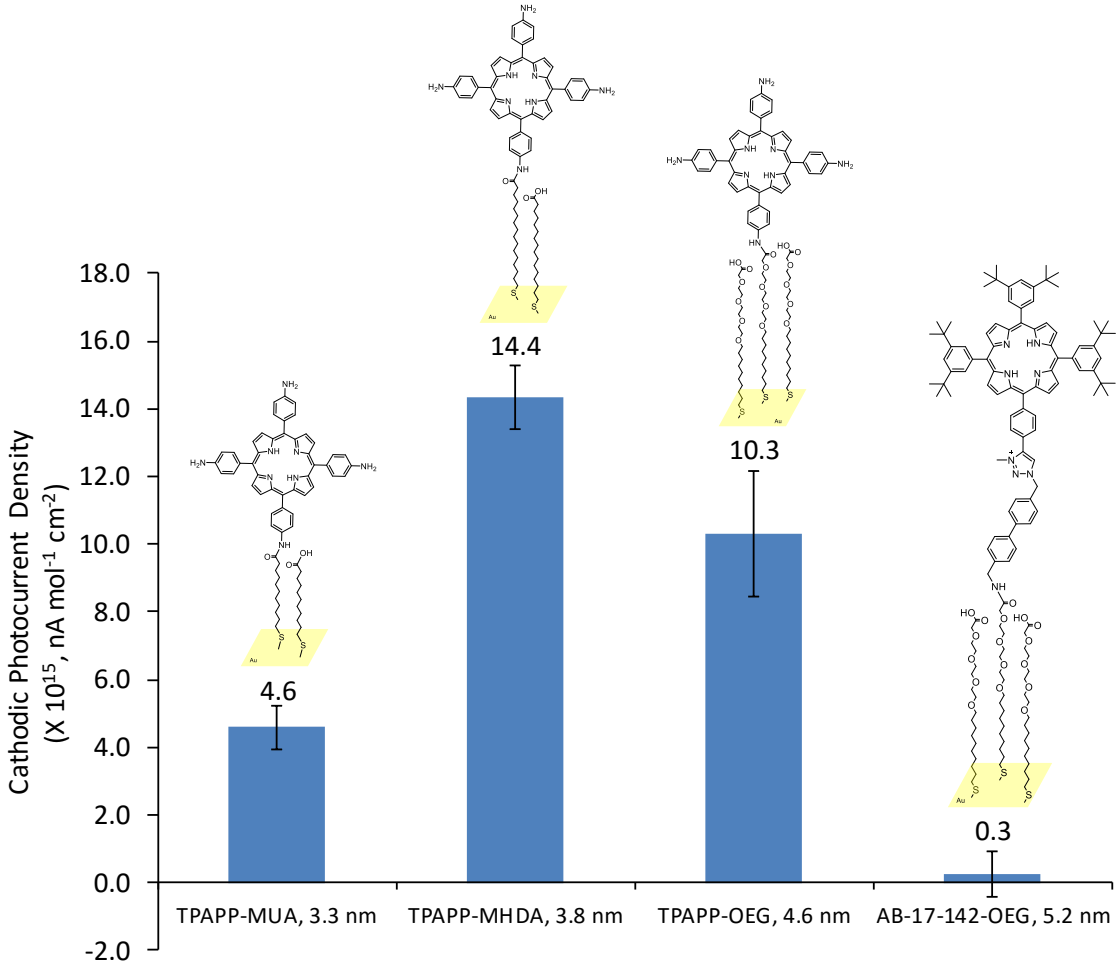


**Figure 17.** Cathodic photocurrent densities acquired at monophasic, porphyrin-appended SAMs formed at Au. All cathodic photocurrents were measured in 0.1 M $Na_2SO_4$ (aq.) containing 5 mM $MV^{2+}$ as an electron acceptor. The electrodes were kept at – 100 mV (*vs.* Ag / AgCl), illuminated with light of wavelength 430 ± 5 nm and the photocurrents normalised for the concentration of porphyrin present at each interface, as determined by cyclic voltammetry (**Appendix, 8.1.2**). Each error bar is equivalent to 3SD and calculated from the data

acquired across four separately prepared electrodes. All porphyrin-Au spatial separations were previously determined by ellipsometry (**Table 2**).

**Figure 17** highlights the fact that upon increasing the distance between the porphyrin moiety and the metallic surface, up until 3.8 nm, the magnitude of the cathodic photocurrent density increased in line with the expected decrease in both the backward rates of electron and energy transfer from $P^*$ to the metallic surface[6,7,8,9,10,11]. A similar observation was made by Imahori *et al*. when investigating the effect of chain length on the structure and photoelectrochemical properties of self-assembled monolayers of porphyrins, linked *via* a symmetrical dialkyl disulfide spacer[10].

Upon increasing the spatial separation further, that is beyond 3.8 nm, by means of utilising the OEGylated thiol derivative, a reduction in the magnitude of cathodic photocurrent density generated was observed. This suppression is attributed to the expected decline in the rate of forward electron transfer between the electrochemically addressable interface and the photoactive moiety[6,7,8,9,10,11].

In conclusion, it can be stated that **X** is approximately equal to 3.8 nm, **Figure 4**, and beyond this distance a relay moiety is required to mediate electron transfer and / or compensate for the drop in the rate of forward electron transfer. Further experiments, in which the spatial separation is set at between 3.8 and 4.6 nm, are required to determine the true value of **X**. The varying level of the unwanted association of the porphyrinic macrocycle (TPAPP and / or AB-14-172 at MUA and / or MHDA) made acquiring consistent data sets difficult. Nevertheless, the spatial separation trend alluded to above (**Figure 17**) held throughout.

### 2.2.3 – Modulating the Magnitude of Photoelectrochemical Output

Prior to simultaneously depositing varying chain length ferrocenethiols, in a bid to mediate electron transfer between the Au substrate and $P^*$, and thus compensate for the predicted drop in the magnitude of the cathodic photocurrent density generated at Por-Au distances > 3.8 nm, an electron mediator was added into solution in a bid to elucidate whether the relay effect could be realised by the addition of a metallocene into solution, **Figure 18** (**Appendix, 8.3.1**).

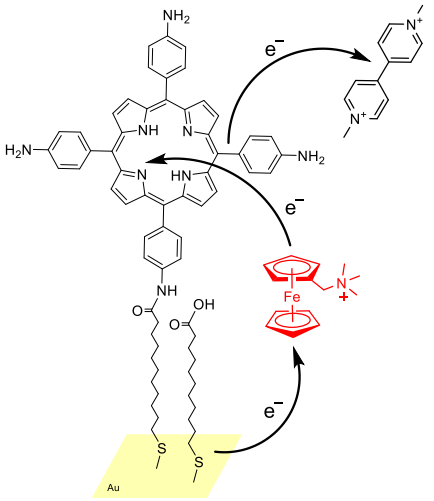


**Figure 18**. Mediating electron transfer within monophasic, porphyrin-appended molecular films. Introducing a diffusive electron mediator into solution, in the form of $FcCH_2NMe_3^+$, compensates for the drop in the rate of forward electron transfer (Au → P*).

Upon adding (ferrocenylmethyl)trimethylamonium iodide ($FcCH_2NMe_3^+$) into solution, the desired relay effect was observed, **Figure 19** (**Appendix, 8.3.1**), that is greater cathodic photocurrent densities were acquired in its presence. Thus, it has been found that a diffusive metallocene can mediate electron transfer between a redox-addressable interface and a photoactive moiety. Its addition into solution, at a concentration of 1 mM, was found to bring about a 286 ± 12 % increase in the magnitude of cathodic photocurrent density acquired at a TPAPP-MUA modified interface, whilst the enhanced photoelectrochemical outputs were shown to be potential dependent in accordance with its $E_{1/2}$ value (610 mV, *vs* Ag / AgCl), **Figure 20** (**Appendix, 8.3.1**).

Furthermore, greater cathodic photocurrent densities were acquired in the presence of the electron acceptor species, $MV^{2+}$. Photoelectrochemical output was however observed in its absence, albeit of significantly lower magnitude, because although oxygen can act as an electron 'sink', electron transfer from the singlet excited state of the porphyrin moiety to $MV^{2+}$ proceeds in preference to the analogous electron transfer process to dissolved $O_2$. Electron transfer to the former derivative is favoured because the redox potential of $^1P_2^*/P_2^{\bullet+}$ (- 800 mV) is energetically closer to the reduction potential of $MV^{2+}$ (- 620 mV), *cf.* $O_2$ (- 480 mV), and $MV^{2+}$ is present at a much higher concentration (mM *vs*. μM)[6,10,11].

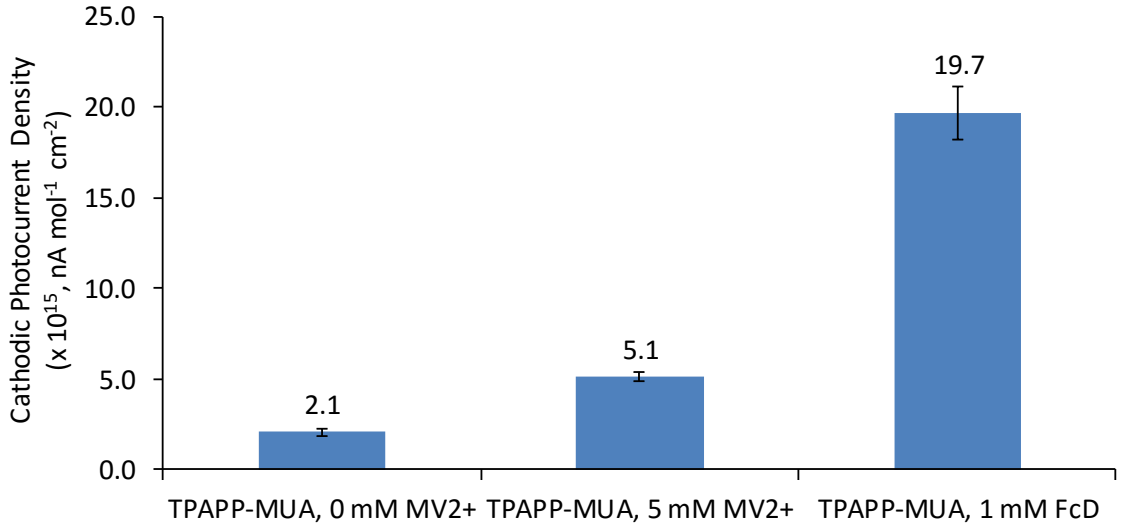


**Figure 19.** Cathodic photocurrent densities acquired at a SAM of TPAPP-MUA deposited at Au, prior to and following the additions of 5 mM $MV^{2+}$ and 1 mM FcD ($FcCH_2NMe_3^+$) to the electrolytic solution. All cathodic photocurrents were measured in 0.1 M $Na_2SO_4$ (aq.) whilst the electrodes were kept at – 100 mV (*vs.* Ag / AgCl), illuminated with light of wavelength 430 ± 5 nm and the photocurrents normalised for the concentration of porphyrin present at the interface, as determined by cyclic voltammetry (**Appendix, 8.1.2**). Each error bar is equivalent to 3SD and calculated from the data acquired across four separately prepared electrodes. Electrochemical Cell Setup: *Working Electrode*: TPAPP-MUA. *Reference Electrode*: Ag / AgCl. *Auxiliary Electrode*: Pt Wire. *Electrolytic Solution*: 0.1 M $Na_2SO_4$, (+ 5 mM $MV^{2+}$, + 1 mM FcD ($FcCH_2NMe_3^+$)). *Solvent*: $H_2O$. *Bias Potential*: - 100 mV. $\lambda_{irr}$: 430 ± 5 nm.

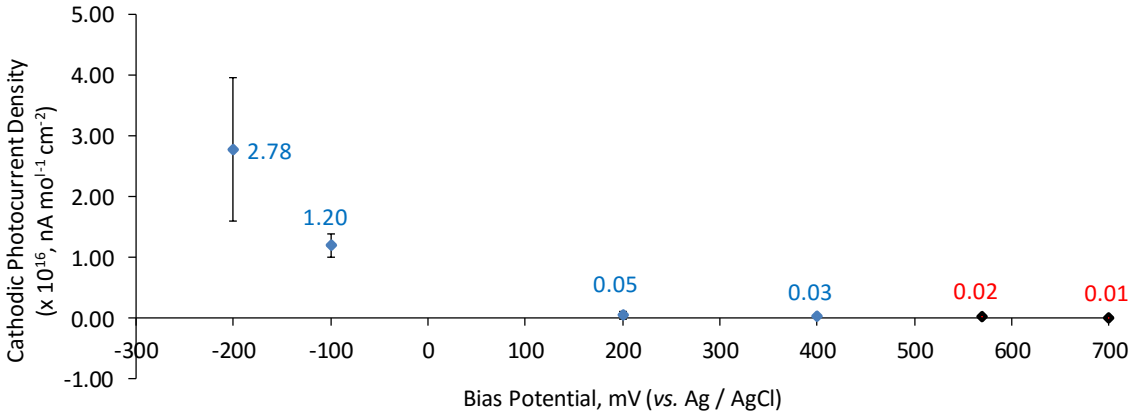


**Figure 20.** Manipulating the cathodic photocurrent density acquired at a SAM of TPAPP-MUA deposited at Au by varying the bias potential of the working electrode. All cathodic photocurrents were measured in 0.1 M $Na_2SO_4$ (aq.) containing 5 mM $MV^{2+}$ as an electron acceptor. The electrodes were illuminated with light of wavelength 430 ± 5 nm and the photocurrents normalised for the concentration of porphyrin present at the interface, as determined by cyclic voltammetry (**Appendix, 8.1.2**). Each error bar is equivalent to 3SD and calculated from the data acquired across four separately prepared electrodes. Electrochemical Cell Setup: *Working Electrode*: TPAPP-MHDA. *Reference Electrode*: Ag / AgCl. *Auxiliary Electrode*: Pt Wire. *Electrolytic Solution*: 0.1 M $Na_2SO_4$, + 5 mM $MV^{2+}$, + 1 mM $FcCH_2NMe_3^+$. *Solvent*: $H_2O$. *Bias Potential*: Variable. $\lambda_{irr}$: 430 ± 5 nm.

Cathodic photocurrent densities were acquired at bias potentials of – 200, - 100, 200 and 400 mV, **Figure 20**, whilst the flow of cathodic photocurrent was supressed at bias potentials ≥ 550 mV. This is in agreement with the $E_{1/2}$ value (610 mV, *vs* Ag / AgCl) of the diffusive metallocene, which when reduced (< 560 mV) accepts an electron from the gold Fermi level, before transferring it to the

photoactive moiety prior to the generation of a stable, cathodic photocurrent[6,7,8,9]. Greater cathodic photocurrents are generated upon loading minus voltage onto the working electrode, **Figure 21** (**Appendix, 8.3.1**), due to the fact that it enhances the forward rate of electron transfer between the metallic substrate and the metallocene, which in turn further highlights the contribution made by the diffusive relay moiety[6].

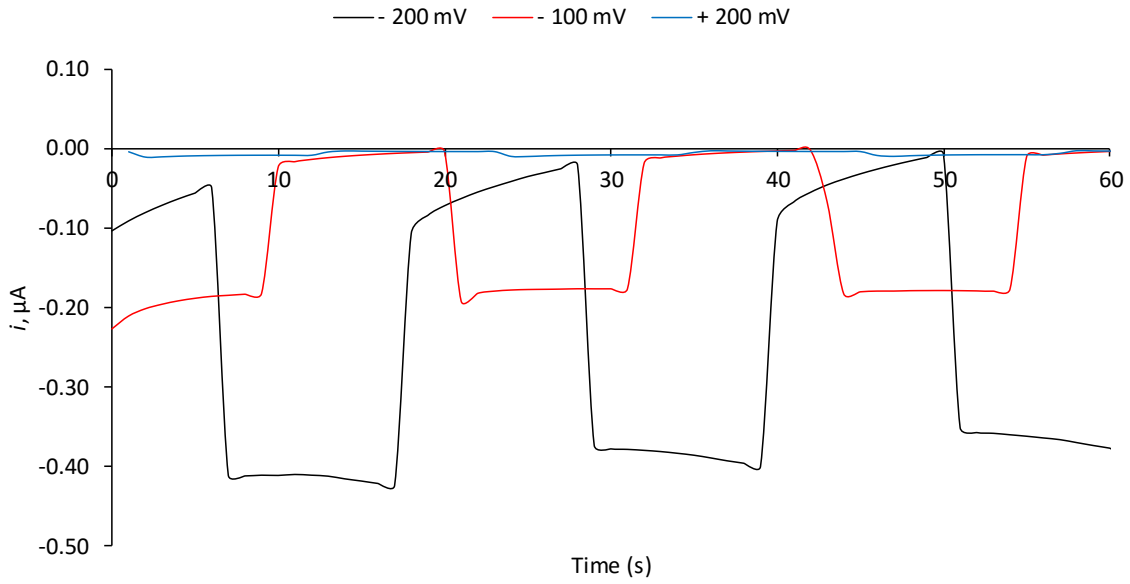


**Figure 21.** Current *vs.* time profiles for a Au electrode at which a SAM of TPAPP-MUA had been deposited. The electrode was kept at either + 200 mV (**Blue**), – 100 mV (**Red**) or – 200 mV (**Black**) and illuminated with light of wavelength 430 ± 5 nm. Electrochemical Cell Setup: *Working Electrode*: TPAPP-MHDA. *Reference Electrode*: Ag / AgCl. *Auxiliary Electrode*: Pt Wire. *Electrolytic Solution*: 0.1 M $Na_2SO_4$, + 5 mM $MV^{2+}$, + 1 mM $FcCH_2NMe_3^+$. *Solvent*: $H_2O$. *Bias Potential*: Variable.

However, at bias potentials more positive than the reduction potential of $FcCH_2NMe_3^+$ (570 and 700 mV), the flow of cathodic photocurrent is suppressed, and it is likely that the flow of an anodic photocurrent would have been initiated upon the addition of a sacrificial electron donor such as triethanolamine[33].

In conclusion, it has been demonstrated that cathodic photocurrent density can be generated at a variety of porphyrin-functionalised SAMs, of which have been fabricated on polycrystalline Au macroelectrodes. The magnitude of the photoelectrochemical output acquired is enhanced upon tethering the photoactive moiety further from the interface, and / or upon the addition of either an electron acceptor ($MV^{2+}$) and / or an electron mediator ((ferrocenylmethyl)trimethylamonium iodide) into solution. The electron acceptor moiety acts as an electron 'sink', whilst the electron mediator serves to mediate electron transfer and / or compensate for the drop in the forward rate of electron transfer between the metallic substrate and $P^*$.[6,7,8,9,10,11] A drop in the rate of forward electron transfer arises as the photoactive moiety is tethered further from the interface (> 3.8 nm) in order to reduce the rates of both backward electron and backward energy transfer from $P^*$ to the Au

surface[6,7,8,9,10,11]. Furthermore, the mediation of electron transfer has been shown to be potential dependent, thus highlighting the metallocene's ability to act as an effective relay group, paving the way to investigate this phenomenon upon the simultaneous deposition of varying chain length ferrocenethiols within biphasic SAMs, **Figure 3**.

## 2.3 – Establishing a Conformational 'Ruler' within Biphasic, Porphyrin-Appended SAMs

After utilising a diffusive electron mediator to enhance the magnitude of cathodic photocurrent density generated at monophasic monolayers (**Figures 2** and **19**), biphasic SAMs were generated in a bid to probe the distance dependency associated with this intermolecular relay effect, **Figure 22**. To recap, it was hoped that this would shed light on at what distance two molecular stations needed to be set apart, within a dynamic supramolecular architecture, to allow for the differentiation of the GSCC and the MSCC[1,2,3,4,5]. Thus, this would ensure that the position of a ferrocene-appended macrocycle could be photoelectrochemically resolved within such a system.

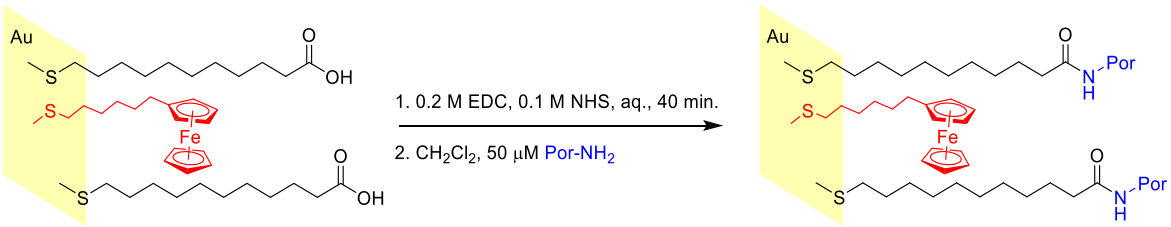


**Figure 22.** Covalent attachment of TPAPP and AB-14-172 to biphasic SAMs deposited at Au.

Prior to investigating the generation of cathodic photocurrent density at each of the fabricated biphasic SAMs, **Figure 3**, CV (**Appendix, 8.1.3**) was used to demonstrate that both the porphyrin derivative (TPAPP or AB-14-172) and ferrocene thiol ($Fc(CH_2)_6SH$ or $Fc(CH_2)_{11}SH$) were present at the interface, and at what concentration relative to one another. Unlike in the case of the porphyrin-appended, monophasic monolayers, **Figure 2**, ellipsometry and UV-Vis spectroscopy were not utilised when trying to characterise the biphasic monolayers, **Figure 3**. Ellipsometry was not employed because the film thickness value acquired by means of this optical technique is calculated upon analysing the change in polarisation upon the reflection of light from the surface of the sample. This typically occurs across a large surface area, and thus assumes that the monolayer is both homogenous and isotropic (*cf.* angle resolved XPS), something that the biphasic monolayers fabricated are unlikely to be following the probable event of phase segregation and / or the formation of molecular domains[34,35,36,37,38,39,40,41]. Hence, any film thickness value acquired is likely to have been an average of that acquired from each molecular domain. However, monolayers of both 6-(ferrocenyl)hexanethiol and 11-(ferrocenyl)undecanethiol were deposited, revealing close to ideal ellipsometric film thickness values in the process, 1.2 and 1.7 ± 0.2 nm, respectively. It was expected

for these derivatives to align surface normal when simultaneously deposited with carboxy-functionalised thiols of varying chain length (**Figure 22**), and thus this assumption is the origin of both the Au-Fc and Fc-Por distances quoted herein. In addition, UV-Vis spectroscopy was not of use when trying to verify the interfacial presence of both the porphyrinic macrocycle and the metallocene; a signature confirming the presence of ferrocene was not acquired upon analysis of SAMs of either 6-(ferrocenyl)hexanethiol or 11-(ferrocenyl)undecanethiol, *cf.* when analysing monolayers appended with either TPAPP or AB-14-172, **Figures 3 and 15**. This was not unexpected as the molar extinction coefficient of ferrocene (96 $cm^{-1}$ $M^{-1}$, at 442 nm, cyclohexane)[42,43,44] is significantly lower than that of a porphyrin (tetraphenylporphyrin, 413, 698 $cm^{-1}$ $M^{-1}$, at 419 nm, toluene)[43,44,45,46,47,48].

The simultaneous deposition of the photoactive (TPAPP or AB-14-172) and relay ($Fc(CH_2)_6SH$ or $Fc(CH_2)_{11}SH$) moieties was however confirmed by both CV, **Figure 23** (**Appendix, 8.1.3**), and XPS, **Figure 24**. That is, upon analysis of the biphasic SAMs, both redox couples, Fc / $Fc^+$ ($E_{1/2}$ 510 mV, *vs*. Ag / AgCl) and $P^0$ / $P^{+1}$ ($E_{1/2}$ 1084 mV, *vs*. Ag / AgCl), were observed, and peaks at approximately 400 and in the range 700 – 740 eV were observed in the corresponding x-ray photoelectron spectra; peaks at these respective binding energies confirm that the –N= functionalities of the porphyrinic macrocycle (440 eV)[7] and the Fe centre (700 – 740 eV)[7,49] of the metallocene were both present at the interface, as was desired.

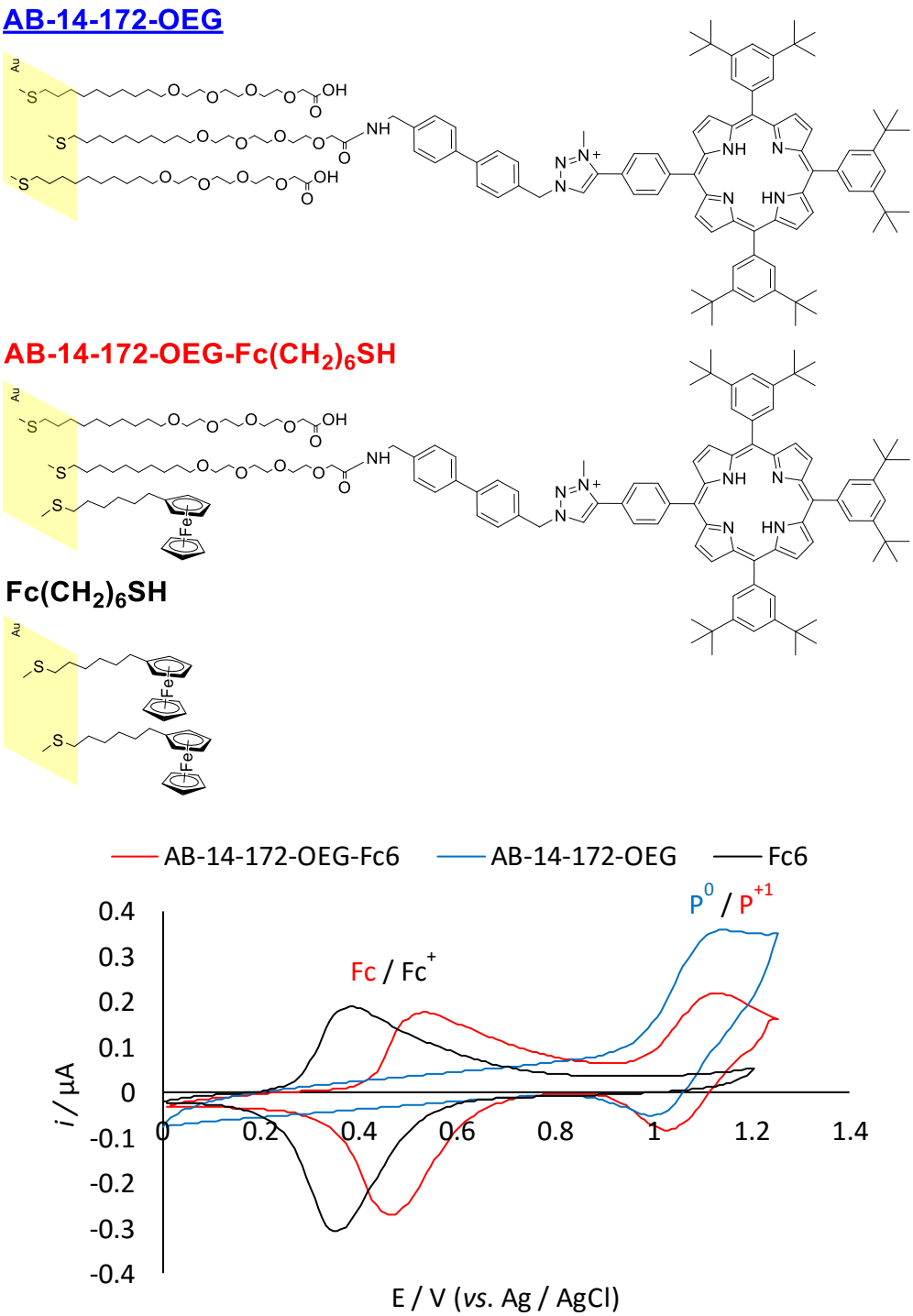


**Figure 23.** Cyclic voltammograms of an activated SAM of OEG following immersion in a solution (50 µM, anhydrous $CH_2Cl_2$) of AB-14-172, in the presence (**Red**) and absence (**Blue**) of $Fc(CH_2)_6SH$ (Fc6). A cyclic voltammogram of a SAM of Fc6 (**Black**) deposited at Au is also given. Electrochemical Setup: *Working Electrode*: SAM. *Reference Electrode*: Ag / AgCl. *Auxiliary Electrode*: Pt wire. *Electrolytic Solution*: 0.1 M $TBAPF_6$, anhydrous $CH_2Cl_2$. *Scan Rate:* 1000 mV / s.

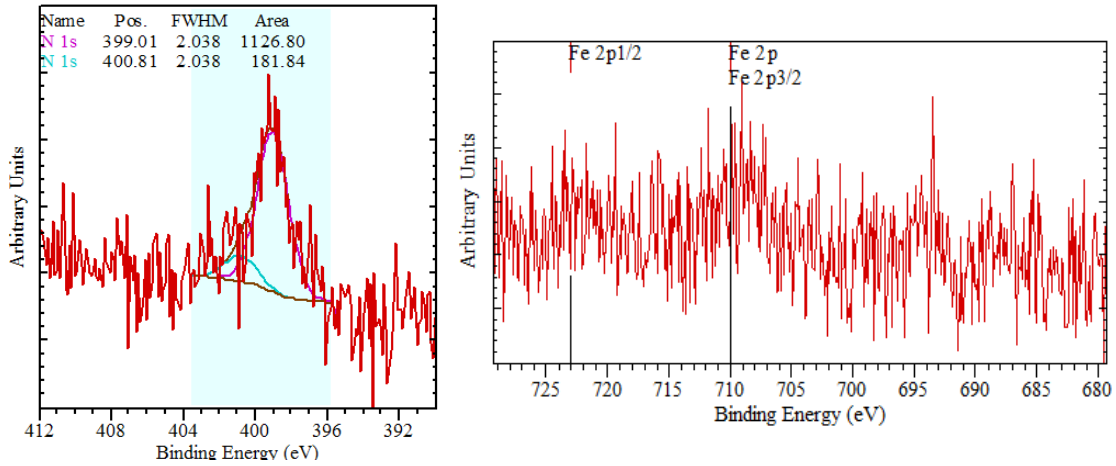


**Figure 24.** Narrow scan (N 1s (**Left**), Fe 2p (**Right**)) XPS spectra of a SAM of AB-14-172-OEG-Fc$(CH_2)_6$SH deposited at Au (**Figure 23**).

As in the case of the monophasic monolayers, the surface concentration of each moiety (Fc$(CH_2)_{6/11}$SH, TPAPP or AB-14-172) was established by integrating the area under the oxidative peak of the respective redox couple, and normalising the response for the geometric surface area of the electrode on which the biphasic monolayers had been deposited. The acquired surface concentration of each moiety present within all the fabricated biphasic interfaces, **Figure 3**, is given in **Table 4** (**Appendix, 8.1.3**).

| **Underlying Biphasic Monolayer** | **Porphyrin Derivative** | **Fc / $Fc^+$ []** (x $10^{-10}$ mol $cm^{-2}$) (% of Pure Monolayer of Fc$(CH_2)_6$SH or Fc$(CH_2)_{11}$SH) | **$P^0$ / $P^{+1}$ []** (x $10^{-10}$ mol $cm^{-2}$) (% of Pure Monolayer of TPAPP or AB-14-172) |
|---|---|---|---|
| MUA – Fc$(CH_2)_6$SH | TPAPP | 0.80 ± 0.05 (21 %) | 0.52 ± 0.08 (8.3 %) |
| MUA – Fc$(CH_2)_{11}$SH | TPAPP | 1.7 ± 0.60 (43 %) | 0.24 ± 0.03 (3.8 %) |
| MHDA – Fc$(CH_2)_6$SH | TPAPP | 0.91 ± 0.04 (24 %) | 0.45 ± 0.06 (7.1 %) |
| MHDA – Fc$(CH_2)_{11}$SH | TPAPP | 1.7 ± 0.50 (43 %) | 0.26 ± 0.04 (4.1 %) |
| OEG – Fc$(CH_2)_6$SH | TPAPP | 0.87 ± 0.04 (23 %) | 0.49 ± 0.06 (7.7 %) |
| | AB-14-172 | 0.88 ± 0.06 (23 %) | 0.31 ± 0.03 (68 %) |
| OEG – Fc$(CH_2)_{11}$SH | TPAPP | 1.4 ± 0.40 (35 %) | 0.27 ± 0.04 (4.3 %) |
| | AB-14-172 | 1.3 ± 0.30 (33 %) | 0.28 ± 0.04 (62 %) |
| Fc$(CH_2)_6$SH | N / A | 3.8 ± 1.20 (*3.8 ± 1.0) | N / A |
| Fc$(CH_2)_{11}$SH | N / A | 4.0 ± 1.02 (*5.5 ± 1.0) | N / A |

**Table 4.** Concentration of **Fc / $Fc^+$** and **$P^0$ / $P^{+1}$** at biphasic, porphyrin-appended monolayers deposited at Au. All concentrations were determined by cyclic voltammetry (**Appendix, 8.1.3**), and each error bar is equivalent to 3SD and was calculated from the data acquired across five separately prepared electrodes. *As determined by Walczak *et al.*[21] and Lee *et al.*[50].

Upon inspection of **Table 4**, in all cases lower surface concentrations of 6-(ferrocenyl)hexanethiol (Fc$(CH_2)_6$SH) (21 – 23 % of that acquired for a pure monolayer (100 % Fc$(CH_2)_6$SH at Au, 3.8 ± 1.2 x $10^{-10}$ mol $cm^{-2}$)) were acquired in comparison to those obtained for 11-

(ferrocenyl)undecanethiol ($Fc(CH_2)_{11}SH$) (33 – 43 % of that acquired for a pure monolayer (100 % $Fc(CH_2)_{11}SH$ at Au, $4.0 \pm 1.0 \times 10^{-10}$ mol $cm^{-2}$)). It is not yet known why this is the case, although a difference in the rate of deposition is likely to be key. It is assumed that this observation arises because 11-(ferrocenyl)undecanethiol (1.7 ± 0.2 nm) can deposit at a much quicker rate and / or possesses a similar deposition rate to the carboxy-functionalised, alkylated thiols utilised, of which are similar in length (MUA: 1.4 ± 0.2 nm, MHDA: 2.0 ± 0.2 nm, OEG: 2.6 ± 0.2 nm), *cf.* 6-(ferrocenyl)hexanethiol (1.2 ± 0.2 nm), as supported by ellipsometry (**Table 1**). In addition, it can be seen that relatively low surface concentrations of TPAPP (3.8 – 8.3 % of that acquired for a pure monolayer (the monolayer(s) assembled in the absence of either $Fc(CH_2)_6SH$ or $Fc(CH_2)_{11}SH$, $4.0 \pm 1.0 \times 10^{-10}$ mol $cm^{-2}$)) were acquired throughout, although if it is presumed that the biphasic monolayers deposited resist unwanted, physical association of the aminated derivative, then this equates to surface concentrations of between 26 and 55 % of that expected for a monolayer of TPAPP ($9.4 \times 10^{-11}$ mol $cm^{-2}$), based on its size (MM2, Chem 3D 15.0). This range is closer to what was expected when considering the relative ratio (1 mM: 1 mM) of the two components present within the deposition solution. Steric hindrance is also likely to have prevented 100 % tethering efficiency being reached.

Upon assessing the concentration of the photoactive moiety (TPAPP or AB-14-172) present at each biphasic interface, **Figure 3**, cathodic photocurrent densities were acquired, **Figure 25** (**Appendix, 8.3.2**); the raw cathodic current data was normalised for the concentration of the porphyrinic macrocycle present. The data was not normalised for the concentration of ferrocene and / or ferrocenium present due to the fact that although this appeared more consistent, and the redox couple more stable, in comparison to the amount of either TPAPP or AB-14-172 present at the interface, which varied significantly, and was observed to decline over the course of the investigation(s), as discussed previously (**Figure 16**), normalising the data for the concentration of porphyrin present at the interface, ensured that comparison could be made with the cathodic photocurrents generated upon illumination of the monophasic monolayers.

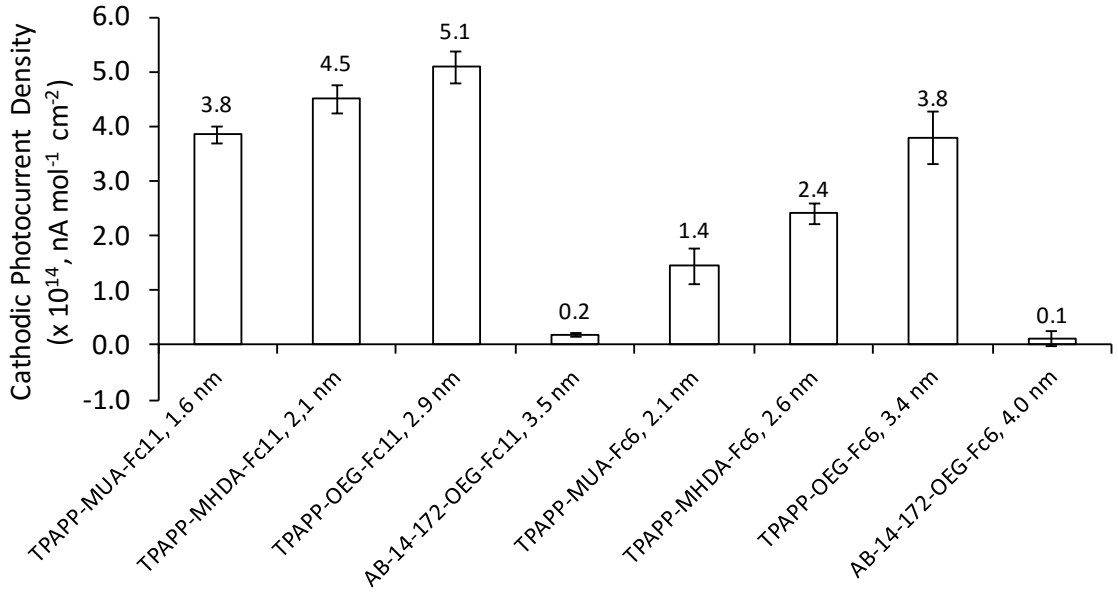


**Figure 25.** Cathodic photocurrent densities acquired at biphasic, porphyrin-appended SAMs deposited at Au. All cathodic photocurrents were measured in 0.1 M $Na_2SO_4$ (aq.) containing 5 mM $MV^{2+}$ as an electron acceptor. $Fc(CH_2)_6SH$: Fc6. $Fc(CH_2)_{11}SH$: Fc11. The electrodes were kept at – 100 mV (*vs.* Ag / AgCl), illuminated with light of wavelength 430 ± 5 nm and the photocurrents normalised for the concentration of porphyrin present at each interface, as determined by cyclic voltammetry (**Appendix, 8.1.3**). Each error bar is equivalent to 3SD and calculated from the data acquired across three separately prepared electrodes.

Upon the simultaneous deposition of varying chain length ferrocene-thiols, the expected enhancement in the magnitude of cathodic photocurrent density acquired was not observed, that is cathodic photocurrent densities of lesser magnitude were acquired upon covalently tethering the relay entity to the surface, **Figure 25**, *cf.* the monophasic systems, **Figure 2**. This is thought to occur as the result of significantly more porphyrin intercalation into the monophasic films, whereby the amount of intercalated material is greater than that covalently tethered to the periphery of the interface. This hypothesis only holds if it is assumed that the intercalated material is not electrochemically addressable, but is somehow able to prolong the lifetime of the photoexcited state of the tethered photoactive moieties. Furthermore, the effect of phase segregation on the magnitude of the photoelectrochemical output acquired is yet to be elucidated; that is, it is not known how a porphyrinic macrocycle is orientated upon becoming tethered to an underlying, biphasic interface. It has been assumed, in the absence of ellipsometric film thickness data, that all the deposited thiols align surface normal within the biphasic systems assembled (**Figure 3**). It could be that within biphasic systems, where this hypothesis does not hold and / or where phase segregation is more than likely to occur, bringing about a conformational change, the tethered porphyrin derivative is much closer to the quenching metallic surface than was modelled, thus any photoelectrochemical output is inherently supressed and the results acquired (**Figures 17** and **25**) are in line with what should be expected.

Irrespective of this observation, clear trends were observed within the data set acquired, **Figure 26** (**Appendix, 8.4**).

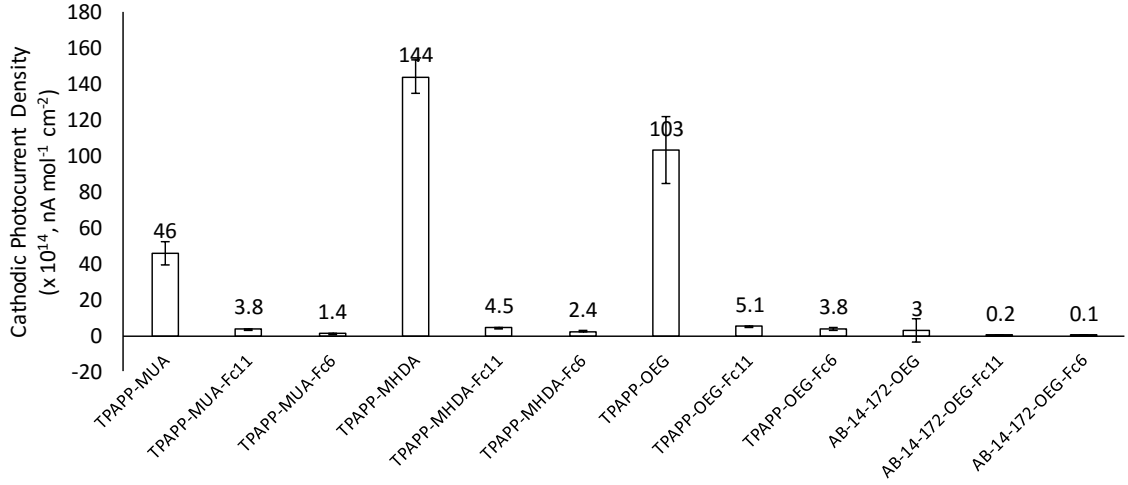


**Figure 26.** Cathodic photocurrent densities acquired at monophasic and biphasic porphyrin-appended SAMs deposited at Au. All cathodic photocurrents were measured in 0.1 M $Na_2SO_4$ (aq.) containing 5 mM $MV^{2+}$ as an electron acceptor. $Fc(CH_2)_6SH$: Fc6. $Fc(CH_2)_{11}SH$: Fc11. The electrodes were kept at – 100 mV (*vs.* Ag / AgCl), illuminated with light of wavelength 430 ± 5 nm and the photocurrents normalised for the concentration of porphyrin present at each interface, as determined by cyclic voltammetry (**Appendix, 8.1.2 and 8.1.3**). Each error bar is equivalent to 3SD and calculated from the data acquired across three (biphasic) or four (monophasic) separately prepared electrodes.

Unlike in the case of the monophasic films assembled (**Figure 26, Blue**), the magnitude of the cathodic photocurrent density acquired is not limited by the vertical spatial separation between the electronically addressable substrate and the photoactive moiety. That is, in the presence of either 6-(ferrocenyl)hexanethiol ($Fc(CH_2)_6SH$) or 11-(ferrocenyl)undecanethiol ($Fc(CH_2)_{11}SH$), increasingly greater cathodic photocurrent densities are acquired upon increasing the distance between the porphyrin moiety and the Au surface, *i.e.* TPAPP-MUA-$Fc(CH_2)_{11}SH$ < TPAPP-MHDA-$Fc(CH_2)_{11}SH$ < OEG-$Fc(CH_2)_{11}SH$ and TPAPP-MUA-$Fc(CH_2)_6SH$ < TPAPP-MHDA-$Fc(CH_2)_6SH$ < OEG-$Fc(CH_2)_6SH$. This dissimilarity highlights the fact that a covalently tethered relay moiety is able to mediate electron transfer between the metallic substrate and $Por^*$.[6,7,8,9] Thus, it is able to compensate for the drop in the rate of forward electron transfer, whilst ensuring that suppression of the rates of both backward electron and backward energy transfer from $Por^*$ to the Au surface is upheld[6,7,8,9,10,11]. This was not the case following analysis of the analogous monophasic systems, where it was concluded that the magnitude of the cathodic photocurrent density generated declined upon increasing the porphyrin-Au distance beyond 3.8 nm, *i.e.* MUA-TPAPP < MHDA-TPAPP > OEG-TPAPP > OEG-AB-14-172, **Figure 17**. A decline in the magnitude of the cathodic photocurrent density acquired upon irradiation of the biphasic monolayers was only observed upon increasing the distance between the relay ($Fc(CH_2)_6SH$ or $Fc(CH_2)_{11}SH$) and photoactive (TPAPP or AB-14-172) moieties to > 3.4 nm (**Figures 3 and 25**, **AB-14-172-OEG-$Fc(CH_2)_{11}SH$**). This was

attributed to the fact that beyond ferrocene-porphyrin separations of 3.4 nm, it was assumed that the distance was too great as to facilitate efficient electron transfer between the two moieties. In addition, it is thought that the inherently smaller surface coverages acquired for the shorter chain ferrocenethiol derivative ($Fc(CH_2)_6SH$), **Table 4**, limit the magnitude of the photoelectrochemical response observed, *cf.* $Fc(CH_2)_{11}SH$. Throughout, involvement of the relay moiety was highlighted by demonstrating the cathodic photocurrent output to be potential dependent in accordance with the $E_{1/2}$ value (490 mV, *vs*. Ag / AgCl) of the surface-tethered metallocene, **Figure 27** (**Appendix, 8.3.2**); greater cathodic photocurrent densities were acquired upon poising the electrode more negative than the reductive potential (468 mV, *vs*. Ag / AgCl) of the surface-tethered redox moiety. This occurs for the same reason as to why greater cathodic photocurrent densities are generated at monophasic, porphyrin appended SAMs upon adding (ferrocenylmethyl)trimethylamonium iodide into solution, and poising the electrode more negative than 560 mV (*vs*. Ag / AgCl) (**Section 2.2.3**).

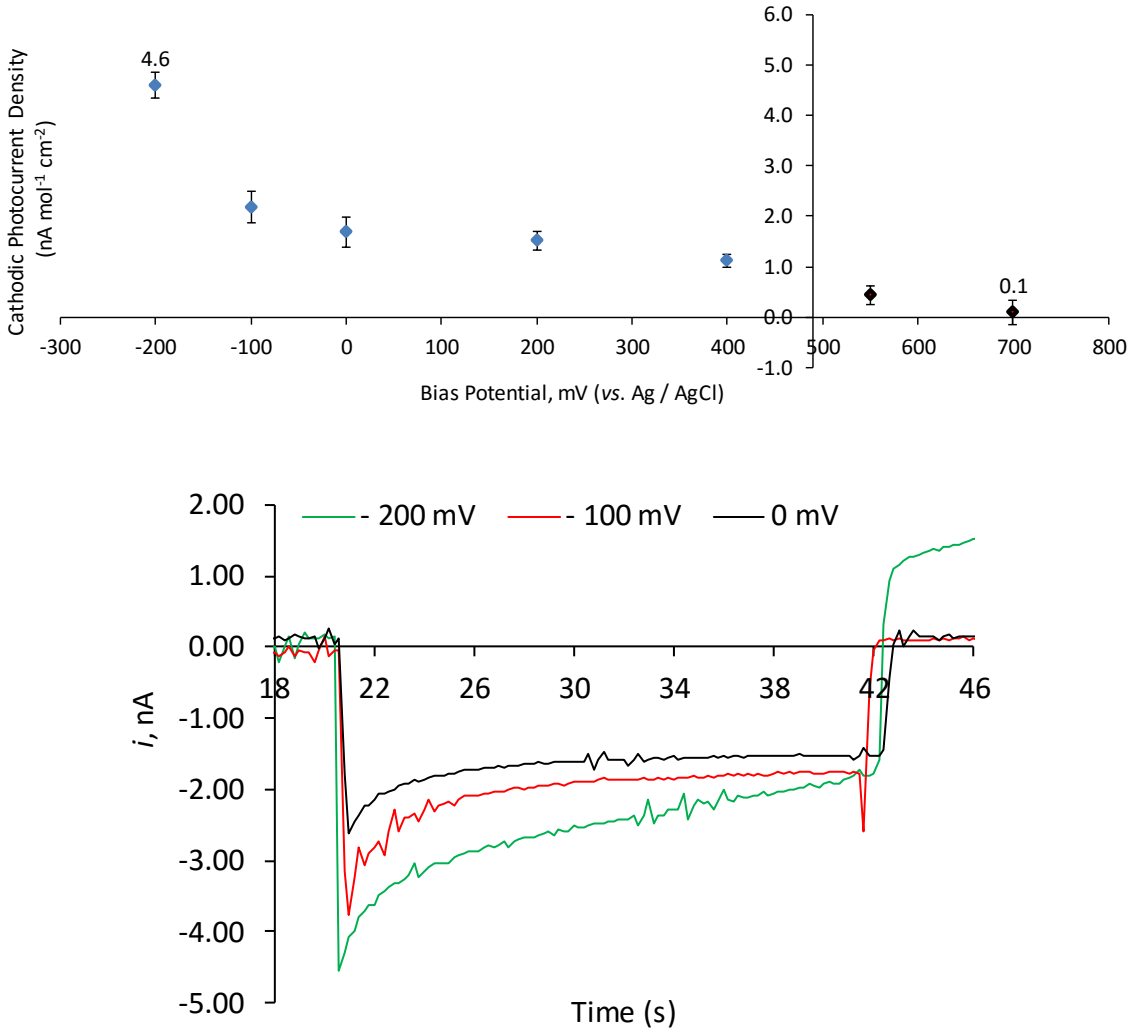


**Figure 27.** **Top.** Manipulating the cathodic photocurrent density acquired at a SAM of AB-14-172-OEG-$Fc(CH_2)_{11}SH$ deposited at Au by varying the bias potential of the working electrode. All cathodic photocurrents were measured in 0.1 M $Na_2SO_4$ (aq.) containing 5 mM $MV^{2+}$ as an electron acceptor. The electrodes were illuminated with light of wavelength 430 ± 5 nm and the photocurrents normalised for

the concentration of porphyrin present at the interface, as determined by cyclic voltammetry (**Appendix, 8.1.3**). Each error bar is equivalent to 3SD and calculated from the data acquired across three separately prepared electrodes. **Bottom.** Current *vs.* time profiles for a Au electrode at which a SAM of AB-14-172-OEG-Fc$(CH_2)_{11}$SH had been deposited. All profiles were measured in 0.1 M $Na_2SO_4$ (aq.) containing 5 mM $MV^{2+}$ as an electron acceptor. The electrode was kept at either 0 mV (**Black**), – 100 mV (**Red**) or – 200 mV (**Green**) and illuminated with light of wavelength 430 ± 5 nm. Electrochemical Cell Setup: *Working Electrode*: OEG-AB-14-172-Fc$(CH_2)_{11}$SH. *Reference Electrode*: Ag / AgCl. *Auxiliary Electrode*: Pt Wire. *Electrolytic Solution*: 0.1 M $Na_2SO_4$ + 5 mM $MV^{2+}$. *Solvent*: $H_2O$. *Bias Potential*: Variable.

## 2.4 – Concluding Remarks and Moving Forwards

In conclusion, the novel incorporation of an intermolecular relay moiety serves to extend the distance from the interface at which a drop in the magnitude of normalised cathodic photocurrent is realised. It serves to mediate electron transfer between the electronically addressable interface and $P^*$. This is essential when the porphyrin-Au distance is increased beyond 3.8 nm (**Figures 3** and **17**, TPAPP-MHDA), although the magnitude of the cathodic photocurrent density acquired then becomes dependent upon the spatial separation between the relay group and both the metallic interface and the photoactive moiety. Greatest cathodic photoelectrochemical output was observed when the photoactive moiety and the metallic interface were separated by a vertical distance of 4.6 nm, and the relay moiety was positioned 1.7 nm from the interface and / or 2.9 nm from the porphyrinic macrocycle, **Figures 3** and **25**, **TPAPP-OEG-Fc$(CH_2)_{11}$SH**. Following the analysis of such spatial dependencies and / or the construction of a conformational ruler, it is plausible to suggest that 'mapping' the anion-induced, translational motion of a ferrocene-appended macrocycle within such a molecular architecture as the one depicted in **Figure 28,** should be possible by the novel photoelectrochemical approach documented.

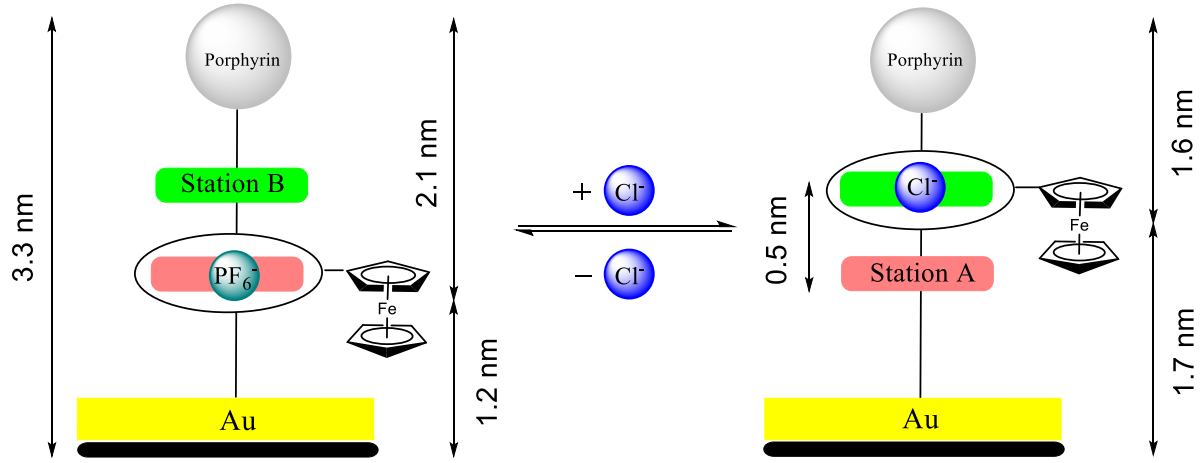


**Figure 28.** Implementing the conformational ruler established within the design of a novel bistable [2]rotaxane. All quoted distances were estimated by a minimisation approach (MM2) performed in Chem3D 15.0.

This system was designed based on the cathodic photocurrent densities acquired at the mono- and biphasic films incorporating MUA, whereby the porphyrin-Au distance was experimentally shown to equal 3.3 nm (**Table 2**), and the ferrocene-porphyrin distance assumed to equal either 1.6 (**Figure**

**3**, **TPAPP-MUA-Fc$(CH_2)_{11}$SH)** or 2.1 nm (**Figure 3**, **TPAPP-MUA-Fc$(CH_2)_6$SH**), depending at which station the ferrocene-appended macrocycle was located at. Although larger cathodic photocurrent densities were acquired upon the irradiation of porphyrin-appended MHDA interfaces (**Figures 17** and **25**), and the analogous OEGylated thiol films shown to resist unwanted association of the aminated porphyrin derivatives to greatest degree (**Figure 14** *vs*. **Figure 16**), the use of MUA brought about a larger difference in the cathodic photocurrent densities acquired upon the deposition of 6-(ferrocenyl)hexanethiol and 11-(ferrocenyl)undecanethiol, **Table 5**.

**Cathodic Photocurrent Density (nA $mol^{-1}$ $cm^{-2}$)**

| SAM | | **+ Fc$(CH_2)_6$SH** | **+ Fc$(CH_2)_{11}$SH** | **% Difference** |
|---|---|---|---|---|
| TPAPP-MUA | 4.60 x $10^{15}$ | 1.40 x $10^{14}$ | 3.80 x $10^{14}$ | 92 |
| TPAPP-MHDA | 1.44 x $10^{16}$ | 2.40 x $10^{14}$ | 4.50 x $10^{14}$ | 61 |
| TPAPP-OEG | 10.3 x $10^{15}$ | 3.80 x $10^{14}$ | 5.10 x $10^{14}$ | 29 |

**Table 5.** Comparison of the cathodic photocurrent densities acquired upon tethering TPAPP to SAMs of MUA, MHDA and OEG deposited at Au, in the absence and presence of Fc$(CH_2)_6$SH and Fc$(CH_2)_{11}$SH.

It was thought that this would aid in the photoelectrochemical differentiation of the GSCC and the MSCC; upon translocation of the ferrocene-appended macrocycle, from molecular station A (Fc$(CH_2)_6$SH, 1.2 ± 0.2 nm) to molecular station B (Fc$(CH_2)_{11}$SH, 1.7 ± 0.2 nm), an increase of 171 % ((3.80 x $10^{14}$ - 1.4 x $10^{14}$) / 1.40 x $10^{14}$) *100)) in the magnitude of the cathodic photocurrent density was to be expected, given the above result(s) (**Table 5**). With this is mind, a static interlocked supramolecular architecture was assembled, **Figure 29**, and its covalent attachment to a MUA-modified interface investigated. Since the axle component (AB-14-172) is significantly larger than TPAPP, the resulting molecular film was envisaged to closely resemble that, in terms of the vertical spatial separations invoked, of coupling TPAPP to an underlying, OEGylated thiol interface, **Figure 2**, and / or the intermediate distance regime ($PC_8FcC_{11}SH$) reported by the group of Uosaki[6,7,8,9], **Figure 5**.

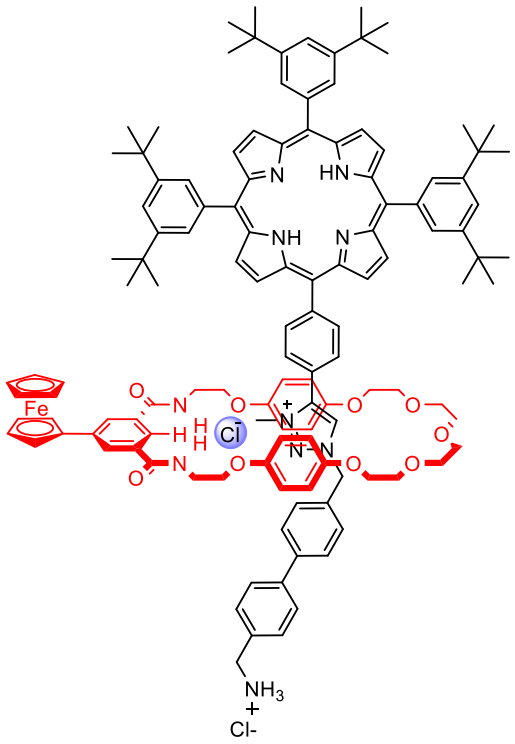


**Figure 29.** Solution phase formation of the pseudorotaxane, AB-14-172-JL241; mixing stoichiometric amounts of AB-14-172 and JL241led to the formation of the interlocked supramolecular architecture. JL241 was synthesised by Mr Jason Lim of the Paul Beer Group (University of Oxford).

Upon covalently coupling the assembly to an underlying SAM of MUA, it was predicted (MM2, Chem3D 15.0) for the porphyrin-Au distance to equal 4.3 nm, the ferrocene-macrocycle to reside at either 2.0 or 2.5 nm from the interface, and porphyrin-ferrocene spatial separations of either 1.8 and 2.3 nm to be attained. In all cases, based on the results presented within this chapter, cathodic photocurrents of differentiable magnitude were expected to be acquired at each molecular station, presuming that the metallocene was not electrochemically decoupled from the interface at distances greater than 1.7 nm. Thus, the deposition of the static, interpenetrated assembly (**Figure 29**) at a SAM of MUA, **Figure 30**, set out to determine whether upon the interlocking of a ferrocene-appended macrocycle, at 2.5 nm from the interface, and 1.8 nm from the porphyrinic macrocycle, cathodic photocurrent could be induced and subsequently quantified.

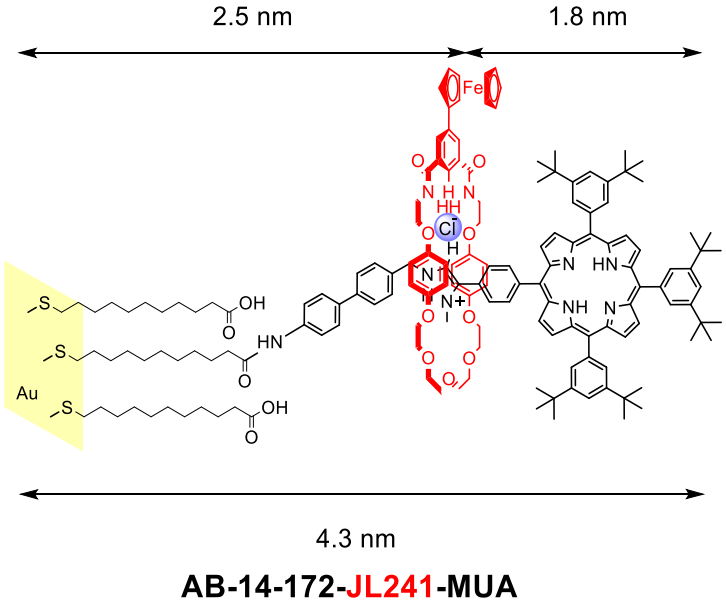


**Figure 30.** Tethering AB-14-172-JL241to an activated SAM of MUA deposited at Au. All quoted distances were estimated by a minimisation approach (MM2) performed in Chem3D 15.0.

If successful, it was intended for another molecular station to be integrated into the molecular architecture, at a distance closer to the interface, to permit macrocyclic translocation and thus permit photoelectrochemical transduction of the dynamic and reversible process thereafter. **Chapter 3** documents the research performed on this front.

## List of References

1. Cheng Wang, Dennis Cao, Albert C. Fahrenbach, Lei Fang, Mark A. Olson, Douglas C. Friedman, Subhadeep Basu, Sanjeev K. Dey, Youssry Y. Botros, J. Fraser Stoddart, *J. Phys. Org. Chem*. **2012**, 25, 544-552.
2. Albert C. Fahrenbach, Carson J. Bruns, Hao Li, Ali Trabolsi, Ali Coskun, J. Fraser Stoddart, *Acc. Chem. Res*., **2014**, 47, 482-493.
3. Seung Soon Jang, Yun Hee Jang, Yong-Hoon Kim, William A. Goddard III, Amar H. Flood, Bo W. Laursen, Hsian-Rong Tseng, J. Fraser Stoddart, Jan O. Jeppesen, Jang Wook Choi, David W. Steuerman, Erica DeIonno, James R. Heath, *J. Am. Chem. Soc*., **2005**, 127, 1563-1575.
4. Albert C. Fahrenbach, Jonathan C. Barnes, Hao Li, Diego Benítez, Ashish N. Basuray, Lei Fang, Chi-Hau Sue, Gokhan Barina, Sanjeev K. Dey, William A. Goddard III, J. Fraser Stoddart, *PNAS*, **2011**, 108, 20416-20421.
5. Sandrine Garaudée Dr., Serena Silvi, Margherita Venturi Prof., Alberto Credi Dr., Amar H. Flood Dr., J. Fraser Stoddart Prof., ChemPhysChem., **2005**, 6, 2145-2152.

6. Kohei Uosaki, Toshihiro Kondo, Xue-Qun Zhang, Masatoshi Yanagida, *J. Am. Chem. Soc.*, **1997**, 119, 8367-8368.
7. M. Yanagida, T. Kanai, X.-Q. Zhang, T. Kondo, K. Uosaki, *Bull. Chem. Soc. Jpn.*, **1998**, 71, 2555-2559.
8. T. Kondo, T. Kanai, K. Isoo, K. Uosaki, *Z. Phys. Chem.*, **1999**, 212, 23-30.
9. Toshihiro Kondo, Masatoshi Yanagida, Xue-Qun Zhang, Kohei Uosaki, *Chem. Lett*., **2000**, 29, 964-965.
10. Hiroshi Imahori, Hiroyuki Norieda, Yoshinobu Nishimura, Iwao Yamazaki, Kazuo Higuchi, Naohiko Kato, Tomoyoshi Motohiro, Hiroko Yamada, Koichi Tamaki, Masatoshi Arimura, Yoshiteru Sakata, *J. Phys. Chem. B*, **2000**, 104, 1253-1260.
11. Hiroshi Imahori, Taku Hasobe, Hiroko Yamada, Yoshinobu Nishimura, Iwao Yamazaki, Shunichi Fukuzumi, *Langmuir*, **2001**, 17, 4925-4931.
12. Philip Leighton, J. A. Cowan, Raymond J. Abraham, Jeremy K. M. Sanders, *J. Org. Chem*., **1988**, 53, 733-740.
13. F. Ricchelli, *Journal of Photochemistry and Photobiology B: Biology*, **1995**, 29, 109-118.
14. Joshua Lehr, Jamie Bennett, Manuel Tropiano, Thomas J. Sørensen, Stephen Faulkner, Paul D. Beer, Jason J. Davis, *Langmuir*, **2013**, 29, 1475-1482.
15. Sandra M. Mendoza, Imad Arfaoui, Simone Zanarini, Francesco Paolucci, Petra Rudolf, *Langmuir*, **2007**, 23, 582-588.
16. Joshua Lehr, Manuel Tropiano, Paul D. Beer, Stephen Faulkner, Jason J. Davis, *Chem. Commun.*, **2015**, 51, 15944-15947.
17. Dr. Joshua Lehr, Dr. Thomas Lang, Dr. Octavia A. Blackburn, Timothy A. Barendt, Prof. Stephen Faulkner, Dr. Jason J. Davis, Prof. Paul D. Beer, *Chem. Eur. J*., **2013**, 19, 15898-15906.
18. Cindra A. Widrig, Chinkap Chung, Marc D. Porter, *J. Electroanal. Chem.*, **1991**, 310, 335-359.
19. D.-F. Yang, C. P. Wilde, M. Morin, *Langmuir*, **1996**, 12, 6570-6577.
20. D.-F. Yang, C. P. Wilde, M. Morin, *Langmuir*, **1997**, 13, 243-249.
21. Mary M. Walczak, Darwin D. Popenoe, Randall S. Deinhammer, Brian D. Lamp, Chinkap. Chung, Marc D. Porter, *Langmuir*, **1991**, 7, 2687-2693.
22. Y. W. Yang, L. J. Fan, *Langmuir*, **2002**, 18, 1157-1164.
23. Colin D. Bain, Hans A. Biebuyck, George M. Whitesides, *Langmuir*, **189**, 5, 723-727.
24. Marie-Caroline Bourg, Antonella Badia, R. Bruce Lennox, *J. Phys. Chem. B*., **2000**, 104, 6562-6567.
25. Sirnegeda D. Techane, Lara J. Gamble, David G. Castner, *Biointerphases*, **2011**, 6, 98-104.
26. Mikael Wirde, Ulrik Gelius, *Langmuir*, **1999**, 15, 6370-6378.

27. Paul E. Laibinis, George M. Whitesides, David L. Allara, Yu Tai Tao, Atul N. Parikh, Ralph G. Nuzzo, *J. Am. Chem. Soc.*, **1991**, 113, 7152-7167.
28. Nakul C. Maiti, Shyamalava Mazumdar, N. Periasamy, *J. Phys. Chem B.*, **1998**, 102, 1528-1538.
29. R. F. Khairutdinov, *J. Phys. Chem B.*, **1999**, 103, 761-769.
30. Atsuhiro. Osuka, Kazuhiro. Maruyama, *J. Am. Chem. Soc.*, **1988**, 110, 4454-4456.
31. Mikael Andersson, Jan Davidsson, Leif Hammarström, *J. Phys. Chem. B.*, **1999**, 103, 3258-3262.
32. Jan Tkac, Jason J. Davis, *J. Electroanal. Chem.*, **2008**, 621, 117-120.
33. Hirotaka Uji, Yuji Yatsunami, Shunsaku Kimura, *J. Phys. Chem. C.*, **2015**, 119, 8054-8061.
34. Colin D. Bain, George M. Whitesides, *J. Am. Chem. Soc.*, **1989**, 111, 7164-7175.
35. S. J. Stranick, A. N. Parikh, Y.-T. Tao, D. L. Allara, P. S. Weiss, *J. Phys. Chem.*, **1994**, 98, 7636-7646.
36. John P. Folkers, Paul E. Laibinis, George M. Whitesides, *Langmuir*, **1992**, 8, 1330-1341.
37. C. D. Bain, G. M. Whitesides, *Science*, **1988**, 240, 62-63.
38. Paul E. Laibinis, Ralph G. Nuzzo, George M. Whitesides, *J. Phys. Chem.*, **1992**, 96, 5097-5105.
39. Kaoru Tamada, Masahiko Hara, Hiroyuki Sasabe, Wolfgang Knoll, *Langmuir*, **1997**, 13, 1558-1566.
40. John P. Folkers, Paul E. Laibinis, George M. Whitesides, John Deutch, *J. Phys. Chem.*, **1994**, 98, 563-571.
41. Daisuke Hobara, Masayuki Ota, Shin-ichiro Imabayashi, Katsumi Niki, Takashi Kakiuchi, *J. Electroanal. Chem.*, **1998**, 444, 113-119.
42. Bozak, R. E. (1971) Photochemistry in the metallocenes. In Advances in Photochemistry (Edited by J. N. Pitts, Jr., G. S. Hammond and W. A. Noyes, Jr.), 8, pp. 227-244. Wiley Interscience, New York.
43. James M. Dixon, Masahiko Taniguchi, Jonathan S. Lindsey, *Photochemistry and Photobiology*, **2005**, 81, 212-213.
44. Hai Du, Ru-Chun Amy Fuh, Junzhong Li, L. Andrew Corkan, Jonathan S. Lindsey, *Photochemistry and Photobiology*, **1998**, 68, 141-142.
45. V. M. Albers, H. V. Knorr, *J. Chem. Phys.*, **1936**, 4, 422-425.
46. G. M. Badger, R. Alan Jones, Robert L. Laslett, *Aust. J. Chem.*, **1964**, 17, 1028-1035.
47. Graham H. Barnett, Mervyn F. Hudson, Kevin M. Smith, *J. Chem. Soc. Perkin Trans. 1*, **1975**, 1401-1403.

48. Jean B. Kim, John J. Leonard, Frederick R. Longo, *J. Am. Chem. Soc.*, **1972**, 94, 3986-3992.
49. Satoshi Shogen, Masahiro Kawasaki, Toshihiro Kondo, Yukari Sato, Kohei Uosaki, *Appl. Organomet. Chem*., **1992**, 6, 533-536.
50. Lawrence Yoon Suk Lee, Todd C. Sutherland, Simona Rucareanu, R. Bruce Lennox, *Langmuir*, **2006**, 22, 4438-4444.

## List of Figures

**Figure 1.** Anion-induced translocation of a redox-active macrocycle within a photoelectrochemically active, bistable [2]rotaxane; formation of the MSCC is brought about upon addition of the chloride anion. $MV^{2+}$: Methyl Viologen. *hv:* Photoirradiation. $\mathbf{e}^-$: Electron.

**Figure 2.** Varying the distance between the porphyrin 'stopper' and the Au surface. **MUA**: 11-Mercaptoundecanoic acid. **MHDA**: 16-Mercaptohexadecanoic acid. **OEG**: HS-$(CH_2)_{10}$-$EG_3$-$OCH_2$-COOH. **TPAPP**: Tetra(4-aminophenyl)porphyrin. **AB-14-172**: a porphyrin-appended axle component synthesised by Dr Asha Brown of the Paul Beer Group (University of Oxford). All quoted distances were estimated by a minimisation approach (MM2) performed in Chem3D 15.0.

**Figure 3.** Varying the distances between the porphyrin 'stopper', the relay moiety and the Au surface. Varying chain length carboxy-terminated (MUA, MHDA, OEG) and ferrocene-functionalised (6-(ferrocenyl)hexanethiol ($Fc(CH_2)_6SH$) or 11-(ferrocenyl)undecanethiol ($Fc(CH_2)_{11}SH$)) thiols were deposited. **AB-14-172**: a porphyrin-appended axle component synthesised by Dr Asha Brown of the Paul Beer Group (University of Oxford). All quoted distances were estimated by a minimisation approach (MM2) performed in Chem3D 15.0.

**Figure 4.** The electron (et) and energy transfer (**P*→Au**) processes governing the magnitude of cathodic photocurrent density deposited at the interface. In the absence of an electron relay group (**Left**), the magnitude of cathodic photocurrent density is limited by the rate of forward electron transfer ($K_{et}$), an effect more dominant upon increasing the spatial separation, d, between the Au interface and the porphyrinic macrocycle, as to limit the rates of both backward electron and backward energy transfer from the excited state of the porphyrinic macrocycle ($P^*$) to the Au surface. Thus, upon increasing d, the magnitude of cathodic photocurrent density should increase in accordance with a drop in the rates of both backward electron and backward energy transfer from $P^*$ to the Au surface, as implied by the **green line**. These otherwise act to reduce the magnitude of photoelectrochemical output. Upon integrating a relay group (**Right**), this effect is reduced, that is the drop in $K_{et}$ is not as dominant, and **X** is moved further away from the interface (**X'**).[6,7,8,9,10,11]

**Figure 5.** The molecular dyads deposited at Au by the group of Uosaki[6,7,8,9]. Fc = ferrocene. All quoted distances were estimated by a minimisation approach (MM2) performed in Chem3D 15.0.

**Figure 6.** Photoelectrochemically 'mapping' the translocation of a ferrocene-appended macrocycle within a bistable [2]rotaxane deposited at Au.

**Figure 7.** Current *vs.* time profile showing how the magnitude of cathodic photocurrent density is calculated. Δ denotes change.

**Figure 8.** Covalent attachment of TPAPP and AB-14-172 to SAMs of carboxy-functionalised, alkylated thiols deposited at Au.

**Figure 9.** SAMs of MUA (**Left**, 1.4 nm), MHDA (**Centre**, 2.1 nm) and OEG (**Right**, 2.5 nm) deposited at Au. All quoted distances were estimated by a minimisation approach (MM2) performed in Chem3D 15.0.

**Figure 10.** Cyclic voltammograms of a 1 mM solution (aqueous) of $K_3[Fe(CN_6)]$ recorded at a bare Au electrode (**Red**), and those modified with SAMs of MUA (**Black**), MHDA (**Green**) and OEG (**Blue**), **Figure 9**. Electrochemical Setup: *Working Electrode*: SAM. *Reference Electrode*: SCE. *Auxiliary Electrode*: Pt wire. *Electrolytic Solution*: 0.1 M $NaClO_4$, aq. *Scan Rate:* 100 mV / s.

**Figure 11.** The characteristic peak acquired upon reductively 'stripping' thiols from Au interfaces. Above example acquired upon repeatedly sweeping (100 mV / s) the potential of a MHDA-modified Au electrode between – 0.5 and – 1.5 V (*vs.* Ag wire) in a 0.5 M solution (50:50, EtOH: $H_2O$, degassed) of KOH.

**Figure 12.** Narrow scan (S 2p) XPS spectra of SAMs of MUA, MHDA and OEG deposited at Au.

**Figure 13.** Narrow scan (O 1s (**Left**), N 1s (**Right**)) XPS spectra of a SAM of MUA-TPAPP deposited at Au.

**Figure 14.** Cyclic voltammograms of a SAM of OEG following exposure to AB-14-172 in the presence (**Blue**) and absence (**Black**) of EDC / NHS. Electrochemical Setup: *Working Electrode*: SAM. *Reference Electrode*: Ag / AgCl. *Auxiliary Electrode*: Pt wire. *Electrolytic Solution*: 0.1 M $TBAPF_6$, anhydrous $CH_2Cl_2$. *Scan Rate:* 1000 mV / s. **Note.** Prior to immersion of the substrate, diffusive voltammograms of a solution of AB-14-172 were recorded at glassy carbon and Au (**Appendix, 8.1.1**); **Experimental, 7.2.4**.

**Figure 15.** UV-Vis spectra of a solution (25 μM, anhydrous $CH_2Cl_2$) of TPAPP (**Green**, primary y-axis), and of SAMs of MUA-TPAPP/AB-14-172 (**Red**, secondary y-axis) deposited at Au.

**Figure 16.** Cyclic voltammograms of activated (**Red**) and unactivated (**Black**) SAMs of MUA following exposure to a solution (50 μM, anhydrous $CH_2Cl_2$) of TPAPP. Electrochemical Setup: *Working Electrode*: SAM. *Reference Electrode*: Ag / AgCl. *Auxiliary Electrode*: Pt wire. *Electrolytic Solution*: 0.1 M $TBAPF_6$, anhydrous $CH_2Cl_2$. *Scan Rate:* 1000 mV / s.

**Figure 17.** Cathodic photocurrent densities acquired at monophasic, porphyrin-appended SAMs formed at Au. All cathodic photocurrents were measured in 0.1 M $Na_2SO_4$ (aq.) containing 5 mM $MV^{2+}$ as an electron acceptor. The electrodes were kept at – 100 mV (*vs.* Ag / AgCl), illuminated with light of wavelength 430 ± 5 nm and the photocurrents normalised for the concentration of porphyrin present at each interface, as determined by cyclic voltammetry (**Appendix, 8.1.2**). Each error bar is equivalent to 3SD and calculated from the data acquired across four separately prepared electrodes. All porphyrin-Au spatial separations were previously determined by ellipsometry (**Table 2**).

**Figure 18**. Mediating electron transfer within monophasic, porphyrin-appended molecular films. Introducing a diffusive electron mediator into solution, in the form of $FcCH_2NMe_3^+$, compensates for the drop in the rate of forward electron transfer (Au → P*).

**Figure 19.** Cathodic photocurrent densities acquired at a SAM of TPAPP-MUA deposited at Au, prior to and following the additions of 5 mM $MV^{2+}$ and 1 mM FcD ($FcCH_2NMe_3^+$) to the electrolytic solution. All cathodic photocurrents were measured in 0.1 M $Na_2SO_4$ (aq.) whilst the electrodes were kept at – 100 mV (*vs.* Ag / AgCl), illuminated with light of wavelength 430 ± 5 nm and the photocurrents normalised for the concentration of porphyrin present at the interface, as determined by cyclic voltammetry (**Appendix, 8.1.2**). Each error bar is equivalent to 3SD and calculated from the data acquired across four separately prepared electrodes. Electrochemical Cell Setup: *Working Electrode*: TPAPP-MUA. *Reference Electrode*: Ag / AgCl. *Auxiliary Electrode*: Pt Wire. *Electrolytic Solution*: 0.1 M $Na_2SO_4$, (+ 5 mM $MV^{2+}$, + 1 mM FcD ($FcCH_2NMe_3^+$)). *Solvent*: $H_2O$. *Bias Potential*: - 100 mV. $\lambda_{irr}$: 430 ± 5 nm.

**Figure 20.** Manipulating the cathodic photocurrent density acquired at a SAM of TPAPP-MUA deposited at Au by varying the bias potential of the working electrode. All cathodic photocurrents were measured in 0.1 M $Na_2SO_4$ (aq.) containing 5 mM $MV^{2+}$ as an electron acceptor. The electrodes were illuminated with light of wavelength 430 ± 5 nm and the photocurrents normalised for the concentration of porphyrin present at the interface, as determined by cyclic voltammetry (**Appendix, 8.1.2**). Each error bar is equivalent to 3SD and calculated from the data acquired across four separately prepared electrodes. Electrochemical Cell Setup: *Working Electrode*: TPAPP-MHDA. *Reference Electrode*: Ag / AgCl. *Auxiliary Electrode*: Pt Wire. *Electrolytic Solution*: 0.1 M $Na_2SO_4$, + 5 mM $MV^{2+}$, + 1 mM $FcCH_2NMe_3^+$. *Solvent*: $H_2O$. *Bias Potential*: Variable. $\lambda_{irr}$: 430 ± 5 nm.

**Figure 21.** Current *vs.* time profiles for a Au electrode at which a SAM of TPAPP-MUA had been deposited. The electrode was kept at either + 200 mV (**Blue**), – 100 mV (**Red**) or – 200 mV (**Black**) and illuminated with light of wavelength 430 ± 5 nm. Electrochemical Cell Setup: *Working Electrode*: TPAPP-MHDA. *Reference Electrode*: Ag / AgCl. *Auxiliary Electrode*: Pt Wire. *Electrolytic Solution*: 0.1 M $Na_2SO_4$, + 5 mM $MV^{2+}$, + 1 mM $FcCH_2NMe_3^+$. *Solvent*: $H_2O$. *Bias Potential*: Variable.

**Figure 22.** Covalent attachment of TPAPP and AB-14-172 to biphasic SAMs deposited at Au.

**Figure 23.** Cyclic voltammograms of an activated SAM of OEG following immersion in a solution (50 μM, anhydrous $CH_2Cl_2$) of AB-14-172, in the presence (**Red**) and absence (**Blue**) of $Fc(CH_2)_6SH$ (Fc6). A cyclic voltammogram of a SAM of Fc6 (**Black**) deposited at Au is also given. Electrochemical Setup: *Working Electrode*: SAM. *Reference Electrode*: Ag / AgCl. *Auxiliary Electrode*: Pt wire. *Electrolytic Solution*: 0.1 M $TBAPF_6$, anhydrous $CH_2Cl_2$. *Scan Rate:* 1000 mV / s.

**Figure 24.** Narrow scan (N 1s (**Left**), Fe 2p (**Right**)) XPS spectra of a SAM of AB-14-172-OEG-$Fc(CH_2)_6SH$ deposited at Au (**Figure 23**).

**Figure 25.** Cathodic photocurrent densities acquired at biphasic, porphyrin-appended SAMs deposited at Au. All cathodic photocurrents were measured in 0.1 M $Na_2SO_4$ (aq.) containing 5 mM $MV^{2+}$ as an electron acceptor. $Fc(CH_2)_6SH$: Fc6. $Fc(CH_2)_{11}SH$: Fc11. The electrodes were kept at – 100 mV (*vs.* Ag / AgCl), illuminated with light of wavelength 430 ± 5 nm and the photocurrents normalised for the concentration of porphyrin present at each interface, as determined by cyclic voltammetry (**Appendix, 8.1.3**). Each error bar is equivalent to 3SD and calculated from the data acquired across three separately prepared electrodes.

**Figure 26.** Cathodic photocurrent densities acquired at monophasic and biphasic porphyrin-appended SAMs deposited at Au. All cathodic photocurrents were measured in 0.1 M $Na_2SO_4$ (aq.) containing 5 mM $MV^{2+}$ as an electron acceptor. $Fc(CH_2)_6SH$: Fc6. $Fc(CH_2)_{11}SH$: Fc11. The electrodes were kept at – 100 mV (*vs.* Ag / AgCl), illuminated with light of wavelength 430 ± 5 nm and the photocurrents normalised for the concentration of porphyrin present at each interface, as determined by cyclic voltammetry (**Appendix, 8.1.2 and 8.1.3**). Each error bar is equivalent to 3SD and calculated from the data acquired across three (biphasic) or four (monophasic) separately prepared electrodes.

**Figure 27. Top.** Manipulating the cathodic photocurrent density acquired at a SAM of AB-14-172-OEG-$Fc(CH_2)_{11}SH$ deposited at Au by varying the bias potential of the working electrode. All cathodic photocurrents were measured in 0.1 M $Na_2SO_4$ (aq.) containing 5 mM $MV^{2+}$ as an electron acceptor. The electrodes were illuminated with light of wavelength 430 ± 5 nm and the photocurrents normalised for the concentration of porphyrin present at the interface, as determined by cyclic voltammetry (**Appendix, 8.1.3**). Each error bar is equivalent to 3SD and calculated from the data acquired across three separately prepared electrodes. **Bottom.** Current *vs.* time profiles for a Au electrode at which a SAM of AB-14-172-OEG-$Fc(CH_2)_{11}SH$ had been deposited. All profiles were measured in 0.1 M $Na_2SO_4$ (aq.) containing 5 mM $MV^{2+}$ as an electron acceptor. The electrode was kept at either 0 mV (**Black**), – 100 mV (**Red**) or – 200 mV (**Blue**) and illuminated with light of wavelength 430 ± 5 nm. Electrochemical Cell Setup: *Working Electrode*: OEG-AB-14-172-$Fc(CH_2)_{11}SH$. *Reference Electrode*: Ag / AgCl. *Auxiliary Electrode*: Pt Wire. *Electrolytic Solution*: 0.1 M $Na_2SO_4$ + 5 mM $MV^{2+}$. *Solvent*: $H_2O$. *Bias Potential*: Variable.

**Figure 28.** Implementing the conformational ruler established within the design of a novel bistable [2]rotaxane. All quoted distances were estimated by a minimisation approach (MM2) performed in Chem3D 15.0.

**Figure 29.** Solution phase formation of the pseudorotaxane, AB-14-172-JL241; mixing stoichiometric amounts of AB-14-172 and JL241led to the formation of the interlocked supramolecular architecture. JL241 was synthesised by Mr Jason Lim of the Paul Beer Group (University of Oxford).

**Figure 30.** Tethering AB-14-172-JL241to an activated SAM of MUA deposited at Au. All quoted distances were estimated by a minimisation approach (MM2) performed in Chem3D 15.0.

## List of Tables

**Table 1.** Ellipsometric film thicknesses for SAMs of MUA, MHDA and OEG deposited at Au. *Estimated by means of minimisation (MM2) in Chem3D 15.0. ** Calculated by either attenuation of the Au 4*f* x-ray photoelectron spectroscopy signature[15] or ellipsometry[14,16,17]. *** Experimentally determined by ellipsometry. Reported film thicknesses are those determined from, and averaged over, four separately prepared samples, with two measurements per sample.

**Table 2.** Ellipsometric film thickness increases following the covalent attachment of TPAPP or AB-14-172 to SAMs of MUA, MHDA and OEG deposited at Au. Reported film thicknesses are those determined from, and averaged over, four separately prepared samples, with two measurements per sample. *Estimated by minimisation (MM2) in Chem3D 15.0.

**Table 3.** C/N ratio for SAMs of TPAPP-MUA (Bottom) and AB-14-172-OEG (Top) deposited at Au.

**Table 4.** Concentration of **$Fc$ / $Fc^+$** and **$P^0$ / $P^{+1}$** at biphasic, porphyrin-appended monolayers deposited at Au. All concentrations were determined by cyclic voltammetry (**Appendix, 8.1.3**), and each error bar is equivalent to 3SD and was calculated from the data acquired across five separately prepared electrodes. *As determined by Walczak *et al.*[21]and Lee *et al.*[50].

**Table 5.** Comparison of the cathodic photocurrent densities acquired upon tethering TPAPP to SAMs of MUA, MHDA and OEG deposited at Au, in the absence and presence of $Fc(CH_2)_6SH$ and $Fc(CH_2)_{11}SH$.

# 3. Towards Photoelectrochemically 'Mapping' the Position of Redox-Active Macrocycles within Dynamic Supramolecular Architectures

## 3.1 – Confirming Solution Phase Pseudorotaxane Assembly

Prior to covalently coupling the supramolecular architecture to an activated, thiolated substrate, in a bid to generate the desired interlocked assembly, **Figure 1**, formation of the pseudorotaxane was confirmed by both $^{1}$H NMR (**Figure 2**) and rotating frame nuclear overhauser effect (ROESY) spectroscopy (**Figure 3**); **Experimental, 7.7**. If formation of the desired pseudorotaxane was successful, then it was expected that a significant cathodic photocurrent density would be acquired upon photoirradiation of the resultant monolayer, which had been assembled upon tethering the interpenetrated assembly to a SAM deposited at Au, having taken the conformational ruler established previously (**Chapter 2**) into account.

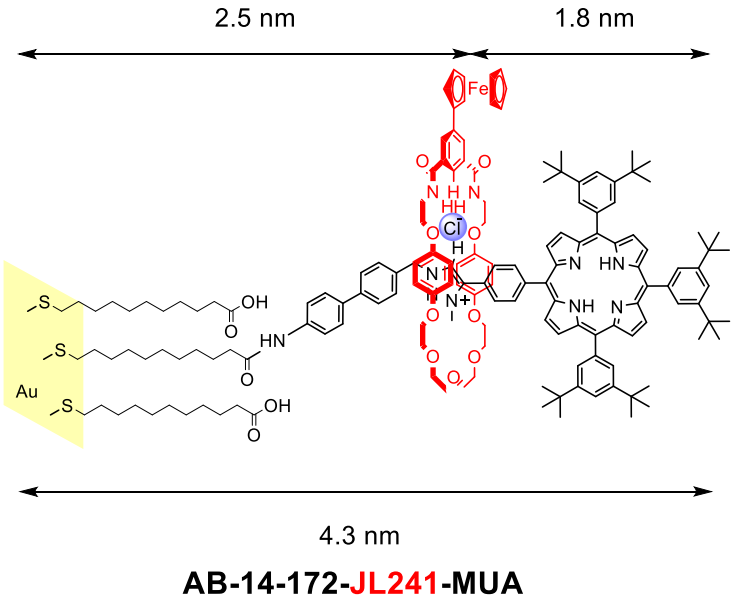


**Figure 1.** Tethering AB-14-172-JL241 to an activated SAM of MUA deposited at Au. All quoted distances were estimated by a minimisation approach (MM2) performed in Chem3D 15.0.

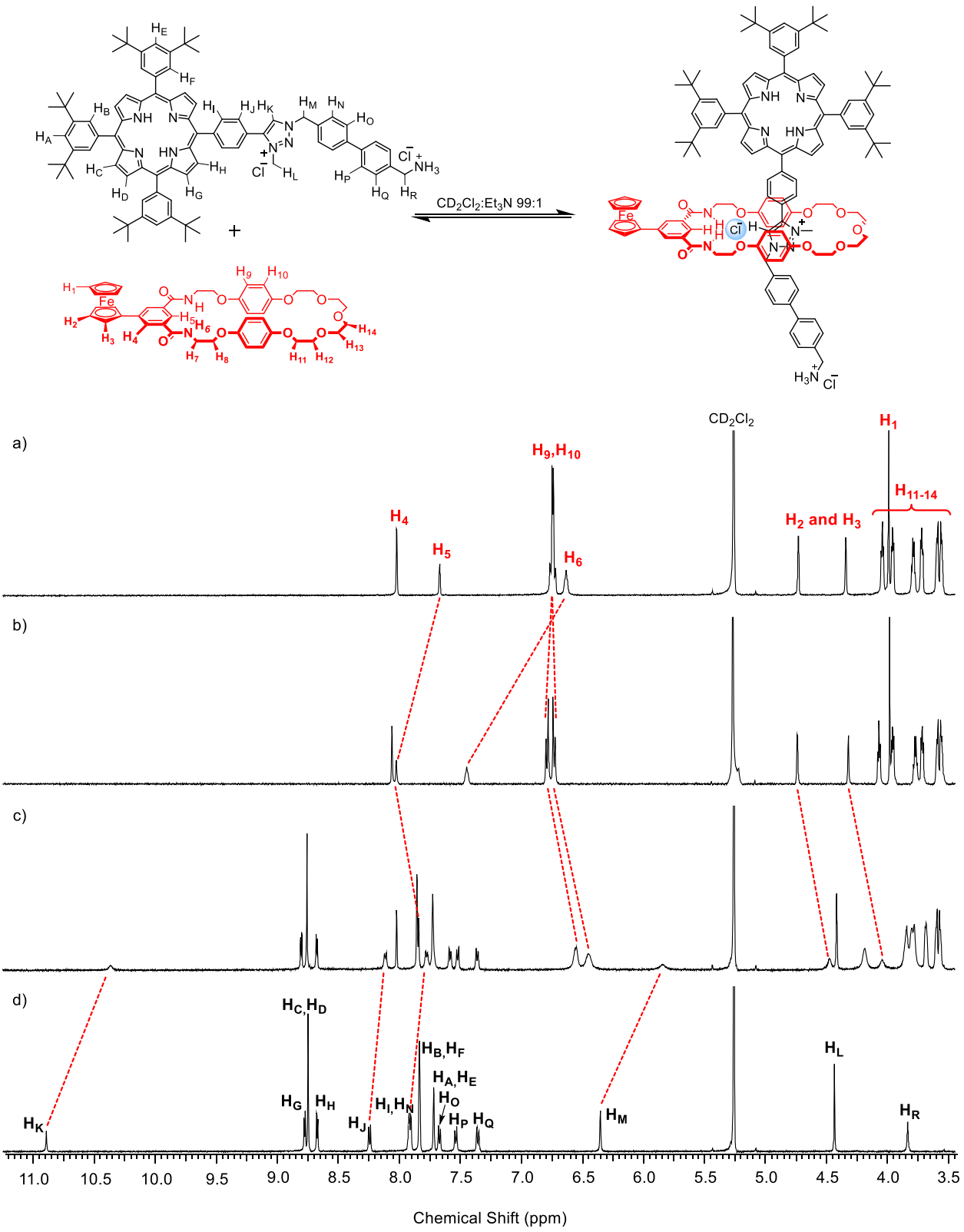


**Figure 2.** Partial $^{1}H$ NMR spectra ($CD_2Cl_2$:$Et_3N$, 99:1, 298 K, 500 MHz) of **a**) JL241, **b**) an equimolar mixture of JL241 and TBACl, **c**) an equimolar mixture of JL241 and AB-14-172 and **d**) AB-14-172. All components were used at a concentration of 1.5 mM and spectra recorded by Dr Asha Brown of the Paul Beer Group (University of Oxford).

Formation of the pseudorotaxane (**Figure 2, Top**) was inferred from a splitting of and an upfield shift of the macrocyclic (JL241) hydroquinone protons (**H$_9$** and **H$_{10}$**), a slight downfield shift of the internal macrocyclic isophthalamide proton (**H$_5$**), and concomitant upfield shifts of the thread protons (**H$_K$**, **H$_L$**, **H$_J$** and **H$_M$**)[1,2]. Concomitant upfield shifts of the thread protons (**H$_K$**, **H$_L$**, **H$_J$** and **H$_M$**) suggests that the templating chloride anion is slightly polarised away from the axle's triazolium binding cleft, that is it forms additional hydrogen bonds with the macrocyclic isophthalamide motif, and thus is consistent with the formation of the desired pseudorotaxane[1,2]. In addition, the slight downfield shift of the internal macrocyclic isophthalamide proton (**H$_5$**) highlights the fact that upon the addition of AB-14-172, hydrogen bonding interactions are induced between the templating anion and the isophthalamide motif of the macrocyclic species[1,2]. Unfortunately, broadening of its amide proton (**H$_6$**), into the baseline of the spectrum (**Figure 2**, **Trace C**), arose in the solvent system. Furthermore, the splitting of and an upfield shift in the position of the macrocyclic hydroquinone protons (**H$_9$** and **H$_{10}$**) is apparent due to the fact that upon the interlocking of the two components in solution, donor-acceptor interactions are induced between the macrocycle's electron-rich hydroquinone motif, and the electron-deficient triazolium station present within AB-14-172[1,2]. Finally, slight shielding of the ferrocene ring protons (**H$_1$**, **H$_2$** and **H$_3$**) may arise due to the influence of the porphyrin ring currents. Similar observations, indicative of pseudorotaxane formation, were observed in a more competitive medium (99:1, acetone: $Et_3N$), although complete dissolution of both derivatives was not apparent. On the other hand, ROESY spectroscopy, **Figure 3**, confirmed intercomponent interaction between the methyl triazolium protons on AB-14-172 (**H$_L$**) and the polyether entity of JL241 (**H$_{11}$**, **H$_{13}$**, **H$_{14}$**).

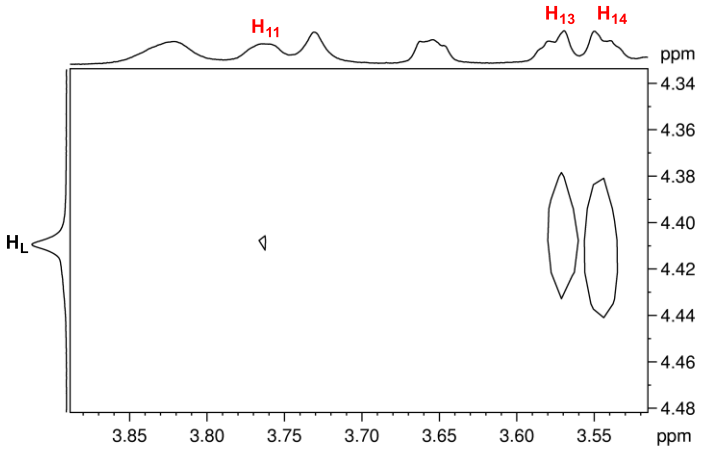


**Figure 3.** ROESY spectrum ($CD_2Cl_2$:$Et_3N$, 99:1, 298 K, 500 MHz) of an equimolar (1.5 mM) mixture of JL241 and AB-14-172. Spectrum recorded by Dr Asha Brown of the Paul Beer Group (University of Oxford).

Chloride templation of the single-station, interlocked architecture was also probed by cyclic voltammetry (**Experimental, 7.2.4**), although the expected reduction in the diffusion coefficient (***D***) of the macrocyclic species (JL241, $E_{1/2}$ 290 mV, *vs*. Ag / $AgNO_3$) upon assembly was not observed, **Figure 4**. It was thought that upon the addition of a slight excess of AB-14-172 (1.2 equivalents), and thus the formation of the pseudorotaxane (**Figure 2**, **Top**), which was thought would possess a smaller diffusion coefficient, *cf*. the macrocyclic species, the peak current ($\boldsymbol{i_p}$) would decline because the interpenetrated assembly possesses greater molecular mass, thus is likely to induce greater steric hindrance at the diffusive interface. This relationship was first highlighted by Valencia *et al.*[3,4], albeit for molecular entities with molecular weight ≤ 350 Da. The stated relationship between $\boldsymbol{i_p}$ and ***D*** can be perceived upon consideration of the Randles-Sevcik equation,

$$i_p = 0.4463\, nF\, AC\, (\frac{nFvD}{RT})^{0.5}$$

where $\boldsymbol{i_p}$ is the current maximum (A), ***n*** the number of electrons involved in the redox process, ***F*** Faraday's constant (C $mol^{-1}$), ***A*** the electrode area ($cm^{-2}$), ***C*** the concentration of the redox-active species (mol $cm^{-3}$), ***v*** the scan rate (v $s^{-1}$), ***D*** the diffusion coefficient ($cm^2$ $s^{-1}$), ***R*** the gas constant (J $K^{-1}$ $mol^{-1}$) and ***T*** temperature (K)[5-8].

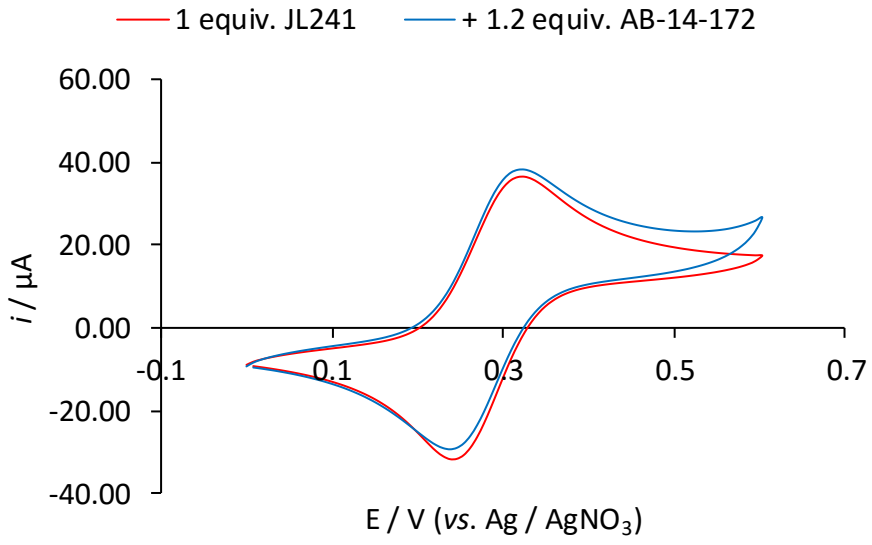


**Figure 4**. Cyclic voltammogram of a 0.21 mM solution ($CH_2Cl_2$, anhydrous) of JL241 prior to (**Red**) and following (**Blue**) the addition of 1.2 equivalents of AB-14-172. The expected reductions in ***D*** and $\boldsymbol{i_p}$ of the macrocyclic species (JL241, $E_{1/2}$ 290 mV *vs.* Ag / $AgNO_3$, 1000 mV / s) were not observed upon the addition of AB-14-172 into solution. Electrochemical Setup: *Working Electrode*: Glassy Carbon. *Reference Electrode*: Ag / $AgNO_3$SCE. *Auxiliary Electrode*: Pt wire. *Electrolytic Solution*: 0.1 M $TBAPF_6$, anhydrous $CH_2Cl_2$. *Scan Rate:* 1000 mV / s.

It is thought that the drop in current was not observed because the high salt concentration (0.1 M $TBAPF_6$) and / or the absence of trimethylamine ($Et_3N$) is likely to have prevented the formation of

the pseudorotaxane; a trace amount of $Et_3N$ was utilised when acquiring the $^1H$ NMR spectra (**Figure 2** and **33**) to further solubilise AB-14-172, and thus reduce aggregation. In addition, it was not known if the relationship between $\boldsymbol{i_p}$ and $\boldsymbol{D}$ was expected to hold upon increasing the molecular weight beyond 350 Da.

In summary, based on the evidence acquired from $^1H$ NMR and ROESY spectroscopy, it was concluded that formation of the desired pseudorotaxane was successful. Hence, a pseudorotaxane suitable for deposition at Au was established, and this work will be described in the next section. If a photoelectrochemical output was to be acquired upon irradiation of the resultant monolayer, then it would be the first example of such a system, and a secondary station could be incorporated to investigate the use of photoelectrochemical analysis in the transduction of macrocyclic motion.

## 3.2 – Tethering AB-14-172-JL241 to an Underlying, Thiolated Interface Deposited at Au

### 3.2.1 – Covalent Attachment of AB-14-172-JL241 to a SAM of MUA

As before (**Chapter 2**, **Figures 8** and **22**), carbodiimide coupling (**Experimental, 7.3.3**) was exploited in a bid to tether the pseudorotaxane to a OEGylated thiol interface, **Figure 5**.

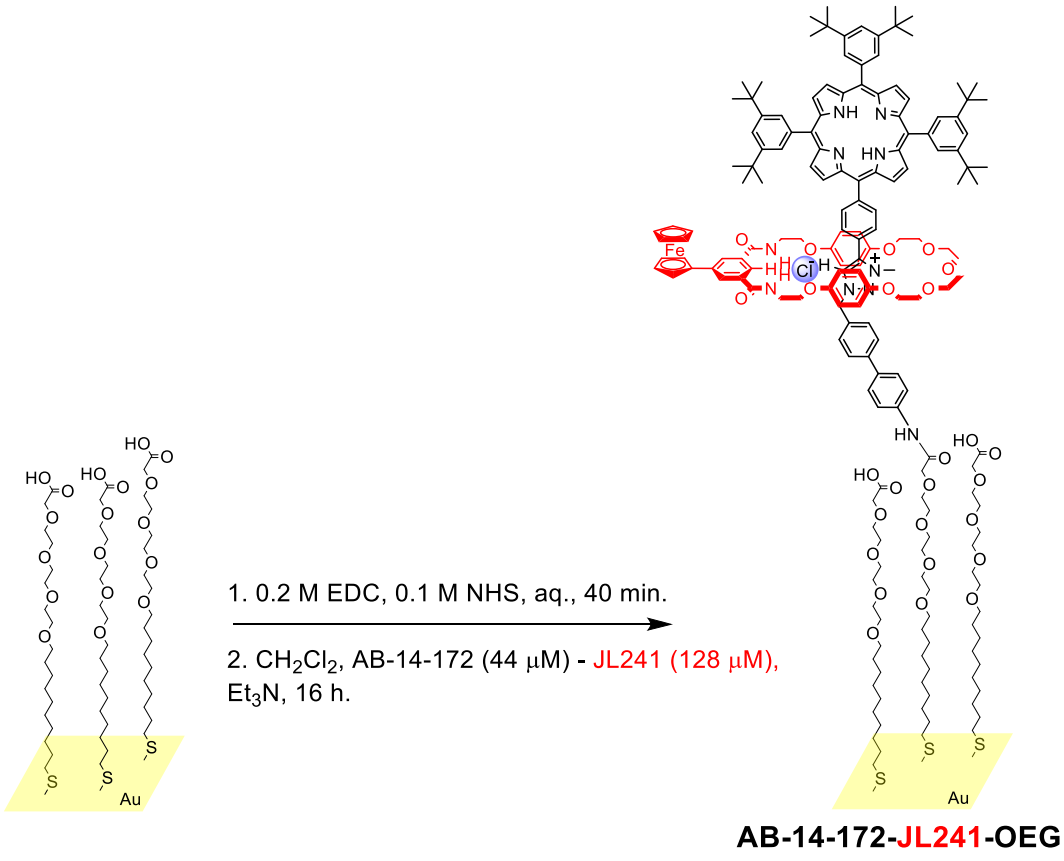


**Figure 5.** Tethering AB-14-172-JL241 to a SAM of OEG deposited at Au.

The OEGylated thiol was deposited (**Experimental, 7.3.2**) in preference to MUA, even though the original model (**Figure 1**) was based upon tethering the pseudorotaxane to a SAM of the latter, due to the fact that in the absence of the coupling reagents (EDC and NHS), a greater degree of unwanted association of the axle component (AB-14-172) was apparent at a SAM of MUA, **Figure 6** (**Bottom**, **Purple Trace**); similarly to a SAM of the OEGylated thiol, the porphyrinic macrocycle should not have been apparent upon exposure of a SAM of MUA to AB-14-172.

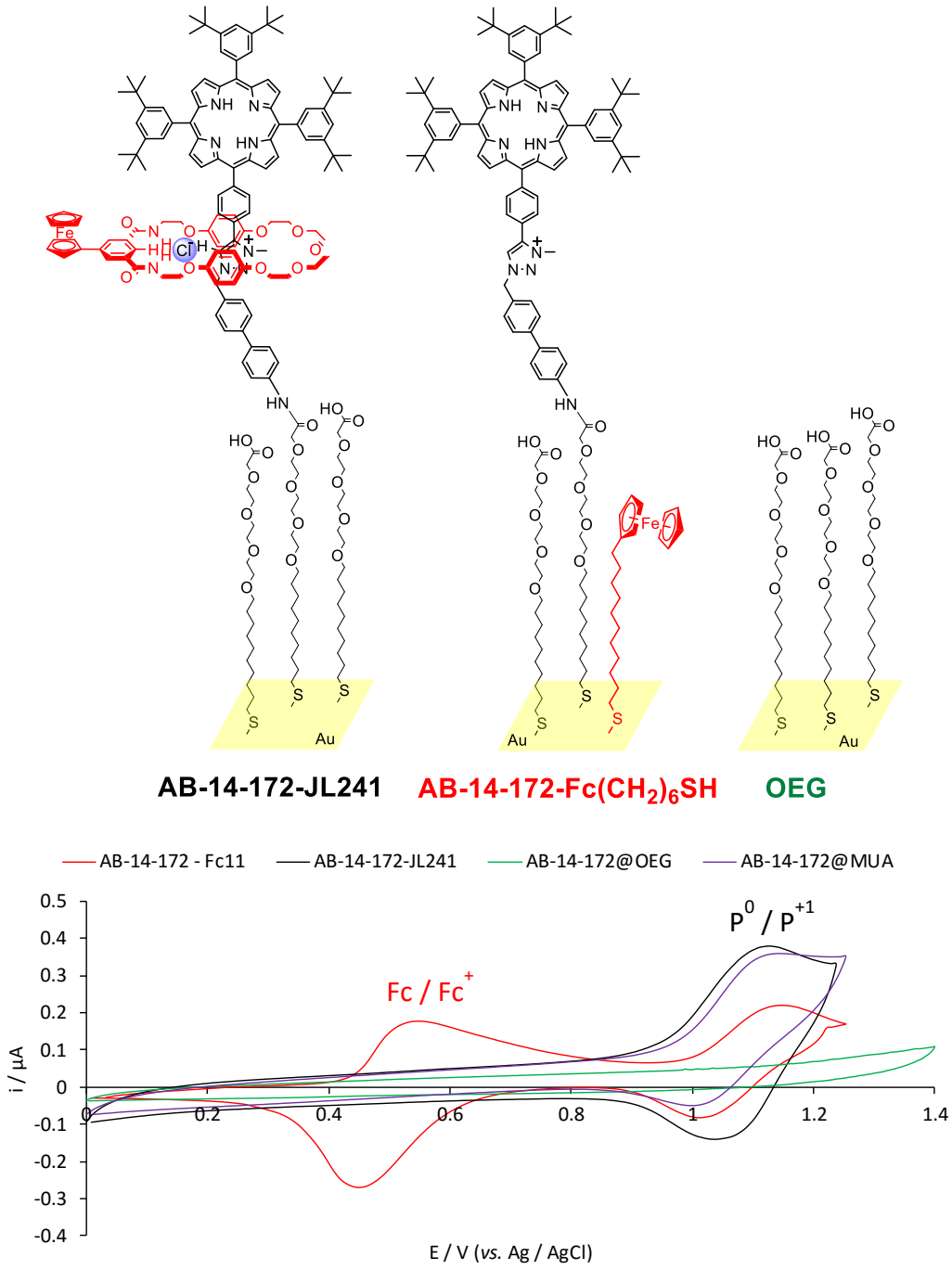


**Figure 6.** Cyclic voltammograms of SAMs of AB-14-172- Fc11-OEG (**Red**) and AB-14-172-JL241-OEG (**Black**) deposited at Au, and of SAMs of OEG (**Green**) and MUA (**Purple**) following exposure to a solution (50 µM, $CH_2Cl_2$, anhydrous) of AB-14-172 in the absence of EDC / NHS. Fc11: $Fc(CH_2)_{11}SH$. Electrochemical Setup: *Working Electrode*: SAM. *Reference Electrode*: Ag / AgCl. *Auxiliary Electrode*: Pt wire. *Electrolytic Solution*: 0.1 M $TBAPF_6$, anhydrous $CH_2Cl_2$. *Scan Rate:* 1000 mV / s.

Upon exchanging the MUA tether for the OEGylated analogue, modulation of the spatial separation between each of the molecular entities (photoactive (AB-14-172), relay (JL241) and metallic interface (Au)) within the film resulted, **Figure 7**. The generation of substantial cathodic photocurrent, upon photoirradiation of the film (**Experimental, 7.2.3**), was still expected, given the

magnitude of the response observed in the absence of the macrocyclic species (**Chapter 2**, **Figure 17**), and the reduced distance employed between the integrated relay (JL241) and photoactive (AB-14-172) moieties (1.8 nm (**Figure 7**) (*cf.* 3.5 (AB-14-172-Fc$(CH_2)_{11}$SH) and 4.0 nm (AB-14-172-Fc$(CH_2)_6$SH), **Chapter 2**, **Figure 3**). However, it was anticipated that the increased distance between the metallic interface and the relay moiety would prove problematic; at a distance of 3.4 nm (*cf.* 2.5 nm) from the interface (**Figure 7**), it was not known whether the metallocene would be electrochemically decoupled from the macroelectrode on which the monolayer was assembled.

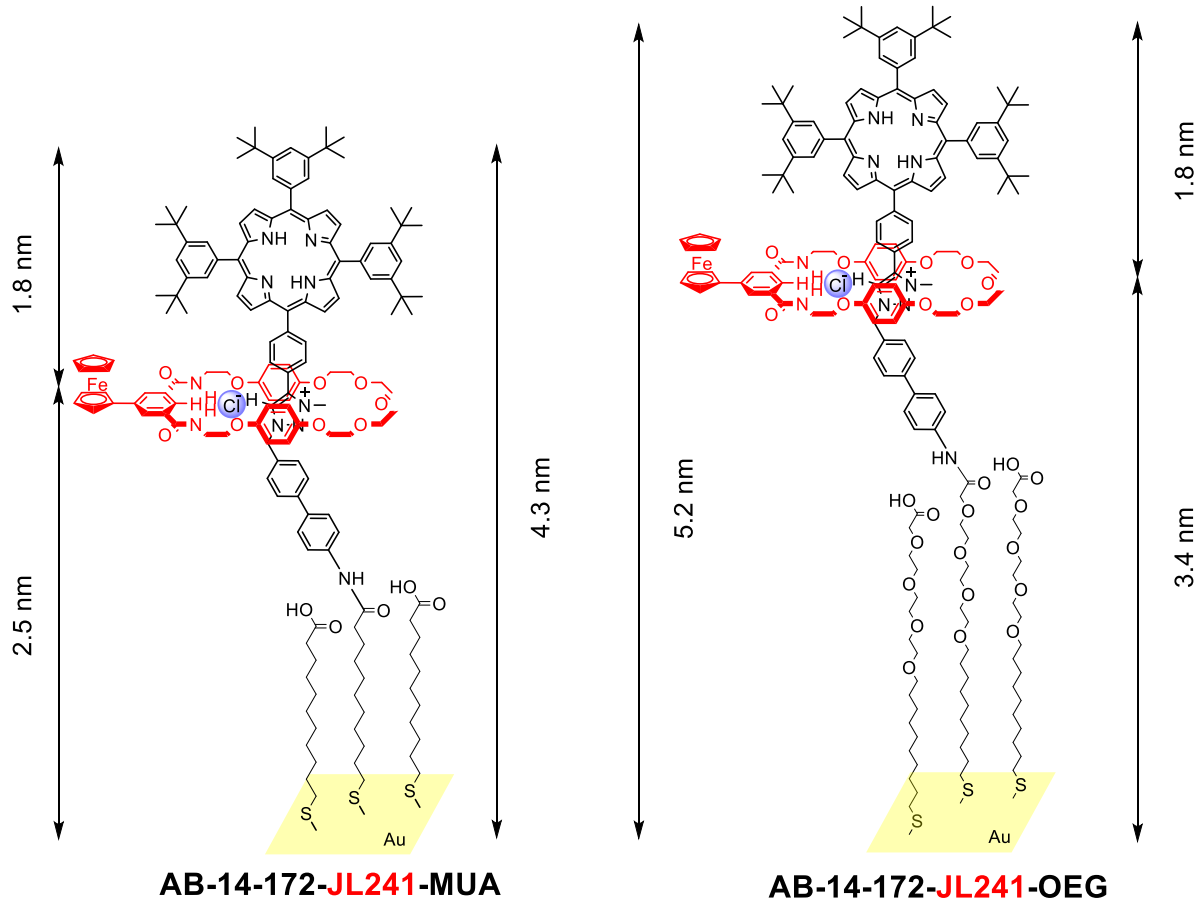


**Figure 7.** Tethering AB-14-172-JL241 to SAMs of MUA and OEG deposited at Au. All quoted distances were estimated by a minimisation approach (MM2) performed in Chem3D 15.0

Upon exposure of an activated SAM of the OEGylated thiol to a solution of the pseudorotaxane (**Figure 5**), covalent attachment of the interlocked assembly was not apparent. Whilst the $P^0$ / $P^{+1}$ redox couple was observed ($E_{1/2}$ 1083 mV, *vs.* Ag / AgCl, **Figure 6, Black Trace**) and a film thickness increase of 2.5 nm (± 0.2) acquired by ellipsometry (**Experimental, 7.4**), both highlighting the interfacial presence of the axle component, AB-14-172, the presence of the ferrocene-appended macrocycle, JL241, was not evident, as it had been upon the simultaneous deposition of 11-(ferrocenyl)undecanethiol, **Figure 6, Red Trace**, where the Fc / $Fc^+$ redox couple ($E_{1/2}$ 496 mV, *vs.* Ag / AgCl) was observed. These observations suggest that the macrocycle is either not present at the

interface, or is electrochemically decoupled from the Au substrate at 3.4 nm from it, *i.e*. the rate of electron transfer is negligible at this distance, and thus a cyclic voltammogram cannot be attained. X-ray photoelectron spectroscopy (XPS, **Experimental, 7.6**) was used to confirm that the ferrocene-appended macrocycle was not present at the interface; no peak at a binding energy of approximately 710 eV (Fe) was observed upon analysis of the film (**Appendix, 8.5.2**). It was therefore concluded that the axle component, AB-14-172, preferentially tethers to the interface. Additionally, it is reasonable to suggest that steric hindrance prevents assembly of the desired molecular film (**Figure 5**); sterically restricted access to the amine tether is likely to prevent formation of the desired amide bond and / or tethering of the pseudorotaxane to the activated carboxy-functionalised interface. A surface concentration of $2.1 \pm 0.4 \times 10^{-11}$ mol $cm^{-2}$ was determined (**Experimental, 7.2.2**) upon integration of the $P^0$ / $P^{+1}$ redox couple (**Figure 6**, **Bottom**, **Black Trace**), further highlighting the assembly of a monophasic, porphyrin-appended monolayer, in preference to the desired rotaxanated interface. The surface concentration ($2.1 \pm 0.4 \times 10^{-11}$ mol $cm^{-2}$) is similar in magnitude to that acquired when purposely tethering AB-14-172 to an underlying monolayer of the OEGylated thiol in the absence of JL241, $4.5 \pm 0.9 \times 10^{-11}$ mol $cm^{-2}$ (**Appendix, 8.5.1**).

### 3.2.2 – Generation of Cathodic Photocurrent at Rotaxanated Interfaces

Upon photoirradiation of the resultant interface, in the absence of the ferrocene-appended macrocycle, it was expected for a negligible photoelectrochemical output to be shown, as was observed upon selectively tethering AB-14-172 to a SAM of the OEGylated thiol (**Chapter 2**, **Figure 17**). No cathodic photocurrent was generated as it had been previously ($3.0 \times 10^{14}$ nA $mol^{-1}$ $cm^{-2}$), and upon irradiation of the analogous biphasic film (**Figure 8** and **Appendix, 8.6.1**). It suggested that the presence of JL241 and / or the pseudorotaxane prevents AB-14-172 tethering to the interface with the same orientation (surface normal). Thus, the porphyrin derivative could be in much closer proximity to the Au surface than was envisaged (≤ 5.2 nm), **Figure 7**, which would explain why the flow of cathodic current was not induced upon photoirradiation of the interface (**Figure 8**, **Top**, **Black Trace**); backwards electron and / or energy transfer, from $P^*$ to the gold surface, is more dominant[9-14].

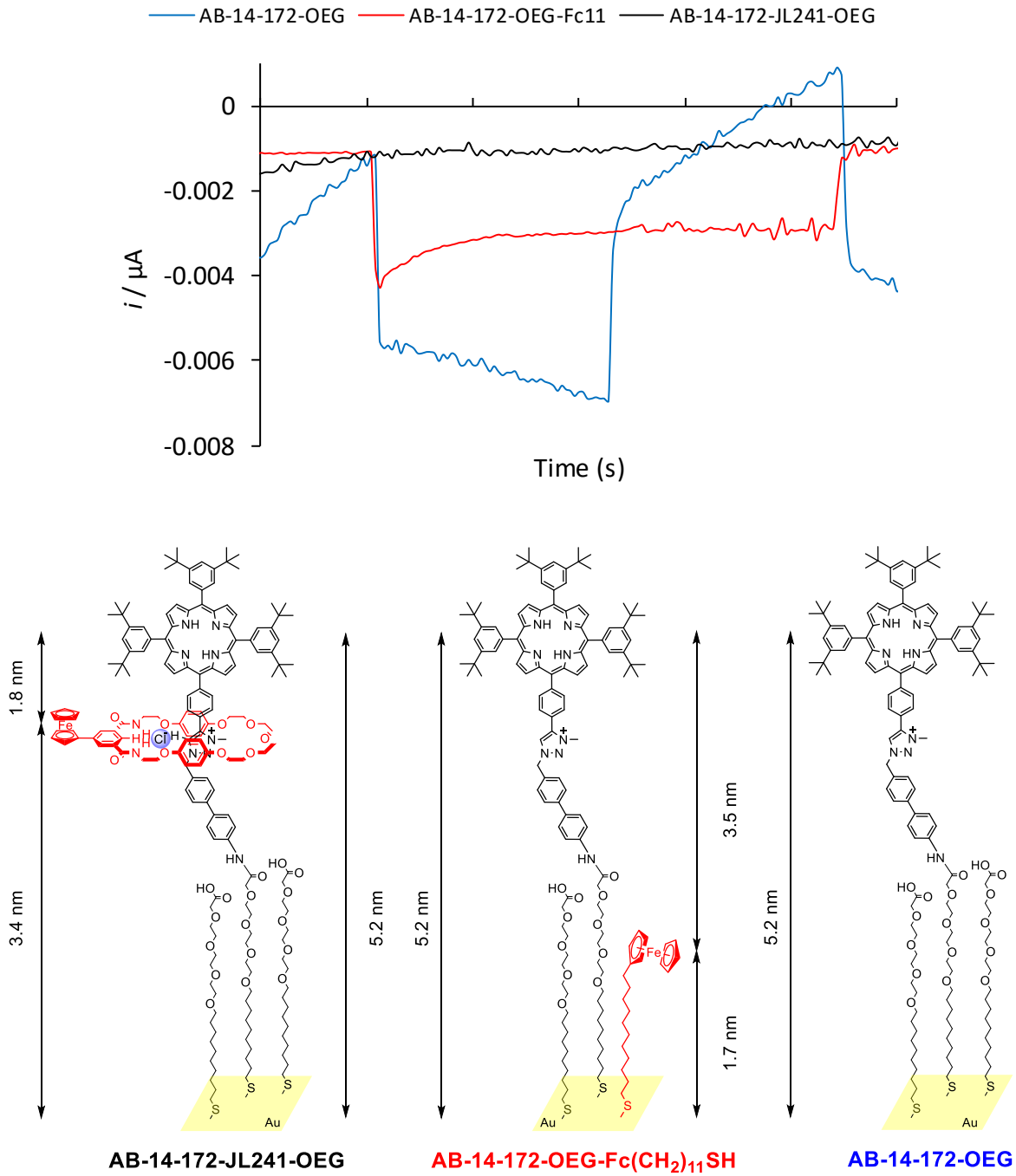


**Figure 8.** Current *vs.* time profiles for SAMs of AB-14-172-OEG (**Blue**), AB-14-172-OEG-Fc11 (**Red**) and AB-14-172-JL241-OEG (**Black**) deposited at Au. Fc11: $Fc(CH_2)_{11}SH$. The structure of each monolayer is given. Electrochemical Cell Setup: *Working Electrode*: SAM. *Reference Electrode*: Ag / AgCl. *Auxiliary Electrode*: Pt Wire. *Electrolytic Solution*: 0.1 M $Na_2SO_4$ + 5 mM $MV^{2+}$. *Solvent*: $H_2O$. *Bias Potential*: - 100 mV. $\lambda_{irr}$: 430 ± 5 nm.

To try to induce the flow of cathodic current and / or ensure that the pseudorotaxane became tethered to the interface, the concentration of the macrocyclic species (JL241) was increased, relative to that of AB-14-172, in a bid to drive the equilibrium towards favouring formation of the interpenetrated structure. Thus, it was expected that no unthreaded AB-14-172 would remain in solution, and that

the presence of JL241 at the interface would be inferred by XPS, CV and photoelectrochemical analyses. Prior to modulating the deposition ratio (AB-14-172: JL241), it was important to ensure that the macrocyclic species (JL241) did not become physically adsorbed to the underlying monolayer and / or the bare Au substrates. Upon exposure of the OEGylated thiol interface to increasing amounts (40 → 1000 μM) of JL241, the Fc / $Fc^+$ redox couple was not observed by CV (**Figure 9** (**Experimental, 7.2.4**)) permitting use of the macrocycle in excess. Deposition ratios of 1:1, 1:3 and 1:10, all in favour of JL241, were employed in the formation of the pseudorotaxane, although in each case the presence of Fc / $Fc^+$ was not observed at the interface, by CV or XPS, upon exposure of the activated interface to a solution of the pseudorotaxane. Thus, the flow of cathodic current was not detected upon illumination of the resultant films.

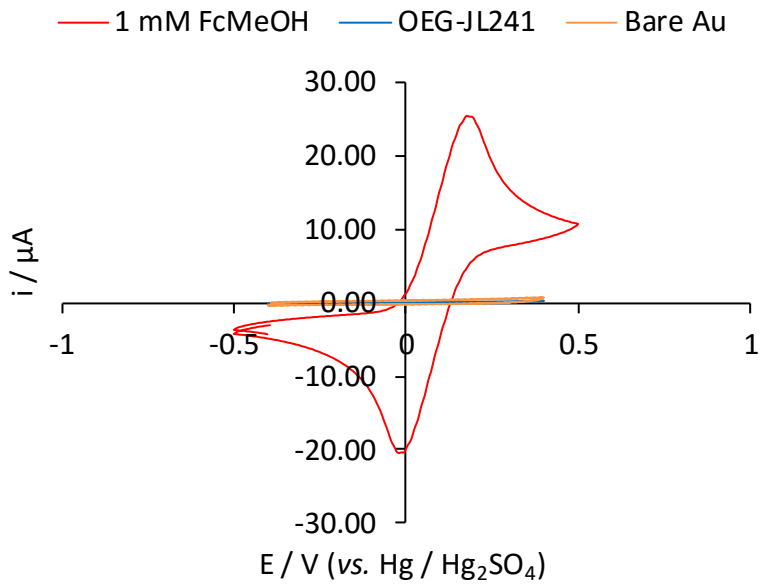


**Figure 9.** Cyclic voltammograms of a 1 mM solution of ferrocenemethanol (**Red**), and of both a SAM of OEG (**Blue**) and a bare Au electrode (**Orange**) following exposure to a 450 μM solution of JL241. Electrochemical Cell Setup: *Working Electrode:* Au or SAM. *Reference Electrode:* Hg / $Hg_2SO_4$. *Auxiliary Electrode:* Pt Wire. *Supporting Electrolyte*: ~ 0.1 M $TBAPF_6$. *Solvent:* $CH_2Cl_2$ (anhydrous).

## 3.3 – Utilising Thioctic Acid-Appended Axle Components in the Assembly of Interlocked Molecular Films

### 3.3.1 – Direct Deposition of Interlocked Architectures at the Interface

To permit the surface deposition of such single-station, rotaxanated architectures, and thus subsequently acquire substantial cathodic photocurrent densities from interlocked, molecular films, incorporating a ferrocene-appended macrocycle, thioctic acid-appended axle components were utilised in a bid to directly deposit the interpenetrated molecular assemblies at Au, **Figure 10**. It was anticipated that this approach would not only serve to ensure that the ferrocene-appended macrocycle was attached to the interface, thus permitting the mediation of electron transfer within a surface-

bound rotaxane, but would circumvent the problems associated with forming an amide bond in the presence of a large molecular entity witnessed thus far. In addition, it was expected that intercalation and / or physical adsorption of the derivative would be limited, *cf.* when exposing activated monolayers of carboxy-functionalised thiols to aminated porphyrin derivatives (**Chapter 2**, **Figures 8** and **16**).

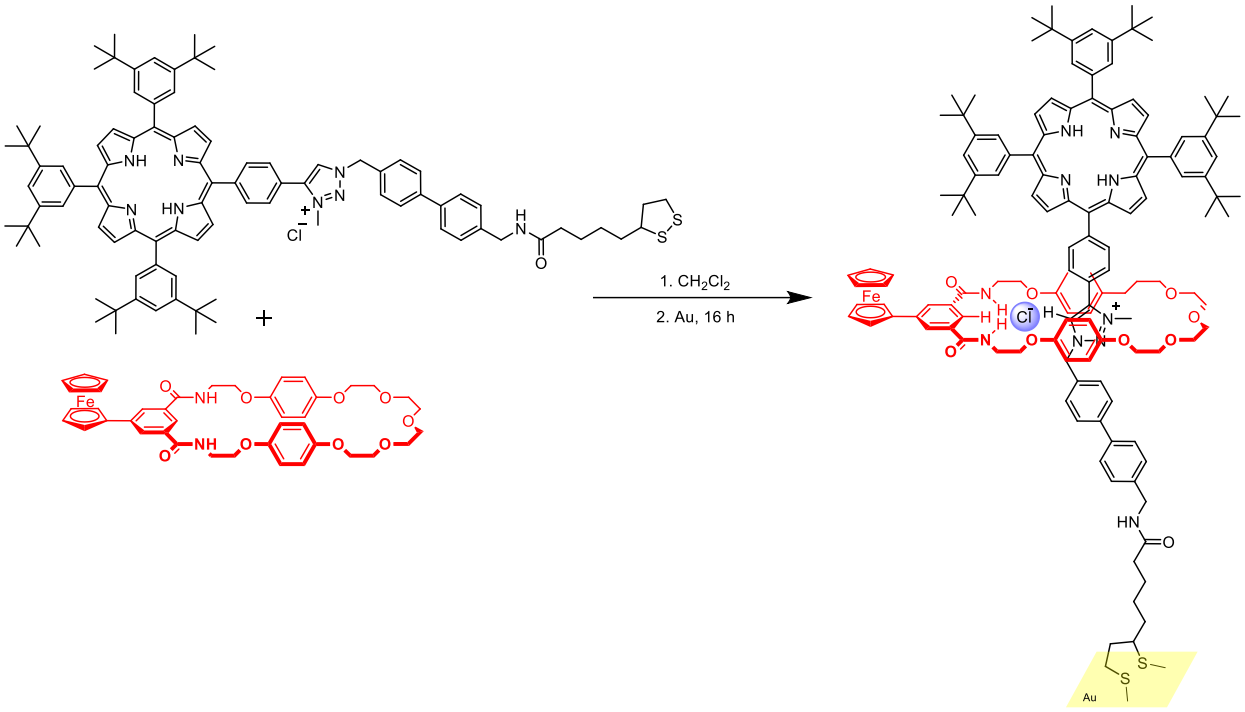


**Figure 10.** Solution phase pseudorotaxane formation (between JL241 and a thioctic acid-appended, porphyrin-stoppered axle component), prior to deposition of the resultant interlocked assembly at Au.

Prior to synthesising and depositing the interlocked assembly shown in **Figure 10** at Au, AB-18-088, **Figure 11** (**M = $H_2$**), was synthesised to gauge the viability of utilising the thioctic acid-tether in such an approach. It was expected for this derivative to become tethered to Au upon exposure of the metallic substrate to a solution (50 µM, $CH_2Cl_2$ (anhydrous), 16 h) of the thioctic acid-appended motif (AB-18-088), both in the presence and absence of either 6-(ferrocenyl)hexanethiol or 11-(ferrocenyl)undecanethiol, **Figure 11**. The concentration of AB-18-088 present within each molecular film, **Figure 11**, was to be determined by CV, the uniformity of each SAM deposited assessed upon consideration of the ellipsometric film thickness data acquired, and the flow of cathodic photocurrent to be induced upon photoirradiation of the films.

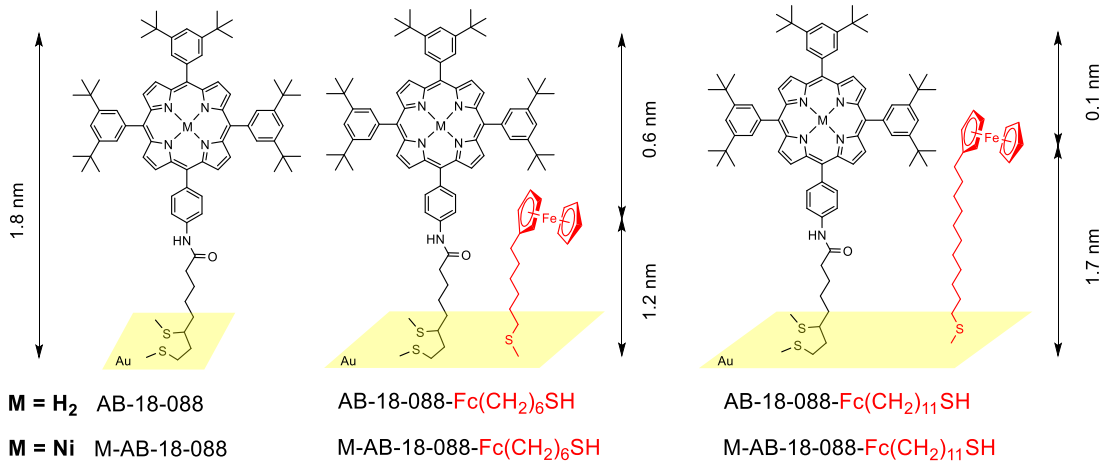


**Figure 11.** Deposition of free-base (**M = $H_2$**) and metallated (**M = Ni**), thioctic acid-appended porphyrin derivatives at Au. AB-18-088 was synthesised by Dr Asha Brown of the Paul Beer Group (University of Oxford).

Upon exposing pristine Au substrates to micromolar (25 μM) solutions ($CH_2Cl_2$, anhydrous, 16 h) of AB-18-088, no change in film thickness was observed by ellipsometry, and the presence of the porphyrinic macrocycle at the interface was not inferred by cyclic voltammetry. Thus, a photoelectrochemical study was not performed, and it was concluded that the generation of singlet oxygen by the free-base porphyrin derivative[15,16] prevented the surface deposition of AB-18-088.

Upon analysis (**Experimental, 7.7**) of a solution (degassed $CH_2Cl_2$ (anhydrous)) of AB-20-042, **Figure 12**, a peak at 1521.86 m / z was observed, demonstrating the effect of singlet oxygen generation in preventing the deposition of free-base, thioctic acid-appended porphyrin derivatives at Au; the presence of singlet oxygen induces formation of the thiosulfonate analogue which is not able to covalently bind to the Au surface. **Note.** AB-20-042 was utilised because its increased molecular weight (1522.01 g / mol), in comparison to that of AB-18-088 (1154.72 g / mol), permitted higher spectral resolution.

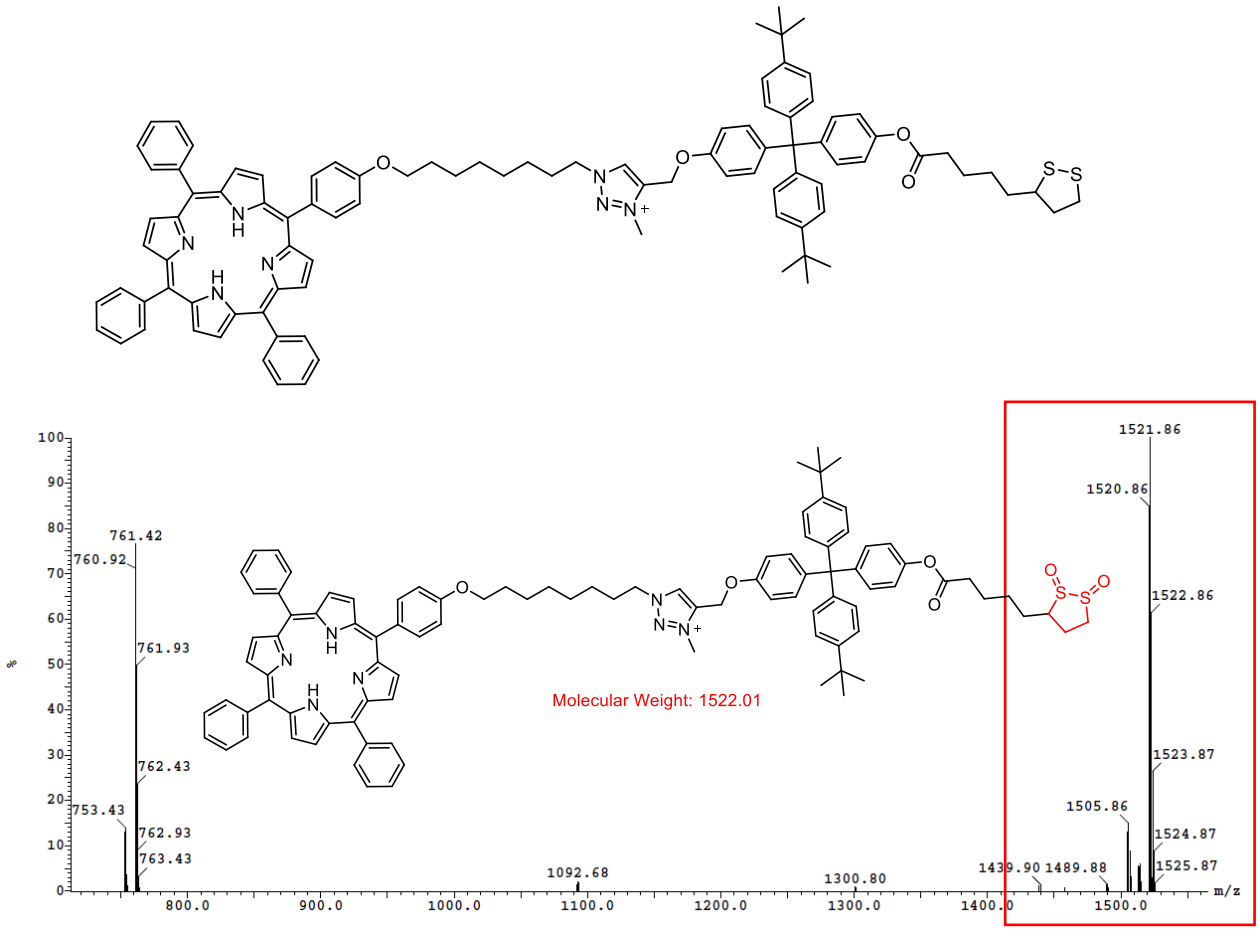


**Figure 12.** ESI-MS of a solution of AB-20-042 following oxidation of the thioctic acid tether. Its molecular structure prior to and following oxidation of the thioctic acid tether is given. AB-20-042 was synthesised by Dr Asha Brown of the Paul Beer Group (University of Oxford).

This was not the case upon metallation of the porphyrinic macrocycle with $Ni^{II}$, **Figure 11, M = Ni**, which has been shown to quench the generation of singlet oxygen[15]. Upon deposition of the metallated derivative, M-AB-18-088, a film thickness increase of 1.6 ± 0.2 nm was observed, as was to be expected given the length of its minimised energy conformer (**Figure 11**, 1.8 nm, Chem3D 15.0 (MM2)), and a surface concentration of 2.4 ± 0.3 x $10^{-11}$ mol $cm^{-2}$ acquired upon integration of the $P^0$ / $P^{+1}$ ($E_{1/2}$ 1052 mV, *vs.* Ag / AgCl) redox couple, **Figure 13**; the $P^{+1}$ / $P^{+2}$ ($E_{1/2}$ 1223 mV, *vs.* Ag / AgCl) redox couple was also apparent, as expected.

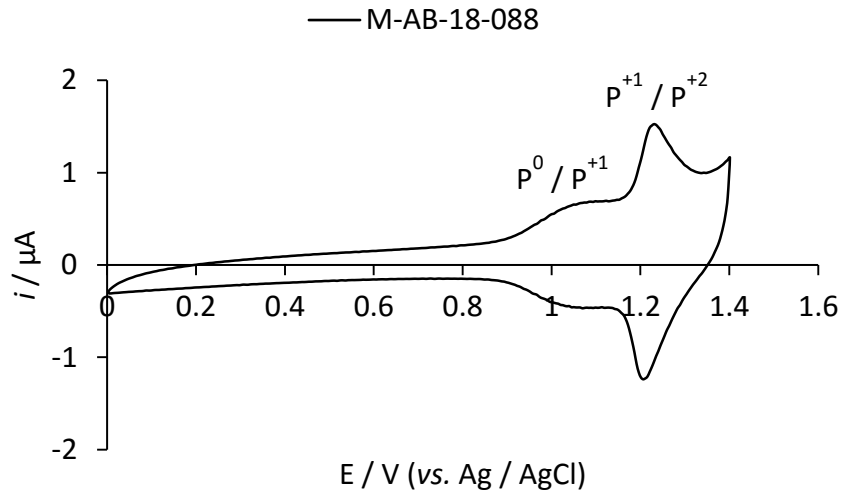


**Figure 13.** Cyclic voltammogram of a SAM of M-AB-18-088 deposited at Au. Upon deposition, the presence of M-AB-18-088 at the interface is inferred from the appearance of both porphyrin-centred redox couples ($P^0$ / $P^{+1}$ ($E_{1/2}$ 1052 mV, *vs.* Ag / AgCl) and $P^{+1}$ / $P^{+2}$ ($E_{1/2}$ 1223 mV, *vs.* Ag / AgCl)), *cf.* when the free-base analogue AB-18-088 is deposited. Electrochemical Setup: *Working Electrode*: SAM. *Reference Electrode*: Ag / AgCl. *Auxiliary Electrode*: Pt wire. *Electrolytic Solution*: 0.1 M $TBAPF_6$, anhydrous $CH_2Cl_2$. *Scan Rate:* 1000 mV / s.

Both confirm the presence of the metallated porphyrinic macrocyclic derivative at the interface, although no cathodic photocurrent was observed (**Appendix, 8.6.2**) upon photoirradiation of the monolayers, even upon the simultaneous deposition of 11-(ferrocenyl)undecanethiol (**Figure 11, M = Ni**). It is thought that the flow of cathodic photocurrent was not induced in either case because the distance between the porphyrinic macrocycle and the quenching metallic surface is too short (1.6 ± 0.2 nm as determined by ellipsometry) to prevent the domination of the backward rate of either energy or electron transfer from the excited state of the porphyrinic macrocycle to the Au surface[9-14]. Furthermore, in the case of the analogous biphasic films (**Figure 11, M = Ni**), it is thought that the reduced distance between the porphyrinic macrocycle and the tethered metallocene (0.1 or 0.6 nm as modelled in Chem3D 15.0 (MM2)) prevents the expected enhancement in the magnitude of the cathodic photocurrent being realised because the photoexcited state of the porphyrinic macrocycle is more efficiently quenched by the oxidised form of the electron relay group[14]. Simultaneous deposition of the photoactive (M-AB-18-088) and relay moieties ($Fc(CH_2)_6SH$ or $Fc(CH_2)_{11}SH$) was confirmed by CV, **Figure 14**, and XPS, **Figure 15**. Upon integration of each of the redox couples present ($P^0$ / $P^{+1}$ ($E_{1/2}$ 958 mV, *vs.* Ag Wire) and Fc / $Fc^+$ ($E_{1/2}$ 288 mV, *vs.* Ag Wire)), **Figure 14**, the surface concentration of both the porphyrinic macrocycle (1.2 ± 0.4 x $10^{-11}$ mol $cm^{-2}$), and the varying-length, surface-tethered metallocenes ($Fc(CH_2)_{11}SH$: 4.6 ± 1.0 x $10^{-11}$ mol $cm^{-2}$, $Fc(CH_2)_6SH$: 4.2 ± 0.8 x $10^{-11}$ mol $cm^{-2}$) was calculated. As expected, the concentration of M-AB-18-088 was lower than that acquired in the absence of either 6-(ferrocenyl)hexanethiol or 11-

(ferrocenyl)undecanethiol, 2.4 ± 0.3 x $10^{-11}$ mol $cm^{-2}$. Moreover, both Ni (854 eV) and Fe (≈ 710 eV) were observed upon XPS analysis of the biphasic interfaces, **Figure 15**.

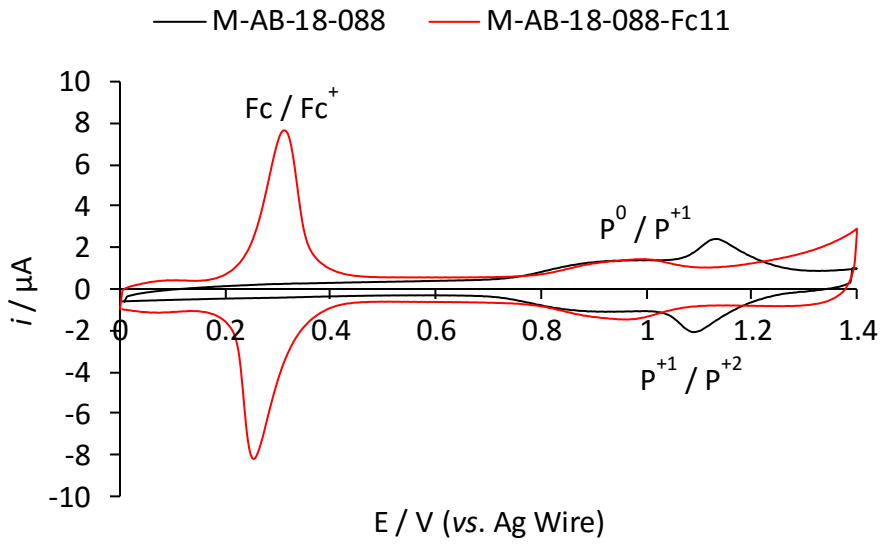


**Figure 14.** Cyclic voltammograms of SAMs of M-AB-18-088 (**Black**, 25 µM, $CH_2Cl_2$ (anhydrous), 16 h) and M-AB-18-088: Fc11 (**Red**, 1:1, 25 µM, $CH_2Cl_2$ (anhydrous), 16 h) deposited at Au. Fc11: $Fc(CH_2)_{11}SH$. Electrochemical Setup: *Working Electrode*: SAM. *Reference Electrode*: Ag / AgCl. *Auxiliary Electrode*: Pt wire. *Electrolytic Solution*: 0.1 M $TBAPF_6$, anhydrous $CH_2Cl_2$. *Scan Rate:* 1000 mV / s.

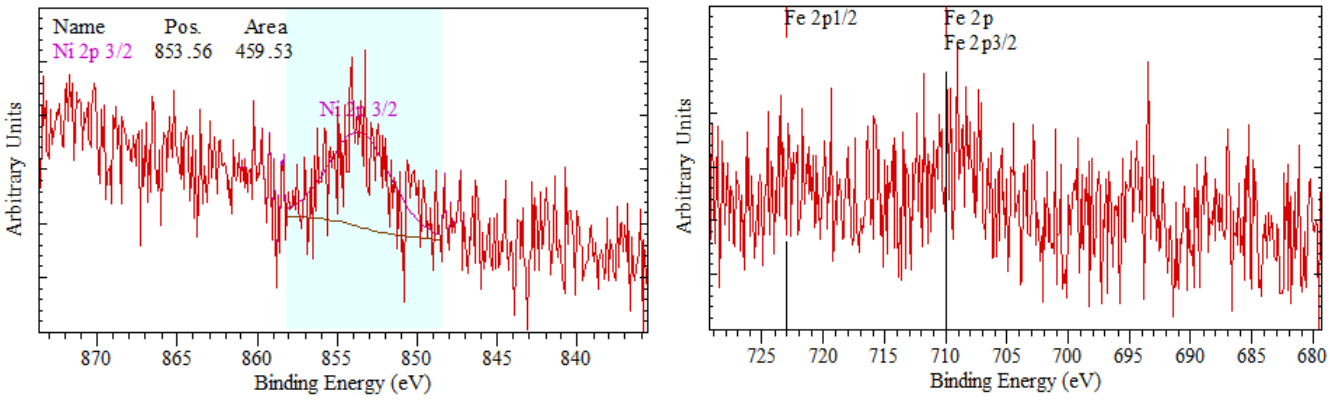


**Figure 15.** Narrow scan (Ni 2p (**Left**), Fe 2p (**Right**)) XPS spectra of a SAM of M-AB-18-088- $Fc(CH_2)_{11}SH$ deposited at Au.

Following the successful surface deposition of M-AB-10-088, AB-19-144 (**Figure 16**) was synthesised in a bid to achieve a cathodic photocurrent output from such an architecture, by increasing the distance between the metallated porphyrinic macrocycle and the metallic interface, **Figure 16**, from 1.6 ± 0.2 nm (M-AB-18-088, **Figure 11**) to 3.3 nm (AB-19-144). The integration of either 6-(ferrocenyl)hexanethiol or 11-(ferrocenyl)undecanethiol was then expected to bring about an enhancement in the magnitude of the photoelectrochemical output.

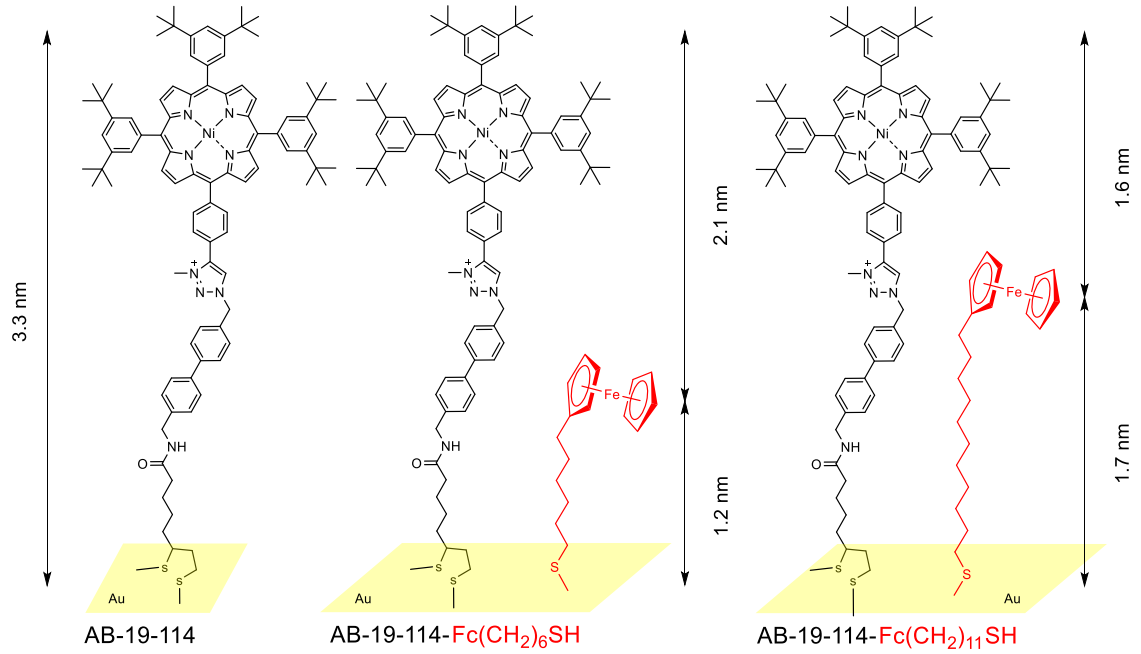


**Figure 16.** SAMs of AB-19-114, AB-19-114- $Fc(CH_2)_6SH$ and AB-19-114- $Fc(CH_2)_{11}SH$ deposited at Au. All quoted distances were estimated by a minimisation approach (MM2) performed in Chem3D 15.0. AB-19-114 was synthesised by Dr Asha Brown of the Paul Beer Group (University of Oxford).

The envisaged monolayers (**Figure 16**) were equivalent in structure, in regards to the interfacial molecular distances employed, to those documented in Chapter 2, **Figure 17**, from which cathodic photocurrent densities were found.

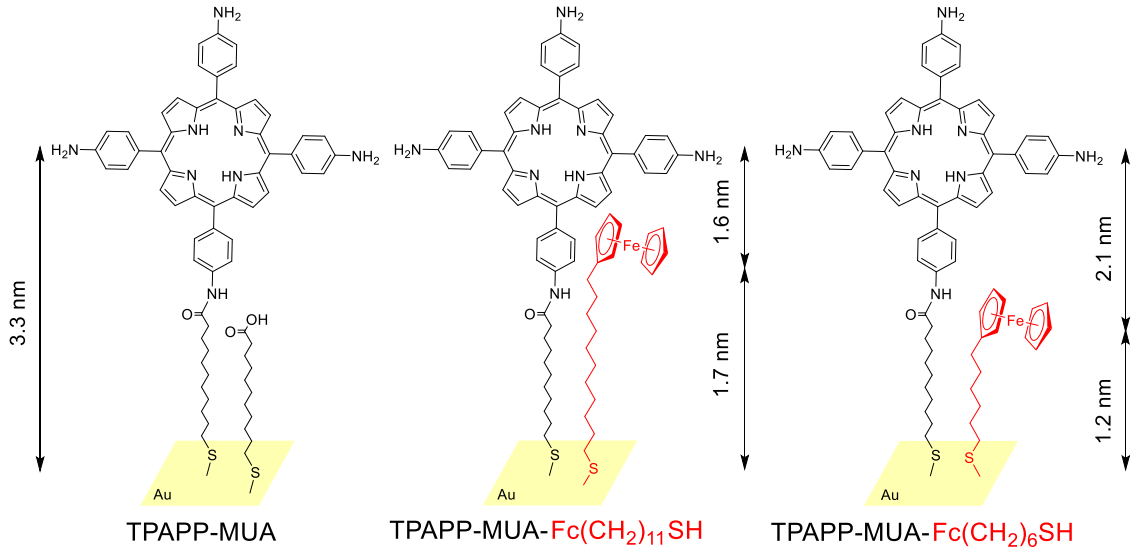


**Figure 17.** SAMs of TPAPP-MUA, TPAPP-MUA-$Fc(CH_2)_{11}SH$ and TPAPP-MUA-$Fc(CH_2)_6SH$ deposited at Au. All spatial separations were previously determined by ellipsometry (**Chapter 2**, **Table 2**).

Hence, upon the deposition of AB-19-114-JL241, **Figure 18**, cathodic photocurrent density was expected to be achieved upon the photoelectrochemical analysis of the resultant interlocked

molecular film, if the macrocyclic species (JL241) remained present and / or could mediate electron transfer.

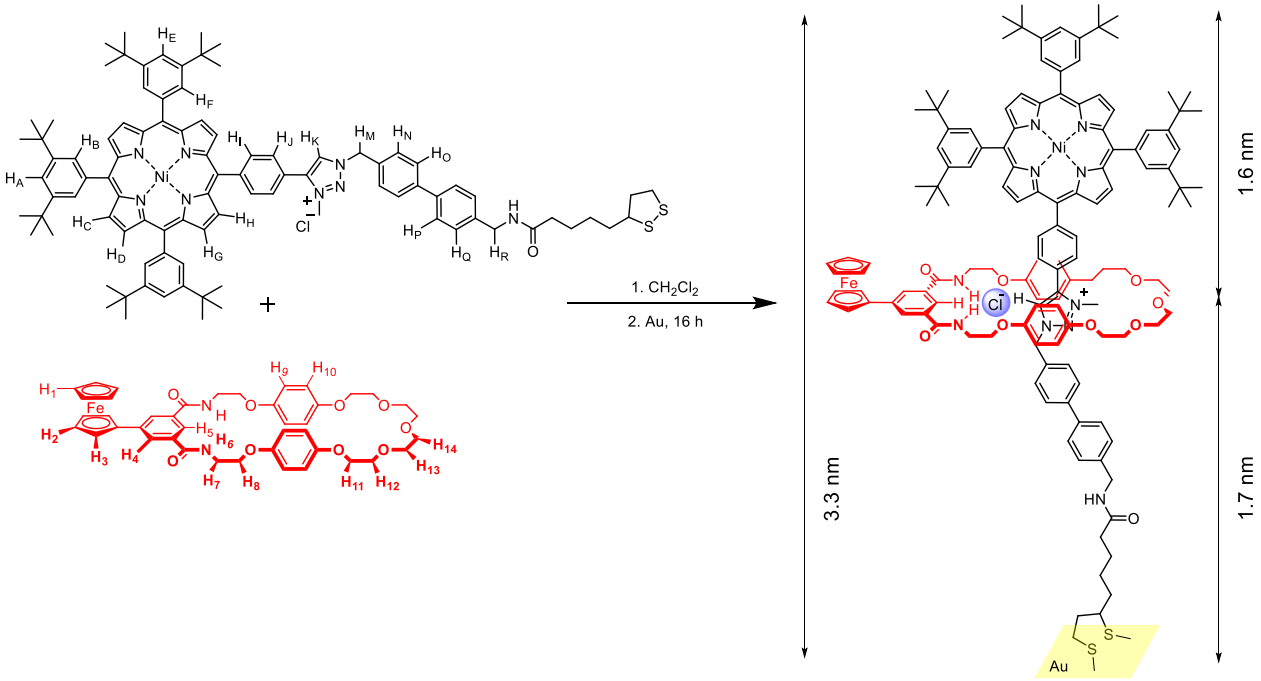


**Figure 18.** Solution phase pseudorotaxane formation (AB-19-144-JL241) prior to deposition of the interlocked assembly at Au.

Upon the deposition (25 μM, $CH_2Cl_2$ (anhydrous), 16 h) of AB-19-114, in the absence of JL241, **Figure 16**, both porphyrinic-centred redox couples ($P^0$ / $P^{+1}$ ($E_{1/2}$ 1116 mV, *vs.* Ag / AgCl) or $P^{+1}$ / $P^{+2}$ ($E_{1/2}$ 1294 mV, *vs.* Ag / AgCl)) were observed, **Figure 19**, a film thickness of 3.2 ± 0.2 nm acquired, by ellipsometry, and the presence of $Ni^{II}$ (854 eV) and / or the porphyrinic macrocycle confirmed by virtue of XPS (**Figure 20** and **Appendix, 8.5.3**).

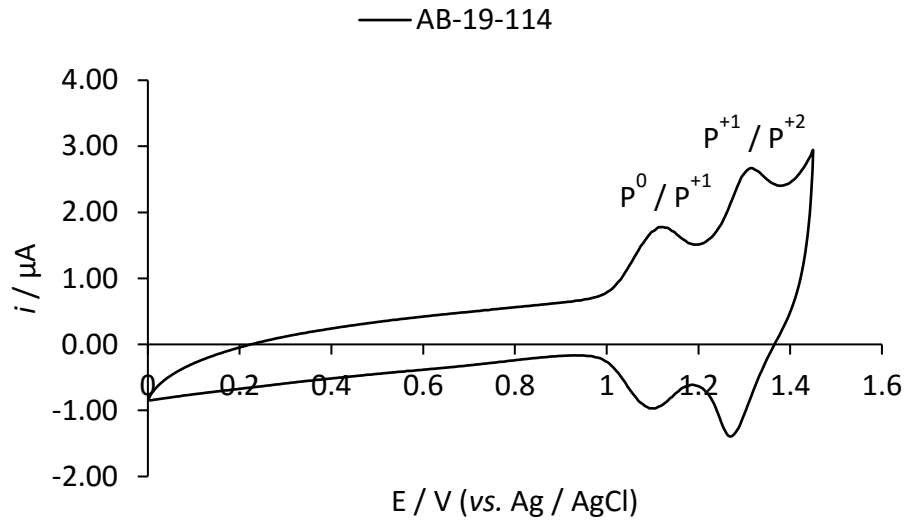


**Figure 19.** Cyclic voltammogram of a SAM of AB-19-144 deposited (25 µM, $CH_2Cl_2$ (anhydrous), 16 h) at Au. Electrochemical Setup: *Working Electrode*: SAM. *Reference Electrode*: Ag / AgCl. *Auxiliary Electrode*: Pt wire. *Electrolytic Solution*: 0.1 M $TBAPF_6$, anhydrous $CH_2Cl_2$. *Scan Rate:* 1000 mV / s.

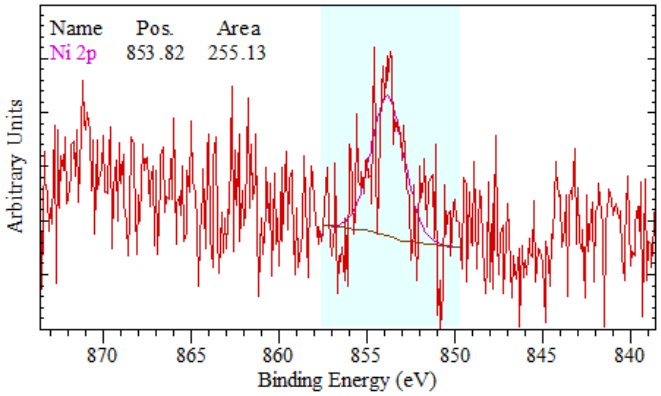


**Figure 20.** Narrow scan (Ni 2p) XPS spectrum of a SAM of AB-19-144 deposited at Au.

A surface concentration of 1.9 ± 0.5 x $10^{-11}$ mol $cm^{-2}$ was calculated upon integration of the $P^0$ / $P^{+1}$ ($E_{1/2}$ 1116 mV, *vs.* Ag / AgCl) redox couple, which is similar in magnitude to that obtained upon the deposition of M-AB-18-088, **Figure 11**. Surprisingly, the flow of cathodic current was not induced upon photoirradiation of the resultant film (**Appendix, 8.6.3**), thus the biphasic monolayers (**Figure 16**) were not assembled because it was desired for an enhancement in the magnitude of cathodic photocurrent density to be realised upon the addition of 1 mM FcMeOH into solution.

Similar observations were made upon the attempted deposition of the corresponding interpenetrated architecture, **Figure 18**, after its formation was probed by $^{1}$H NMR spectroscopy, **Figure 21**. Shifts similar to those observed upon the formation of AB-14-172-JL241 were apparent (**Figure 2**), indicating formation of the desired pseudorotaxane; an upfield shift of the macrocyclic (JL241) hydroquinone protons (**$H_9$** and **$H_{10}$**), and a slight downfield shift of the internal macrocyclic isophthalamide proton (**$H_5$**) was observed[1,2]. Although the expected increase in film thickness was observed by ellipsometry (3.1 ± 0.2 nm), no cathodic photocurrent output was observed upon photoirradiation of the interface, and the data acquired by virtue of CV, **Figure 22**, suggests that the ferrocene-appended macrocycle was not incorporated into the molecular film (**Blue Trace**); the Fc / $Fc^{+}$ redox couple is assumed to be absent for a similar reason as it was upon the attempted tethering of AB-14-172-JL241 to an activated film of the OEGylated thiol, **Figure 5**. To recap, it is thought that the steric hindrance associated with the formation of the interpenetrated assembly (AB-19-114-JL241) brings about the preferential deposition of the uncomplexed axle (AB-19-114). Furthermore, the resultant interface appears to resemble the monolayer acquired in the absence of JL241, that is the porphyrinic macrocycle is present at a surface concentration of 1.5 ± 0.5 x $10^{-11}$ mol $cm^{-2}$ ($P^{0}$ / $P^{+1}$ ($E_{1/2}$ 1030 mV, *vs.* Ag / AgCl)), *cf.* 1.9 ± 0.5 x $10^{-11}$ mol $cm^{-2}$ (AB-19-114 only), whilst only the $Ni^{II}$ signature (854 eV) is present in the associated XPS spectrum, **Figure 23**.

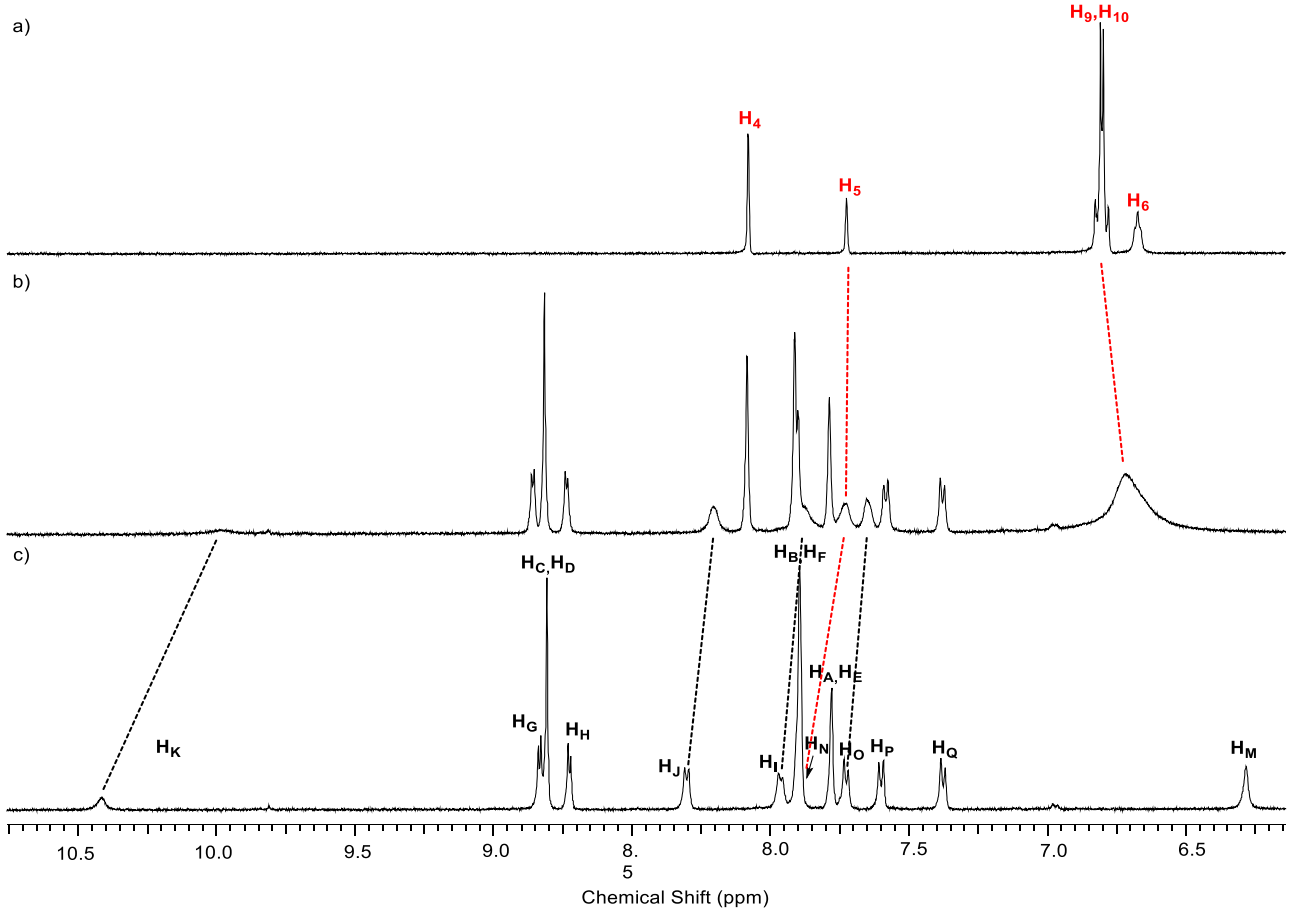


**Figure 21.** Partial $^{1}$H NMR spectra ($CD_2Cl_2$:$Et_3N$, 99:1, 298 K, 500 MHz) of 1.5 mM solutions of **a**) JL241, **b**) an equimolar mixture of JL241 and AB-19-144 and **c**) AB-19-144. Spectra recorded by Dr Asha Brown of the Paul Beer Group (University of Oxford).

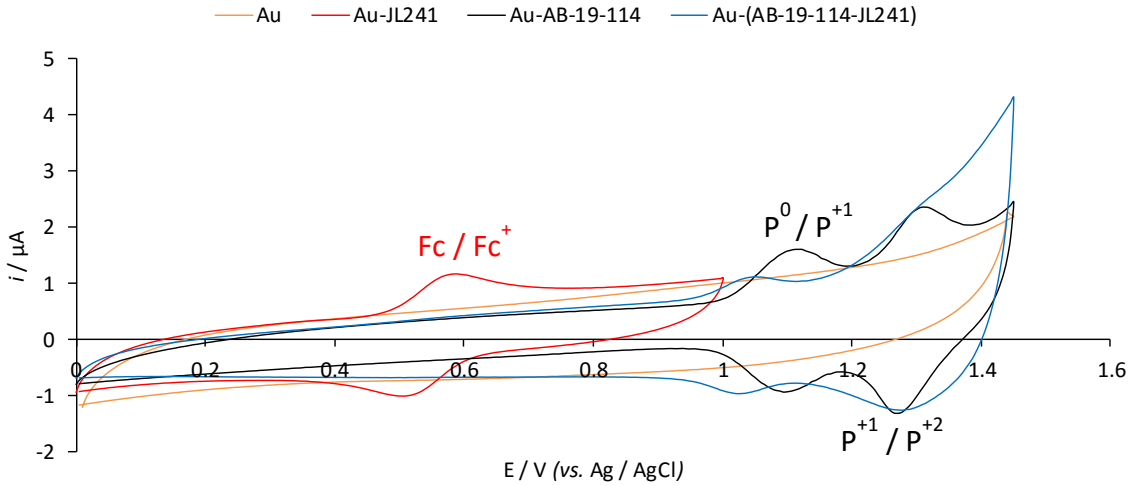


**Figure 22.** Cyclic voltammograms of a bare Au electrode prior to (**Orange**) and following the deposition of AB-19-114 (25 µM, $CH_2Cl_2$ (anhydrous), 16 h, **Black**) and AB-19-114-JL241 (**Blue**) (1:10, 25 µM, $CH_2Cl_2$ (anhydrous), 16 h). A diffusive voltammogram of JL241 (250 µM, $CH_2Cl_2$ (anhydrous), **Red**) is given. Electrochemical Setup: *Working Electrode*: SAM. *Reference Electrode*: Ag / AgCl. *Auxiliary Electrode*: Pt wire. *Electrolytic Solution*: 0.1 M $TBAPF_6$, anhydrous $CH_2Cl_2$. *Scan Rate:* 1000 mV / s.

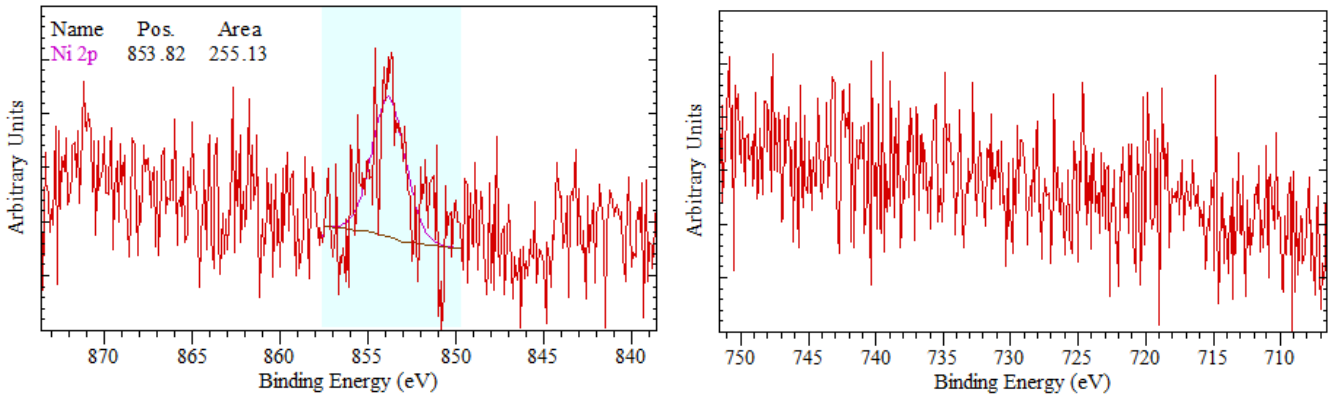


**Figure 23.** Narrow scan (Ni 2p (**Left**), Fe 2p (**Right**)) XPS spectra of a SAM of AB-19-144-JL241 deposited at Au.

In summary, whilst the presence of a free-base porphyrin derivative has been demonstrated to bring about the generation of singlet oxygen and / or the formation of the corresponding thiosulfonate, **Figure 12**, preventing the deposition of the porphyrin-stoppered, thioctic acid-functionalised axle component, AB-18-088, **Figure 11**, cathodic photocurrent density was not acquired upon metallation ($Ni^{II}$) of the porphyrinic macrocycle. Thus, fluorescence spectroscopy experiments were conducted as to elucidate the effect that incorporating $Ni^{II}$ has on the singlet excited state of the porphyrinic core.

### 3.3.2 – Role of Coordinated Metal Ions and the Triazolium Motif in the Generation of Cathodic Photocurrent

Upon the analysis of equimolar solutions of free-base, metallated and triazolium-containing porphyrin derivatives, the quenching effect of incorporating both $Ni^{II}$, into the core of the porphyrinic macrocycle, and a triazolium moiety, into the backbone of the molecular axle, on the fluorescent output ($Q_x$ (0,0) and $Q_x$ (0,1)) of the porphyrinic macrocycle, was highlighted, **Figure 24**.

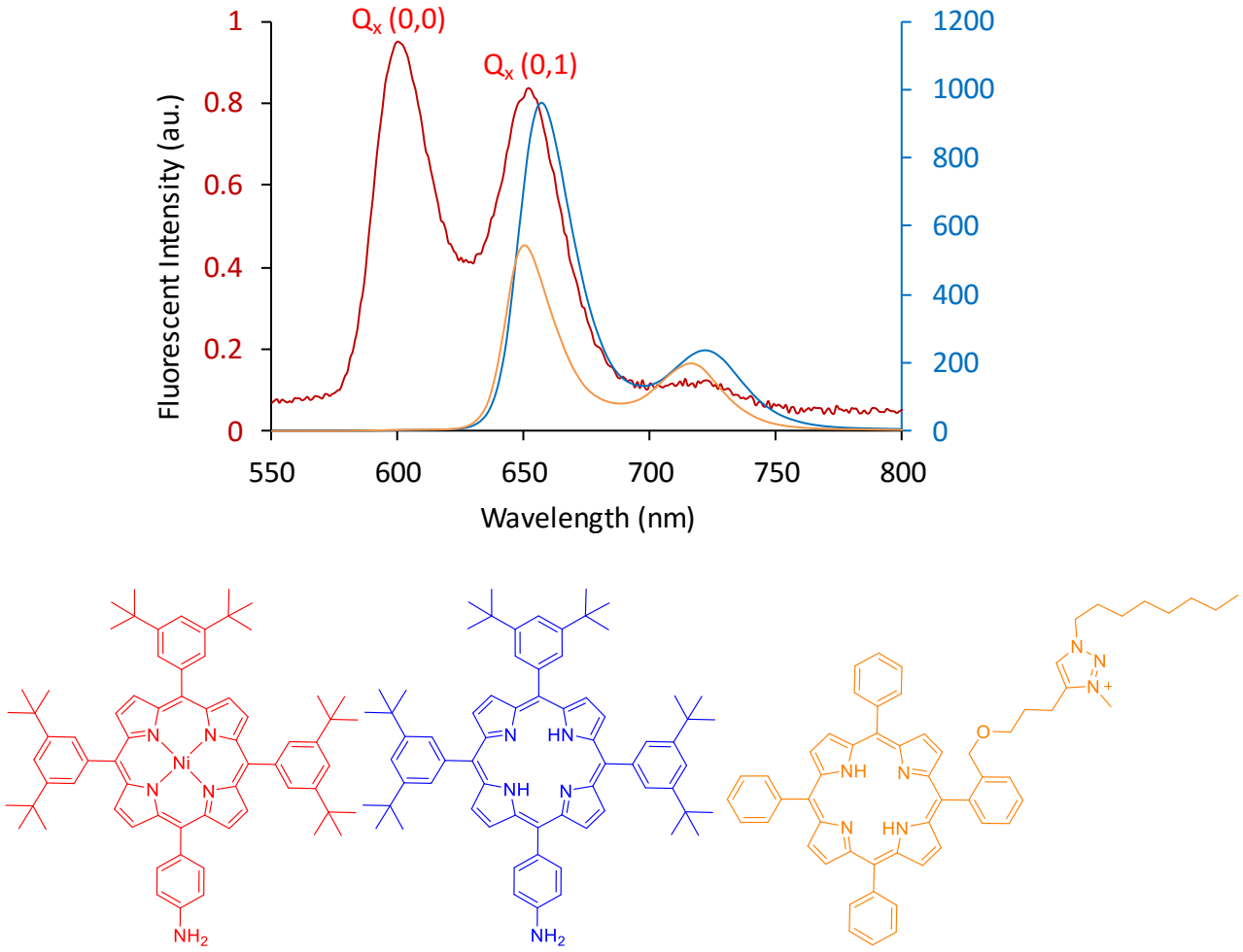


**Figure 24.** Fluorescent emission spectra of solutions (5 μM, $CH_2Cl_2$ (anhydrous)) of free-base (**Blue**, $\lambda_{irr}$. 423 nm, secondary y-axis), metallated (**Red**, $\lambda_{irr}$. 419 nm, primary y-axis) and triazolium-containing (**Orange**, $\lambda_{irr}$. 418 nm, secondary y-axis) porphyrin derivatives. Experimental Parameters: $\lambda_{ex}$ = variable, excitation slit width = 10 nm, emission slit width = 10 nm, PMT Voltage (V) = 600, CAT 30, 298 K. Absorption spectra (**Experimental, 7.5**) of porphyrins given in **Appendix, 8.7**.

Upon metallation of the porphyrinic core, a decrease in the intensity of both $Q_x$ (0,0) and $Q_x$ (0,1) was observed (**Experimental, 7.8**), **Figure 24**, illustrating the quenching nature of $Ni^{II}$ insertion. Nickel, a metal ion possessing partially filled *d*-orbitals, has been shown to act as an efficient excited-state quencher[15]; $Ni^{II}$ can quench the singlet excited state of the porphyrinic macrocycle by means of either electron or energy transfer[15]. Thus, it is not surprising that the flow of cathodic photocurrent was inhibited in its presence. This effect has also been witnessed upon the insertion of both $Ag^{II}$ and $Cu^{II}$.[15]

A reduction in the intensity of fluorescent emission was also observed upon the addition of methyl viologen dichloride, **Figure 25**, as was expected given the mechanism by which cathodic photocurrent is induced (**Introduction**, **Chapter 2**, **Section 2.3.1**, **Figure 13**); reports suggest that the photoinduced electron transfer process from an excited porphyrinic macrocycle to methyl

viologen occurs directly from the $S_2$ state of the porphyrin, before internal conversion to $S_1$, from which a reduced fluorescent output is acquired[17].

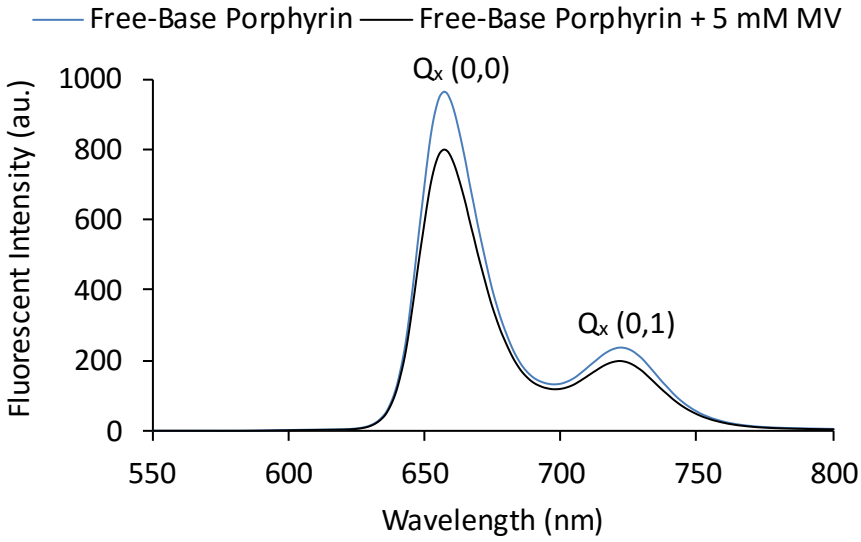


**Figure 25.** Fluorescent emission spectra of a solution (5 μM, $CH_2Cl_2$ (anhydrous)) of a free-base porphyrin derivative (**Figure 24**) prior to (**Blue**) and following the addition (**Black**) of $MV^{2+}$ (5 mM). Experimental Parameters: $\lambda_{ex}$ = 423 nm, excitation slit width = 10 nm, emission slit width = 5 nm, PMT Voltage (V) = 600, CAT 30, 298 K.

## 3.4 – Concluding Remarks and Moving Forwards

In conclusion, the generation of cathodic photocurrent is yet to be realised within an interlocked supramolecular architecture, which has been assembled at an interface. The formation of two interlocked molecular assemblies (**Figures 32** and **48**) was established by $^1$H NMR spectroscopy, although neither were successfully tethered to the interface, whether by directly depositing a thioctic acid-appended, pseudorotaxane at Au (**Figure 18**), or by covalently tethering the aminated analogue, by means of carbodiimide coupling, to an activated SAM of the OEGylated thiol (**Figure 2**). It is thought that the generation of singlet oxygen, by free-base porphyrin 'stoppers', prevents the deposition of thioctic acid-appended molecular systems, whilst although the insertion of $Ni^{II}$ into the porphyrinic core inhibits the formation of the corresponding thiosulfonate, and thus permits surface deposition, the metal ion, which possesses partially filled *d*-orbitals ($d^8$), has been shown to efficiently quench the singlet excited state ($Q_x$ (0,0), $Q_x$ (0,1)) of the porphyrinic macrocycle. It is for this reason that the flow of cathodic photocurrent was not induced upon the photoirradiation of metallated porphyrin-appended films. Furthermore, chloride templation of the ferrocene-appended macrocycle was not found in either case, that is JL241 was not observed at the interface throughout, thus electron transfer could not be mediated, as was demonstrated in Chapter 2 (**Section 2.3**) upon the simultaneous deposition of both 6-(ferrocenyl)hexanethiol and 11-(ferrocenyl)undecanethiol. The reason(s) for this is not yet known, although it might arise due to variation in the rates of

deposition and / or a shift in the equilibrium concerned with the formation of the pseudorotaxane. Given the difference in size between the axle (AB-14-172) and the pseudorotaxane (AB-14-172-JL241), it is reasonable to suggest that preferential tethering, at the interface, of the latter arises.

To bring about the surface deposition of such interlocked molecular architectures, and utilise the conformational ruler established in the process, the incorporation of non-quenching metal ions should be explored, as should the deposition of free-base porphyrin derivatives under an argon atmosphere. For example, it is reported that both $Zn^{II}$ and $Pd^{II}$ do not quench the singlet excited state of the porphyrinic macrocycle[15], but instead bring about an enhancement in fluorescent emission. They are however known to generate singlet oxygen[15], but this could be avoided upon depositing the derivatives under an inert atmosphere. However, the insertion of $Zn^{II}$ is likely to disrupt macrocyclic chloride templation and / or formation of the pseudorotaxane, because it is likely that the templating chloride anion would coordinate axially to the metal centre[18]. Thus, $Pd^{II}$ is likely to be the best option in terms of trying to ensure that the fluorescent emission from the porphyrinic macrocycle is not quenched upon metal insertion. However, upon optimisation of the molecular system, which appears to warrant careful consideration of both the metal ion's ability to generate singlet oxygen and / or luminesce, thiosulfonate formation may still prove to be an issue, as may recruiting the pseudorotaxane in preference to its axle component. Thus, incorporating free-base porphyrin derivatives into the supramolecular architecture, *via* an alternative self-assembly approach in which the ferrocene-appended macrocycle is already present at the interface, may prove to be the way forward in regards to the development of a bistable [2]rotaxane, whereby the position of a redox-active macrocyclic component is inferred by the magnitude of the cathodic photocurrent density acquired at each molecular station.

One approach envisaged, based on the work of Morin and co-workers[19], is centred on the formation of a SAM in which the macrocyclic component resides at an initial molecular station. The idea would be to then covalently couple a free-base porphyrin derivative to the SAM, bringing about the formation of a further molecular station in the process. Translocation of the redox-active macrocycle could then be photoelectrochemically monitored upon anion exchange. For example, the ferrocene-appended macrocycle could originally reside at an incorporated naphthalimide.$BF_4^-$ station[1], whilst upon the generation of a triazolium motif, following the attachment of a free-base porphyrin derivative, by means of a copper-free click cycloaddition reaction (phenyl azide + cyclooctyne[20]), translocation of the macrocycle could be induced upon the addition of a smaller anion, such as chloride or bromide, **Figure 26.** The cathodic photocurrent density acquired at each molecular station is expected to vary upon implementation of the conformational ruler established (**Chapter 2**), thus permitting novel photoelectrochemical transduction of macrocyclic motion within the dynamic, supramolecular architecture.

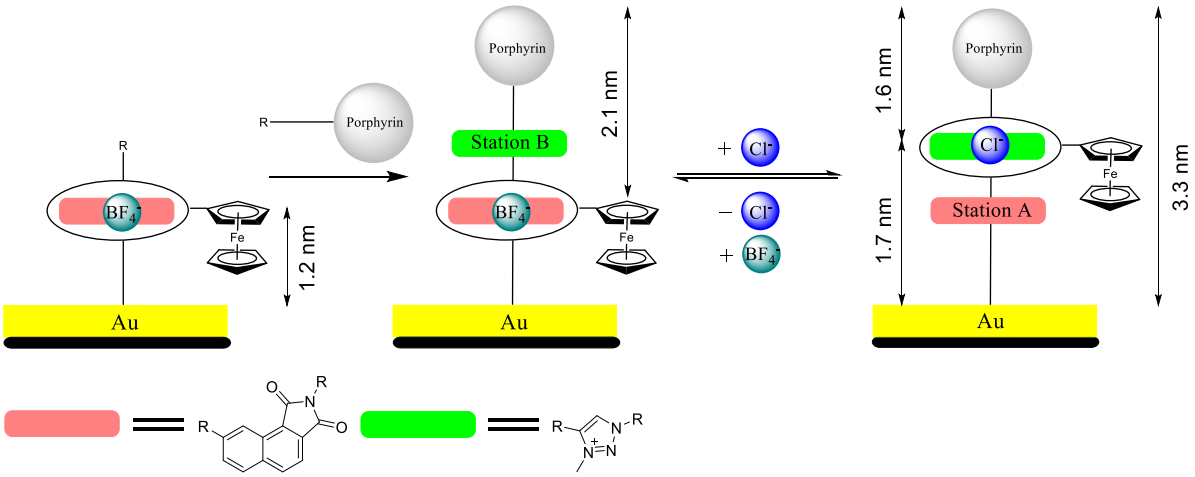


**Figure 26.** An alternative approach to the development of the desired bistable [2]rotaxane.

Although the interfacial assembly of such an architecture has proven very difficult to date, and thus the flow of cathodic photocurrent has yet to be realised within an interpenetrated molecular film, it is anticipated that this approach would serve to negate the physical adsorption issues associated with the covalent attachment of aminated free-base porphyrin derivatives to SAMs of carboxy-functionalised thiols. In addition, it would also ensure that the ferrocene-appended macrocycle was incorporated into the film, permitting the mediation of electron transfer and / or the induction of enhanced cathodic current in the process. Finally, the systematic approach highlighted (**Figure 26**) should allow for the incorporation, into the molecular assembly, of both a free-base porphyrin derivative and the thioctic acid tether, making it viable to suggest that stable films will be acquired thus, and that the photoelectrochemical output will not be inherently quenched, as was the case upon the insertion of $Ni^{II}$ into the porphyrinic core.

Alternatively, the use of thioctic acid, and thus formation of the corresponding thiosulfonate, in the presence of a free-base porphyrin derivative, could be circumvented by virtue of exploiting host-guest chemistry at the interface, **Figure 27**; an adamantane derivative, possessing a greater affinity constant for the hydrophobic cavity of CB[7], than those reported for ferrocene and analogues thereof, would serve to form an inclusion complex with CB[7] at the interface[21], thus bringing about surface normal deposition of the rotaxane. By permitting the use of a free-base porphyrin derivative, this approach would again ensure that the generation of singlet oxygen was no longer an issue, and that the singlet excited-state of the porphyrinic macrocycle was not inherently quenched.

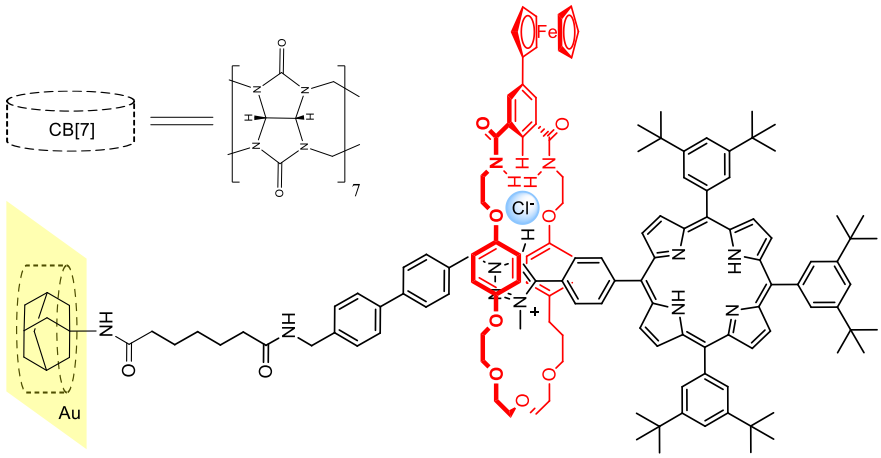


**Figure 27.** Utilising host-gust chemistry at the interface to recruit porphyrin-appended pseudorotaxanes.

If either of the interlocked architectures (**Figures 56** and **57**) are assembled at the interface, and the conformational ruler applied when doing so, as is inferred in **Figure 26**, and upon the integration of a secondary molecular station in the case of **Figure 27**, cathodic photocurrents of varying magnitude will be acquired at each of the incorporated molecular stations, thereby allowing the position of the ferrocene-appended macrocycle to be resolving by virtue of a novel, photoelectrochemical approach.

## List of References

1. Graeme T. Spence, Dr. Mateusz B. Pitak, Prof. Paul D. Beer, *Chem. Eur. J.*, **2012**, 18, 7100–7108.
2. Asha Brown, Paul D. Beer, *Dalton Trans.*, **2012**, 41, 118-129.
3. Drochss P. Valencia, Felipe J. González, *Electrochemistry Communications*, **2011**, 13, 129-132.
4. Drochss P. Valencia, Felipe J. González, *Journal of Electroanalytical Chemistry*, **2012**, 681, 121-126.
5. Alaa A. A. Aljabali, J. Elaine Barclay, Julea N. Butt, George P. Lomonossoff, David J. Evans, *Dalton Trans.*, **2010**, 39, 7569-7574.
6. Nicole F. Steinmetz, George P. Lomonossoff Dr., David. J. Evans Dr., *Small*, **2006**, 2, 530-533.
7. Nicole F. Steinmetz, George P. Lomonossoff, David J. Evans, *Langmuir*, **2006**, 22, 3488-3490.
8. *Electrochemistry at Solid Electrodes*, ed. R. N. Adams, Marcel Dekker, New York, 1969.
9. Hiroshi Imahori, Hiroyuki Norieda, Yoshinobu Nishimura, Iwao Yamazaki, Kazuo Higuchi, Naohiko Kato, Tomoyoshi Motohiro, Hiroko Yamada, Koichi Tamaki, Masatoshi Arimura, Yoshiteru Sakata, *J. Phys. Chem. B*, **2000**, 104, 1253-1260.

10. Hiroshi Imahori, Taku Hasobe, Hiroko Yamada, Yoshinobu Nishimura, Iwao Yamazaki, Shunichi Fukuzumi, *Langmuir*, **2001**, 17, 4925-4931.
11. Toshihiro Kondo, Masatoshi Yanagida, Xue-Qun Zhang, Kohei Uosaki, *Chem. Lett*., **2000**, 29, 964-965.
12. Kohei Uosaki, Toshihiro Kondo, Xue-Qun Zhang, Masatoshi Yanagida, *J. Am. Chem. Soc.*, **1997**, *119*, 8367-8368.
13. M. Yanagida, T. Kanai, X. Q. Zhang, T. Kondo, K. Uosaki, *Bull. Chem. Soc. Jpn.*, **1998**, 71, 2555-2559.
14. T. Kondo, T. Kanai, K. Isoo, K. Uosaki, *Z. Phys. Chem.*, **1999**, 212, 23-30.
15. Jason R. McCarthy, Ralph Weissleder, *ChemMedChem*., **2007**, 2, 360-365.
16. Sean Mathai, Trevor A. Smith, Kenneth P. Ghiggino, *Photochem. Photobiol. Sci*., **2007**, 6, 995-1002.
17. Mikael Andersson, Jan Davidsson, Leif Hammarström, *J. Phys. Chem. B*, **1999**, 103, 3258-3262.
18. *The Porphyrin Handbook: Inorganic, Organometallic and Coordination Chemistry (Volume 3)*, ed. K. M. Kadish, K. M. Smith, R. Guilard, Elsevier, 2000.
19. Jean-Sébastien Marois, Jean-François Morin, *Langmuir*, **2008**, 24, 10865-10873.
20. Jeremy M. Baskin, Jennifer A. Prescher, Scott T. Laughlin, Nicholas J. Agard, Pamela V. Chang, Isaac A. Miller, Anderson Lo, Julian A. Codelli, Carolyn R. Bertozzi, PNAS, **2007**, 104, 16793-16797.
21. Steven J. Barrow, Setu Kasera, Matthew J. Rowland, Jesús del Barrio, Oren A. Scherman, *Chem.Rev*., **2015**, 115, 12320-12406.

## List of Figures

**Figure 1.** Tethering AB-14-172-JL241 to an activated SAM of MUA deposited at Au. All quoted distances were estimated by a minimisation approach (MM2) performed in Chem3D 15.0.

**Figure 2.** Partial $^{1}$H NMR spectra ($CD_2Cl_2$:$Et_3N$, 99:1, 298 K, 500 MHz) of **a**) JL241, **b**) an equimolar mixture of JL241 and TBACl, **c**) an equimolar mixture of JL241 and AB-14-172 and **d**) AB-14-172. All components were used at a concentration of 1.5 mM and spectra recorded by Dr Asha Brown of the Paul Beer Group (University of Oxford).

**Figure 3.** ROESY spectrum ($CD_2Cl_2$:$Et_3N$, 99:1, 298 K, 500 MHz) of an equimolar (1.5 mM) mixture of JL241 and AB-14-172. Spectrum recorded by Dr Asha Brown of the Paul Beer Group (University of Oxford).

**Figure 4**. Cyclic voltammogram of a 0.21 mM solution ($CH_2Cl_2$, anhydrous) of JL241 prior to (**Red**) and following (**Blue**) the addition of 1.2 equivalents of AB-14-172. The expected reductions in ***D*** and $\boldsymbol{i_p}$ of the macrocyclic species (JL241, $E_{1/2}$ 290 mV *vs.* Ag / $AgNO_3$, 1000 mV / s) were not observed upon the addition of AB-14-172 into solution. Electrochemical Setup: *Working Electrode*: Glassy Carbon. *Reference Electrode*: Ag / $AgNO_3$SCE. *Auxiliary Electrode*: Pt wire. *Electrolytic Solution*: 0.1 M $TBAPF_6$, anhydrous $CH_2Cl_2$. *Scan Rate:* 1000 mV / s.

**Figure 5.** Tethering AB-14-172-JL241 to a SAM of OEG deposited at Au.

**Figure 6.** Cyclic voltammograms of SAMs of AB-14-172- Fc11-OEG (**Red**) and AB-14-172-JL241-OEG (**Black**) deposited at Au, and of SAMs of OEG (**Green**) and MUA (**Purple**) following exposure to a solution (50 µM, $CH_2Cl_2$, anhydrous) of AB-14-172 in the absence of EDC / NHS. Fc11: $Fc(CH_2)_{11}SH$. Electrochemical Setup: *Working Electrode*: SAM. *Reference Electrode*: Ag / AgCl. *Auxiliary Electrode*: Pt wire. *Electrolytic Solution*: 0.1 M $TBAPF_6$, anhydrous $CH_2Cl_2$. *Scan Rate:* 1000 mV / s.

**Figure 7.** Tethering AB-14-172-JL241 to SAMs of MUA and OEG deposited at Au. All quoted distances were estimated by a minimisation approach (MM2) performed in Chem3D 15.0

**Figure 8.** Current *vs.* time profiles for SAMs of AB-14-172-OEG (**Blue**), AB-14-172-OEG-Fc11 (**Red**) and AB-14-172-JL241-OEG (**Black**) deposited at Au. Fc11: $Fc(CH_2)_{11}SH$. The structure of each monolayer is given. Electrochemical Cell Setup: *Working Electrode*: SAM. *Reference Electrode*: Ag / AgCl. *Auxiliary Electrode*: Pt Wire. *Electrolytic Solution*: 0.1 M $Na_2SO_4$ + 5 mM $MV^{2+}$. *Solvent*: $H_2O$. *Bias Potential*: - 100 mV. $\lambda_{irr}$*:* 430 ± 5 nm.

**Figure 9.** Cyclic voltammograms of a 1 mM solution of ferrocenemethanol (**Red**), and of both a SAM of OEG (**Blue**) and a bare Au electrode (**Orange**) following exposure to a 450 µM solution of JL241. Electrochemical Cell Setup: *Working Electrode:* Au or SAM. *Reference Electrode:* Hg / $Hg_2SO_4$. *Auxiliary Electrode:* Pt Wire. *Supporting Electrolyte*: ~ 0.1 M $TBAPF_6$. *Solvent:* $CH_2Cl_2$ (anhydrous).

**Figure 10.** Solution phase pseudorotaxane formation (between JL241 and a thioctic acid-appended, porphyrin-stoppered axle component), prior to deposition of the resultant interlocked assembly at Au.

**Figure 11.** Deposition of free-base (**M = $H_2$**) and metallated (**M = Ni**), thioctic acid-appended porphyrin derivatives at Au. AB-18-088 was synthesised by Dr Asha Brown of the Paul Beer Group (University of Oxford).

**Figure 12.** ESI-MS of a solution of AB-20-042 following oxidation of the thioctic acid tether. Its molecular structure prior to and following oxidation of the thioctic acid tether is given. AB-20-042 was synthesised by Dr Asha Brown of the Paul Beer Group (University of Oxford).

**Figure 13.** Cyclic voltammogram of a SAM of M-AB-18-088 deposited at Au. Upon deposition, the presence of M-AB-18-088 at the interface is inferred from the appearance of both porphyrin-centred redox couples ($P^0$ / $P^{+1}$ ($E_{1/2}$ 1052 mV, *vs.* Ag / AgCl) and $P^{+1}$ / $P^{+2}$ ($E_{1/2}$ 1223 mV, *vs.* Ag / AgCl)), *cf.* when the free-base analogue AB-18-088 is deposited. Electrochemical Setup: *Working Electrode*: SAM. *Reference Electrode*: Ag / AgCl. *Auxiliary Electrode*: Pt wire. *Electrolytic Solution*: 0.1 M $TBAPF_6$, anhydrous $CH_2Cl_2$. *Scan Rate:* 1000 mV / s.

**Figure 14.** Cyclic voltammograms of SAMs of M-AB-18-088 (**Black**, 25 µM, $CH_2Cl_2$ (anhydrous), 16 h) and M-AB-18-088: Fc11 (**Red**, 1:1, 25 µM, $CH_2Cl_2$ (anhydrous), 16 h) deposited at Au. Fc11: $Fc(CH_2)_{11}SH$. Electrochemical Setup: *Working Electrode*: SAM. *Reference Electrode*: Ag / AgCl. *Auxiliary Electrode*: Pt wire. *Electrolytic Solution*: 0.1 M $TBAPF_6$, anhydrous $CH_2Cl_2$. *Scan Rate:* 1000 mV / s.

**Figure 15.** Narrow scan (Ni 2p (**Left**), Fe 2p (**Right**)) XPS spectra of a SAM of M-AB-18-088- $Fc(CH_2)_{11}SH$ deposited at Au.

**Figure 16.** SAMs of AB-19-114, AB-19-114- $Fc(CH_2)_6SH$ and AB-19-114- $Fc(CH_2)_{11}SH$ deposited at Au. All quoted distances were estimated by a minimisation approach (MM2) performed in Chem3D 15.0. AB-19-114 was synthesised by Dr Asha Brown of the Paul Beer Group (University of Oxford).

**Figure 17.** SAMs of TPAPP-MUA, TPAPP-MUA-$Fc(CH_2)_{11}SH$ and TPAPP-MUA-$Fc(CH_2)_6SH$ deposited at Au. All spatial separations were previously determined by ellipsometry (**Chapter 2**, **Table 2**).

**Figure 18.** Solution phase pseudorotaxane formation (AB-19-144-JL241) prior to deposition of the interlocked assembly at Au.

**Figure 19.** Cyclic voltammogram of a SAM of AB-19-144 deposited (25 µM, $CH_2Cl_2$ (anhydrous), 16 h) at Au. Electrochemical Setup: *Working Electrode*: SAM. *Reference Electrode*: Ag / AgCl. *Auxiliary Electrode*: Pt wire. *Electrolytic Solution*: 0.1 M $TBAPF_6$, anhydrous $CH_2Cl_2$. *Scan Rate:* 1000 mV / s.

**Figure 20.** Narrow scan (Ni 2p) XPS spectrum of a SAM of AB-19-144 deposited at Au.

**Figure 21.** Partial $^1$H NMR spectra ($CD_2Cl_2$:$Et_3N$, 99:1, 298 K, 500 MHz) of 1.5 mM solutions of **a**) JL241, **b**) an equimolar mixture of JL241 and AB-19-144 and **c**) AB-19-144. Spectra recorded by Dr Asha Brown of the Paul Beer Group (University of Oxford).

**Figure 22.** Cyclic voltammograms of a bare Au electrode prior to (**Orange**) and following the deposition of AB-19-114 (25 μM, $CH_2Cl_2$ (anhydrous), 16 h, **Black**) and AB-19-114-JL241 (**Blue**) (1:10, 25 μM, $CH_2Cl_2$ (anhydrous), 16 h). A diffusive voltammogram of JL241 (250 μM, $CH_2Cl_2$ (anhydrous), **Red**) is given. Electrochemical Setup: *Working Electrode*: SAM. *Reference Electrode*: Ag / AgCl. *Auxiliary Electrode*: Pt wire. *Electrolytic Solution*: 0.1 M $TBAPF_6$, anhydrous $CH_2Cl_2$. *Scan Rate:* 1000 mV / s.

**Figure 23.** Narrow scan (Ni 2p (**Left**), Fe 2p (**Right**)) XPS spectra of a SAM of AB-19-144-JL241 deposited at Au.

**Figure 24.** Fluorescent emission spectra of solutions (5 μM, $CH_2Cl_2$ (anhydrous)) of free-base (**Blue**, $\lambda_{irr}$. 423 nm, secondary y-axis), metallated (**Red**, $\lambda_{irr}$. 419 nm, primary y-axis) and triazolium-containing (**Orange**, $\lambda_{irr}$. 418 nm, secondary y-axis) porphyrin derivatives. Experimental Parameters: $\lambda_{ex}$ = variable, excitation slit width = 10 nm, emission slit width = 10 nm, PMT Voltage (V) = 600, CAT 30, 298 K. Absorption spectra of porphyrins given in **Appendix, 8.7**.

**Figure 25.** Fluorescent emission spectra of a solution (5 μM, $CH_2Cl_2$ (anhydrous)) of a free-base porphyrin derivative (**Figure 24**) prior to (**Blue**) and following the addition (**Black**) of $MV^{2+}$ (5 mM). Experimental Parameters: $\lambda_{ex}$ = 423 nm, excitation slit width = 10 nm, emission slit width = 5 nm, PMT Voltage (V) = 600, CAT 30, 298 K.

**Figure 26.** An alternative approach to the development of the desired bistable [2]rotaxane.

**Figure 27.** Utilising host-gust chemistry at the interface to recruit porphyrin-appended pseudorotaxanes.

# 4. Host-Guest Recognition & the Generation of Ternary Complexes in Solution

The interest in this family of homologous macrocyclic compound (cucurbit[*n*]uril, CB[*n*]) arises as the result of its ability to include guest species within its molecular cavities[1,2], a recognition process aided by both the polar carbonyl groups situated at their periphery, and the apolar, hydrophobic nature of their cavity[3]. Although this branch of supramolecular chemistry is attracting significant interest of late, especially within the disciplines of catalysis, sensing, molecular machines and self-assembly,[4] the use of CB[8] in the construction of an optically switchable ternary complex, exploiting charge transfer, has yet to be reported, something that this project set out to address. The strategy employed to try and generate such a complex, centred on confining the donor-acceptor interaction induced between an electron-rich naphthalene derivative (EuNap) and an electron-deficient methyl viologen ($MV^{2+}$) derivative (FcMV), within the cavity of CB[8], **Figure 1** (**A**). The electron-rich naphthalene derivative was to be tethered to a complex of europium(III) ($Eu^{3+}$), whilst it was planned for the electron-deficient methyl viologen to be appended with ferrocene (Fc). Thus, one would be able to see whether it was possible to modulate the luminescent emission from the lanthanide ion confined within this assembly, upon altering the oxidation state of the metallocene. This concept was previously reported by members of our group[5,6], who could demonstrate that the low-lying excited states of ferrocenium ($Fc^{+}$) act to quench sensitised emission to a greater degree than those of a Fc chromophore[5,6].

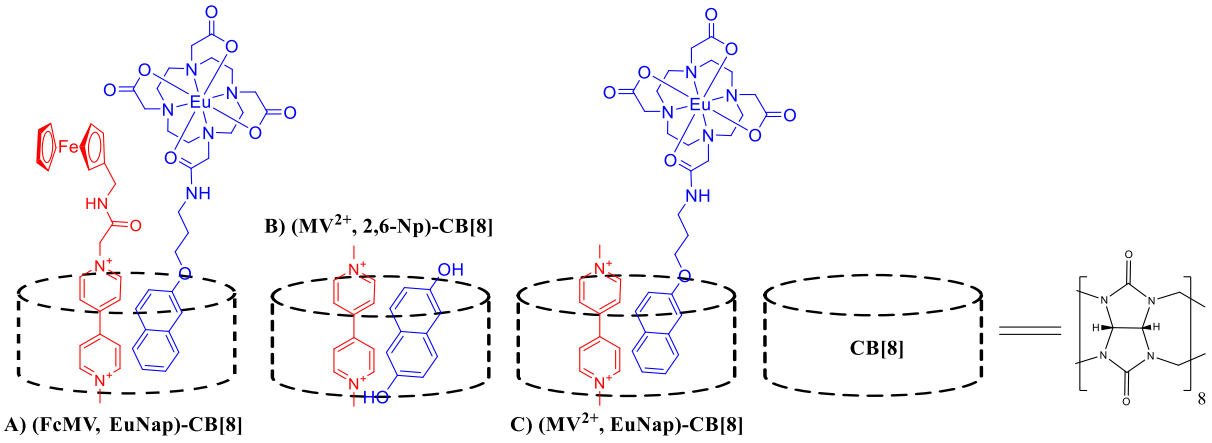


**Figure 1.** The envisaged ternary complexes; (FcMV, EuNap)-CB[8] (**A**), ($MV^{2+}$, 2,6-Np)-CB[8] (**B**) and ($MV^{2+}$, EuNap)-CB[8] (**C**).

Prior to utilising CB[8] in the assembly of ternary complexes, the inclusion of a variety of ferrocene derivatives, within the hydrophobic cavity of the smaller homologue, CB[7], to give complexes of stoichiometric ratio 1:1 (host : guest)[7-10], rather than 1:2 in the case of CB[8][11-20], was investigated to acquire understanding of the inclusion of a guest species within the cavity of a macrocyclic host.

Their inclusion within the cavity of CB[7] was confirmed upon the observation of an anodic shift of the guest's $E_{1/2}$ value, corresponding to increased stabilisation of the neutral form,[21] a decrease in current, something which coincides with the inclusion complex having a smaller diffusion coefficient than the derivative in solution,[22-27] and a blue spectral shift of the metal-to-ligand charge-transfer (MLCT) band, brought about by the fact that the guest is migrating from an aqueous medium into a non-polar environment,[28-30] **Figure 2**.

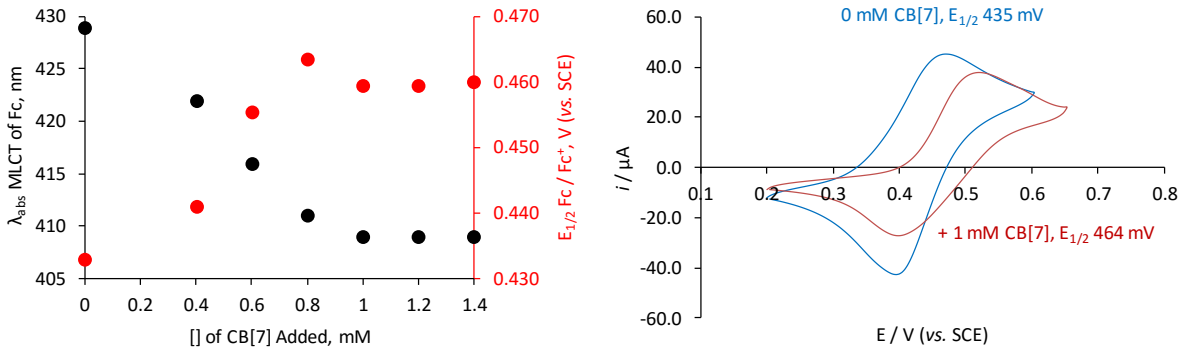


**Figure 2.** Monitoring the inclusion of ferrocenylmethyltrimethylamine ($FcCH_2NMe_3^+$) within the apolar cavity of CB[7] by cyclic voltammetry (**Experimental, 7.2.4**) and UV-Vis spectroscopy (**Experimental, 7.5**). Upon the addition of an increasing number of equivalents of CB[7] (0 → 1.4) to a solution (1 mM, aq.) of $FcCH_2NMe_3^+$, inclusion of the guest species is confirmed by an anodic shift in the $E_{1/2}$ value (**Left** (**secondary *y*-axis**) **and Right**), and a blue spectral shift in the metal-to-ligand charge-transfer (MLCT) band of the guest species (**Left, primary *y*-axis**). No further change was observed following the addition of 1 equivalent of CB[7], highlighting the formation of a 1:1 host-guest complex.

## 4.1 – Ternary Complex Formation

Charge-transfer was first evident upon generation of the model system, that is the charge-transfer complex in which both 2,6-dihydroxynaphthalene (2,6-Np) and $MV^{2+}$ are confined within the cavity of CB[8], **Figure 1** (**B**). Formation of the model system (**Experimental, 7.10**) was confirmed by means of $^1$H NMR (**Experimental, 7.7**), ESI-MS (**Experimental, 7.7**), UV-Vis (**Experimental, 7.5**), and luminescence spectroscopy (**Experimental, 7.8**), respectively. For example, all peaks in the $^1$H NMR spectrum, **Figure 3**, were shifted upfield (shifts of 0.2 and 0.8 ppm were evident in the case of the aromatic protons of $MV^{2+}$ (*a* and *b*) in the presence of CB[8], and subsequently shifted downfield, by the equivalent magnitude,[31] upon the addition of an excess of amantadine hydrochloride (**Figure 3, Trace B**). This was expected given the fact that it possesses a greater association constant for the hydrophobic cavity of the macrocyclic host[7], *cf.* both $MV^{2+}$ and 2,6-Np. This is likely to be because it is both cationic, and reported to be of an idealised molecular geometry for binary inclusion into the cavity of CB[8].[32,33]

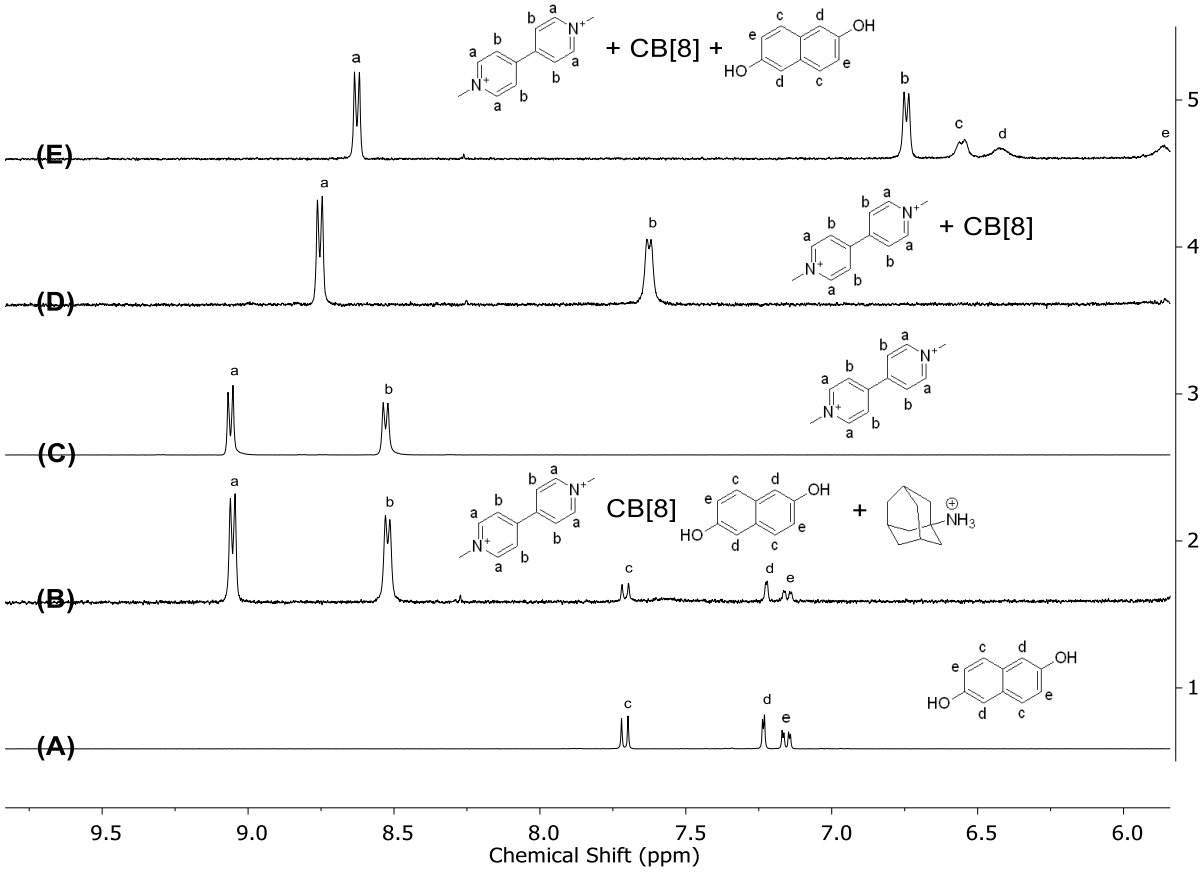


**Figure 3.** $^{1}$H NMR spectra ($H_2O$, 298 K, 400 MHz) of a solution of ($MV^{2+}$, 2,6-Np)-CB[8] prior to (**Trace E**) and following the addition of 1 equivalent of amantadine hydrochloride (**Trace B**). $^{1}$H NMR spectra ($H_2O$, 298 K, 400 MHz) of solutions of $MV^{2+}$-CB[8] (**Trace D**), $MV^{2+}$ (**Trace C**) and 2,6-Np (**Trace A**) are also given. Ternary complex formation was confirmed when upfield chemical shifts of the resonances corresponding to protons *a*, *b*, *c*, *d* and *e* were observed upon the addition of a stoichiometric amount of the macrocyclic host, CB[8]. Upfield shifts of 0.2 and 0.8 ppm of the aromatic peaks of $MV^{2+}$ (*a* and *b*) post complexation result from shielding of the proton environments due to their interaction with the carbonyl portals and the negative electrostatic potential of the CB[8] cavity. The peaks of the 2,6-Np protons (*c*, *d* and *e*) are broadened and similarly shifted upfield on formation of the ternary complex, the negative EP of CB[8] causing similar shielding effects, and the interruption of aromaticity from charge-transfer reducing paramagnetic contribution to the shifts from ring currents of the naphthalene core.[31] All complexes were generated at a concentration of 2 mM. **Traces A – E, Bottom – Top**.

Additionally, upon formation of the model ternary complex, ($MV^{2+}$, 2,6-Np)-CB[8], a peak at *m / z* 837.28 was observed in the ESI-MS spectrum recorded, **Figure 4** (**Right**), and a charge transfer band observed at 570 nm, the molar absorption coefficient (ε) of which dramatically increased upon confinement of both species within the molecular cavity of CB[8], **Figure 4** (**Left**); ε is intensified as the result of face-to-face π-π stacking of the guest species within CB[8].

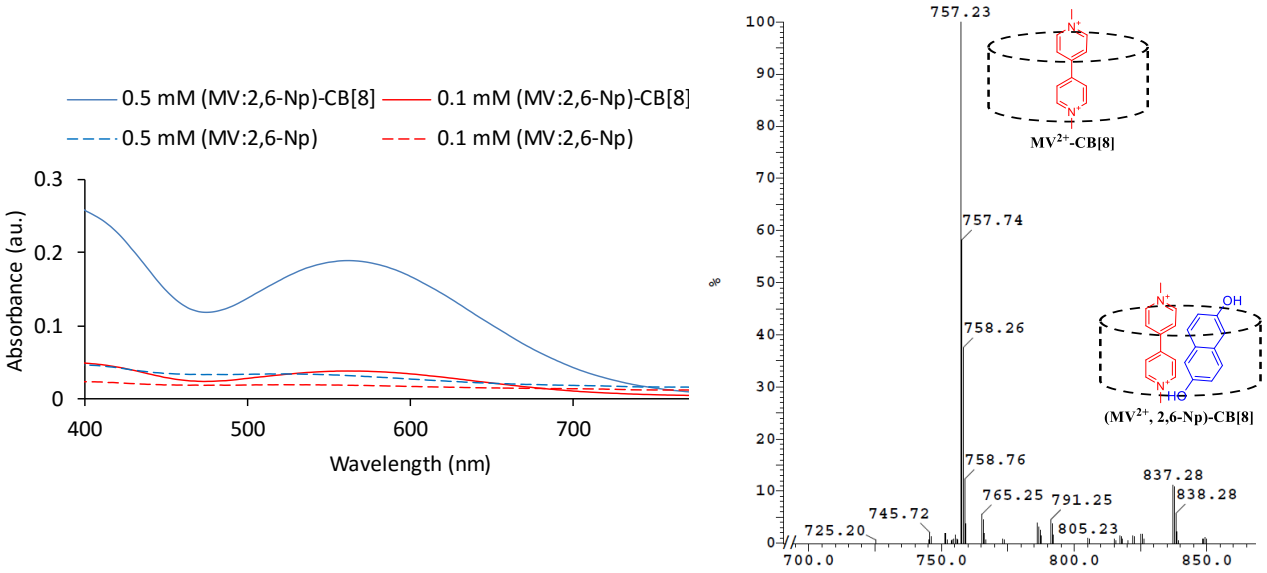


**Figure 4.** An increase in ε of the charge-transfer band ($\lambda_{max}$ 570 nm) is seen upon the addition of a stoichiometric amount of CB[8] (**Left**). This is accompanied by the appearance of a peak in the ESI-MS at *m / z* 837.33 (**Right**); both signify formation of the model ternary complex, ($MV^{2+}$, 2,6-Np)-CB[8]. Presence of the binary complex ($MV^{2+}$-CB[8], *m / z* 757.23, **Right**) is still apparent to some extent. Both give similar spectra which differ to that of the free dimer ($MV^{2+}$-2,6-Np) in solution, **Figure 4**. All complexes were generated in aqueous solution at 298 K.

## 4.2 – Formation of the Model Homoternary Dimer Complex, $(MV^{+\bullet})_2$-CB[8]

It was found that upon reduction of a solution of the model ternary complex, *via* the addition into solution of an excess of sodium dithionite ($Na_2S_2O_4$), the charge transfer band at 570 nm disappeared in accordance with the formation of the homoternary dimer complex, $(MV^{+\bullet})_2$-CB[8], **Figure 5** (**Top**).[20] This complex was also afforded, as expected[20], upon reduction of the binary complex ($MV^{2+}$-CB[8], *m / z* 757.23, **Figure 4** (**Right**)). Both give similar spectra which differ to that of the free dimer in solution, **Figure 5** (**Top Right, Red Trace**). This transition ($\lambda_{max}$ 570 nm) did however reappear upon the application of oxygen to the solution, suggesting that the process is reversible and that the method may be of potential use in the switching of lanthanide luminescence.

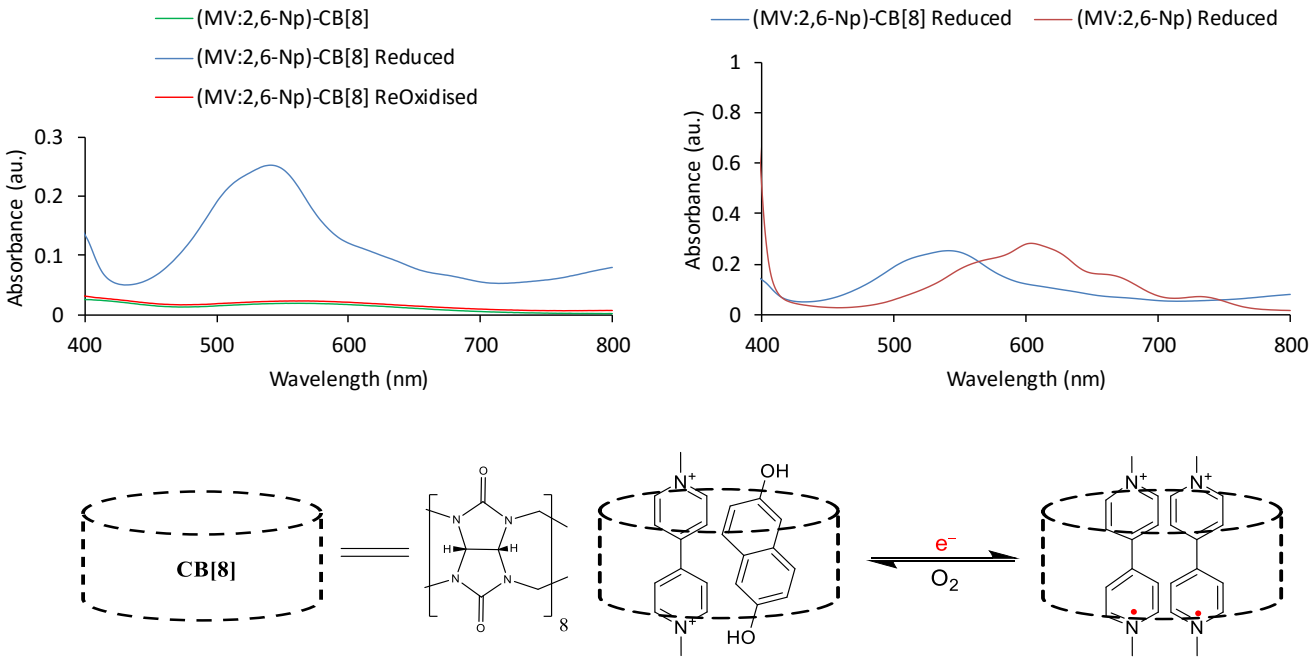


**Figure 5.** Formation of the homoternary complex ($(MV^{+\bullet})_2$-CB[8]) and the switching of lanthanide luminescence within a novel heteroternary assembly. Demonstrating the reversibility of the redox process in the presence (**Top Left**) and absence (**Top Right**) of CB[8]. **Bottom**. The effect of reducing, and subsequently oxidising, a solution of the model ternary complex, ($MV^{2+}$, 2,6-Np)-CB[8]. All complexes were generated in aqueous solution at 298 K, and at a concentration of 0.5 mM. $e^-$ denotes one electron reduction, whilst $O_2$ denotes oxidation.

However, exploiting this chemically-triggered method in a bid to optically switch the radiative output from the excited state of $Eu^{3+}$, $^7D_0$, confined within the two ternary complexes of interest, (MV, EuNap)-CB[8] and (FcMV, EuNap)-CB[8], was likely to prove problematic due to the slow rate of regeneration of the ternary complex, following prior reduction, and the competitive binding of sodium cations to the periphery of the macrocyclic host. Both factors proved to be an issue in the case of the model complex, ($MV^{2+}$, 2,6-Np)-CB[8], **Figure 5.** The binding of sodium cations to the weakly basic carbonyl portals of the macrocyclic host was seen to bring about decomplexation of the ternary system, by displacing the already encapsulated guest species ($MV^{2+}$ and 2,6-Np), *via* depolarisation of the carbonyl portals permitting inclusion of the guest species within the molecular cavity. In addition, precipitation of the CB[8] motif was accelerated upon saturation of the solution with the sulphite ion, formed upon oxidation of the disulphite ion. Thus, a proportion of free $MV^{2+}$ remained in solution, portraying its characteristic monomer-dimer equilibrium spectral signature (**Figure 5** (**Top Right, Red Trace**)); the dimer solution spectrum is derivable by deconvolution of the full spectrum of reduced $MV^{2+}$, which constitutes an equilibrium between the free monomer and dimer radical species. In the absence of competitive cation-carbonyl interactions, and precipitation of the macrocyclic host species, the reduction and reoxidation process is likely to be fully reversible, delivering a molecular switch that can be followed qualitatively by a visible colour change. Nevertheless, electrochemical modulation of emission was expected to be far less destructive, in the sense that it does not involve displacement, and subsequent rerecruitment, of the optically-active

moiety, as was the case when using $Na_2S_2O_4$ to bring about the desired reductive change. It was assumed that careful modulation of the incorporated metallocene's oxidation state would have the same effect, **Figure 1**, as was demonstrated previously[5,6] when ferrocenium ($Fc^+$) was shown to quench the excited state of $Eu^{3+}$ to a greater extent than its neutral precursor, Fc.

Thus, research centred on investigating the use of another reducing agent, in a bid to generate the homoternary complex, and reduce cation-carbonyl interaction, thereby increasing the reversibility of the chemically-induced switching process, was not deemed a necessity; the project aimed to culminate in the development of an interfacial, molecular switch, not a solution phase, optically tuneable inclusion complex. In addition, the same thought process was applied when deciding not to elucidate whether it was possible to follow the modulation in optical emission, by monitoring changes in the emission profile of the europium centre of the naphthalene-appended derivative, as it was released from, and recruited back, into the molecular cavity of the CB[8] host. This was however likely to have proven problematic because one would have had to ensure that 100 % complexation and decomplexation arose prior to the recording of the respective spectra.

In summary, the model ternary complex, ($MV^{2+}$, 2,6-Np)-CB[8], was generated, before being characterised by UV-Vis, ESI-MS and $^1$H NMR spectroscopy. Subsequent chemical reduction yielded the homoternary complex, $(MV^{+\bullet})_2$-CB[8], and this process was shown to be fully reversible, upon the application of a stream of oxygen, thus highlighting its potential in the fabrication of a molecular switch that can be followed quantitatively by a visible colour change.

## 4.3 – Elucidating the Effect of Charge Transfer on the Sensitised Radiative Output Acquired from a Lanthanide Centre, Confined within a Ternary Complex

Following characterization of the model ternary complex, ($MV^{2+}$, 2,6-Np)-CB[8], a lanthanide centre was incorporated in the form of a EuNap derivative (Andrew Baxter, Professor Paul Beer Group (University of Oxford), **Experimental, 7.12**), **Figure 1** (**C**). ($MV^{2+}$, EuNap)-CB[8] was characterised, and its optical switching properties investigated, as was done for ($MV^{2+}$, 2,6-Np)-CB[8]. Upon confirmation of complexation, by UV-Vis spectroscopy and ESI-MS (*m / z* 1125.89) respectively, **Figure 6**, the effect, if any, that the induced charge-transfer interaction has upon the luminescent emission from the europium centre of the complex was probed by luminescence spectroscopy.

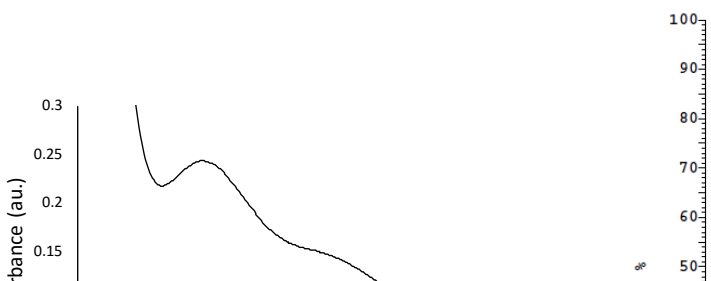

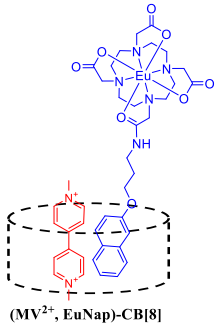


**Figure 6.** UV-Vis (**Left**) and ESI-MS (**Right**) of a solution of ($MV^{2+}$, EuNap)-CB[8]. Upon formation of the complex, a peak at *m / z* 1125.89 appeared, along with two charge-transfer peaks in the expected region; a shoulder peak at ca. 490 nm, and a more defined peak at ca. 390 nm. Both are of similar intensity to the charge-transfer peak observed in the case of the model ternary complex (($MV^{2+}$, 2,6-Np)-CB[8], **Figure 4**), denoting similarly confined inclusion. The hypsochromic shift of the charge-transfer bands from that witnessed in the model complex is in good agreement with the Mulliken model of charge-transfer electronics. As the two complexes are structurally similar, it may be approximated that the reorganisation energy *J* is comparable, with $\Delta E_{CT}$ ascribable to the difference in $E_{HOMO}$ of the donor compound. With only one electron-releasing substituent conjugated to the naphthalene core, $E_{HOMO}$ should be lower for EuNap, increasing the frontier orbital energy gap. $\lambda^{-1} \propto E_{CT} = E_{HOMO} - E_{LUMO} + J$, the wavelength of absorption is decreased and the charge-transfer complex now absorbs in the blue region of the electromagnetic spectrum, consequently appearing red in colour. All complexes were generated in aqueous solution at 298 K, and at a concentration of 2 mM.

It was important to investigate the effect of charge-transfer due to the fact that it was envisaged that the recruitment of this complex to a functionalised surface, such as gold (Au) or silicon (Si) would bring about the development of a novel, electrochemically switchable, emissive interface, whereby the sensitised emissive output from the lanthanide centre could be modulated upon either varying the oxidation state of the co-included, metallocene-containing species[5,6] (FcMV) (**Figure 7,** (**A**)), or by reversibly generating the homoternary complex[20], and subsequently monitoring the change in emissive output, from the lanthanide centre, at both the interface (loss) and in solution (increase), **Figure 7** (**B**).

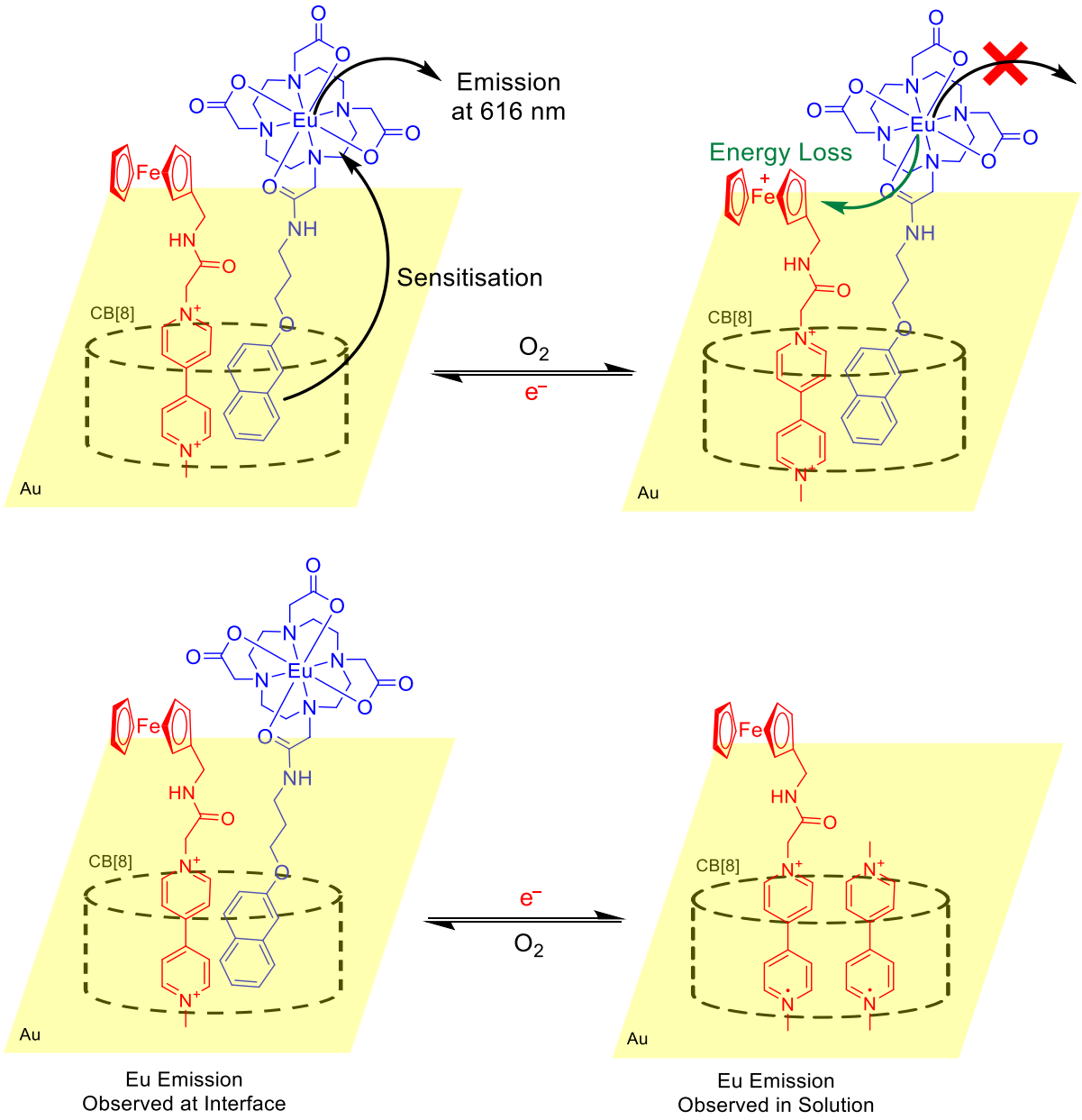


**Figure 7.** Modulating the emissive output from (FcMV, EuNap)-CB[8] at the interface by varying the oxidation state of the coincluded FcMV derivative (**Top** (**A**)), or *via* reversible generation of $(MV^{+\bullet})_2$-CB[8] (**Bottom** (**B**)). Upon oxidation of the Fc motif to $Fc^+$, the emissive state of $Eu^{3+}$ should be quenched, and hence no luminescent output observed. Whilst upon formation of the homoternary complex, $(MV^{+\bullet})_2$-CB[8], following one electron reduction of the $MV^{2+}$ appendage, in the presence of an excess of $MV^{2+}$, the EuNap species should be released into solution, hence all emissive output will be lost from the surface, and an optical signature only acquired upon analysis of the resultant solution. $e^-$ denotes one electron reduction, whilst $O_2$ denotes oxidation.

It was hoped that the induced charge transfer interaction would not inherently quench the excited state of the lanthanide ion, due to the fact that the presence of a metallic substrate, at the projected (Chem3D 15.0, MM2) distance of approximately 1.6 nm from the lanthanide ion itself, is reported to be capable of doing so to some degree.[34-37] Thus, if both quenching pathways are apparent, it is highly likely that no sensitised emissive output will be observed upon excitation of the assembly

highlighted in **Figure 7**. This is discussed in more detail within **Chapter 5**: **'The Surface Assembly of Molecular Switches'**.

Unfortunately, the induced charge-transfer interaction was seen to adversely affect the intensity of sensitised emission ($\lambda_{ex}$ 227 nm, 2,6-Np), **Figure 8**.

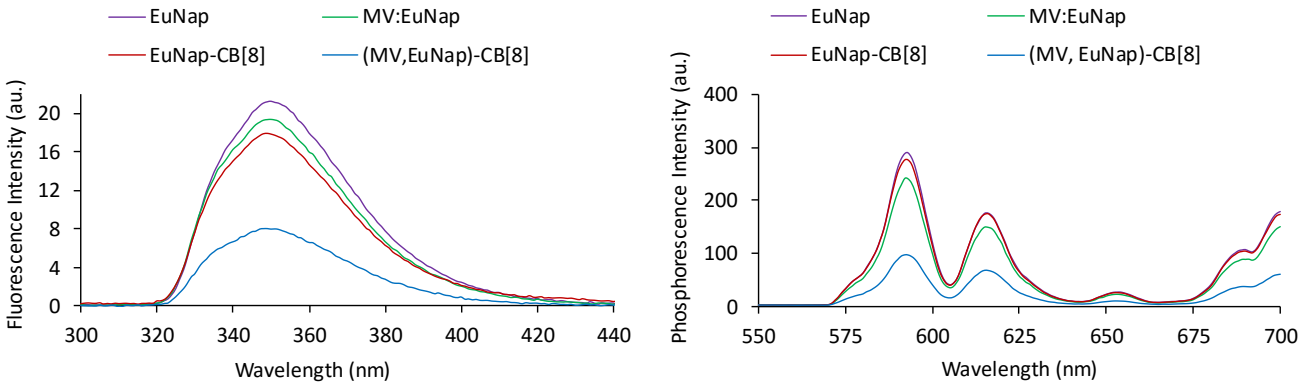


**Figure 8.** Quenching of the fluorescent (**Left**) and luminescent (**Right**) output of a solution of ($MV^{2+}$, EuNap)-CB[8]. Upon generation of the charge-transfer complex, a reduction in sensitised emission is observed. All complexes were generated in aqueous solution at 298 K, and at a concentration of 0.5 mM. Experimental Parameters (Fluorescent Output of EuNap): $\lambda_{ex}$ = 227 nm, excitation slit width = 5 nm, emission slit width = 5 nm, PMT Voltage (V) = 500, CAT 10, 298 K. Experimental Parameters (Phosphorescent Output of EuNap): $\lambda_{ex}$ = 227 nm, excitation slit width = 10 nm, emission slit width = 10 nm, PMT Voltage (V) = 1000, CAT 10, total decay time = 0.020 s, delay time = 0.20 ms, gate time = 0.50 ms, 298 K.

As is inferred by **Figure 8**, the spatial confinement of both $MV^{2+}$ and EuNap within the cavity of CB[8] brings about a decrease in both the fluorescent and phosphorescent emission intensities acquired upon excitation of the complex. This suggests that the charge-transfer interaction, induced upon bringing the two guest moieties into close proximity[12-20], within the cavity of the macrocyclic host species, quenches the excited state of the naphthalene antenna, resulting in a decreased radiative output from the excited state of $Eu^{3+}$, $^7D_0$. It has been hypothesised that the excited state of the naphthalene chromophore is subject to energy transfer within the confined nanocavity of the CB[8] host. Thus, an excited charge-transfer state, (2,6-Np, MV)*, is generated, and this decays *via* charge transfer fluorescence at a longer $\lambda_{max}$ to what was probed here. This energy loss from the excited state of the naphthalene antenna leads to a decrease in the quanta of energy available for sensitisation of $Eu^{3+}$, and thus brings about the concomitant diminution in luminescent radiation from the $^7D_0$ excited state of $Eu^{3+}$. Formation of the charge-transfer complex therefore acts as a luminescence switch, since both the charge-transfer band and $Eu^{3+}$ are competing for energy transfer from the antenna species. In addition, the control experiments (**Appendix, 8.8.2**), in which CB[8] and $MV^{2+}$ were not present, infer that the latter derivative does not collisionally quench lanthanide luminescence, and enhances the suggestion that confinement of the derivatives within the cavity is solely responsible for bringing about the observation(s) The indirect effect of charge-transfer on the

radiative output from the lanthanide centre was demonstrated further by means of luminescent lifetime measurements, **Table 1**.

| **System** | **Schematic** | **Lifetime(s), ms (± 10 %)** |
|---|---|---|
| EuNap | 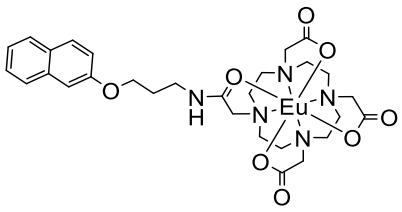 | 0.6 |
| $MV^{2+}$, EuNap | 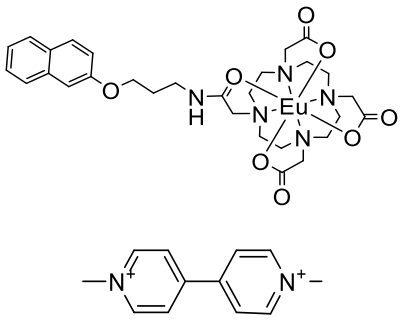 | 0.6 |
| ($MV^{2+}$, EuNap)-CB[8] | 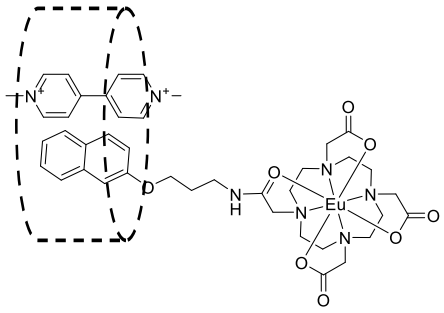 | 0.1 & 0.6 (biexponential) |

**Table 1.** The effect of charge-transfer on the decay of luminescent emission from the lanthanide centre of ($MV^{2+}$, EuNap)-CB[8]. All luminescent lifetime measurements (**Appendix, 8.8**) were performed in aqueous solution at 298 K, where the concentration of each species was 0.5 mM. Experimental Parameters: $\lambda_{ex}$ = 227 nm, $\lambda_{em}$ 616 nm, excitation slit width = 10 nm, emission slit width = 5 nm, PMT Voltage (V) = 1000, CAT 10, time per flash = 41 ms, flash count = 100.

In the case of the ternary complex, **Figure 1** (**C**), the decay of luminescent emission from the europium centre is biexponential (**Appendix, 8.8.3**). A biexponential decay curve is attained because some of the EuNap is confined within the cavity, whist a proportion remains in solution, due to the kinetic barrier to complexation; it is not incorporated within the quenching, apolar environment, and thus decays in a similar manner to the 'free' EuNap species (0.6 ms, **Appendix, 8.8.1**), **Table 1**.

Analysis (**Appendix, 8.9** and **8.10**) revealed that 84.6 % of the EuNap is confined within the cavity, whilst 15.4 % remains in solution. However, upon the addition of $Na_2S_2O_4$, the percentage of uncomplexed EuNap, present in solution, increased to 42.1 %, as was expected in accordance with the likely generation of $(MV^{+\bullet})_2$-CB[8] and the loss of the quenching charge-transfer interaction alluded to previously[20], **Figure 4** (**Right**).

A similar observation, **Figure 9** (**Right**), was made upon exchanging $Eu^{3+}$ for either ytterbium ($Yb^{3+}$, **Appendix, 8.12.1**) or neodymium ($Nd^{3+}$, **Appendix, 8.12.2**), **Experimental, 7.12**. As the excited states of both $Yb^{3+}$ and $Nd^{3+}$ are lower in energy than that of $Eu^{3+}$, **Figure 9** (**Left**),[38] it was hypothesized that upon exchange of $Eu^{3+}$ for either $Yb^{3+}$ or $Nd^{3+}$, the quenching of lanthanide luminescence would be negated. Thus, it was thought that it would be possible to facilitate the population of their excited state(s) in preference to energy transfer to the charge-transfer band, compared with ($MV^{2+}$, EuNap)-CB[8] (**Figure 8** and **Table 1**), where energy transfer to the charge-transfer band was seen to dominate. In addition, the role of oxygen and the effect of confining the sensitizer motif (naphthalene) within the apolar cavity of a macrocyclic host (CB[7]) was elucidated, **Figure 9** (**Right**); all data provided in **Appendix, 8.13**. The effect of confining the organic chromophore within the cavity of CB[7] was investigated because it was not known whether the increase in rigidity, and thus the increase in spatial separation between the organic chromophore and $Nd^{3+}$, brought about upon confinement of the NdNap derivative, was having an adverse effect on the efficiency of sensitisation, **Figure 10**.

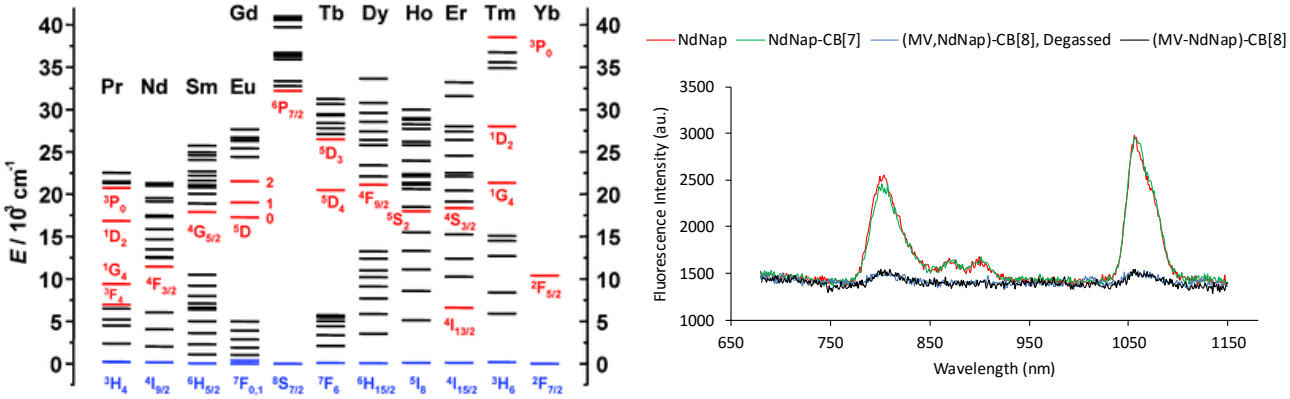


**Figure 9.** Partial energy diagrams for the lanthanide aquo ions (**Left**). The main luminescent levels are drawn in **red**, while the fundamental level is indicated in **blue**. Figure reproduced with permission from reference [38]. The quenching of lanthanide luminescence within ($MV^{2+}$, NdNap)-CB[8] (**Right**). Upon confinement of both guest species within the apolar cavity of CB[8], a reduction in sensitised emission is observed. Removing oxygen from the system and confining the sensitizer motif (2,6-Np) within the cavity of the macrocyclic host, has no effect on the magnitude of sensitised emission. Similar observations were made upon analysis of the Yb analogue (**Appendix, 8.12.1**). All complexes were generated in aqueous solution at 298 K, and at a concentration of 0.5 mM. Experimental Parameters: $\lambda_{ex}$ = 323 nm, excitation slit width = 5 nm, emission slit width = 5 nm, PMT Voltage (V) = 500, CAT 10, 298 K.

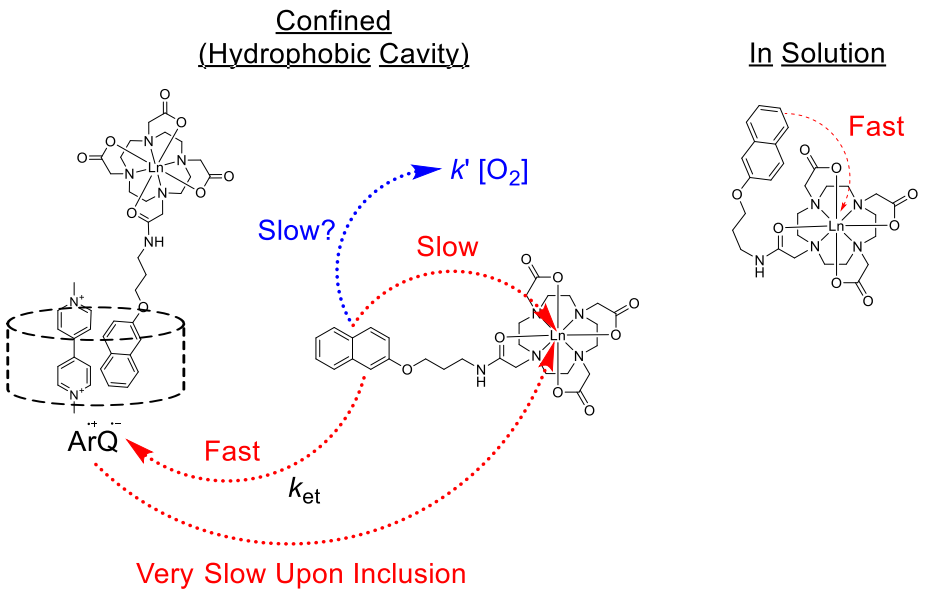


**Figure 10.** All possible pathways preventing generation of the lanthanide ($Eu^{3+}$, $Yb^{3+}$ or $Nd^{3+}$) emissive state(s). When the lanthanide complex is dissolved in solution, sensitisation is extremely efficient, and significant optical output acquired. However, upon formation of the ternary complex, ($MV^{2+}$, LnNap)-CB[8], optical output is suppressed due to the induction of charge-transfer, rigidification of the sensitizer-appended moiety, or *via* quenching of the emissive state of the chromophore by oxygen.

In summary, the presence of oxygen and the rigidification of the sensitizer derivative, brought about upon complexation, have no effect on the magnitude of the optical response acquired. This demonstrates that the induction of charge-transfer is solely responsible for bringing about the quenching of sensitised emission from the lanthanide centre ($Eu^{3+}$, $Yb^{3+}$ or $Nd^{3+}$) confined within the heteroternary complexes generated.

## 4.4 – Formation of the Desired Ternary Complex, (FcMV, EuNap)-CB[8]: a Sterically and Kinetically Impeded Process

Incorporation of the ferrocene-functionalised viologen derivative (FcMV, synthesized by Andrew Baxter of the Beer Group (University of Oxford), **Experimental, 7.13**), in a bid to generate the desired assembly, **Figure 1** (**A**), proved problematic. Ferrocene derivatives appear to have a greater affinity than viologen derivatives for binary inclusion within the nanocavity of CB[8], based on the results acquired from a competition experiment involving both ferrocenemethanol (FcMeOH) and $MV^{2+}$, **Figure 11**. Upon analysis of a 0.5 mM 1:1:1 FcMeOH:$MV^{2+}$:CB[8] solution, the presence of FcMeOH was not inferred by means of either cyclic voltammetry (**Figure 11** (**Inset**), $E_{1/2}$ –189 mV, *vs.* Ag / $AgNO_3$) or $^1$H NMR spectroscopy, respectively, **Figure 11**, whilst the $^1$H NMR resonances associated with $MV^{2+}$ (*a* and *b*) remained unshifted (**Figure 2** (**Trace C**)). This was to be expected given the charge neutrality and larger association constant of the former derivative. That is, whilst FcMeOH preferentially includes, its charge neutrality prevents inclusion bringing about a sufficient increase of the solubility of the complex, thus inhibiting it from remaining in solution with the competitive electrolytic salt. Hence, only $MV^{2+}$ remains in solution, and a voltammogram of

FcMeOH is not acquired as a result, **Figure 11** (**Inset**). However, the addition of one equivalent of 2,6-Np resulted in the reappearance of an unshifted FcMeOH peak ($E_{1/2}$ – 189 mV, *vs.* Ag / $AgNO_3$), and an upfield shift, indicative of ternary complex formation, of the $^1$H NMR resonances associated with $MV^{2+}$, **Figure 11** (**Trace A *vs.* Trace B**).

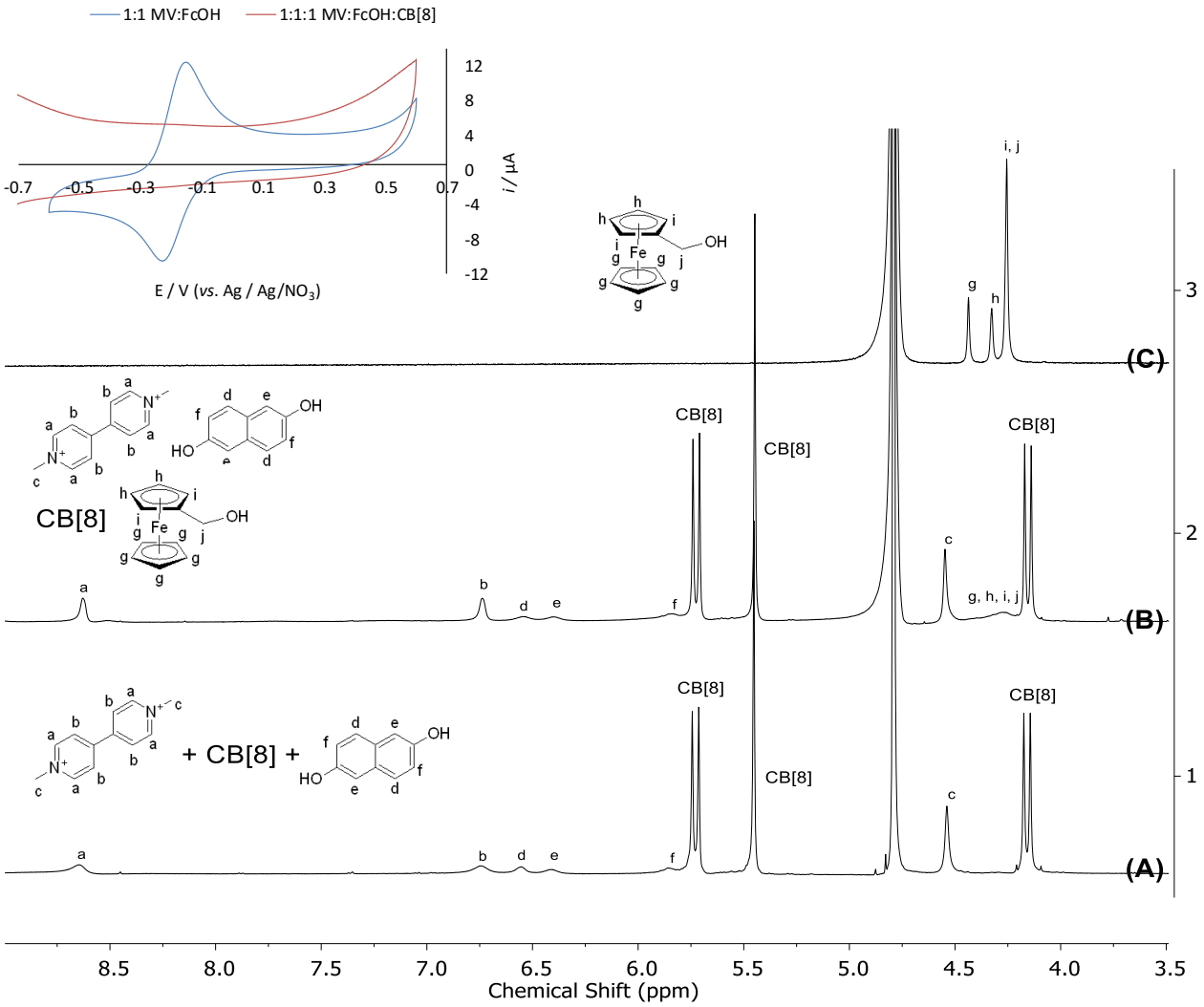


**Figure 11.** $^1$H NMR spectra ($D_2O$, 298 K, 400 MHz) of solutions of ($MV^{2+}$, 2,6-Np)-CB[8] (**Trace A**), 1:1:1:1 $MV^{2+}$:2,6-Np:FcMeOH:CB[8] (**Trace** B) and FcMeOH (**Trace C**) **Traces A – C, Bottom – Top**. Cyclic voltammograms (**Inset**) highlighting the loss of ferrocene from solution upon the addition of CB[8] to a 1:1 solution of $MV^{2+}$:FcMeOH; precipitation of FcMeOH as an included species in binary complexation is induced, but this is displaced, to give the charge-transfer complex, ($MV^{2+}$, EuNap)-CB[8], upon the subsequent addition of 2,6-Np. All spectra were recorded at a concentration of 0.5 mM. Electrochemical Setup: *Working Electrode*: Glassy Carbon. *Reference Electrode*: Ag / $AgNO_3$. *Auxiliary Electrode*: Pt wire. *Electrolytic Solution*: 0.1 M $NaClO_4$, aq. *Scan Rate:* 300 mV / s.

Nevertheless, formation of the desired ternary complex, (FcMV, EuNap)-CB[8], is preferred over formation of the ferrocene binary complex, or a theoretical ferrocene ternary complex. Favourable electrostatic interactions present in the model complex, and the steric challenge of coincluding a secondary guest species and the ferrocene appendage within the apolar cavity of the macrocyclic host are most likely to be responsible for this outcome, **Figure 12**. The desired complex ((FcMV,

EuNap)-CB[8]) was observed at an extremely low relative intensity (2 % by ESI-MS, *m / z* 1247.36 (**Appendix, 8.15**)), and only weak shoulder peaks were observed in the region expected for charge transfer within either (FcMV, 2,6-Np)-CB[8] (**Appendix, 8.14** (**Figure 57**)) or (FcMV, EuNap)-CB[8] (**Appendix, 8.14** (**Figure 57**)), *cf.* ($MV^{2+}$, 2,6-Np)-CB[8], **Figure 4**, and ($MV^{2+}$, EuNap)-CB[8], **Figure 6**. These observations suggest that the desired ternary complex is not afforded to an appreciable extent, or that the positioning of the species within the cavity is not conclusive to bring about face-face alignment of the two derivatives, a necessity to bring about good π-π stacking interactions, and thus the generation of a strong charge-transfer band[12-20].

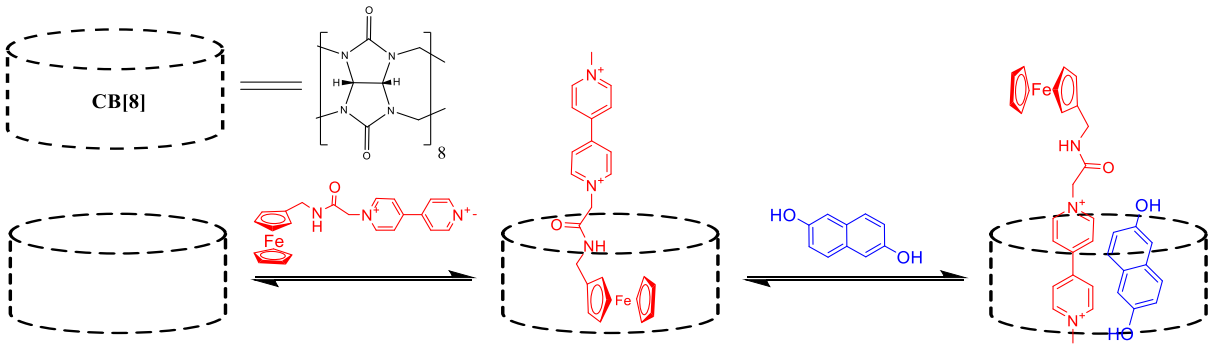


**Figure 12.** Possible complexation pathway to the desired ternary complex, (FcMV, 2,6-Np)-CB[8] (*n.b.* also valid for EuNap secondary guest inclusion).

In addition, *in-situ* oxidation of the ferrocene-functionalised viologen derivative (FcMV) was observed, **Figure 13**; a significant peak appears in many of the mass spectra at a *m / z* of 585.84 **Figure 13** (**Left**)), corresponding to a triply charged analogue of the binary complex. This implies that ferrocene is being oxidised to ferrocenium, as highlighted by the appearance of a peak at approximately 620 nm in many of the UV-vis spectra acquired, **Figure 13** (**Right**). This is not prevalent in the UV-Vis spectrum of the lone FcMV species, and suggests onset of decomposition on complexation, either due to the acid of crystallisation present in the commercially-acquired CB[8] or the heat imparted by the extended sonication process to the species. This partial oxidation appears to manifest optically as a colour change to a slight yellow-green, the full oxidation as seen in attempted purification yielding a turquoise product.

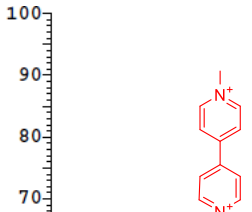

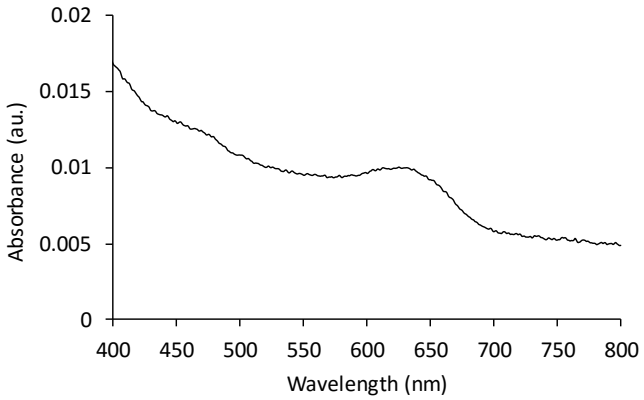


**Figure 13.** ESI-MS (**Left**) and UV-Vis spectra (**Right**) demonstrating oxidation of the FcMV derivative to $(FcMV\text{-}CB[8])^{3+}$. The characteristic UV-Vis signature of ferrocenium was acquired at ca. 630 nm, whilst a peak at a *m / z* of 585.84 was observed in the ESI-MS spectrum.

## 4.5 – Quenching Effect of Charge-Transfer by Reducing Conjugation

Since assembly of the desired ternary complex, **Figure 1** (**C**), proved detrimental to acquire a sensitized, optical output of significant magnitude, that is the luminescent lifetime of the europium centre decreased by 83 % upon inclusion, the non-aromatic analogue of $MV^{2+}$, **Figure 14**, was synthesized with a H-Cube hydrogenation reactor, **Experimental, 7.11**. Hydrogen is generated *in-situ via* the electrolysis of water[39]. The complete loss of aromaticity, confirmed by $^{1}H$ NMR spectroscopy, **Figure 15**, and the appearance of a peak at a *m / z* 198 in the ESI-MS, **Figure 15** (**Inset**), inferred that the reaction had proceeded to completion.

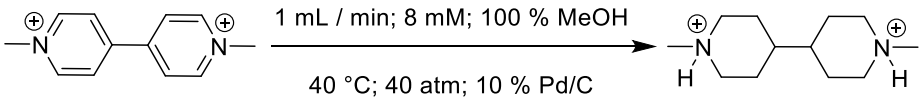


**Figure 14.** Generating *N,N'*-dimethyl-[4,4'-bipiperidine]-1,1'-diium (NAMV) by complete hydrogenation of $MV^{2+}$.

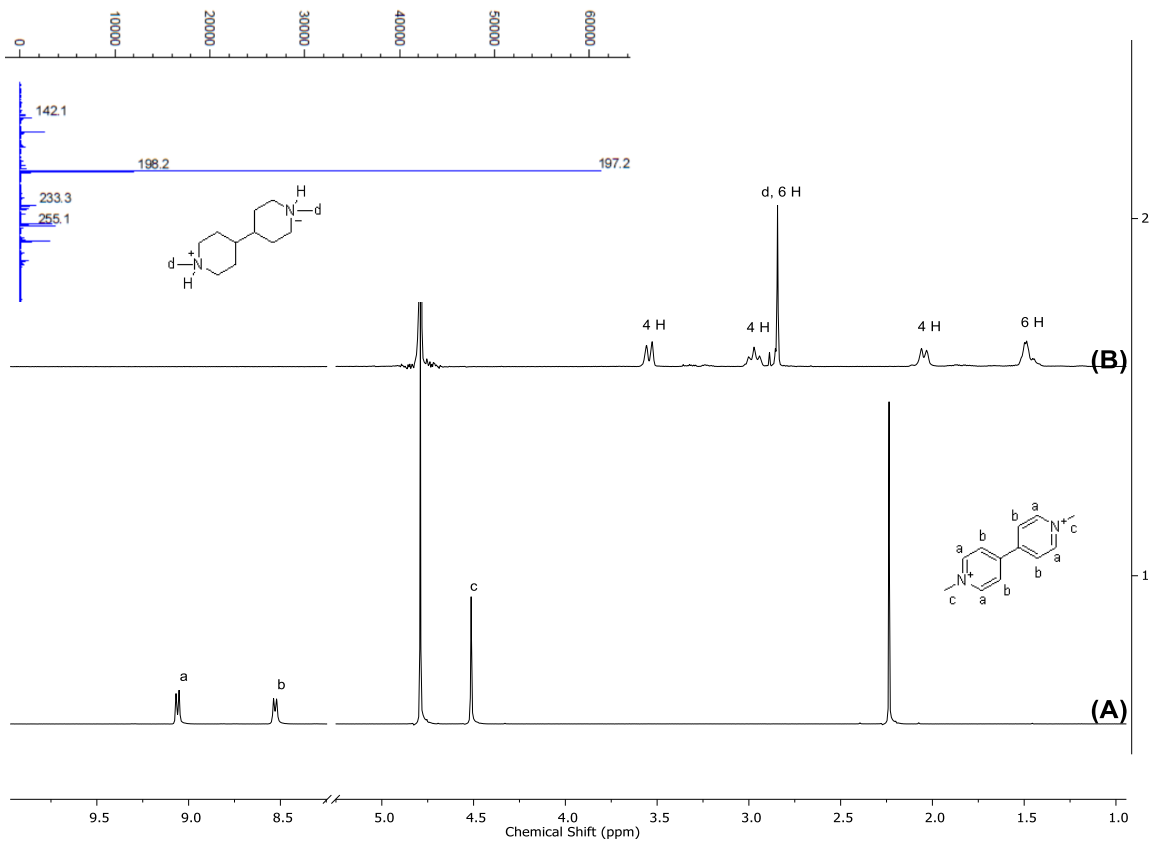


**Figure 15**. $^{1}$H NMR spectra ($D_2O$, 298 K, 400 MHz) of a solution of $MV^{2+}$ prior to (**Trace A**) and following complete hydrogenation (**Trace B**). Hydrogenation resulted in loss of aromaticity (8.45 – 9.5 ppm) and the appearance of additional aliphatic multiplets in the range, 1.00 – 4.00 ppm. A peak at a *m / z* 198 in the ESI-MS also arose (**Inset**). **Traces A – B, Bottom – Top.**

Following isolation, and subsequent characterisation, **Figure 15** (**Trace B**), of the non-aromatic analogue, NAMV, its binary, **Figure 16**, and ternary, **Figure 17**, inclusion properties were investigated as a non-quenching substitute, for $MV^{2+}$, in the generation of ternary complexes, both in solution and at the interface. Its incorporation into an interfacial molecular assembly was of most interest because Au substrates are inherently quenching in nature, hence trying to negate the additional quenching of lanthanide emission, brought about upon the induction of charge-transfer, is vital to facilitate the generation of an optically-responsive, molecular assembly.

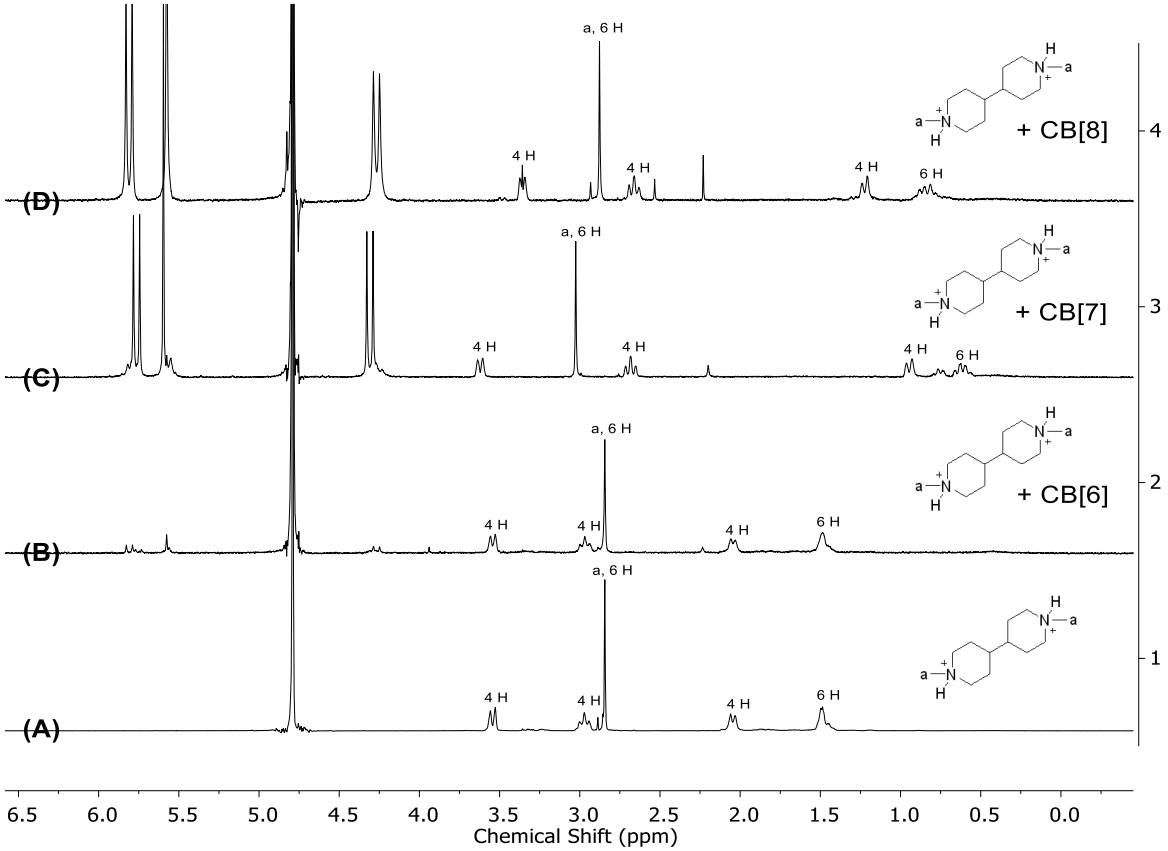


**Figure 16**. $^{1}$H NMR spectra ($D_2O$, 298 K, 400 MHz) of solutions of NAMV prior to (**Trace A**) and following the addition of a stoichiometric amount of CB[6] (**Trace B**), CB[7] (**Trace C**) or CB[8] (**Trace D**). All complexes were generated in aqueous solution at a concentration of 2 mM. **Traces A – D, Bottom – Top.**

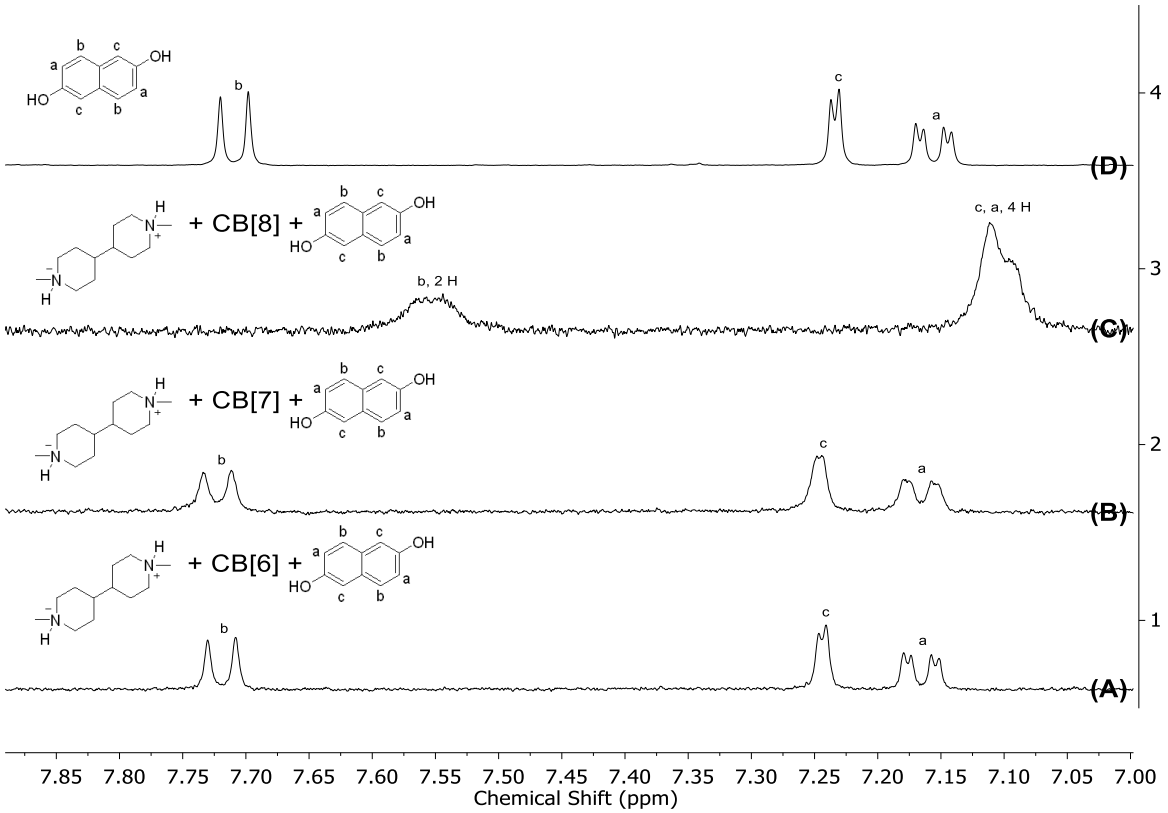


**Figure 17.** $^{1}$H NMR spectra ($D_2O$, 298 K, 400 MHz) of solutions of NAMV-CB[6] (**Trace A**), NAMV-CB[7] (**Trace B**) and NAMV-CB[8] (**Trace C**) following the addition of a stoichiometric amount of 2,6-Np. All complexes were generated in aqueous solution at a concentration of 2 mM. **Traces A – D, Bottom – Top.**

It can be seen, **Figure 16**, that the binary inclusion of NAMV occurs only in the case of CB[7] and CB[8], presumably because the cavity of CB[6] is too small to accommodate a guest species of its size; no change in the position of the aliphatic resonances of NAMV is brought about upon the addition n of a stoichiometric amount of CB[6], **Figure 16** (**Trace B**).

Moreover, the addition of a stoichiometric amount of 2,6-Np to solutions of the binary complexes (**Figure 16**) only brings about the characteristic spectral shift indicative of ternary complex formation when CB[8] is present, **Figure 17**. Only when CB[8] is present in solution, are the multiplets corresponding to the naphthalene moiety shifted upfield, (*a*, *b* and *c*, **Figure 17** (**Trace C**)), *cf*. CB[6] (**Figure 17** (**Trace A**)) and CB[7] (**Figure 17** (**Trace B**)). This was expected, given the larger dimensions of its apolar cavity, *cf.* both CB[6] and CB[7], and tentatively suggests that ternary complex formation was successful in the absence of charge-transfer, **Figure 18**, an interaction previously considered a necessity when trying to generate complexes of this type. As no UV-Vis signature was acquired upon the formation of the envisaged ternary complex, (NAMV, 2,6-Np)-CB[8], as was to be expected given the loss of conjugation and the resultant reduction in face-to-face, π-π stacking within the molecular cavity of CB[8], no further evidence to suggest co-confinement of the two guest species (NAMV and 2,6-Np) was obtained.

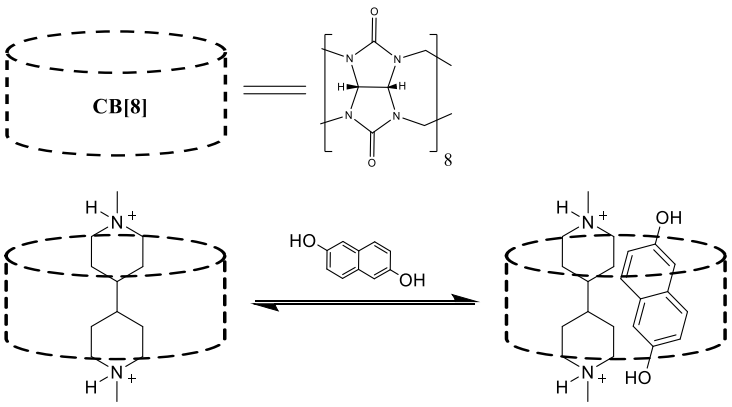


**Figure 18.** Assembly of (NAMV, 2,6-Np)-CB[8]. The complex was generated in aqueous solution at 298 K, and at a concentration of 2 mM.

To ensure that the resultant complex, **Figure 18**, did not quench the excited state of the naphthalene antenna, resulting in a decreased radiative output from the excited state of $Eu^{3+}$, $^7D_0$, as was observed upon the cooperative confinement of $MV^{2+}$ and EuNap within the cavity of CB[8], luminescent lifetime experiments, analogous to those previously discussed (**Table 1**), were undertaken in $D_2O$, **Table 2**. Both samples were prepared in $D_2O$, and to ensure that complete complexation was brought about, following the addition of EuNap to a solution of the binary complex, (NAMV)-CB[8], EuNap was added into solution at a slightly lower concentration (0.7 mM *cf.* 1 mM (both $MV^{2+}$ and CB[8])), to increase the likelihood that 100 % of the EuNap molecules added into solution would become, and remain, confined within a ternary environment throughout the optical analysis.

In the case of the model ternary complex, **Figure 1** (**C**), the decay of luminescent emission from the europium centre was again negligible (**Table 2**, 0.58 ms). This was expected given the fact that the two moieties had been brought into proximity, thereby influencing charge-transfer, **Table 2**. However, when the non-aromatic derivative, NAMV, was incorporated, this effect was absent (**Table 2**, 1.96 ms), that is the profile of decay of luminescent emission from the europium centre was comparable to that acquired when the derivative, EuNap, was 'free' in solution, and not 'held' within the apolar cavity of the macrocyclic host, CB[8], **Table 2**; when complexes of this type are dissolved in $D_2O$, the luminescent emission from the lanthanide ion ($Eu^{3+}$) is reported to decay within approximately 2.4 ms[40,41]. All data is provided in **Appendix, 8.11**.

| System | Schematic | Lifetime(s), ms (± 10 %) |
|---|---|---|
| (NAMV, EuNap)-CB[8] | 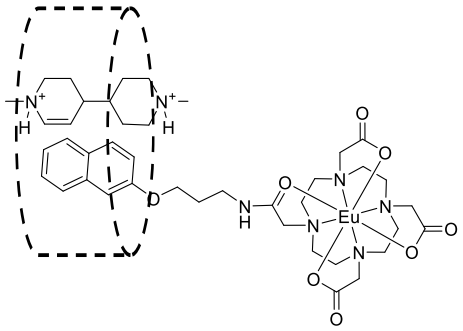 | 1.96 |
| ($MV^{2+}$, EuNap)-CB[8] | 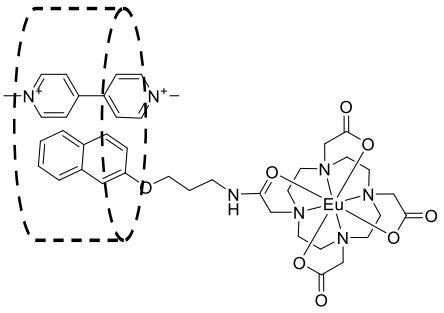 | 0.58 |

**Table 2.** The effect of nullifying charge-transfer on the decay of luminescent emission from a lanthanide centre confined within a ternary environment. Confinement of both NAMV and EuNap within the apolar cavity of CB[8] has no effect on the lifetime of luminescent emission from the lanthanide centre, *cf.* when both $MV^{2+}$ and 2,6-Np are confined and charge-transfer inducted. All complexes were generated in $D_2O$ at 298 K, and at a concentration of 2 mM. Experimental Parameters: $\lambda_{ex}$ = 397 nm, $\lambda_{em}$ 616 nm, excitation slit width = 14 nm, emission slit width = 5 nm, PMT Voltage (V) = 1000, CAT 10, time per flash = 41 ms, flash count = 10, 298 K.

In summary, N,N'-dimethyl-[4,4'-bipiperidine]-1,1'-diium (NAMV) was obtained *via* the hydrogenation of $MV^{2+}$. $^1H$ NMR and luminescence spectroscopy were employed in a bid to confirm that both derivatives (NAMV and EuNap) were included within the cavity of CB[8], prior to it being demonstrated that their interaction had no effect on the emissive state of the confined lanthanide ion ($Eu^{3+}$), as was witnessed upon the assembly and characterisation of the heteroternary complexes incorporating $MV^{2+}$, ($MV^{2+}$, LnNap)-CB[8], where Ln = $Eu^{3+}$, $Yb^{3+}$ or $Nd^{3+}$.

## 4.6 – Negating the Quenching Effect of Charge Transfer at the Interface

Since the confinement of both NAMV and 2,6-Np within the apolar cavity of CB[8] was seen to have no effect on the sensitised emission intensity of a $Eu^{3+}$-complex, 1-(10-mercaptodecyl)-1'-methyl-[4,4'-bipyridine]-diium bromide, **Figure 19** (D), and 1-methyl-1'-(10-(naphthalen-2-yloxy)decyl)-[4,4'-bipyridine]-1,1'-diium bromide iodide, **Figure 20** (F), were synthesised (**Experimental, 7.15** (D) and **7.16** (F)). It was envisaged that these derivatives (**Figure 19** (D) and **Figure 20** (F)) and their non-aromatic analogues (**Figure 21**), synthesised *via* hydrogenation, could exploited in the assembly of two surface-immobilised, molecular switches, **Figure 22**.

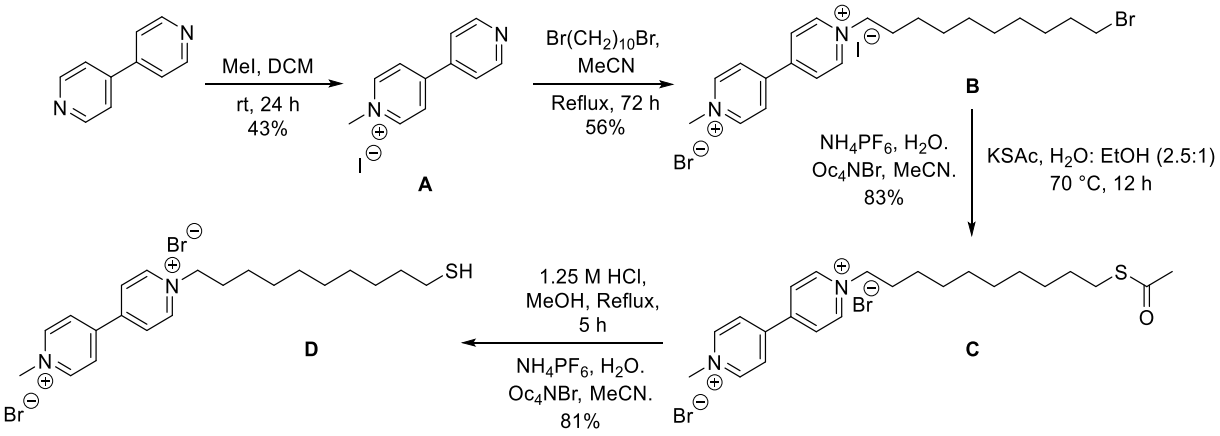


**Figure 19.** Synthesis of 1-(10-mercaptodecyl)-1'-methyl-[4,4'-bipyridine]-diium bromide, **D**. Scheme devised upon consideration of references [20], [42] and [43].

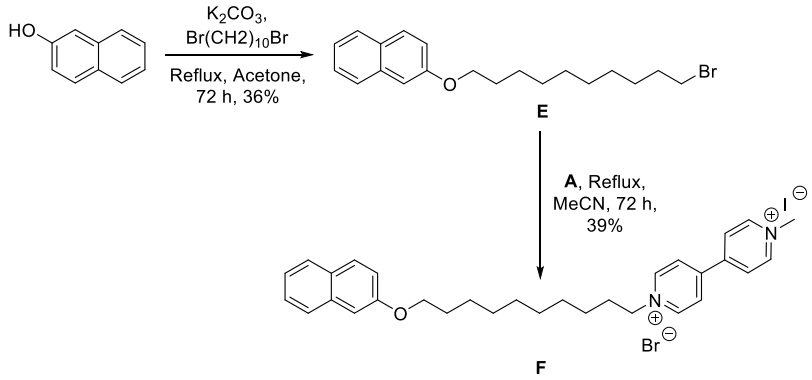


**Figure 20.** Synthesis of 1-methyl-1'-(10-(naphthalen-2-yloxy)decyl)-[4,4'-bipyridine]-1,1'-diium bromide iodide, **F**. Scheme devised upon consideration of references [44-46].

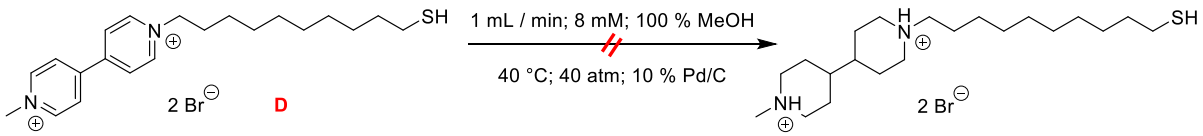


**Figure 21.** Attempted hydrogenation of 1-(10-Mercaptodecyl)-1'-methyl-[4,4'-bipyridine]-diium bromide, **D**.

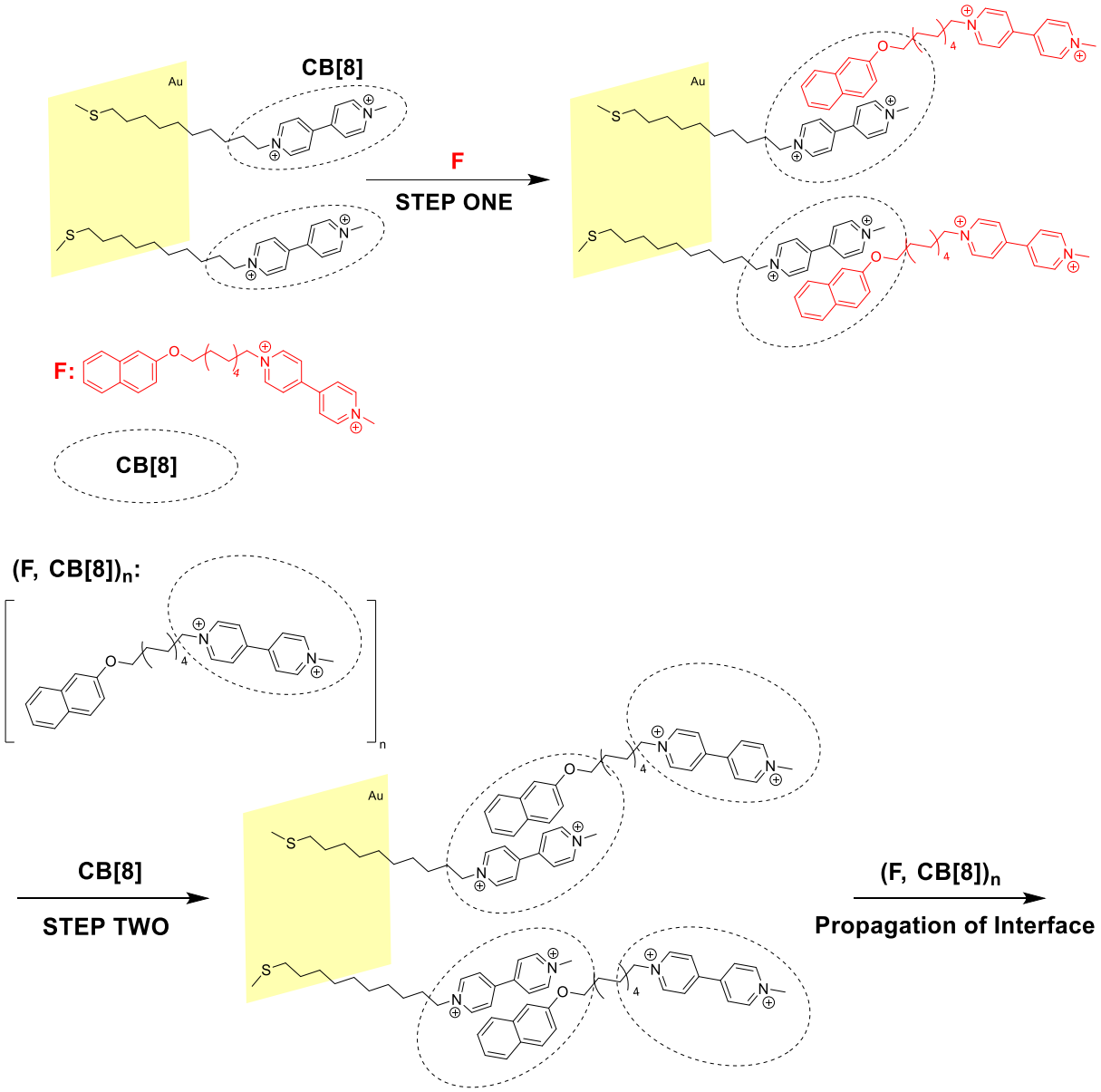
CB[8]
Au
F
STEP ONE
F:
CB[8]
(F, CB[8])n:
CB[8]
STEP TWO
(F, CB[8])n
Propagation of Interface

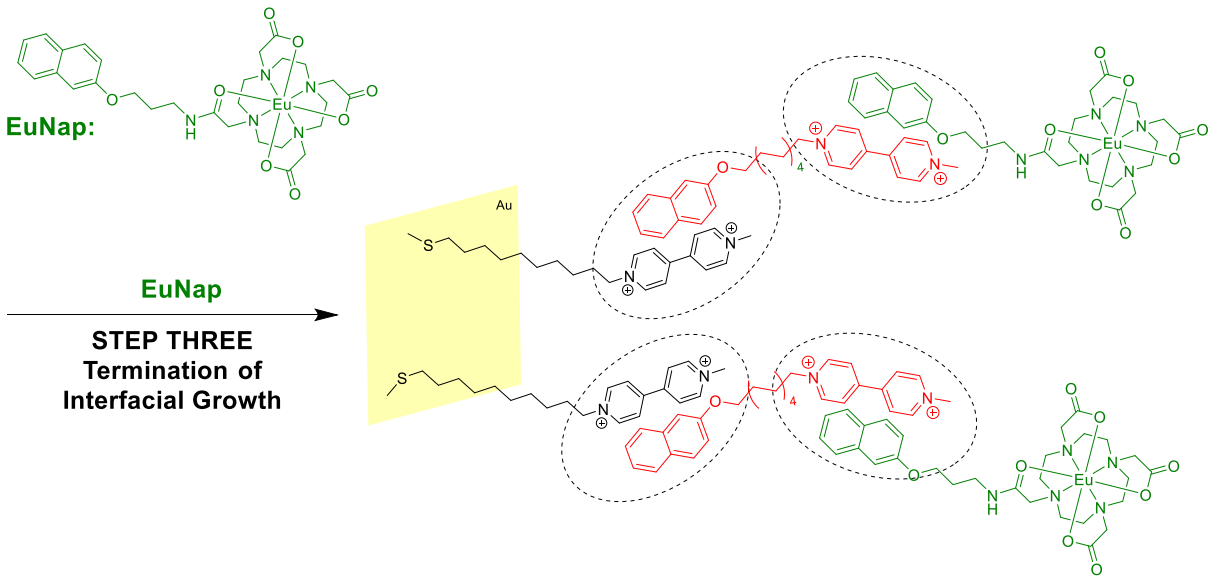


**Figure 22.** Surface assembly of an interfacial, molecular switch, in which a lanthanide ion is confined within a charge-transfer complex. Stepwise growth of the interface is feasible because the number of **F**-CB[8] complexes recruited to the underlying film can be varied prior to propagation being terminated *via* the recruitment of a functionalised naphthalene derivative, EuNap.

By exploiting, and subsequently comparing, the use of both the aromatic thiolate, **Figure 19 (D)**, and its hydrogenated analogue, **Figure 21**, in the construction of an interfacial molecular switch, **Figure 22**, it was assumed that it would be possible to compare, and modulate, the emission intensity from both assemblies at a variety of distances from the interface, in the presence and absence of the quenching, charge-transfer interaction, respectively, **Figure 23**. It was intended for the modulation of any optical output acquired from the lanthanide centre situated at the periphery of each polymeric network to be brought about upon the integration of either 6-(mercaptohexyl)ferrocene or 11-ferrocenyl-1-undecanethiol into the self-assembled monolayer; electrochemical modulation was envisaged because the low-lying excited states of $Fc^{+}$ are reported to quench sensitised lanthanide emission to a greater extent than those of Fc. It was thought that this would nullify the steric impediment which prevented incorporation of the FcMV adduct, to any significant extent (a relative intensity of only 2 % by ESI-MS), and thus generation of the desired ternary complex, (FcMV, EuNap)-CB[8]. The assembly and luminescent characterisation of these interfacial molecular switches, **Figure 23**, will be discussed in more detail within **Chapter 5**: **'The Surface Assembly of Molecular Switches'**.

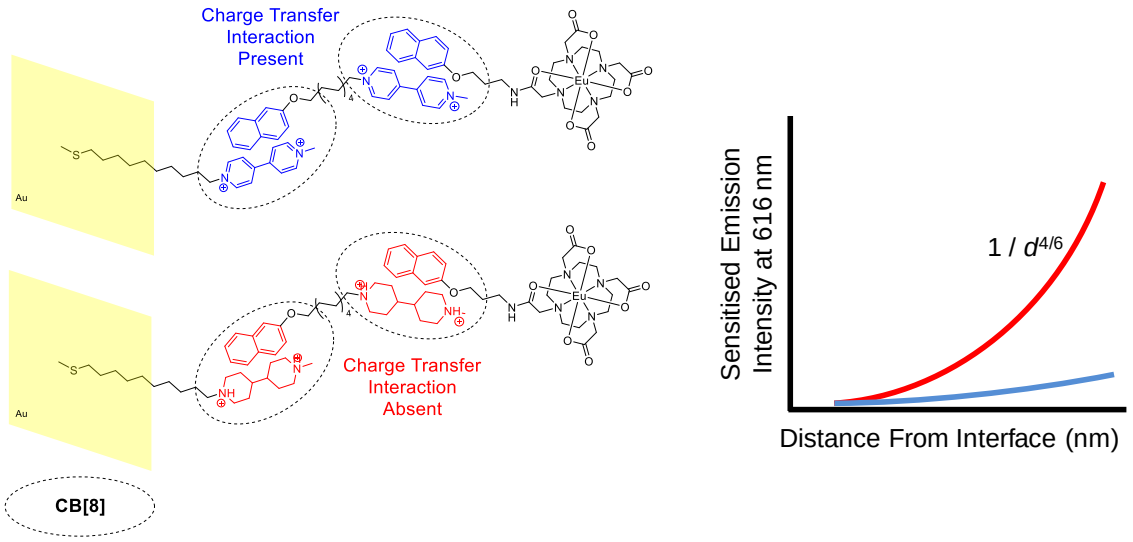


**Figure 23.** A schematic representation highlighting the expected difference in the intensity of sensitised emission acquired from a lanthanide-appended, molecular assembly in the **absence** and **presence** of charge-transfer (**Left**). As the lanthanide ion is recruited further from the metallic interface, in the absence charge-transfer, its emissive output is assumed to increase in line with a decline in energy transfer, both to the Au surface (SET), and the nearby acceptor chromophore (naphthalene motif), *via* nonradiative, dipole-dipole coupling (**Right**). However, in the presence of charge-transfer, an interaction which has been shown to quench lanthanide luminescence (**Table 1**), it is unlikely that increasing the distance between the metallic interface and the lanthanide ion will have the desired effect (**Right**). *d* denotes the distance between the donor (Ln emissive state) and acceptor (Au) moieties present.

Following the synthesis of 1-(10-Mercaptodecyl)-1'-methyl-[4,4'-bipyridine]-diium bromide, **Figure 19** (**D**), 1-methyl-1'-(10-(naphthalen-2-yloxy)decyl)-[4,4'-bipyridine]-1,1'-diium bromide iodide (**F**) was isolated by means of subsequent $S_N2$ reactions, **Figure 20**. It was anticipated that the recruitment of **F**, to a CB[8]-'capped', self-assembled monolayer of **D,** would initiate and allow for the growth of the interfacial, molecular switch, **Figure 22**. Following the synthesis of **D** and **F**, and prior to utilising them both in the surface-assembly of an optical switch, **Figure 22**, use of a H-Cube hydrogenation reactor to prepare the non-aromatic analogue of **D**, **Figure 21**, was investigated.

As is inferred by the $^1$H NMR spectrum given in **Figure 24**, the hydrogenation of **D** proved ineffective. Following the attempted hydrogenation of **D**, a large degree of aromaticity (7.9 – 9.2 ppm) remained, and the aliphatic region of the spectrum (1.2 – 3.8 ppm) resembled that of N,N'-dimethyl-[4,4'-bipiperidine]-1,1'-diium. It is thought that the thiol derivative partially decomposed under the reaction conditions employed; this was also evident at a range of applied pressures and temperatures.

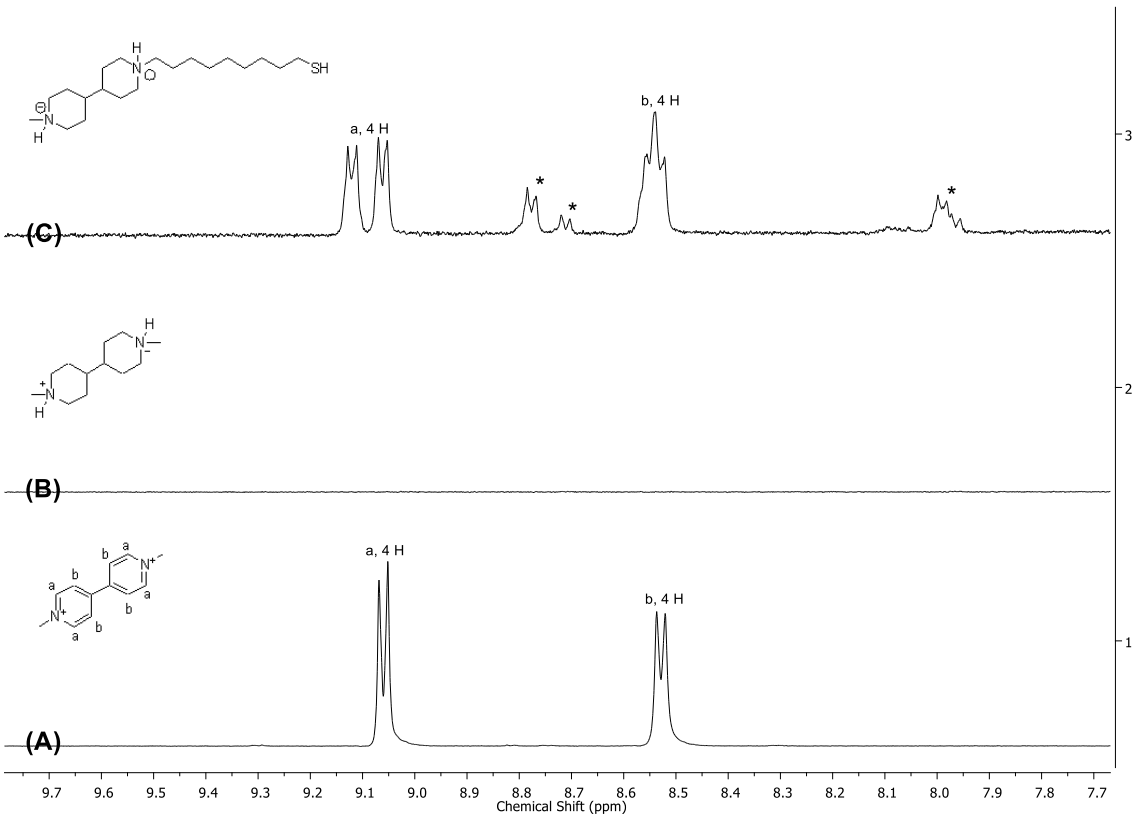


**Figure 24.** $^{1}$H NMR spectrum ($D_2O$, 298 K, 400 MHz) of a solution of 1-(10-Mercaptodecyl)-1'-methyl-[4,4'-bipyridine]-diium bromide (**D**) following attempted hydrogenation. $MV^{2+}$-centred multiplets (**Trace A**) are still present in the resultant spectrum (**Trace C**), unlike upon the formation of NAMV (**Trace B**). All complexes were generated at a concentration of 2 mM. *denotes the resonances that cannot be resolved. **Traces A – B, Bottom – Top.**

As the hydrogenation of **D** proved problematic, attempts were made to hydrogenate **A** (**Figure 19**), **Figure 25**. If successful, it was expected that the required non-aromatic thiol derivative could be acquired from the hydrogenated product precursor, by the three-step synthetic strategy detailed, **Figure 25.**

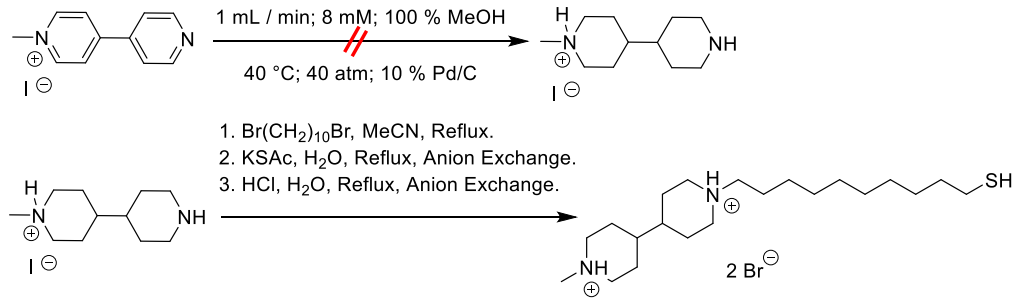


**Figure 25. Top.** Hydrogenation of 1-methyl-[4,4'-bipyridin]-1-ium iodide. **Bottom.** A possible synthetic approach for acquiring the non-aromatic analogue of **D**; the direct hydrogenation of **D** did not proceed to completion, and subsequent decomposition of **D** was observed by $^{1}$H NMR spectroscopy.

Unfortunately, the aromatic precursor, 1-methyl-[4,4'-bipyridin]-1-ium iodide, appeared to decompose upon attempted hydrogenation. Thus, the hydrogenation of **F** (**Figure 16**) was not investigated. It was hypothesised that upon exposure of **F** to excess hydrogen, the derivative was

likely to either decompose, or the naphthalene moiety become converted to either the corresponding tetralin or decalin functionality[47]. In addition, it is plausible to suggest that the $MV^{2+}$ appenditure would have been fully hydrogenated, as in the case of $MV^{2+}$, **Figures 14 and 15**.

## 4.7 – Utilising Ternary Complex Formation in the Stepwise Growth of an Emissive Interface

It was established that to synthesise all three non-aromatic derivatives, with good selectivity, 4,4'-bipiperidine would need to be systematically functionalised, although this was likely to prove very difficult due to the nucleophilicity of the nitrogen atoms. That is, nucleophilic substitution is likely to have occurred at each nitrogen centre, permitting the need to systematically utilise a range of protecting groups. It was intended for all three non-aromatic derivatives to be synthesised following the assembly and characterisation of the molecular switch, incorporating the aromatic precursor components, **Figure 22**. The non-aromatic assembly, **Figure 23**, whereby the charge-transfer interaction was absent, was to be constructed in the same way, just from the non-aromatic synthons acquired as the result of the selective functionalization of 4,4'-bipiperidine. **Note**: Stepwise growth of the interface is viable because it is possible to bypass step three, **Figure 22**, in favour of further additions of CB[8] and **F**, respectively. The ability to initiate and terminate the growth of the highlighted assemblies, **Figure 23**, at set distances from the interface, should, in theory, allow for a comparison to be made to the sensitised emission intensity acquired upon excitation of the respective optically-responsive assembly, in the absence or presence of the quenching charge-transfer interaction, **Figure 23**, whilst doing the upmost to lessen the characteristic quenching effect of the underlying metallic (Au) substrate[34-37].

It is foreseen that in the absence of the quenching, charge-transfer interaction, the sensitised emission intensity from the lanthanide centre will increase upon growth of the assembly, *i.e.* as the lanthanide centre is positioned further from the quenching metallic interface. This spatial dependency, depicted in **Figure 23**, is reported to arise due to the occurrence of two distinct mechanisms, Förster Resonance Energy Transfer (FRET)[48,49] and Surface Energy Transfer (SET)[50-52], of which have distance dependencies of $1 / d^6$ and $1 / d^4$, respectively. FRET and SET differ in the fact that the former originates from the weak electromagnetic coupling of two dipoles[48,49], whilst the latter does not require a resonant electronic transition[50-52], something fundamental to the shorter-range, Förster process. SET is documented to arise following the interaction of the electromagnetic field of the donor-dipole with the nearly free conduction electrons of the accepting metal surface[50-52]. Although SET is generally accepted to occur in proximity to a metallic interface, the quenching of lanthanide luminescence herein is likely to occur from a combination of both energy transfer mechanisms.

Nevertheless, in the presence of the charge-transfer interaction brought about upon the confinement of both **D** and **F** within the apolar cavity of CB[8], the sensitised emission intensity is expected to

remain negligible, even upon migration of the lanthanide centre away from the interface. Although the known quenching effect of the metallic substrate will be reduced, the quenching effect brought about upon the induction of charge-transfer will remain, and hence a significantly decreased radiative output from the excited state of $Eu^{3+}$ will be detected upon analysis of the former assembly, irrespective of the distance between the lanthanide ion and the metallic surface.

Prior to fabricating the aromatic assembly, **Figure 22**, it was necessary to investigate the inclusion properties of the two derivatives, **D** and **F**, as to ensure that propagation of the assembly was viable. If both derivatives could be confined within the cavity of the macrocyclic host, as was expected, the assembly (**Figure 22**) was to be generated as proof of concept, prior to fabrication of the non-aromatic analogue (**Figure 23**). It was then expected for an appreciable luminescent signature to be acquired upon recruitment of the EuNap derivative, at a distance where both the effects of FRET and SET are negligible, > 3.2 nm.

It was evident ($^1$H NMR) that **D** forms binary inclusion complexes with both CB[7] and CB[8], **Figure 26**. Although the aromatic protons (*a* and *b*) of the $MV^{2+}$ moiety were shifted upfield upon inclusion, the multiplets were not as well defined as those acquired upon the inclusion of $MV^{2+}$, **Figure 3**.

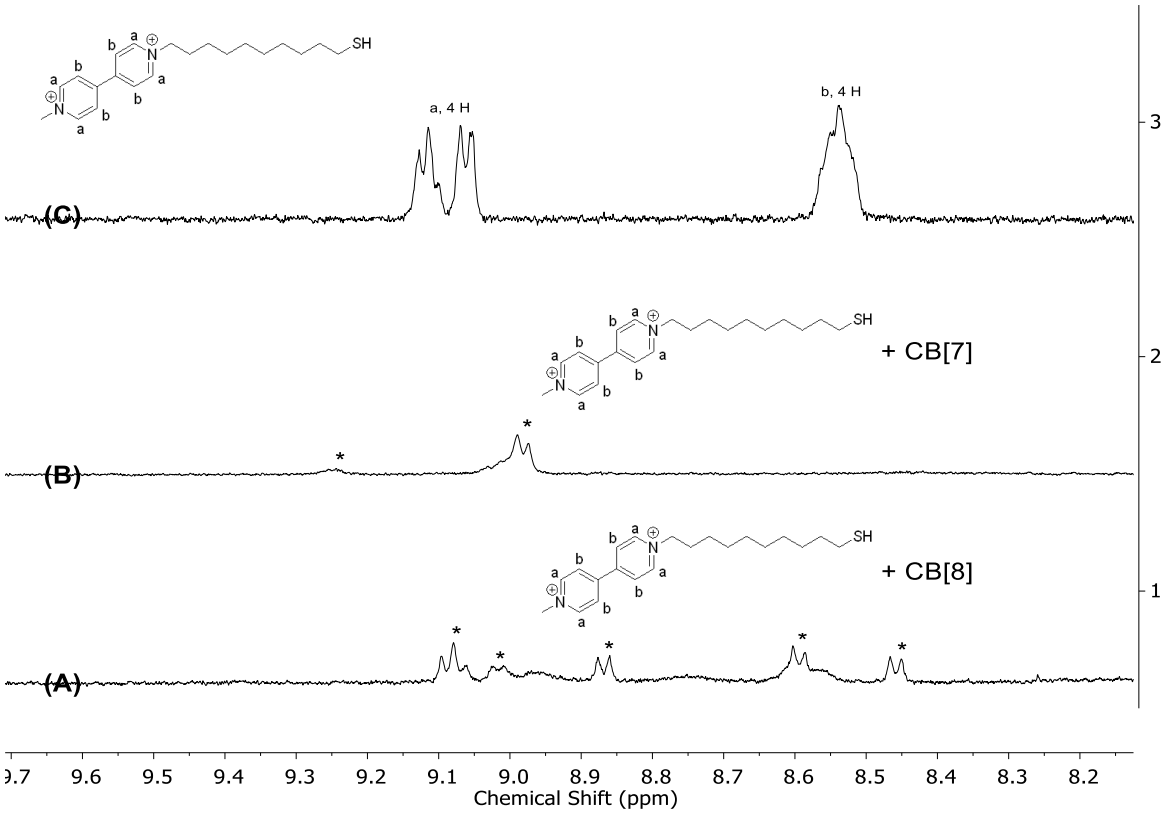


**Figure 26**. $^{1}$H NMR spectra ($D_2O$, 298 K, 400 MHz) of solutions of **D** prior to (**Trace C**) and following the addition of stoichiometric amounts of CB[7] (**Trace B**) or CB[8] (**Trace A**). All complexes were generated at a concentration of 2 mM. *denotes the resonances that cannot be resolved. **Traces A – C, Bottom – Top.**

It is understood that the resonances broaden and coalesce due to the presence of the alkylated, thiolated linker, which is likely to increase the conformational flexibility of the derivative. Thus, the guest species, **D**, is less likely to be 'held' tightly within the cavity of the macrocyclic host, and it is plausible that two, or even more, conformers are in equilibrium, **Figure 27,** leading to a broadening of the multiplets in question, and the appearance of additional resonances. This is less likely to occur when **D**-CB[8] is confined at the interface, where conformational freedom is restricted, *cf.* in solution.

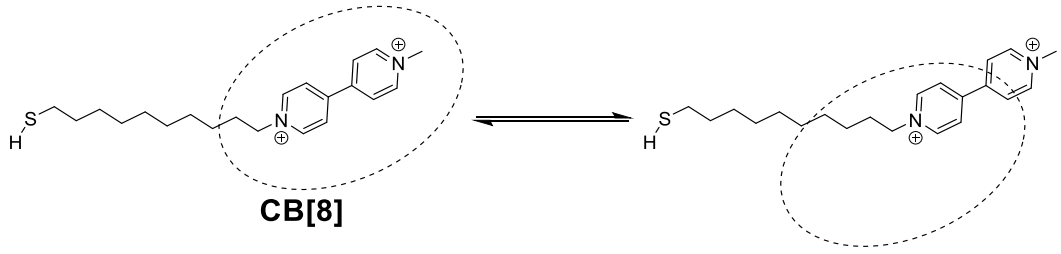


**Figure 27.** A schematic representation highlighting the likely mode of encapsulation of **D** by CB[8].

## 4.8 – Ensuring that the Stepwise Growth of an Emissive Interface is Viable

Following characterisation of the binary complex, **D**-CB[8], the ternary complex, (**D**, 2,6-Np)-CB[8], was obtained ($\lambda_{max}$ 557 nm, **Appendix, 8.14** (**Figure 57**)) following the addition of one equivalent of 2,6-Np into solution. This was evident because upon the addition of the secondary guest species, both signal sets, that are those corresponding to both the $MV^{2+}$ (*a*, *b*; 8.40 – 9.20 ppm) and naphthalene (*c*, *d* and *e*; 7.00 – 7.90 ppm) moieties, were shifted upfield, **Figure 28**. Moreover, the signal sets were much better resolved than those observed upon binary inclusion (**Figure 26**), suggesting that the inclusion of a secondary guest species rigidifies the complex, pushing the proposed equilibrium, **Figure 27**, towards the left.

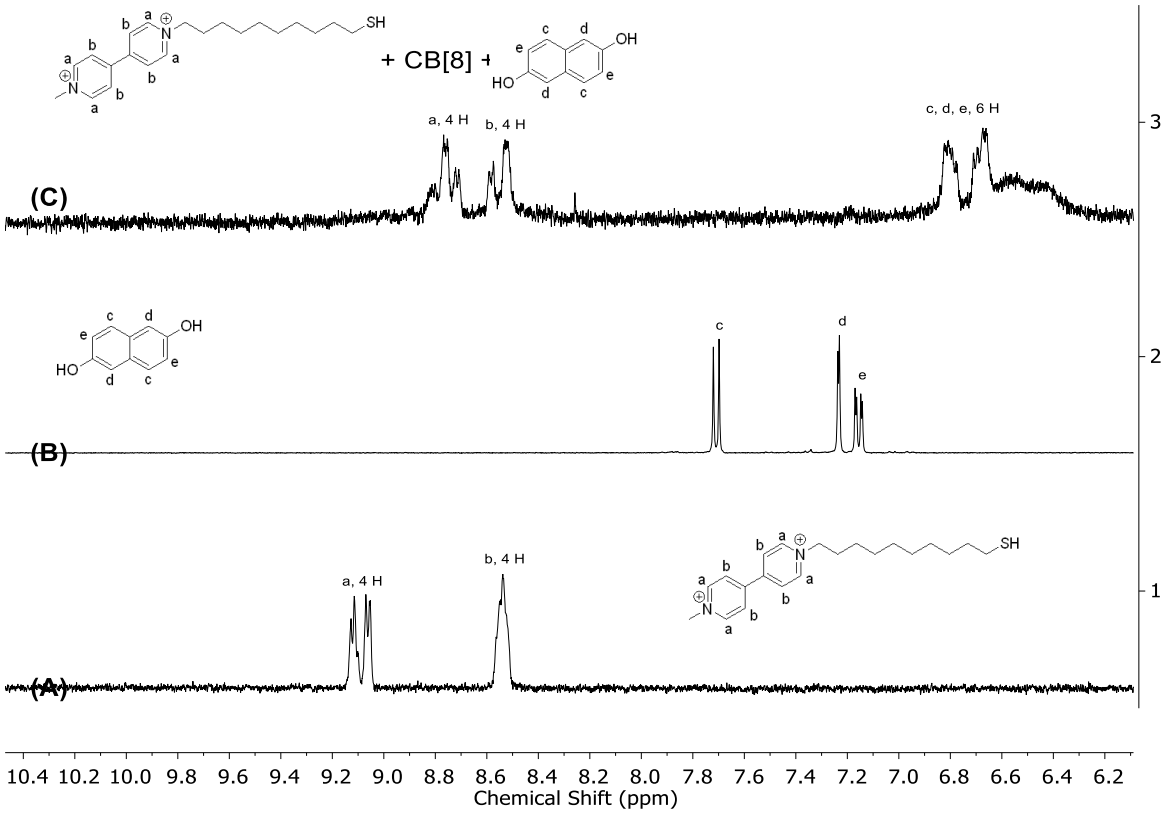


**Figure 28.** $^1$H NMR spectrum ($D_2O$, 298 K, 400 MHz) of a solution of **D**-CB[8] following the addition of a stoichiometric amount of 2,6-Np (**Trace C**). $^1$H NMR spectra ($D_2O$, 298 K, 400 MHz) of solutions of **D** and 2,6-Np are also given. All complexes were generated at a concentration of 2 mM. **Traces A – C, Bottom – Top.**

Furthermore, upon the addition of one equivalent of **F**, as opposed to 2,6-Np, to a solution of the binary complex (**D**-CB[8]), a ternary complex ($\lambda_{max}$ 515 nm, **Appendix, 8.14** (**Figure 57**)) was also generated, **Figure 29**. It must however be noted that at this stage there was a slight suspicion that the addition of **F** brought about the displacement of **D** from the apolar cavity of the macrocyclic host, CB[8], thus generating the 1:1 *intra*molecular heteroternary complex ($\lambda_{max}$ 541 nm, **Appendix, 8.14** (**Figure 57**)) at the expense of the 1:1 *inter*molecular heteroternary complex, **Figure 30**.[44-46]

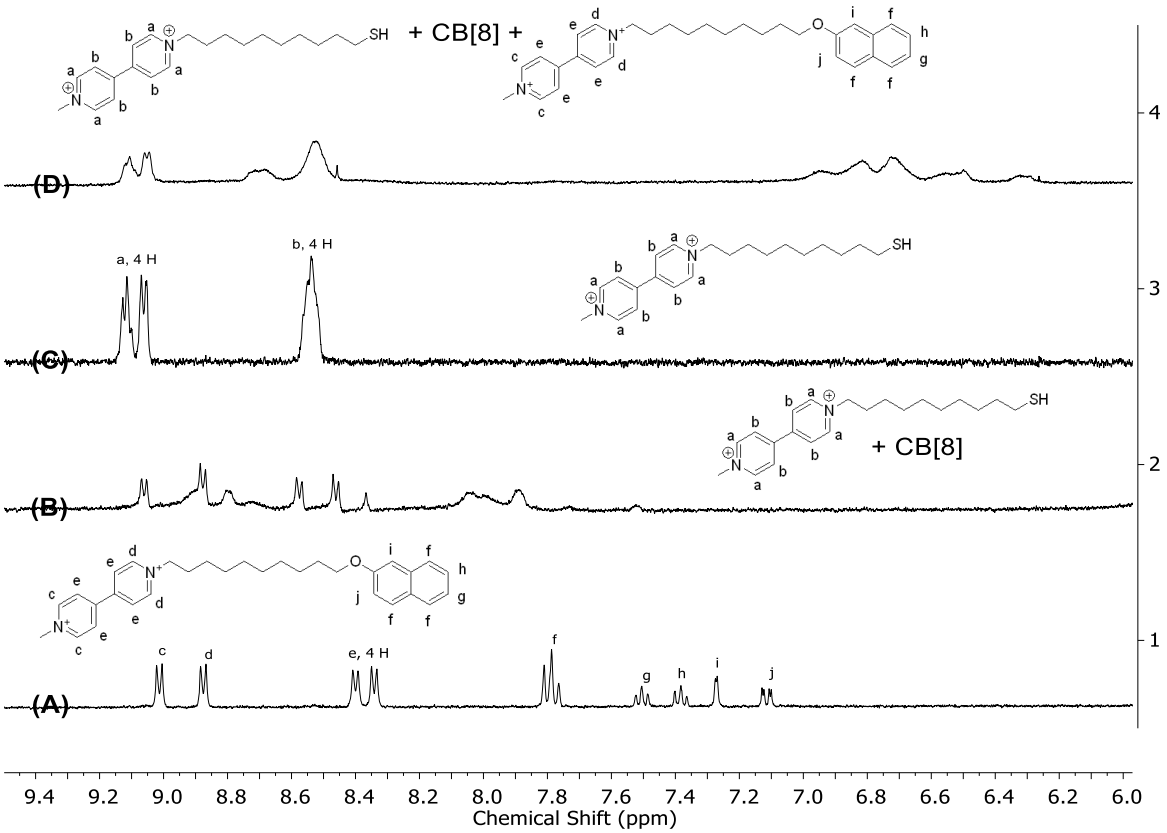


**Figure 29.** $^{1}$H NMR spectra ($D_2O$, 298 K, 400 MHz) of solutions of **F** (**Trace A**), **D**-CB[8] (**Trace B**), **D** (**Trace C**) and (**D**, **F**)-CB[8] (**Trace D**). All complexes were generated at a concentration of 2 mM. **Note.** Not all the resonances associated with the host-guest complexes (**Traces B and D**) could be resolved. **Traces A – D, Bottom – Top.**

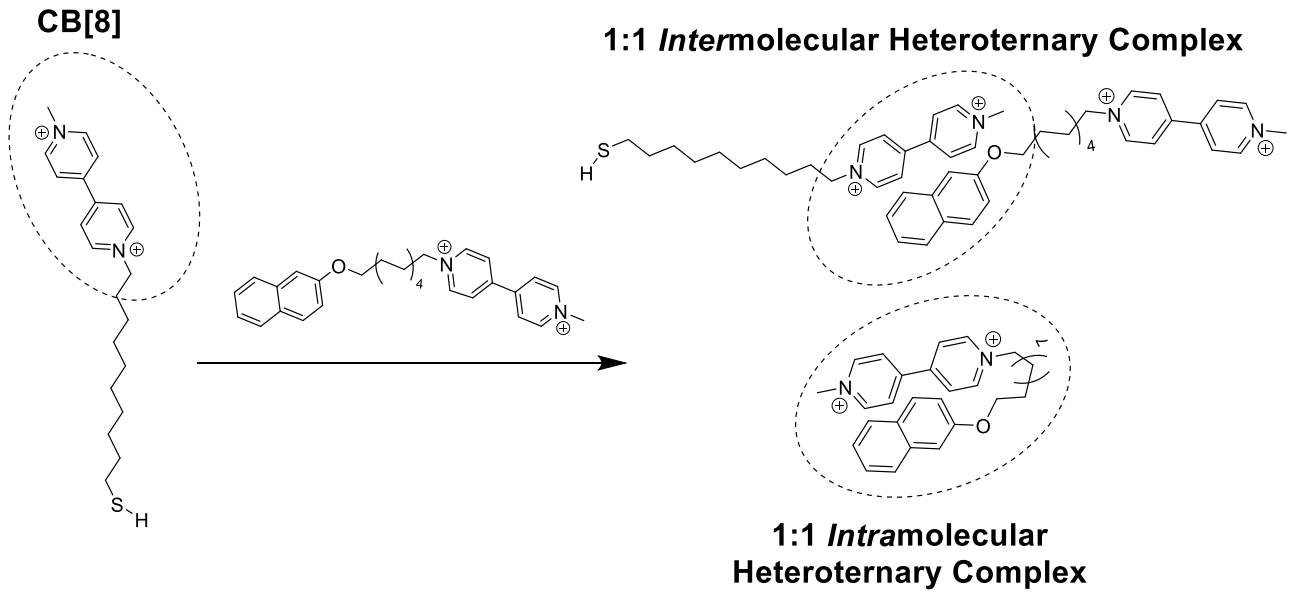


**Figure 30.** A schemtaic representation highlighting possible generation of both the 1:1 *inter*molecular heteroternary complex and the 1:1 *intra*molecular heteroternary complex upon the addition of **F** into a solution of the binary complex, **D**-CB[8].[44-46]

Although the formation of the 1:1 *intra*molecular heteroternary complex was considered a possibility, **Figure 30**, it was not deemed to pose an adverse effect on the growth of the desired

polymeric interface, **Figure 22**. It was assumed that the enhanced rigidity of an underlying **D**-CB[8]-functionalised interface, **Figure 22**, and the fewer degress of freedom present at the interface, would serve to push the equilibrium towards favouring the formation of the 1:1 *inter*molecular heteroternary complex, as was desired. Thus, the assembly of the interfacial, molecular switch, designed to incorporate both a lanthanide centre and a charge-transfer complex, **Figure 22**, was established. It was envisaged that this assembly could be utilised to assess the likelihood of being able to acquire the non-aromatic assembly, from which it was thought that a significant optical output could be detected, and subsequently modulated upon manipulation of the oxidation state of a surface-confined metallocene[5,6].

## List of References


1. Galit Parvari, Ofer Reany, Ehud Keinan, *Isr. J. Chem.*, **2011**, 51, 646–663.
2. Jean-Marie Lehn, *Angew. Chem. Int. Ed.*, **1988**, 27, 89–112.
3. Jae Wook Lee, S. Samal, N. Selvapalam, Hee-Joon Kim, Kimoon Kim, *Acc. Chem. Res.*, **2003**, 36, 621–630.
4. Pedro Montes-Navajas, Hermenegildo García, *J. Phys. Chem. C*, **2010**, 114, 18847–18852.
5. Manuel Tropiano, Nathan L. Kilah, Michael Morten, Habibur Rahman, Jason J. Davis, Paul D. Beer, Stephen Faulkner, *J. Am. Chem. Soc.*, **2011**, 133, 11847–11849.
6. Joshua Lehr, Manuel Tropiano, Paul D. Beer, Stephen Faulkner, Jason J. Davis, *Chem. Commun.*, **2015**, 51, 6515–6517.
7. Steven J. Barrow, Setu Kasera, Matthew J. Rowland, Jesús del Barrio, Oren A. Scherman, *Chem. Rev.*, **2015**, 115, 12320–12406.
8. Woo Sung Jeon, Kwangyul Moon, Sang Hyun Park, Hyungpil Chun, Young Ho Ko, Jin Yong Lee, Eun Sung Lee, S. Samal, N. Selvapalam, Mikhail V. Rekharsky, Vladimir Sindelar, David Sobransingh, Yoshihisa Inoue, Angel E. Kaifer, Kimoon Kim, *J. Am. Chem. Soc.*, **2005**, 127, 12984–12989.
9. Lu Cui, Suresh Gadde, Wei Li, Angel E. Kaifer, *Langmuir*, **2009**, 25, 13763–13769.
10. Wei Wang, Angel E. Kaifer, *Supramol. Chem.*, **2010**, 22, 710–716.
11. Y. M. Jeon, D, Whang, J. Kim, K. Kim, *Chem. Lett.*, **1996**, 27, 503–504.
12. Jae Wook Lee, S. Samal, N. Selvapalam, Hee-Joon Kim, Kimoon Kim, *Acc. Chem. Res.*, **2003**, 36, 621–630.
13. K. Kim, N. Selvapalam, D. H. Oh, *J. Incl. Phenom. Macrocycl. Chem.*, **2004**, 50, 31–36.
14. Frank Biedermann, Oren A. Scherman, *J. Phys. Chem. B.*, **2012**, 116, 2842–2849.
15. Woo Sung Jeon, Hee-Joon Kim, Chongmok Lee, Kimoon Kim, *Chem. Commun.*, **2002**, 38, 1828–1829.

16. Hee-Joon Kim Dr., Jungseok Heo, Woo Sung Jeon, Eunsung Lee, Jaheon Kim Dr., Shigeru Sakamoto, Kentaro Yamaguchi Prof. Dr., Kimoon Kim Prof. Dr., *Angew. Chem. Int. Ed*., **2001**, 40, 1526–1529.
17. Young Ho Ko, Kyungpil Kim, Jin-Koo Kang, Hyungphil Chun, Jae Wook Lee, Shigeru Sakamoto, Kentaro Yamaguchi, James C. Fettinger, Kimoon Kim, *J. Am. Chem. Soc*., **2004**, 126, 1932–1933.
18. Y. H. Ko, K. Kim, E. Kim, K. Kim, *Supramol. Chem.*, **2007**, 19, 287–293.
19. Tadashi Mori, Young Ho Ko, Kimoon Kim, Yoshihisa Inoue, *J. Org. Chem*., **2006**, 71, 3232–3247.
20. Feng Tian, Dezhi Jiao, Frank Biedermann, Oren A. Scherman, *Nat. Commun*., **2012**, 3, 1–8.
21. Woo Sung Jeon, Kwangyul Moon, Sang Hyun Park, Hyungpil Chun, Young Ho Ko, Jin Yong Lee, Eun Sung Lee, S. Samal, N. Selvapalam, Mikhail V. Rekharsky, Vladimir Sindelar, David Sobransingh, Yoshihisa Inoue, Angel E. Kaifer, Kimoon Kim, *J. Am. Chem. Soc*., **2005**, 127, 12984–12989.
22. Drochss P. Valencia, Felipe J. González, *Electrochemistry Communications*, **2011**, 13, 129-132.
23. Drochss P. Valencia, Felipe J. González, *Journal of Electroanalytical Chemistry*, **2012**, 681, 121-126.
24. Alaa A. A. Aljabali, J. Elaine Barclay, Julea N. Butt, George P. Lomonossoff, David J. Evans, *Dalton Trans*., **2010**, 39, 7569-7574.
25. Nicole F. Steinmetz, George P. Lomonossoff Dr., David. J. Evans Dr., *Small*, **2006**, 2, 530-533.
26. Nicole F. Steinmetz, George P. Lomonossoff, David J. Evans, *Langmuir*, **2006**, 22, 3488-3490.
27. *Electrochemistry at Solid Electrodes*, ed. R. N. Adams, Marcel Dekker, New York, **1969**.
28. Winston Ong , Marielle Gómez-Kaifer, Angel E. Kaifer, *Org*. Lett., **2002**, 4, 1791–1794.
29. Winston Ong, Angel E. Kaifer, *Organometallics*., **2003**, 22, 4181–4183.
30. R. Chadha, N. Kashid, A. Saini, *JSIR*, **2004**, 63, 211–229.
31. Eric Masson, Xiaoxi Ling, Roymon Joseph, Lawrence Kyeremeh-Mensah, Xiaoyong Lu, *RSC Adv*., **2012**, 2, 1213–1247.
32. Simin Liu, Christian Ruspic, Pritam Mukhopadhyay, Sriparna Chakrabarti, Peter Y. Zavalij, Lyle Isaacs, *J. Am. Chem. Soc*., **2005**, 127, 15959 –15967.
33. Dinesh Shetty, Jayshree K. Khedkar, Kyeng Min Park, Kimoon Kim, *Chem. Soc. Rev*., **2015**, 44, 8747–8761.

34. C. S. Yun, A. Javier, T. Jennings, M. Fisher, S. Hira, S. Peterson, B. Hopkins, N. O. Reich, G. F. Strouse, *J. Am. Chem. Soc*., **2005**, 127, 3115–3119.

35. Guillermo P. Acuna, Martina Bucher, Ingo H. Stein, Christian Steinhauer, Anton Kuzyk, Phil Holzmeister, Robert Schreiber, Alexander Moroz, Fernando D. Stefani, Tim Lied, Friedrich C. Simmel, Philip Tinnefeld, *ACS Nano*., **2012**, 6, 3189–3195.

36. Chhabra R, Sharma J, Wang H, Zou S, Lin S, Yan H, Lindsay S, Liu Y., *Nanotechnology*, **2009**, 20, 485201.

37. B. N. J. Persson, N. D. Lang, *Phys. Rev. B: Condens. Matter Mater. Phys*., **1982**, 26, 5409.

38. Jean-Claude G. Bünzli, Claude Piguet, *Chem. Soc. Rev*., **2005**, 34, 1048–1077.

39. Richard V. Jones, Lajos Godorhazy, Norbert Varga, Daniel Szalay, Laszlo Urge, Ferenc Darvas, *J. Comb. Chem.*, **2006**, 8, 110–116.

40. Octavia A. Blackburn, Jack D. Routledge, Laura B. Jennings, Nicholas H. Rees, Alan M. Kenwright, Paul D. Beer, Stephen Faulkner, *Dalton Trans*., **2016**, 45, 3070.

41. Robert C. Leif, Lidia M. Vallarino, Margie C. Becker, Sean Yang, *Cytometry A*, **2006**, 69A, 767–778.

42. Feng Tian, Nan Cheng, Nicolas Nouvel, Jin Geng, Oren A. Scherman, *Langmuir*, **2010**, 26, 5323–5328.

43. Feng Tian, Monika Cziferszky, Dezhi Jiao, Karolina Wahlström, Jin Geng, Oren A. Scherman, *Langmuir*, **2011**, 27, 1387–1390.

44. Young Ho Ko, Kyungpil Kim, Jin-Koo Kang, Hyungphil Chun, Jae Wook Lee, Shigeru Sakamoto, Kentaro Yamaguchi, James C. Fettinger, Kimoon Kim, *J. Am. Chem. Soc*., **2004**, 126, 1932–1933.

45. Tadashi Mori, Young Ho Ko, Kimoon Kim, Yoshihisa Inoue, *J. Org. Chem*., **2006**, 71, 3232–3247.

46. Y. H. Ko, K. Kim, E. Kim, K. Kim, *Supramol. Chem*, **2007**, 19, 287–293.

47. Thomas P. Wilson, Edward G. Caflisch, G. F. Hurley, *J. Phys. Chem*., **1958**, 62, 1059–1061.

48. T. H. Förster, *Radiation Research Supplement*, **1960**, 2, 326–339.

49. Aaron R. Clapp Dr., Igor L. Medintz Dr., Hedi Mattoussi Dr., *ChemPhysChem*., **2006**, 7, 47–57.

50. A. Campion, A.R. Gallo, C.B. Harris, H.J. Robota, P.M. Whitmore, *Chem. Phys. Lett*., **1980**, 73, 447–450.

51. C. S. Yun, A. Javier, T. Jennings, M. Fisher, S. Hira, S. Peterson, B. Hopkins, N. O. Reich, G. F. Strouse, *J. Am. Chem. Soc*., **2005**, 127, 3115–3119.

52. Guillermo P. Acuna, Martina Bucher, Ingo H. Stein, Christian Steinhauer, Anton Kuzyk, Phil Holzmeister, Robert Schreiber, Alexander Moroz, Fernando D. Stefani, Tim Lied, Friedrich C. Simmel, Philip Tinnefeld, *ACS Nano*., **2012**, 6, 3189–3195.

## List of Figures

**Figure 1.** The envisaged ternary complexes; (FcMV, EuNap)-CB[8] (**A**), ($MV^{2+}$, 2,6-Np)-CB[8] (**B**) and ($MV^{2+}$, EuNap)-CB[8] (**C**).

**Figure 2.** Monitoring the inclusion of ferrocenylmethyltrimethylamine ($FcCH_2NMe_3^+$) within the apolar cavity of CB[7] by cyclic voltammetry and UV-Vis spectroscopy. Upon the addition of an increasing number of equivalents of CB[7] (0 → 1.4) to a solution (1 mM, aq.) of $FcCH_2NMe_3^+$, inclusion of the guest species is confirmed by an anodic shift in the $E_{1/2}$ value (**Left** (**secondary *y*-axis**) **and Right**), and a blue spectral shift in the metal-to-ligand charge-transfer (MLCT) band of the guest species (**Left, primary *y*-axis**). No further change was observed following the addition of 1 equivalent of CB[7], highlighting the formation of a 1:1 host-guest complex.

**Figure 3.** $^1$H NMR spectra ($H_2O$, 298 K, 400 MHz) of a solution of ($MV^{2+}$, 2,6-Np)-CB[8] prior to (**Trace E**) and following the addition of 1 equivalent of amantadine hydrochloride (**Trace B**). $^1$H NMR spectra ($H_2O$, 298 K, 400 MHz) of solutions of $MV^{2+}$-CB[8] (**Trace D**), $MV^{2+}$ (**Trace C**) and 2,6-Np (**Trace A**) are also given. Ternary complex formation was confirmed when upfield chemical shifts of the resonances corresponding to protons *a*, *b*, *c*, *d* and *e* were observed upon the addition of a stoichiometric amount of the macrocyclic host, CB[8]. Upfield shifts of 0.2 and 0.8 ppm of the aromatic peaks of $MV^{2+}$ (*a* and *b*) post complexation result from shielding of the proton environments due to their interaction with the carbonyl portals and the negative electrostatic potential of the CB[8] cavity. The peaks of the 2,6-Np protons (*c*, *d* and *e*) are broadened and similarly shifted upfield on formation of the ternary complex, the negative EP of CB[8] causing similar shielding effects, and the interruption of aromaticity from charge-transfer reducing paramagnetic contribution to the shifts from ring currents of the naphthalene core.[31] All complexes were generated at a concentration of 2 mM. **Traces A – E, Bottom – Top**.

**Figure 4.** An increase in ε of the charge-transfer band ($\lambda_{max}$ 570 nm) is seen upon the addition of a stoichiometric amount of CB[8] (**Left**). This is accompanied by the appearance of a peak in the ESI-MS at *m / z* 837.33 (**Right**); both signify formation of the model ternary complex, ($MV^{2+}$, 2,6-Np)-CB[8]. Presence of the binary complex ($MV^{2+}$-CB[8], *m / z* 757.23, **Right**) is still apparent to some extent. Both give similar spectra which differ to that of the free dimer ($MV^{2+}$-2,6-Np) in solution, **Figure 4**. All complexes were generated in aqueous solution at 298 K.

**Figure 5.** Formation of the homoternary complex (($MV^{+\bullet}$)$_2$-CB[8]) and the switching of lanthanide luminescence within a novel heteroternary assembly. Demonstrating the reversibility of the redox process in the presence (**Top Left**) and absence (**Top Right**) of CB[8]. **Bottom**. The effect of reducing, and subsequently oxidising, a solution of the model ternary complex, ($MV^{2+}$, 2,6-Np)-CB[8]. All complexes were generated in aqueous solution at 298 K, and at a concentration of 0.5 mM. $e^-$ denotes one electron reduction, whilst $O_2$ denotes oxidation.

**Figure 6.** UV-Vis (**Left**) and ESI-MS (**Right**) of a solution of ($MV^{2+}$, EuNap)-CB[8]. Upon formation of the complex, a peak at *m / z* 1125.89 appeared, along with two charge-transfer peaks in the expected region; a shoulder peak at ca. 490 nm, and a more defined peak at ca. 390 nm. Both are of similar intensity to the charge-transfer peak observed in the case of the model ternary complex (($MV^{2+}$, 2,6-Np)-CB[8], **Figure 4**), denoting similarly confined inclusion. The hypsochromic shift of the charge-transfer bands from that witnessed in the model complex is in good agreement with the Mulliken model of charge-transfer electronics. As the two complexes are structurally similar, it may be approximated that the reorganisation energy *J* is comparable, with $\Delta E_{CT}$ ascribable to the difference in $E_{HOMO}$ of the donor compound. With only one electron-releasing substituent conjugated to the naphthalene core, $E_{HOMO}$ should be lower for EuNap, increasing the frontier orbital energy gap. $\lambda^{-1} \propto E_{CT} = E_{HOMO} - E_{LUMO} + J$, the wavelength of absorption is decreased and the charge-transfer complex now absorbs in the blue region of the electromagnetic spectrum, consequently appearing red in colour. All complexes were generated in aqueous solution at 298 K, and at a concentration of 2 mM.

**Figure 7.** Modulating the emissive output from (FcMV, EuNap)-CB[8] at the interface by varying the oxidation state of the coincluded FcMV derivative (**Top** (**A**)), or *via* reversible generation of ($MV^{+\bullet}$)$_2$-CB[8] (**Bottom** (**B**)). Upon oxidation of the Fc motif to $Fc^+$, the emissive state of $Eu^{3+}$ should be quenched, and hence no luminescent output observed. Whilst upon formation of the homoternary complex, ($MV^{+\bullet}$)$_2$-CB[8], following one electron reduction of the $MV^{2+}$ appendage, in the presence of an excess of $MV^{2+}$, the EuNap species should be released into solution, hence all emissive output will be lost from the surface, and an optical signature only acquired upon analysis of the resultant solution. $e^-$ denotes one electron reduction, whilst $O_2$ denotes oxidation.

**Figure 8.** Quenching of the fluorescent (**Left**) and luminescent (**Right**) output of a solution of ($MV^{2+}$, EuNap)-CB[8]. Upon generation of the charge-transfer complex, a reduction in sensitised emission is observed. All complexes were generated in aqueous solution at 298 K, and at a concentration of 0.5 mM. Experimental Parameters (Fluorescent Output of EuNap): $\lambda_{ex}$ = 227 nm, excitation slit width = 5 nm, emission slit width = 5 nm, PMT Voltage (V) = 500, CAT 10, 298 K. Experimental Parameters (Phosphorescent Output of EuNap):

$\lambda_{ex}$ = 227 nm, excitation slit width = 10 nm, emission slit width = 10 nm, PMT Voltage (V) = 1000, CAT 10, total decay time = 0.020 s, delay time = 0.20 ms, gate time = 0.50 ms, 298 K.

**Figure 9.** Partial energy diagrams for the lanthanide aquo ions (**Left**). The main luminescent levels are drawn in **red**, while the fundamental level is indicated in **blue**. Figure reproduced with permission from reference [38]. The quenching of lanthanide luminescence within ($MV^{2+}$, NdNap)-CB[8] (**Right**). Upon confinement of both guest species within the apolar cavity of CB[8], a reduction in sensitised emission is observed. Removing oxygen from the system and confining the sensitizer motif (2,6-Np) within the cavity of the macrocyclic host, has no effect on the magnitude of sensitised emission. Similar observations were made upon analysis of the Yb analogue (**Appendix, 8.12.1**). All complexes were generated in aqueous solution at 298 K, and at a concentration of 0.5 mM. Experimental Parameters: $\lambda_{ex}$ = 323 nm, excitation slit width = 5 nm, emission slit width = 5 nm, PMT Voltage (V) = 500, CAT 10, 298 K.

**Figure 10.** All possible pathways preventing generation of the lanthanide ($Eu^{3+}$, $Yb^{3+}$ or $Nd^{3+}$) emissive state(s). When the lanthanide complex is dissolved in solution, sensitisation is extremely efficient, and significant optical output acquired. However, upon formation of the ternary complex, ($MV^{2+}$, LnNap)-CB[8], optical output is suppressed due to the induction of charge-transfer, rigidification of the sensitizer-appended moiety, or *via* quenching of the emissive state of the chromophore by oxygen.

**Figure 11.** $^1$H NMR spectra ($D_2O$, 298 K, 400 MHz) of solutions of ($MV^{2+}$, 2,6-Np)-CB[8] (**Trace A**), 1:1:1:1 $MV^{2+}$:2,6-Np:FcMeOH:CB[8] (**Trace** B) and FcMeOH (**Trace C**) **Traces A – C, Bottom – Top**. Cyclic voltammograms (**Inset**) highlighting the loss of ferrocene from solution upon the addition of CB[8] to a 1:1 solution of $MV^{2+}$:FcMeOH; precipitation of FcMeOH as an included species in binary complexation is induced, but this is displaced, to give the charge-transfer complex, ($MV^{2+}$, EuNap)-CB[8], upon the subsequent addition of 2,6-Np. All spectra were recorded at a concentration of 0.5 mM. Electrochemical Setup: *Working Electrode*: Glassy Carbon. *Reference Electrode*: Ag / $AgNO_3$. *Auxiliary Electrode*: Pt wire. *Electrolytic Solution*: 0.1 M $NaClO_4$, aq. *Scan Rate:* 300 mV / s.

**Figure 12.** Possible complexation pathway to the desired ternary complex, (FcMV, 2,6-Np)-CB[8] (*n.b*. also valid for EuNap secondary guest inclusion).

**Figure 13.** ESI-MS (**Left**) and UV-Vis spectra (**Right**) demonstrating oxidation of the FcMV derivative to $(FcMV\text{-}CB[8])^{3+}$. The characteristic UV-Vis signature of ferrocenium was acquired at ca. 630 nm, whilst a peak at a *m / z* of 585.84 was observed in the ESI-MS spectrum.

**Figure 14.** Generating *N*,*N'*-dimethyl-[4,4'-bipiperidine]-1,1'-diium (NAMV) by complete hydrogenation of $MV^{2+}$.

**Figure 15**. $^1$H NMR spectra ($D_2O$, 298 K, 400 MHz) of a solution of $MV^{2+}$ prior to (**Trace A**) and following complete hydrogenation (**Trace B**). Hydrogenation resulted in loss of aromaticity (8.45 – 9.5 ppm) and the appearance of additional aliphatic multiplets in the range, 1.00 – 4.00 ppm. A peak at a *m / z* 198 in the ESI-MS also arose (**Inset**). **Traces A – B, Bottom – Top.**

**Figure 16**. $^1$H NMR spectra ($D_2O$, 298 K, 400 MHz) of solutions of NAMV prior to (**Trace A**) and following the addition of a stoichiometric amount of CB[6] (**Trace B**), CB[7] (**Trace C**) or CB[8] (**Trace D**). All complexes were generated in aqueous solution at a concentration of 2 mM. **Traces A – D, Bottom – Top.**

**Figure 17.** $^1$H NMR spectra ($D_2O$, 298 K, 400 MHz) of solutions of NAMV-CB[6] (**Trace A**), NAMV-CB[7] (**Trace B**) and NAMV-CB[8] (**Trace C**) following the addition of a stoichiometric amount of 2,6-Np. All complexes were generated in aqueous solution at a concentration of 2 mM. **Traces A – D, Bottom – Top.**

**Figure 18.** Assembly of (NAMV, 2,6-Np)-CB[8]. The complex was generated in aqueous solution at 298 K, and at a concentration of 2 mM.

**Figure 19.** Synthesis of 1-(10-mercaptodecyl)-1'-methyl-[4,4'-bipyridine]-diium bromide, **D**. Scheme devised upon consideration of references [20], [42] and [43].

**Figure 20.** Synthesis of 1-methyl-1'-(10-(naphthalen-2-yloxy)decyl)-[4,4'-bipyridine]-1,1'-diium bromide iodide, **F**. Scheme devised upon consideration of references [44-46].

**Figure 21.** Attempted hydrogenation of 1-(10-Mercaptodecyl)-1'-methyl-[4,4'-bipyridine]-diium bromide, **D**.

**Figure 22.** Surface assembly of an interfacial, molecular switch, in which a lanthanide ion is confined within a charge-transfer complex. Stepwise growth of the interface is feasible because the number of **F**-CB[8] complexes recruited to the underlying film can be varied prior to propagation being terminated *via* the recruitment of a functionalised naphthalene derivative, EuNap.

**Figure 23.** A schematic representation highlighting the expected difference in the intensity of sensitised emission acquired from a lanthanide-appended, molecular assembly in the **absence** and **presence** of charge-transfer (**Left**). As the lanthanide ion is recruited further from the metallic interface, in the absence charge-transfer, its emissive output is assumed to increase in line with a decline in energy transfer, both to the Au surface (SET), and the nearby acceptor chromophore (naphthalene motif), *via* nonradiative, dipole-dipole coupling (**Right**). However, in the presence of charge-transfer, an interaction which has been shown to quench lanthanide luminescence (**Table 1**), it is unlikely that increasing the distance between the metallic interface and the lanthanide ion will have the desired effect (**Right**). *d* denotes the distance between the donor (Ln emissive state) and acceptor (Au) moieties present.

**Figure 24.** $^{1}$H NMR spectrum ($D_2O$, 298 K, 400 MHz) of a solution of 1-(10-Mercaptodecyl)-1'-methyl-[4,4'-bipyridine]-diium bromide (**D**) following attempted hydrogenation. $MV^{2+}$-centred multiplets (**Trace A**) are still present in the resultant spectrum (**Trace C**), unlike upon the formation of NAMV (**Trace B**). All complexes were generated at a concentration of 2 mM. *denotes the resonances that cannot be resolved. **Traces A – B, Bottom – Top.**

**Figure 25. Top.** Hydrogenation of 1-methyl-[4,4'-bipyridin]-1-ium iodide. **Bottom.** A possible synthetic approach for acquiring the non-aromatic analogue of **D**; the direct hydrogenation of **D** did not proceed to completion, and subsequent decomposition of **D** was observed by $^{1}$H NMR spectroscopy.

**Figure 26**. $^{1}$H NMR spectra ($D_2O$, 298 K, 400 MHz) of solutions of **D** prior to (**Trace C**) and following the addition of stoichiometric amounts of CB[7] (**Trace B**) or CB[8] (**Trace A**). All complexes were generated at a concentration of 2 mM. *denotes the resonances that cannot be resolved. **Traces A – C, Bottom – Top.**

**Figure 27.** A schematic representation highlighting the likely mode of encapsulation of **D** by CB[8].

**Figure 28.** $^{1}$H NMR spectrum ($D_2O$, 298 K, 400 MHz) of a solution of **D**-CB[8] following the addition of a stoichiometric amount of 2,6-Np (**Trace C**). $^{1}$H NMR spectra ($D_2O$, 298 K, 400 MHz) of solutions of **D** and 2,6-Np are also given. All complexes were generated at a concentration of 2 mM. **Traces A – C, Bottom – Top.**

**Figure 29.** $^{1}$H NMR spectra ($D_2O$, 298 K, 400 MHz) of solutions of **F** (**Trace A**), **D**-CB[8] (**Trace B**), **D** (**Trace C**) and (**D**, **F**)-CB[8] (**Trace D**). All complexes were generated at a concentration of 2 mM. **Note.** Not all the resonances associated with the host-guest complexes (**Traces B and D**) could be resolved. **Traces A – D, Bottom – Top.**

**Figure 30.** A schemtaic representation highlighting possible generation of both the 1:1 *inter*molecular heteroternary complex and the 1:1 *intra*molecular heteroternary complex upon the addition of **F** into a solution of the binary complex, **D**-CB[8].[44-46]

## List of Tables

**Table 1.** The effect of charge-transfer on the decay of luminescent emission from the lanthanide centre of ($MV^{2+}$, EuNap)-CB[8]. All luminescent lifetime measurements (**Appendix, 8.8**) were performed in aqueous solution at 298 K, where the concentration of each species was 0.5 mM. Experimental Parameters: $\lambda_{ex}$ = 227 nm, $\lambda_{em}$ 616 nm, excitation slit width = 10 nm, emission slit width = 5 nm, PMT Voltage (V) = 1000, CAT 10, time per flash = 41 ms, flash count = 100.

**Table 2.** The effect of nullifying charge-transfer on the decay of luminescent emission from a lanthanide centre confined within a ternary environment. Confinement of both NAMV and EuNap within the apolar cavity of CB[8] has no effect on the lifetime of luminescent emission from the lanthanide centre, *cf.* when both $MV^{2+}$ and 2,6-Np are confined and charge-transfer inducted. All complexes were generated in $D_2O$ at 298 K, and at a concentration of 2 mM. Experimental Parameters: $\lambda_{ex}$ = 397 nm, $\lambda_{em}$ 616 nm, excitation slit width = 14 nm, emission slit width = 5 nm, PMT Voltage (V) = 1000, CAT 10, time per flash = 41 ms, flash count = 10, 298 K.

# 5. The Surface Assembly of Molecular Switches

It was aimed for lanthanide complexes to be immobilised at the surface, facilitating device integration, and permitting the conformational dynamics of such systems to be analysed. Variations in lanthanide-centred luminescent emission can be utilised to monitor conformational, coordinative, and electronic change.[1,2,3,4] The incorporation of a redox-active moiety into the molecular architecture allows for the electrochemical switching of sensitised emission[5,6], as was alluded to in Chapter 4. As only a relatively few examples of such a system have been reported to date, not much is known about the emissive characteristics of lanthanides at interfaces. To try to shed further light on this topic, prior to utilising charge-transfer in the construction of an emissive assembly, a variety of cucurbit[*n*]uril-functionalised interfaces were generated, to which *d*-*f* dyads could be potentially recruited and their emissive properties subsequently modulated by varying the oxidation state of the ferrocene (Fc) chromophore[5,6], **Figure 1**, thereby obtaining interfacial, molecular switches.

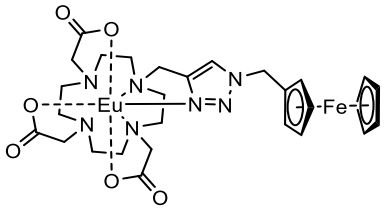


**Figure 1.** Ferrocene-europium dyad, Eu.2. Oxidation of the Fc chromophore brings about the formation of the quenching ferrocenium ($Fc^+$) moiety, and a reduction in the intensity of sensitised luminescent emission from the lanthanide centre ($\lambda_{ex}$ 340 nm, $\lambda_{em}$ 616 nm).[5,6]

## 5.1 – Recruiting Redox-Active Derivatives to CB[*n*]-Functionalised Surfaces

### 5.1.1 – Exploiting Multivalent Interactions in the Assembly of CB[*n*]-Functionalised Interfaces

The strong multivalent interaction between the carbonyl portals of cucurbit[7]uril (CB[7]) and gold (Au) was exploited to form a receptive self-assembled monolayer (SAM)[7], that is one in which the recognition properties of CB[7] are maintained, and to which ferrocene-appended molecular assemblies can be recruited. The formation of these SAMs (**Experimental, 7.3.1**) and the inclusion of redox-active moieties within the hydrophobic cavities of the surface-bound CB[7] molecules was probed by x-ray photoelectron spectroscopy (XPS, **Experimental, 7.6**), cyclic voltammetry (CV, **Experimental, 7.2.4**), luminescence spectroscopy (**Experimental, 7.8**), and ellipsometry (**Experimental, 7.4**). SAMs in which the carbonyl portals of CB[7] are held perpendicular with respect to the Au surface were formed upon the spontaneous adsorption of the macrocyclic host[7]. The presence of CB[7] molecules on the Au surface was confirmed by XPS, CV, ellipsometry and contact angle measurements (**Experimental, 7.9**).

Upon deposition of the macrocyclic host, CB[7], peaks at binding energies of 285 (C-C), 287 (C-N) and 289 (C=O) eV were observed in the XPS spectrum, whilst increases in film thickness, indicative of monolayer coverage, and surface wettability were observed, **Figure 2**.

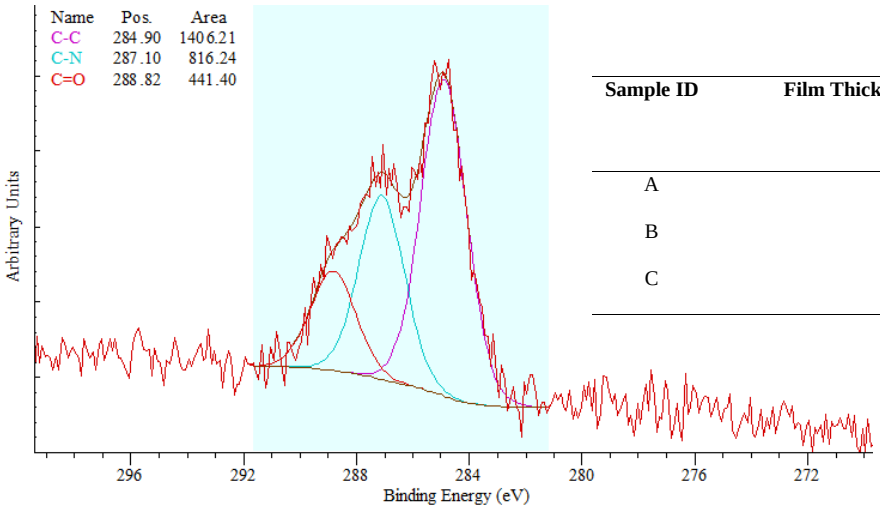


| Sample ID | Film Thickness Increase (nm) (± 0.2) | Contact Angle (°) (± 5) |
|---|---|---|
| A | 1.0 | 47 |
| B | 1.1 | 47 |
| C | 0.9 | 48 |

**Figure 2.** XPS spectrum of a CB[7]-modified Au surface. **Inset.** Increases in ellipsometric film thickness and surface wettablity recorded following the deposition of CB[7] at Au. Reported increases are those determined from, and averaged over, three separately prepared samples (A, B and C), with four measurements per sample.

Electrochemical data was also acquired in support of the formation of a monolayer of CB[7] on Au. When a CB[7]-modified Au electrode was exposed to a 1 mM acetonitrile (AcN) solution of FcMV, **Figure 3**, a well-defined redox couple ($Fc / Fc^+$, $E_{1/2}$ 312 mV *vs.* $Hg / HgSO_4$) was detected following thorough washing, **Figure 4** (**Left**), whilst a linear relationship ($R^2 = 0.9983$) between scan rate and peak current, **Figure 4** (**Right**), confirmed that the FcMV derivative was confined at the electrode surface[7].

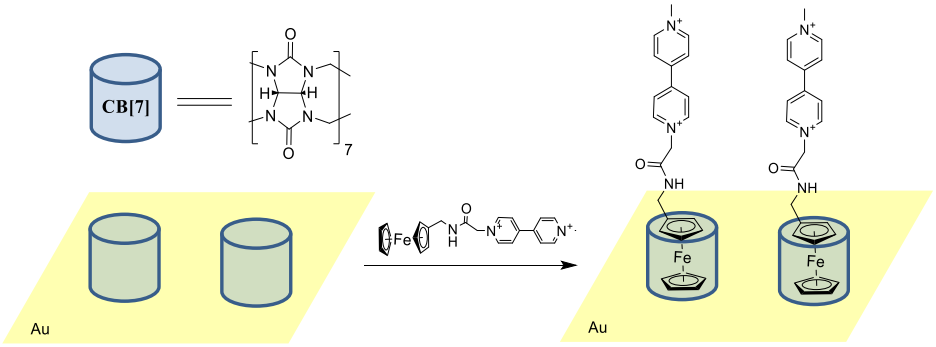


**Figure 3.** Recruitment of FcMV at a CB[7]-functionalised Au substrate.

Confinement of the derivative at the interface was also confirmed by the fact that upon the inclusion of FcMV within the apolar cavity of the macrocyclic host, a pronounced anodic shift (171 mV) in the position of the corresponding $E_{1/2}$ value for oxidation of the ferrocene residue was observed[8], **Figure 4** (**Left**). The anodic shift reveals that the ferrocene form of the guest is considerably more stabilized by CB[7] complexation than the oxidized form[8]. In other words, oxidation of the ferrocene

residue considerably weakens the stability of the inclusion complex[8]. The expected current level decrease brought about by the host-guest association was also apparent[8-14], **Figure 4** (**Left**). Similar results were acquired upon the recruitment of $FcCH_2NMe_3^+$, Eu.2 and Fc at CB[7]-modified Au electrodes (**Experimental, 8.16**).

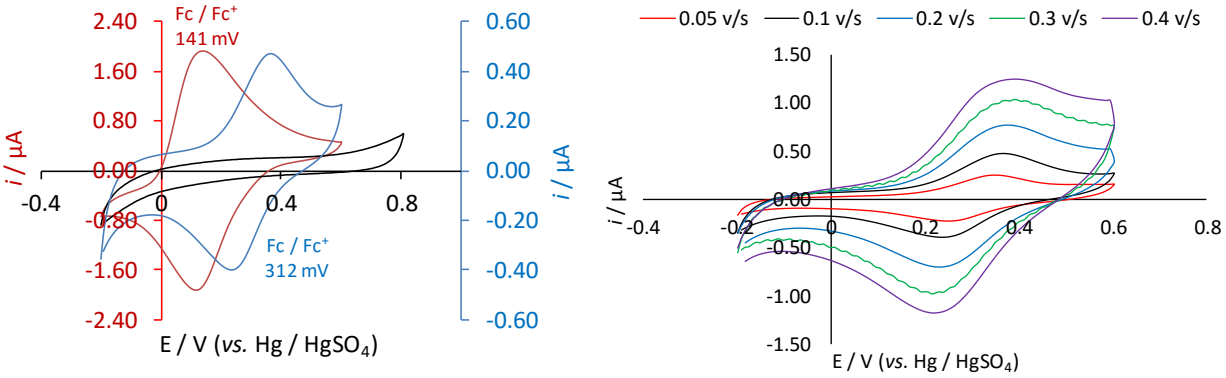


**Figure 4.** **Left.** Cyclic voltammograms of a CB[7]-modified Au electrode (**Black**), a 0.1 mM aqueous solution of FcMV (**Red**) and a FcMV@CB[7]-modified Au electrode (**Blue**). **Right.** Cyclic voltammograms of a FcMV@CB[7]-modified Au electrode recorded at variable scan rates.

Following the formation and characterisation of SAMs of CB[7], in which the recognition properties of the macrocyclic host are maintained, the recruitment of Eu.2 was probed in a bid to acquire an emissive assembly, the optical output of which could be modulated upon varying the oxidation state of the Fc chromophore[5,6]. Subsequent to the recruitment of Eu.2 ($Fc / Fc^+$, $E_{1/2}$ 284 mV *vs.* SCE, **Experimental, 8.16**), **Figure 5** (**Left**), and the deposition of the preformed host-guest complex, Eu.2-CB[7], **Figure 5** (**Right**), no emissive output (**Experimental, 8.19** ($\lambda_{ex}$ 340 nm, $\lambda_{em}$ 616 nm)) was detected, as in solution[5] (**Experimental, 8.18**). It was assumed that the lanthanide centre was in too close a proximity to the quenching, Au interface[15-18].

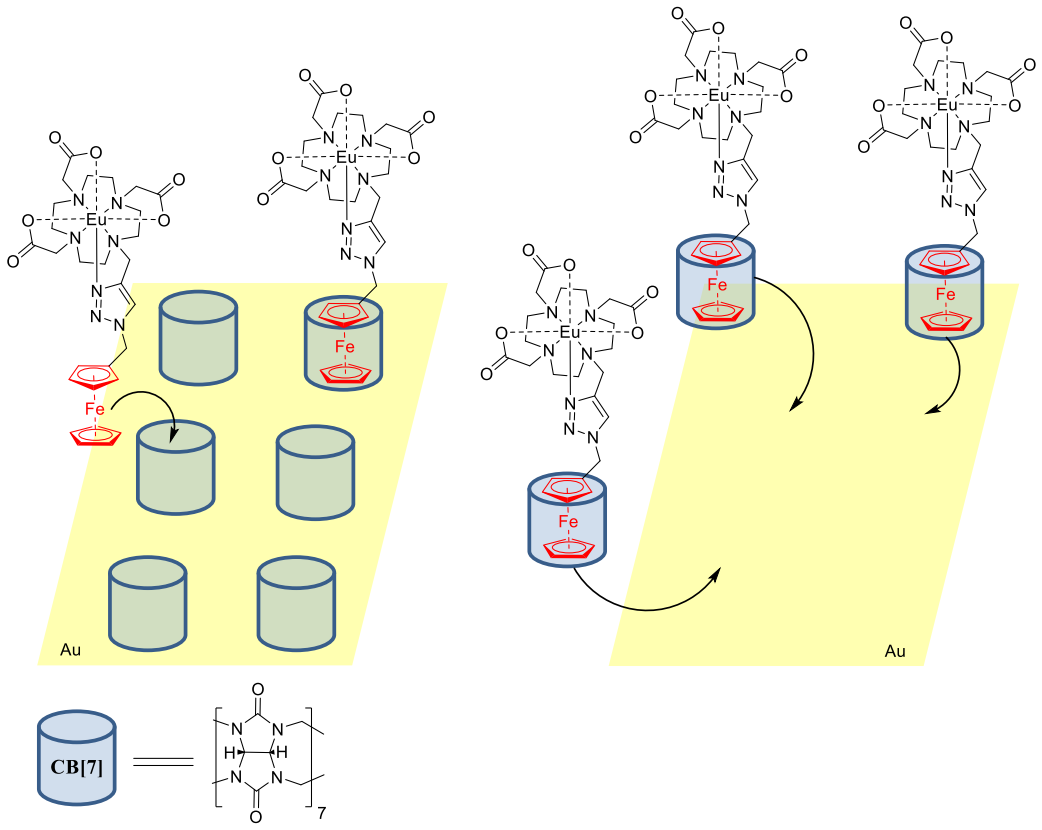


**Figure 5.** Recruitment of Eu.2 at a CB[7]-functionalised Au interface (**Left**), and deposition of Eu.2-CB[7] at Au (**Right**).

In addition to the fact that optical emission ($\lambda_{em}$ 616 nm) was not detected upon excitation of the Fc chromophore ($\lambda_{ex}$ 340 nm, **Appendix, 8.19**), physical adsorption of the guest species (Eu.2) at bare Au was apparent (**Appendix, 8.17**). In the absence of the macrocyclic host, CB[7], redox couples were also detected upon the exposure of pristine Au substrates to micromolar solutions of both $FcCH_2NH_2$ (**Appendix, 8.17**) and $FcCH_2NMe_3^+$, **Figure 6**. This made quantifying the level of inclusion at the receptive interface extremely difficult, and thus prohibited the calculation of the surface density (molecules $cm^{-2}$) of CB[7]; for the surface density of CB[7] to be calculated, it has to be assumed that all redox-active moieties are confined within the cavity of the deposited macrocyclic host molecules[7], which is clearly not the case given the data in **Figure 6**.

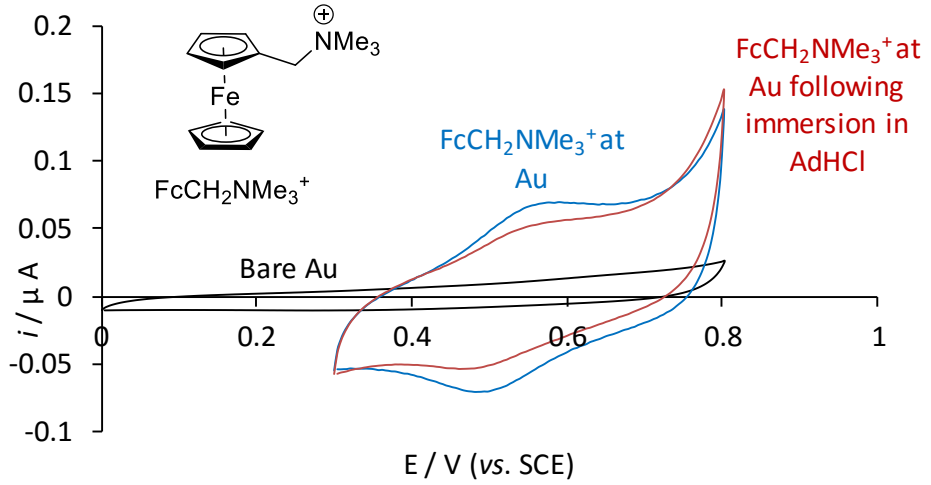


**Figure 6.** Cyclic voltammograms of a bare Au electrode prior to (**Black**) and following exposure to a 1 mM AcN solution of $FcCH_2NMe_3^+$ (**Blue**), and of a $FcCH_2NMe_3^+$@CB[7]-modified electrode following immersion in a 10 mM aqueous solution of amantadine hydrochloride (AdHCl) (**Red**). Significant physical adsorption of $FcCH_2NMe_3^+$ at bare Au is apparent. That is, the Fc / $Fc^+$ redox couple (529 mV *vs.* SCE) is present following immersion of the interface in a 10 mM aqueous solution of AdHCl.

Such observations were also made following the prior recruitment of AdHCl to a SAM of CB[7], **Figure 7**, highlighting the fact that the deposited monolayers are of low-density, that is a high proportion of the Au surface remains exposed following deposition of the macrocyclic host from aqueous solution. In theory, a redox signature should not be detected upon the attempted recruitment of $FcCH_2NMe_3^+$ at an AdHCl@CB[7]-modified electrode because AdHCl-CB[7] possesses a greater binding constant (logK 14.32)[19] than $FcCH_2NMe_3^+$-CB[7] (logK 12.61)[19].

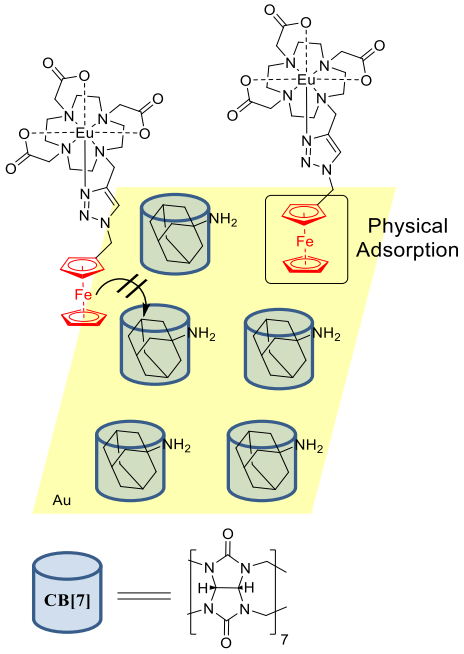


**Figure 7.** Recruitment of AdHCl to a CB[7]-functionalised interface, and the undesirable interaction between Au and both cationic and neutral Fc-appended derivatives. The Fc-appended derivatives physically adsorb to the functionalised Au substrate, irrespective of whether AdHCl has been previously recruited to the CB[7]-functionalised interface.

Thus, and since CB[7] does not directly interact with either silicon (Si), indium tin oxide (ITO) or glass, an alternative interface was assembled in a bid to acquire an optical signature upon the recruitment of Eu.2, **Figure 8**. Si, ITO and glass are all surfaces at which the quenching of lanthanide luminescence is likely to be greatly reduced in comparison to that observed at Au. The deposition of CB[7] at Si, ITO and glass was probed by ellipsometry, where possible, and by monitoring changes in the wettability of the interface upon exposure to an aqueous solution of the macrocyclic host, CB[7]. The desired increase (0.9 nm)[20] in film thickness was not recorded at Si, whilst a change in contact angle was not observed at any of the substrates (Si, ITO and glass) upon attempted deposition of the hydrophobic macrocycle.

### 5.1.2 – Electrostatic Recruitment of CB[7] at Non-Quenching Substrates

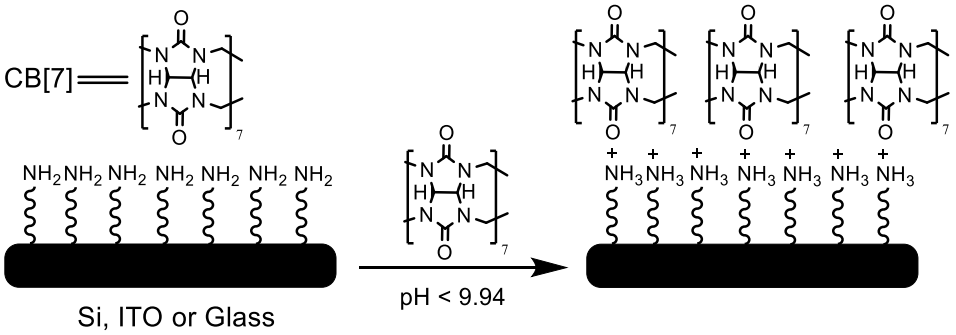


**Figure 8.** Formation of CB[7]-functionalised self-assembled monolayers (SAM) at Si, ITO and glass; **Experimental, 7.3.5**.

The recruitment of CB[7] to an underlying monolayer of (3-aminopropyl)triethoxysilane (APTES) centres on the electrostatic interaction induced, following a reduction in pH, between the positively charged amine terminus of APTES and the negatively polarised carbonyl portals lining the periphery of the macrocyclic host, **Figure 8**.[21] Thus it has been shown, by monitoring the associated change in ellipsometric film thickness, that the recruitment of CB[7] at a monolayer of APTES is pH dependent. An increase in film thickness of 1.0 (± 0.2) nm, corresponding to the recruitment of CB[7][20], is only observed when the pH of the deposition solution is lowered below that of the pKa of the amine terminus of APTES (pKa 9.94)[22-25]. However, when trying to demonstrate that the macrocyclic host is not recruited when the pH of the solution is raised above 9.94, that is when the amine functionality is deprotonated, etching of the Si surface arose. Thus, a weaker base (NaOH (aq.) *cf*. KOH (aq.)) was utilised to demonstrate the true reversibility of the recruitment process. In addition, no increase in ellipsometric film thickness was observed upon exposure of the monolayer (APTES-Si) to a solution of the binary complex formed (**Experimental, 7.10**) between CB[7] and AdHCl, AdHCl-CB[7], as was expected given the fact that CB[7] and AdHCl are reported to associate strongly in solution ($1.7 \pm 0.8 \times 10^{14}$ $M^{-1}$)[26,27]. It was therefore concluded that formation of the CB[7]-functionalised assembly, AdHCl-CB[7]@APTES-Si, was prevented as a result of the carbonyl periphery of the host being unable to interact with the positively charged interface.

The receptive assembly was constructed on highly-doped Si and ITO, **Figure 8**, although the interfacial recruitment of Fc, FcMeOH and methyl viologen ($MV^{2+}$) from both aqueous ($H_2O$) and non-aqueous (AcN) media proved unsuccessful. Upon exposure of the interface to solutions of Fc, FcMeOH and $MV^{2+}$, CVs were not acquired that inferred confinement of the redox-active moieties at the interface, and the CB[7] moiety was displaced from the interface; the ellipsometric film thickness declined to that determined for a monolayer of APTES (0.8 (± 0.2) nm).

It was hypothesised that the electrostatic interaction thought to be driving assembly of the monolayer diminished the host's ability to recruit guest moieties from solution, and the macrocyclic host migrates into solution upon the preferential formation of a more stable binary complex. In addition, the recruitment of $MV^{2+}$ is likely to be further discouraged as the result of electrostatic repulsion between the cationic periphery of the monolayer and itself. However, as both Fc and FcMeOH, neutral guest species, were not recruited at the interface, this interaction was deemed not significant in the disassembly of the monolayer, and thus partial inclusion of the aminosilane within the apolar cavity of the macrocycle was considered.

The partial inclusion of APTES within the apolar cavity of CB[7] was inferred from $^1$H NMR (**Experimental, 7.7**) spectroscopy data, **Figures 9** and **10**. The binary inclusion properties of 1,4-diaminobutane, **Figure 9**, and hexylamine, **Figure 10**, were probed to try to elucidate what was preventing the recruitment of a further guest species at the periphery of the APTES monolayer, following the electrostatic recruitment of CB[7]. 1,4-Diaminobutane and hexylamine were utilised due to their similarity to APTES; they are both water soluble and functionalised with a primary amine which is protonated in aqueous media ($pKa_{hexylamine}$ 10.56[28], $pKa_{1,4\text{-diaminobutane}}$ 10.80[28]). Note: The ratio of macrocyclic host: guest species was fixed at 1:1 to prevent the formation, where possible, of 1:1 homoternary complexes. Upon the addition of a stoichiometric amount of the respective macrocyclic host, CB[6], CB[7] or CB[8], binary inclusion of the guest species, hexylamine (**Figure 9**) or 1,4-diaminobutane (**Figure 10**), was confirmed upon observing an upfield chemical shift of the proton resonances in question.

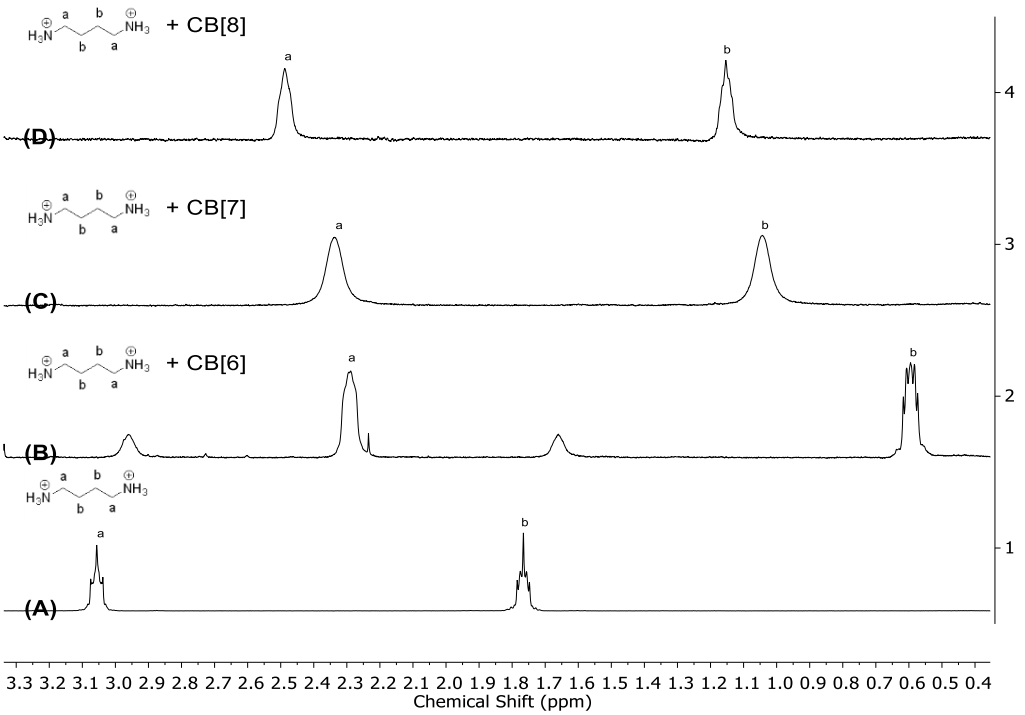


**Figure 9**. $^{1}$H NMR spectra ($D_2O$, 298 K, 400 MHz) of solutions of 1,4-diaminobutane prior to (**Trace A**) and following the addition of a stoichiometric amount of CB[6] (**Trace B**), CB[7] (**Trace C**) or CB[8] (**Trace D**). All complexes were generated at a concentration of 2 mM. The unassigned multiplets in **Trace B** are attributed to the presence of uncomplexed 1,4-diaminobutane. **Traces A – D, Bottom – Top**.

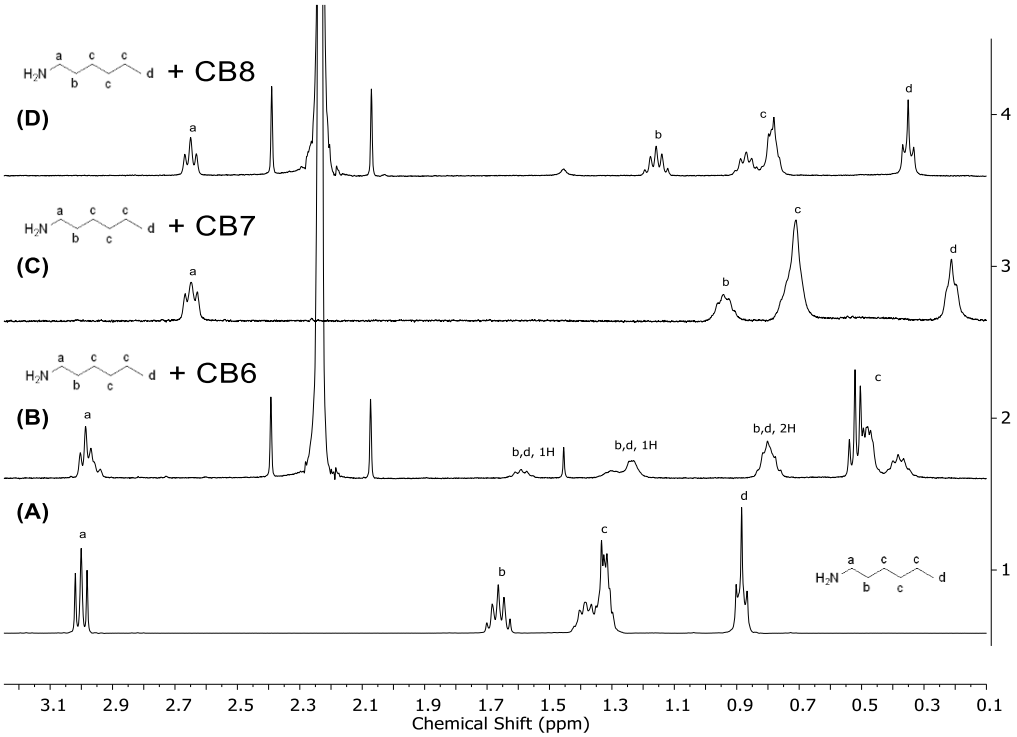


**Figure 10**. $^{1}$H NMR spectra ($D_2O$, 298 K, 400 MHz) of solutions of hexylamine prior to (**Trace A**) and following the addition of a stoichiometric amount of CB[6] (**Trace B**), CB[7] (**Trace C**) or CB[8] (**Trace D**). All complexes were generated at a concentration of 2 mM. **Traces A – D, Bottom – Top**.

Although 1,4-diaminobutane appears to become encapsulated within the apolar cavity of all three macrocyclic hosts, CB[6], CB[7] and CB[8], the $^{1}$H NMR spectra acquired (**Figure 9, Traces A - C**) infer that migration into the cavity of CB[6] is favoured, as was expected given its optimal portal diameter. The signals associated with the aliphatic protons of 1,4-diaminobutane ($H_a$ and $H_b$) are shifted upfield to a greater extent upon the addition of CB[6] (($H_a$, + 0.76 ppm), ($H_b$, + 1.17 ppm), **Trace B**), than they are upon the addition of either CB[7] (($H_a$, + 0.71 ppm), ($H_b$, + 0.72 ppm), **Trace C**), or CB[8] (($H_a$, + 0.56 ppm), ($H_b$, + 0.61ppm), **Trace D**). The binary inclusion of hexylamine however, is favoured, albeit surprisingly, in the hydrophobic cavities of the larger macrocyclic host species, CB[7] (**Trace C**) and CB[8] (**Trace D**), **Figure 10**. This is again inferred from the magnitude of the upfield chemical shifts (monoamine ($H_a$-$H_d$)) induced upon the addition of the respective macrocyclic host species. It has yet to be established as to why this is the case, although it is possible that the larger homologues can interact with more than one monoamine moiety at any given time. This would manifest itself in a greater upfield chemical shift because each aliphatic derivative would essentially be encapsulated within the cavity of more than one macrocyclic host moiety.

Although it has been shown that both 1,4-diamonbutane and hexylamine form binary inclusion complexes with CB[7] in solution, it is still not evident as to why the recruitment of both $MV^{2+}$ and

FcMeOH at the CB[7]-functionalised APTES interface proved ineffective, especially in the case of the latter neutral guest moiety where electrostatic repulsion is assumed to be negligible.

### 5.1.3 – Recruiting $MV^{2+}$ and FeMeOH at CB[7]-Functionalised Monolayers Deposited at Non-Quenching Surfaces

Further $^{1}$H NMR experiments were conducted to clarify why the attempted recruitment of both $MV^{2+}$ and FeMeOH proved ineffective. In the presence of a stoichiometric amount of 1,4-diaminobutane, $MV^{2+}$ is observed to preferentially 'include' within the cavity of the macrocyclic host, CB[7], **Figure 11** (**Figure D**). That is, upon the addition of stoichiometric amounts of $MV^{2+}$ and 1,4-diaminobutane to an aqueous solution of CB[7], the aromatic region (6.8 – 9.2 ppm) of the resultant $^{1}$H NMR spectrum (**Trace D**) resembles that of the spectrum acquired upon the analysis of the $MV^{2+}$-CB[7] complex (**Trace E**). The resonances associated with the protons of the bipyridine motif ($H_c$ and $H_d$) shift upfield, whilst those associated with the aliphatic species ($H_a$ and $H_b$) appear at a chemical shift value closer to that observed in the absence of the macrocyclic host (**Inset, Traces A, B** and **D**). The spectrum (**Inset, Trace D**) is however not identical to that of 1,4-diaminobutane in solution (**Inset, Trace A**) because it is assumed that the derivative is still within the vicinity of the macrocyclic host species, *i.e*. electrostatically ligated to its carbonyl fringed-portal framework. This suggests that the macrocyclic host migrates from the interface, into solution, upon the attempted recruitment of the cationic motif, $MV^{2+}$, **Figure 12**, prior to formation of the binary complex, $MV^{2+}$-CB[7]. It is likely that the binary complex, $MV^{2+}$-CB[7], is then electrostatically repelled from the positively charged monolayer.

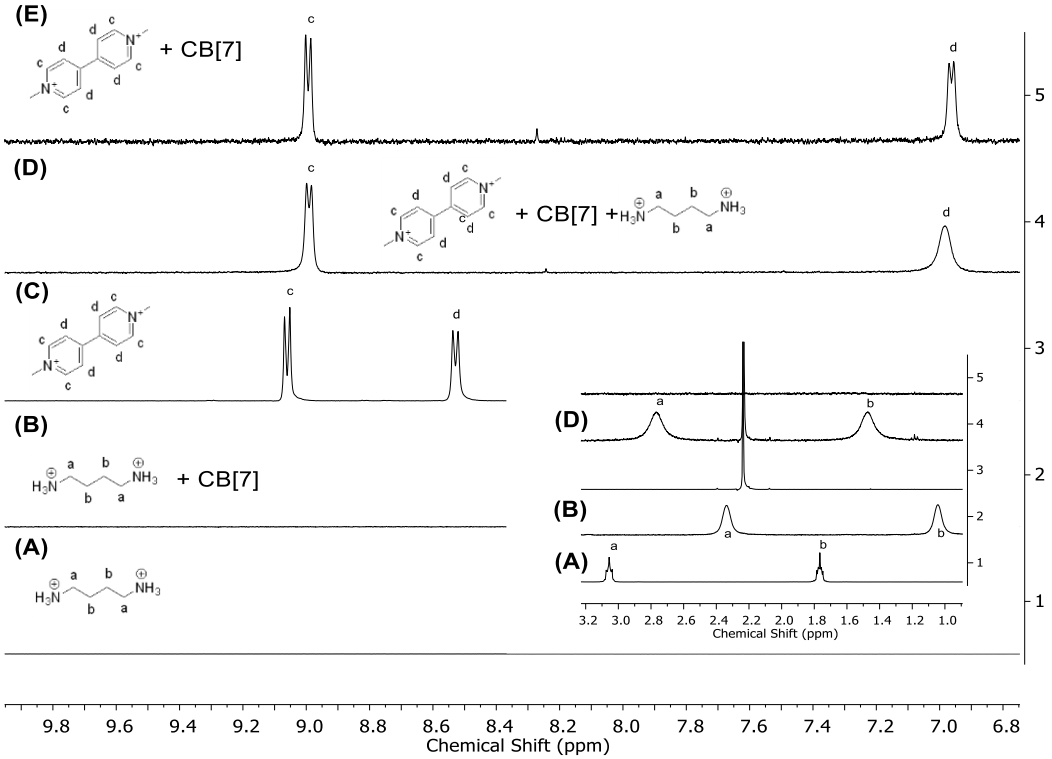


**Figure 11.** $^{1}$H NMR spectra ($D_2O$, 298 K, 400 MHz) of solutions of 1,4-diaminobutane (**Trace A**), 1,4-diaminobutane-CB[7] (**Trace B**), $MV^{2+}$ (**Trace C**), a 1:1:1 mixture of 1,4-diaminobutane, $MV^{2+}$ and CB[7] (**Trace D**) and $MV^{2+}$-CB[7] (**Trace E**). **Inset.** The aliphatic region of each $^{1}$H NMR spectrum. All complexes were generated at a concentration of 2 mM. **Traces A – E, Bottom – Top.**

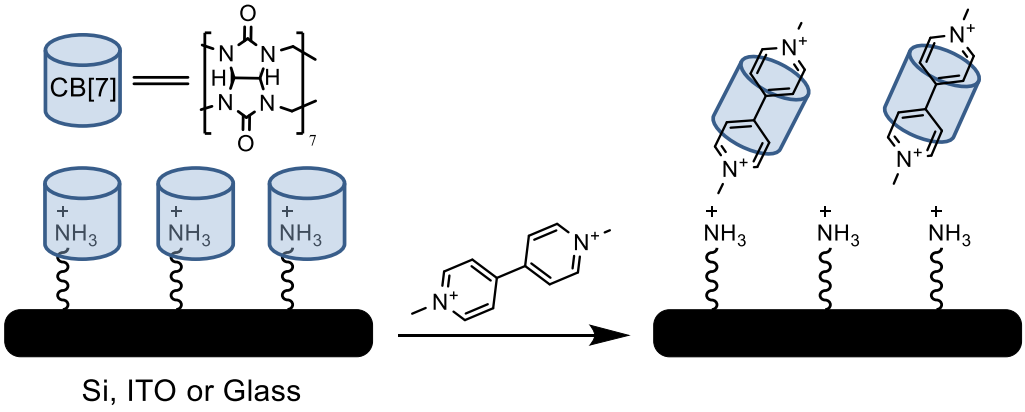


**Figure 12.** Depicting the loss of $MV^{2+}$-CB[7] from the interface upon the attempted recruitment of $MV^{2+}$ from solution.

Analogous observations were made upon the attempted recruitment of FcMeOH; it was demonstrated that FcMeOH can displace both hexylamine and 1,4-diaminobutane from the hydrophobic cavity of CB[7], **Figures 13** and **14**, whilst both are unable to displace FcMeOH from the cavity of the macrocyclic host, **Figures 15** and **16**.

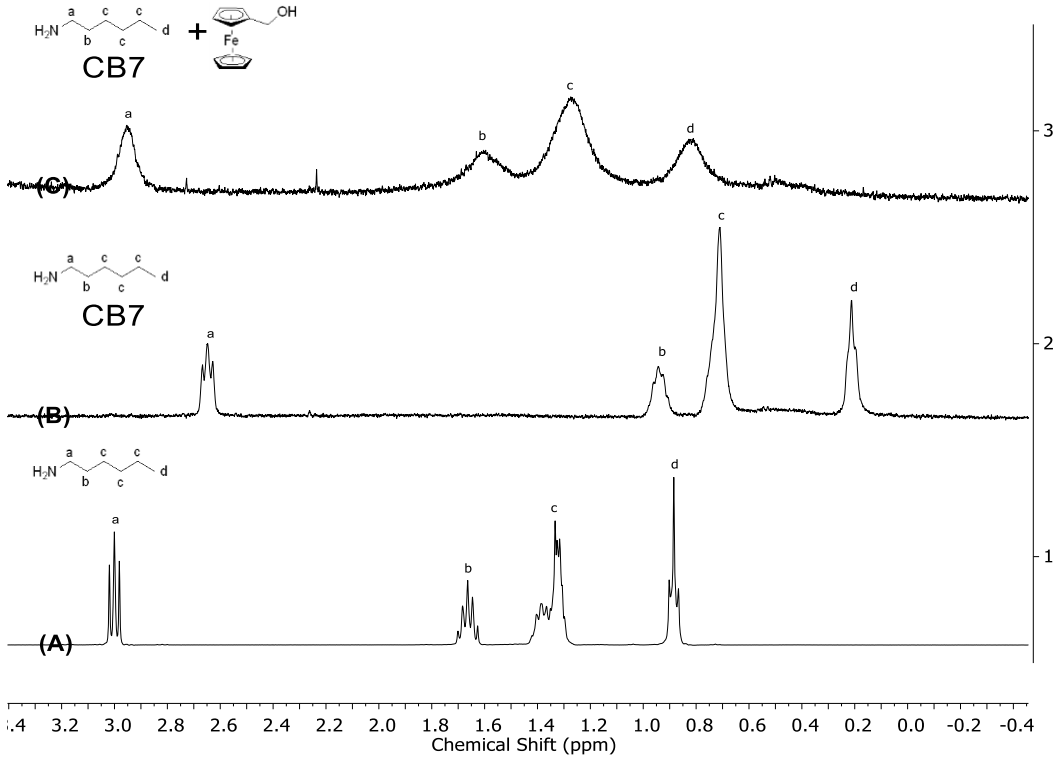


**Figure 13.** $^{1}$H NMR spectra ($D_2O$, 298 K, 400 MHz) of a solution of hexylamine prior to (T**race A**) and following the additions of CB[7] (**Trace B**) and FcMeOH (**Trace C**). All complexes were generated at a concentration of 2 mM. **Traces A – C, Bottom – Top**.

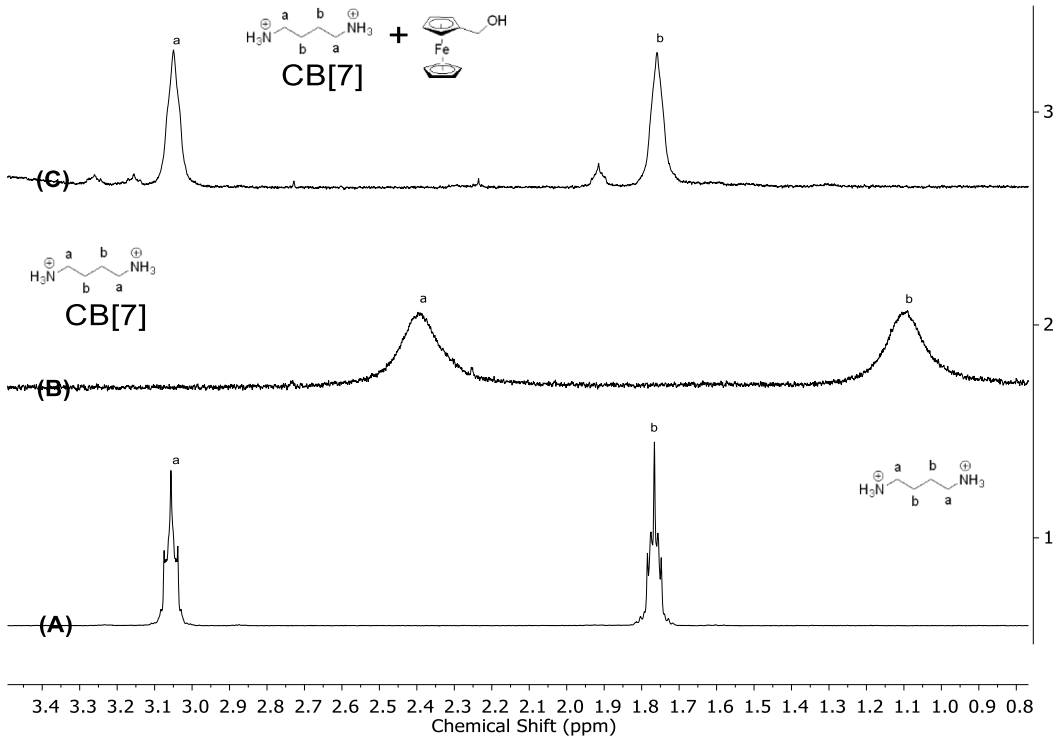


**Figure 14.** $^{1}$H NMR spectra ($D_2O$, 298 K, 400 MHz) of a solution of 1,4-diaminobutane prior to (T**race A**) and following the additions of CB[7] (**Trace B**) and FcMeOH (**Trace C**). All complexes were generated at a concentration of 2 mM. **Traces A – C, Bottom – Top**.

**Figures 13** and **14** indicate that upon the addition of FcMeOH to a solution of each binary complex, hexylamine-CB[7] (**Figure 13**) and 1,4-diaminobutane-CB[7] (**Figure 14**), the respective amine is displaced from the hydrophobic cavity of the host, prior to the formation of the more stable binary complex, FcMeOH-CB[7]. When FcMeOH is added into solution, the resultant spectra (**Trace C, Figures 13** and **14**) resemble that of either hexylamine or 1,4-diaminobutane in solution (**Trace A, Figures 13** and **14**). Addition of the secondary guest species, FcMeOH, brings about a downfield chemical shift of the resonances associated with the protons of the primary amines (hexylamine, $H_a$-$H_d$, 1, 4-diaminobutane, $H_a$ and $H_b$). Note: The initial binary inclusion of each brings about an upfield chemical shift of all the associated resonances, thus decomplexation manifests itself as a downfield chemical shift.

In addition, when hexylamine (**Figure 15, Trace C**) and 1,4-diaminobutane (**Figure 16, Trace C**) are added to a solution of FcMeOH-CB[7], an upfield chemical shift of each of the aliphatic resonances (hexylamine ($H_a$-$H_d$) and 1,4-diaminobutane ($H_a$ and $H_b$)) is not seen, suggesting that the inclusion of either amine or the displacement of FcMeOH from the cavity of the macrocyclic host is not induced. This was expected given the difference in association constants for CB[7] inclusion complexes of FcMeOH and aliphatic guest species ($3.0 \pm 0.5 \times 10^9$ $M^{-1}$ (FcMeOH)[29] *vs*. $4.7 \pm 0.3 \times 10^5$ $M^{-1}$ (1,6-diaminohexane)[30]), and the observations made previously (**Figures 13** and **14**).

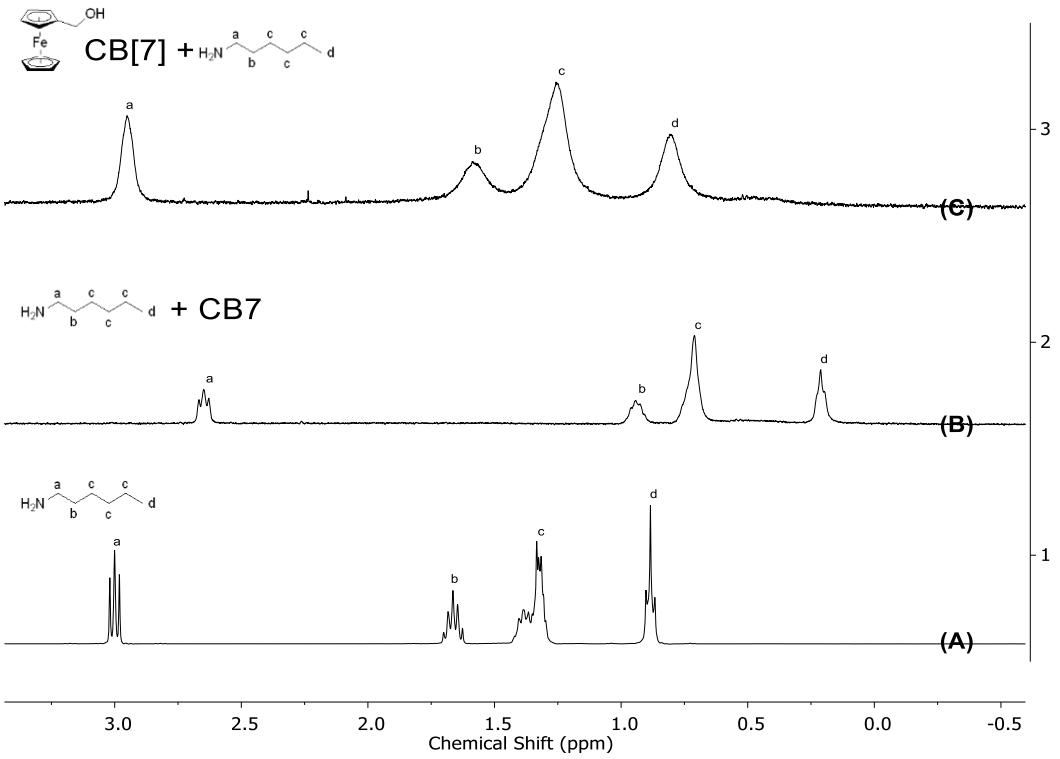


**Figure 15.** $^1$H NMR spectra ($D_2O$, 298 K, 400 MHz) of solutions of hexylamine (**Trace A**) and hexylamine-CB[7] (**Trace B**), and of a solution of FcMeOH-CB[7] following the addition of a stoichiometric amount of hexylamine (**Trace C**). All complexes were generated at a concentration of 2 mM. **Traces A – C, Bottom – Top.**

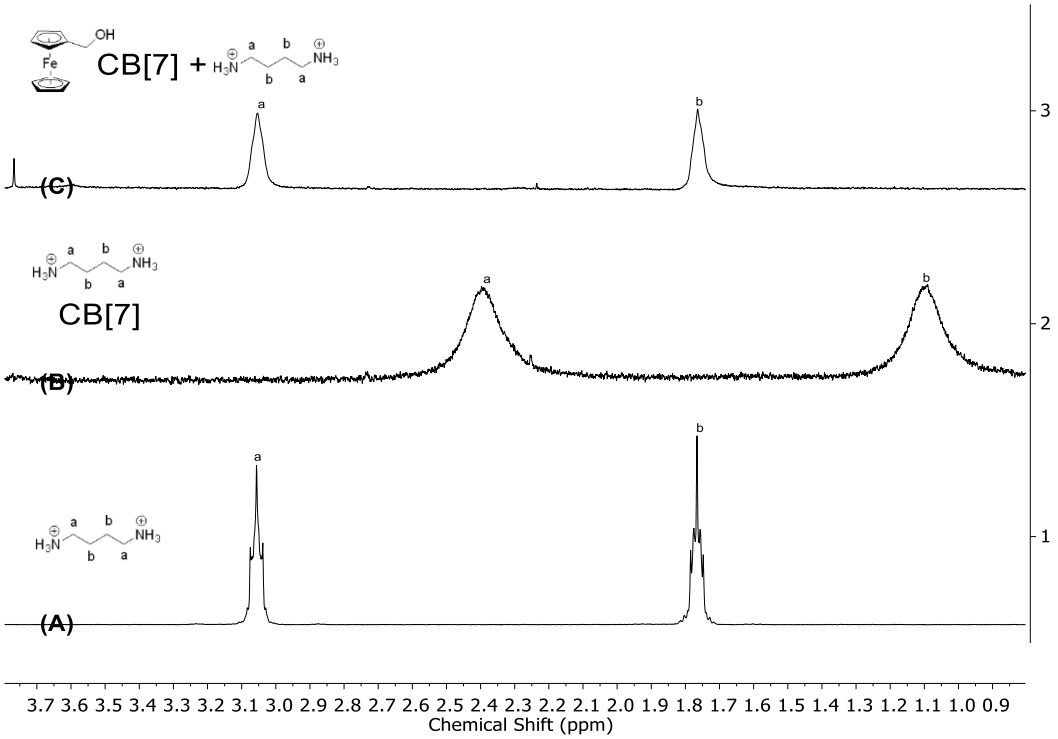


**Figure 16.** $^{1}$H NMR spectra ($D_2O$, 298 K, 400 MHz) of solutions of 1,4-diaminobutane (**Trace A**) and 1,4-diaminobutane -CB[7] (**Trace B**), and of a solution of FcMeOH-CB[7] following the addition of a stoichiometric amount of 1,4-diaminobutane (**Trace C**). All complexes were generated at a concentration of 2 mM. **Traces A – C, Bottom – Top.**

The displacement of FcMeOH from the macrocyclic cavity of CB[7] was probed by monitoring changes within the aliphatic region of the spectra only. The resonances associated with FcMeOH were broad, which was in part assumed to arise due to its limited solubility in aqueous media, and thus could not be assigned with 100 % confidence. Thus, it was assumed that upon the displacement of either hexylamine or 1,4-diaminobutane, FeMeOH-CB[7] formed at a rate considered quick on the NMR timescale. The binary complexes (hexylamine-CB[7] and 1,4-diaminobutane-CB[7]) were formed at a concentration of 2 mM to ensure that highly resolved $^{1}$H NMR spectra were acquired within the spectral region of interest.

In summary, FcMeOH and $MV^{2+}$ are capable of displacing both 1,4-diamonbutane and hexylamine form the hydrophobic cavity of CB[7], and it was for this reason that the recruitment of Eu.2 (**Figure 1**) was not attempted in a bid to acquire an interfacial, molecular switch. Although the addition of both FcMeOH and $MV^{2+}$ into solution induced displacement of the aliphatic guest moieties from the cavity of the macrocyclic host, it was not known which interaction(s) was responsible for driving the assembly of the receptive monolayer, **Figure 8**.

### 5.1.4 – Elucidating the Mechanism of Assembly of a SAM of CB[7] at APTES-Modified Substrates

To clarify the origin of self-assembly, that is highlight the interaction driving recruitment of the macrocyclic host (CB[7]) at the cationic, APTES-modified interface, **Figure 8**, further $^{1}$H NMR experiments were conducted involving $MV^{2+}$. The objective was to determine whether recruitment of the macrocyclic host species was driven electrostatically, or by the partial inclusion of APTES within the hydrophobic cavity of CB[7]. Alternatively, it is possible that the two occur concurrently.

Although an upfield chemical shift of the resonances associated with the protons of 1,4-diaminobutane ($H_a$ (+ 0.29 ppm) and $H_b$ (+ 0.30 ppm)) is observed when both $MV^{2+}$ and CB[7] are added *in-situ* to a solution of the diamine, **Figure 11** (**Inset**), the magnitude of such shifts is significantly reduced in comparison to those induced upon the addition of only CB[7] ($H_a$ (+ 0.72 ppm) and $H_b$ (+ 0.73 ppm)), **Figure 9**. Thus, when all three components are added *in-situ* within the NMR tube (**Figure 11, Trace C**), it is assumed that the diamine ligates to the periphery of the macrocyclic host, compared with $MV^{2+}$ which is encapsulated within its apolar cavity.

At the interface however, the situation is likely to be different. $MV^{2+}$ is not initially present in solution and thus cannot kinetically compete with the diamine for inclusion within the hydrophobic cavity of the macrocyclic host. Consequently, assembly of the interface proceeds unhindered, **Figure 8**, either *via* partial inclusion of the APTES tether or electrostatic ligation to the macrocyclic host. This was modelled in solution by $^{1}$H NMR spectroscopy, and the mechanism(s) by which the interface assembles and disassembles upon the addition of secondary guest species deduced.

Initially, 1,4-diaminobutane and CB[7] were added into solution and a $^{1}$H NMR spectrum recorded (**Figure 17, Trace A**), before the effect of adding a stoichiometric amount of $MV^{2+}$ was realised (**Figure 17, Trace B**). If prior inclusion of 1,4-diaminobutane into the hydrophobic cavity of CB[7] was observed, before it was subsequently displaced upon the addition of $MV^{2+}$, then it is likely that the partial inclusion of the APTES tether drives formation of the receptive SAM, **Figure 8**. In this case, it was expected for the aliphatic proton resonances of the diamine ($H_a$ and $H_b$) to shift downfield, to the value (**Figure 11** (**Inset**), $H_a$ (0.29 ppm) and $H_b$ (0.30 ppm)) understood to be indicative of the presence of the diamine at the periphery of the macrocyclic host, following the addition of the cationic, secondary guest species, $MV^{2+}$. However, if the initial spectrum, **Figure 17** (**Trace A**), resembled the one recorded following the addition of all three components *in-situ*, **Figures 11** and **17** (**Trace D**), then it can be concluded that electrostatic ligation, and not binary inclusion, is key. Electrostatic repulsion between the encapsulated $MV^{2+}$ motif and the protonated periphery of the interface is then expected to bring about the loss of the more stable host-guest complex from the interface.

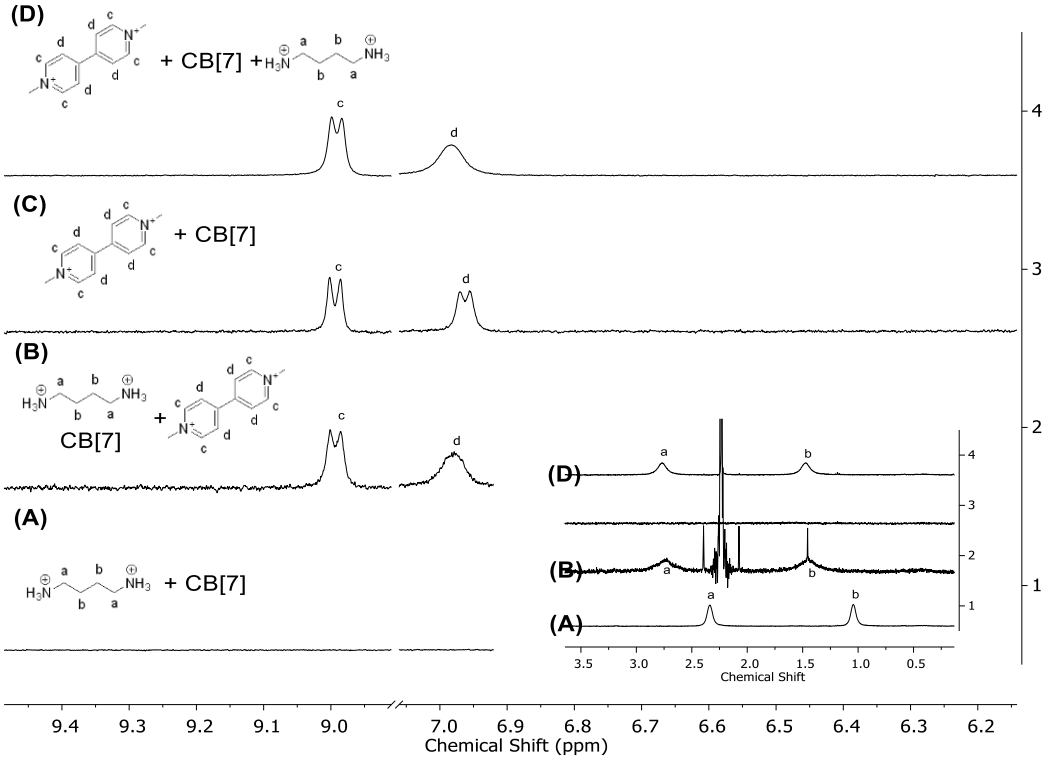


**Figure 17.** $^{1}$H NMR spectra ($D_2O$, 298 K, 400 MHz) of solutions of 1,4-diaminobutane-CB[7] (**Trace A**), (1,4-diaminobutane-CB[7]) + $MV^{2+}$ (**Trace B**), $MV^{2+}$-CB[7] (**Trace C**) and a 1:1:1 mixture of 1,4-diaminobutane, $MV^{2+}$ and CB[7] (**Trace D**). **Inset.** The aliphatic region of each $^{1}$H NMR spectrum. All complexes were generated at a concentration of 2 mM. **Traces A – D, Bottom – Top.**

**Figure 17** (**Trace B**) indicates that when a stoichiometric amount of $MV^{2+}$ is added to a solution of the binary complex, 1,4-diaminobutane-CB[7], $MV^{2+}$ inclusion takes preference and the diamine derivative migrates to the carbonyl periphery of the host, after being displaced from its hydrophobic cavity. That is, the resonances associated with the aliphatic protons of the diamine ($H_a$ and $H_b$) are shifted downfield to the chemical shift values observed for these protons when all three components, 1,4-diaminobutane, CB[7] and $MV^{2+}$, are added *in*-situ (**Figure 17** (**Inset, Trace D**)). Furthermore, the resonances associated with the protons of the bipyridine motif ($H_c$ and $H_d$) are positioned at chemical shift values indicative of binary inclusion (**Figure 17, Trace B**). The fact that the aliphatic resonances associated with the protons of the diamine ($H_a$ and $H_b$) still appear further upfield (**Trace B, Inset, Figure 17**) than they do in the absence of the macrocyclic host (**Trace A, Figure 9**), implies that the diamine remains associated with the periphery of the macrocyclic host following its displacement from the apolar cavity, and the subsequent formation of the more stable host-guest complex, $MV^{2+}$-CB[7]. This weak associative interaction is assumed to be nullified at the interface upon the introduction of the cationic derivative, $MV^{2+}$, which serves to electrostatically repel the APTES-tether. In addition, washing of the substrate is likely to remove any loosely associated, binary complex, ($MV^{2+}$-CB[7]), from the interface.

In summary, $^{1}$H NMR spectroscopy implies that formation of the CB[7]-functionalised interface (**Figure 8**) is driven by the inclusion of the APTES tether within the apolar cavity of CB[7], and that

disassembly of the monolayer arises following displacement of the diamine, and thus formation of the more favourable binary complex, $MV^{2+\cdot}$-CB[7]. This process is aided by the onset of intrinsic charge repulsion between the protonated terminus of APTES and $MV^{2+}$, which is now preferentially confined within the cavity of the macrocyclic host.

This concept of a secondary guest species competing for the hydrophobic cavity of a surface-confined macrocycle was further demonstrated in the analogous $^{1}$H NMR study, where $MV^{2+\cdot}$ was exchanged for 2,6-dihydoxynapthalene (2,6-Np), **Figures 19** and **20**. The objective of the experiment was to elucidate whether or not it was possible to preferentially recruit 2,6-Np into the hydrophobic cavity of CB[7], in the presence of 1,4-diaminobutane, whether 1,4-diaminobutane be present in solution (**Figure 18**) or already confined within the apolar cavity of the macrocyclic host, (**Figure 19**). If the interaction between the two formal charges present (the negatively charged carbonyl portals of CB[7] and the positively charged amine terminus of APTES) is significant in the assembly of the receptive interface, then it is likely that the recruitment of 2,6-Np is possible. Unlike upon the recruitment of $MV^{2+}$, charge repulsion would not be induced upon the attempted recruitment of 2,6-Np, thus migration of the host-guest complex, 2,6-Np-CB[7], is less likely to occur, especially given the diminished association constants reported for the complexation of functionalised naphthalene derivatives by CB[7] ($1.17 \times 10^{4}$ $M^{-1}$)[31], *cf*. that seen in the case of the binary complex formed between CB[7] and $MV^{2+}$ ($2.24 \times 10^{5}$ $M^{-1}$)[32].

In short, the viability of recruiting EuNap (**Figure 18**) at the interface (**Figure 8**) would be inferred, and successful recruitment of the lanthanide-containing species would allow for the generation of an optical assembly, the output from which could be modulated upon incorporation of a suitable metallocene-appended tether[5,6], such as 11-(ferrocenyl)undecanethiol or 6-(ferrocenyl)hexanethiol.

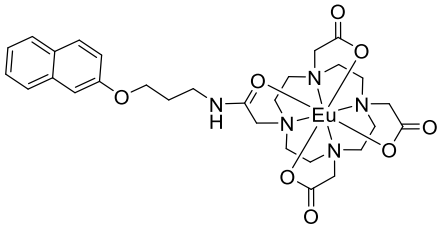


**Figure 18.** Naphthalene-appended, emissive europium derivative, EuNap.

The simultaneous inclusion of 2,6-Np within the cavity of CB[7] and association of 1,4-diaminobutane with the periphery of the macrocycle was desired. It has been demonstrated that the binding constant between $MV^{2+}$ and CB[7] is too great as to facilitate the surface confinement of $MV^{2+\cdot}$CB[7], whilst maintaining the peripheral association between the carbonyl portals of CB[7] and the amine terminus of APTES.

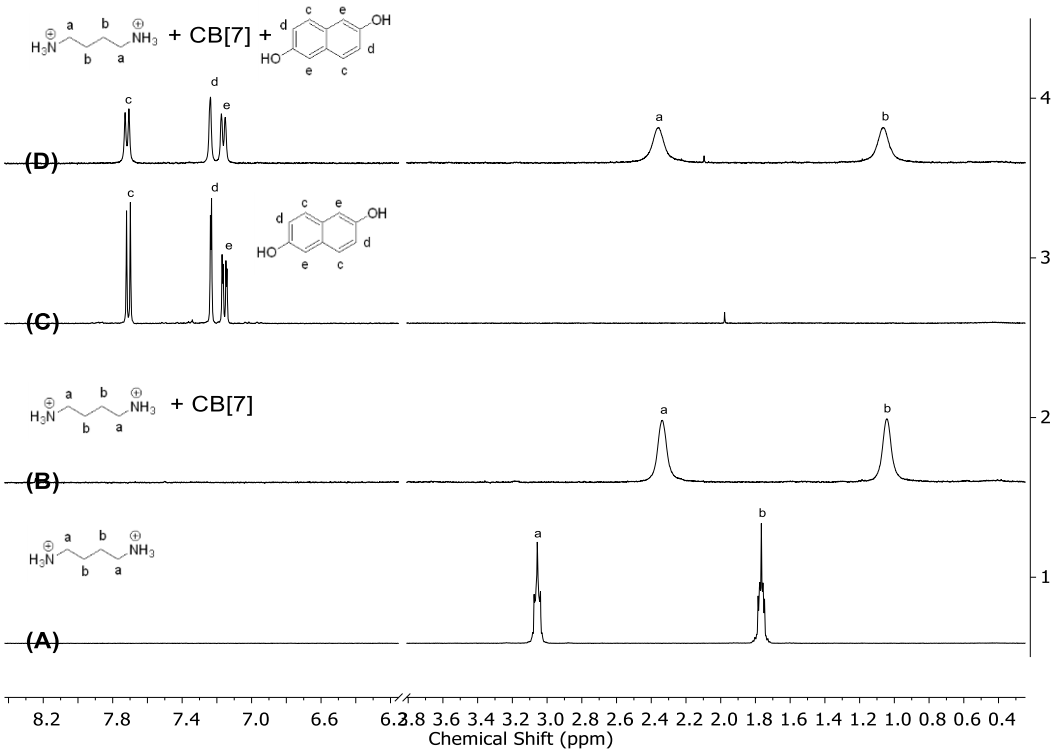


**Figure 19.** $^{1}$H NMR spectra ($D_2O$, 298 K, 400 MHz) of solutions of 1,4-diaminobutane (**Trace A**), 1,4-diaminobutane-CB[7] (**Trace B**), 2,6-Np (**Trace C**) and a 1:1:1 mixture of 1,4-diaminobutane, 2,6-Np and CB[7] (**Trace D**). All complexes were generated at a concentration of 2 mM. **Traces A – D, Bottom – Top.**

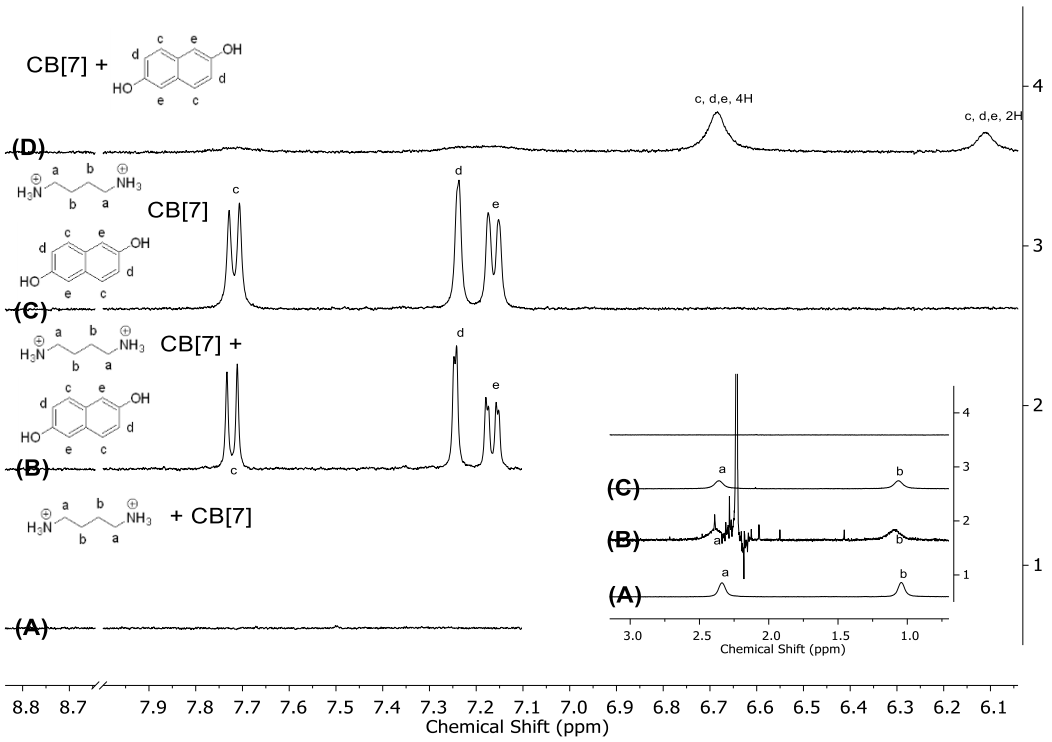


**Figure 20.** $^{1}$H NMR spectra ($D_2O$, 298 K, 400 MHz) of solutions of 1,4-diaminobutane-CB[7] (**Trace A**), (1,4-diaminobutane-CB[7]) + 2,6-Np (**Trace B**), a 1:1:1 mixture of 1,4-diaminobutane, 2,6-Np and CB[7] (**Trace C**) and 2,6-Np-CB[7] (**Trace D**). **Inset.** The aliphatic region of each $^{1}$H NMR spectrum. All complexes were generated at a concentration of 2 mM. **Traces A – D, Bottom – Top**.

Upfield chemical shifts of the resonances associated with the aliphatic diamine protons ($H_a$ and $H_b$), equivalent to those observed in the absence of 2,6-Np (**Figure 20** (**Inset, Trace B**)), were observed (**Figure 20** (**Inset, Trace B**) upon the addition of a stoichiometric amount of 2,6-Np to a solution of the binary complex, 1,4-diaminobutane-CB[7] complex. In addition, all multiplets present within the region expected for 2,6-Np remained unchanged ($H_c$, $H_d$ and $H_e$), irrespective of if the secondary guest species (2,6-Np) was initially present in solution, **Figure 19** (**Trace D**), or added upon the formation of the 1,4-diaminobutane-CB[7] complex, **Figure 20** (**Trace B**). These observations imply that 1,4-diaminobutane is preferentially encapsulated by the macrocyclic host, and highlights why the recruitment of naphthalene-appended (2,6-Np and EuNap) derivatives was not attempted at the constructed interface (**Figure 8**).

Contrary to what has been reported[21], it has again been demonstrated that the recruitment of CB[7] at the interface is not electrostatic in nature. Based on the observations made by $^1$H NMR spectroscopy, **Figure 21** illustrates what is likely to occur upon the attempted recruitment of 2,6-Np at a CB[7]-functionalised interface, and thus indicates why it would have not been possible to assemble an optically-responsive interface based on the recruitment of EuNap.

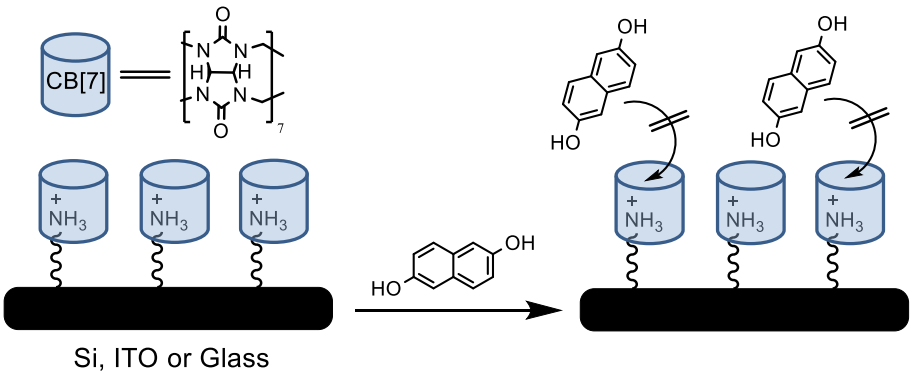


**Figure 21.** Recruitment of 2,6-Np (*n.b.* also valid for the recruitment of EuNap) at a CB[7]-functionalised interface.

In conclusion, it has been shown that a CB[7]-functionalised interface is generated upon exposure of a SAM of APTES, deposited on Si, to an aqueous solution of CB[7]. The data acquired implies that inclusion of the alkyl derivative, within the apolar cavity of the macrocyclic host species, drives the assembly of the analogous interface. It was originally hypothesised that this would not be the case, and in fact the electrostatic interaction, which is reported to occur between the carbonyl periphery of the host and the amine terminus of the interface, would be responsible. Furthermore, the assembly of the interface has been shown to be pH dependent in accordance with the pKa of the amine terminus of APTES. Inclusion of the alkyl derivative and thus recruitment of the macrocyclic host, CB[7], is only observed when the pH of the host solution is reduced (< 9.94), as to ensure protonation of the amine functionality[22-25]. However, this is not the case in solution where the inclusion of both hexylamine and 1,4-diaminobutane is not pH dependent. It was expected, in

accordance with the pH-dependent data acquired at the interface, that upon increasing the pH of the binary complex solutions, 1,4-diaminobutane-CB[7] and hexylamine-CB[7], *via* the addition of a 1 M $D_2O$ solution of NaOD, the binding constant would decrease, and thus the $^1H$ NMR resonances associated with both 1,4-diaminobutane and hexylamine would shift downfield. Such behaviour would signify deprotonation of the amine groups and release of the free guest species, 1,4-diaminobutane and hexylamine, into solution. However, no significant downfield shift was observed, **Figure 22**, suggesting that the ion-dipole interaction between the amine group(s) and the carbonyl portals of the macrocyclic host plays no role in the inclusion of the aliphatic guest derivatives in solution. Therefore, it is likely that the hydrophobic effect and hydrogen bonding interactions drive inclusion within solution *cf*. at the interface where inclusion is predominantly driven by electrostatic interaction.

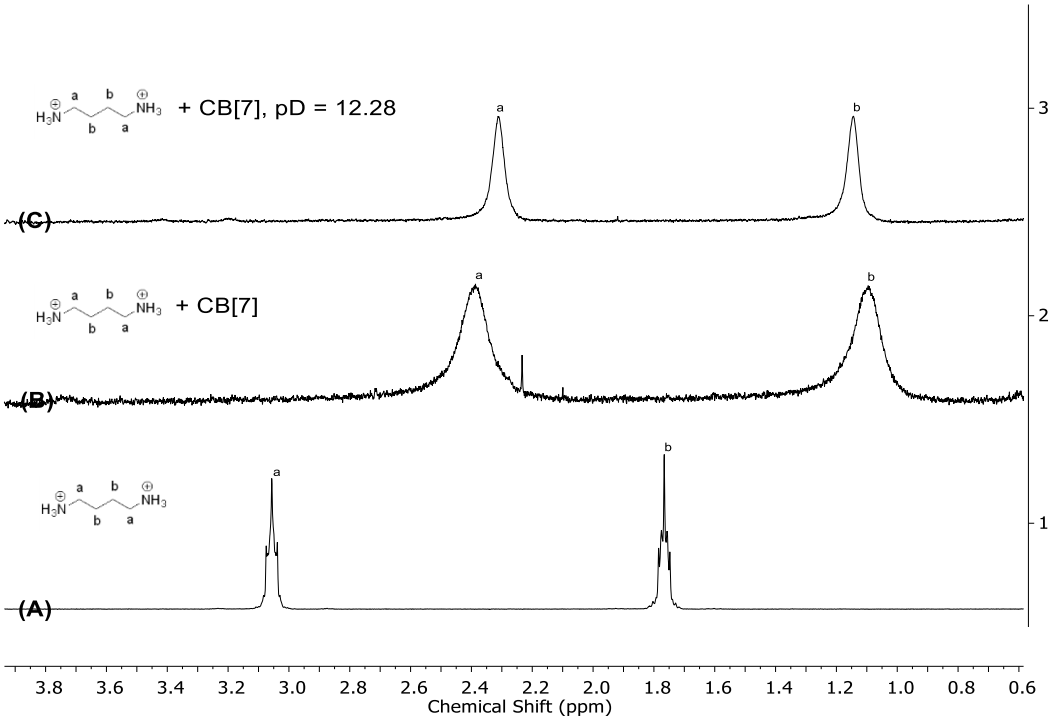


**Figure 22.** $^1H$ NMR spectra ($D_2O$, 298 K, 400 MHz) of solutions of 1,4-diaminobutane (**Trace A**), 1,4-diaminobutane-CB[7] (**Trace B**) and 1,4-diaminobutane-CB[7], pD 12.28 (**Trace C**). The pH of the binary complex solution was altered *via* the addition of a 1 M $D_2O$ solution of NaOD. No significant change in the spectrum of the binary complex (1,4-diaminobutane-CB[7]) arose upon increasing the pD of the solution; the guest species remained confined within the apolar cavity of the macrocyclic host upon deprotonation of its terminal amine groups, that is the resultant spectrum (**Trace C**) did not resemble that of 1,4-diaminobutane in solution, **Trace A**; *cf.* when FcMeOH was added to a solution of the binary complex, **Figure 14**. The above observations were also made in the case of hexylamine. All complexes were generated at a concentration of 2 mM. **Traces A – C, Bottom – Top**.

It is still not known as to why the complexation of amine-terminated derivatives appeared to be pH-dependent at the interface, but not in solution. It is reasonable to suggest that at the interface, on which a highly ordered, dense, silanated monolayer has been deposited, the likelihood of the macrocyclic host species being able to penetrate the monolayer, in order for the recruitment of CB[7]

to be driven by the hydrophobic effect and hydrogen bonding interactions, is low. This is not the case in solution where the increased number of degrees of freedom permits recruitment of the macrocyclic host species *via* the hydrophobic effect and hydrogen bonding interactions. In short, at the interface, the macrocyclic host species is recruited to the underlying monolayer, with electrostatic interaction(s) dominating, **Figure 23**, whilst in solution recruitment of the aliphatic guest species is driven by the presence of both the hydrophobic effect and hydrogen bonding interactions, **Figure 23**, and is therefore less dependent on pH.

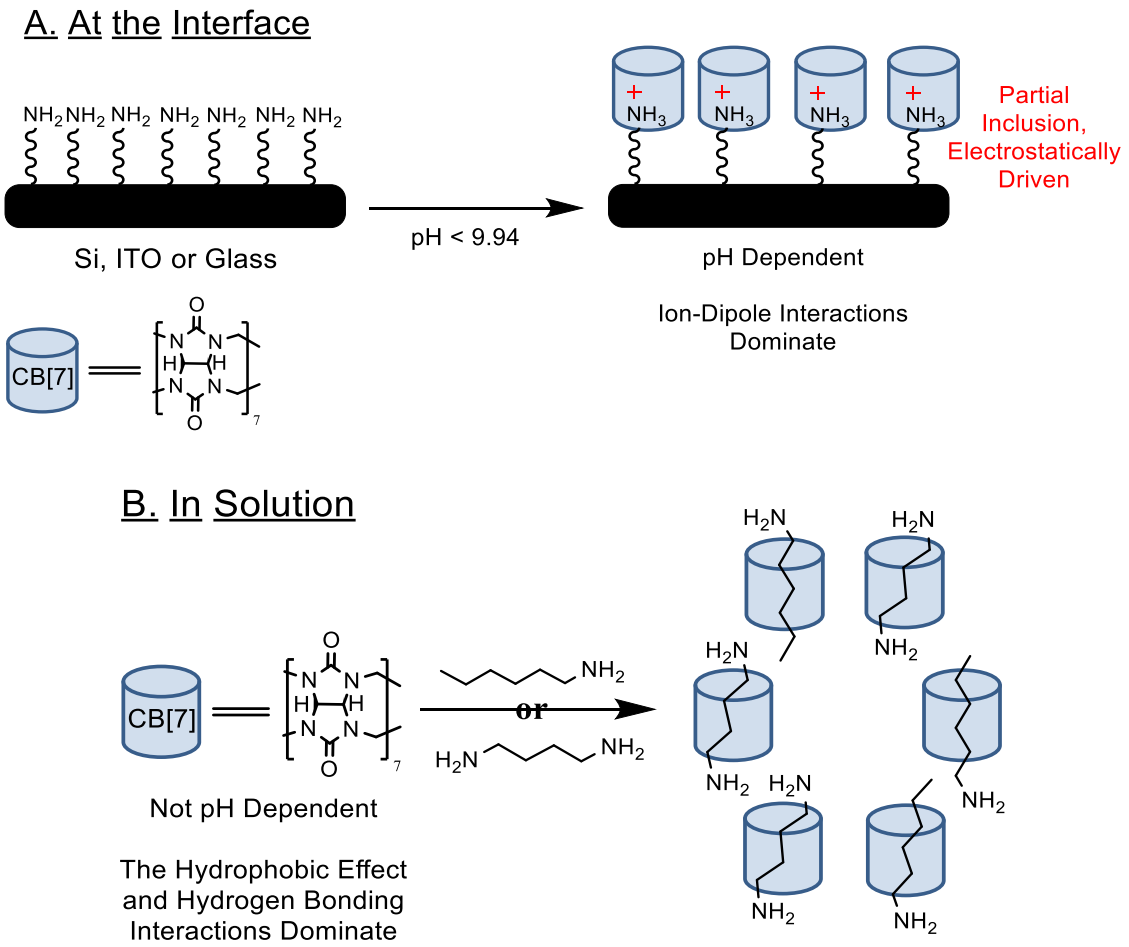


**Figure 23.** Interactions governing the recruitment of CB[7] at the interface (**Top**), and the complexation of hexylamine and 1,4-diaminobutane by CB[7] in solution (**Bottom**).

Furthermore, the attempted recruitment of both neutral (2,6-Np, FcMeOH) and cationic ($MV^{2+}$) guest species to the CB[7]-functionalised interface proved unsuccessful. The preferential recruitment of secondary guest species brought about the generation of more stable inclusion complexes, with the only exception being 2,6-Np. 2,6-Np is unable to displace primary amine derivatives from the cavity of CB[7]. At the interface, it is presumed that the more stable inclusion complexes subsequently migrate into solution upon the displacement of the 'included' APTES tether. Since the molecular recognition properties of CB[7] were essentially nullified by means of this assembly route, an alternative method of generating a receptive interface was sought after.

### 5.1.5 – Maintaining the Recognition Properties of CB[7] at the Interface

To ensure that the carbonyl portals of the macrocyclic host were available to drive host-guest complexation, a nitrene based approach was explored in a bid to covalently tether CB[7] to both Si and Au[33] (**Experimental, 7.3.6**). At Au, it was thought that any recruited lanthanide complex would be at a distance of ≥ 3.2 nm (MM2, Chem3D 15.0) from the quenching, metallic interface, and therefore an emissive signature would be detected upon excitation of an appropriate chromophore, in the absence of both Förster Resonance Energy Transfer (FRET) and Surface Energy Transfer (SET), *cf*. the assembly generated at Au upon the physical adsorption of CB[7], **Figure 5** (**Left**). The objective was to generate azide-functionalised surfaces from which highly reactive singlet or triplet nitrene could be generated (UV irradiation (254, 366 nm))[33-36]. This highly reactive species could then be inserted into either the C-H bond located at the 'waist' of the CB[7] moiety, or into the bridging $CH_2$ groups, **Figure 24**.[33]

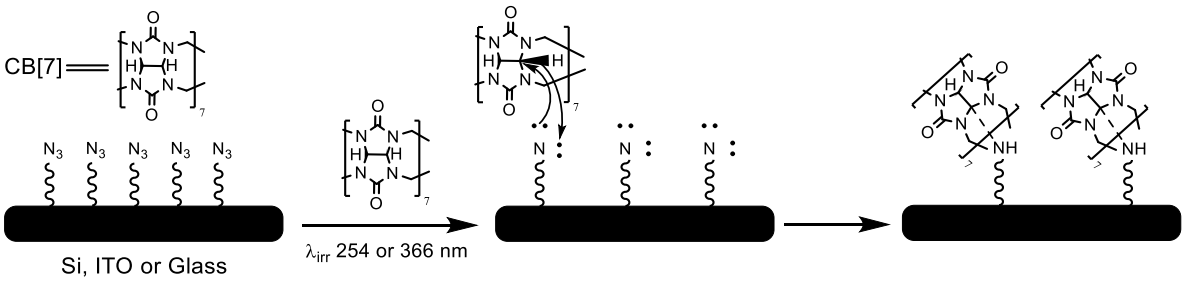


**Figure 24.** Formation of SAMs of CB[7] on Si and Au by way of nitrene insertion.[33]

Unfortunately, prior to the attempted recruitment of a suitable *d-f* dyad, negative controls were observed at Si, that is upon exposure of the irradiated azido interface to an aqueous solution of CB[7], a large degree of unwanted association of the macrocyclic host was observed. Ellipsometric film thickness increases of ≈ 15 (± 0.2) nm were recorded over duplicate samples, when a film thickness increase of 0.9 (± 0.2) nm was expected given the height of the macrocyclic cavitand[20]. The excess organic material could not be removed by means of sonication in either $H_2O$ or dimethyl sulfoxide (DMSO). In addition, when the insertion reaction was performed at Au, no change in either film thickness or surface wettability was recorded upon irradiation of the interface with light of wavelengths 366 and 254 nm. Light of wavelength 254 nm was applied because CB[7] is reported to be chemically inert and the insertion reaction associated with a high activation energy.[37,38,39] However, utilising high energy radiation is likely to have brought about degradation of the azido-terminated monolayer. Due to the lack of nitrene insertion observed, **Figure 24**, the solution phase functionalization of CB[7] was probed, **Figure 25**.

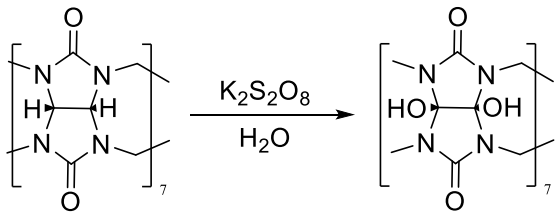


**Figure 25.** Hydroxylation of CB[7].

To screen the validity of the oxidative approach reported by Kim *et al*. in 2003[37], **Figure 25**, CB[6] was reacted with potassium persulphate to obtain perhydroxy-CB[6]. The potassium ion complex of perhydroxy-CB[6] yielded (*m / z* 1132.27, 1148.31 (MALDI-TOF), $((HO)_{6,7}CB[6]) + K^+$, **Experimental, 7.17**), but the CB[7] analogue could not be detected. This was not unexpected given the fact the perhydroxylated products of the higher homologues (CB[7] and CB[8]) are reported to be inherently less stable[37].

It was anticipated that the highly reactive product, perhydroxy-CB[7], would be isolated, and it used as a building block in the synthesis of CB[7]-functionalised derivatives that could be directly deposited at Si or Au (**Figure 26**), respectively. Research aimed at obtaining these derivatives (**Figures 25** and **26**) is still ongoing.

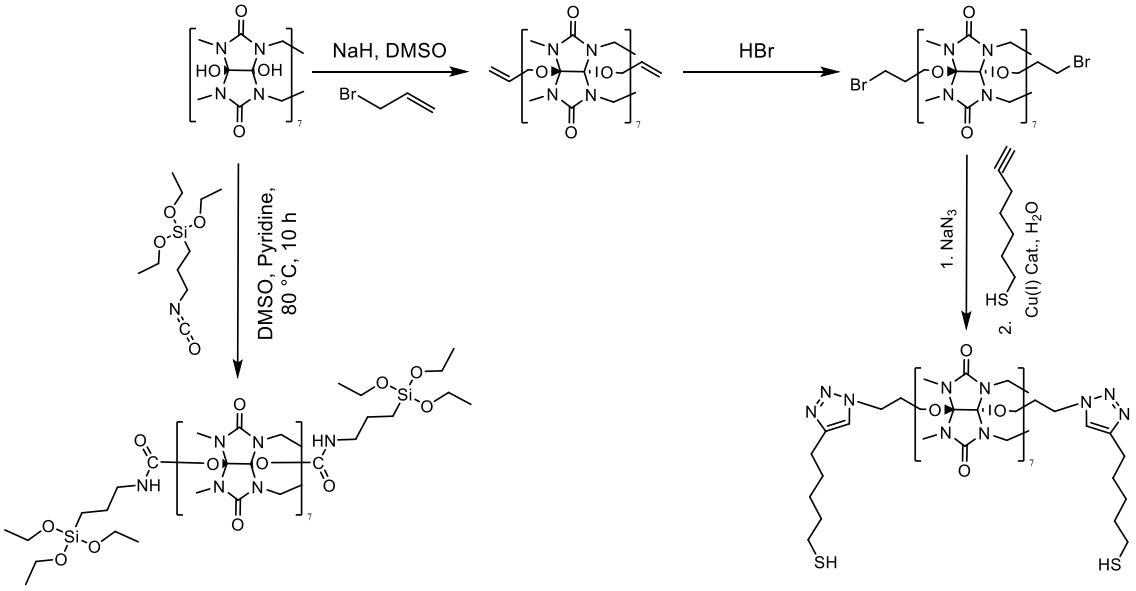


**Figure 26.** Functionalisation of CB[7].

In conclusion, the formation of a receptive CB[7]-functionalised interface proved problematic. An assembly was not generated in which the host's molecular recognition ability remained unaffected. The competitive inclusion of a cationic surface tether prevented the electrostatically-induced recruitment of CB[7], whilst CB[7]'s inherent inertness prohibited its structural functionalization; the utilisation of a free radical generated in solution, and conventional synthetic methodologies were ineffective. Thus, focus shifted towards generating the polymeric-like assembly first highlighted in

**Chapter 4** (**Figure 22**), where it was believed that CB[7] would be incorporated into the molecular architecture with the same level of host-guest affinity it displays in solution.

## 5.2 – Utilising Charge-Transfer in the Surface Assembly of Switchable, Lanthanide-Appended Molecular Systems

1:2 Heteroternary complex formation was exploited in a bid to assemble the interface alluded to in Chapter 4 (**Figure 22**). It was anticipated that the interface could be systematically assembled, thus ensuring that CB[*n*] is incorporated into the molecular architecture with the same level of host-guest affinity it displays in solution. In addition, it was assumed that the distance between the lanthanide centre and the metallic interface could be optimised as to permit the detection of optical output from the analogous non-aromatic assembly generated in the absence of charge-transfer (**Chapter 4, Figure 23**). It was expected for an efficient, interfacial molecular switch to be yielded upon the integration of either 6-(mercaptohexyl)ferrocene or 11-ferrocenyl-1-undecanethiol.

### 5.2.1 – Formation and Characterisation of $MV^{2+}$-Functionalised Monolayers

To exploit 1:2 heteroternary complex formation in the assembly of lanthanide-appended molecular films, stable SAMs of $MV^{2+}$ were a prerequisite; 1-(10-mercaptodecyl)-1'-methyl-[4,4'-bipyridine]-diium bromide was synthesised and characterised using CV (**Figure 28**), $^{1}$H NMR (**Experimental**, **7.15**) and UV-Vis spectroscopy (**Appendix**, **8.14, Figures 58** and **59**), prior to the derivative being deposited at Au, **Figure 27**.

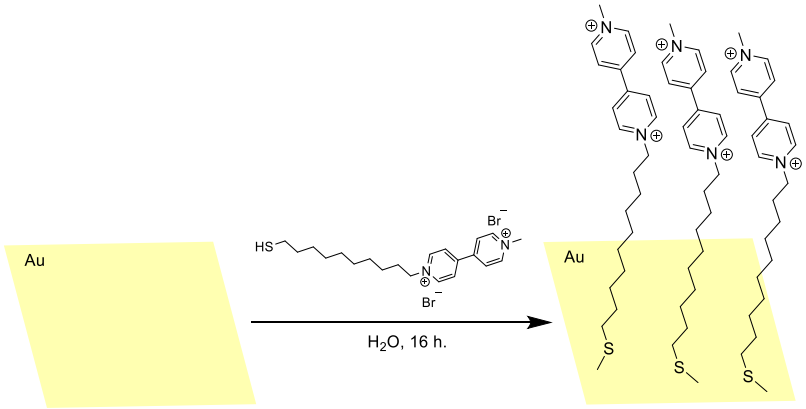


**Figure 27.** Deposition of 1-(10-mercaptodecyl)-1'-methyl-[4,4'-bipyridine]-diium bromide at Au substrates. Deposition of the thiolate was undertaken from both aqueous ($H_2O$) and non-aqueous media (AcN, $CH_2Cl_2$), depending on the identity of the counter ion(s) present (aqueous: $Br^-$ or $Cl^-$, non-aqueous: $PF_6^-$).

Formation of the desired monolayer(s) (**Experimental, 7.3.2**) was inferred from the resultant voltammetric response, **Figure 28**, and the ellipsometric film thickness values acquired across multiple samples. The surface concentration of the deposited thiol ($5.5 \pm 0.75 \times 10^{-11}$ mol cm$^{-2}$) was quantified by normalising the integrated faradaic response ($MV^{2+}$ / $MV^{+\cdot}$, $E_{1/2}$ -520 mV *vs*. SCE) for

the geometric surface area of the electrode on which the monolayer was deposited (**Experimental, 7.7.2**). The geometric area of each electrode was established prior to use by integrating the peak associated with the reduction of the Au/α gold oxide layer (+750 → +1000 mV, *vs* SCE), revealed upon sweeping (sweep rate: 100 mV $s^{-1}$) the potential of the electrode in a 100 mM aqueous solution of $H_2SO_4$[40] (**Experimental, 7.2.1**).

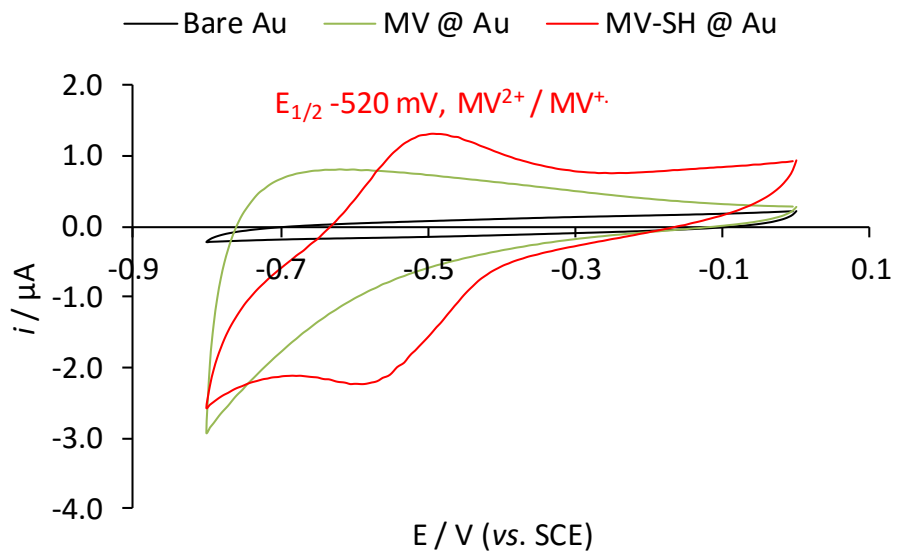


**Figure 28.** Cyclic voltammograms recorded following the deposition of 1-(10-mercaptodecyl)-1'-methyl-[4,4'-bipyridine]-diium bromide at Au (**Red**), and upon exposure of a bare Au electrode (**Black**) to a 5 mM aqueous solution of $MV^{2+}$ (**Green**).

Even though the $MV^{2+}$-functionalised monolayers remained stable following repeated cycling (≤ 200 scans) within the electrochemical window of interest (0 → -800 mV *vs*. SCE), that is the peak current associated with the $MV^{2+}$ / $MV^{+\cdot}$ redox couple remained constant, the surface coverage calculated for each ($5.5 \pm 0.75 \times 10^{-11}$ mol $cm^{-2}$) was significantly lower (≈ 4 % of theoretical) than that predicted by way of approximation (MM2) in Chem3D 15.0, $13.2 \times 10^{-10}$ mol $cm^{-2}$. This estimate was calculated based on the size of the bipyridinium motif, whilst the error associated with the surface coverage acquired has been calculated based on the difference in the concentration of the thiol deposited across five separately prepared electrodes, with the error being 3SD from the mean.

In addition, ellipsometric film thickness measurements infer that 1-(10-mercaptodecyl)-1'-methyl-[4,4'-bipyridine]-diium bromide is unable to deposit surface normal, as is reported for alkylated thiols[41]. An increase in film thickness of 0.9 ± 0.2 nm was consistently acquired, when an increase of 2.1 nm was expected (MM2, Chem3D 15.0) given the dimensions of the synthesised thiolate. It is understood that this discrepancy arises because neighbouring $MV^{2+}$ moieties act to electrostatically repel one another, thus preventing surface normal deposition of the derivative.

In a bid to increase the surface coverage of 1-(10-mercaptodecyl)-1'-methyl-[4,4'-bipyridine]-diium bromide, by way of minimising this repulsive interaction, and bring about surface normal alignment

of the thiolate, the deposition of the preformed binary complexes ($MV^{2+}$-SH,CB[7]) and ($MV^{2+}$-SH,CB[8]) was probed, **Figure 29**.

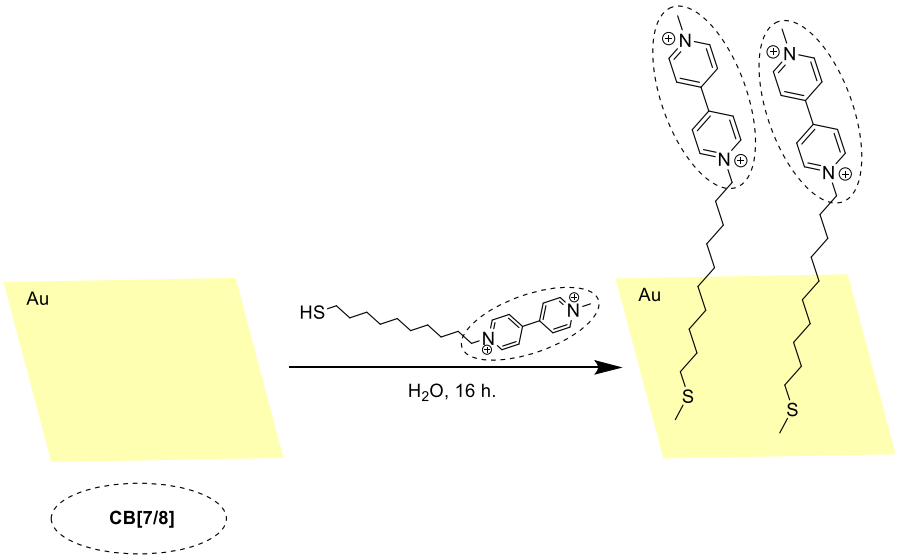


**Figure 29.** Deposition of ($MV^{2+}$-SH,CB[7]) and ($MV^{2+}$-SH,CB[8]) at Au.

The effect of covalently tethering 1-(3-aminopropyl)-1'-methyl-[4,4'-bipyridine]-1,1'-diium ($MVNH_3^+$, **Experimental, 7.14**) to an underlying SAM of MHDA, **Figure 30** (**Top**), and utilising the Huisgen cycloaddition reaction (**Experimental, 7.3.4**) between an azido-terminated interface and 1-(3-azidopropyl)-1'-methyl-[4,4'-bipyridine]-1,1'-diium ($MVN_3^+$, **Experimental, 7.14**), **Figure 30** (**Bottom**), was also probed as a means of alleviating this problem in a bid to increase the surface concentration of the redox active moiety, $MV^{2+}$, to which CB[8] could be recruited and a 1:2 heteroternary complex subsequently generated.

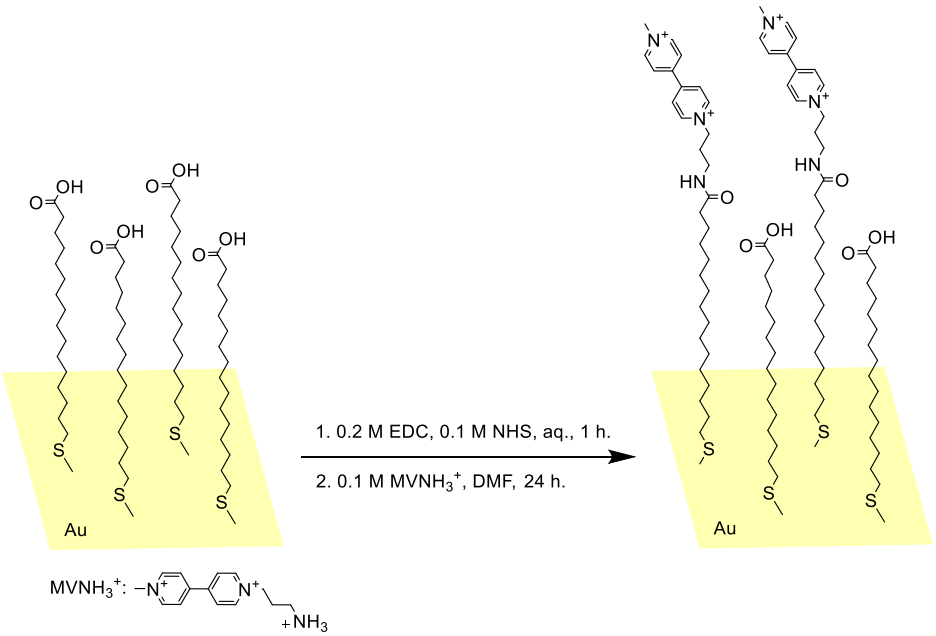

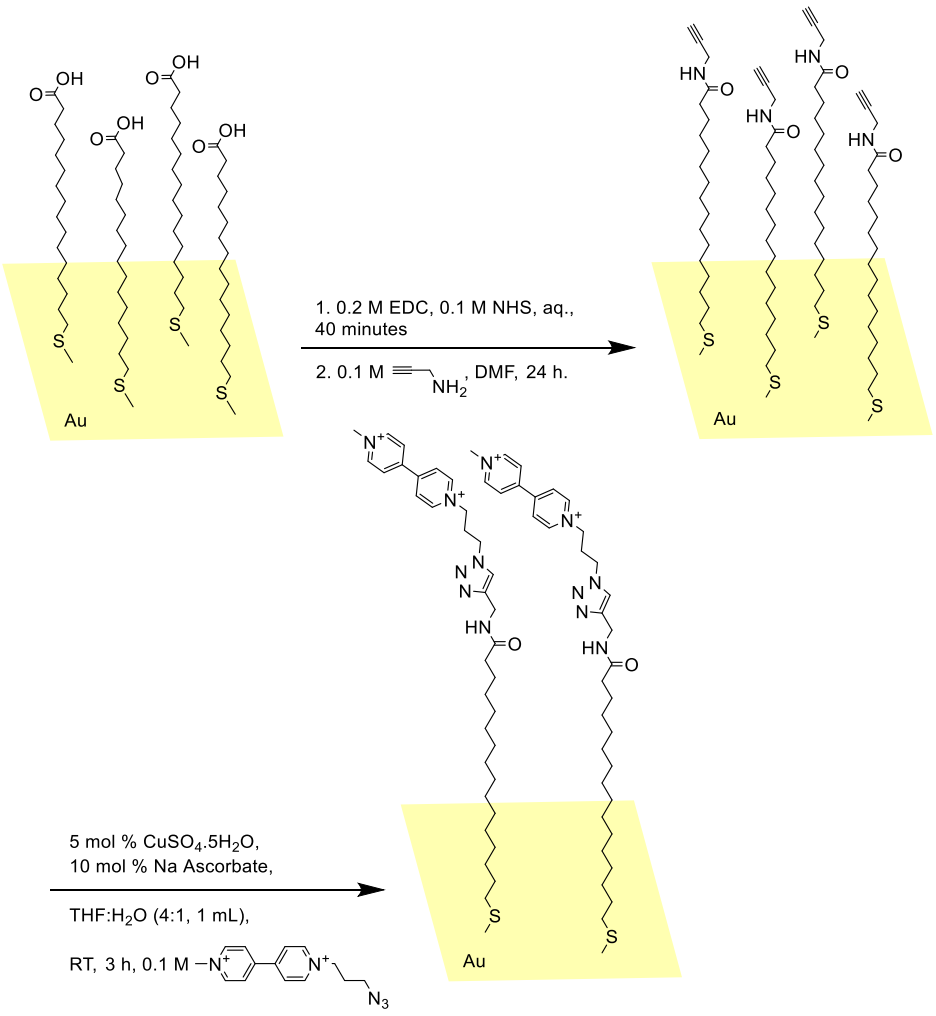


**Figure 30.** Covalent attachment of $MVNH_3^+$ to a SAM of MHDA (**Top**), and $MVN_3^+$ to an azido-terminated interface (**Bottom**). $MVNH_3^+$ and $MVN_3^+$ were synthesised by Alexander Hess of the Paul Beer Group (University of Oxford). All precursor molecular films were characterised by cyclic voltammetry (diffusive redox probe and thiolate stripping) and ellipsometric film thickness measurements prior to use, as to ensure that the Au surface was passivated and that the SAMs formed were uniform in structure.

The covalent attachment of both $MVNH_3^+$ and $MVN_3^+$ to underlying SAMs of varying chain length did not yield the desired molecular films (**Figure 30**) with great enough stability. That is, formation of the neutral quinoid compound, **Figure 31**, was consistently observed, particularly in the presence of a trace amount of triethylamine ($Et_3N$) which was required to bring about the deprotonation of $MVNH_3^+$, and thus facilitate carbodiimide coupling (**Experimental, 7.3.3**) at the interface, **Figure 41** (**Top**).

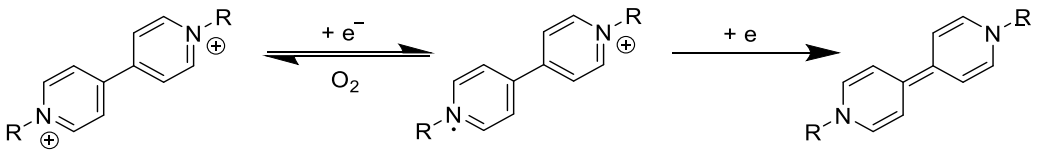


**Figure 31.** Formation of the cyclic diketone analogue of paraquat.

Irreversible formation of the quinoid analogue brought about the expected change in the colour of the deposition solution (clear to yellow), and a progressive reduction in the magnitude of the integrated charge associated with the surface-tethered, $MV^{2+}$ derivative.

However, deposition of the 1:1 binary complexes, ($MV^{2+}$-SH,CB[7]) and ($MV^{2+}$-SH,CB[8]), **Figure 29**, proved successful, as was shown by CV data, **Figure 32**, which indicated the presence of the paraquat-centred redox couple at the interface.

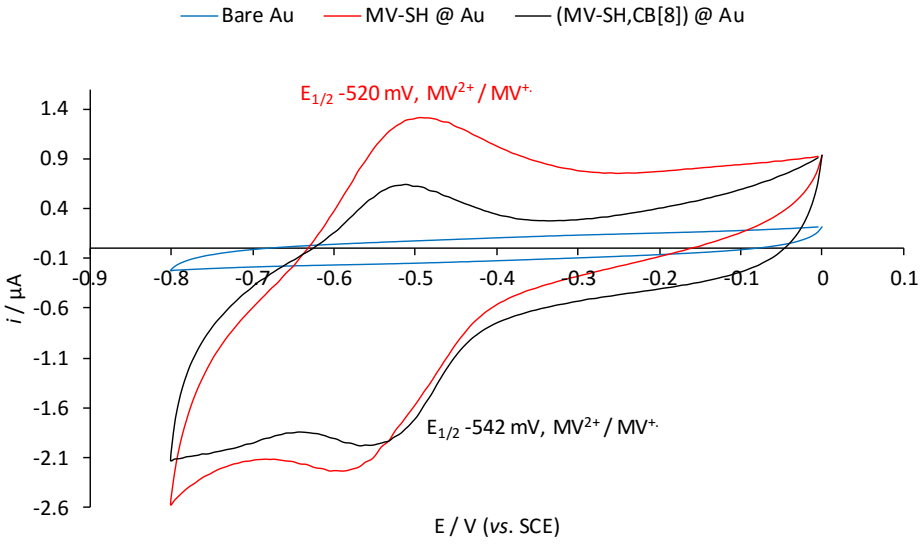


**Figure 32.** Cyclic voltammograms recorded following the deposition of 1-(10-mercaptodecyl)-1'-methyl-[4,4'-bipyridine]-diium bromide (**Red**) and 1-(10-mercaptodecyl)-1'-methyl-[4,4'-bipyridine]-diium bromide-CB[8] (**Black**) at Au (**Blue**).

Although a greater surface coverage of the redox-active moiety ($2.9 \pm 0.20 \times 10^{-11}$ mol $cm^{-2}$, ≈ 25 % of the theoretical surface coverage calculated based on the size of the macrocyclic host, CB[8]) was not acquired, the resultant monolayers were seen to align normal to the surface. An ellipsometric film thickness of 2.1 ± 0.2 nm was consistently acquired in the presence of the macrocyclic hosts, CB[7] and CB[8]. This value decreased to that acquired previously (0.9 ± 0.2 nm) upon removal of the macrocyclic host species, following the addition of the more competitive guest moiety, AdHCl, into solution. This demonstrates that prior inclusion of the $MV^{2+}$ terminus within the apolar cavity of the macrocyclic host(s) serves to prevent collapse of the monolayer, and minimises interfacial repulsion between neighbouring $MV^{2+}$ moieties. It is likely that a reduction in interfacial repulsion arises because the presence of either macrocyclic host induces greater spatial separation within the monolayer structure, that is the $MV^{2+}$ termini are segregated. In addition, the 22 mV cathodic shift of the half-way potential of the $MV^{2+}$ / $MV^{+\cdot}$ redox couple observed upon deposition of the binary complex, ($MV^{2+}$-SH,CB[8]), reveals that the cation radical form of the $MV^{2+}$ terminus interacts slightly less strongly with CB[8][42]. It also implies that the $MV^{2+}$ terminus of 1-(10-mercaptodecyl)-1'-methyl-[4,4'-bipyridine]-diium bromide is encapsulated within the apolar cavity of the macrocyclic host species at the periphery of the interface, as opposed to being weakly associated

with it. An anodic shift of 22 mV arose following displacement of the CB[8] moiety, whilst no shift in the half-way potential of the $MV^{2+}$ / $MV^{+\cdot}$ redox couple was observed following immersion in a solution of the binary complex, (AdHCl,CB[8]), **Figure 33**. This was expected given the difference in association constants of the two binary complexes, (AdHCl,CB[8], logK 11.63)[19] and ($MV^{2+}$-SH,CB[8], logK 5.04)[19].

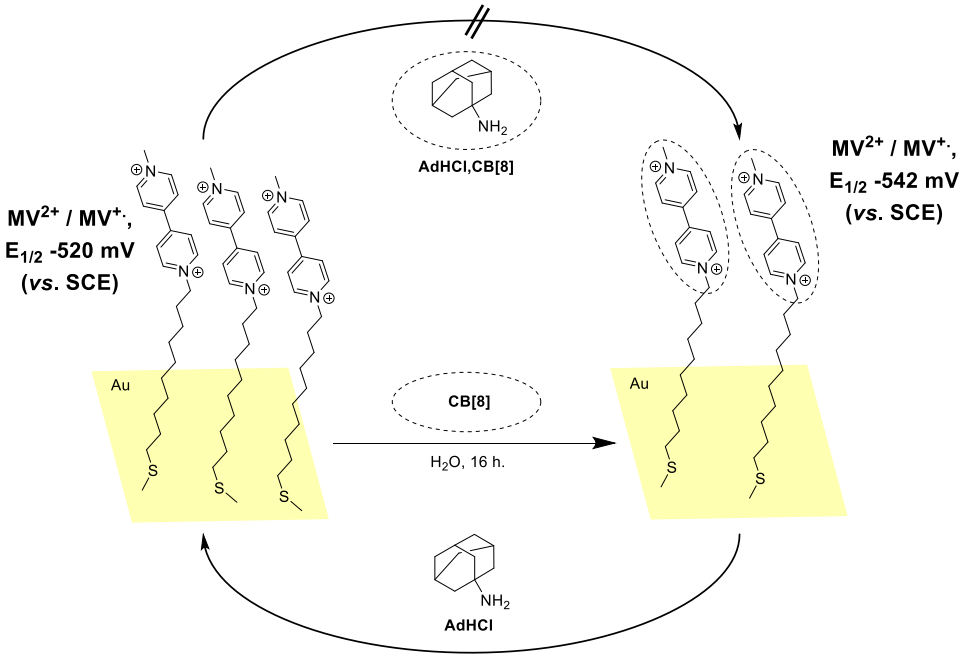


**Figure 33.** Reversible formation of the binary complex, $MV^{2+}$-SH,CB[8], at a SAM of 1-(10-mercaptodecyl)-1'-methyl-[4,4'-bipyridine]-diium bromide deposited at Au.

Thiolate stripping peaks ($E_{1/2}$ -1052 mV, *vs.* Ag Wire) were observed in all cases, **Figure 34**, dismissing the possibility that the macrocyclic cavitand (CB[7] or CB[8]) deposits at the interface in preference to S-Au bond formation.

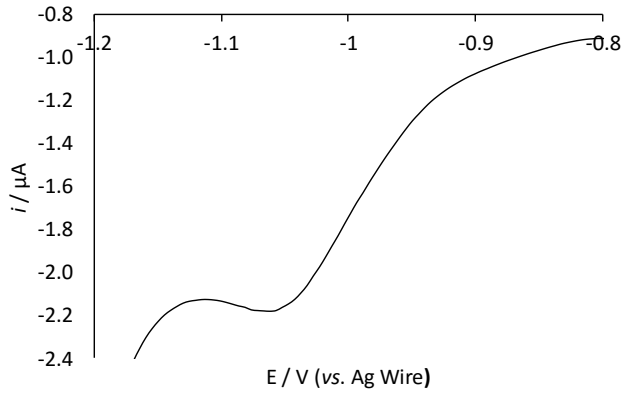


**Figure 34.** Cyclic voltammogram recorded following the reductive desorption of 1-(10-mercaptodecyl)-1'-methyl-[4,4'-bipyridine]-diium bromide-CB[8] from the interface.

In summary, the deposition of 1-(10-mercaptodecyl)-1'-methyl-[4,4'-bipyridine]-diium bromide leads to the formation of monolayers in which the thiolate is not orientated surface normal, whilst formation of the quinoid analogue prevents the covalent attachment of $MVNH_3^+$ and $MVN_3^+$ to appropriately functionalised interfaces. Upon prior inclusion within the cavity of either CB[7] or CB[8], 1-(10-mercaptodecyl)-1'-methyl-[4,4'-bipyridine]-diium bromide is deposited surface normal, with the macrocyclic host residing at the periphery of the interface, as implied by the appearance of a thiolate stripping peak and a cathodic shift (22 mV *vs.* SCE) of the $MV^{2+}$ / $MV^{+\cdot}$ redox couple. This increase in surface normality was deemed significant because the stepwise assembly of the lanthanide-appended interface, **Chapter 4**, **Figure 22**, is likely to have proven very inefficient in the presence of a poorly formed monolayer, where the recognition properties of CB[8] were likely to have been hindered and the lanthanide centre in much closer proximity to the metallic substrate than was desired.

### 5.2.2 – Towards the Stepwise Growth of Lanthanide-Appended Interfaces

Following the formation (**Experimental, 7.16**) and characterisation of the $MV^{2+}$-CB[8]-functionalised interface, **Figure 29**, the recruitment of 1-methyl-1'-(10-(naphthalen-2-yloxy)decyl)-[4,4'-bipyridine]-1,1'-diium bromide iodide was probed in a bid to obtain a bilayer from which further growth could occur, **Figure 35**.

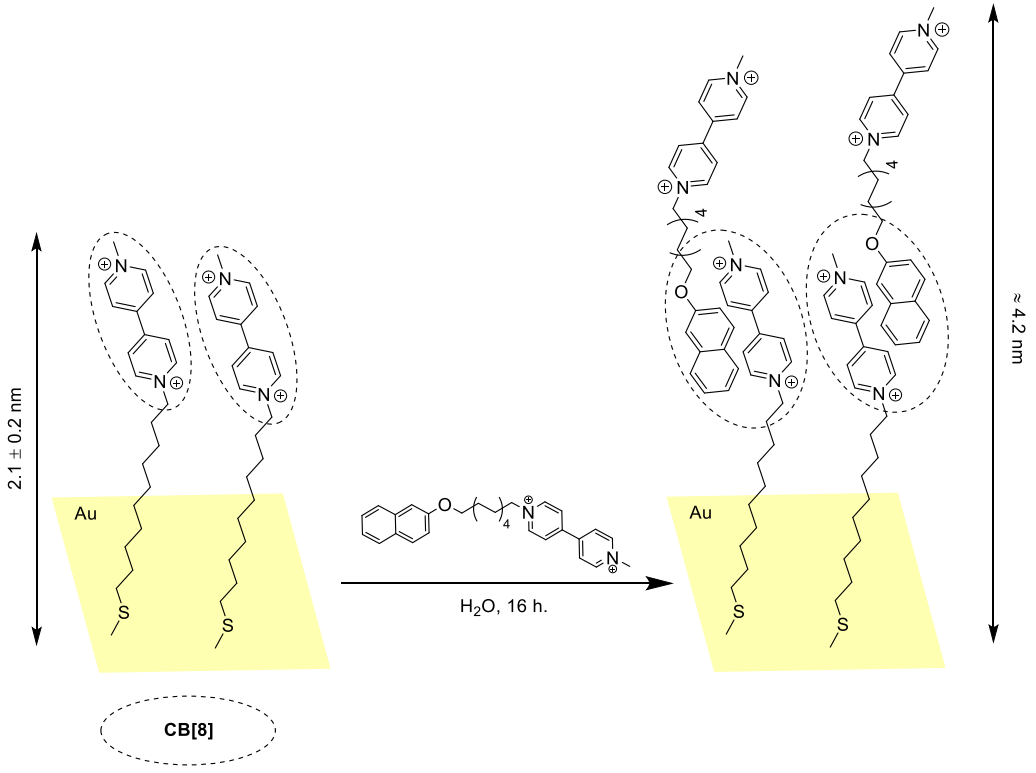


**Figure 35.** Forming a bilayer at the interface by exploiting 1:2 heteroternary complex formation. Quoted interfacial distances were determined by either ellipsometry, that is if an error bar is given, or estimated by a minimisation approach (MM2) conducted in Chem3D 15.0. This holds from here on in, unless otherwise stated.

Formation of the bilayer, following the attempted recruitment of 1-methyl-1'-(10-(naphthalen-2-yloxy)decyl)-[4,4'-bipyridine]-1,1'-diium bromide iodide at a $MV^{2+}$-CB[8]-functionalised interface, was not successful; the desired increase (+ 2.1 nm, as modelled (MM2) in Chem 3D 15.0) in ellipsometric film thickness was not observed. The ellipsometric film thickness declined from 2.1 ± 0.2 nm to that observed for a monolayer of 1-(10-mercaptodecyl)-1'-methyl-[4,4'-bipyridine]-diium bromide, 0.9 ± 0.2 nm (**Figure 27**), suggesting that a 1:1 *intra*molecular heteroternary complex had formed, **Figure 36**, in preference to the desired 1:1 *inter*molecular heteroternary complex, **Figure 35**. Furthermore, an anodic shift in the half-way potential of the encapsulated $MV^{2+}$ terminus ($MV^{2+}$ / $MV^{+\cdot}$, $E_{1/2}$ -520 mV *vs*. SCE) was observed, as opposed to a further cathodic shift, upon the attempted recruitment of 1-methyl-1'-(10-(naphthalen-2-yloxy)decyl)-[4,4'-bipyridine]-1,1'-diium. This was not unexpected given loss of the macrocyclic host and the fact that no further cathodic shift in the half-way potential of $MV^{2+}$ was observed upon formation of the model ternary complex, ($MV^{2+}$, 2,6-Np)-CB[8], in solution.

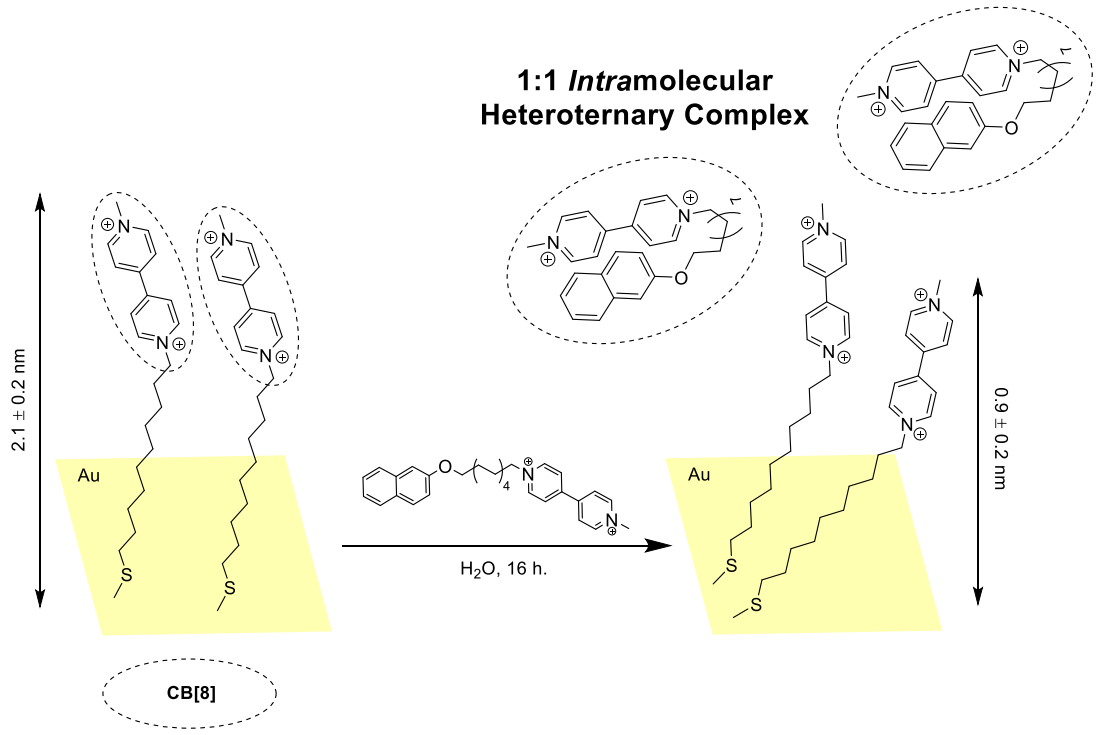


**Figure 36.** Formation of the 1:1 *intra*molecular heteroternary complex upon recruitment of 1-methyl-1'-(10-(naphthalen-2-yloxy)decyl)-[4,4'-bipyridine]-1,1'-diium bromide iodide at a $MV^{2+}$-CB[8]-functionalised interface.

It was assumed that the flexibility of the alkyl linker within 1-methyl-1'-(10-(naphthalen-2-yloxy)decyl)-[4,4'-bipyridine]-1,1'-diium would not be great enough as to facilitate the formation of a 1:1 *intra*molecular heteroternary complex in which both the N,N′-dimethyl-4,4′-bipyridinium and naphthalene units are confined within the hydrophobic cavity of CB[8]. In addition, it was assumed that the reduced number of degrees of freedom present at the interface would favour formation of the *inter*molecular analogue.

Prior to investigating this further by $^1$H NMR spectroscopy, the recruitment of 1-methyl-1'-(10-(naphthalen-2-yloxy)decyl)-[4,4'-bipyridine]-1,1'-diium bromide iodide-CB[7] was probed, **Figure 37**. It was thought that the presence of CB[7] would prevent formation of the 1:1 *intra*molecular heteroternary complex and thus disassembly of the supramolecular architecture.

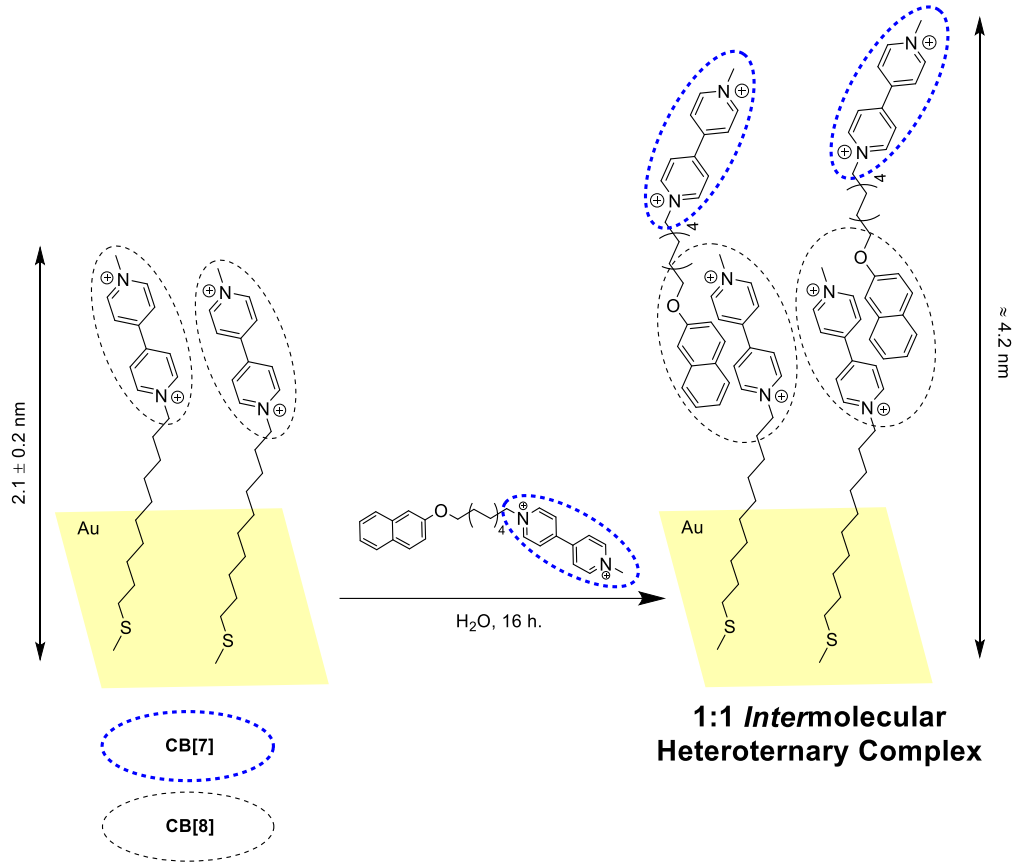


**Figure 37.** Recruitment of 1-methyl-1'-(10-(naphthalen-2-yloxy)decyl)-[4,4'-bipyridine]-1,1'-diium bromide iodide-CB[7] at a $MV^{2+}$-CB[8]-functionalised interface. Formation of the 1:1 *intra*molecular heteroternary complex should have been prevented.

This approach centred on the fact that in the presence of CB[7], binary complex formation preferentially occurs at the bipyridine terminus of 1-methyl-1'-(10-(naphthalen-2-yloxy)decyl)-[4,4'-bipyridine]-1,1'-diium bromide, **Figure 38**; the $^1$H NMR resonances associated with the naphthalene protons (*d*, *e*, *f*, *g* and *h*) remain relatively unshifted relative to those of the free guest species, whilst those of the bipyridinium unit (*a*, *b* and *c*) broaden, coalesce and are shifted upfield upon the addition of a stoichiometric amount of CB[7] into solution.

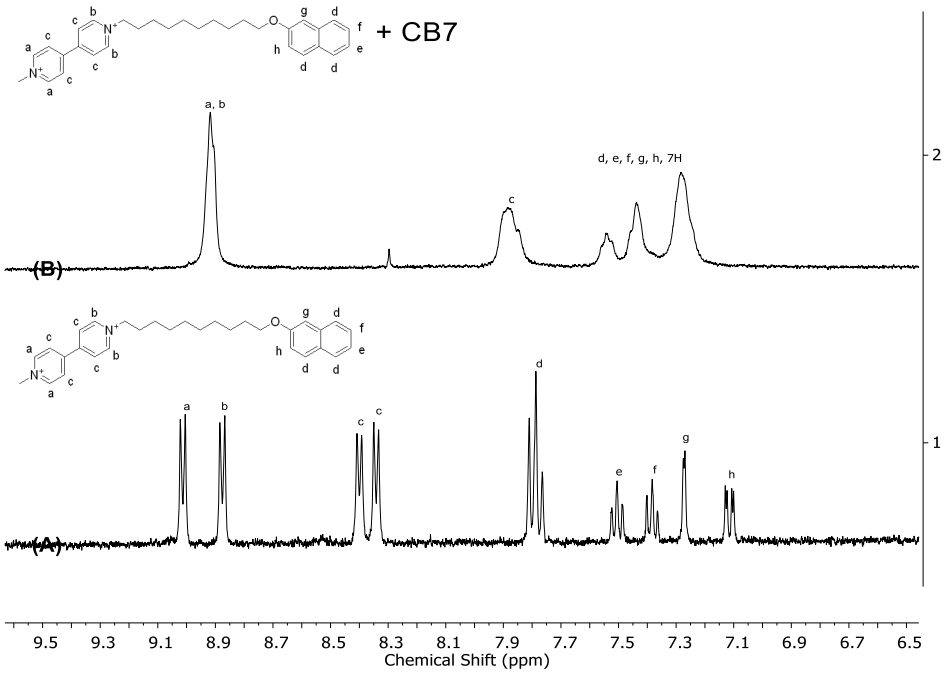


**Figure 38.** $^{1}$H NMR spectra ($D_2O$, 298 K, 400 MHz) of solutions of 1-methyl-1'-(10-(naphthalen-2-yloxy)decyl)-[4,4'-bipyridine]-1,1'-diium prior to (**Trace A**) and following the addition of a stoichiometric amount of CB[7]. All complexes were generated at a concentration of 2 mM. **Traces A – B, Bottom – Top**.

Following the attempted recruitment of 1-methyl-1'-(10-(naphthalen-2-yloxy)decyl)-[4,4'-bipyridine]-1,1'-diium bromide iodide-CB[7], collapse of the monolayer was observed, as it was in the absence of CB[7], hence further $^{1}$H NMR studies were performed in a bid to confirm the origin of disassembly.

In summary, preferential formation of the 1:1 *intra*molecular heteroternary complex prevents the recruitment of both 1-methyl-1'-(10-(naphthalen-2-yloxy)decyl)-[4,4'-bipyridine]-1,1'-diium bromide and 1-methyl-1'-(10-(naphthalen-2-yloxy)decyl)-[4,4'-bipyridine]-1,1'-diium bromide iodide-CB[7] at a $MV^{2+}$-CB[8]-functionalised interface, and thus induces disassembly of the interface.

### 5.2.3 – Formation of the 1:1 *Intra*molecular Heteroternary Charge-Transfer Complex and Subsequent Disassembly of the Supramolecular Architecture

The inclusion of 1-methyl-1'-(10-(naphthalen-2-yloxy)decyl)-[4,4'-bipyridine]-1,1'-diium bromide iodide within the apolar cavity of CB[8] was first examined using $^{1}$H NMR spectroscopy, **Figure 39**, in a bid to elucidate if incorporation of the alkyl linker facilitates formation of the 1:1 *intra*molecular heteroternary complex assumed to bring about disassembly of the $MV^{2+}$-CB[8]-functionalised interface. In short, the objective was to establish whether increased conformational flexibility permits formation of the 1:1 *intra*molecular heteroternary complex in preference to the *inter*molecular analogue.

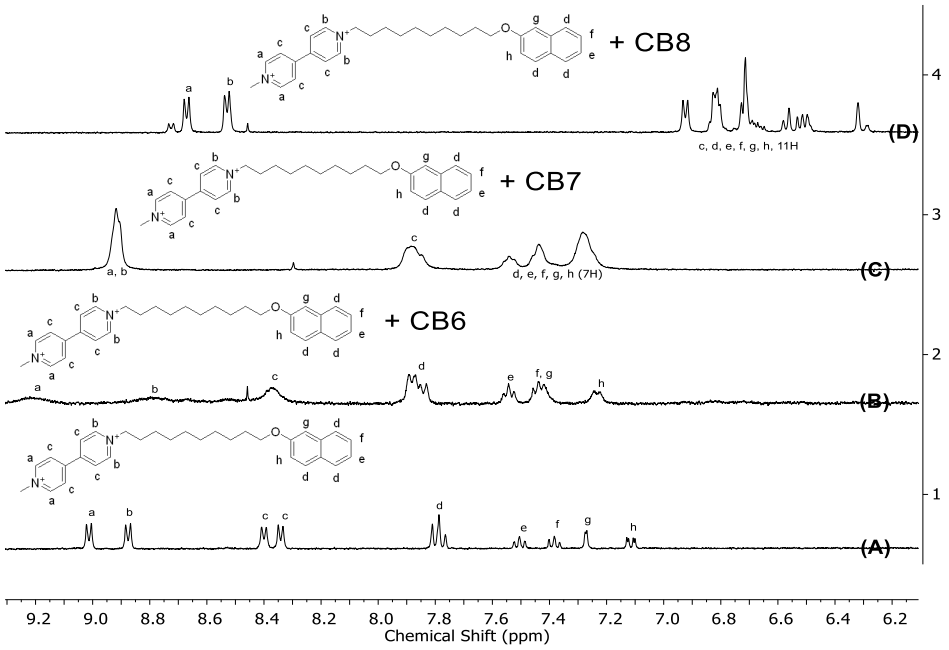


**Figure 39.** $^{1}$H NMR spectra ($D_2O$, 298 K, 400 MHz) of solutions of 1-methyl-1'-(10-(naphthalen-2-yloxy)decyl)-[4,4'-bipyridine]-1,1'-diium prior to (**Trace A**) and following the addition of a stoichiometric amount of CB[6] (**Trace B**), CB[7] (**Trace C**) or CB[8] (**Trace D**). All complexes were generated at a concentration of 2 mM. **Traces A – D, Bottom – Top**.

The addition of a stoichiometric amount of CB[8] to a solution of 1-methyl-1'-(10-(naphthalen-2-yloxy)decyl)-[4,4'-bipyridine]-1,1'-diium bromide iodide has been shown to bring about the formation of a 1:1 *intra*molecular heteroternary complex, in which both the N,N′-dimethyl-4,4′-bipyridinium and naphthalene termini are confined within the hydrophobic cavity of CB[8]. The addition of CB[8] (**Figure 39, Trace D**) induces an upfield chemical shift of both the bipyridinium (*a*, *b* and *c*) and naphthalene-centred (*d*, *e*, *f*, *g* and *h*) resonances, relative to the free guest derivative (**Figure 39, Trace A**).

Such inclusion behaviour is not witnessed upon the addition of either CB[6] or CB[7]. This was expected given the fact that the size of their respective apolar cavities does not permit the inclusion of more than one guest species, and thus the formation of either *inter*- or *intra*molecular heteroternary complexes is not viable. That is, upon the addition of a stoichiometric amount of CB[7] (**Figure 39, Trace C**), only the resonances associated with the bipyridinium motif (*a*, *b* and *c*) coalescence, broaden and migrate upfield. A slight upfield chemical shift of the naphthalene proton (*d*) is however also observed, and this is assumed to have arisen because the system is likely to be in equilibrium; CB[7] is also able to form binary complexes with neutral, aromatic guest species. No such upfield chemical shifts were witnessed upon the addition of CB[6], because its apolar cavity is only large enough to accommodate aliphatic guest species, such as 1,4-diaminobutane (**Figure 9**) and hexylamine (**Figure 10**). However, considerable broadening of the bipyridinium resonances (*a*, *b* and *c*) and a downfield shift of the naphthalene-centred multiplets (*d*, *e*, *f*, *g* and *h*) was observed,

both of which are ascribed to the poor solubility of CB[6] and the fact that inclusion of the guest species is not permitted.

Upon verifying formation of the 1:1 *intra*molecular heteroternary complex by way of $^{1}$H NMR spectroscopy, the effect of adding a stoichiometric amount of CB[8] to a solution of 1-methyl-1'-(10-(naphthalen-2-yloxy)decyl)-[4,4'-bipyridine]-1,1'-diium bromide iodide-CB[7], and *vice versa*, was investigated, **Figure 40**. This experiment set out to confirm why growth of the lanthanide-appended monolayer was not observed upon the attempted recruitment of 1-methyl-1'-(10-(naphthalen-2-yloxy)decyl)-[4,4'-bipyridine]-1,1'-diium-CB[7] at a 1-(10-mercaptodecyl)-1'-methyl-[4,4'-bipyridine]-diium-CB[8]-functionalised interface, **Figure 35**, *i.e*. highlight why the prior complexation of 1-methyl-1'-(10-(naphthalen-2-yloxy)decyl)-[4,4'-bipyridine]-1,1'-diium with CB[7] did not deter formation of the 1:1 *intra*molecular heteroternary complex at the interface.

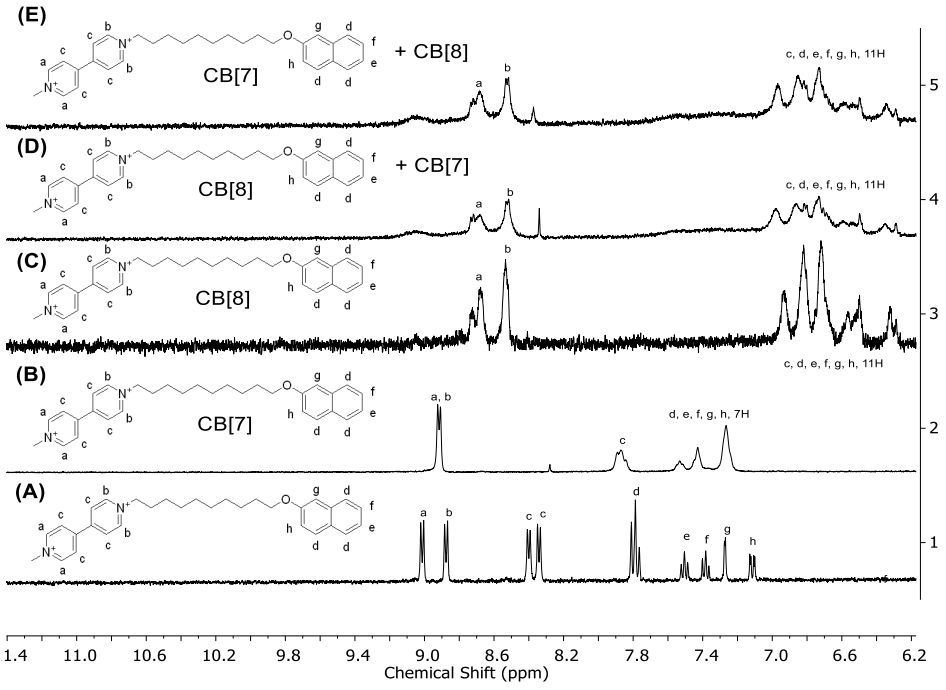


**Figure 40.** $^{1}$H NMR spectra ($D_2O$, 298 K, 400 MHz) of solutions of 1-methyl-1'-(10-(naphthalen-2-yloxy)decyl)-[4,4'-bipyridine]-1,1'-diium (**Trace A**), 1-methyl-1'-(10-(naphthalen-2-yloxy)decyl)-[4,4'-bipyridine]-1,1'-diium-CB[7] (**Trace B**), 1-methyl-1'-(10-(naphthalen-2-yloxy)decyl)-[4,4'-bipyridine]-1,1'-diium-CB[8] (**Trace C**), (1-methyl-1'-(10-(naphthalen-2-yloxy)decyl)-[4,4'-bipyridine]-1,1'-diium-CB[8]) + CB[7] (**Trace D**) and (1-methyl-1'-(10-(naphthalen-2-yloxy)decyl)-[4,4'-bipyridine]-1,1'-diium-CB[7]) + CB[8] (**Trace E**). All complexes were generated at a concentration of 2 mM. **Traces A – E, Bottom – Top.**

**Figure 40** implies that upon the addition of a stoichiometric amount of CB[8] to a solution of the binary complex, 1-methyl-1'-(10-(naphthalen-2-yloxy)decyl)-[4,4'-bipyridine]-1,1'-diium bromide iodide-CB[7], the bipyridinium motif is displaced from the hydrophobic cavity of CB[7] and the 1:1 *intra*molecular heteroternary complex generated. This is evident upon comparing **Traces B**, **C** and **E**; upon the addition of CB[8], the multiplets associated with both the bipyridinium (*a*, *b* and *c*) and naphthalene motifs migrate upfield (*d*, *e*, *f*, *g* and *h*), with the resultant spectrum (**Trace E**)

resembling that of the one acquired of the 1:1 *intra*molecular heteroternary complex (**Trace C**) and not the binary complex (**Trace B**).

Further to this, the addition of CB[7] to a solution of the 1:1 *intra*molecular heteroternary complex, 1-(10-(naphthalen-2-yloxy)decyl)-[4,4'-bipyridine]-1,1'-diium-CB[8], does not bring about any form of spectral change, that is the resulting spectrum (**Trace D**) is identical to those acquired upon the addition of CB[8] to a solution of the 1-(10-(naphthalen-2-yloxy)decyl)-[4,4'-bipyridine]-1,1'-diium-CB[7] complex (**Trace E**) and of a solution of the 1:1 *intra*molecular heteroternary complex (**Trace C**).

In summary, $^{1}$H NMR and ellipsometric film thickness measurements highlight the fact that the 1:1 *intra*molecular heteroternary complex is generated in preference to the *inter*molecular analogue, both in solution and at the interface. This clarifies why growth of the lanthanide-appended interface was not possible, and this preference for *intra*molecular ternary inclusion was further highlighted when 1-(10-(naphthalen-2-yloxy)decyl)-[4,4'-bipyridine]-1,1'-diium was added to a 1:1 mixture of CB[7] and CB[8], **Figure 41**; upon the addition of 1-(10-(naphthalen-2-yloxy)decyl)-[4,4'-bipyridine]-1,1'-diium to a solution containing each macrocyclic cavitand, CB[7] and CB]8], the spectrum acquired (**Trace D**) was equivalent to that recorded for a solution of the 1:1 *intramolecular* heteroternary complex (**Trace C**), *cf*. **Traces A** and **B**.

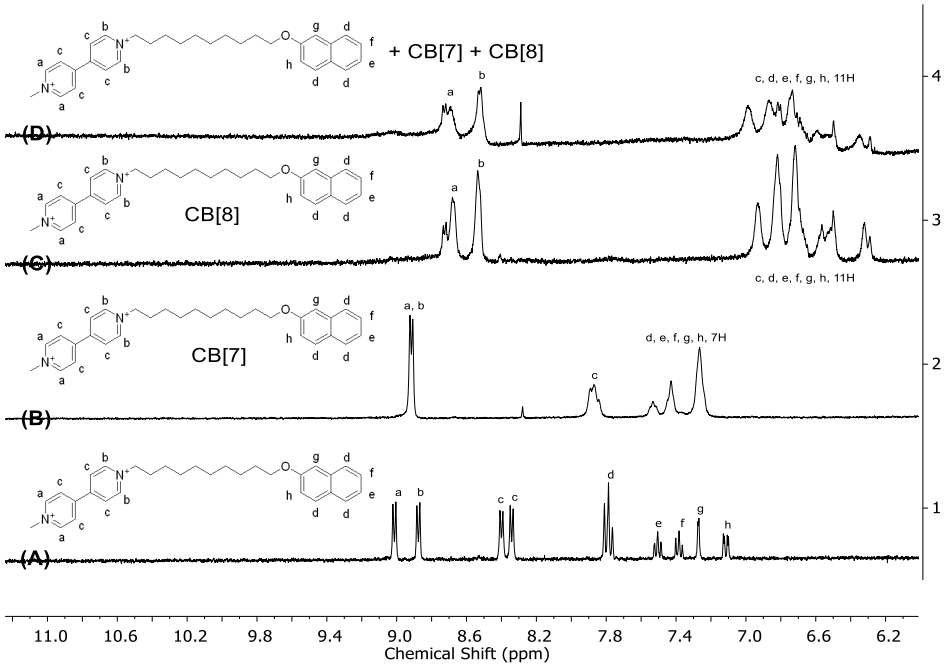


**Figure 41.** $^{1}$H NMR spectra ($D_2O$, 298 K, 400 MHz) of solutions of 1-methyl-1'-(10-(naphthalen-2-yloxy)decyl)-[4,4'-bipyridine]-1,1'-diium prior to (**Trace A**) and following the addition of a stoichiometric amount of CB[7] (**Trace B**), CB[8] (**Trace C**) or a 1:1 mixture of CB[7] and CB[8] (**Trace D**). All complexes were generated at a concentration of 2 mM. **Traces A – E, Bottom – Top.**

### 5.2.4 – Assembling *Inter*molecular Charge-Transfer Complexes from their *Intra*molecular Analogues

To shed further light on the strength of the interaction driving formation of the 1:1 *intra*molecular heteroternary complex, the effect of adding 2,6-Np to a solution of the ternary complex, **Figure 42**, was probed by $^{1}$H NMR, **Figure 43**, and UV-Vis spectroscopy. This was made possible by the fact that the $^{1}$H NMR spectrum of the naphthalene motif within each environment differs, **Figure 44**, allowing the proton resonances of 2,6-Np and 1-methyl-1'-(10-(naphthalen-2-yloxy)decyl)-[4,4'-bipyridine]-1,1'-diium to be isolated independently from one another within the convoluted spectrum, **Figure 43**. That is, it was possible to distinguish whether 2,6-Np had been incorporated within the apolar cavity of CB[8] and the 1:1 *inter*molecular heteroternary complex subsequently generated, at the expense of the naphthalene terminus of 1-(10-(naphthalen-2-yloxy)decyl)-[4,4'-bipyridine]-1,1'-diium.

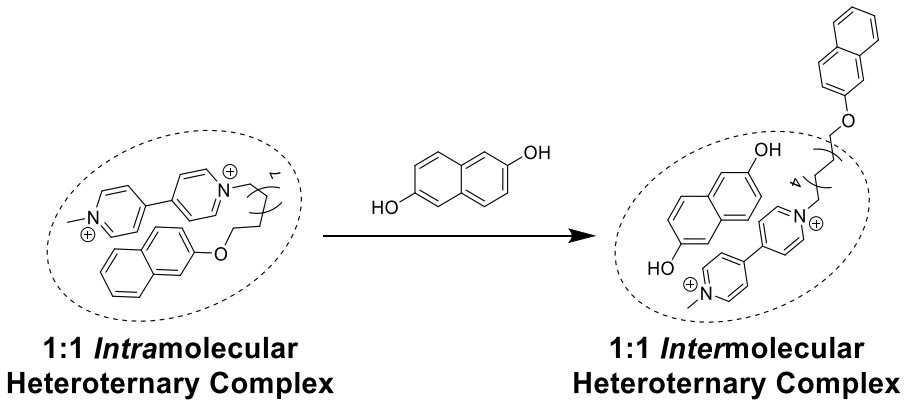


**Figure 42.** A possible way of transforming the 1:1 *intra*molecular heteroternary complex into the desired 1:1 *inter*molecular analogue.

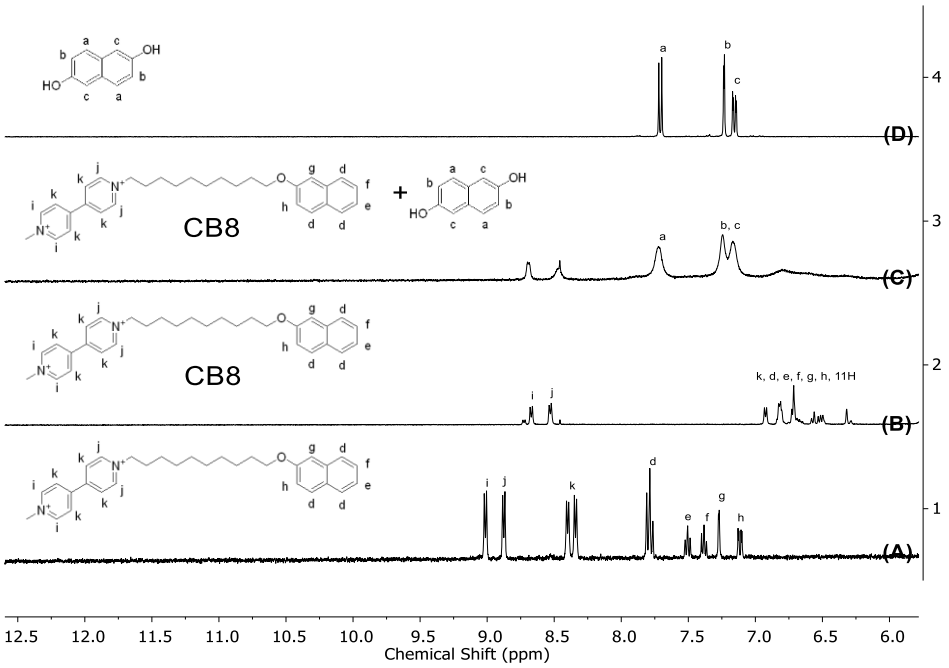


**Figure 43**. $^{1}$H NMR spectra ($D_2O$, 298 K, 400 MHz) of solutions of 1-methyl-1'-(10-(naphthalen-2-yloxy)decyl)-[4,4'-bipyridine]-1,1'-diium (**Trace A**), 1-methyl-1'-(10-(naphthalen-2-yloxy)decyl)-[4,4'-bipyridine]-1,1'-diium-CB[8] (**Trace B**), (1-methyl-1'-(10-(naphthalen-2-yloxy)decyl)-[4,4'-bipyridine]-1,1'-diium-CB[8]) + 2,6-Np (**Trace C**) and 2,6-Np (**Trace D**). All complexes were generated at a concentration of 2 mM. **Traces A – E, Bottom – Top.**

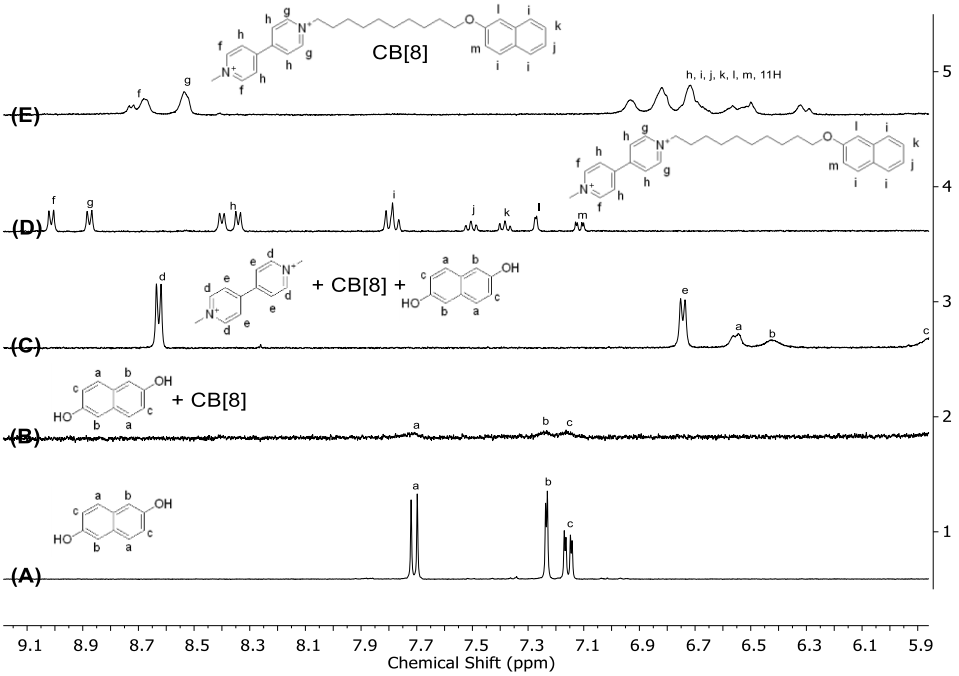


**Figure 44**. $^{1}$H NMR spectra ($D_2O$, 298 K, 400 MHz) of solutions of 2,6-Np (**Trace A**), 2,6-Np-CB[8] (**Trace B**), ($MV^{2+}$, 2,6-Np)-CB[8] (**Trace C**), 1-methyl-1'-(10-(naphthalen-2-yloxy)decyl)-[4,4'-bipyridine]-1,1'-diium (**Trace D**) and (1-methyl-1'-(10-(naphthalen-2-yloxy)decyl)-[4,4'-bipyridine]-1,1'-diium-CB[8] (**Trace E**). All complexes were generated at a concentration of 2 mM. **Traces A – E, Bottom – Top.**

**Figure 43** tentatively suggests that upon the addition of 2,6-Np to a solution of the 1:1 *intra*molecular heteroternary complex, the *inter*molecular analogue is not obtained, with 1-(10-(naphthalen-2-yloxy)decyl)-[4,4'-bipyridine]-1,1'-diium remaining encapsulated within the apolar cavity of CB[8], leaving 2,6-Np in solution; the naphthalene-centred proton resonances of 1-(10-(naphthalen-2-yloxy)decyl)-[4,4'-bipyridine]-1,1'-diium (*d, e, f, g* and *h*) are not shifted downfield, and an upfield shift of the 2,6-Np protons (*a, b,* and *c*) is not observed (**Trace C**). **Note:** Suppression of the multiplets corresponding to the presence of the 1:1 *intra*molecular heteroternary complex arises as the result of 2,6-Np being added in slight excess (1.1 equivalents). In addition, no change in the UV-Vis spectrum (**Experimental, 7.5**) of the 1:1 *intra*molecular heteroternary complex arose upon the addition of 2,6-Np; the charge-transfer interaction remained at $\lambda_{max}$ 541 nm (**Experimental, 8.14, Figure 58**), when a red spectral shift was expected upon formation of the *intermolecular* analogue, of which bares greater resemblance to the model system (($MV^{2+}$, 2,6-Np)-CB[8], $\lambda_{max}$ 570 nm (**Experimental, 8.14, Figure 57**), **Chapter 4**, **Figure 4**).

In summary, the data suggests that preferential formation of the 1:1 *intra*molecular heteroternary complex, 1-(10-(naphthalen-2-yloxy)decyl)-[4,4'-bipyridine]-1,1'-diium-CB[8], induces migration of the macrocyclic host into solution, which in turn prevents formation of the supramolecular architecture, **Figure 35**. Disassembly of the interface occurs irrespective of whether 1-methyl-1'-(10-(naphthalen-2-yloxy)decyl)-[4,4'-bipyridine]-1,1'-diium or 1-methyl-1'-(10-(naphthalen-2-yloxy)decyl)-[4,4'-bipyridine]-1,1'-diium-CB[7] is recruited to the underlying, SAM, 1-(10-mercaptodecyl)-1'-methyl-[4,4'-bipyridine]-diium-CB[8], **Figures 35 and 37**, respectively, and the *inter*molecular analogue is not afforded upon the addition of a secondary guest species into solution, **Figure 42**. The above is depicted in **Figure 45**.

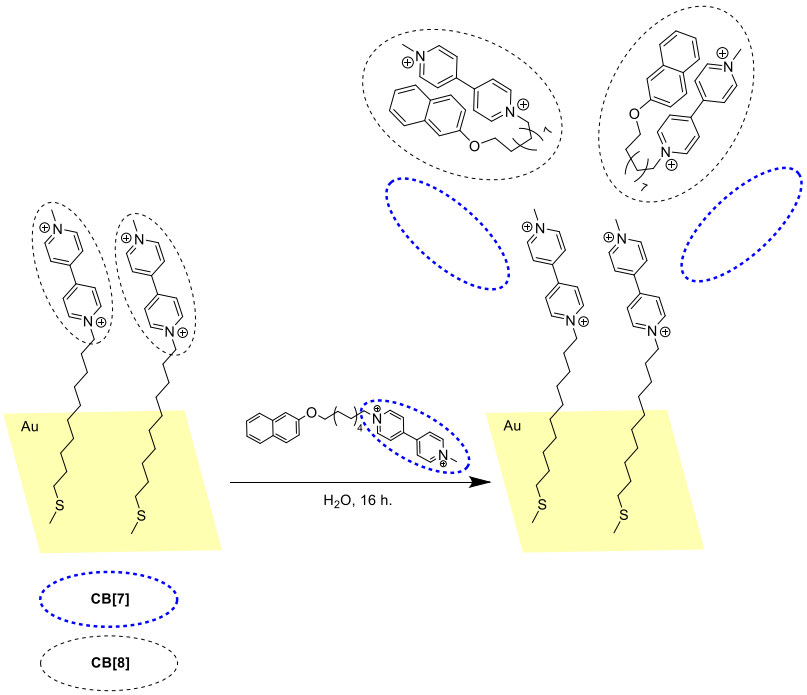


**Figure 45**. 1:1 *intra*molecular heteroternary complex formation upon the recruitment of 1-methyl-1'-(10-(naphthalen-2-yloxy)decyl)-[4,4'-bipyridine]-1,1'-diium bromide iodide-CB[7] at a $MV^{2+}$-CB[8]-functionalised interface. Exposure of the interface to a solution of the binary complex, 1-methyl-1'-(10-(naphthalen-2-yloxy)decyl)-[4,4'-bipyridine]-1,1'-diium-CB[7], does not bring about preferential formation of the *inter*molecular analogue.

### 5.2.5 – Modelling Migration of the Macrocyclic Host from the Periphery of the Interface

This concept of the macrocyclic host species migrating from the periphery of the interface into solution, in order to form the 1:1 *intra*molecular heteroternary complex, was further highlighted upon adding a solution of 1-(10-mercaptodecyl)-1'-methyl-[4,4'-bipyridine]-diium bromide-CB[8] to a solution of 1-(10-mercaptodecyl)-1'-methyl-[4,4'-bipyridine]-diium bromide-CB[7], **Figure 46**; this experiment mimics what is thought to prevent growth of the monolayer, **Figure 45**.

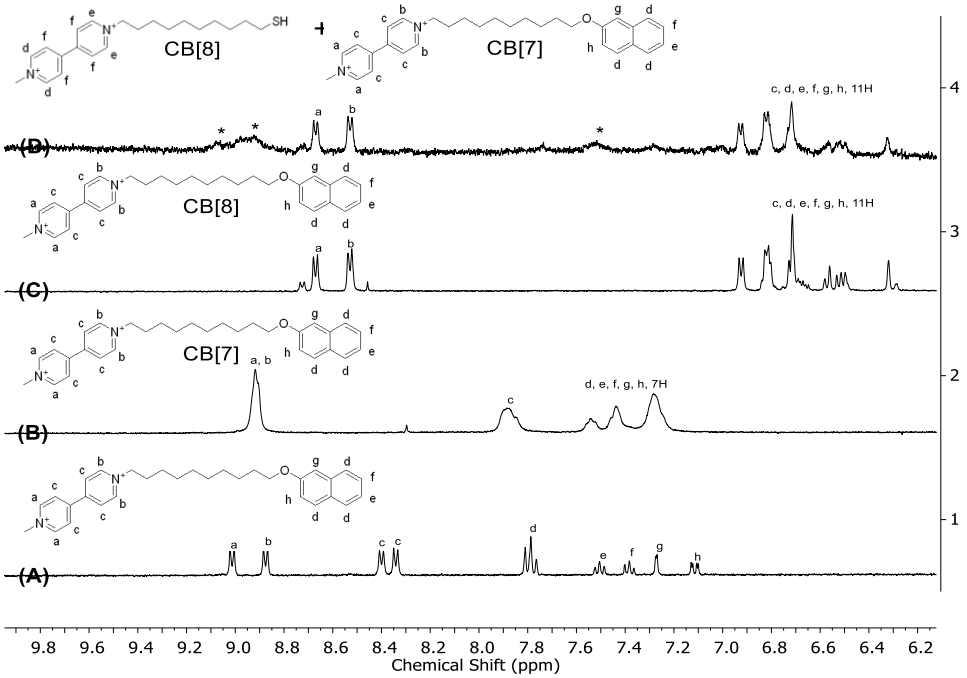


**Figure 46.** $^{1}$H NMR spectra ($D_2O$, 298 K, 400 MHz) of solutions of 1-methyl-1'-(10-(naphthalen-2-yloxy)decyl)-[4,4'-bipyridine]-1,1'-diium bromide iodide (**Trace A**), 1-methyl-1'-(10-(naphthalen-2-yloxy)decyl)-[4,4'-bipyridine]-1,1'-diium bromide iodide-CB[7] (**Trace B**), 1-methyl-1'-(10-(naphthalen-2-yloxy)decyl)-[4,4'-bipyridine]-1,1'-diium bromide iodide-CB[8] (**Trace C**) and (1-(10-mercaptodecyl)-1'-methyl-[4,4'-bipyridine]-diium bromide-CB[8] + 1-methyl-1'-(10-(naphthalen-2-yloxy)decyl)-[4,4'-bipyridine]-1,1'-diium bromide iodide-CB[7]) (**Trace D**). All complexes were generated at a concentration of 2 mM. **Traces A – E, Bottom – Top.**

The spectrum acquired upon the addition of a solution of 1-(10-mercaptodecyl)-1'-methyl-[4,4'-bipyridine]-diium bromide-CB[8] to a solution of 1-(10-mercaptodecyl)-1'-methyl-[4,4'-bipyridine]-diium bromide-CB[7], **Figure 46**, **Trace D**, resembles that of the $^{1}$H NMR spectrum acquired for a solution of the 1:1 *intra*molecular heteroternary complex, **Figure 46**, **Trace C**. This implies that macrocyclic exchange occurs and formation of the 1:1 *intra*molecular heteroternary complex is favoured at the expense of the *inter*molecular analogue, as was first thought. This exchange process did however not proceed to completion, **Figure 47**; resonances corresponding to the presence of the binary complex, 1-(10-mercaptodecyl)-1'-methyl-[4,4'-bipyridine]-diium bromide-CB[7], are still apparent within the spectrum (**Figure 47, Trace C**), although these trace multiplets, of which have not been assigned, may correspond to the presence of uncomplexed 1-(10-mercaptodecyl)-1'-methyl-[4,4'-bipyridine]-diium bromide (**Trace D**) or 1-methyl-1'-(10-(naphthalen-2-yloxy)decyl)-[4,4'-bipyridine]-1,1'-diium bromide iodide (**Trace A**). Additionally, 1-(10-mercaptodecyl)-1'-methyl-[4,4'-bipyridine]-diium bromide may precipitate out of solution upon displacement from the cavity of CB[8]. Nevertheless, macrocyclic exchange was seen to occur to a significant degree, as expected.

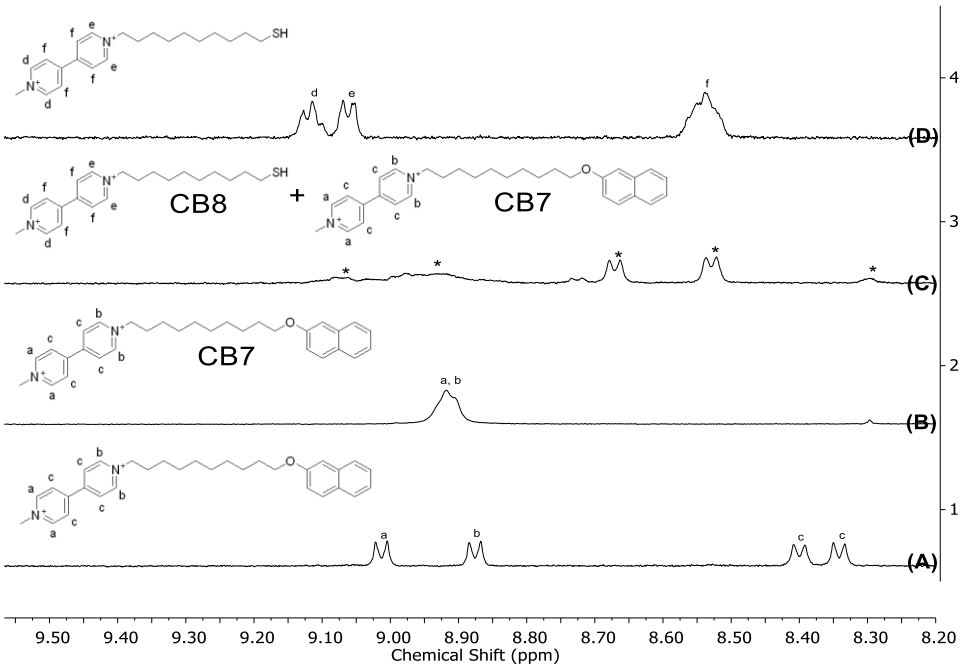


**Figure 47.** $^{1}$H NMR spectra ($D_2O$, 298 K, 400 MHz) of solutions of 1-methyl-1'-(10-(naphthalen-2-yloxy)decyl)-[4,4'-bipyridine]-1,1'-diium bromide iodide (**Trace A**), 1-methyl-1'-(10-(naphthalen-2-yloxy)decyl)-[4,4'-bipyridine]-1,1'-diium bromide iodide-CB[7] (**Trace B**), (1-(10-mercaptodecyl)-1'-methyl-[4,4'-bipyridine]-diium bromide-CB[8] + 1-methyl-1'-(10-(naphthalen-2-yloxy)decyl)-[4,4'-bipyridine]-1,1'-diium bromide iodide-CB[7]) (**Trace C**) and 1-(10-mercaptodecyl)-1'-methyl-[4,4'-bipyridine]-diium bromide (**Trace D**). All complexes were generated at a concentration of 2 mM. **Traces A – E, Bottom – Top.**

In conclusion, the force driving formation of the 1:1 *intra*molecular heteroternary complex is too great to overcome, and does not facilitate growth of the desired supramolecular architecture. Although the strength of this interaction was not quantified, it is believed to be much greater than the reported binary interaction which arises between CB[8] and AdHCl, $8.19 \pm 1.75 \times 10^{8}$ $M^{-1}$,[43] based on the evidence acquired by $^{1}$H NMR spectroscopy, **Figure 48**. Upon the addition of a stoichiometric amount of CB[8]-1-aminoadamantane to a solution of 1-methyl-1'-(10-(naphthalen-2-yloxy)decyl)-[4,4'-bipyridine]-1,1'-diium bromide iodide-CB[7], the 1:1 *intra*molecular heteroternary complex is generated. The resultant spectrum (**Trace D**) resembles that acquired of the 1:1 *intra*molecular heteroternary complex (**Trace C**), highlighting the fact that AdHCl is displaced from the apolar cavity of CB[8] by 1-methyl-1'-(10-(naphthalen-2-yloxy)decyl)-[4,4'-bipyridine]-1,1'-diium bromide iodide.

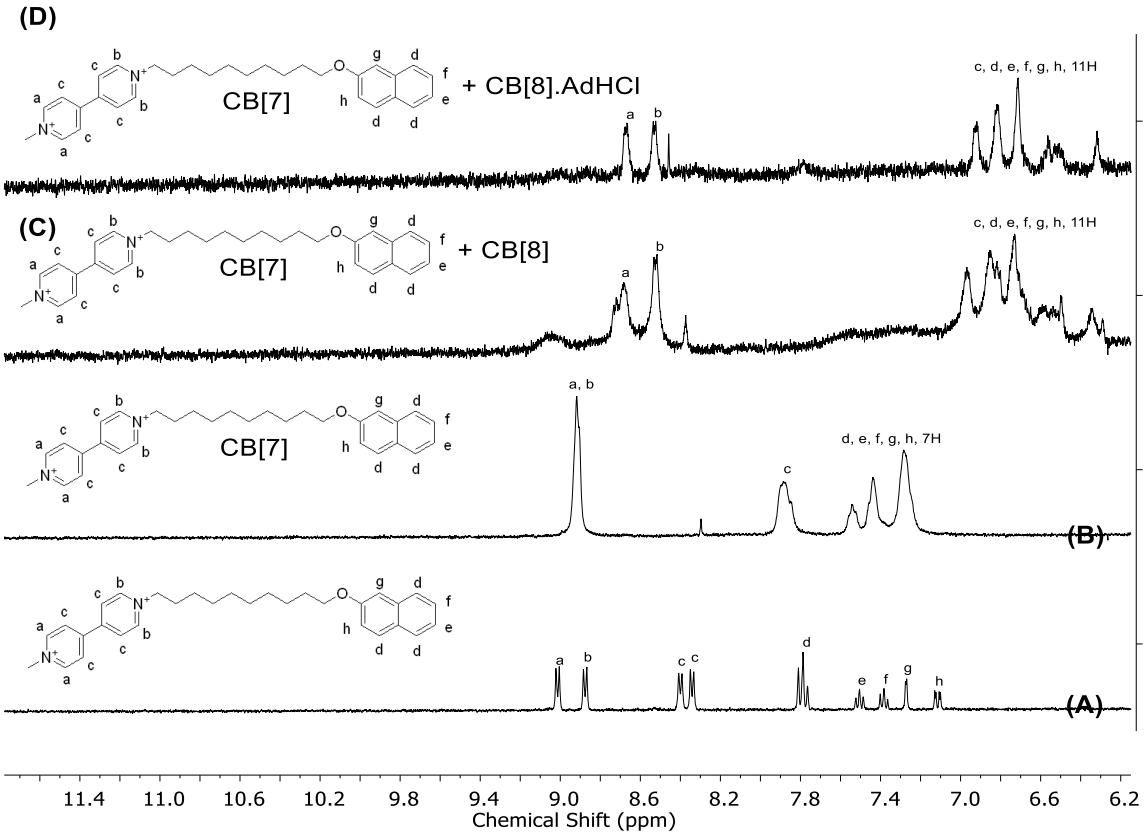


**Figure 48.** $^{1}H$ NMR spectra ($D_2O$, 298 K, 400 MHz) of solutions of 1-methyl-1'-(10-(naphthalen-2-yloxy)decyl)-[4,4'-bipyridine]-1,1'-diium bromide iodide (**Trace A**), 1-methyl-1'-(10-(naphthalen-2-yloxy)decyl)-[4,4'-bipyridine]-1,1'-diium bromide iodide-CB[7] (**Trace B**), (1-methyl-1'-(10-(naphthalen-2-yloxy)decyl)-[4,4'-bipyridine]-1,1'-diium bromide iodide-CB[7]) + CB[8] (**Trace C**), (1-methyl-1'-(10-(naphthalen-2-yloxy)decyl)-[4,4'-bipyridine]-1,1'-diium bromide iodide-CB[7]) + CB[8]-AdHCl (**Trace D**). All complexes were generated at a concentration of 2 mM. **Traces A – E, Bottom – Top.**

## 5.3 – Moving Forwards

To facilitate growth of the supramolecular architecture, focus must switch towards synthesising a more rigid linker derivative, **Figure 49**, as to prevent preferential formation of the 1:1 *intra*molecular heteroternary complex at the interface.

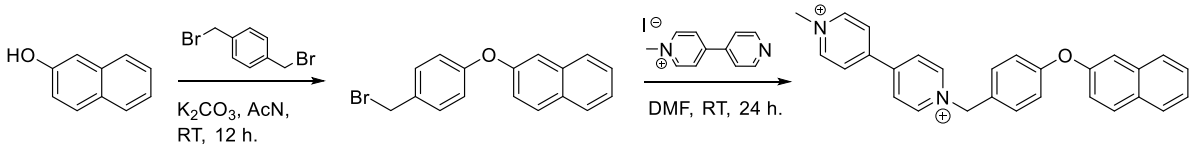


**Figure 49.** Synthesis of 1-methyl-1'-(4-(naphthalen-2-yloxy)benzyl)-[4,4'-bipyridine]-1,1'-diium.

Reducing the flexibility of the linker motif by incorporating an aryl group into its backbone is reported to prevent folding of the derivative[44-46], and complexation is therefore likely to favour formation of the *inter*molecular analogue, thus permitting growth of the interface, **Figure 50**.

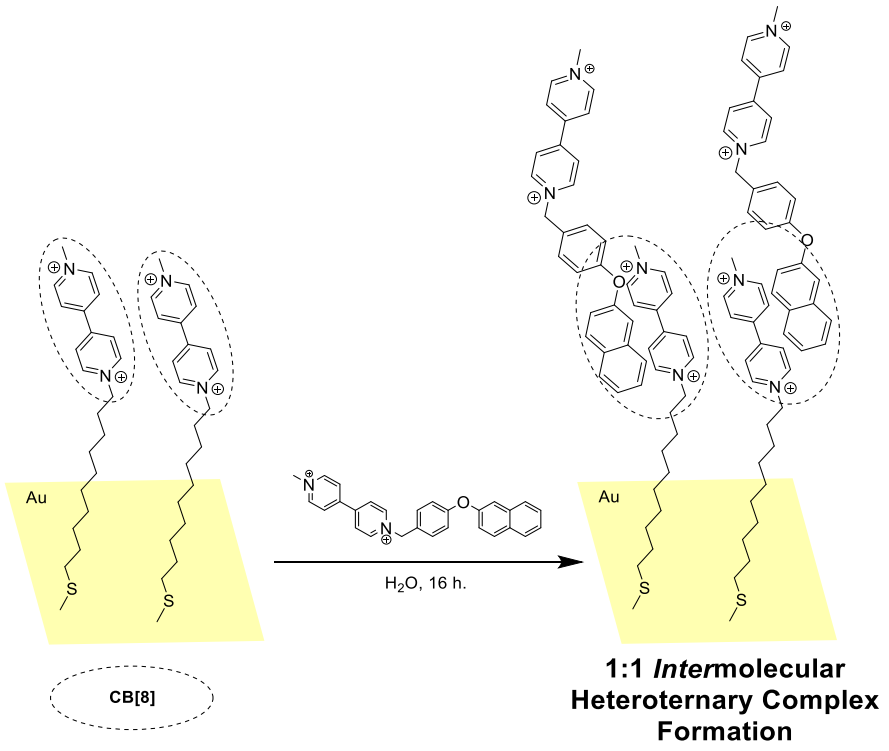


**Figure 50.** Recruitment of 1-methyl-1'-(4-(naphthalen-2-yloxy)benzyl)-[4,4'-bipyridine]-1,1'-diium at a $MV^{2+}$-CB[8]-functionalised interface. It is feasible that incorporation of an aryl moiety into the backbone of the rigid linker derivative will drive formation of the 1:1 *inter*molecular heteroternary complex at the expense of the 1:1 *intra*molecular analogue.

This was demonstrated by a molecular modelling study (MM2) performed in Chem3D 15.0, **Figure 51**. Formation of the 1:1 *intra*molecular heteroternary complex is only possible in the case of 1-methyl-1'-(10-(naphthalen-2-yloxy)decyl)-[4,4'-bipyridine]-1,1'-diium bromide iodide, where the long alkyl chain, incorporated in a bid to increase the distance between the lanthanide centre and the quenching metallic interface, as to enhance the magnitude of the optical output detected upon irradiation of the interface, permits folding of the derivative within the apolar cavity of CB[8].

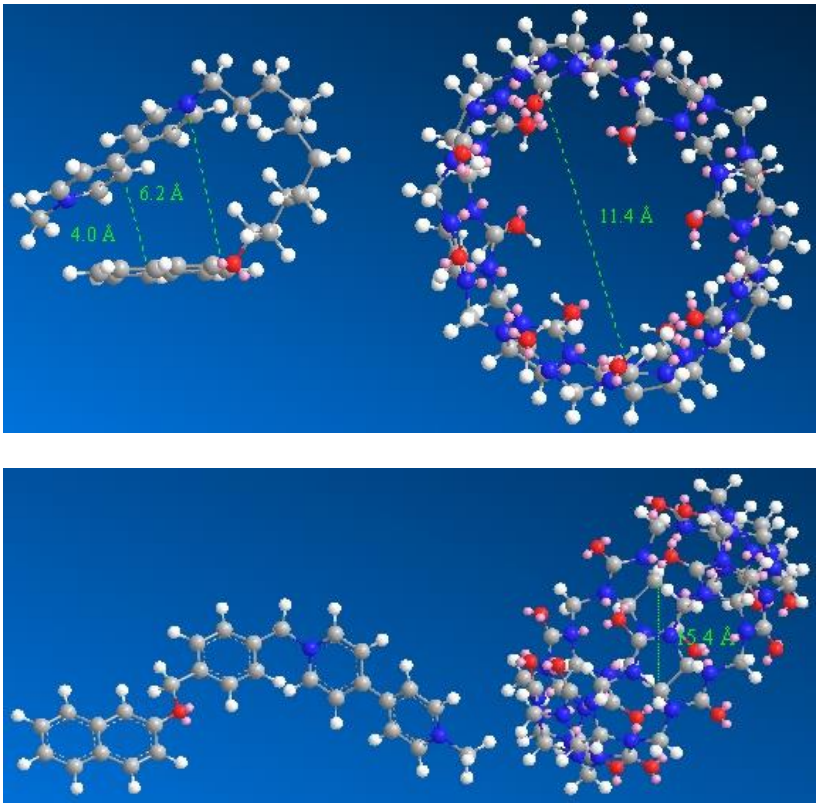


**Figure 51.** Inclusion of both 1-methyl-1'-(10-(naphthalen-2-yloxy)decyl)-[4,4'-bipyridine]-1,1'-diium bromide iodide (**Top**) and 1-methyl-1'-(4-(naphthalen-2-yloxy)benzyl)-[4,4'-bipyridine]-1,1'-diium (**Bottom**) within the apolar cavity of CB[8], as modelled in Chem3D 15.0. Inclusion of 1-methyl-1'-(10-(naphthalen-2-yloxy)decyl)-[4,4'-bipyridine]-1,1'-diium bromide iodide proceeds to generate the 1:1 *intra*molecular heteroternary complex; this is not possible in the case of the conformationally restricted derivative, 1-methyl-1'-(4-(naphthalen-2-yloxy)benzyl)-[4,4'-bipyridine]-1,1'-diium.

Following expected growth of the interface upon incorporation of the more rigid linker derivative, **Figure 50**, the use of functionalised triazolium and bistriazolium derivatives, **Figure 52**, should be explored to nullify the effect of charge transfer.

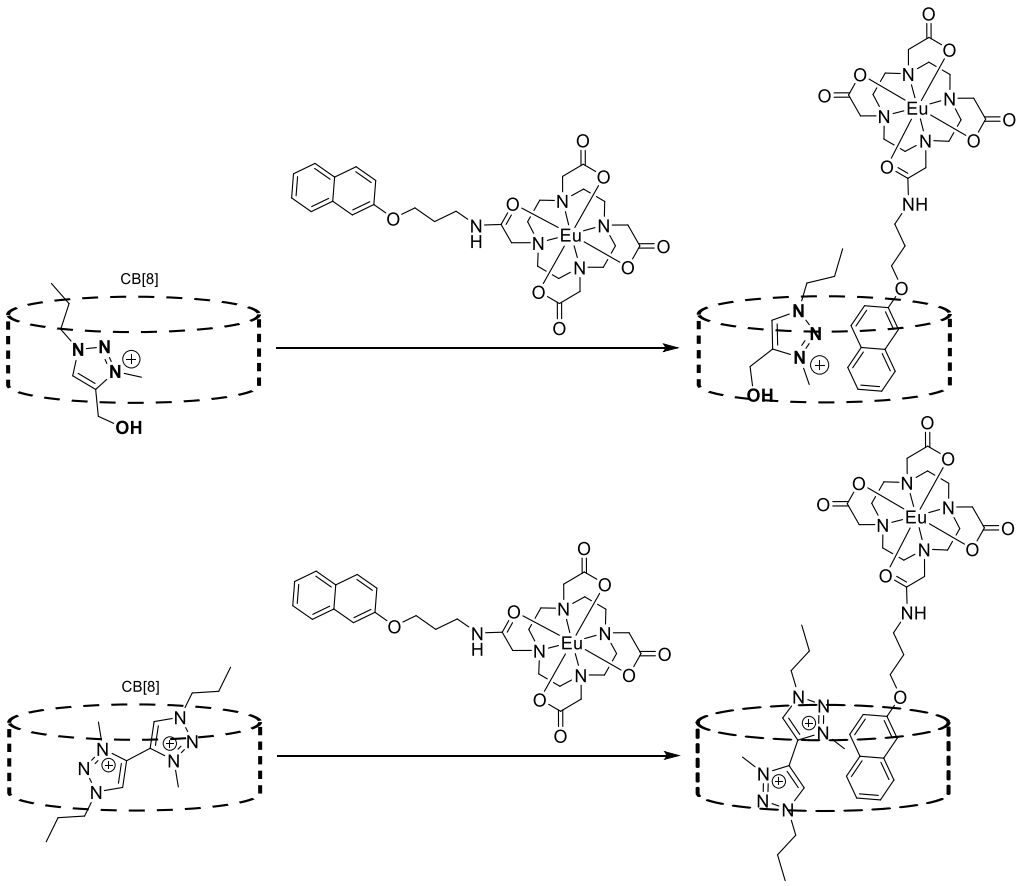


**Figure 52.** Incorporating triazolium (**Top**) and bistriazolium (**Bottom**) derivatives within the apolar cavity of CB[8], at the expense of $MV^{2+}$, to try to nullify the effect of charge-transfer on the emissive state of the lanthanide ion.

The incorporation of $MV^{2+}$-functionalised derivatives within heteroternary complexes has been shown to quench lanthanide ($Eu^{3+}$, $Nd^{3+}$, $Yb^{3+}$) luminescence (**Chapter 4, Section 4.3**). It is anticipated that heteroternary complexes incorporating either of the derivatives will absorb at lower wavelength (< 570 nm), and thus the quenching of sensitised emission will not be detected, enabling formation of a novel supramolecular platform, **Figure 22** (**Chapter 4**), from which significant optical output can be detected and subsequently modulated by manipulating the oxidation state of a surface-confined metallocene.

## List of References

1. David Curiel, Paul D. Beer, *Chem. Commun*., **2005**, 14, 1909–1911.
2. Graeme T. Spence, Dr. Mateusz B. Pitak, Prof. Paul D. Beer, *Chem. Eur. J*., **2012**, 18, 7100–7108.
3. Matthew J. Langton, Prof. Paul D. Beer, *Chem. Eur. J*., **2012**, 18, 14406–14412.
4. Joshua Lehr, Paul D. Beer, Stephen Faulkner, Jason J. Davis, *Chem. Commun*., **2014**, 50, 5678–5687.
5. Manuel Tropiano, Nathan L. Kilah, Michael Morten, Habibur Rahman, Jason J. Davis, Paul D. Beer, Stephen Faulkner, *J. Am. Chem. Soc*., **2011**, 133, 11847–11849.

6. Joshua Lehr, Manuel Tropiano, Paul D. Beer, Stephen Faulkner, Jason J. Davis, *Chem. Commun*., **2015**, 51, 6515–6517.
7. Qi An, Guangtao Li, Chengan Tao, Yan Li, Yiguang Wu, Weixia Zhang, *Chem. Commun.*, **2008**, 1989–1991.
8. Woo Sung Jeon, Kwangyul Moon, Sang Hyun Park, Hyungpil Chun, Young Ho Ko, Jin Yong Lee, Eun Sung Lee, S. Samal, N. Selvapalam, Mikhail V. Rekharsky, Vladimir Sindelar, David Sobransingh, Yoshihisa Inoue, Angel E. Kaifer, Kimoon Kim, *J. Am. Chem. Soc*., **2005**, 127, 12984–12989.
9. Drochss P. Valencia, Felipe J. González, *Electrochemistry Communications*, **2011**, 13, 129-132.
10. Drochss P. Valencia, Felipe J. González, *Journal of Electroanalytical Chemistry*, **2012**, 681, 121-126.
11. Alaa A. A. Aljabali, J. Elaine Barclay, Julea N. Butt, George P. Lomonossoff, David J. Evans, *Dalton Trans*., **2010**, 39, 7569-7574.
12. Nicole F. Steinmetz, George P. Lomonossoff Dr., David. J. Evans Dr., *Small*, **2006**, 2, 530-533.
13. Nicole F. Steinmetz, George P. Lomonossoff, David J. Evans, *Langmuir*, **2006**, 22, 3488-3490.
14. *Electrochemistry at Solid Electrodes*, ed. R. N. Adams, Marcel Dekker, New York, 1969.
15. C. S. Yun, A. Javier, T. Jennings, M. Fisher, S. Hira, S. Peterson, B. Hopkins, N. O. Reich, G. F. Strouse, *J. Am. Chem. Soc*., **2005**, 127, 3115.
16. Acuna GP, Bucher M, Stein IH, Steinhauer C, Kuzyk A, Holzmeister P, Schreiber R, Moroz A, Stefani FD, Liedl T, Simmel FC, Tinnefeld P., *ACS Nano*, **2012**, 6, 3189 –3195.
17. Chhabra R, Sharma J, Wang H, Zou S, Lin S, Yan H, Lindsay S, Liu Y., *Nanotechnology*, **2009**, 20, 485201.
18. B. N. J. Persson, N. D. Lang, *Phys. Rev. B: Condens. Matter Mater. Phys*., **1982**, 26, 5409.
19. Steven J. Barrow, Setu Kasera, Matthew J. Rowland, Jesús del Barrio, Oren A. Scherman, *Chem. Rev.*, **2015**, 115, 12320–12406.
20. Khaleel I. Assaf, Werner M. Nau, *Chem. Soc. Rev*., **2015**, 44, 394–418.
21. Wei Zhu, Chen Wang, Weina Li, Cheng-an Tao, Jiecheng Cui, Haowei Yang, Yin Jiang, Guangtao Li, *J. Mater. Chem. A.*, **2013**, 1, 11741–11747.
22. Koen van der Maaden, Karen Sliedregt, Alexander Kros, Wim Jiskoot, Joke Bouwstra, *Langmuir*, **2012**, 28, 3403–3411.
23. Dmitri V. Vezenov, Aleksandr Noy, Lawrence F. Rozsnyai, Charles M. Lieber, *J. Am. Chem. Soc.*, **1997**, 119, 2006–2015.

24. Tadesse Z. Mengistu, Vishya Goel, J. Hugh Horton, Sylvie Morin, *Langmuir*, **2006**, 22, 5301–5307.
25. Poobalasingam Abiman, Gregory G. Wildgoose Dr., Alison Crossley Dr., John H. Jones Dr., Richard G. Compton Prof., *Chem. Eur. J.*, **2007**, 13, 9663–9667.
26. Sarvin Moghaddam, Cheng Yang, Mikhail Rekharsky, Young Ho Ko, Kimoon Kim, Yoshihisa Inoue, Michael K. Gilson, *J. Am. Chem. Soc.*, **2011**, 133, 3579–3581.
27. Hao Chen, Shengzhen Hou, Haili Ma, Xu Li, Yebang Tan, *Sci. Rep*., **2016**, 6, 1–10.
28. Dissociation Constants of Organic Bases in Aqueous Solution; Perrin, D. D., Ed.; Butterworths: London, UK, **1965**.
29. Woo Sung Jeon, Kwangyul Moon, Sang Hyun Park, Hyungpil Chun, Young Ho Ko, Jin Yong Lee, Eun Sung Lee, S. Samal, N. Selvapalam, Mikhail V. Rekharsky, Vladimir Sindelar, David Sobransingh, Yoshihisa Inoue, Angel E. Kaifer, Kimoon Kim, *J. Am. Chem. Soc*., **2005**, 127, 12984–12989.
30. Shin Jung C. Lee, Jong Wha Lee, Hong Hee Lee, Jongcheol Seo, Dong Hun Noh, Young Ho Ko, Kimoon Kim, Hugh I. Kim, *J. Phys. Chem. B*, **2013**, 117, 8855–8864.
31. Yoshimi Sueishi, Tomonori Fujita, Shinichiro Nakatani, Naoya Inazumi, Yoshihiro Osawa, *Spectrochim. Acta Mol. Biomol. Spectrosc.*, **2013**, 114, 344–349.
32. Winston Ong, Angel E. Kaifer, *J. Org. Chem*., **2004**, 69, 1383–1385.
33. Xiaoqun Zhu, Xiuwei Fan, Guannan Ju, Mengjiao Cheng, Qi An, Jun Nie, Feng Shi, *Chem. Commun*., **2013**, 49, 8093–8095.
34. Alan K. Schrock, Gary B. Schuster, *J. Am. Chem. Soc*., **1984**, 106, 5228.
35. Karen L. Buchmueller, Brian T. Hill, Matthew S. Platz, Kevin M. Weeks, *J. Am. Chem. Soc*., **2003**, 125, 10850.
36. Yan Zhao, Zhiguang Xu, Xungai Wang, Tong Lin, *Langmuir*, **2012**, 28, 6328–6335.
37. Sang Yong Jon, Narayanan Selvapalam, Dong Hyun Oh, Jin-Koo Kang, Soo-Young Kim, Young Jin Jeon, Jae Wook Lee, Kimoon Kim, *J. Am. Chem. Soc*., **2003**, 125, 10186–10187.
38. Kimoon Kim, Narayanan Selvapalam, Young Ho Ko, Kyeng Min Park, Dongwoo Kim, Jeeyeon Kim, *Chem. Soc. Rev*., **2007**, 36, 267–279.
39. Jason Lagona, Pritam Mukhopadhyay, Sriparna Chakrabarti, Lyle Isaacs, *Angew. Chem. Int. Ed*., **2005**, 44, 4844–4870.
40. Jan Tkac, Jason J Davis, *Journal of Electroanalytical Chemistry*, **2008**, 621, 117–120.
41. Mary M. Walczak, Darwin D. Popenoe, Randall S. Deinhammer, Brian D. Lamp, Chinkap. Chung, Marc D. Porter, *Langmuir*, **1991**, 7, 2687–2693.
42. Hee-Joon Kim, Woo Sung Jeon, Young Ho Ko, Kimoon Kim, *PNAS*, **2002**, 99, 5007–5011.

43. Simin Liu, Christian Ruspic, Pritam Mukhopadhyay, Sriparna Chakrabarti, Peter Y. Zavalij, Lyle Isaacs, *J. Am. Chem. Soc*., **2005**, 127, 15959–15967.
44. Young Ho Ko, Kyungpil Kim, Jin-Koo Kang, Hyungphil Chun, Jae Wook Lee, Shigeru Sakamoto, Kentaro Yamaguchi, James C. Fettinger, Kimoon Kim, *J. Am. Chem. Soc*., **2004**, 126, 1932–1933.
45. Tadashi Mori, Young Ho Ko, Kimoon Kim, Yoshihisa Inoue, *J. Org. Chem*., **2006**, 71, 3232–3247.
46. Young Ho Ko, Kyungpil Kim, Eunju Kim, Kimoon Kim, *Supramol. Chem*, **2007**, 19, 287–293.

## List of Figures

**Figure 1.** Ferrocene-europium dyad, Eu.2. Oxidation of the Fc chromophore brings about the formation of the quenching ferrocenium ($Fc^{+}$) moiety, and a reduction in the intensity of sensitised luminescent emission from the lanthanide centre ($\lambda_{ex}$ 340 nm, $\lambda_{em}$ 616 nm).[5,6]

**Figure 2.** XPS spectrum of a CB[7]-modified Au surface. **Inset.** Increases in ellipsometric film thickness and surface wettablity recorded following the deposition of CB[7] at Au. Reported increases are those determined from, and averaged over, three separately prepared samples (A, B and C), with four measurements per sample.

**Figure 3.** Recruitment of FcMV at a CB[7]-functionalised Au substrate.

**Figure 4. Left.** Cyclic voltammograms of a CB[7]-modified Au electrode (**Black**), a 0.1 mM aqueous solution of FcMV (**Red**) and a FcMV@CB[7]-modified Au electrode (**Blue**). **Right.** Cyclic voltammograms of a FcMV@CB[7]-modified Au electrode recorded at variable scan rates.

**Figure 5.** Recruitment of Eu.2 at a CB[7]-functionalised Au interface (**Left**), and deposition of Eu.2-CB[7] at Au (**Right**).

**Figure 6.** Cyclic voltammograms of a bare Au electrode prior to (**Black**) and following exposure to a 1 mM AcN solution of $FcCH_2NMe_3^{+}$ (**Blue**), and of a $FcCH_2NMe_3^{+}$@CB[7]-modified electrode following immersion in a 10 mM aqueous solution of amantadine hydrochloride (AdHCl) (**Red**). Significant physical adsorption of $FcCH_2NMe_3^{+}$ at bare Au is apparent. That is, the Fc / $Fc^{+}$ redox couple (529 mV *vs.* SCE) is present following immersion of the interface in a 10 mM aqueous solution of AdHCl.

**Figure 7.** Recruitment of AdHCl to a CB[7]-functionalised interface, and the undesirable interaction between Au and both cationic and neutral Fc-appended derivatives. The Fc-appended derivatives physically adsorb to the functionalised Au substrate, irrespective of whether or not AdHCl has been previously recruited to the CB[7]-functionalised interface.

**Figure 8.** Formation of CB[7]-functionalised self-assembled monolayers (SAM) at Si, ITO and glass; **Experimental, 7.3.5**.

**Figure 9**. $^{1}$H NMR spectra ($D_2O$, 298 K, 400 MHz) of solutions of 1,4-diaminobutane prior to (**Trace A**) and following the addition of a stoichiometric amount of CB[6] (**Trace B**), CB[7] (**Trace C**) or CB[8] (**Trace D**). All complexes were generated at a concentration of 2 mM. The unassigned multiplets in **Trace B** are attributed to the presence of uncomplexed 1,4-diaminobutane. **Traces A – D, Bottom – Top**.

**Figure 10**. $^{1}$H NMR spectra ($D_2O$, 298 K, 400 MHz) of solutions of hexylamine prior to (**Trace A**) and following the addition of a stoichiometric amount of CB[6] (**Trace B**), CB[7] (**Trace C**) or CB[8] (**Trace D**). All complexes were generated at a concentration of 2 mM. **Traces A – D, Bottom – Top**.

**Figure 11.** $^{1}$H NMR spectra ($D_2O$, 298 K, 400 MHz) of solutions of 1,4-diaminobutane (**Trace A**), 1,4-diaminobutane-CB[7] (**Trace B**), $MV^{2+}$ (**Trace C**), a 1:1:1 mixture of 1,4-diaminobutane, $MV^{2+}$ and CB[7] (**Trace D**) and $MV^{2+}$-CB[7] (**Trace E**). **Inset.** The aliphatic region of each $^{1}$H NMR spectrum. All complexes were generated at a concentration of 2 mM. **Traces A – E, Bottom – Top.**

**Figure 12.** Depicting the loss of $MV^{2+}$-CB[7] from the interface upon the attempted recruitment of $MV^{2+}$ from solution.

**Figure 13.** $^1$H NMR spectra ($D_2O$, 298 K, 400 MHz) of a solution of hexylamine prior to (T**race A**) and following the additions of CB[7] (**Trace B**) and FcMeOH (**Trace C**). All complexes were generated at a concentration of 2 mM. **Traces A – C, Bottom – Top**.

**Figure 14.** $^1$H NMR spectra ($D_2O$, 298 K, 400 MHz) of a solution of 1,4-diaminobutane prior to (T**race A**) and following the additions of CB[7] (**Trace B**) and FcMeOH (**Trace C**). All complexes were generated at a concentration of 2 mM. **Traces A – C, Bottom – Top**.

**Figure 15.** $^1$H NMR spectra ($D_2O$, 298 K, 400 MHz) of solutions of hexylamine (**Trace A**) and hexylamine-CB[7] (**Trace B**), and of a solution of FcMeOH-CB[7] following the addition of a stoichiometric amount of hexylamine (**Trace C**). All complexes were generated at a concentration of 2 mM. **Traces A – C, Bottom – Top.**

**Figure 16.** $^1$H NMR spectra ($D_2O$, 298 K, 400 MHz) of solutions of 1,4-diaminobutane (**Trace A**) and 1,4-diaminobutane -CB[7] (**Trace B**), and of a solution of FcMeOH-CB[7] following the addition of a stoichiometric amount of 1,4-diaminobutane (**Trace C**). All complexes were generated at a concentration of 2 mM. **Traces A – C, Bottom – Top.**

**Figure 17.** $^1$H NMR spectra ($D_2O$, 298 K, 400 MHz) of solutions of 1,4-diaminobutane-CB[7] (**Trace A**), (1,4-diaminobutane-CB[7]) + $MV^{2+}$ (**Trace B**), $MV^{2+}$-CB[7] (**Trace C**) and a 1:1:1 mixture of 1,4-diaminobutane, $MV^{2+}$ and CB[7] (**Trace D**). **Inset.** The aliphatic region of each $^1$H NMR spectrum. All complexes were generated at a concentration of 2 mM. **Traces A – D, Bottom – Top.**

**Figure 18.** Naphthalene-appended, emissive europium derivative, EuNap.

**Figure 19.** $^1$H NMR spectra ($D_2O$, 298 K, 400 MHz) of solutions of 1,4-diaminobutane (**Trace A**), 1,4-diaminobutane-CB[7] (**Trace B**), 2,6-Np (**Trace C**) and a 1:1:1 mixture of 1,4-diaminobutane, 2,6-Np and CB[7] (**Trace D**). All complexes were generated at a concentration of 2 mM. **Traces A – D, Bottom – Top.**

**Figure 20.** $^1$H NMR spectra ($D_2O$, 298 K, 400 MHz) of solutions of 1,4-diaminobutane-CB[7] (**Trace A**), (1,4-diaminobutane-CB[7]) + 2,6-Np (**Trace B**), a 1:1:1 mixture of 1,4-diaminobutane, 2,6-Np and CB[7] (**Trace C**) and 2,6-Np-CB[7] (**Trace D**). **Inset.** The aliphatic region of each $^1$H NMR spectrum. All complexes were generated at a concentration of 2 mM. **Traces A – D, Bottom – Top**.

**Figure 21.** Recruitment of 2,6-Np (*n.b.* also valid for the recruitment of EuNap) at a CB[7]-functionalised interface.

**Figure 22.** $^1$H NMR spectra ($D_2O$, 298 K, 400 MHz) of solutions of 1,4-diaminobutane (**Trace A**), 1,4-diaminobutane-CB[7] (**Trace B**) and 1,4-diaminobutane-CB[7], pD 12.28 (**Trace C**). The pH of the binary complex solution was altered *via* the addition of a 1 M $D_2O$ solution of NaOD. No significant change in the spectrum of the binary complex (1,4-diaminobutane-CB[7]) arose upon increasing the pD of the solution; the guest species remained confined within the apolar cavity of the macrocyclic host upon deprotonation of its terminal amine groups, that is the resultant spectrum (**Trace C**) did not resemble that of 1,4-diaminobutane in solution, **Trace A**; *cf.* when FcMeOH was added to a solution of the binary complex, **Figure 14**. The above observations were also made in the case of hexylamine. All complexes were generated at a concentration of 2 mM. **Traces A – C, Bottom – Top**.

**Figure 23.** Interactions governing the recruitment of CB[7] at the interface (**Top**), and the complexation of hexylamine and 1,4-diaminobutane by CB[7] in solution (**Bottom**).

**Figure 24.** Formation of SAMs of CB[7] on Si and Au by way of nitrene insertion.[33]

**Figure 25.** Hydroxylation of CB[7].

**Figure 26.** Functionalisation of CB[7].

**Figure 27.** Deposition of 1-(10-mercaptodecyl)-1'-methyl-[4,4'-bipyridine]-diium bromide at Au substrates. Deposition of the thiolate was undertaken from both aqueous ($H_2O$) and non-aqueous media (AcN, $CH_2Cl_2$), depending on the identity of the counter ion(s) present (aqueous: $Br^-$ or $Cl^-$, non-aqueous: $PF_6^-$).

**Figure 28.** Cyclic voltammograms recorded following the deposition of 1-(10-mercaptodecyl)-1'-methyl-[4,4'-bipyridine]-diium bromide at Au (**Red**), and upon exposure of a bare Au electrode (**Black**) to a 5 mM aqueous solution of $MV^{2+}$ (**Green**).

**Figure 29.** Deposition of ($MV^{2+}$-SH,CB[7]) and ($MV^{2+}$-SH,CB[8]) at Au.

**Figure 30.** Covalent attachment of $MVNH_3^+$ to a SAM of MHDA (**Top**), and $MVN_3^+$ to an azido-terminated interface (**Bottom**). $MVNH_3^+$ and $MVN_3^+$ were synthesised by Alexander Hess of the Paul Beer Group (University of Oxford). All precursor molecular films were

characterised by cyclic voltammetry (diffusive redox probe and thiolate stripping) and ellipsometric film thickness measurements prior to use, as to ensure that the Au surface was passivated and that the SAMs formed were uniform in structure.

**Figure 31.** Formation of the cyclic diketone analogue of paraquat.

**Figure 32.** Cyclic voltammograms recorded following the deposition of 1-(10-mercaptodecyl)-1'-methyl-[4,4'-bipyridine]-diium bromide (**Red**) and 1-(10-mercaptodecyl)-1'-methyl-[4,4'-bipyridine]-diium bromide-CB[8] (**Black**) at Au (**Blue**).

**Figure 33.** Reversible formation of the binary complex, $MV^{2+}$-SH,CB[8], at a SAM of 1-(10-mercaptodecyl)-1'-methyl-[4,4'-bipyridine]-diium bromide deposited at Au.

**Figure 34.** Cyclic voltammogram recorded following the reductive desorption of 1-(10-mercaptodecyl)-1'-methyl-[4,4'-bipyridine]-diium bromide-CB[8] from the interface.

**Figure 35.** Forming a bilayer at the interface by exploiting 1:2 heteroternary complex formation. Quoted interfacial distances were determined by either ellipsometry, that is if an error bar is given, or estimated by a minimisation approach (MM2) conducted in Chem3D 15.0. This holds from here on in, unless otherwise stated.

**Figure 36.** Formation of the 1:1 *intra*molecular heteroternary complex upon recruitment of 1-methyl-1'-(10-(naphthalen-2-yloxy)decyl)-[4,4'-bipyridine]-1,1'-diium bromide iodide at a $MV^{2+}$-CB[8]-functionalised interface.

**Figure 37.** Recruitment of 1-methyl-1'-(10-(naphthalen-2-yloxy)decyl)-[4,4'-bipyridine]-1,1'-diium bromide iodide-CB[7] at a $MV^{2+}$-CB[8]-functionalised interface. Formation of the 1:1 *intra*molecular heteroternary complex should have been prevented.

**Figure 38.** $^1$H NMR spectra ($D_2O$, 298 K, 400 MHz) of solutions of 1-methyl-1'-(10-(naphthalen-2-yloxy)decyl)-[4,4'-bipyridine]-1,1'-diium prior to (**Trace A**) and following the addition of a stoichiometric amount of CB[7]. All complexes were generated at a concentration of 2 mM. **Traces A – B, Bottom – Top**.

**Figure 39.** $^1$H NMR spectra ($D_2O$, 298 K, 400 MHz) of solutions of 1-methyl-1'-(10-(naphthalen-2-yloxy)decyl)-[4,4'-bipyridine]-1,1'-diium prior to (**Trace A**) and following the addition of a stoichiometric amount of CB[6] (**Trace B**), CB[7] (**Trace C**) or CB[8] (**Trace D**). All complexes were generated at a concentration of 2 mM. **Traces A – D, Bottom – Top**.

**Figure 40.** $^1$H NMR spectra ($D_2O$, 298 K, 400 MHz) of solutions of 1-methyl-1'-(10-(naphthalen-2-yloxy)decyl)-[4,4'-bipyridine]-1,1'-diium (**Trace A**), 1-methyl-1'-(10-(naphthalen-2-yloxy)decyl)-[4,4'-bipyridine]-1,1'-diium-CB[7] (**Trace B**), 1-methyl-1'-(10-(naphthalen-2-yloxy)decyl)-[4,4'-bipyridine]-1,1'-diium-CB[8] (**Trace C**), (1-methyl-1'-(10-(naphthalen-2-yloxy)decyl)-[4,4'-bipyridine]-1,1'-diium-CB[8]) + CB[7] (**Trace D**) and (1-methyl-1'-(10-(naphthalen-2-yloxy)decyl)-[4,4'-bipyridine]-1,1'-diium-CB[7]) + CB[8] (**Trace E**). All complexes were generated at a concentration of 2 mM. **Traces A – E, Bottom – Top.**

**Figure 41.** $^1$H NMR spectra ($D_2O$, 298 K, 400 MHz) of solutions of 1-methyl-1'-(10-(naphthalen-2-yloxy)decyl)-[4,4'-bipyridine]-1,1'-diium prior to (**Trace A**) and following the addition of a stoichiometric amount of CB[7] (**Trace B**), CB[8] (**Trace C**) or a 1:1 mixture of CB[7] and CB[8] (**Trace D**). All complexes were generated at a concentration of 2 mM. **Traces A – E, Bottom – Top.**

**Figure 42.** A possible way of transforming the 1:1 *intra*molecular heteroternary complex into the desired 1:1 *inter*molecular analogue.

**Figure 43**. $^1$H NMR spectra ($D_2O$, 298 K, 400 MHz) of solutions of 1-methyl-1'-(10-(naphthalen-2-yloxy)decyl)-[4,4'-bipyridine]-1,1'-diium (**Trace A**), 1-methyl-1'-(10-(naphthalen-2-yloxy)decyl)-[4,4'-bipyridine]-1,1'-diium-CB[8] (**Trace B**), (1-methyl-1'-(10-(naphthalen-2-yloxy)decyl)-[4,4'-bipyridine]-1,1'-diium-CB[8]) + 2,6-Np (**Trace C**) and 2,6-Np (**Trace D**). All complexes were generated at a concentration of 2 mM. **Traces A – E, Bottom – Top.**

**Figure 44**. $^1$H NMR spectra ($D_2O$, 298 K, 400 MHz) of solutions of 2,6-Np (**Trace A**), 2,6-Np-CB[8] (**Trace B**), ($MV^{2+}$, 2,6-Np)-CB[8] (**Trace C**), 1-methyl-1'-(10-(naphthalen-2-yloxy)decyl)-[4,4'-bipyridine]-1,1'-diium (**Trace D**) and (1-methyl-1'-(10-(naphthalen-2-yloxy)decyl)-[4,4'-bipyridine]-1,1'-diium-CB[8] (**Trace E**). All complexes were generated at a concentration of 2 mM. **Traces A – E, Bottom – Top.**

**Figure 45**. 1:1 *intra*molecular heteroternary complex formation upon the recruitment of 1-methyl-1'-(10-(naphthalen-2-yloxy)decyl)-[4,4'-bipyridine]-1,1'-diium bromide iodide-CB[7] at a $MV^{2+}$-CB[8]-functionalised interface. Exposure of the interface to a solution of the binary complex, 1-methyl-1'-(10-(naphthalen-2-yloxy)decyl)-[4,4'-bipyridine]-1,1'-diium-CB[7], does not bring about preferential formation of the *inter*molecular analogue.

**Figure 46.** $^1$H NMR spectra ($D_2O$, 298 K, 400 MHz) of solutions of 1-methyl-1'-(10-(naphthalen-2-yloxy)decyl)-[4,4'-bipyridine]-1,1'-diium bromide iodide (**Trace A**), 1-methyl-1'-(10-(naphthalen-2-yloxy)decyl)-[4,4'-bipyridine]-1,1'-diium bromide iodide-CB[7] (**Trace B**), 1-methyl-1'-(10-(naphthalen-2-yloxy)decyl)-[4,4'-bipyridine]-1,1'-diium bromide iodide-CB[8] (**Trace C**) and (1-(10-mercaptodecyl)-1'-methyl-[4,4'-bipyridine]-diium bromide-CB[8] + 1-methyl-1'-(10-(naphthalen-2-yloxy)decyl)-[4,4'-bipyridine]-1,1'-diium bromide iodide-CB[7]) (**Trace D**). All complexes were generated at a concentration of 2 mM. **Traces A – E, Bottom – Top.**

**Figure 47.** $^1$H NMR spectra ($D_2O$, 298 K, 400 MHz) of solutions of 1-methyl-1'-(10-(naphthalen-2-yloxy)decyl)-[4,4'-bipyridine]-1,1'-diium bromide iodide (**Trace A**), 1-methyl-1'-(10-(naphthalen-2-yloxy)decyl)-[4,4'-bipyridine]-1,1'-diium bromide iodide-CB[7] (**Trace B**), (1-(10-mercaptodecyl)-1'-methyl-[4,4'-bipyridine]-diium bromide-CB[8] + 1-methyl-1'-(10-(naphthalen-2-yloxy)decyl)-[4,4'-bipyridine]-1,1'-diium bromide iodide-CB[7]) (**Trace C**) and 1-(10-mercaptodecyl)-1'-methyl-[4,4'-bipyridine]-diium bromide (**Trace D**). All complexes were generated at a concentration of 2 mM. **Traces A – E, Bottom – Top.**

**Figure 48.** $^1$H NMR spectra ($D_2O$, 298 K, 400 MHz) of solutions of 1-methyl-1'-(10-(naphthalen-2-yloxy)decyl)-[4,4'-bipyridine]-1,1'-diium bromide iodide (**Trace A**), 1-methyl-1'-(10-(naphthalen-2-yloxy)decyl)-[4,4'-bipyridine]-1,1'-diium bromide iodide-CB[7] (**Trace B**), (1-methyl-1'-(10-(naphthalen-2-yloxy)decyl)-[4,4'-bipyridine]-1,1'-diium bromide iodide-CB[7]) + CB[8] (**Trace C**), (1-methyl-1'-(10-(naphthalen-2-yloxy)decyl)-[4,4'-bipyridine]-1,1'-diium bromide iodide-CB[7]) + CB[8]-AdHCl (**Trace D**). All complexes were generated at a concentration of 2 mM. **Traces A – E, Bottom – Top.**

**Figure 49.** Synthesis of 1-methyl-1'-(4-(naphthalen-2-yloxy)benzyl)-[4,4'-bipyridine]-1,1'-diium.

**Figure 50.** Recruitment of 1-methyl-1'-(4-(naphthalen-2-yloxy)benzyl)-[4,4'-bipyridine]-1,1'-diium at a $MV^{2+}$-CB[8]-functionalised interface. It is feasible that incorporation of an aryl moiety into the backbone of the rigid linker derivative will drive formation of the 1:1 *inter*molecular heteroternary complex at the expense of the 1:1 *intra*molecular analogue.

**Figure 51.** Inclusion of both 1-methyl-1'-(10-(naphthalen-2-yloxy)decyl)-[4,4'-bipyridine]-1,1'-diium bromide iodide (**Top**) and 1-methyl-1'-(4-(naphthalen-2-yloxy)benzyl)-[4,4'-bipyridine]-1,1'-diium (**Bottom**) within the apolar cavity of CB[8], as modelled in Chem3D 15.0. Inclusion of 1-methyl-1'-(10-(naphthalen-2-yloxy)decyl)-[4,4'-bipyridine]-1,1'-diium bromide iodide proceeds to generate the 1:1 *intra*molecular heteroternary complex; this is not possible in the case of the conformationally restricted derivative, 1-methyl-1'-(4-(naphthalen-2-yloxy)benzyl)-[4,4'-bipyridine]-1,1'-diium.

**Figure 52.** Incorporating triazolium (**Top**) and bistriazolium (**Bottom**) derivatives within the apolar cavity of CB[8], at the expense of $MV^{2+}$, to try to nullify the effect of charge-transfer on the emissive state of the lanthanide ion.

# 6. Summary and Outlook

This thesis has described the development and application of a conformational ruler within porphyrin-appended self-assembled monolayers (SAMs), and utilised host-guest chemistry, both in solution and at the interface, to assemble novel lanthanide-containing heteroternary complexes able to function as supramolecular switches. The conformational ruler has been used to optimise photoelectrochemical output and highlight at what distance, relative to one another, the molecular stations within a bistable [2]rotaxane should be set apart to permit differentiation of the ground state (GSCC) and metastable state co-conformations (MSCC).

In chapter 2, the concept of photoinduced electron transfer was introduced, and cathodic photocurrent density (CPCD) measurements undertaken at monophasic and biphasic, porphyrin-appended SAMs. The magnitude of CPCD acquired was demonstrated to increase upon the introduction of both an electron acceptor (methyl viologen, $MV^{2+}$, $\leq$ 160 % nA $mol^{-1}$ $cm^{-2}$) and an electron mediator ((ferrocenylmethyl)trimethylamonium iodide, $\leq$ 283 % nA $mol^{-1}$ $cm^{-2}$) into solution, and upon the integration of ferrocenethiols of varying chain length (1.2 nm (6-(ferrocenyl)hexanethiol, Fc6SH) and 1.7 nm (11-(ferrocenyl)undecanethiol, Fc11SH) within the molecular film. The electron acceptor moiety acts as an electron 'sink', whilst the electron mediator serves to mediate electron transfer and compensate for the drop in the forward rate of electron transfer between the metallic substrate and the excited state of the porphyrinic macrocycle ($P^*$), induced upon tethering the porphyrinic macrocycle further from the interface to reduce the rates of both backward electron and backward energy transfer from $P^*$ to the gold (Au) surface. Involvement of the relay moiety, both in solution and at the interface, was highlighted by the fact that it was possible to modulate the magnitude of the CPCD acquired by gating the forward rate of electron transfer between the Au surface and the metallocene. This intermolecular relay effect was also observed to be dependent upon the distances between the metallic interface, the electron relay moiety and the porphyrinic macrocycle. Greatest photoelectrochemical output ($5.1 \times 10^{14}$ nA $mol^{-1}$ $cm^{-2}$) is realised when the porphyrinic macrocycle is covalently tethered at 4.6 nm from the quenching metallic interface, and the relay moiety integrated at 1.7 nm from the interface and 2.9 nm from the porphyrinic macrocycle respectively. This conformational ruler was utilised in the design of a novel bistable [2]rotaxane to ensure that the photoelectrochemical differentiation of its GSCC and MSCC was viable. The research conducted on this front is presented in chapter 3.

Initially, the formation of a pseudorotaxane consisting of a ferrocene-appended macrocycle and a porphyrin-appended axle was confirmed by means of nuclear magnetic resonance (NMR) ($^1$H and rotating frame nuclear overhauser effect (ROESY)) spectroscopy. Covalent attachment of the assembly to an underlying carboxy-functionalised interface (PEG: HS-$(CH_2)_{10}$-$EG_3$-$OCH_2$-COOH) proved problematic: the presence of the ferrocene-appended macrocycle was not detected by either cyclic

voltammetry (CV) or x-ray photoelectron spectroscopy (XPS). Thus, the use of thioctic-acid functionalised axles in the assembly of porphyrin-appended, rotaxanated molecular films was explored. However, the generation of singlet oxygen, by the free-base porphyrin derivative and thus the subsequent formation of the analogous thiosulfinates and / or thiosulfonates, prevented their surface deposition. The effect of singlet oxygen was negated upon metalation (nickel(II) ($Ni^{II}$)) of the porphyrinic core, but no CPCD was acquired upon the irradiation ($\lambda_{irr}$ = 430 ± 5 nm) of SAMs incorporating metallated porphyrin derivatives at the periphery. A decrease in the intensity of the fluorescent output from the porphyrinic macrocycle ($Q_x$ (0,0) and $Q_x$ (0,1)) illustrates the ability of $Ni^{II}$, a metal ion possessing partially filled *d*-orbitals, to act as an efficient excited-state quencher. Although the interfacial assembly of such porphyrin-appended architectures has proven very difficult to date and thus the flow of cathodic photocurrent has yet to be realised within an interpenetrated molecular film, it is anticipated that such an objective will be met upon the generation of an assembly by means of an approach centred on the formation of a SAM in which the macrocyclic component resides at an initial molecular station (**Chapter 3, Figure 56**). The attachment of a free-base porphyrin derivative, by means of a copper-free click cycloaddition reaction, serves to incorporate an additional molecular station. Additionally, formation of the thiosulfonate analogue could be circumvented by exploiting host-guest chemistry at the interface (**Chapter 3, Figure 57**). In conjunction with the conformational ruler established, either approach is likely to permit novel photoelectrochemical transduction of macrocyclic motion within dynamic, supramolecular architectures.

In chapter 4, the concept of ternary complex formation was introduced and a model ternary complex generated in which both 2,6-dihydroxynaphthalene (2,6-Np) and methyl viologen ($MV^{2+}$) are confined within the cavity of cucurbit[8]uril (CB[8]), ($MV^{2+}$, 2,6-Np)-CB[8]. Charge-transfer was observed ($\lambda_{max}$ = 570 nm) but disappeared following subsequent generation of the homoternary dimer complex, $(MV^{+\bullet})_2$-CB[8] ($\lambda_{max} \approx$ 535 nm), upon the addition of sodium dithionite ($Na_2S_2O_4$) into solution. Following characterisation of the model ternary complex, a lanthanide centre was incorporated in the form of a synthesised EuNap derivative (($MV^{2+}$, EuNap)-CB[8]) and its optical switching properties investigated. The induction of charge-transfer was demonstrated to quench sensitised lanthanide emission ($Eu^{3+}$, $Nd^{3+}$, $Yb^{3+}$), and this concept was utilised in the development of a novel supramolecular switch (($MV^{2+}$, EuNap)-CB[8] ↔ $(MV^{+\bullet})_2$-CB[8] + EuNap). Development of the switch was facilitated by the fact that the charge-transfer band ($\lambda$ = 390, 490 nm) and europium (III) ($Eu^{3+}$) compete for energy transfer from the antenna species, naphthalene; $\tau_{Eu}$= 0.6 ms → $\tau_{Eu}$ = 0.1 ms upon confinement within the apolar cavity of CB[8]. Exploiting this chemically-triggered method in a bid to optically switch the radiative output from the excited state of $Eu^{3+}$, $^7D_0$, confined within the desired complex, (FcMV, EuNap)-CB[8], proved problematic due to the slow rate of regeneration of the ternary complex following prior reduction and the competitive binding of sodium cations to the periphery of the macrocyclic host. In addition, formation of the desired ternary complex ((FcMV, EuNap)-CB[8]) was

sterically and kinetically impeded, whilst *in-situ* oxidation of the ferrocene-functionalised viologen derivative (FcMV) was observed throughout. (FcMV, EuNap)-CB[8] was observed at an extremely low relative intensity (2 % by ESI MS, *m / z* 1247.36), thus research moved towards trying to negate the effect of charge transfer by hydrogenation and synthesise both 1-(10-mercaptodecyl)-1'-methyl-[4,4'-bipyridine]-diium bromide ($MV^{2+}$-SH) and 1-methyl-1'-(10-(naphthalen-2-yloxy)decyl)-[4,4'-bipyridine]-1,1'-diium bromide iodide. It was assumed that the synthesis of both $MV^{2+}$-SH and 1-methyl-1'-(10-(naphthalen-2-yloxy)decyl)-[4,4'-bipyridine]-1,1'-diium bromide iodide would permit the assembly of a lanthanide-appended interface, whereby modulation of any optical output acquired from the lanthanide centre could be brought about upon the integration of either Fc6SH or Fc11SH into the molecular film. This approach was examined in chapter 5, along with other methods of immobilising lanthanide complexes at a variety of interfaces.

Initially, the recruitment of a ferrocene-europium dyad, Eu.2, was probed at a SAM of cucurbit[7]uril (CB[7]) deposited at Au; a strong multivalent interaction is reported to arise between the carbonyl portals of the macrocyclic host and the metallic substrate. No emissive output ($\lambda_{ex}$ 340 nm, $\lambda_{em}$ 616 nm) was detected upon analysis of the substrate and it was assumed that the lanthanide centre was in too close a proximity to the quenching Au interface. Thus, and as CB[7] does not directly interact with either silicon (Si), indium tin oxide (ITO) or glass, an alternative interface was assembled in a bid to acquire an optical signature upon the recruitment of Eu.2. CB[7] was recruited to an underlying monolayer of (3-aminopropyl)triethoxysilane (APTES). Recruitment of the macrocyclic host centres on the electrostatic interaction induced, following a reduction in pH, between the positively charged amine terminus of APTES and the negatively polarised carbonyl portals lining the periphery of the macrocyclic host. The recruitment of CB[7] was shown to be pH dependent. The macrocyclic host is only recruited to the periphery of the interface when the pH of the deposition solution is lowered below that of the pKa of the amine terminus of APTES (pKa 9.94). The recruitment of guest species was prohibited by the fact that inclusion of the alkyl derivative, within the apolar cavity of the macrocyclic host species, was shown to drive assembly of the underlying interface. To ensure that the carbonyl portals of the macrocyclic host were available to drive host-guest complexation, and the recognition properties of CB[7] maintained, a radical based approach was explored in a bid to covalently tether CB[7] to both Si and Au. Azide-functionalised surfaces from which highly reactive singlet and triplet nitrene could be generated (UV irradiation (254, 366 nm)) were fabricated. It was assumed that singlet nitrene could then be inserted into either the C-H bond located at the 'waist' of the CB[7] moiety, or into the bridging $CH_2$ groups. Unfortunately, nitrene insertion was not observed, thus the use of $MV^{2+}$-SH and 1-methyl-1'-(10-(naphthalen-2-yloxy)decyl)-[4,4'-bipyridine]-1,1'-diium bromide iodide, in incorporating CB[*n*] into a molecular film was probed, whilst ensuring that it displays the same level of host-guest affinity it does in solution. To try to exploit 1:2 *inter*molecular heteroternary complex formation in the assembly of lanthanide-appended molecular films, stable SAMs of ($MV^{2+}$- SH,CB[8])

were deposited. However, preferential formation of the *intra*molecular analogue prevented this objective being met; the attempted recruitment of 1-methyl-1'-(10- (naphthalen-2-yloxy)decyl)-[4,4'-bipyridine]-1,1'-diium bromide iodide resulted in loss of the macrocyclic host from the interface and confinement of both termini (N,N′-dimethyl-4,4′-bipyridinium and naphthalene) within its apolar cavity. Growth of the supramolecular architecture is likely to be facilitated in conjunction with the use of a more rigid linker derivative (1-methyl-1'-(4-(naphthalen-2-yloxy)benzyl)-[4,4'-bipyridine]-1,1'-diium), and the effect of charge-transfer may be negated *via* the use of functionalised triazolium and bistriazolium derivatives, which are hoped will absorb at lower wavelength (< 570 nm).

# 7. Experimental

## 7.1 – Material and Reagents

All chemicals and solvents, except ethyl(dimethylaminopropyl) carbodiimide (EDC, Alfa Aesar), tetra(4-aminophenyl) porphyrin (TPAPP, TCI Chemicals), HS-$(CH_2)_{10}$-$EG_3$-$OCH_2$-COOH (OEG, ProChimia), 3-aminopropyltriethoxysilane (APTES, Alfa Aesar) and 4-azidobenzoic acid (PA, J&K Scientific) were purchased from Sigma Aldrich and used as received. Dr Asha Brown (AB-14-172, AB-19-114, AB-18-088, M-AB-18-088, AB-20-042), Dr Manuel Tropiano (Eu.2 (redox-active, ferrocene-europium dyad)), Dr Alexander Hess (YbNap, NdNap, $MVNH_3^+$, $MVN_3^+$, (ferrocenylmethyl)trimethylamonium iodide), Jason Lim (JL241) and Andrew Baxter (FcMV, EuNap) provided a range of derivatives for use. De-ionised water (18.2 MΩ·cm, Millipore Ltd.) was used throughout to prepare aqueous solutions.

Gold substrates for ellipsometric film thickness measurements and luminescent analyses were prepared by vapour deposition of 10 nm of chromium, followed by 100 nm of gold, onto silicon (Si) substrates (Silicon Materials (USA): Si(100), N+/Sb doped, 0.005 – 0.025 Ω·cm (resistivity), 525 ± 25 μm (thickness)). Gold substrates for transmissive UV analyses were prepared by vapour deposition of 2 nm of chromium, followed by 8 nm of gold, onto circular borosilicate glass microscope slides (VWR International, 22 mm in diameter, Product No. 631 – 015). All substrates were prepared by Dr Robert Jacobs (Surface Analysis Facility, University of Oxford). Prior to use, all substrates were cleaned by immersion in piranha solution (a 3:1 by volume mixture of 18 M sulphuric acid and 30% hydrogen peroxide, handle with caution) for 15 seconds and washed with copious amounts of $H_2O$ (18.2 MΩ·cm). They were then dried in a gentle stream of $N_2$ (g).

## 7.2 – Electrochemistry

Electrochemistry was carried out on an Autolab PGSTAT-12 system and all cyclic voltammograms were analysed using General Purpose Electrochemical Software (GPES, Metrohm Autolab, version 4.9).

### 7.2.1 – Electrode Preparation

Polycrystalline gold disk electrodes (BASi, 1.6 mm diameter) were mechanically polished with alumina slurry (0.05 μM) on a polishing cloth (Buehler, UK, Product No. 407212) for 4 minutes. The electrodes were then thoroughly rinsed with de-ionised $H_2O$, cleaned by means of ultrasonication (2 minutes, $H_2O$) to remove residual alumina particles, and immersed into hot piranha solution for ca. 15 minutes. The electrodes were then removed and rinsed with de-ionised $H_2O$, before being electropolished (500 cycles, 0 → 1250 mV *vs.* Ag Wire, Pt auxiliary electrode, 100 mV / s) in a 0.1 M aqueous solution of $H_2SO_4$. The geometric area of each electrode was established prior to use by integrating the peak associated with the reduction of the Au/α gold oxide layer (+ 750 to +

1000 mV, *vs*. Ag Wire, **A**) revealed upon sweeping (sweep rate: 100 mV $s^{-1}$) the potential of the electrode in a 100 mM aqueous solution of $H_2SO_4$, **Figure 1**, and applying **Equation 1**[1,2].

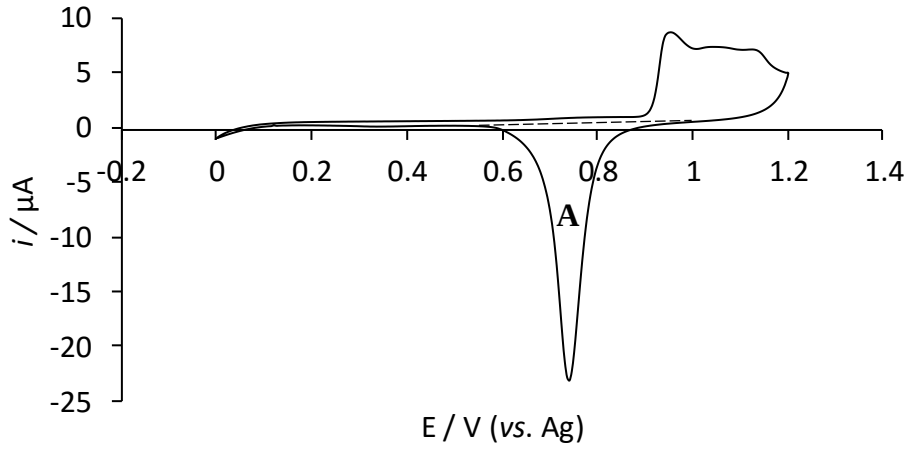


**Figure 1.** A cyclic voltammogram of a gold electrode following electrochemical polishing in a 100 mM aqueous solution of $H_2SO_4$. The surface area of each electrode was calculated upon integrating the peak labelled **A** (reduction of the Au/α gold oxide layer formed in an anodic scan). Electrochemical Setup: *Working Electrode*: Bare Au. *Reference Electrode*: Ag Wire. *Auxiliary Electrode*: Pt wire. *Electrolytic Solution*: 0.1 M $H_2SO_4$ (aqueous). *Scan Rate:* 100 mV / s.

$$A\ (cm^2) = \frac{Q\ (C)}{482\ \mu C\ cm^{-2}}$$

**Equation 1.** Calculating the geometric area (**A**, $cm^2$) of a polycrystalline Au electrode, where **Q** (C, coulombs) is the current obtained upon integrating the reduction peak of the Au/α gold oxide layer (+ 750 to + 1000 mV, vs Ag Wire) and 482 µC $cm^{-2}$ the theoretical amount of current required to remove a monolayer of Au/α gold oxide from the surface of 1 $cm^2$ of Au.[3]

All glassy carbon electrodes, at which diffusive voltammetry was performed, were mechanically polished with alumina slurry (0.05 µM) on a polishing cloth (Buehler, UK, Product No. 407212) for 4 minutes, before being rinsed with copious amounts of $H_2O$, sonicated in $H_2O$ for 10 mins, and subjected to three cycles of washing and drying in a gentle stream of $N_2$ (g).

### 7.2.2 – Calculating the Surface Coverage

The surface coverage of each thiol deposited was calculated, and compared to the theoretical maximum, by considering the area of the reductive stripping peaks (**R**) acquired upon repeatedly sweeping the potential of the modified substrates between – 0.5 and – 1.5 V, in a degassed 0.5 M solution (50:50, EtOH: $H_2O$) of KOH, **Figure 2**.[4,5,6,7]

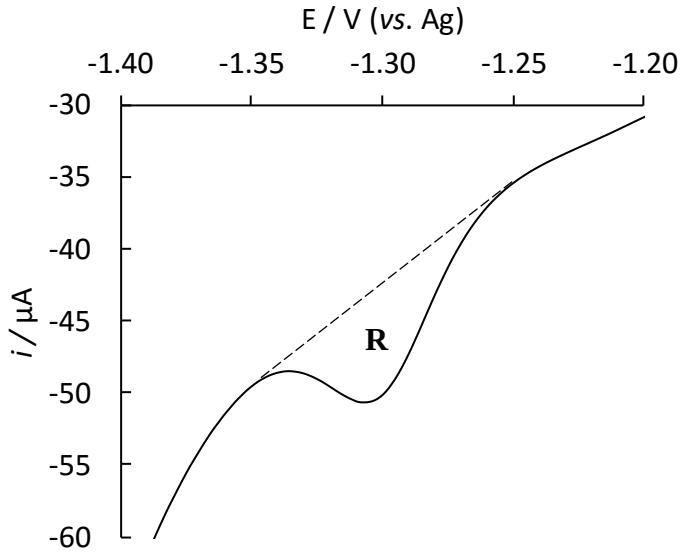


**Figure 2.** The characteristic peak acquired upon reductively 'stripping' thiols from gold interfaces. The above example was acquired upon repeatedly sweeping the potential of a MHDA-modified gold electrode between – 0.5 and – 1.5 V in a degassed 0.5 M solution (50:50, EtOH: $H_2O$) of KOH at a scan rate of 100 mV / s.

The surface coverage of all electroactive thiols deposited was estimated by integrating either the oxidation or reduction peaks acquired upon sweeping the potential of the modified substrates between 0 and + 1.4 V in a degassed 0.1 M solution ($CH_2Cl_2$) of $TBAPF_6$ (**Figure 3**).

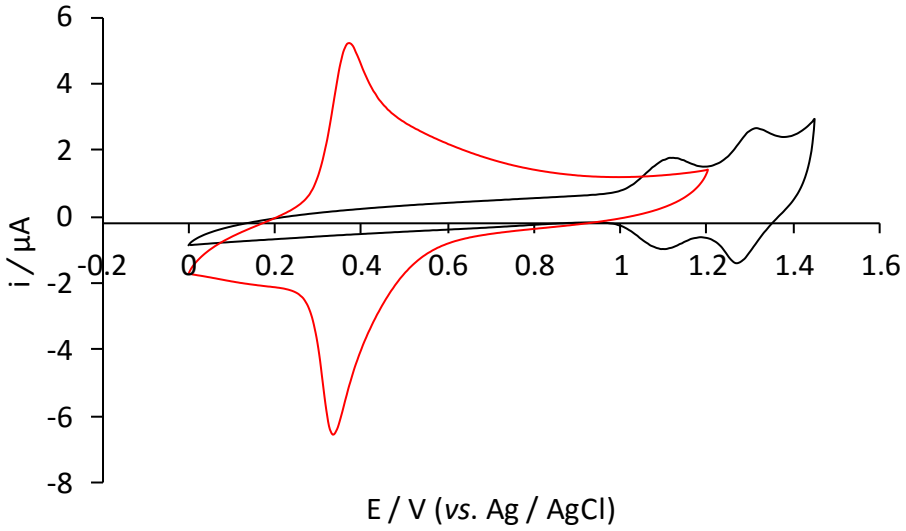


**Figure 3.** Cyclic voltammograms recorded following the deposition of both 11-(ferrocenyl)undecanethiol (**Red**) and a porphyrin-appended thiol (**Black**) at Au. Both CVs were obtained in a 0.1 M solution ($CH_2Cl_2$) of $TBAPF_6$ at a scan rate of 1000 mV /s.

The removal of a thiol layer, and the reductions of both the ferrocenium ion ($Fc/Fc^+$) and the porphyrin moiety ($P^0/P^{+1}$, $P^{+1}/P^{+2}$) at the periphery of the self-assembled monolayer are all one electron processes. The following equation (**Equation 2**) was used to calculate the surface concentration of each (mol $cm^{-2}$), where the cathodic area is the integral of the reductive peak, in

coulombs (C), *n* the number of electrons transferred in the electrochemical process, and F is Faraday's constant (C $mol^{-1}$).

$$\textbf{Equation 2}.\ \text{Surface Concentration (mol } cm^{-2}) = \frac{Cathodic\ Area\ (C)}{n\text{F x Area of Electrode } (cm^2)}$$

**7.2.3 – Calculating the Cathodic Photocurrent Density**

Cathodic photocurrent density measurements were performed in a one-compartment glass cell (50 x 25 mm), **Figure 4**, and all data was acquired on a μAutolabIII/FRA2 electrochemical system, set in chronoamperometry mode, and analysed using GPES (version 4.9). The SAMs (0.020 $cm^2$) were illuminated with light of wavelength 430 ± 5 nm (LUXEON Z UV High Power LED, Part No. LHUV-0425-0650), unless otherwise stated, and the photocurrent measured within a deoxygenated electrolytic solution (0.1 M $Na_2SO_4$) containing 5 mM $MV^{2+}$ as the electron acceptor. All measurements were acquired within a Faraday cage as to reduce the amount of electrical noise and block out any external light. The modified gold electrode served as the working electrode, whilst a platinum wire was used as the auxiliary electrode and a Ag/AgCl electrode (saturated with KCl) used as the reference electrode. The light intensity was monitored using an optical power meter setup (compact power and energy meter console (PM100D, Thorlabs), standard photodiode power sensor (S120VC, Thorlabs)), and the illumination source manipulated and switched on (6.0 mW $cm^{-2}$) and off (0.0 mW $cm^{-2}$) *via* the use of an arbitrary waveform function generator (DG1022, Rigol). The bias potential was held at - 100 mV and reported cathodic photocurrent densities (nA $mol^{-1}$ $cm^{-2}$) are those determined from, and averaged over, two separately prepared electrodes, two measurements per SAM, unless otherwise stated.

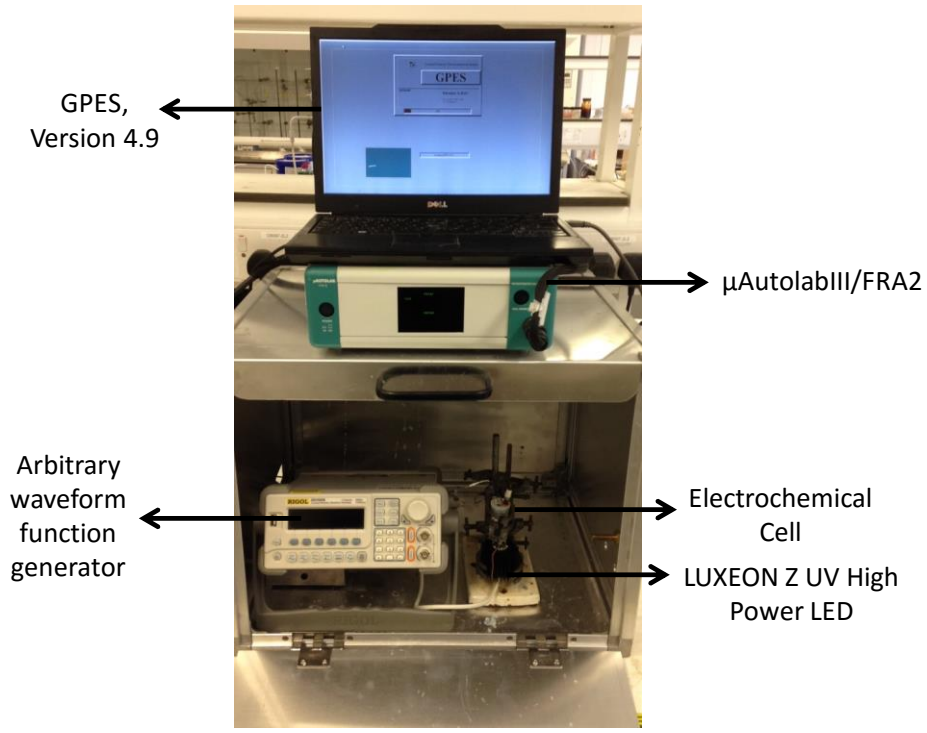


**Figure 4.** An overview of the experimental setup employed to measure cathodic photocurrent density.

All cathodic photocurrent densities were calculated by taking the increase in cathodic current brought about upon irradiation of the porphyrin-terminated monolayer, and normalising the response for the concentration of porphyrin present at the interface. For example, a typical plot of photocurrent *vs.* time is given in **Figure 5**; turning on the irradiation source brought about an increase (-1.09 → -2.88 nA) in the magnitude of the cathodic current generated.

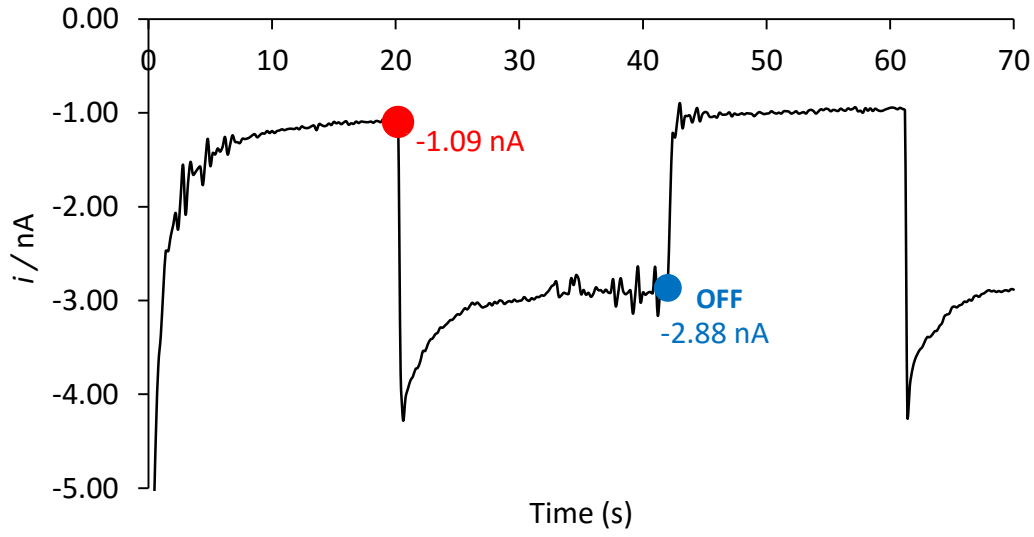


**Figure 5.** A plot of current *vs.* time acquired upon irradiation (**'ON'**, 430 ± 5 nm) of a porphyrin-appended monolayer.

The increase in photocurrent (+ 1.79 nA) was then normalised for the concentration of porphyrin present at the interface, and the geometric surface area of the Au electrode on which the monolayer

was deposited. A representative cathodic photocurrent density (nA $mol^{-1}$ $cm^{-2}$) was yielded. Both the concentration of porphyrin at the interface and the area of the Au electrode were determined by cyclic voltammetry prior to the photoelectrochemical measurements being taken. An example calculation is given below.

**Step 1.** Difference in Cathodic Current, nA = ((-1.09 nA) – (-2.88 nA)) = **1.79**

**Step 2.** Surface Coverage of Porphyrin Moiety, mol $cm^{-2}$ = Q / nFA = **$7.20 \times 10^{-11}$**

**Step 3.** Geometric Area of Au Electrode, $cm^{-2}$ = **0.032**

**Step 4.** Surface Coverage of Porphyrin Moiety, mol = Q / nF = **$2.30 \times 10^{-12}$**

**Step 5.** Cathodic Photocurrent Density, nA $mol^{-1}$ $cm^{-2}$ = (1.79 / 2.30 $\times 10^{-12}$ / 0.032) = **$2.43 \times 10^{13}$**

**7.2.4 – Electrochemical Parameters**

**Redox Probe Voltammetry at SAMs of MUA, MHDA and OEG:** *Working Electrode*: SAM. *Reference Electrode*: SCE. *Auxiliary Electrode*: Pt wire. *Electrolytic Solution*: 0.1 M $NaClO_4$, aqueous. *Scan Rate:* 100 mV / s.

**Solution-Phase Characterisation of AB-14-172:** *Working Electrode*: **Glassy Carbon or Au**. *Reference Electrode*: Ag / $AgNO_3$. *Auxiliary Electrode*: Pt wire. *Electrolytic Solution*: 0.1 M $TBAPF_6$, anhydrous $CH_2Cl_2$. *Scan Rate:* 100 mV / s.

**Characterisation of Porphyrin-Appended SAMs:** *Working Electrode*: Porphyrin-appended SAM deposited at Au. *Reference Electrode*: Ag / AgCl. *Auxiliary Electrode*: Pt wire. *Electrolytic Solution*: 0.1 M $TBAPF_6$, anhydrous $CH_2Cl_2$. *Scan Rate:* 1000 mV / s.

**Reductively Stripping Thiolate from Gold Surface:** *Working Electrode*: SAM deposited at Au. *Reference Electrode*: Ag Wire. *Auxiliary Electrode*: Pt wire. *Electrolytic Solution*: 0.5 M solution (50:50, EtOH: $H_2O$, degassed) of KOH. *Scan Rate:* 100 mV / s.

**Monitoring Anion Templation in Solution:** *Working Electrode:* Glassy Carbon. *Reference Electrode:* Ag / $AgNO_3$. *Auxiliary Electrode:* Pt Wire. *Electrolytic Solution*: 0.1 M $TBAPF_6$, anhydrous $CH_2Cl_2$. *Scan Rate:* 1000 mV / s.

**Monitoring the Inclusion of Ferrocenylmethyltrimethylamine within the Apolar Cavity of CB[7]:** *Working Electrode*: Glassy Carbon. *Reference Electrode*: SCE. *Auxiliary Electrode*: Pt wire. *Electrolytic Solution*: 0.3 M NaCl, aqueous. *Scan Rate:* 100 mV / s.

**Monitoring the Recruitment of Ferrocene-Functionalised Derivatives at SAMs of CB[7]:** *Working Electrode*: CB[7]-functionalised Au. *Reference Electrode*: SCE (unless otherwise stated). *Auxiliary Electrode*: Pt wire. *Electrolytic Solution*: 0.1 M $NaClO_4$, aqueous. *Scan Rate:* 100 mV / s, unless otherwise stated.

**Characterisation of SAMs of 1-(10-mercaptodecyl)-1'-methyl-[4,4'-bipyridine]-diium bromide and 1-(10-mercaptodecyl)-1'-methyl-[4,4'-bipyridine]-diium bromide-CB[8]:** *Working Electrode*: SAM deposited at Au. *Reference Electrode*: SCE. *Auxiliary Electrode*: Pt wire. *Electrolytic Solution*: 0.1 M $NaClO_4$, aqueous. *Scan Rate:* 1000 mV / s.

## 7.3 – The Formation of Self-Assembled Monolayers (SAMs)

### 7.3.1 – The Formation of SAMs of CB[7] at Gold

SAMs of CB[7] were generated upon incubating freshly prepared gold substrates in an aqueous solution (0.1 mM) of CB[7] for 24 hours at room temperature (RT). A monolayer was afforded once the substrates had been rinsed with $H_2O$, subjected to a period of sonication (2 minutes) and been dried in a gentle steam of $N_2$(g).[8]

### 7.3.2 – The Formation of Thiolated SAMs

All SAMs (MUA, MHDA, OEG, AB-19-114, AB-18-088, M-AB-18-088 and 1-(10-mercaptodecyl)-1'-methyl-[4,4'-bipyridine]-diium bromide) were acquired upon immersion (> 10 hours) of gold substrates (cleaned by immersion in piranha solution, and subsequent washing with $H_2O$) in 2 mM ethanolic solutions (HPLC grade) of the respective thiol, before being rinsed with copious amounts of ethanol (for SAMs of MUA, MHDA, OEG), $H_2O$ (for SAMs of 1-(10-mercaptodecyl)-1'-methyl-[4,4'-bipyridine]-diium bromide) or $CH_2Cl_2$ (for SAMs of AB-19-114, AB-18-088, M-AB-18-088) and dried in a gentle stream of $N_2$ (g).

### 7.3.3 – Carbodiimide Coupling

SAMs of TPAPP, AB-14-172 and $MVNH_3$ were afforded when carboxy-functionalised gold substrates were immersed in an aqueous solution consisting of 0.2 M EDC and 0.1 M NHS for 40 minutes. The substrates were then quickly washed with $H_2O$, dried in a gentle stream of $N_2$ (g) and transferred to a 50 μM solution (anhydrous $CH_2Cl_2$) of either TPAPP or AB-14-172, or a 0.1 M solution (DMF) of $MVNH_3$. After 24 hours, all SAMs were washed with the respective solvent and dried in a gentle stream of $N_2$ (g). **Note**. The formation of a neutral quinoid species, in the presence of a trace amount of $Et_3N$, prevented the covalent attachment of $MVNH_3$ to carboxy-functionalised gold substrates.

### 7.3.4 – Azide-Alkyne Huisgen Cycloaddition

A SAM of $MVN_3$ was afforded when carboxy-functionalised gold substrates were immersed in an aqueous solution of 0.2 M EDC and 0.1 M NHS for 1 hour. The substrate was then quickly washed with $H_2O$, dried in a gentle stream of $N_2$ (g) and transferred to a 0.1 M solution (DMF) of propargylamine for 24 hours. All SAMs were then washed with DMF and sonicated in DMF for 3 minutes, before being dried in a gentle stream of $N_2$ (g) and immersed into a solution (4 : 1, THF: $H_2O$, 1 mL) of 5 mol% $CuSO_4$•$5H_2O$, 10 mol% sodium ascorbate and 0.1 M $MVN_3^+$ at RT for 3 hours. After 3 hours, the SAM was washed with THF and dried in a gentle stream of $N_2$ (g). **Note**. The formation of a neutral quinoid species also prevented the cycloaddition of $MVN_3$ to alkyne-terminated gold substrates.

### 7.3.5 – CB[7]-Functionalised Silicon

Monolayers of CB[7] were generated at Si (1 x 1.5 cm, Si (100), Silicon Materials) following immersion (16 hours) in an aqueous solution (pH < 9.94) of CB[7]. The pH of the deposition solution was changed *via* the addition of a 0.1 M aqueous solution of NaOH. Prior to their immersion in a solution of the macrocyclic cavitand, CB[7], a monolayer of APTES had been deposited (0.4%, anhydrous toluene, 30 minutes)[9] and the resultant substrate thoroughly washed with toluene, ethanol and $H_2O$ before being dried in a gentle stream of $N_2$ (g).[10]

### 7.3.6 – Towards The Covalent Immobilisation of CB[7] on Silicon

Following the deposition of a monolayer of APTES (0.4%, anhydrous toluene, 30 minutes), the substrate was immersed in a 0.15 mM aqueous solution of 4-azidobenzoic acid (PA), activated by an equal molarity of EDC, for 48 hours at RT. The substrate was then rinsed three times with $H_2O$ (3 x 5 mL) and dried after each in a gentle stream of $N_2$ (g). The substrate was then immersed in a 0.1 mM aqueous solution of CB[7], dried in a desiccator in the presence of potassium pentoxide for 12 hours and irradiated with UV light (254 and 366 nm) from a commercially available 200 W high-pressure mercury lamp for 10 mins. Finally, the substrate was rinsed with copious amounts of $H_2O$ and dried in a gentle stream of $N_2$ (g).[11] **Note**. Formation of the desired assembly was prohibited by the use of high energy radiation. Degradation of the interface was consistently observed.

## 7.4 – Ellipsometry

Ellipsometric film thickness measurements were performed on a Beaglehole Instruments Picometer ellipsometer assuming a refractive index of 1.45 for the monolayer over the gold layer (with pseudo optical constants of approximately $n + ik = 0.52 + i \times 3.570$ determined from a fit to each individual gold sample prior to modification).[12] Reported film thicknesses are those determined from, and averaged over, four separately prepared samples, with two measurements per sample. The errors are given as three standard deviations of the average.

## 7.5 – UV-Vis and Transmissive UV-Vis Spectroscopy

All UV-Vis spectra were acquired on a UV-2401PC spectrometer within the ranges 350 – 800 (solution) and 380 – 480 nm (interface), respectively. Solution phase spectra were acquired using a 10 mm Hellma Synthetic Far-UV Quartz cuvette (1 or 3 mL) within either anhydrous $CH_2Cl_2$ (25 μM TPAPP, AB-14-172) or $H_2O$ (0.1 → 2 mM, homo- and heteroternary complexes) at 298 K. The sampling interval was set to 0.5 nm, the sampling speed to medium and the slit width to 5.0 nm. Spectra displayed are those averaged over two scans as to increase the reliability of the data acquired.

## 7.6 – X-Ray Photoelectron Spectroscopy (XPS)

X-ray-photoelectron spectroscopy was undertaken by Dr Ashley Shepherd (Surface Analysis Facility, University of Oxford) using a VG Escalab II spectrometer employing aluminium kalpha radiation (1486.6 eV, 150 W) and a hemispherical analyser to collect the electrons. The pass energy was set to 20 eV, whilst the operating pressure within the analysis chamber was set to below $10^{-8}$ Torr. All spectra were collected with a dwell time of 0.1 s, and a scan step of 0.05 eV. The resulting spectra were analysed using CasaXPS peak fitting software, and sample charging corrected using the C 1s signal at 285.0 eV.

## 7.7 – NMR and Mass Spectroscopy

$^1$H NMR spectra were recorded at 298 K on a Bruker Avance III HD NanoBay 400MHz spectrometer, and all spectra were referenced to the residual solvent peak. Take this to be $D_2O$ (4.79 ppm) unless otherwise stated.

When analysing the complexation of guest species by macrocyclic host derivatives, the ratio of macrocyclic host: guest species was fixed at 1:1 to prevent the formation of 1:1 homoternary complexes.

Electrospray ionisation mass spectra (ESI-MS) were recorded on a Waters Micromass LCT Premier XE mass spectrometer, HR-ESI on a Bruker μTOF mass spectrometer and MALDI-TOF MS on a Waters MALDI Micromass spectrometer.

## 7.8 – Luminescence Spectroscopy

All luminescence measurements were performed using an Agilent Cary Eclipse Fluorescence Spectrophotometer. Emission spectra of porphyrin luminescence (550 – 800 nm) were obtained using slit widths of either 5 or 10 nm, a PMT voltage of 600 V and excitation wavelengths between 418 and 423 nm. Emission spectra of lanthanide luminescence (550 – 1150 nm) were obtained using slit widths of 5 nm, a PMT voltage of 500 V and an excitation wavelength of 227 nm, unless otherwise stated. Phosphorescent spectra were acquired using a total decay time of 0.02 s, a delay time of 0.2 ms and a gate time of 0.5 ms. Slit widths of 10 nm were used and a PMT voltage of 1000

V applied, unless otherwise stated. All spectra supplied are those acquired following averaging over at least 10 scans, as to ensure spectral variation was ≤ 5%; the main source of error is likely to lie in generating an accurate concentration of such low volume and molarity, particularly in the case of some of the less soluble components. Lifetimes ($\lambda_{ex}$ 227 nm, $\lambda_{em}$ 616 nm) were determined by fitting a single exponential decay function; no statistically significant improvement in fit was observed when multiexponential models were applied.

## 7.9 – Contact Angle Measurements

All measurements were taken using an FTA 1000 B Class Economical Drop Shape Instrument, and all contact angles determined from a photo taken (CCD camera) of the droplet using FTA Droplet Analysis Software (Version 32). All quoted angles are averages of at least two measurements with agreement to at least 5 °, and all measurements were made using a syringe which expelled 100 µL of $H_2O$ onto the surface being studied. A piston ensured that the volume expelled was consistent throughout. The contact angle was recorded between the centre of the droplet and the contact point of the droplet, as shown in **Figure 6**.

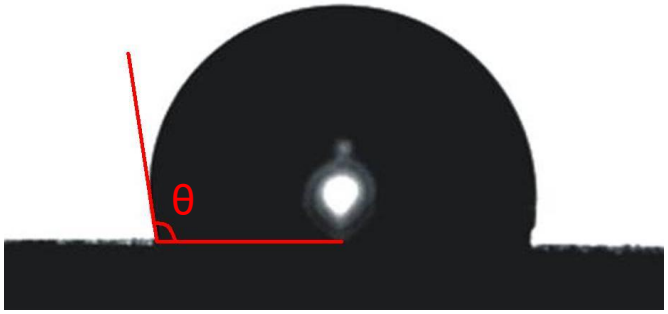


**Figure 6.** An image of a water droplet (100 µL) on the surface of a Au substrate modified with 11-mercaptoundecanoic acid. The contact angle (**θ**) was taken as the angle between the centre of the droplet and the contact point of the droplet.

## 7.10 – Ternary Complex Formation

CB[8]•16$H_2O$ (1.30 mg, 1 mM) was added to an aqueous solution (1.0 mL) of the first guest species (1 mM) and subjected to an extended period of sonication (3 hours, 25 °C). An optically transparent solution of the binary complex ($MV^{2+}$-CB[8]) was afforded, and the secondary guest species added (1 mM). The heteroternary complex was generated following further sonication (60 seconds).

## 7.11 – Hydrogenation Reaction

All hydrogenation reactions were carried out using a H-Cube continuous-flow hydrogenation reactor. An 8.00 mM solution (100% MeOH, 20 mL) of each reactant was passed through the system (10% Pd/C) at a rate of 1 mL/min, a temperature of 40 °C and a pressure of 40 atm. $^1$H NMR spectroscopy and MS were used to monitor the reaction.

## 7.12 – Synthesis of naphthalene-appended lanthanide DO3A (1,4,7,10-tetraazacyclododecane-1,4,7,10-tetraacetic acid) complexes, LnNap

**All derivatives synthesized by Dr Alexander Hess and Mr Andrew Baxter of Professor Paul Beer's research group (University of Oxford).*

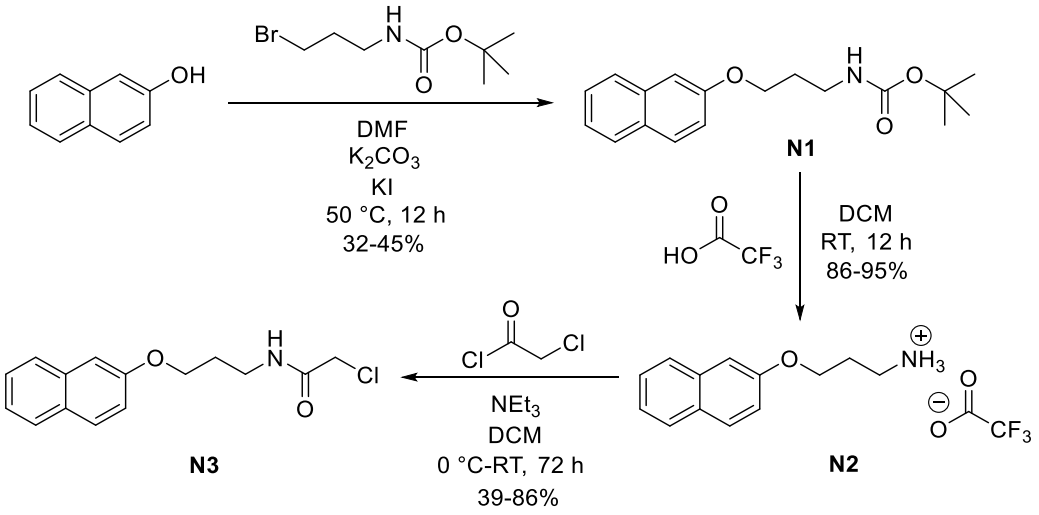


**Figure 7.** Synthesis of naphthoxy amidoacetyl chloride, **N3**.

*Bromopropylamine-Boc*[13]

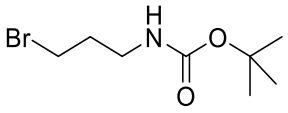


3-Bromopropylamine hydrobromide (1.00 g, 7.19 mmol) was suspended in dry DCM (40 mL) and di-*tert*-butyl dicarbonate (1.88 g, 8.63 mmol) was added to the stirring suspension. $NEt_3$ (3.3 mL, 28.8 mmol) was added drop-wise to the stirring suspension which became homogenous once the addition was complete. The reaction mixture was placed under an atmosphere of $N_2$ and stirred at room temperature for 16 hours. The reaction mixture was then washed with 1M $HCl_{(aq.)}$ (20 mL), 1M $NaOH_{(aq.)}$ (20 mL) and brine (10 mL). The organic layer was dried over $MgSO_4$, filtered and the solvent removed *in vacuo* to give a crude white solid which was purified *via* silica gel column chromatography (20:80, EtOAc: hexane) to give bromopropylamine-Boc as a light-yellow oil (1.17 g, 68%). **$^1$H NMR** (400 MHz, $CDCl_3$) δ (ppm): 4.65 (bs, Carbamate N-H, 1H), 3.44 (t, $CH_2$-Br, $J$ = 6.5 Hz, 2H), 3.26 (m, 2H), 2.05 (m, $CH_2$-$CH_2$-$CH_2$, $J$ = 6.5 Hz, 2H), 1.44 (s, Boc-tBu, 9H).

*Boc-protected naphthoxy amine, **N1***

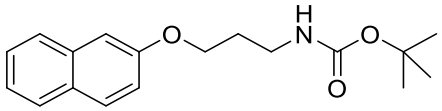

2-naphthol (1.40 g, 9.69 mmol) and bromopropylamine-Boc (3.00 g, 12.6 mmol) were dissolved in acetone (50 mL), to which $Cs_2CO_3$ (4.73 g, 14.8 mmol) and NaI (1.89 g, 12.6 mmol) were added. The reaction mixture was placed under an atmosphere of $N_2$ and heated at 60 °C overnight with stirring. The reaction mixture was diluted with DCM (50 mL), washed with brine (2 x 30 mL), dried over $MgSO_4$, filtered and dried *in vacuo* to give the crude product which was purified by silica gel column chromatography (20% ethyl acetate in hexane) to yield the Boc-protected naphthoxyl amine **N1** as a white solid (2.50 g, 86%). **$^1$H NMR** (400 MHz, $CD_3OD$) δ(ppm): 7.74 (m, Ar-H, 3H), 7.40 (m, Ar-H, 1H), 7.30 (m, Ar-H, 1H), 7.21 (d, Ar-H, *J* = 2.3 Hz, 1H), 7.12 (dd, Ar-H, *J* = 9.0 Hz, 2.0 Hz, 1H), 4.13 (t, naphthol-OC$H_2$, *J* = 6.2 Hz, 2H), 3.28 (t, C$H_2$-NH, *J* = 6.9 Hz,), 2.00 (p, $CH_2CH_2CH_2$, *J* = 6.5 Hz, 2H), 1.43 (s, Boc-tBu, 9H). **$^{13}$C NMR** (125 MHz, $CDCl_3$) δ(ppm): 156.70, 156.02, 134.51, 129.40, 128.98, 127.62, 126.71, 126.37, 123.63, 118.82, 106.62, 79.24, 65.77, 38.06, 29.52, 28.40. **MS** (ESI +ve) m/z: 324.2 ($[M+Na]^+$, $C_{18}H_{23}NO_3^+$ requires 324.2). **HRMS** (ESI +ve) m/z: 324.1578 ($[M]^{2+}$, $C_{18}H_{23}NO_3^+$ requires 324.1570).

*Naphthoxy amine, **N2***

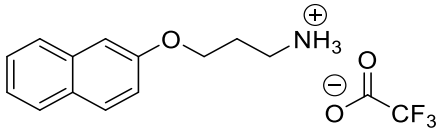

Boc-protected naphthoxy amine **N1** (316 mg, 1.05 mmol) was dissolved in dry DCM (20 mL), cooled to 0 °C and placed under an atmosphere of $N_2$. TFA (0.80 mL, 10.5 mmol) was added drop-wise to the stirring solution, and the reaction mixture allowed to gradually warm to room temperature and left to stir for 48 hours. The solvent was removed *in vacuo* and the resultant solid redissolved in MeOH (5 mL) and dried again three times to remove any residual TFA to give naphthoxy amine as its trifluoroacetate salt **N2** as a brown solid (293 mg, 89%). **$^1$H NMR** (400 MHz, $CD_3OD$) δ(ppm): 7.77 (m, Ar-H, 3H), 7.43 (m, Ar-H, 1H), 7.33 (m, Ar-H, 1H), 7.26 (d, *J* = 2.6 Hz, Ar-H, 1H), 7.16 (dd, *J* = 9.0 Hz, 2.6 Hz, Ar-H, 1H), 4.25 (t, *J* = 5.7 Hz, Napthol-C$H_2$, 2H), 3.21 (t, *J* = 7.3 Hz, C$H_2$-$NH_3^+$, 2H), 2.21 (p, $CH_2$-C$H_2$-$CH_2$, *J* = 6.5 Hz, 2H). **$^{13}$C NMR** (125 MHz, $CD_3OD$) δ (ppm): 156.40, 134.67, 129.26, 129.06, 127.20, 126.45, 126.03, 123.43, 118.19, 106.43, 64.79, 37.28, 26.97. **MS**

(ESI +ve) m/z: 202.1 ($[M+H]^+$, $C_{13}H_{16}NO^+$ requires 202.1). **HRMS** (ESI +ve) m/z: 202.1226 ($[M+H]^+$, $C_{13}H_{16}NO^+$ requires 202.1226).

*Naphthoxy amidoacetyl chloride, **N3***

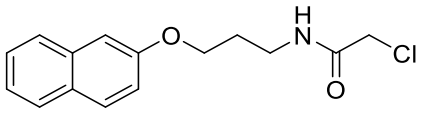


Naphthoxy amine **N2** (292 mg, 0.930 mmol) was dissolved in DCM (10 mL) and placed under an atmosphere of $N_2$. $NEt_3$ (0.60 mL, 4.65 mmol) was added and the reaction mixture was cooled to 0 °C with an ice bath, at which point chloroacetyl chloride (0.22 mL, 2.78 mmol) was added drop-wise to the solution. The reaction mixture was allowed to warm to room temperature and left stirring for 48 hours. The reaction mixture was then washed with water (20 mL), 1M $HCl_{(aq.)}$ (2 x 20 mL) and brine (2 x 20 mL). The solvent was removed *in vacuo* and the crude product was purified by silica gel column chromatography (gradient, 20 » 80% EtOAc/hexane) to give the product naphthoxy amidoacetyl chloride **N3** as an off-white solid (222 mg, 86%). **$^1$H NMR** (400 MHz, $CDCl_3$) δ(ppm): 7.76 (m, Ar-H, 3H), 7.46 (m, Ar-H, *J* = 7.0 Hz, 1H), 7.36 (m, Ar-H, 1H), 7.17 (m, Ar-H, 2H), 4.22 (t, Napthol-$CH_2$, *J* = 5.7 Hz, 2H), 4.09 (s, NHCO-$CH_2$-Cl, 2H), 3.61 (t, $CH_2$-NH, *J* = 7.3 Hz, 2H), 2.14 (p, $CH_2$-$CH_2$-$CH_2$, *J* = 6.0 Hz, 2H). **$^{13}$C NMR** (125 MHz, $CDCl_3$) δ(ppm): 165.94, 156.43, 134.46, 129.55, 129.12, 127.66, 126.76, 126.47, 123.81, 118.64, 106.64, 66.68, 42.71, 38.32, 28.60. **MS** (ESI +ve) m/z: 278.1 ($[M+H]^+$, $C_{15}H_{17}ClNO_2^+$ requires 278.1). **HRMS** (ESI +ve) m/z: 300.0759 ($[M+Na]^+$, $C_{15}H_{16}ClNaNO_2^+$ requires 300.0762).

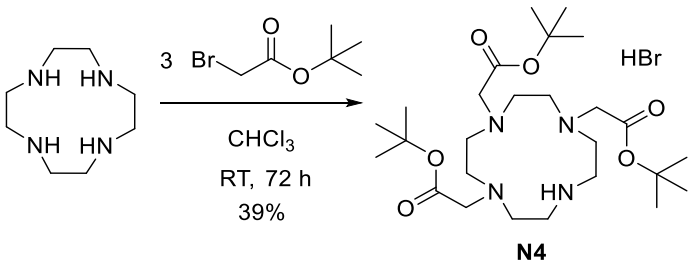


**Figure 8.** Synthesis of DO3A tri-*tert*-butyl ester, **N4**.

*DO3A tri-tert-butyl ester, **N4***[14]

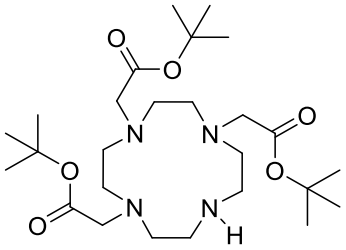

Cyclen (1.78 g, 10.0 mmol) and $NaHCO_3$ (2.78 g, 31.0 mmol) were suspended in dry MeCN (50 mL) and left to stir under a $N_2$ atmosphere and cooled to 0 °C with an ice bath. *Tert*-butyl bromoacetate (4.9 mL, 31.0 mmol) was dissolved in dry MeCN (10 mL) and added drop-wise over a 30-minute period and left to stir at room temperature for 48 hours. The reaction mixture was diluted with DCM (50 mL), filtered and dried *in vacuo* to give a crude beige solid that was redissolved in the minimum of refluxing toluene (~10 mL) and left to stand in a freezer at -27 °C for several hours at which point the product precipitated. The precipitate was isolated *via* vacuum filtration and rinsed with cold $Et_2O$ (10 mL) and dried under high-vacuum to give pure DO3A tri-*tert*-butyl ester **N4** as a fluffy white solid (1.98 g, 39%). **$^1$H NMR** (400 MHz, $CDCl_3$) δ (ppm): 10.06 (bs, N-H, 1H), 3.54 – 2.75 (m, Cyclen arm $CH_2$ + Cyclen ring $CH_2$, 22H), 1.46 (s, COO-tBu, 27H). **MS** (ESI +ve) m/z: 515.4 ($[M+H]^+$, $C_{26}H_{51}N_4O_6^+$ requires 515.4).

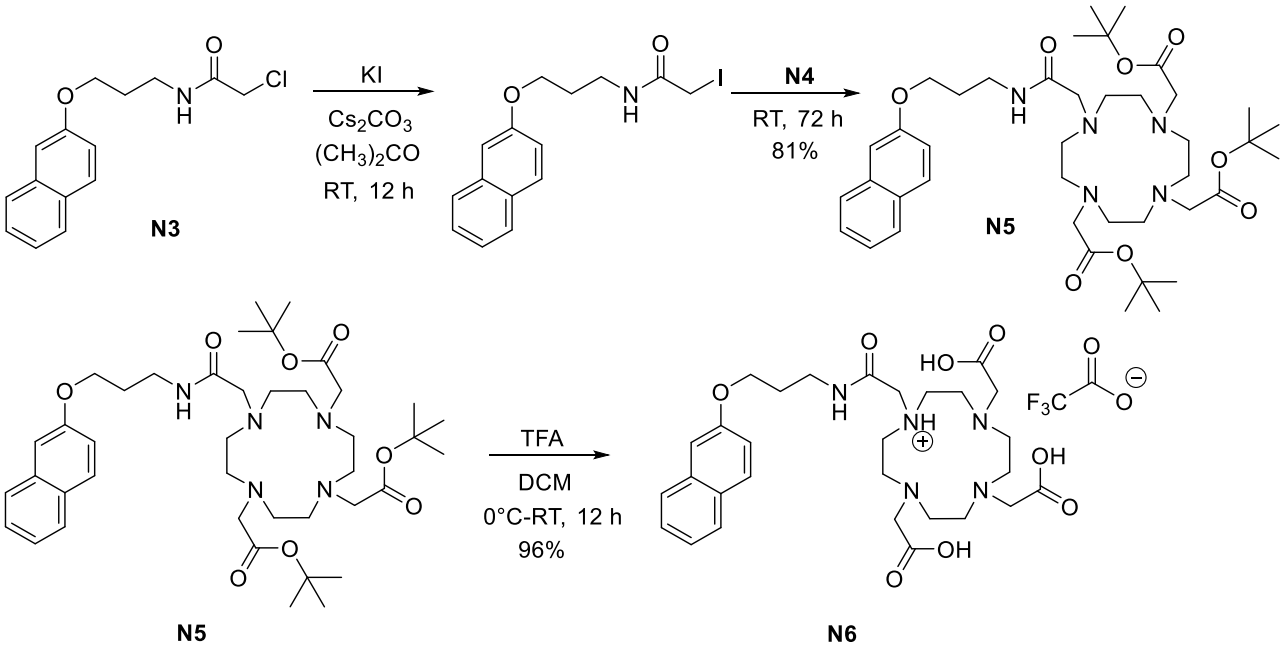


**Figure 9.** Synthesis of naphthol DO3A tri-acid, **N6**.

*Naphthol DO3A tri-tBu ester, **N5***

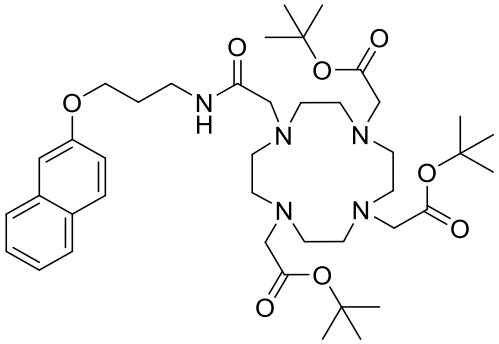

Naphthoxy amidoacetyl chloride **N3** (1.03 g, 3.74 mmol) and KI (1.13 g, 6.80 mmol) were dissolved in acetone (50 mL) and halogen exchange conducted under an atmosphere of $N_2$ at room temperature for 16 hours. $K_2CO_3$ (1.41 g, 10.2 mmol) and DO3A tri-*tert*-butyl ester **N4** were added and the reaction mixture stirred under an atmosphere of $N_2$ at room temperature for 72 hours until mass spectrometry showed no DO3A starting material remaining in the reaction mixture. The solvent was removed *in vacuo* and the crude product purified by column chromatography (silica, 5% methanol in chloroform) to yield the product naphthol DO3A tri-tBu ester **N5** as a viscous yellow oil (2.28 g, 81%). **$^1$H NMR** (400 MHz, $CDCl_3$) δ(ppm): 7.87 (t, *J* = 5.6 Hz, CON-H), 7.72 (dd, *J* = 8.1 Hz, 3.7 Hz, Ar-H, 2H), 7.68 (d, *J* = 8.9 Hz, Ar-H, 1H), 7.39 (m, Ar-H, 1H), 7.30 (d, Ar-H, *J* = 7.7 Hz, 1H), 7.18 (d, Ar-H, *J* = 2.1 Hz, 1H), 7.10 (dd, Ar-H, *J* = 8.9 Hz, 2.4 Hz, 1H), 4.15 (t, Napthol-$CH_2$, *J* = 5.9 Hz, 2H), 3.44 (m, $CH_2$-NH, 2H), 3.37 (s, NHCO-$CH_2$- cyclen), 2.14 (p, $CH_2$-$CH_2$-$CH_2$, *J* = 6.3 Hz, 2H), 3.30 – 1.72 (m, Cyclen arm $CH_2$ + Cyclen ring $CH_2$, 22H), 1.45 – 1.40 (m, COO-tBu, 27H). **$^{13}$C NMR** (125 MHz, $CDCl_3$) δ(ppm): 172.34, 172.08, 171.69, 156.85, 134.55, 129.03, 128.74, 127.38, 126.80, 126.10, 123.31, 118.90, 106.76, 81.73, 66.18, 56.31, 55.62, 55.46, 53.5- 47.5 (broad region due cyclen ring inversion, 4 resonances expected), 36.35, 28.93, 27.91, 27.84. **MS** (ESI +ve) m/z: 756.4 ($[M+H]^+$, $C_{41}H_{66}N_5O_8^+$ requires 756.5); also found: 700.4 [M-tBu+H]$^+$, 644.3 [M-2tBu+H]$^+$, 588.3 [M-3tBu+H]$^+$ fragments. **HRMS** (ESI +ve) m/z: 756.4890 ($[M+H]^+$, $C_{41}H_{66}N_5O_8^+$ requires 756.4906).

*Naphthol DO3A tri-acid, **N6***

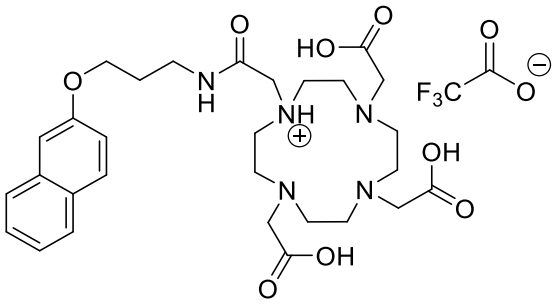

Naphthol DO3A tri-tBu ester **N5** (48.0 mg, 0.0600 mmol) was dissolved in a 1:1 DCM/TFA solvent mixture (4.0 mL) at 0 °C and allowed to gradually warm to room temperature whilst stirring. Once the reaction was judged as complete by TLC (36 hours), the solvent was removed *in vacuo* and repeatedly re-dissolved in MeOH and evaporated to dryness to remove any excess TFA (3 times). The pure product naphthol DO3A tri-acid **N6** was isolated without further purification as a viscous yellow oil (41.0 mg, 96%). **$^{1}$H NMR** (400 MHz, $CD_3OD$) δ(ppm): 7.89 (bs, CON-H, 1H), 7.76 (m, Ar-H, 3H), 7.42 (m, Ar-H, *J* = 7.6 Hz, 1H), 7.31 (m, ArH, 1H), 7.24 (d, Ar-H, *J* = 2.2 Hz, 1H), 7.14 (dd, Ar-H, *J* = 8.9 Hz, 2.4 Hz, 1H), 4.18 (t, Napthol-C$H_2$, *J* = 5.9 Hz, 2H), 3.46 (t, C$H_2$-NH, *J* = 6.4 Hz, 2H), 4.22 – 2.51 (m, Cyclen arm C$H_2$ + Cyclen ring C$H_2$, 24H), 2.07 (p, $CH_2$-C$H_2$-$CH_2$, *J* = 6.3 Hz, 2H). **$^{13}$C NMR** (125 MHz, $CD_3OD$) δ(ppm): 175.17 (suppressed), 174.68 (suppressed), 162.83 (q, *J* = 35 Hz, $^{-}$OOC-C$F_3$), 158.38, 136.27, 130.61, 130.56, 128.74, 127.98, 127.56, 124.81, 120.04, 118.21 (q, *J* = 290 Hz, $^{-}$OOC-$CF_3$), 107.97, 66.83, 57-50 (broad region, 7 resonances expected), 38.03, 30.11. (-CONH- not observable). **MS** (ESI +ve) m/z: 588.3 ($[M+H]^+$, $C_{29}H_{42}N_5O_8^+$ requires 588.3). **HRMS** (ESI +ve) m/z: 588.3022 ($[M+H]^+$, $C_{29}H_{42}N_5O_8^+$ requires 588.3030).

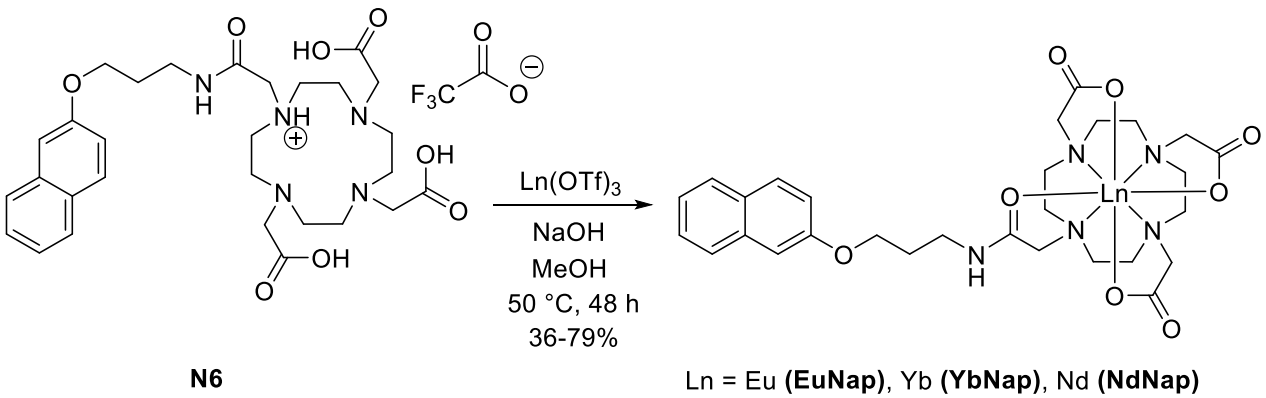


**Figure 10.** Synthesis of LnNap, where Ln = $Eu^{3+}$, $Yb^{3+}$ or $Nd^{3+}$.

*Naphthol DO3A Eu(III) complex,* ***EuNap***

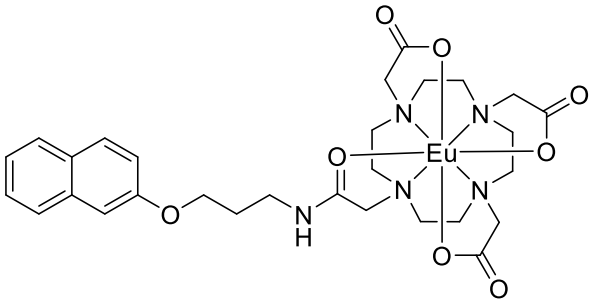

Naphthol DO3A tri-acid **N6** (18.1 mg, 0.0310 mmol) was dissolved in methanol (4.0 mL), and the pH of the solution adjusted, by drop-wise addition of 1 M $NaOH_{(aq.)}$, to 5.5-7.5. $Eu(OTf)_3$ (57.5 mg, 0.0960 mmol) was added and the reaction mixture stirred under an atmosphere of $N_2$ at 50 °C for 48 hours. The crude product was triturated from MeOH using $Et_2O$ to yield the product naphthol Eu(III) complex as an off-white solid (15.0 mg, 79%). **$^1$H NMR** (400 MHz, $D_2O$) δ(ppm): 33.01, 32.23, 30.99, 12.13, 11.67, 8.04, 7.61, 7.52, 7.12, 6.40, 3.30, 2.94, 2.08, 0.84, 0.57, 0.32, -0.63, -0.99, -2.02, -2.32, -3.39, -3.57, -4.45, -5.72, -5.94, -7.95, -8.23, -9.43, -10.46, -11.03, - 11.58, -12.28, -12.83, -14.86, -15.20, -15.58, -16.84. **MS** (ESI +ve) m/z: 736.2 ($[M+H]^+$, $C_{29}H_{39}EuN_5O_8^+$ requires 736.2). **HRMS** (ESI +ve) m/z: 736.1986 ($[M+H]^+$, $C_{29}H_{39}EuN_5O_8^+$ requires 736.1992).

*Naphthol DO3A Yb(III) complex,* ***YbNap***

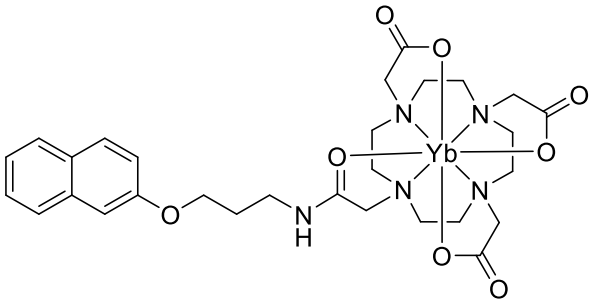

Naphthol DO3A tri-acid **N6** (72.0 mg, 0.122 mmol) was dissolved in methanol (10.0 mL), and the pH of the solution adjusted, by drop-wise addition of 1 M $NaOH_{(aq.)}$, to 5.5-7.5. $Yb(OTf)_3$ (80.0 mg, 0.129 mmol) was added and the reaction mixture stirred under an atmosphere of $N_2$ at 50 °C for 48 hours. The crude product was triturated from MeOH using $Et_2O$ to yield the product naphthol Yb(III) complex **YbNap** as an off-white solid (53.8 mg, 56%). **$^1$H NMR** (400 MHz, $D_2O$) δ (ppm): 131.85, 127.09, 122.83, 121.34, 83.70, 71.07, 32.07, 26.19, 24.82, 20.48, 19.41, 18.65, 17.10, 16.46, 15.77, 15.46, 8.18, 7.94, 7.55, 7.15, 6.84, 4.83, 3.34, 2.44, 2.09, 1.64, 0.70, 0.56, -1.23, -1.35, -12.16, -22.50, -26.11, -27.97, -30.95, -41.60, -44.47, -56.22, -57.97, -76.72, -77.89, -79.11, -79.55. **MS** (ESI

+ve) m/z: 755.1 ($[M+H]^+$, $C_{29}H_{39}YbN_5O_8^+$ requires 755.2). **HRMS** (ESI +ve) m/z: 755.2137 ($[M+H]^+$, $C_{29}H_{39}YbN_5O_8^+$ requires 755.2140).

*Naphthol DO3A Nd(III) complex, **NdNap***

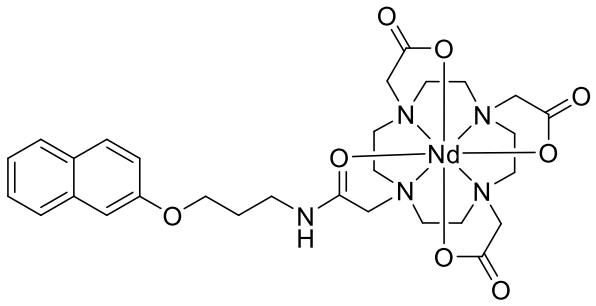

Naphthol DO3A tri-acid **N6** (72.0 mg, 0.122 mmol) was dissolved in methanol (10.0 mL), and the pH of the solution adjusted, by drop-wise addition of 1 M $NaOH_{(aq.)}$, to 5.5-7.5. $Nd(OTf)_3$ (76.2 mg, 0.129 mmol) was added and the reaction mixture stirred under an atmosphere of $N_2$ at 50 °C for 48 hours. The crude product was triturated from MeOH using $Et_2O$ to yield the product naphthol Nd(III) complex **NdNap** as a white solid (34.0 mg, 36%). **$^1$H NMR** (400 MHz, DMSO-$d_6$) δ (ppm): 24.45, 22.45, 22.02, 20.67, 20.13, 15.54, 13.47, 13.43, 12.66, 12.31, 11.69, 9.99, 9.52, 7.92, 7.73, 7.47, 7.29, 7.00, 6.66, 6.31, 5.67, 5.19, 4.53, 3.34, 2.50, 1.82, 1.31, 1.08, 0.54, 0.06, -0.08, -0.68, -0.92, -1.65, -2.68, -4.08, -4.64, -7.91, -9.83, -10.83, -11.87, -12.99, -24.13, -25.03, -28.07. **MS** (ESI +ve) m/z: 727.1 ($[M+H]^+$, $C_{29}H_{39}NdN_5O_8^+$ requires 727.2). **HRMS** (ESI +ve) m/z: 727.1865 ($[M+H]^+$, $C_{29}H_{39}NdN_5O_8^+$ requires 727.1870).

## 7.13 – *Synthesis of the ferrocene functionalised viologen, FcMV

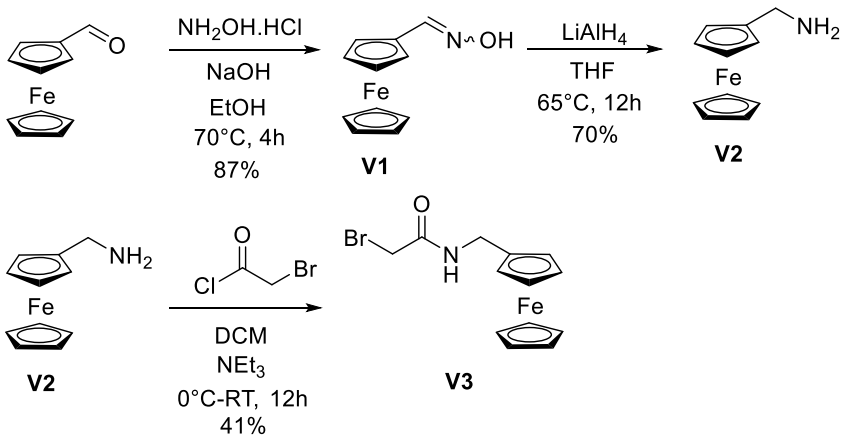


**Figure 11.** Synthesis of ferrocene amido-acetyl bromide, **V3**.

*Ferrocene carboxaldehyde oxime,* ***V1***[15]

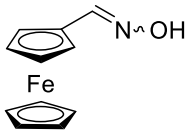


An aqueous solution of hydroxylamine hydrochloride (930 mg, 13.4 mmol) in $H_2O$ (5.0 mL) was added to a solution of ferrocene carboxaldehyde (2.00 g, 9.30 mmol) dissolved in EtOH (20 mL). NaOH pellets (900 mg, 22.6 mmol) were added slowly to the reaction mixture with stirring. The mixture was heated to 70 °C for 4 hours under an atmosphere of $N_2$, left to cool to room temperature and the solvent removed *in vacuo* (CAUTION – dry hydroxylamine is a potentially shock sensitive explosive). $H_2O$ (30 mL) was added and the organic product extracted with $Et_2O$ (3 x 40 mL). The combined organic layers were dried over $MgSO_4$, filtered and the solvent removed *in vacuo* to yield the product as a deep orange solid (1.84 g, 87%). **$^1$H NMR** (400 MHz, $CD_3OD$) δ (ppm): 7.92 (s, C<u>H</u>=NOH, 1H), 7.16 (s, CH=NO<u>H</u>, 1H), 4.53 – 4.35 (m, Ferrocene Ar-<u>H</u>, 4H), 4.20 (s, Ferrocene Ar-<u>H</u>, 5H). **MS** (ESI +ve) m/z: 230.1 ($[M+H]^+$, $C_{11}H_{12}FeNO^+$ requires 230.0).

*Ferrocenyl amine,* ***V2***[15]

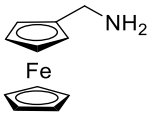


$LiAlH_4$ (1.40 g, 37.0 mmol) was suspended in dry THF (30 mL) and ferrocene carboxaldehyde oxime **V1** (1.84 g, 8.00 mmol) was dissolved in THF (30 mL) and added slowly *via* a dropping funnel to the stirring $LiAlH_4$ suspension under a $N_2$ atmosphere. Once the addition was complete the mixture was heated to 60 °C for 16 hours. The reaction was quenched by cooling the reaction mixture to 0 °C with an ice bath and was water added cautiously to quench the $LiAlH_4$, at which point a large amount of light grey precipitate formed. The solids were filtered and washed with water (50 mL) and DCM (100 mL) and all collected filtrates were combined in a separating funnel and the organic layer separated, dried over $MgSO_4$, filtered and the solvent removed *in vacuo*. The crude product was purified by column chromatography (1M $NH_4OH_{(aq.)}$ (10%) / MeOH) to give ferrocene amine product **V2** as an unstable yellow oil (1.21 g, 70%). **$^1$H NMR** (400 MHz, $CD_3OD$) δ (ppm): 4.22 (m, Ferrocene Ar-<u>H</u>, 2H), 4.15 (s, Ferrocene Ar-<u>H</u>, 5H), 4.13 (m, Ferrocene Ar-<u>H</u>, 2H), 3.54 (s, C<u>H</u>$_2$-$NH_2$, 2H). **MS** (ESI +ve) m/z: 238.0 ($[M+Na]^+$, $C_{11}H_{13}FeNNa^+$ requires 238.0).

*Ferrocene amido-acetyl bromide, **V3***

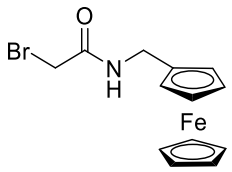


Ferrocene amine **V2** (50.0 mg, 0.230 mmol) and $NEt_3$ (0.010 mL, 0.690 mmol) were dissolved in dry DCM (10 mL) and cooled to 0 °C using an ice bath. Bromoacetyl chloride (0.060 mL, 0.680 mmol) was added drop-wise *via* a syringe and the reaction mixture was placed under a $N_2$ atmosphere, allowed to warm to room temperature and stirred for 16 hours. The reaction mixture was then washed with 1M $HCl_{(aq.)}$ (20 mL), 1M $NaOH_{(aq.)}$ (20 mL) and brine (10 mL). The organic layer was dried over $MgSO_4$, filtered and the solvent removed *in vacuo* to give a crude yellow/brown oil that was purified *via* silica gel column chromatography (gradient, 50 » 100% EtOAc/hexane) to give ferrocene amido-acetyl chloride/bromide **V3** as a yellow solid (31.0 mg, 41%). **$^1$H NMR** for mixed chloride/bromide product (400 MHz, $CD_3OD$) δ(ppm): 4.23 (2x2H, broad s, 2x$C_5H_4$-), 4.19 (2x5H, s, 2x$C_5H_5$), 4.14 (2x2H, broad s, 2x$C_5H_4$-), 4.12 (2H, s, -$CH_2NHCOCH_2Cl$), 4.11 (2H, s, -$CH_2NHCOCH_2Br$), 4.04 (2H, s, - $CH_2NHCOCH_2Cl$), 3.83 (2H, s, -$CH_2NHCOCH_2Br$). **$^{13}$C NMR** for mixed chloride/bromide product (125 MHz, $CD_3OD$) δ(ppm): 167.28, 167.11, 68.43, 68.08, 68.00, 67.87, 41.87, 38.87, 38.66, 27.55. **HRMS** (ESI): m/z calc. for $C_{11}H_{14}BrFeNNaO$ $[M+Na]^+$: 357.9502; found: 357.9508.

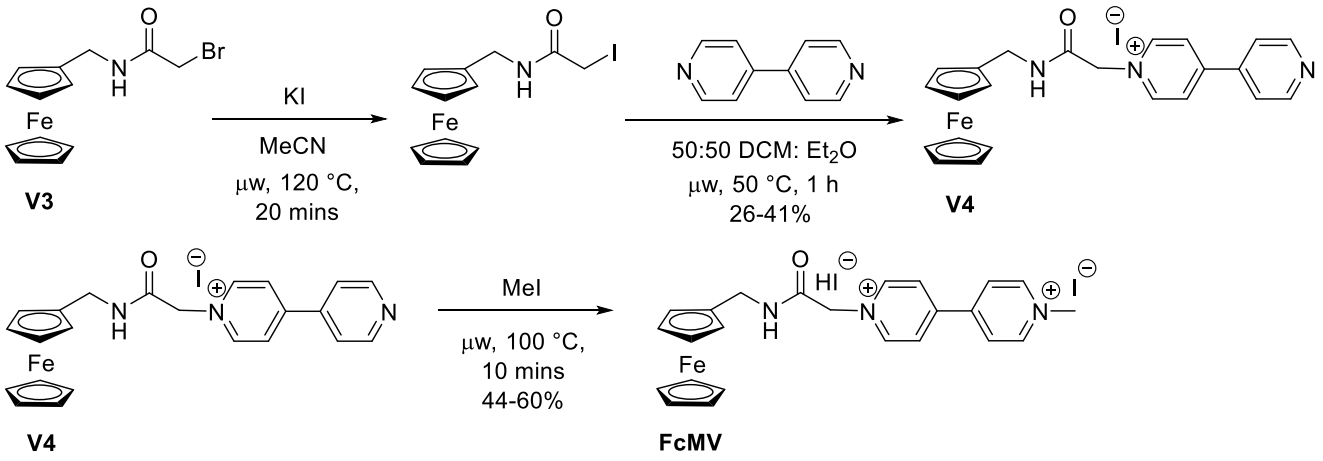


**Figure 12.** Synthesis of **FcMV**.

*Monoalkylated ferrocenyl-bipyridinium iodide, **V4***

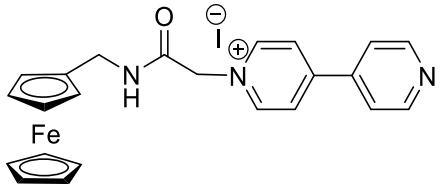

Ferrocene amidoacetyl bromide **V3** (200 mg, 0.580 mmol) and KI (480 mg, 2.89 mmol) were placed in a microwave *via*l and dissolved in MeCN (10 mL). The mixture was heated to 120 °C for 20 minutes in the microwave with stirring to facilitate halogen exchange to ferrocene amidoacetyl iodide, confirmed by TLC and mass spectrometric analysis. 4,4'-bipyridine (181 mg, 1.16 mmol) was added and the reaction mixture heated to 50 °C in the microwave for 1 hour with stirring. The reaction vessel was cooled in an ice bath mix to encourage precipitation of the product, and the crude product filtered and washed with $Et_2O$ (2 x 20 mL). The solvent was reduced *in vacuo* and the filtrate subjected to further reaction cycles until all starting material had been consumed. The monoalkylated ferrocenyl bipyridinium iodide **V4** was obtained as a red-brown solid (128 mg, 41%). **$^1$H NMR** (400 MHz, $CD_3OD$) δ(ppm): 9.02 (d, $Pyr^+$ Ar-H, *J* = 6.5 Hz, 2H), 8.85 (d, $Pyr^+$ Ar-H, *J* = 5.3 Hz, 2H), 8.55 (d, Pyr Ar-H, *J* = 6.4 Hz, 2H) 8.01 (d, Pyr Ar-H, *J* = 5.3 Hz, 2H), 5.47 (s, Pyr-$N^+$-$CH_2$CONH, 2H), 4.25 – 4.15 (m, Ferrocene Ar-H, 11H). **$^{13}$C NMR** (125 MHz, $D_2O$) δ(ppm): 163.99, 154.53, 150.27, 146.38, 142.25, 125.50, 122.38, 70.2-66.8 (broad, 4 resonances expected), 61.32, 39.14. **MS** (ESI +ve) m/z: 412.1 ($[M-I]^+$, $C_{23}H_{22}FeN_3O^+$ requires 412.1). **HRMS** (ESI +ve) m/z: 412.1104 ($[M-I]^+$, $C_{23}H_{22}FeN_3O^+$ requires 412.1107).

*Ferrocene viologen diiodide species, **FcMV***

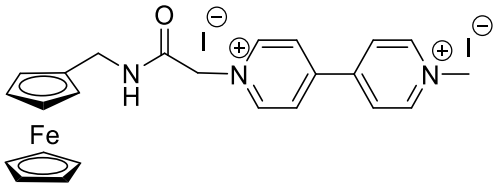

Monoalkylated ferrocenyl-bipyridinium iodide **V4** (127 mg, 0.0800 mmol) was placed in a microwave *via*l, to which MeI (2.0 mL, excess) was added. The reaction mixture was heated in a microwave to 100 °C for 10 minutes with stirring. Upon cooling, diethyl ether (5.0 mL) was added to encourage precipitation of the product. The precipitate was removed by filtration and the filtrate dried *in vacuo*, then subjected to further reaction cycles until no starting material was visible by TLC or mass spectrometry. The combined batches were washed firstly with DCM (10 mL), $Et_2O$ (20 mL), MeCN (20 mL) and MeOH (30 mL) to remove any impurities. The final ferrocene viologen diiodide

**FcMV** was isolated as an orange-brown solid (70.0 mg, 44%). **$^1$H NMR** (400 MHz, DMSO-$d_6$) δ(ppm): 9.28 (m, Pyr$^+$ Ar-H, 4H), 8.84 (bs, CON-H, 1H), 8.80 (d, Pyr$^+$ Ar-H, $J$ = 5.9 Hz, 2H), 8.77 (d, Pyr$^+$ Ar-H, $J$ = 4.9 Hz, 2H), 5.54 (s, Pyr-N$^+$-C$H_2$CONH, 2H), 4.45 (s, PyrN$^+$-Me, 3H), 4.24 – 4.14 (m, Ferrocene Ar-H, 11H). **$^{13}$C NMR** (125 MHz, DMSO-$d_6$) δ(ppm): 163.51, 149.11, 148.18, 147.22, 146.80, 126.21, 125.95, 84.67, 68.46, 68.11, 67.59, 61.45, 48.06, 38.50.

## 7.14 – *Synthesis of functionalised viologen derivatives $MVNH_3$ and $MVN_3$

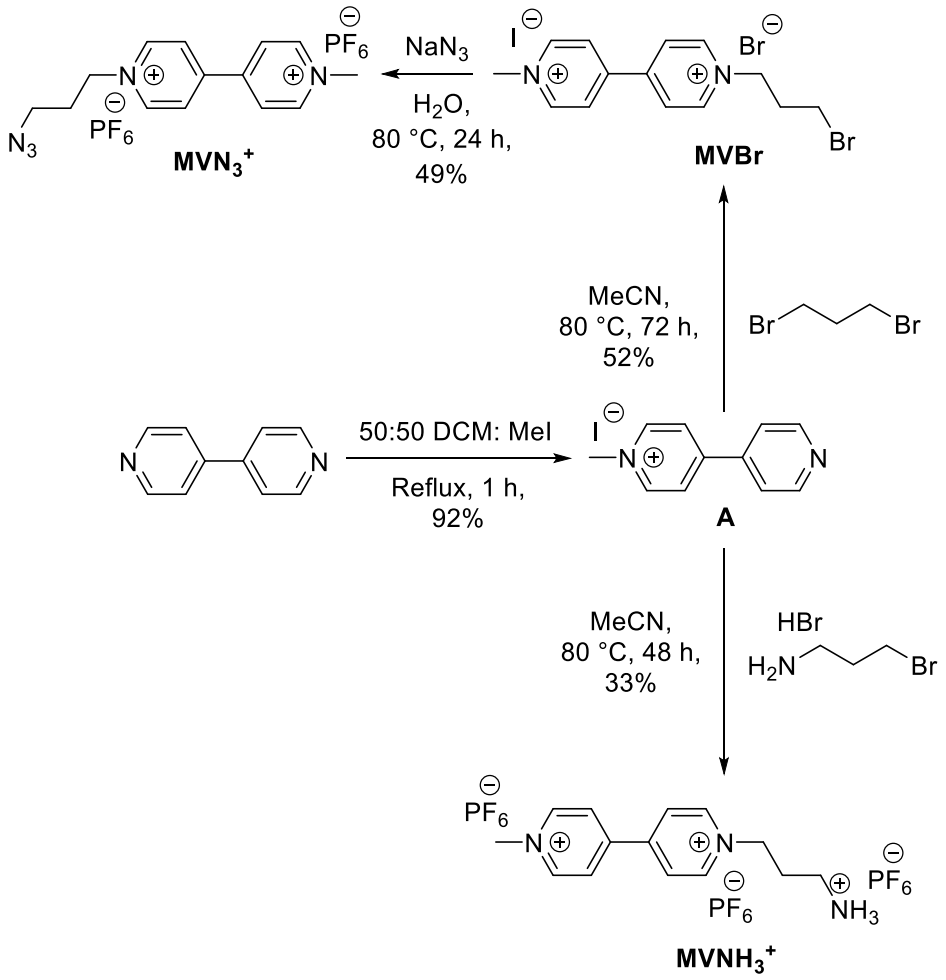


**Figure 13.** Synthesis of $MVN_3^+$ and $MVNH_3^+$.

*Monomethylated 4,4'bipyridine iodide, **A**[16]*

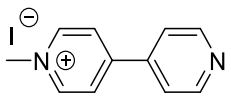

4,4'-bipyridine (2.00 g, 12.8 mmol) was dissolved in DCM/MeI (1:1 v/v, 10.0 mL) and refluxed for 1 hour whereupon a yellow precipitate formed. The precipitate was isolated *via* vacuum filtration

and washed with EtOAc (2 x 10 mL) to remove unreacted starting material, followed by $Et_2O$ (2 x 10 mL). The solid was then dried *in vacuo* to give monomethylated 4,4'bipyridine iodide **A** as a golden yellow powder (3.50 g, 92%). **$^1$H NMR** (400 MHz, $CD_3OD$) δ (ppm): 9.04 (d, $Pyr^+$ Ar-H, *J* = 6.6 Hz, 2H), 8.83 (m, $Pyr^+$ Ar-H, 2H), 8.51 (d, Pyr Ar-H, *J* = 6.6 Hz, 2H) 7.99 (m, Pyr Ar-H, 2H), 4.47 (s, $PyrN^+$-Me, 3H). **MS** (ESI +ve) m/z: 171.1 ($[M-I]^+$, $C_{11}H_{11}N_2^+$ requires 171.1)

*Viologen propyl ammonium[17], **MVNH$_3$***

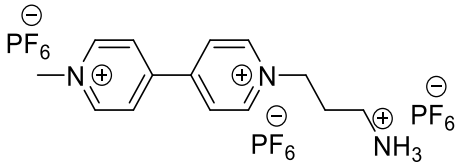


Monomethylated 4,4'bipyridine iodide **A** (2.00 g, 6.71 mmol) and 3-bromo-propylamine hydrobromide (7.34 g, 33.6 mmol) were dissolved in MeCN (40 mL), placed under an atmosphere of $N_2$ and heated to 80 °C for 48 hours, after which a large amount of orange-yellow precipitate had formed. The precipitate was isolated *via* vacuum filtration and washed with MeCN (2 x 20 mL) to remove unreacted starting material. The precipitate was redissolved in the minimum amount of $H_2O$ (~5 mL) and saturated $KPF_{6(aq.)}$ was added drop-wise with gentle stirring to precipitate the tri-$PF_6^-$ salt of the product. The resulting yellow precipitate was isolated *via* vacuum filtration, washed with cold $H_2O$ (2 x 10 mL) and dried *in vacuo* to give viologen propyl ammonium **MVNH$_3$** as a yellow solid (818 mg, 33%). **$^1$H NMR** (400 MHz, DMSO-$d_6$) δ (ppm): 9.33 (d, $Pyr^+$ Ar-H, *J* = 6.5 Hz, 2H), 9.28 (d, $Pyr^+$ Ar-H, *J* = 6.5 Hz, 2H), 8.80 (d, $Pyr^+$ Ar-H, *J* = 6.7 Hz, 2H), 8.73 (d, $Pyr^+$ Ar-H, *J* = 7.0 Hz, 2H), 7.74 (bs, $NH_3^+$, 3H), 4.73 (t, $PyrN^+$-$CH_2$, *J* = 7.2 Hz, 2H), 4.44 (s, $PyrN^+$-Me, 3H), 2.90 (t, $CH_2$-$NH_3^+$, *J* = 7.5 Hz, 2H), 2.26 (p, $CH_2$-$CH_2$-$CH_2$, *J* = 7.3 Hz, 2H). **$^{19}$F NMR** (376 MHz, DMSO-$d_6$) δ (ppm): -70.13 (d, $PF_6$, *J* = 711.3 Hz). **MS** (ESI +ve) m/z: 171.1 ($[M-I]^+$, $C_{11}H_{11}N_2^+$ requires 171.1).

*Viologen propyl bromide, **MVBr**[18]*

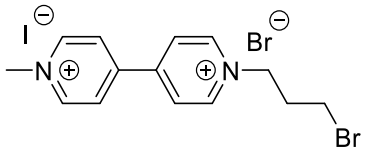


Monomethylated 4,4'bipyridine iodide **A** (700 mg, 2.35 mmol) was dissolved in hot MeCN (80 mL) and di-bromopropane (1.3 mL, 25.0 mmol) was added *via* a syringe, placed under an atmosphere of

$N_2$ and heated to 80 $^0$C for 72 hours, after which a large amount of orange precipitate had formed. The precipitate was isolated *via* vacuum filtration, washed with cold MeCN (2 x 10 mL) and DCM (2 x 10 mL) to remove unreacted starting material. The product was dried *in vacuo* to give viologen propyl ammonium (mixed $I^-$ and $Br^-$ salt) **MVBr** as a yellow solid (616 mg, 52%). **$^1$H NMR** (400 MHz, $D_2O$) δ (ppm): 9.11 (d, $Pyr^+$ Ar-H, *J* = 7.0 Hz, 2H), 8.99 (d, $Pyr^+$ Ar-H, *J* = 6.9 Hz, 2H), 8.51 (d, $Pyr^+$ Ar-H, *J* = 6.4 Hz, 2H), 8.46 (d, $Pyr^+$ Ar-H, *J* = 6.8 Hz, 2H), 4.86 (t, $PyrN^+$-$CH_2$, *J* = 7.1 Hz, 2H), 4.44 (s, $PyrN^+$-Me, 3H), 3.48 (t, $CH_2$-Br *J* = 6.1 Hz, 2H), 2.60 (p, $CH_2$-$CH_2$-$CH_2$, *J* = 6.8 Hz, 2H). **MS** (ESI +ve) m/z: 291.1 ($[M-H]^+$, $C_{14}H_{16}BrN_2^+$ requires 291.0).

*Viologen propyl azide*[19], ***MVN$_3$***

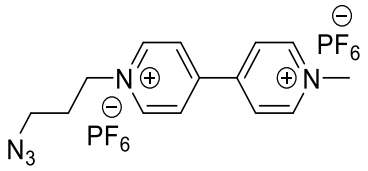


Viologen propyl bromide **MVBr** (150 mg, 0.300 mmol) and $NaN_3$ (200 mg, 3.00 mmol) were dissolved in water, sealed under an atmosphere of $N_2$ and heated for 24 hours at 80 °C (CAUTION – azide compound/salt potentially explosive when dry). The solution was cooled to 0 °C and saturated $KPF_{6(aq.)}$ was added drop-wise with gentle stirring to safely precipitate the di-$PF_6^-$ salt of the product. The resulting grey precipitate was isolated *via* vacuum filtration, washed with cold $H_2O$ (2 x 2 mL) and dried *in vacuo* to give viologen propyl azide **MVN$_3$** as a grey solid (81.0 mg, 49%). **$^1$H NMR** (400 MHz, $CD_3CN$) δ (ppm): 9.10 – 8.78 (m, $Pyr^+$ Ar-H, 4H), 8.64 – 8.30 (m, $Pyr^+$ Ar-H, 4H), 4.71 (m, $PyrN^+$-$CH_2$, 2H), 4.40 (s, $PyrN^+$-Me, 3H), 3.48 (m, $CH_2$-$N_3$, 2H), 2.28 (m, $CH_2$-$CH_2$-$CH_2$, 2H).

## 7.15 – Synthesis of 1-(10-mercaptodecyl)-1'-methyl-[4,4'-bipyridine]-diium bromide, D

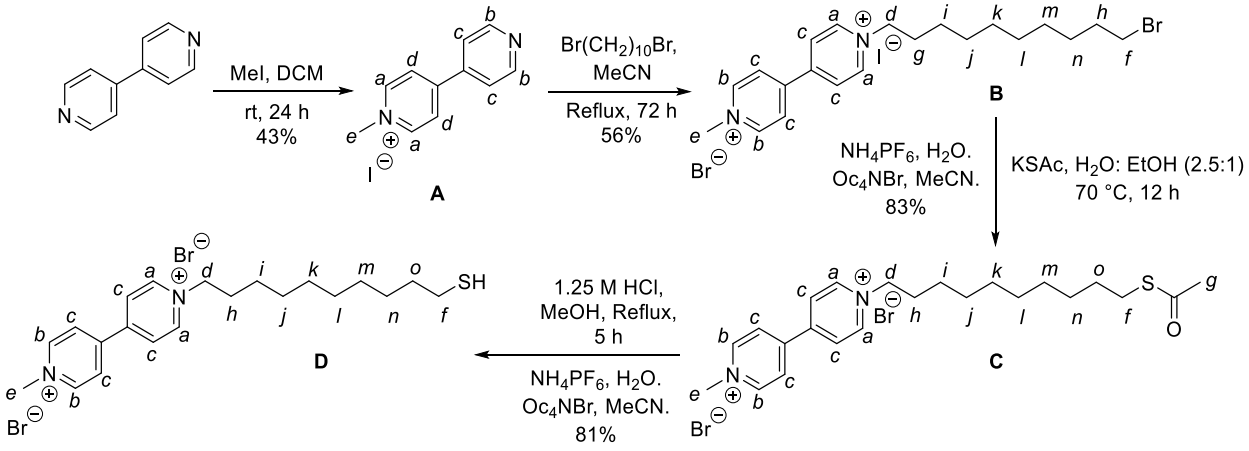


**Figure 14.** Synthesis of 1-(10-mercaptodecyl)-1'-methyl-[4,4'-bipyridine]-diium bromide, **D**.

*Monomethylated 4,4'bipyridine iodide,* ***A***[16]

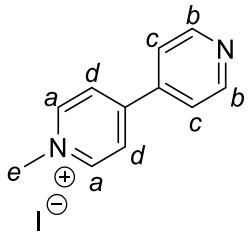

4,4'-bipyridine (2.00 g, 13.1 mmol) was dissolved in DCM/MeI (49:1 v/v, 20.0 mL) and the mixture stirred at RT for 24 hours before a yellow precipitate formed. The precipitate was isolated *via* vacuum filtration and monomethylated 4,4'bipyridine iodide **A** yielded as a golden yellow powder (996 mg, 43%) following recrystallization from MeOH and drying *in vacuo.* **$^1$H NMR** (400 MHz, DMSO-$d_6$) δ (ppm): 9.14 (d, *a*, 2H), 8.88 (d, *b*, 2H), 8.62 (d, *c*, 2H), 8.04 (m, *d*, 2H), 4.38 (s, *e*, 3H); **Figure 15**. **MS** (ESI +ve) m/z: 171.1 ($[M\text{-}I]^+$, $C_{11}H_{11}N_2^+$ requires 171.1).

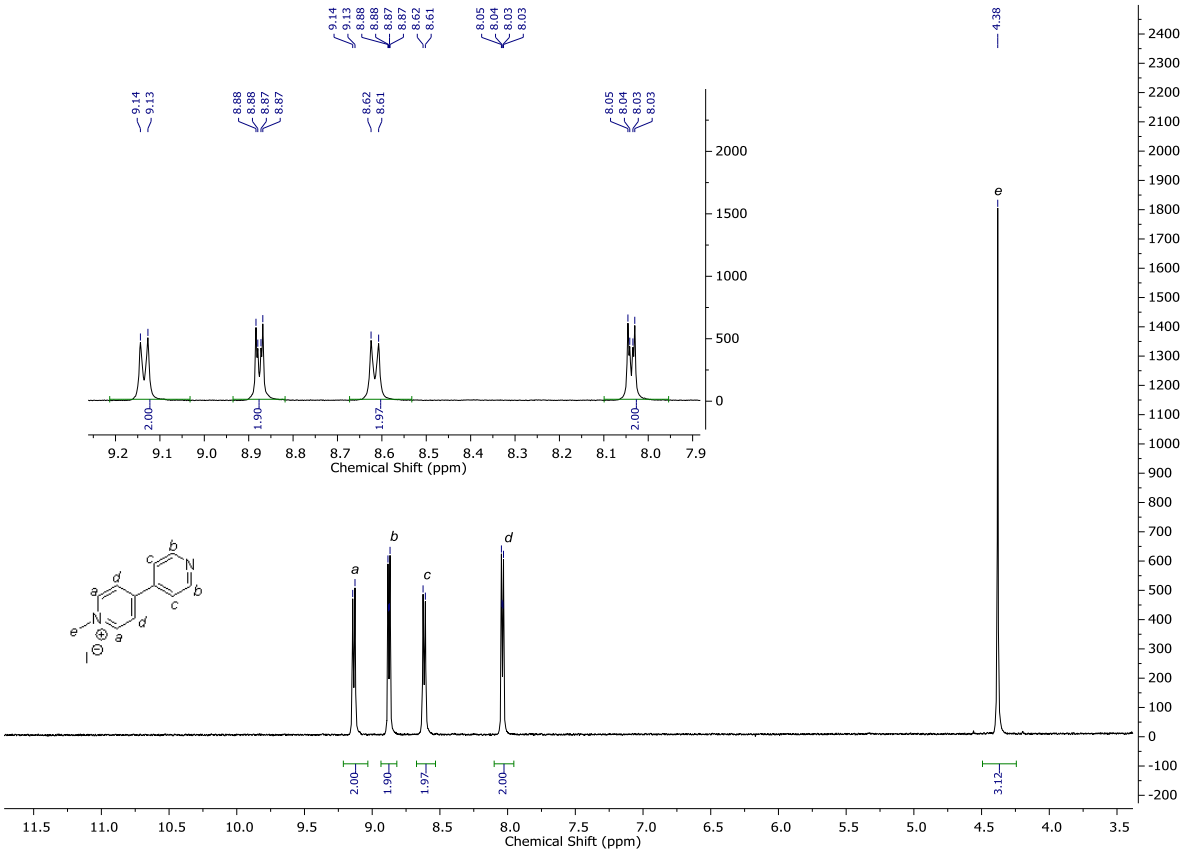


**Figure 15.** $^{1}$H NMR spectrum (400 MHz, DMSO-$d_6$, 298 K) of monomethylated 4,4'bipyridine iodide, **A**. **Inset.** Aromatic region of $^{1}$H NMR spectrum.

***B***[20, 21, 22]

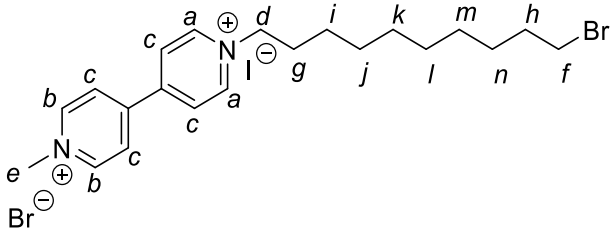


Monomethylated 4,4'bipyridine iodide **A** (966 mg, 3.24 mmol) and 1,10-dibromodecane (998 mg, 3.33 mmol) were refluxed in MeCN (40 mL) for 72 h. The reaction mixture was then allowed to cool to RT and the precipitate filtered off and washed with MeCN (2 x 10 mL). Drying under vacuum gave **B** as an orange solid (1.09 g, 56%).**$^{1}$H NMR** (400 MHz, $D_2O$) δ (ppm): 9.23 (d, *a*, 2H), 9.14 (d, *b*, 2H), 8.62 (t, *c*, 4H), 4.71(t, *d*, 2H), 4.48 (s, *e*, 3H), 3.38 (t, *f*, 1H), 3.17 (t, *f'*, 1H), 2.05 (m, *g*, 2H), 1.75 (m, *h*, 2H), 1.32 (m, *i*→*n*, 12H); **Figure 16**. **MS** (ESI +ve) m/z: 195.1 ($[M\text{-}I\text{-}Br]^{2+}$, $C_{21}H_{31}BrN_2^{2+}$ requires 195.1).

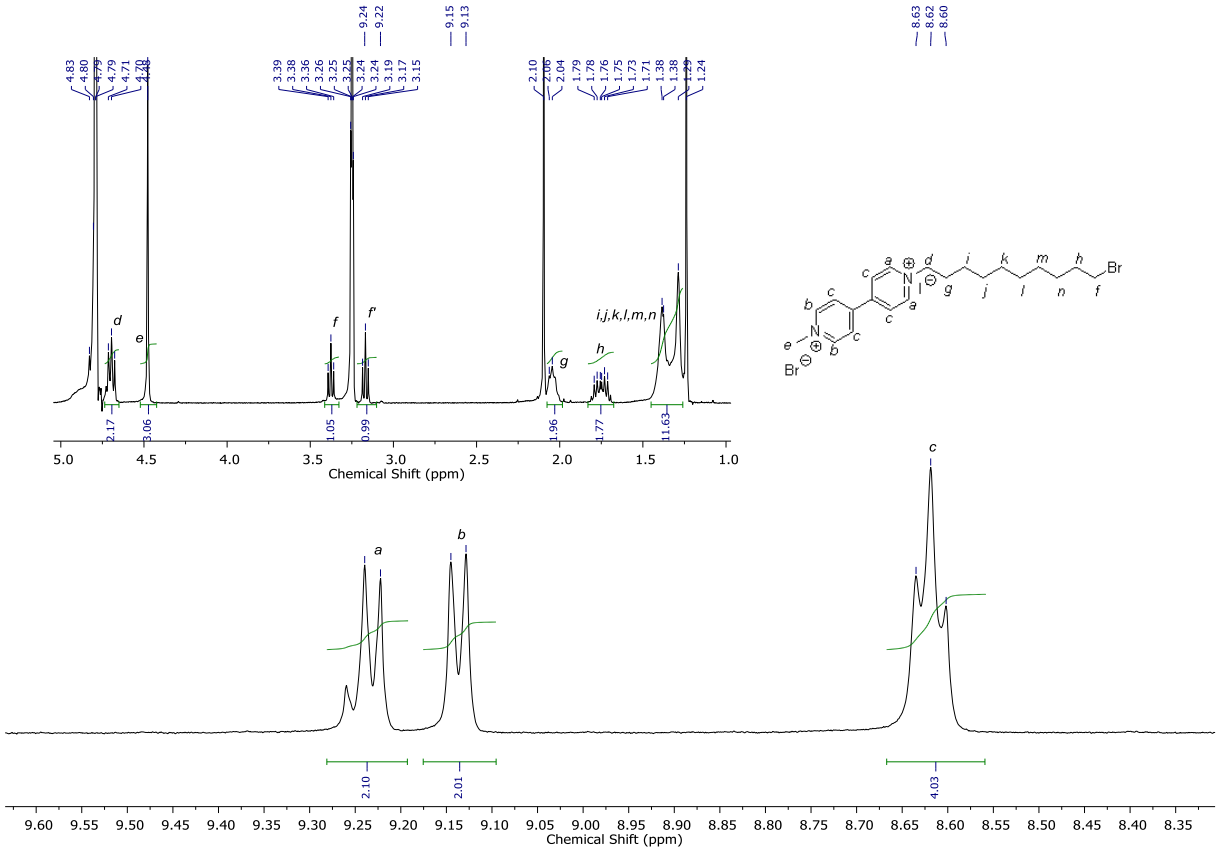


**Figure 16.** $^{1}$H NMR spectrum (400 MHz, $D_2O$, 298 K) of **B**. **Inset.** Aliphatic region of $^{1}$H NMR spectrum.

***C***[20, 21, 22]

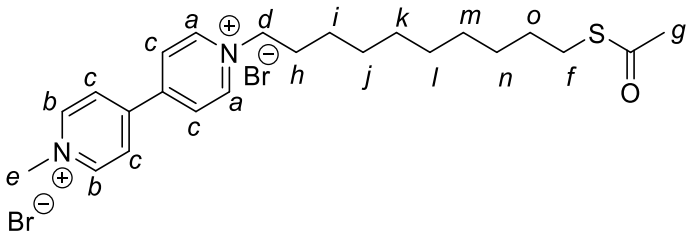


Potassium thioacetate (153 mg, 1.20 mmol) was added to an aqueous solution (40 mL) of **B** (300 mg, 0.500 mmol) and the mixture stirred at 60 °C for 12 h. The clear solution was allowed to cool to RT before being filtered through a pad of wool and cooled to ~ 6 °C in a refrigerator. An aqueous solution (2 mL) of $NH_4PF_6$ (456 mg, 2.80 mmol) was then added to the filtrate and a yellow precipitate collected and dried in air. The solid was then redissolved in MeCN (40 mL), and $Oc_4NBr$ (1.10 g, 2.01 mmol) in MeCN (3 mL) added dropwise. The final product was then filtered off and dried under reduced pressure to yield **C** as light yellow solid (131 mg, 48%). **$^{1}$H NMR** (400 MHz, $D_2O$) δ (ppm): 9.12 (d, *a*, 2H), 9.06 (d, *b*, 2H), 8.54 (m, *c*, 4H), 4.73 (t, *d*, 2H), 4.51 (s, *e*, 3H), 2.87 (t, *f*, 2H), 2.36 (s, *g*, 3H), 2.08 (m, *h*, 2H), 1.56 (m, *o*, 2H), 1.34 (m, *i*→*n*, 12H); **Figure 17**. **$^{13}$C NMR** (125 MHz, $CD_3SOCD_3$) δ (ppm): 195.32, 148.56, 148.19, 146.60, 145.73, 126.52, 126.06, 60.92,

48.04, 30.72, 30.58, 29.10, 28.72, 28.69, 28.40, 28.34, 28.30, 28.08, 25.40; **Figure 18**. **MS** (ESI +ve) m/z: 193.2 ($[M-2Br]^{2+}$, $C_{23}H_{34}N_2OS_2$+ requires 193.1).

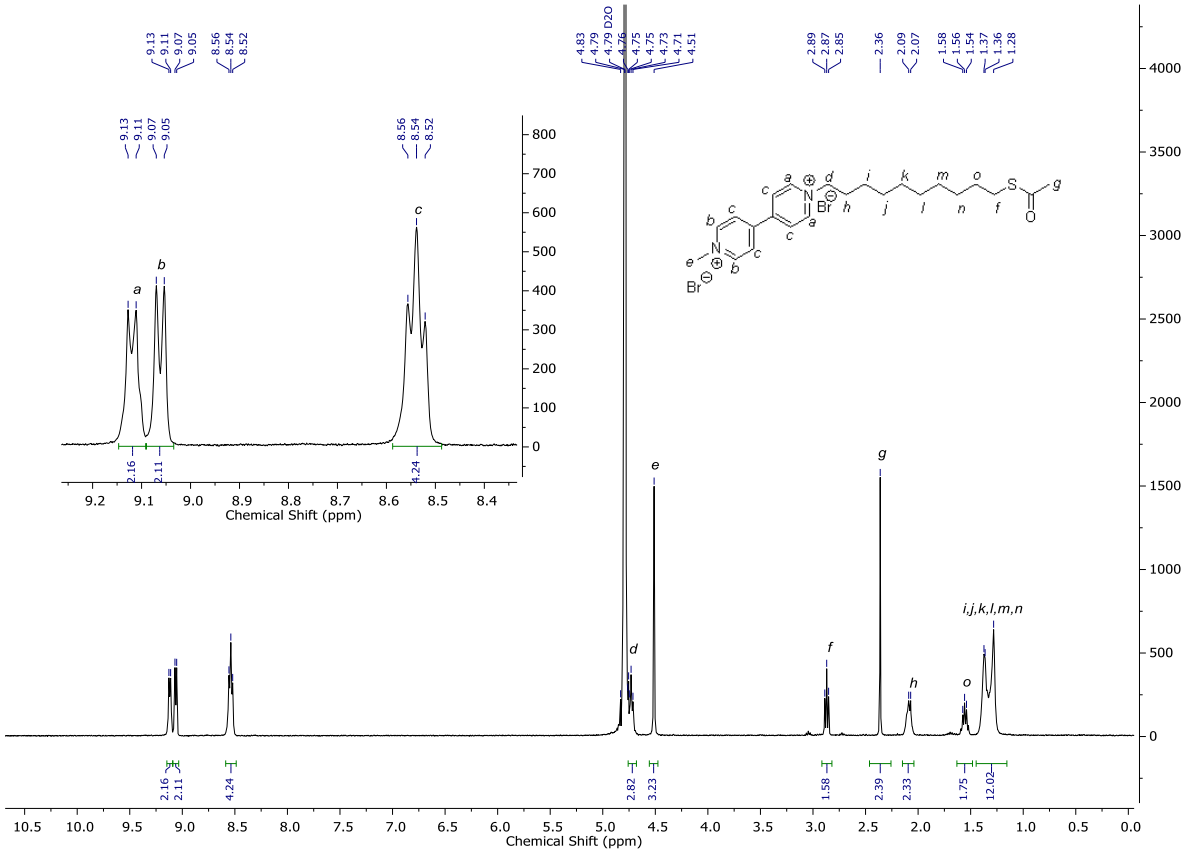


**Figure 17.** $^1$H NMR spectrum (400 MHz, $D_2O$, 298 K) of **C**. **Inset.** Aromatic region of $^1$H NMR spectrum.

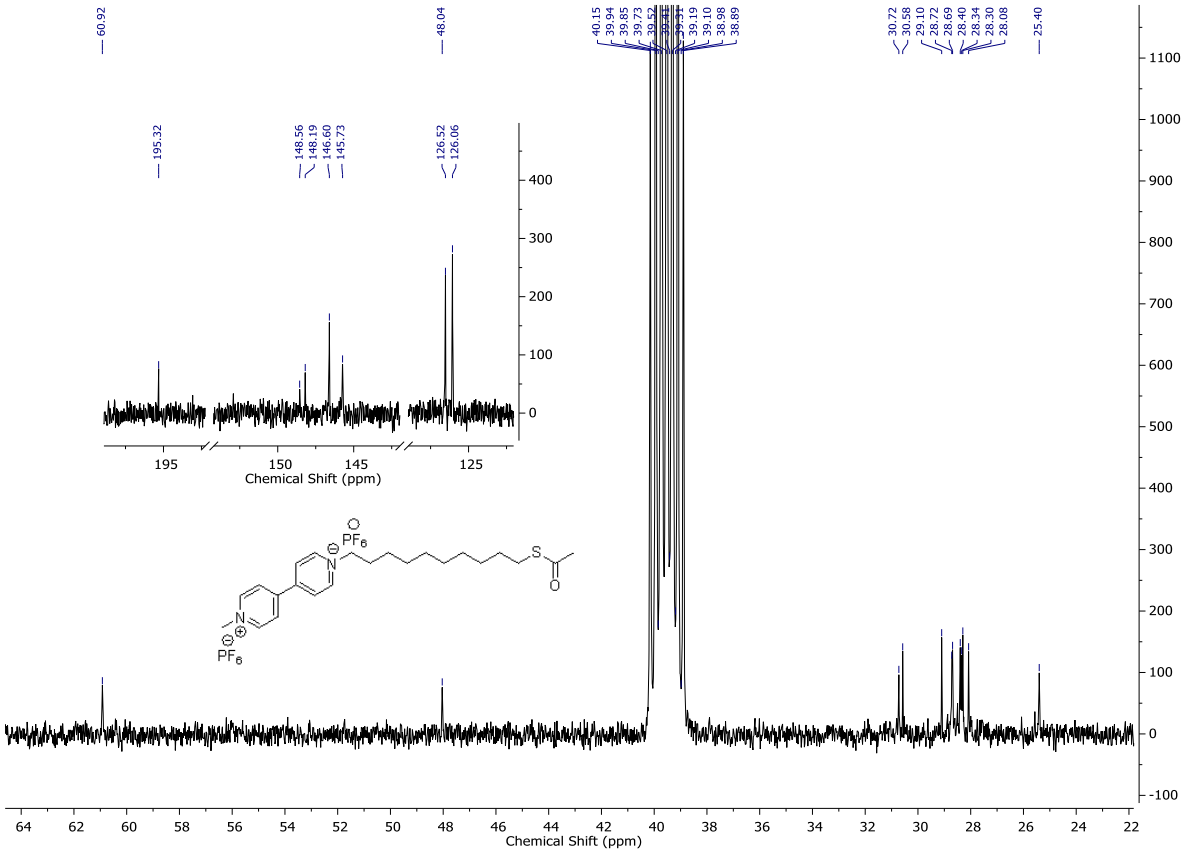


**Figure 18.** $^{13}$C NMR spectrum (125 MHz, $CD_3SOCD_3$, 298 K) of **C** ($PF_6^-$ salt). **Inset.** C=O, aromatic and C=C region of $^{13}$C NMR spectrum.

***D***[20, 21, 22]

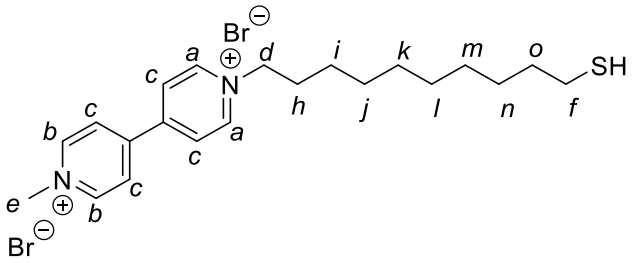


Concentrated HCl (1.25 M, 2.0 mL) was added to an aqueous solution (2.0 mL) of **C** (39.0 mg, 0.0710 mmol) and the mixture stirred for 48 h at 70 °C. Upon allowing the mixture to cool to RT, the crude product was obtained by adding $NH_4PF_6$ (45.0 mg, 0.280 mmol) in $H_2O$ (1.0 mL). The crude product was filtered off and redissolved in MeCN (2.0 mL). Treatment with $Oc_4NBr$ (260 mg, 0.480 mmol) in MeCN (2.0 mL), filtration and drying under vacuum led to the formation of **D** (120 mg, 88%) as a light yellow solid. **$^1$H NMR** (400 MHz, $D_2O$) δ (ppm): 9.03 – 9.15 (m, *a*,*b*, 4H), 8.50 – 8.59 (m, *c*, 4H), 4.51 (s, *e*, 3H), 2.04 – 2.14 (m, *h*, 2H), 1.53 – 1.70 (m, *o*, 2H), 1.33 (m, *i*→*n*, 12H); **Figures 19** and **20**.

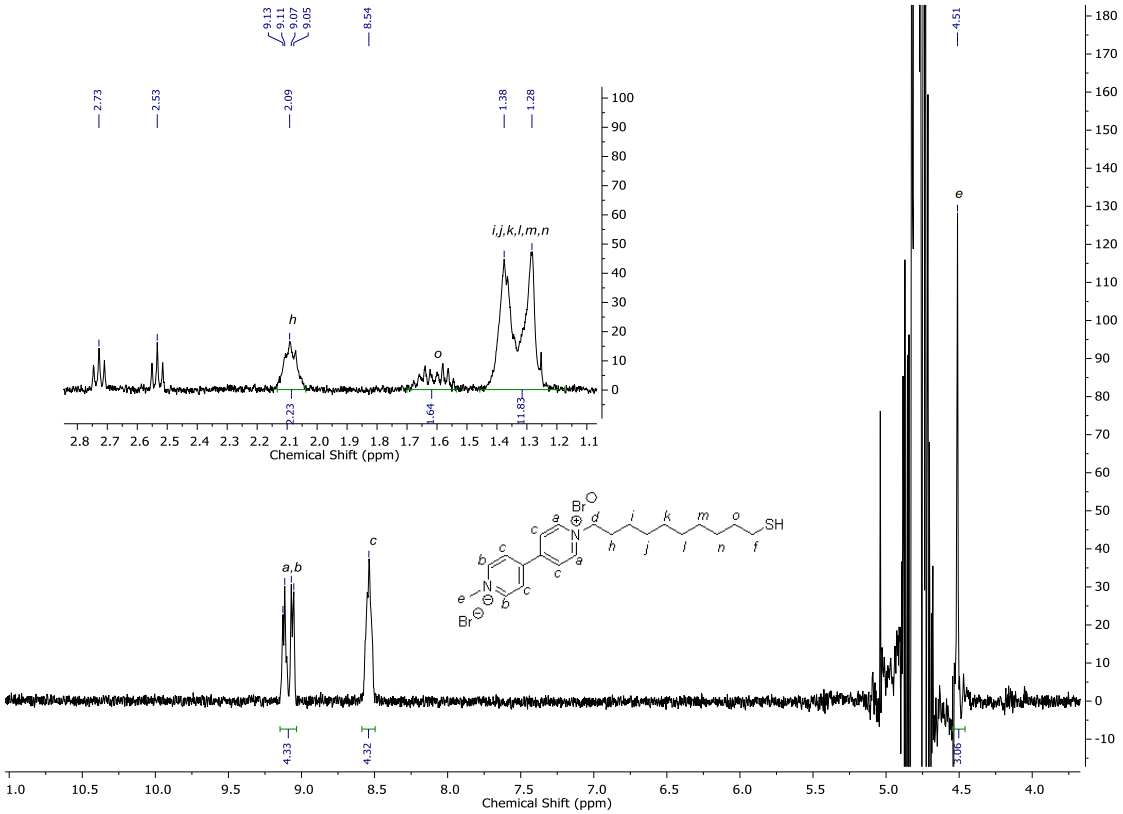


**Figure 19.** $^{1}$H NMR spectrum (400 MHz, $D_2O$, 298 K) of **D**. **Inset.** Aliphatic region of $^{1}$H NMR spectrum.

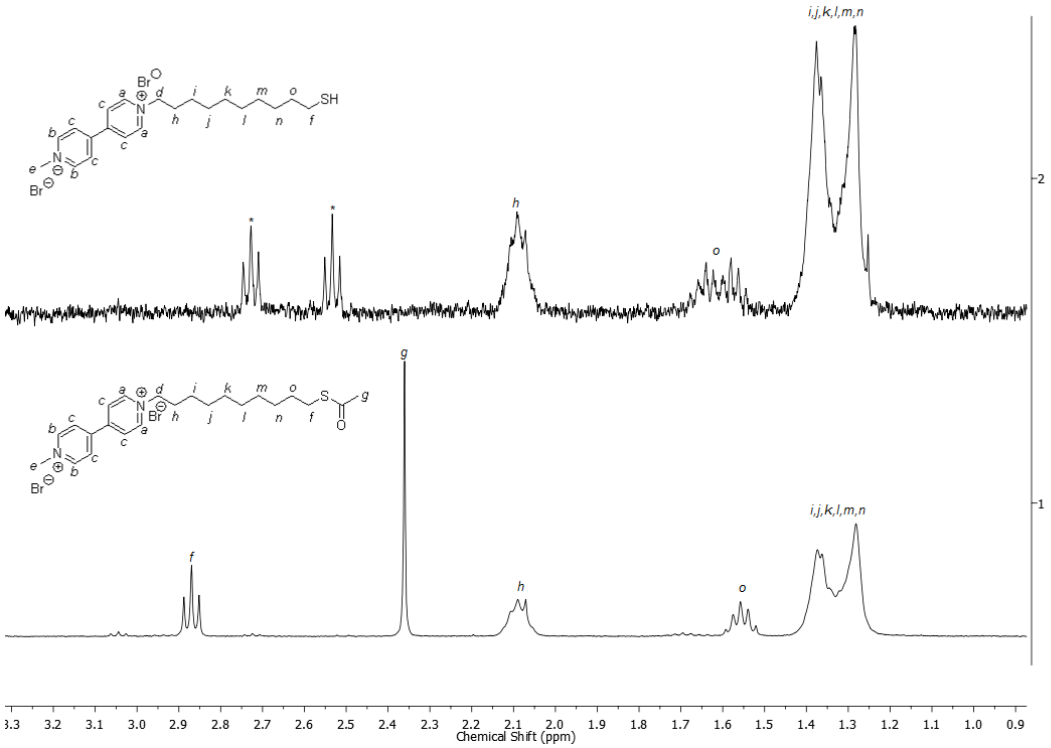


**Figure 20.** $^{1}$H NMR spectra (400 MHz, $D_2O$, 298 K) of **C** (**Bottom**) and **D** (**Top**). Upon thioacetate deprotection, the peak (s, *g*, 3H) at 2.36 ppm disappears as expected.

## 7.16 – Synthesis of 1-methyl-1'-(10-(naphthalen-2-yloxy)decyl)-[4,4'-bipyridine]-1,1'-diium bromide iodide, F

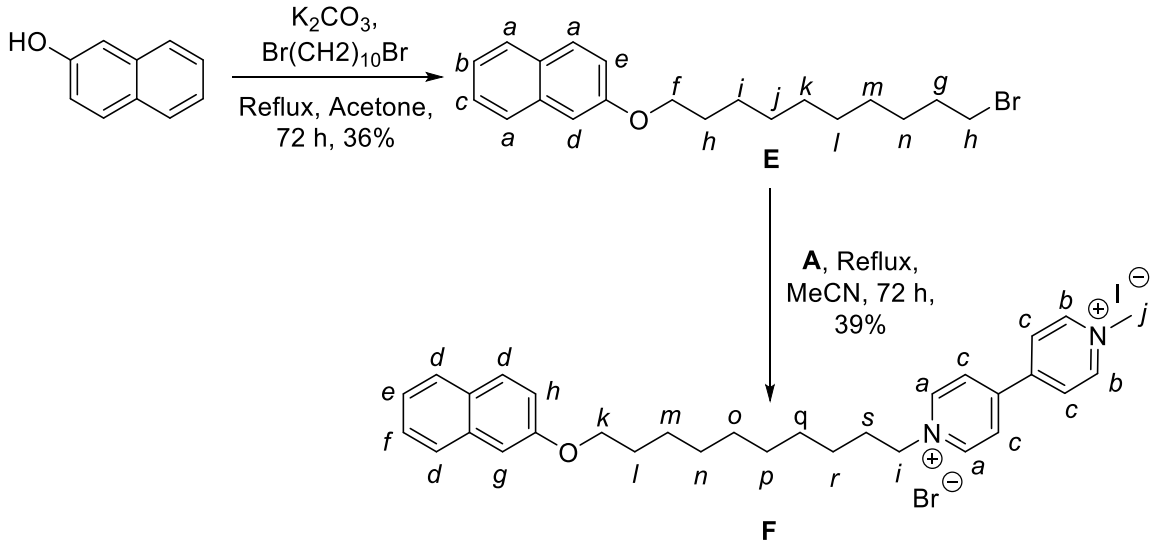


**Figure 21.** Synthesis of 1-methyl-1'-(10-(naphthalen-2-yloxy)decyl)-[4,4'-bipyridine]-1,1'-diium bromide iodide, **F**.

***E***[23, 24, 25]

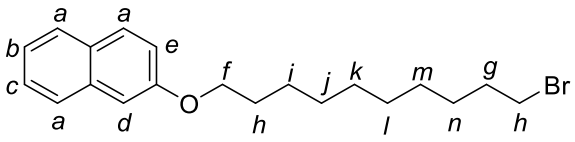

2-Napthol (1.00 g, 6.94 mmol), $K_2CO_3$ (1.00 g, 7.25 mmol) and 1,10-dibromodecane (2.00 g, 6.67 mmol) were refluxed in acetone (50 mL) for 72 h. The reaction mixture was then subject to aqueous workup and the crude product isolated following filtration and drying *in vacuo.* The crude product was then purified by silica gel column chromatography (100:0, 90:10, hexane: ethyl acetate) to give **E** (913 mg, 36%) as a fine cream powder. **$^1$H NMR** (400 MHz, $CDCl_3$) δ (ppm): 7.74 (q, *a*, 3H), 7.43 (t, *b*, 1H), 7.33 (t, *c*, 1H), 7.15 (m, *d*, *e*, 2H), 4.08 (t, *f*, 2H), 3.41 (t, *g*, 2H), 1.85 (m, *h*, 4H), 1.32 – 1.54 (m, *i*→*n*, 12H); **Figure 22**. **$^{13}$C NMR** (125 MHz, $CD_3OD$) δ (ppm): 157.11, 129.31, 128.89, 127.63, 126.68, 126.28, 123.46, 119.03, 106.57, 68.00, 34.05, 32.02, 32.84, 32.82, 29.46, 29.37, 29.31, 29.25, 28.76, 28.72, 28.17, 28.15, 26.10; **Figure 23**. **MS** (ESI +ve) m/z: 362.1 ($[M]^+$, $C_{20}H_{27}BrO$ requires 362.1).

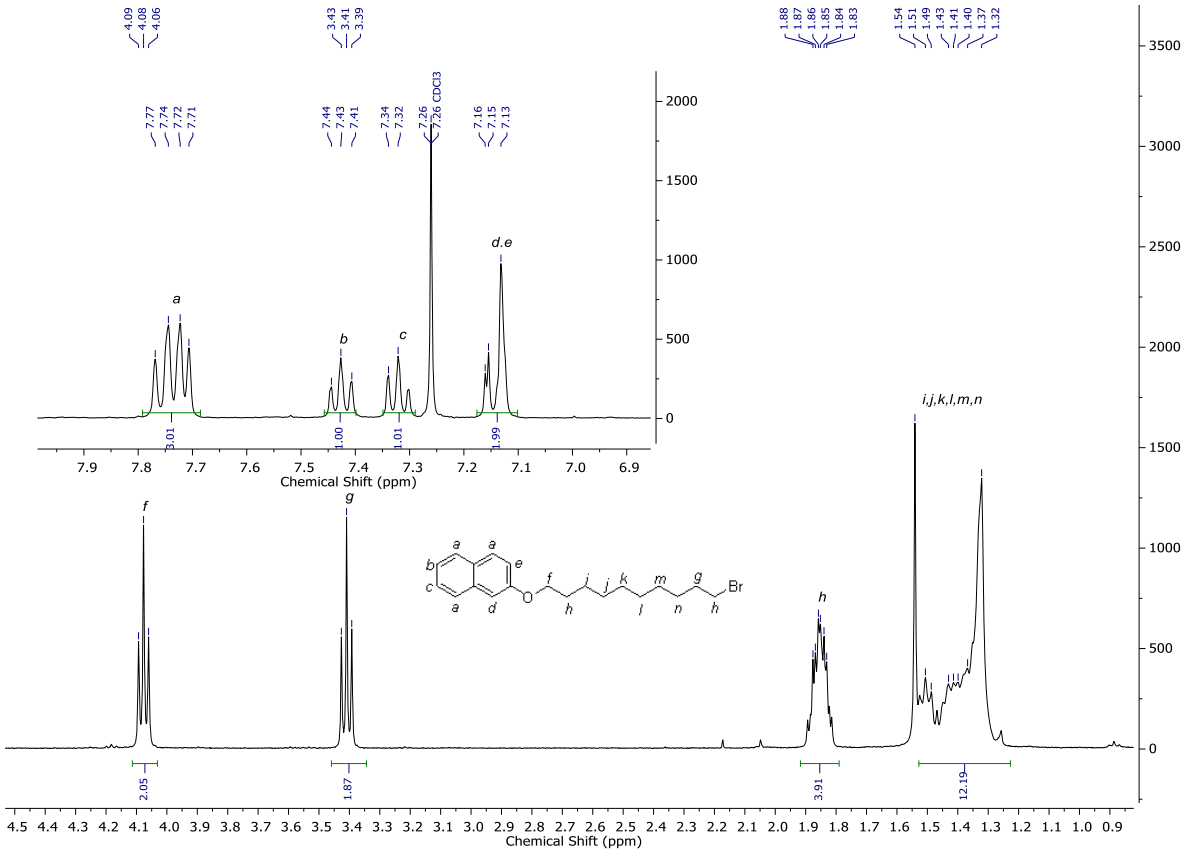


**Figure 22.** $^{1}$H NMR spectrum (400 MHz, $CDCl_3$, 298 K) of **E**. **Inset.** Aromatic region of $^{1}$H NMR spectrum.

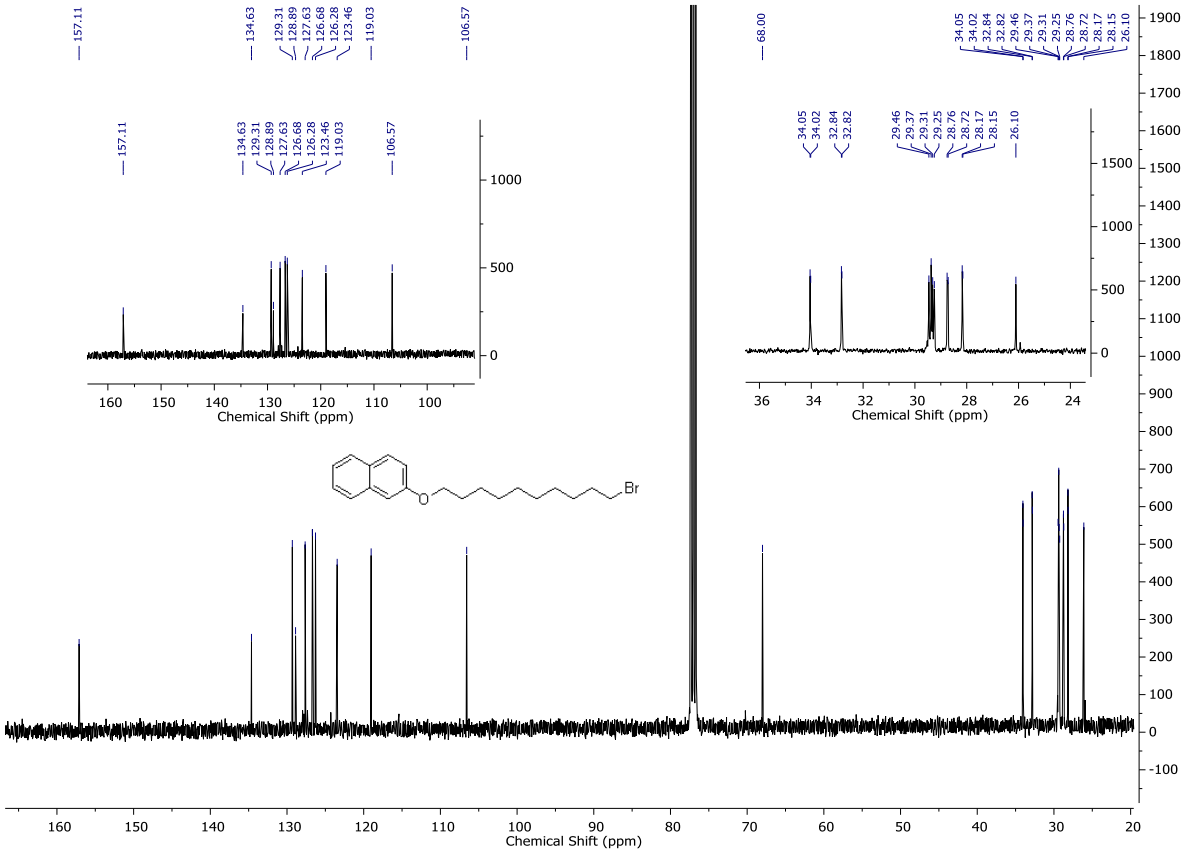


**Figure 23.** $^{13}$C NMR spectrum (125 MHz, $CD_3OD$, 298 K) of **E**. **Inset.** C=O, aromatic and C=C (**Left**) and aliphatic (**Right**) regions of $^{13}$C NMR spectrum.

***F***[23, 24, 25]

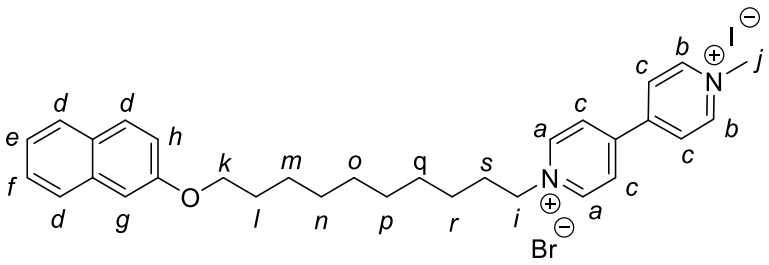


**A** (202 mg, 0.680 mmol) and **E** (229 g, 0.630 mmol) were refluxed in MeCN (45 mL) for 72 h. The reaction mixture was then allowed to cool to RT, before being placed in a refrigerator set to ~ 6 °C for 2 h. The resultant precipitate was then filtered off, washed with MeCN and dried *in vacuo* to yield **F** (109 mg, 39%) as a fine, dark orange powder. **$^1$H NMR** (400 MHz, $D_2O$) δ (ppm): 9.01 (d, *a*, 2H), 8.88 (d, *b*, 2H), 8.33 – 8.41 (2d, *c*, 4H), 7.79 (t, *d*, 3H), 7.51 (t, *e*, 1H), 7.38 (t, *f*, 1H), 7.27 (m, *g*, 1H), 7.12 (2d, *h*, 1H), 4.63 (t, *i*, 2H), 4.36 (s, *j*, 3H), 4.14 (t, *k*, 2H), 1.34-2.07 (m, *l*→*s*, 16H); **Figure 24**. **MS** (ESI +ve) m/z: 227.2 ($[M]^{2+}$ / 2, $C_{31}H_{38}N_2O^{2+}$ requires 227.2), 454.3 ($[M]^+$, $C_{31}H_{38}N_2O^+$ requires 454.3).

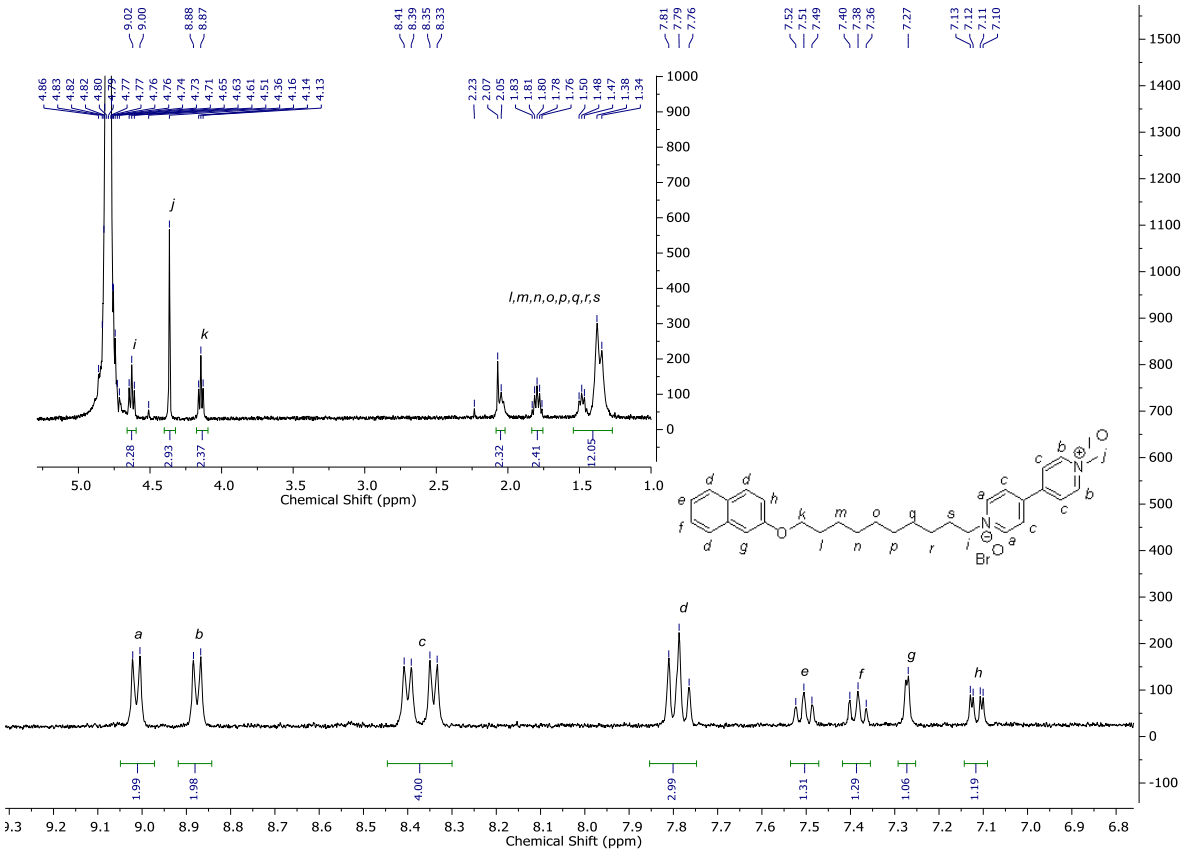


**Figure 24.** $^{1}$H NMR spectrum (400 MHz, $D_2O$, 298 K) of **F**. **Inset.** Aliphatic region of $^{1}$H NMR spectrum.

## 7.17 – Synthesis of PerhydroxyCB[6][26], 1

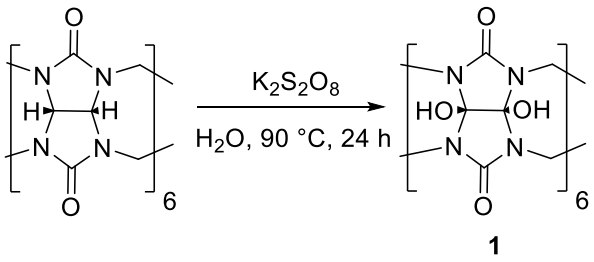


**Figure 25.** Synthesis of perhydroxyCB[6], **1**.

A slurry of CB[6] (99.8 mg, 0.100 mmol) and $K_2S_2O_8$ (398 mg, 1.47 mmol) in distilled $H_2O$ (5.0 mL) was degassed by bubbling $N_2$ (g) through the mixture, and heated to 90 °C for 24 h under a $N_2$ (g) atmosphere. After cooling to RT, the white precipitate was removed by filtration and the filtrate concentrated to 2 mL under reduced pressure. Acetone vapour diffusion (10 min) into the resultant solution yielded a white precipitate, which was collected by filtration, washed with acetone and dried in a vacuum to give the crude product as a fluffy white powder (23.6 mg, 15%). **$^{1}$H NMR** (400 MHz, DMSO-$d_6$) δ (ppm): only crude spectrum acquired. Multiplets can't be assigned with confidence;

**Figure 26**. **MS** (MALDI-TOF): only crude spectrum acquired, infers partial hydroxylation only; **Figure 27**.

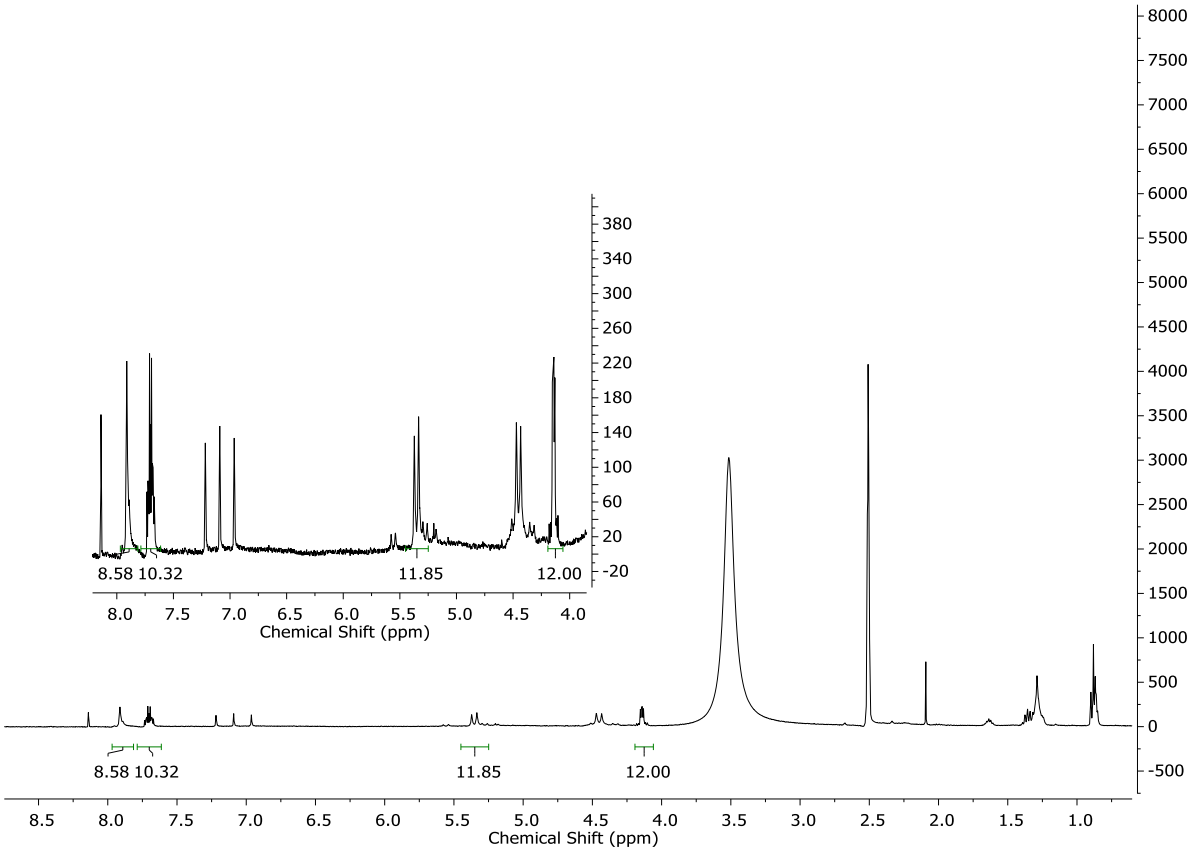


**Figure 26.** $^{1}$H NMR spectrum (400 MHz, DMSO-$d_6$, 298 K) of crude product. **Inset.** Aliphatic and aromatic regions of interest of $^{1}$H NMR spectrum.

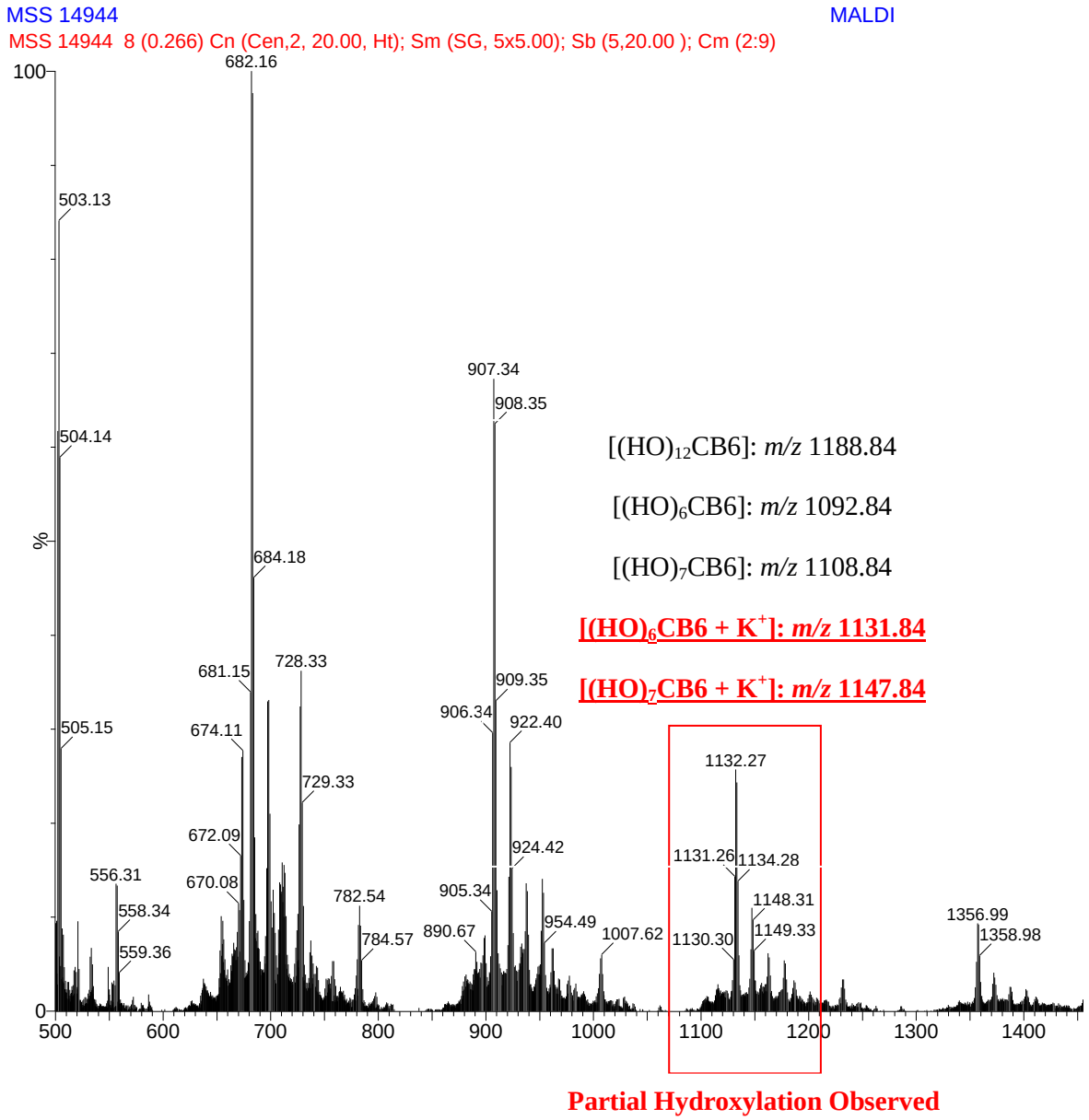


**Figure 27.** MALDI-TOF mass spectrum of crude product. Partial hydroxylation is inferred by the presence of the peaks at m/z between 1130.30 and 1149.33.

## List of References


1. Jan Tkac, Jason J. Davis, *J. Electroanal. Chem*., **2008**, 621, 117–120.
2. Lawrence Yoon Suk Lee, Todd C. Sutherland, Simona Rucareanu, R. Bruce Lennox, *Langmuir*, **2006**, *22*, 4438–4444.
3. J. C. Hoogvliet, M. Dijksma , B. Kamp, W. P. van Bennekom, *Anal. Chem.*, **2000**, 72, 2016–2021.
4. Cindra A. Widrig, Chinkap Chung, Marc D. Porter, *J. Electroanal. Chem.*, **1991**, 310, 335-359.
5. D.-F. Yang, C. P. Wilde, M. Morin, *Langmuir*, **1996**, 12, 6570-6577.
6. D.-F. Yang, C. P. Wilde, M. Morin, *Langmuir*, **1997**, 13, 243-249.
7. Mary M. Walczak, Darwin D. Popenoe, Randall S. Deinhammer, Brian D. Lamp, Chinkap. Chung, Marc D. Porter, *Langmuir*, **1991**, 7, 2687-2693.
8. Qi An, Guangtao Li, Chengan Tao, Yan Li, Yiguang Wu and Weixia Zhang, *Chem. Commun*., **2008**, 1989–1991.
9. Elaine T Vandenberg, Lars Bertilsson, Bo Liedberg, Kajsa Uvdal, Ragnar Erlandsson, Hans Elwing, Ingemar Lundström, *J. Colloid Interface Sci.*, **1991**, 147, 103–118.
10. Wei Zhu, Chen Wang, Weina Li, Cheng-an Tao, Jiecheng Cui, Haowei Yang, Yin Jiang, Guangtao Li, *J. Mater. Chem. A.*, **2013**, 1, 11741–11747.
11. Xiaoqun Zhu, Xiuwei Fan, Guannan Ju, Mengjiao Cheng, Qi An, Jun Nie, Feng Shi, *Chem. Commun.*, **2013**, 49, 8093–8095.
12. Alberto Gomez-Casado, Pascal Jonkheijm, Jurriaan Huskens, *Langmuir*, **2011**, 27, 11508–11513.
13. Alexander Ryabchun, Alexey Bobrovsky, Sung-Ho Chun, Valery Shibaev, *J. Polym. Sci. Part Polym. Chem.*, **2013**, 51, 4031–4041.
14. Anjum Dadabhoy, Stephen Faulkner, Peter G. Sammes, *J. Chem. Soc. Perkin Trans. 2*, **2002**, 2, 348–357.
15. Gnoatto SC, Dassonville-Klimpt A, Da Nascimento S, Galéra P, Boumediene K, Gosmann G, Sonnet P, Moslemi S., *Eur. J. Med. Chem.*, **2008**, 43, 1865–1877.
16. Melissa C. Grenier, Robert W. Davis, Kelsey L. Wilson-Henjum, Jade E. LaDow, Jacob W. Black, Kevin L. Caran, Kyle Seifert, Kevin P.C. Minbiole, *Med. Chem. Lett.*, **2012**, 22, 4055–4058.
17. Noriyuki Asakura, Tomohiro Hiraishi, Toshiaki Kamachi, Ichiro Okura, *Catal. Chem.*, **2001**, 174, 1–5.
18. Samir Andersson, Dapeng Zou, Rong Zhang, Shiguo Sun, Licheng Sun, *Org. Biomol. Chem.*, **2009**, 7, 3605–3609.

19. Jae Wook Lee, Seung Choul Han, Ji Hyeon Kim, Young Ho Ko, Kimoon Kim, *Bull. Korean Chem. Soc.*, **2007**, 28, 1837–1840.
20. Feng Tian, Dezhi Jiao, Frank Biedermann, Oren A. Scherman, *Nat. Commun.*, **2012**, 3, 1–8.
21. Feng Tian, Nan Cheng, Nicolas Nouvel, Jin Geng, Oren A. Scherman, *Langmuir*, **2010**, 26, 5323–5328.
22. Feng Tian, Monika Cziferszky, Dezhi Jiao, Karolina Wahlström, Jin Geng, Oren A. Scherman, *Langmuir*, **2011**, 27, 1387–1390.
23. Ko YH, Kim K, Kang JK, Chun H, Lee JW, Sakamoto S, Yamaguchi K, Fettinger JC, Kim K., *J. Am. Chem. Soc.*, **2004**, 126, 1932–1933.
24. Tadashi Mori, Young Ho Ko, Kimoon Kim, Yoshihisa Inoue, *J. Org. Chem.*, **2006**, 71, 3232–3247.
25. Young Ho Ko, Kyungpil Kim, Eunju Kim, Kimoon Kim, *Supramol. Chem*, **2007**, 19, 287–293.
26. Jon, S. Y., Selvapalam, N., Oh, D. H., Kang, J.-K., Kim, S.-Y., Jeon, Y. J., Lee, J. W., Kim, K., *J. Am. Chem. Soc.*, **2003**, 125, 10186–10187.

## List of Figures

**Figure 1.** A representative cyclic voltammogram of a gold electrode acquired following electrochemical polishing in a 100 mM aqueous solution of $H_2SO_4$. The surface area of each electrode was calculated upon integrating the peak labelled **A** (reduction of an Au/α gold oxide layer formed in an anodic scan). Electrochemical Setup: *Working Electrode*: Bare Au. *Reference Electrode*: Ag Wire. *Auxiliary Electrode*: Pt wire. *Electrolytic Solution*: 0.1 M $H_2SO_4$ (aqueous). *Scan Rate:* 100 mV / s.

**Figure 2.** The characteristic stripping peak acquired upon the reductive desorption of thiols from gold interfaces. The above example was acquired upon repeatedly sweeping the potential of a MHDA-modified gold electrode between – 0.5 and – 1.5 V in a degassed 0.5 M solution (50:50, EtOH: $H_2O$) of KOH at a scan rate of 100 mV / s.

**Figure 3.** Cyclic voltammograms recorded following the deposition of both 11-(ferrocenyl)undecanethiol (**Red**) and a porphyrin-appended thiol (**Black**) at Au. Both CVs were obtained in a 0.1 M solution ($CH_2Cl_2$) of $TBAPF_6$ at a scan rate of 1000 mV /s.

**Figure 4.** An overview of the experimental setup employed to measure cathodic photocurrent density.

**Figure 5.** A plot of current *vs.* time acquired upon irradiation (**'ON'**, 430 ± 5 nm) of a porphyrin-appended monolayer.

**Figure 6.** An image of a water droplet (100 μL) on the surface of a Au substrate modified with 11-mercaptoundecanoic acid. The contact angle (θ) was taken as the angle between the centre of the droplet and the contact point of the droplet.

**Figure 7.** Synthesis of naphthoxy amidoacetyl chloride, **N3**.

**Figure 8.** Synthesis of DO3A tri-*tert*-butyl ester, **N4**.

**Figure 9.** Synthesis of naphthol DO3A tri-acid, **N6**.

**Figure 10.** Synthesis of LnNap, where Ln = $Eu^{3+}$, $Yb^{3+}$ or $Nd^{3+}$.

**Figure 11.** Synthesis of ferrocene amido-acetyl bromide, **V3**.

**Figure 12.** Synthesis of **FcMV**.

**Figure 13.** Synthesis of $MVN_3^+$ and $MVNH_3^+$.

**Figure 14.** Synthesis of 1-(10-mercaptodecyl)-1'-methyl-[4,4'-bipyridine]-diium bromide, **D**.

**Figure 15.** $^{1}$H NMR spectrum (400 MHz, DMSO-$d_6$, 298 K) of monomethylated 4,4'bipyridine iodide, **A**. **Inset.** Aromatic region of $^{1}$H NMR spectrum.

**Figure 16.** $^{1}$H NMR spectrum (400 MHz, $D_2O$, 298 K) of **B**. **Inset.** Aliphatic region of $^{1}$H NMR spectrum.

**Figure 17.** $^{1}$H NMR spectrum (400 MHz, $D_2O$, 298 K) of **C**. **Inset.** Aromatic region of $^{1}$H NMR spectrum.

**Figure 18.** $^{13}$C NMR spectrum (125 MHz, $CD_3SOCD_3$, 298 K) of **C** ($PF_6^-$ salt). **Inset.** C=O, aromatic and C=C region of $^{13}$C NMR spectrum.

**Figure 19.** $^{1}$H NMR spectrum (400 MHz, $D_2O$, 298 K) of **D**. **Inset.** Aliphatic region of $^{1}$H NMR spectrum.

**Figure 20.** $^{1}$H NMR spectra (400 MHz, $D_2O$, 298 K) of **C** (**Bottom**) and **D** (**Top**). Upon thioacetate deprotection, the peak (s, *g*, 3H) at 2.36 ppm disappears as expected.

**Figure 21.** Synthesis of 1-methyl-1'-(10-(naphthalen-2-yloxy)decyl)-[4,4'-bipyridine]-1,1'-diium bromide iodide, **F**.

**Figure 22.** $^{1}$H NMR spectrum (400 MHz, $CDCl_3$, 298 K) of **E**. **Inset.** Aromatic region of $^{1}$H NMR spectrum.

**Figure 23.** $^{13}$C NMR spectrum (125 MHz, $CD_3OD$, 298 K) of **E**. **Inset.** C=O, aromatic and C=C (**Left**) and aliphatic (**Right**) regions of $^{13}$C NMR spectrum.

**Figure 24.** $^{1}$H NMR spectrum (400 MHz, $D_2O$, 298 K) of **F**. **Inset.** Aliphatic region of $^{1}$H NMR spectrum.

**Figure 25.** Synthesis of perhydroxyCB[6], **1**.

**Figure 26.** $^{1}$H NMR spectrum (400 MHz, DMSO-$d_6$, 298 K) of crude product. **Inset.** Aliphatic and aromatic regions of interest of $^{1}$H NMR spectrum.

**Figure 27.** MALDI-TOF mass spectrum of crude product. Partial hydroxylation is inferred by the presence of the peaks at m/z between 1130.30 and 1149.33.

## List of Equations

**Equation 1.** Calculating the geometric area (**A**, $cm^2$) of a polycrystalline Au electrode, where **Q** (C, coulombs) is the current obtained from integrating the reduction peak of the Au/α gold oxide layer (+ 750 to + 1000 mV, vs Ag Wire) and 482 μC $cm^{-2}$ the theoretical amount of current required to remove a monolayer of Au/α gold oxide from the surface of 1 $cm^2$ of Au[3].

# 8. Appendix

## 8.1 – The Characterisation of Porphyrin-Appended SAMs

### 8.1.1 – Solution Phase Characterisation of AB-14-172

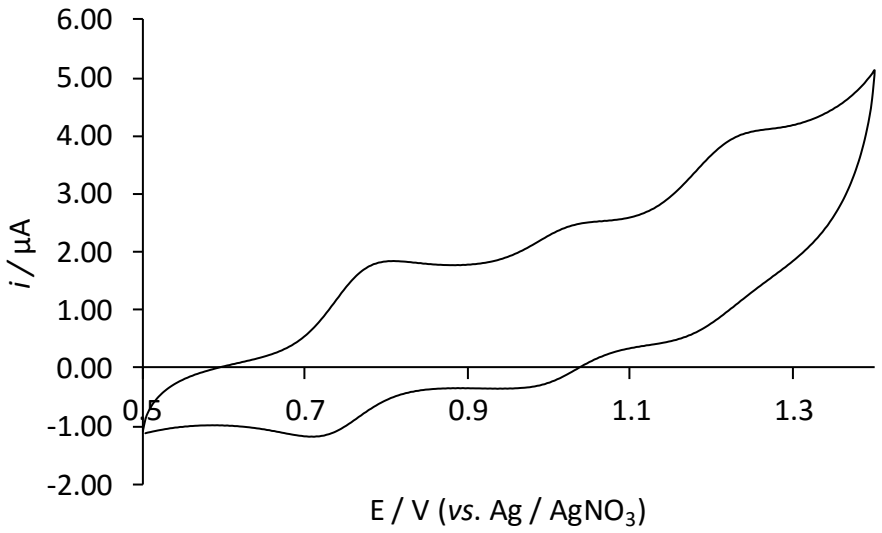


**Figure 1**. Cyclic voltammogram of a 5 µM solution (anhydrous, deoxygenated ($N_2$ (g), 10 min.) $CH_2Cl_2$) of AB-14-172. Electrochemical Setup: *Working Electrode*: Glassy Carbon. *Reference Electrode*: Ag / $AgNO_3$. *Auxiliary Electrode*: Pt wire. *Electrolytic Solution*: 0.1 M $TBAPF_6$ (298 K). *Scan Rate:* 100 mV / s.

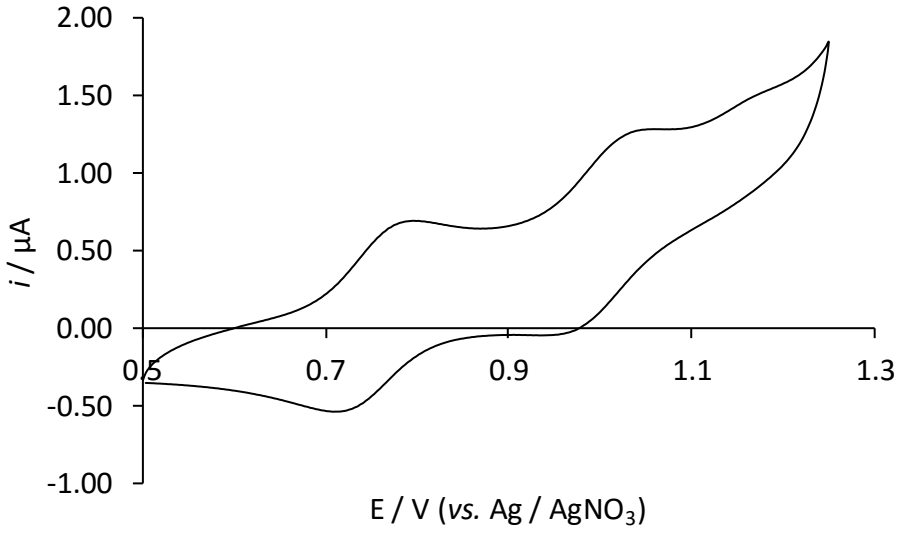


**Figure 2.** Cyclic voltammogram of a 5 µM solution (anhydrous, deoxygenated ($N_2$ (g), 10 min.) $CH_2Cl_2$) of AB-14-172. Electrochemical Setup: *Working Electrode*: Bare Au. *Reference Electrode*: Ag / $AgNO_3$. *Auxiliary Electrode*: Pt wire. *Electrolytic Solution*: 0.1 M $TBAPF_6$ (298 K). *Scan Rate:* 100 mV / s.

## 8.1.2 – Characterisation of Monophasic, Porphyrin-Appended SAMs

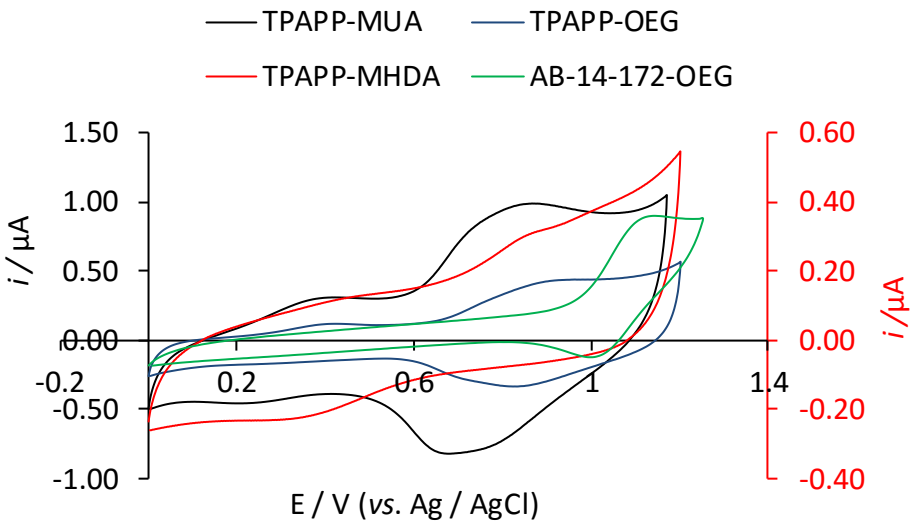


**Figure 3.** Cyclic voltammograms of SAMs of TPAPP-MUA (**Black**), TPAPP-MHDA (**Red**), TPAPP-OEG (**Blue**) and AB-14-172 (**Green**) deposited at Au. Electrochemical Setup: *Working Electrode*: SAM. *Reference Electrode*: Ag / AgCl. *Auxiliary Electrode*: Pt wire. *Electrolytic Solution*: 0.1 M $TBAPF_6$ (anhydrous, deoxygenated ($N_2$ (g), 10 min.) $CH_2Cl_2$, 298 K). *Scan Rate:* 1000 mV / s.

## 8.1.3 – Characterisation of Biphasic, Porphyrin-Appended SAMs

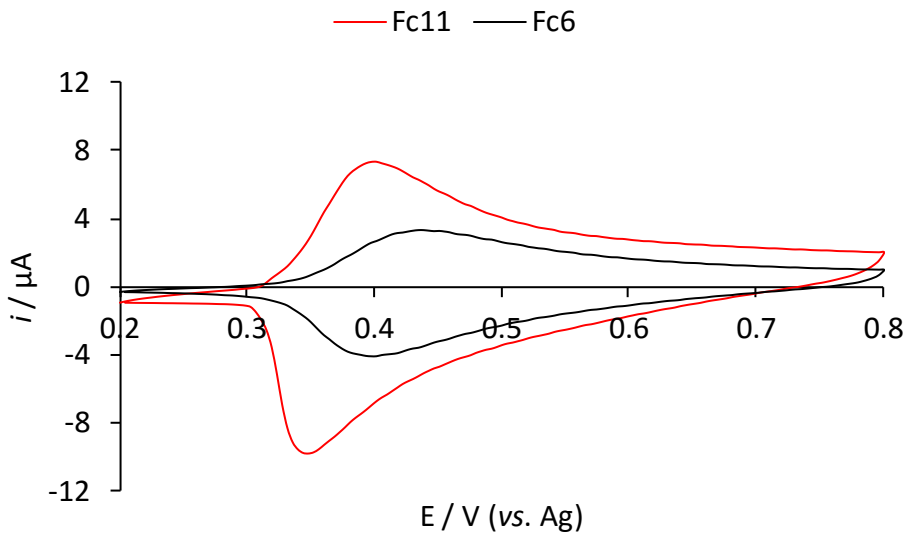


**Figure 4.** Cyclic voltammograms of SAMs of Fc6 (**Black**) and Fc11 (**Red**) deposited at Au. Fc11: $Fc(CH_2)_{11}SH$. Fc6: $Fc(CH_2)_6SH$. Electrochemical Setup: *Working Electrode*: SAM. *Reference Electrode*: Ag Wire. *Auxiliary Electrode*: Pt wire. *Electrolytic Solution*: 0.1 M $TBAPF_6$ (anhydrous, deoxygenated ($N_2$ (g), 10 min.) $CH_2Cl_2$, 298 K). *Scan Rate:* 1000 mV / s.

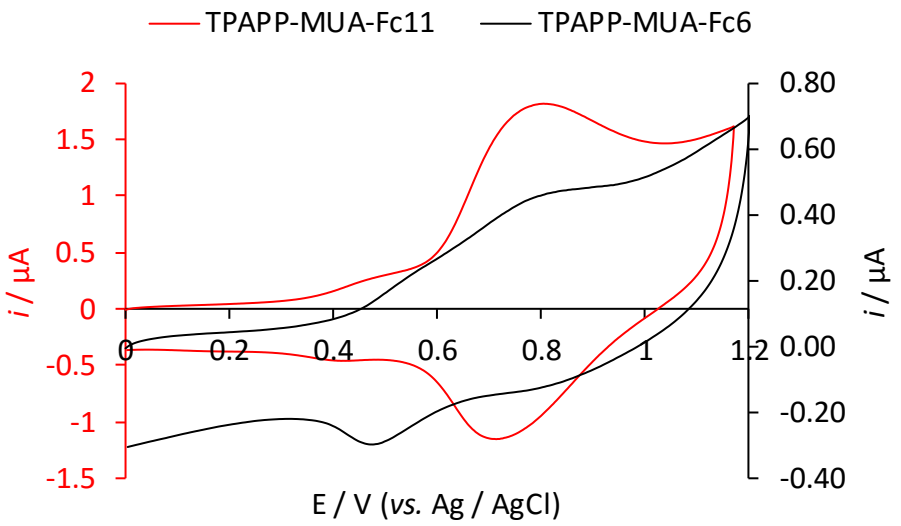


**Figure 5.** Cyclic voltammograms of SAMs of TPAPP-MUA-Fc6 (**Black**) and TPAPP-MUA-Fc11 (**Red**) deposited at Au. Fc11: $Fc(CH_2)_{11}SH$. Fc6: $Fc(CH_2)_6SH$. Electrochemical Setup: *Working Electrode*: SAM. *Reference Electrode*: Ag Wire. *Auxiliary Electrode*: Pt wire. *Electrolytic Solution*: 0.1 M $TBAPF_6$ (anhydrous, deoxygenated ($N_2$ (g), 10 min.) $CH_2Cl_2$, 298 K). *Scan Rate:* 1000 mV / s.

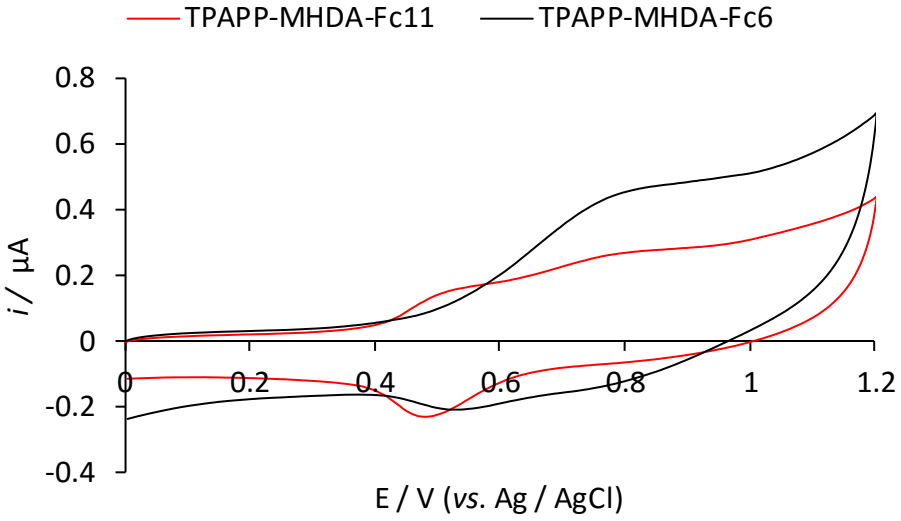


**Figure 6.** Cyclic voltammograms of SAMs of TPAPP-MHDA-Fc6 (**Black**) and TPAPP-MHDA-Fc11 (**Red**) deposited at Au. Fc11: $Fc(CH_2)_{11}SH$. Fc6: $Fc(CH_2)_6SH$. Electrochemical Setup: *Working Electrode*: SAM. *Reference Electrode*: Ag Wire. *Auxiliary Electrode*: Pt wire. *Electrolytic Solution*: 0.1 M $TBAPF_6$ (anhydrous, deoxygenated ($N_2$ (g), 10 min.) $CH_2Cl_2$, 298 K). *Scan Rate:* 1000 mV / s.

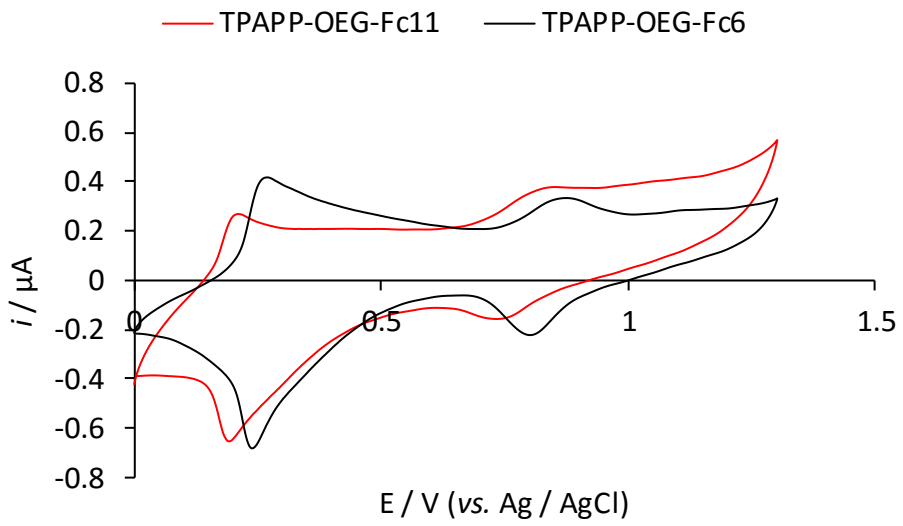


**Figure 7.** Cyclic voltammograms of SAMs of TPAPP-OEG-Fc6 (**Black**) and TPAPP-OEG-Fc11 (**Red**) deposited at Au. Fc11: $Fc(CH_2)_{11}SH$. Fc6: $Fc(CH_2)_6SH$. Electrochemical Setup: *Working Electrode*: SAM. *Reference Electrode*: Ag Wire. *Auxiliary Electrode*: Pt wire. *Electrolytic Solution*: 0.1 M $TBAPF_6$ (anhydrous, deoxygenated ($N_2$ (g), 10 min.) $CH_2Cl_2$, 298 K). *Scan Rate:* 1000 mV / s.

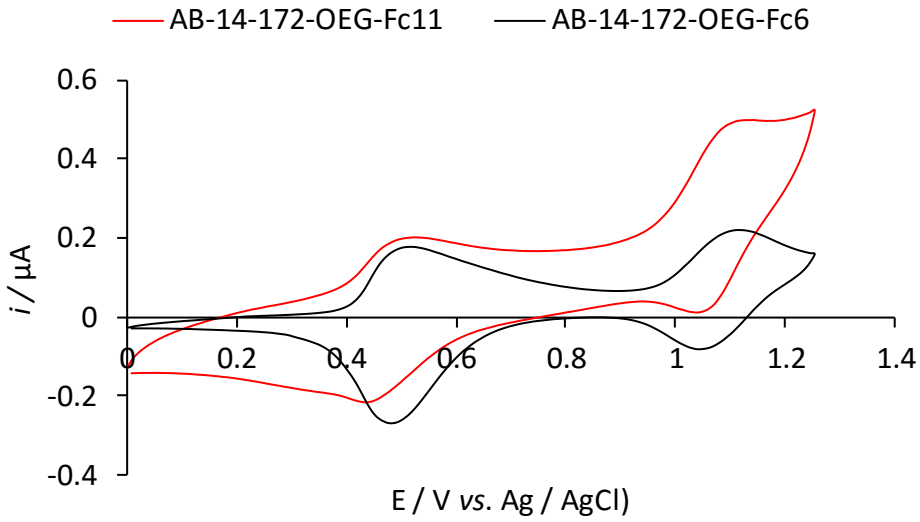


**Figure 8.** Cyclic voltammograms of SAMs of AB-14-172-OEG-Fc6 (**Black**) and AB-14-172-OEG-Fc11 (**Red**) deposited at Au. Fc11: $Fc(CH_2)_{11}SH$. Fc6: $Fc(CH_2)_6SH$. Electrochemical Setup: *Working Electrode*: SAM. *Reference Electrode*: Ag Wire. *Auxiliary Electrode*: Pt wire. *Electrolytic Solution*: 0.1 M $TBAPF_6$ (anhydrous, deoxygenated ($N_2$ (g), 10 min.) $CH_2Cl_2$, 298 K). *Scan Rate:* 1000 mV / s.

| **Underlying Biphasic Monolayer** | **Porphyrin Derivative** | **Fc / $Fc^+$ []** ($\times 10^{-10}$ mol $cm^{-2}$) (% of Pure Monolayer of $Fc(CH_2)_6SH$ or $Fc(CH_2)_{11}SH$) | **$P^0$ / $P^{+1}$ []** ($\times 10^{-10}$ mol $cm^{-2}$) (% of Pure Monolayer of TPAPP or AB-14-172) |
|---|---|---|---|
| MUA – $Fc(CH_2)_6SH$ | TPAPP | 0.80 ± 0.05 (21 %) | 0.52 ± 0.08 (8.3 %) |
| MUA – $Fc(CH_2)_{11}SH$ | TPAPP | 1.7 ± 0.60 (43 %) | 0.24 ± 0.03 (3.8 %) |
| MHDA – $Fc(CH_2)_6SH$ | TPAPP | 0.91 ± 0.04 (24 %) | 0.45 ± 0.06 (7.1 %) |
| MHDA – $Fc(CH_2)_{11}SH$ | TPAPP | 1.7 ± 0.50 (43 %) | 0.26 ± 0.04 (4.1 %) |
| OEG – $Fc(CH_2)_6SH$ | TPAPP | 0.87 ± 0.04 (23 %) | 0.49 ± 0.06 (7.7 %) |
| | AB-14-172 | 0.88 ± 0.06 (23 %) | 0.31 ± 0.03 (68 %) |
| OEG – $Fc(CH_2)_{11}SH$ | TPAPP | 1.4 ± 0.40 (35 %) | 0.27 ± 0.04 (4.3 %) |
| | AB-14-172 | 1.3 ± 0.30 (33 %) | 0.28 ± 0.04 (62 %) |
| $Fc(CH_2)_6SH$ | N / A | 3.8 ± 1.20 (*3.8 ± 1.0) | N / A |
| $Fc(CH_2)_{11}SH$ | N / A | 4.0 ± 1.02 (*5.5 ± 1.0) | N / A |

**Table 1.** Concentration of Fc / $Fc^+$ and $P^0$ / $P^{+1}$ at biphasic, porphyrin-appended monolayers deposited at Au. All concentrations determined by cyclic voltammetry, and each error bar is equivalent to 3SD and calculated from the data acquired across five separately prepared electrodes. Electrochemical Setup: *Working Electrode*: Respective SAM. *Reference Electrode*: Ag / AgCl. *Auxiliary Electrode*: Pt wire. *Electrolytic Solution*: 0.1 M $TBAPF_6$ (anhydrous, deoxygenated ($N_2$ (g), 10 min.) $CH_2Cl_2$, 298 K). *Scan Rate:* 1000 mV / s.

## 8.2 – Characterisation of Porphyrin-Appended SAMs by XPS

| Element | Relative Sensitivity Factor |
|---|---|
| Au ($4f_{7/2}$ and $4f_{5/2}$) | 17.1 |
| O (1s) | 2.93 |
| C (1s) | 1 |
| S ($2p_{3/2}$ $2p_{1/2}$) | 1.68 |
| N (1s) | 1.8 |
| Ni ($2p_{3/2}$) | 14.6 |

**Table 2.** XPS atomic sensitivity factors[1].

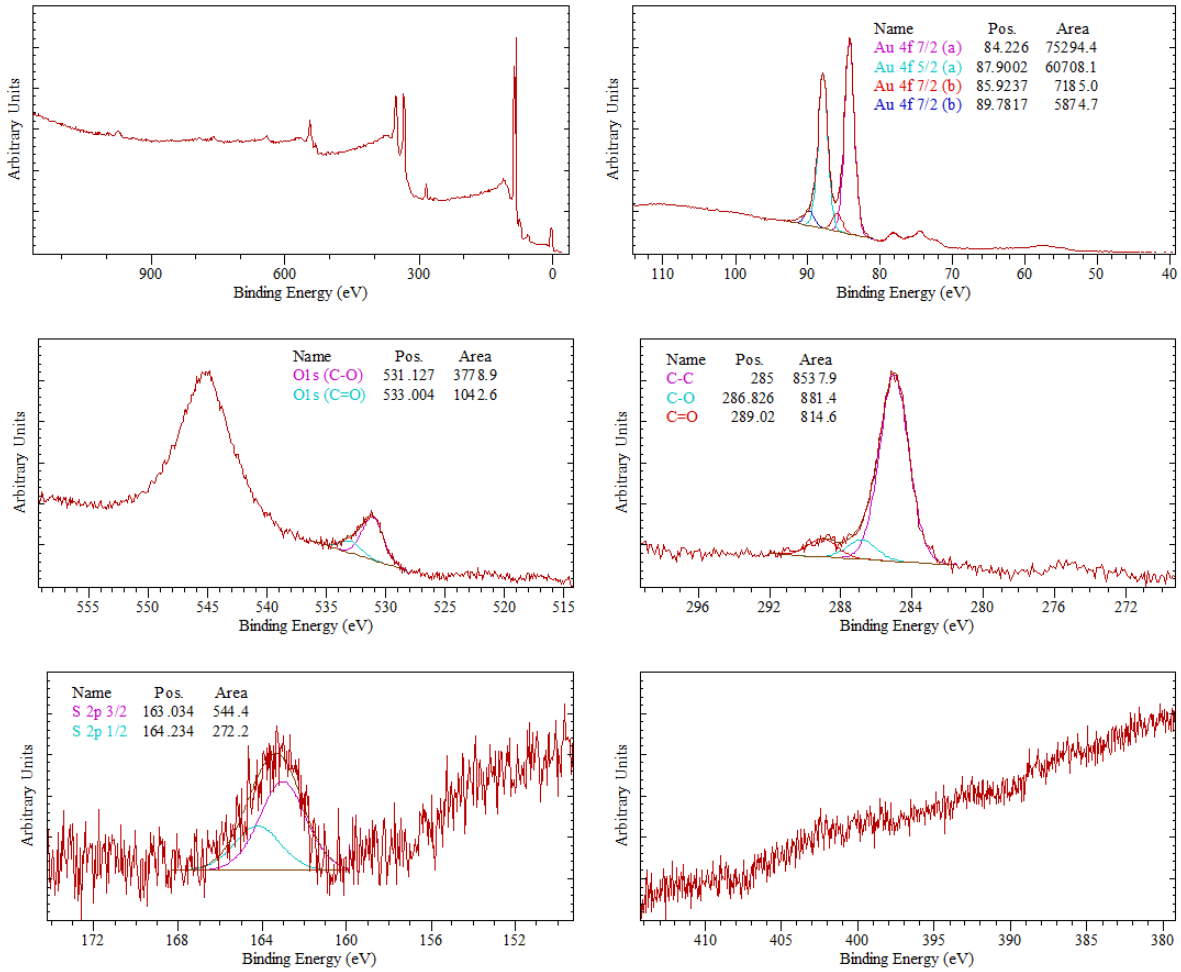


**Figure 9.** XPS spectrum (**Top Left**) of a SAM of MUA deposited at Au. Narrow scan spectra were recorded in the Au 4f (**Top Right**), O 1s (**Middle Left**), C 1s (**Middle Right**), S 2p (**Bottom Left**) and N 1s (**Bottom Right**) regions, and the relative % of each element present at the surface calculated (**Table 3**).

| Element | Normalised Peak Area | Relative % |
|---|---|---|
| **Au** | 8717.1 | 41.3 |
| **O** | 1645.6 | 7.8 |
| **C** | 10233.9 | 48.5 |
| **S** | 486.1 | 2.3 |
| Total | 21082.7 | |

**Table 3.** The relative % of Au, O, C, S, and N observed at a SAM of MUA deposited at Au. No N was observed in either the survey (**Figure 9, Top Left**) or narrow scan (**Figure 9, Bottom Right**) spectra, as was expected in the absence of either TPAPP or AB-14-172.

The relative % of each element at the interface was calculated as follows:

**Step 1.** Normalisation of individual peak area; total elemental peak area / atomic sensitivity factor (**Table 2**).

For example, in **Figure 9**, the normalised peak area for Au is 8717.1 au. ((75294.4 + 60708.1 + 7185.0 + 5874.7) / 17.1).

**Step 2.** The normalised peak area of each element is then divided by the total normalised area and multiplied by 100.

For example, the relative % of Au at a SAM of MUA, **Figure 9**, is (8717.1 / (8717.1 + 1645.6 + 10233.9 + 486.1)), or 41.3 %.

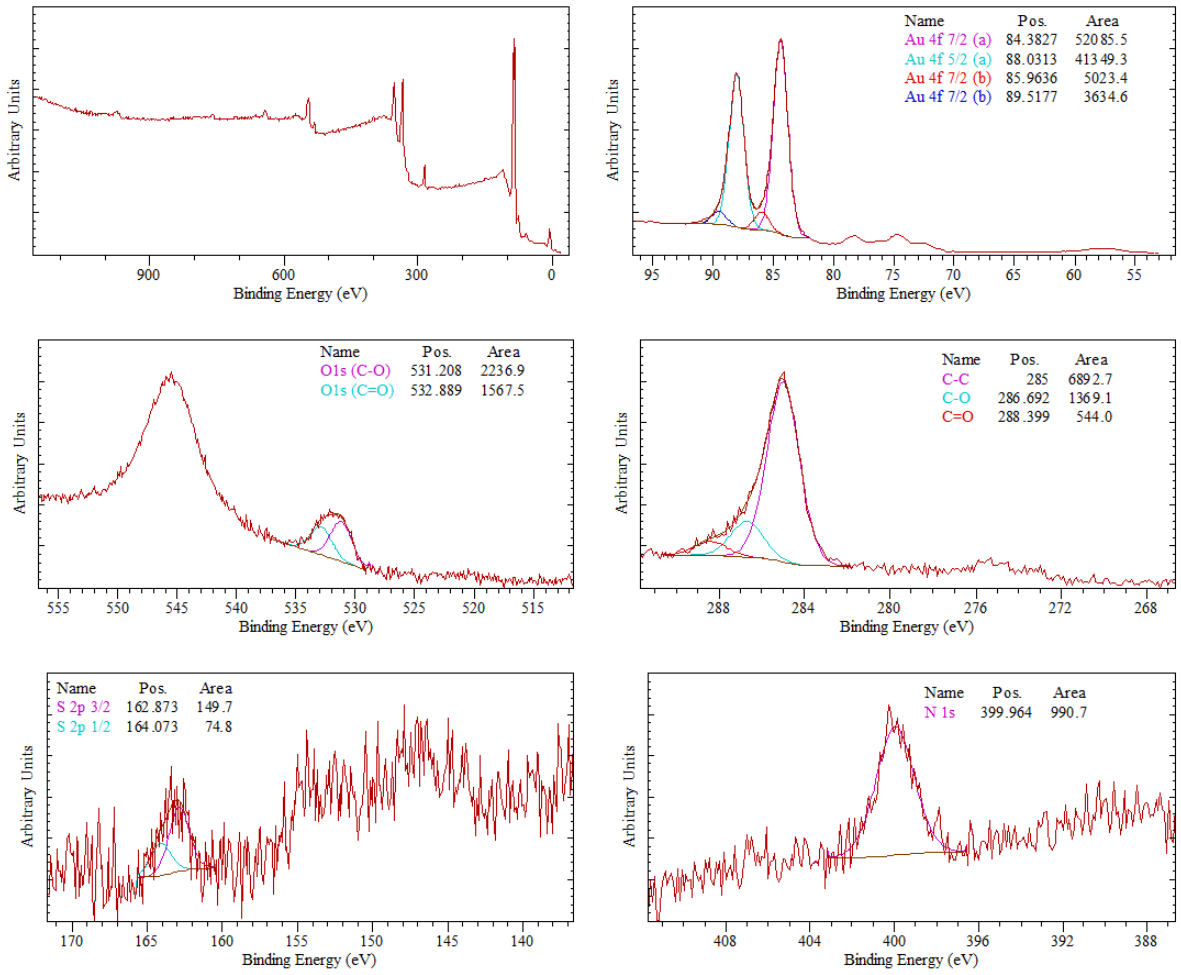


**Figure 10.** XPS spectrum (**Top Left**) of the SAM obtained upon covalent attachment of TPAPP to MUA deposited at Au. Narrow scan spectra were recorded in the Au 4f (**Top Right**), O 1s (**Middle Left**), C 1s (**Middle Right**), S 2p (**Bottom Left**) and N 1s (**Bottom Right**) regions, and the relative % of each element present at the surface calculated (**Table 4**).

| Element | Normalised Peak Area | Relative % |
|---|---|---|
| **Au** | 5970.3 | 35.6 |
| **O** | 1298.4 | 7.7 |
| **C** | 8805.8 | 52.5 |
| **S** | 133.6 | 0.8 |
| **N** | 550.4 | 3.3 |
| Total | 16758.5 | |

| | | | | |
|---|---|---|---|---|
| **Theoretical** | N | 1 | C | 6.9 |
| **Measured** | N | 1 | C | 16.0 |

**Table 4.** The relative % of Au, O, C, S, and N observed at a SAM of TPAPP-MUA.

The theoretical and experimental N:C ratio for all molecular systems was calculated as follows:

Theoretical

Chemical Formula (Calculated in ChemDraw Professional 15.0):

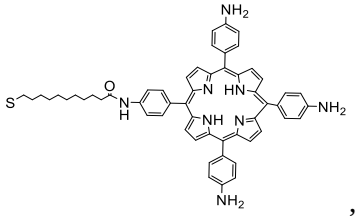


, $C_{55}H_{53}N_8OS$-Au

Theoretical N:C ratio: 55 / 8 = 1 : 6.9

Experimental

Normalised Peak Area of C / Normalised Peak Area of N = (8805.8 / 550.4)

Experimental N:C ratio: 1 : 16.0

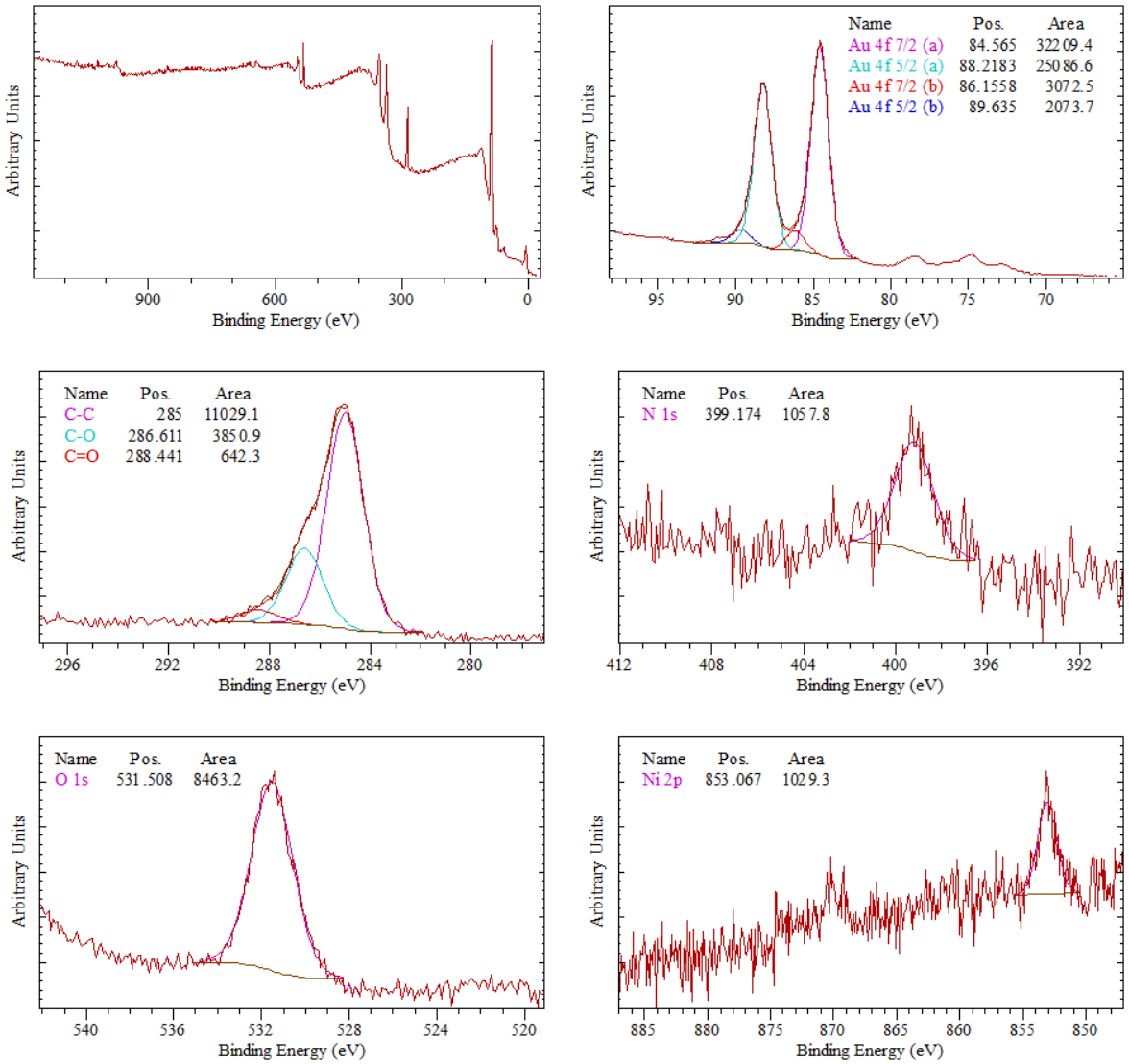


**Figure 11.** XPS spectrum (**Top Left**) of the SAM obtained upon covalent attachment of AB-14-172 to OEG deposited at Au. Narrow scan spectra were recorded in the Au 4f (**Top Right**), C 1s (**Middle Left**), N 1s (**Middle Right**), O 1s (**Bottom Left**) and Ni 2p (**Bottom Right**) regions, and the relative % of each element present at the surface calculated (**Table 5**).

| Element | Normalised Peak Area | Relative % |
|---|---|---|
| **Au** | 3651.6 | 16.1 |
| **O** | 2888.5 | 12.7 |
| **C** | 15522.3 | 68.3 |
| **N** | 587.7 | 2.6 |
| **Ni** | 70.5 | 0.3 |
| Total | 22720.6 | 100.0 |

| | | | | |
|---|---|---|---|---|
| **Theoretical** | N | 1 | C | 12.9 |
| **Measured** | N | 1 | C | 26.4 |

**Table 5.** The relative % of Au, C, N, O, and Ni observed at a SAM of AB-14-172-OEG.

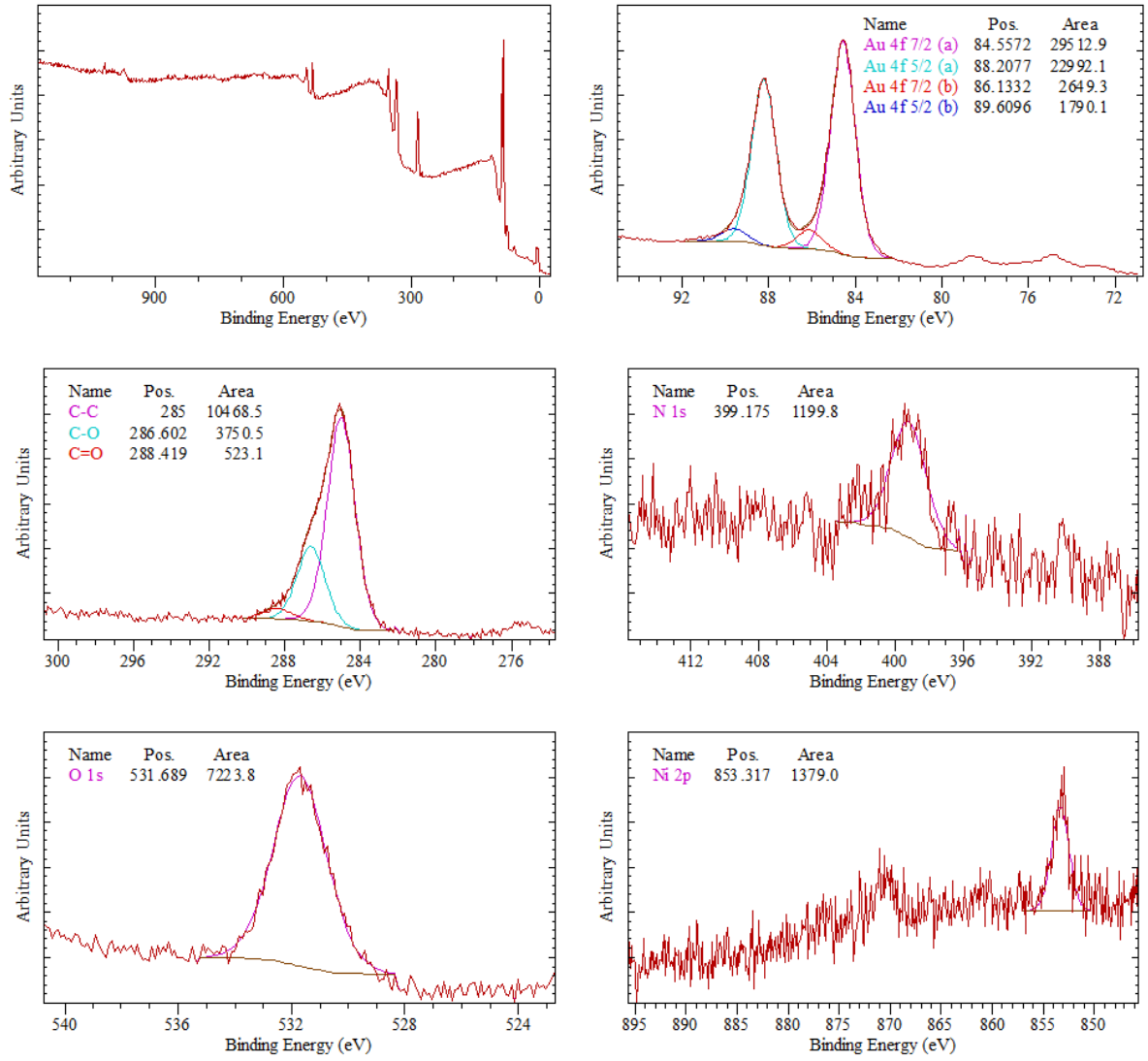


**Figure 12.** XPS spectrum (**Top Left**) of the SAM obtained upon covalent attachment of AB-14-172 to OEG deposited at Au. Narrow scan spectra were recorded in the Au 4f (**Top Right**), C 1s (**Middle Left**), N 1s (**Middle Right**), O 1s (**Bottom Left**) and Ni 2p (**Bottom Right**) regions, and the relative % of each element present at the surface calculated (**Table 6**).

| Element | Normalised Peak Area | Relative % |
|---|---|---|
| **Au** | 3330.1 | 14.7 |
| **O** | 2465.5 | 10.9 |
| **C** | 14742.1 | 64.9 |
| **N** | 666.6 | 2.9 |
| **Ni** | 94.5 | 0.4 |
| Total | 21298.8 | 93.7 |

| | | | | |
|---|---|---|---|---|
| **Theoretical** | N | 1 | C | 12.9 |
| **Measured** | N | 1 | C | 22.1 |

**Table 6.** The relative % of Au, C, N, O, and Ni observed at a SAM of AB-14-172-OEG.

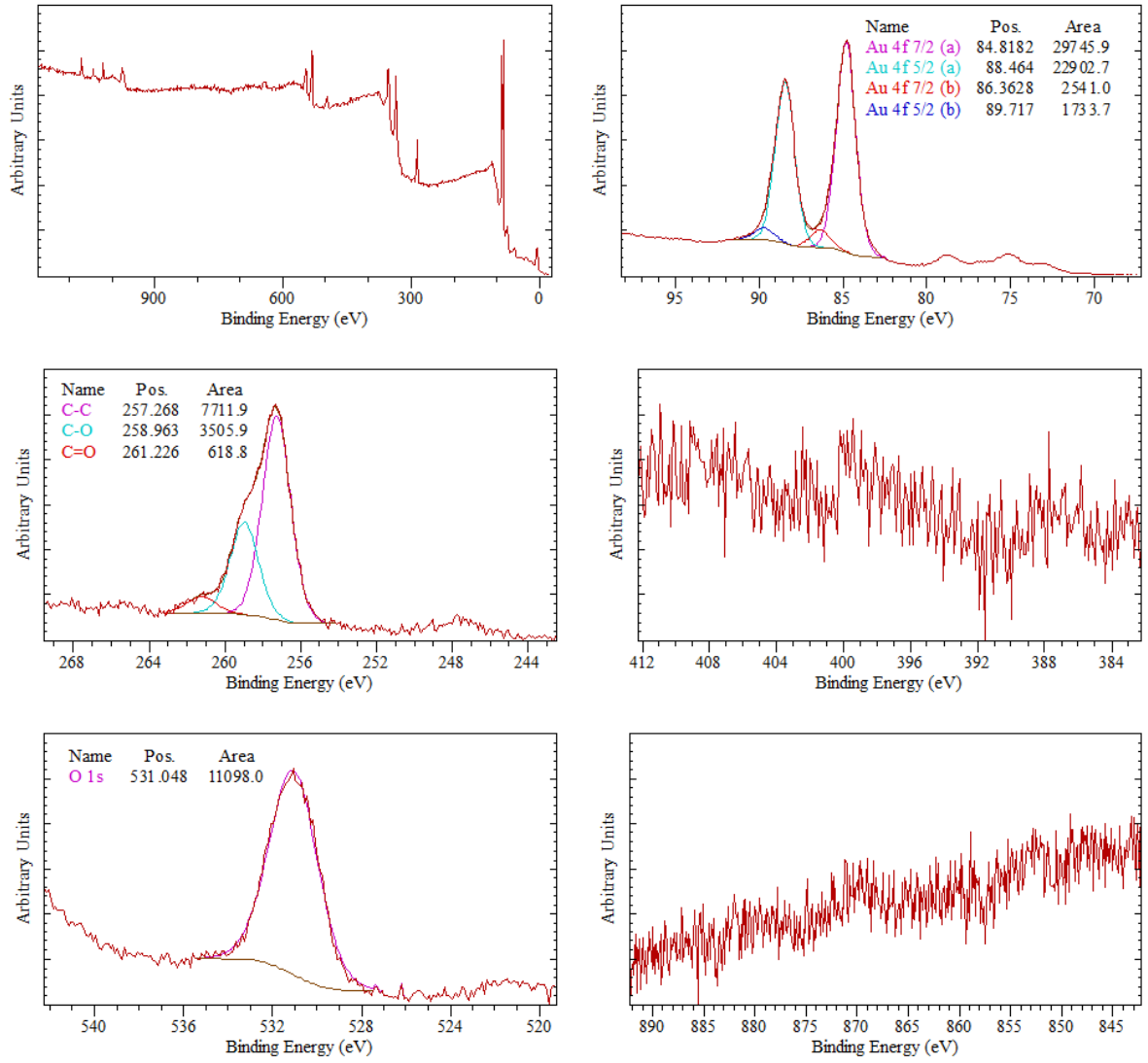


**Figure 13.** XPS spectrum (**Top Left**) of the SAM obtained upon the attempted covalent attachment of AB-14-172 to an unactivated (No EDC / NHS was used) SAM of OEG deposited at Au. Narrow scan spectra were recorded in the Au 4f (**Top Right**), C 1s (**Middle Left**), N 1s (**Middle Right**), O 1s (**Bottom Left**) and Ni 2p (**Bottom Right**) regions, and the relative % of each element present at the surface calculated (**Table 7**).

| Element | Normalised Peak Area | Relative % |
|---|---|---|
| **Au** | 3328.8 | 14.7 |
| **O** | 3787.7 | 16.7 |
| **C** | 11836.6 | 52.1 |
| Total | 18953.1 | |

**Table 7.** The relative % of Au, C, N, O, and Ni observed at a SAM of OEG following exposure to AB-14-172 in the absence of EDC / NHS. No N or Ni was observed in either the survey (**Figure 13, Top Left**) or narrow scan (**Figure 13, Middle and Bottom Right)** spectra, as was expected in the absence of the coupling reagents.

## 8.3 – Photocurrent Density Measurements at Porphyrin-Appended SAMs

### 8.3.1 – Photoelectrochemical Analysis of Monophasic, Porphyrin-Appended SAMs

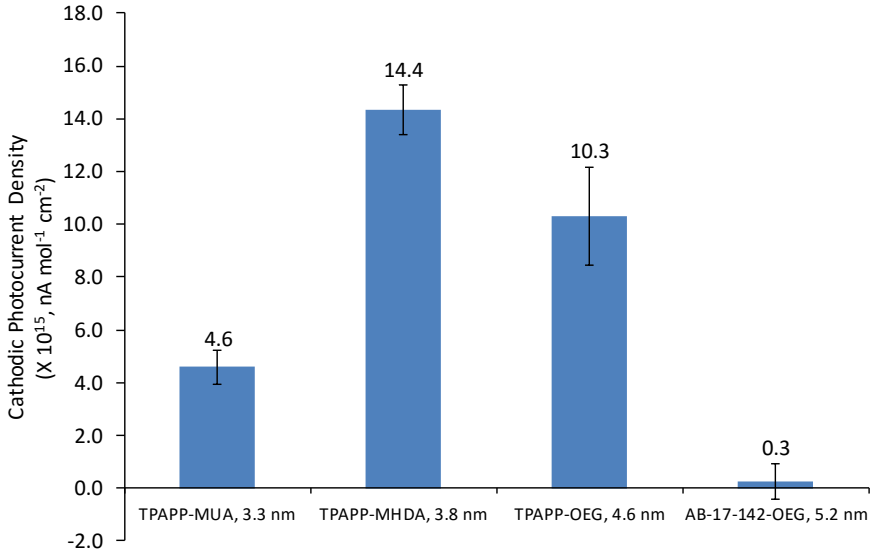

| | ***Experiment 1*** | | ***Experiment 2*** | | ***Experiment 3*** | | ***Experiment 4*** | | ***Average*** | |
|---|---|---|---|---|---|---|---|---|---|---|
| | *Cathodic Photocurrent Density, nA mol$^{-1}$ cm$^{-2}$* | | | | | | | | | *Associated Error* |
| | | x10$^{15}$ | | x10$^{15}$ | | x10$^{15}$ | | x10$^{15}$ | **x10$^{15}$** | SD | 3SD |
| *TPAPP-MUA, 3.3 nm* | 4.37E+15 | 4.37 | 4.56E+15 | 4.56 | 4.87E+15 | 4.87 | 4.51E+15 | 4.51 | **4.6** | 0.21 | 0.63 |
| *TPAPP-MHDA, 3.8 nm* | 1.42E+16 | 14.20 | 1.45E+16 | 14.50 | 1.40E+16 | 14.00 | 1.47E+16 | 14.70 | **14.4** | 0.31 | 0.93 |
| *TPAPP-OEG, 4.6 nm* | 1.10E+16 | 11.00 | 1.04E+16 | 10.40 | 9.50E+15 | 9.50 | 1.04E+16 | 10.40 | **10.3** | 0.62 | 1.86 |
| *AB-17-142-OEG, 5.2 nm* | 8.49E+13 | 0.08 | 5.63E+14 | 0.56 | 1.04E+14 | 0.10 | 2.58E+14 | 0.26 | **0.3** | 0.22 | 0.66 |

**Figure 14.** Cathodic photocurrent densities acquired at monophasic, porphyrin-appended SAMs formed at Au. All cathodic photocurrents were measured in 0.1 M $Na_2SO_4$ (aq.) containing 5 mM $MV^{2+}$ as an electron acceptor. The electrodes were kept at – 100 mV (*vs.* Ag / AgCl), illuminated with light of wavelength 430 ± 5 nm and the photocurrents normalised for the concentration of porphyrin present at each interface, as determined by cyclic voltammetry (**Appendix, 8.1.2**). Each error bar is equivalent to 3SD and calculated from the data acquired across four separately prepared electrodes. All porphyrin-Au spatial separations were previously determined by ellipsometry (**Table 2**).

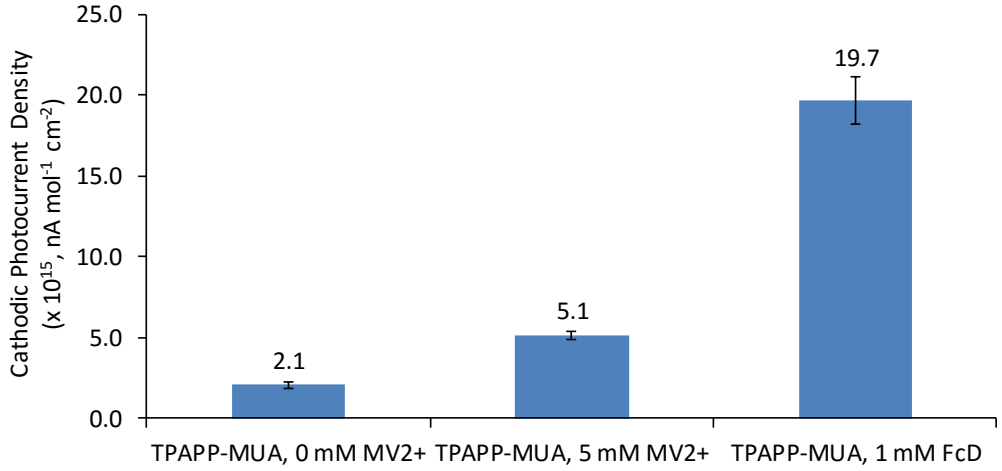


| | ***Experiment 1*** | | ***Experiment 2*** | | ***Experiment 3*** | | ***Average*** | | |
|---|---|---|---|---|---|---|---|---|---|
| | *Cathodic Photocurrent Density, nA mol$^{-1}$ cm$^{-2}$* | | | | | | | *Associated Error* | |
| | | x10$^{15}$ | | x10$^{15}$ | | x10$^{15}$ | **x10$^{15}$** | SD | 3SD |
| *TPAPP-MUA, 0 mM MV$^{2+}$* | 2.08E+15 | 2.08 | 2.15E+15 | 2.15 | 2.00E+15 | 2.00 | **2.1** | 0.08 | 0.23 |
| *TPAPP-MUA, 5 mM MV$^{2+}$* | 5.08E+15 | 5.08 | 5.12E+15 | 5.12 | 5.22E+15 | 5.22 | **5.1** | 0.07 | 0.22 |
| *TPAPP-MUA, 1 mM FcD* | 2.02E+16 | 20.20 | 1.97E+16 | 19.70 | 1.92E+16 | 19.20 | **19.7** | 0.50 | 1.50 |

**Figure 15.** Cathodic photocurrent densities acquired at a SAM of TPAPP-MUA deposited at Au, prior to and following the additions of 5 mM $MV^{2+}$ and 1 mM FcD ($FcCH_2NMe_3^+$) to the electrolytic solution. All cathodic photocurrents were measured in 0.1 M $Na_2SO_4$ (aq.) whilst the electrodes were kept at – 100 mV (*vs.* Ag / AgCl), illuminated with light of wavelength 430 ± 5 nm and the photocurrents normalised for the concentration of porphyrin present at the interface, as determined by cyclic voltammetry (**Appendix, 8.1.2**). Each error bar is equivalent to 3SD and calculated from the data acquired across four separately prepared electrodes. Electrochemical Cell Setup: *Working Electrode*: TPAPP-MUA. *Reference Electrode*: Ag / AgCl. *Auxiliary Electrode*: Pt Wire. *Electrolytic Solution*: 0.1 M $Na_2SO_4$, (+ 5 mM $MV^{2+}$, + 1 mM FcD ($FcCH_2NMe_3^+$)). *Solvent*: $H_2O$. *Bias Potential*: - 100 mV. $\lambda_{irr}$: 430 ± 5 nm.

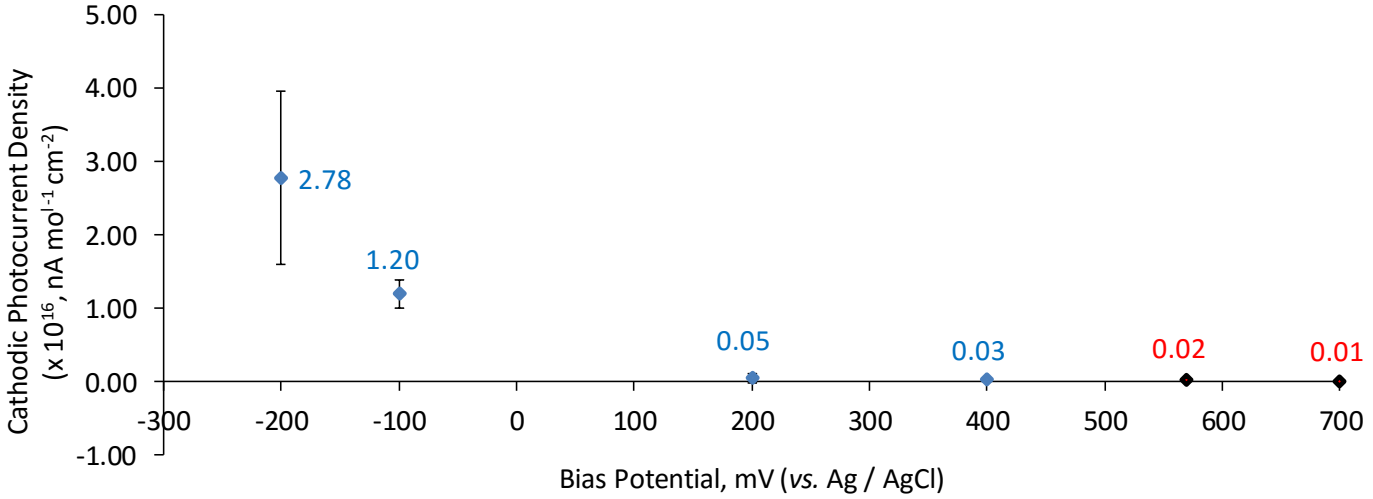
5.00
4.00
3.00
2.00
1.00
0.00
-1.00
Cathodic Photocurrent Density
(x 10^16, nA mo^-1 cm^-2)
2.78
1.20
0.05
0.03
0.02
0.01
-300
-200
-100
0
100
200
300
400
500
600
700
Bias Potential, mV (vs. Ag / AgCl)

| | ***Experiment 1*** | | ***Experiment 2*** | | ***Experiment 3*** | | ***Experiment 4*** | | ***Average*** | Associated Error | |
|---|---|---|---|---|---|---|---|---|---|---|---|
| | *Cathodic Photocurrent Density, nA mol$^{-1}$ cm$^{-2}$* | | | | | | | | | | |
| | | x10$^{16}$ | | x10$^{16}$ | | x10$^{16}$ | | x10$^{15}$ | **x10$^{15}$** | SD | 3SD |
| *-200* | 2.30E+16 | 2.30 | 2.65E+16 | 2.65 | 2.97E+16 | 2.97 | 3.20E+16 | 3.20 | **2.78** | 0.39 | 1.17 |
| *-100* | 1.17E+16 | 1.17 | 1.26E+16 | 1.26 | 1.25E+16 | 1.25 | 1.13E+16 | 1.13 | **1.20** | 0.06 | 0.19 |
| *200* | 2.00E+14 | 0.02 | 7.41E+14 | 0.07 | 3.98E+14 | 0.04 | 6.38E+14 | 0.06 | **0.05** | 0.02 | 0.07 |
| *400* | 2.91E+14 | 0.03 | 2.06E+14 | 0.02 | 4.06E+14 | 0.04 | 3.58E+14 | 0.04 | **0.03** | 0.01 | 0.03 |
| *570* | 1.98E+14 | 0.02 | 1.78E+14 | 0.02 | 2.52E+14 | 0.03 | N / A | | **0.02** | 0.00 | 0.01 |
| *700* | 1.16E+14 | 0.01 | 1.94E+14 | 0.02 | 1.85E+14 | 0.02 | 1.01E+14 | 0.01 | **0.01** | 0.00 | 0.01 |

**Figure 16.** Manipulating the cathodic photocurrent density acquired at a SAM of TPAPP-MUA deposited at Au by varying the bias potential of the working electrode. All cathodic photocurrents were measured in 0.1 M $Na_2SO_4$ (aq.) containing 5 mM $MV^{2+}$ as an electron acceptor. The electrodes were illuminated with light of wavelength 430 ± 5 nm and the photocurrents normalised for the concentration of porphyrin present at the interface, as determined by cyclic voltammetry (**Appendix, 8.1.2**). Each error bar is equivalent to 3SD and calculated from the data acquired across four separately prepared electrodes. Electrochemical Cell Setup: *Working Electrode*: TPAPP-MHDA. *Reference Electrode*: Ag / AgCl. *Auxiliary Electrode*: Pt Wire. *Electrolytic Solution*: 0.1 M $Na_2SO_4$, + 5 mM $MV^{2+}$, + 1 mM $FcCH_2NMe_3^+$. *Solvent*: $H_2O$. *Bias Potential*: Variable. $\lambda_{irr}$: 430 ± 5 nm.

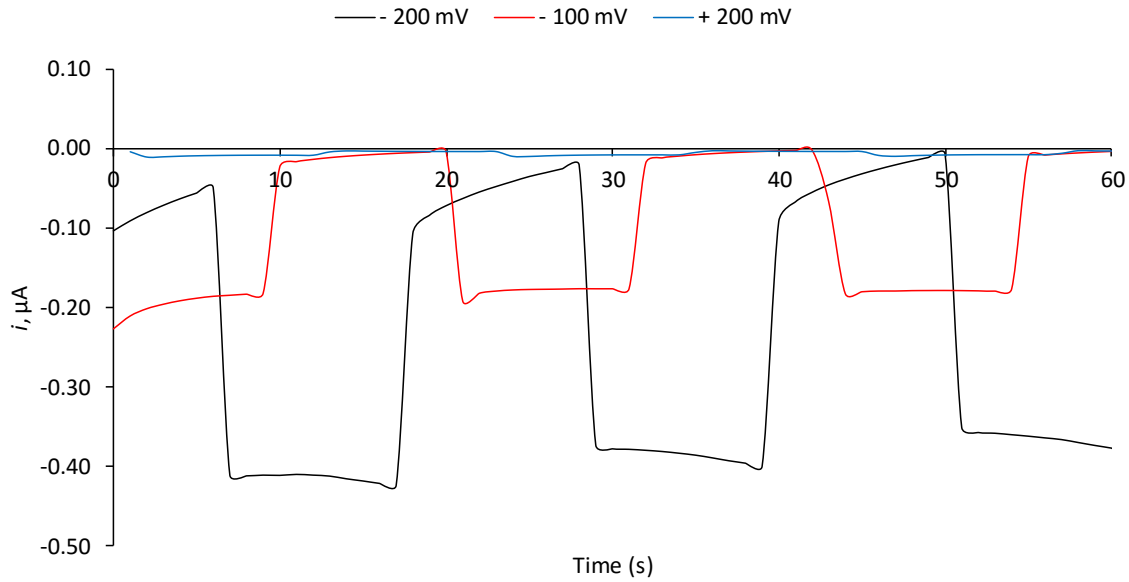


**Figure 17.** Current *vs.* time profiles for a Au electrode at which a SAM of TPAPP-MUA had been deposited. The electrode was kept at either + 200 mV (**Blue**), – 100 mV (**Red**) or – 200 mV (**Black**) and illuminated with light of wavelength 430 ± 5 nm. Electrochemical Cell Setup: *Working Electrode*: TPAPP-MHDA. *Reference Electrode*: Ag / AgCl. *Auxiliary Electrode*: Pt Wire. *Electrolytic Solution*: 0.1 M $Na_2SO_4$, + 5 mM $MV^{2+}$, + 1 mM $FcCH_2NMe_3^+$. *Solvent*: $H_2O$. *Bias Potential*: Variable. The differences in current (dark ('OFF') and light ('ON')) observed (**Table 8**) were used to quantify the photoelectrochemical outputs.

| | Photocurrent, μA | | |
|---|---|---|---|
| | 'OFF' | 'ON' | Difference |
| -200 mV | -0.05 | -0.42 | 0.370 |
| -100 mV | -0.005 | -0.18 | 0.175 |
| 200 mV | -0.004 | -0.008 | 0.004 |

**Table 8.** Gating the magnitude of the photoelectrochemical response observed upon illuminating a SAM of TPAPP-MUA by varying the bias potential of the working electrode. The difference, in conjunction with the concentration of porphyrin present at the interface, as obtained by cyclic voltammetry (**Appendix, 8.1.2**), was used to normalise each photoelectrochemical response. An increase in negative bias resulted in greater cathodic photocurrent densities being generated.

**8.3.2 – Photoelectrochemical Analysis of Biphasic, Porphyrin-Appended SAMs**

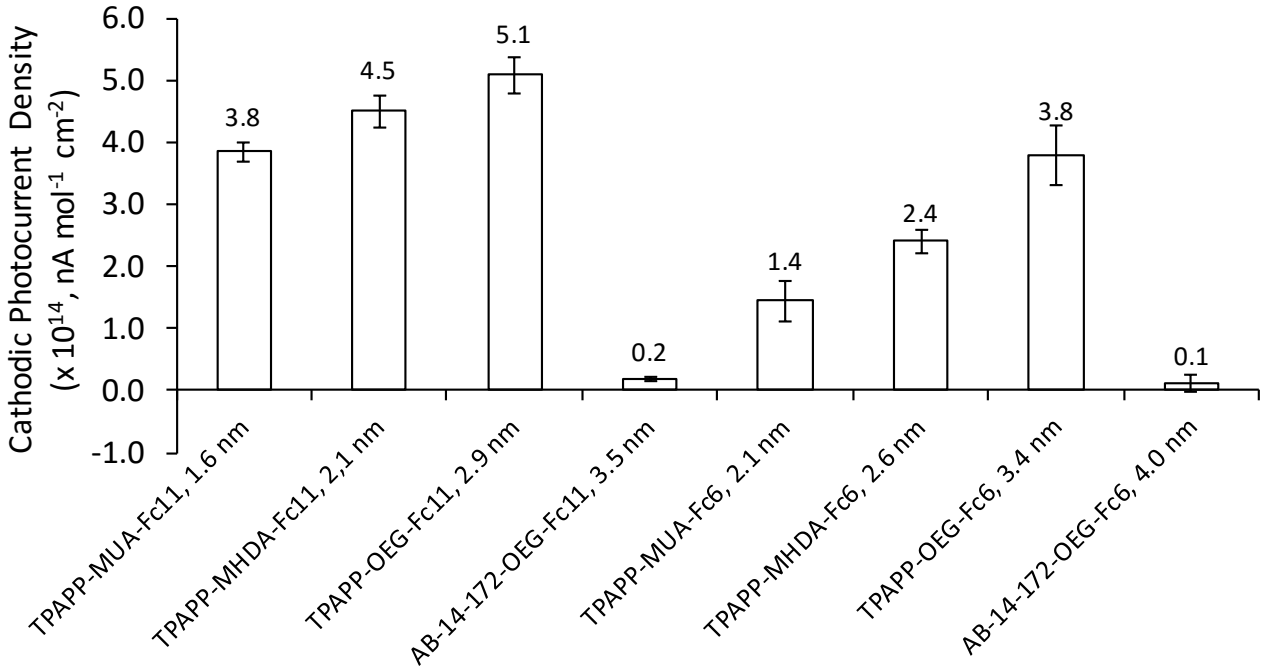

| | ***Experiment 1*** | | ***Experiment 2*** | | ***Experiment 3*** | | ***Average*** | | |
|---|---|---|---|---|---|---|---|---|---|
| | Cathodic Photocurrent Density, nA $mol^{-1}$ $cm^{-2}$ | | | | | | | Associated Error | |
| | | $x10^{14}$ | | $x10^{14}$ | | $x10^{14}$ | **$x10^{14}$** | SD | 3SD |
| TPAPP-MUA-Fc11, 1.6 nm | 3.90E+14 | 3.90 | 3.80E+14 | 3.80 | 3.84E+14 | 3.84 | **3.8** | 0.05 | 0.15 |
| TPAPP-MHDA-Fc11, 2,1 nm | 4.60E+14 | 4.60 | 4.50E+14 | 4.50 | 4.43E+14 | 4.43 | **4.5** | 0.09 | 0.26 |
| TPAPP-OEG-Fc11, 2.9 nm | 5.10E+14 | 5.10 | 4.99E+14 | 4.99 | 5.18E+14 | 5.18 | **5.1** | 0.10 | 0.29 |
| AB-14-172-OEG-Fc11, 3.5 nm | 1.76E+13 | 0.18 | 1.93E+13 | 0.19 | 1.79E+13 | 0.18 | **0.2** | 0.01 | 0.03 |
| TPAPP-MUA-Fc6, 2.1 nm | 1.43E+14 | 1.43 | 1.56E+14 | 1.56 | 1.35E+14 | 1.35 | **1.4** | 0.11 | 0.32 |
| TPAPP-MHDA-Fc6, 2.6 nm | 2.39E+14 | 2.39 | 2.48E+14 | 2.48 | 2.35E+14 | 2.35 | **2.4** | 0.07 | 0.20 |
| TPAPP-OEG-Fc6, 3.4 nm | 3.80E+14 | 3.80 | 3.65E+14 | 3.65 | 3.97E+14 | 3.97 | **3.8** | 0.16 | 0.48 |
| AB-14-172-OEG-Fc6, 4.0 nm | 1.20E+13 | 0.12 | 6.50E+12 | 0.07 | 1.52E+13 | 0.15 | **0.1** | 0.04 | 0.13 |

**Figure 18.** Cathodic photocurrent densities acquired at biphasic, porphyrin-appended SAMs deposited at Au. All cathodic photocurrents were measured in 0.1 M $Na_2SO_4$ (aq.) containing 5 mM $MV^{2+}$ as an electron acceptor. Fc11: $Fc(CH_2)_{11}SH$. Fc6: $Fc(CH_2)_6SH$. The electrodes were kept at – 100 mV (*vs.* Ag / AgCl), illuminated with light of wavelength 430 ± 5 nm and the photocurrents normalised for the concentration of porphyrin present at each interface, as determined by cyclic voltammetry (**Appendix, 8.1.3**). Each error bar is equivalent to 3SD and calculated from the data acquired across three separately prepared electrodes.

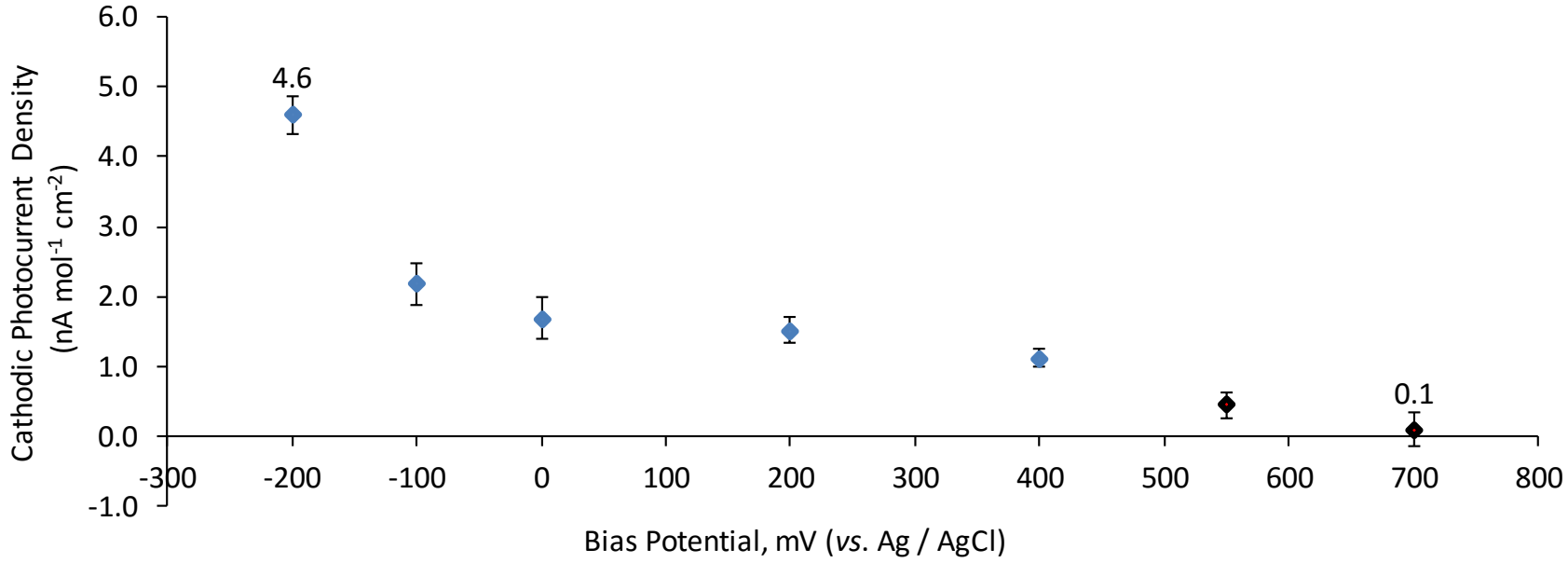
6.0
5.0
4.0
3.0
2.0
1.0
0.0
-1.0
Cathodic Photocurrent Density
(nA mol-1 cm-2)
4.6
0.1
-300
-200
-100
0
100
200
300
400
500
600
700
800
Bias Potential, mV (vs. Ag / AgCl)

| | ***Experiment 1*** | | ***Experiment 2*** | | ***Experiment 3*** | | ***Average*** | | |
|---|---|---|---|---|---|---|---|---|---|
| | Cathodic Photocurrent Density, nA $mol^{-1}$ $cm^{-2}$ | | | | | | | Associated Error | |
| | | $x10^{14}$ | | $x10^{14}$ | | $x10^{14}$ | **$x10^{14}$** | SD | 3SD |
| -200 | 4.58E+13 | 4.58 | 4.69E+13 | 4.69 | 4.52E+13 | 4.52 | **4.6** | 0.09 | 0.26 |
| -100 | 2.20E+13 | 2.20 | 2.07E+13 | 2.07 | 2.27E+13 | 2.27 | **2.2** | 0.10 | 0.30 |
| 0 | 1.77E+13 | 1.77 | 1.58E+13 | 1.58 | 1.72E+13 | 1.72 | **1.7** | 0.10 | 0.30 |
| 200 | 1.52E+13 | 1.52 | 1.46E+13 | 1.46 | 1.58E+13 | 1.58 | **1.5** | 0.06 | 0.18 |
| 400 | 1.08E+13 | 1.08 | 1.11E+13 | 1.11 | 1.16E+13 | 1.16 | **1.1** | 0.04 | 0.12 |
| 550 | 5.10E+12 | 0.51 | 4.30E+12 | 0.43 | 3.90E+12 | 0.39 | **0.4** | 0.06 | 0.18 |
| 700 | 1.80E+12 | 0.18 | 7.00E+11 | 0.07 | 3.10E+11 | 0.03 | **0.1** | 0.08 | 0.23 |

**Figure 19.** Manipulating the cathodic photocurrent density acquired at a SAM of AB-14-172-OEG-Fc$(CH_2)_{11}$SH deposited at Au by varying the bias potential of the working electrode. All cathodic photocurrents were measured in 0.1 M $Na_2SO_4$ (aq.) containing 5 mM $MV^{2+}$ as an electron acceptor. The electrodes were illuminated with light of wavelength 430 ± 5 nm and the photocurrents normalised for the concentration of porphyrin present at the interface, as determined by cyclic voltammetry (**Appendix, 8.1.3**). Each error bar is equivalent to 3SD and calculated from the data acquired across three separately prepared electrodes.

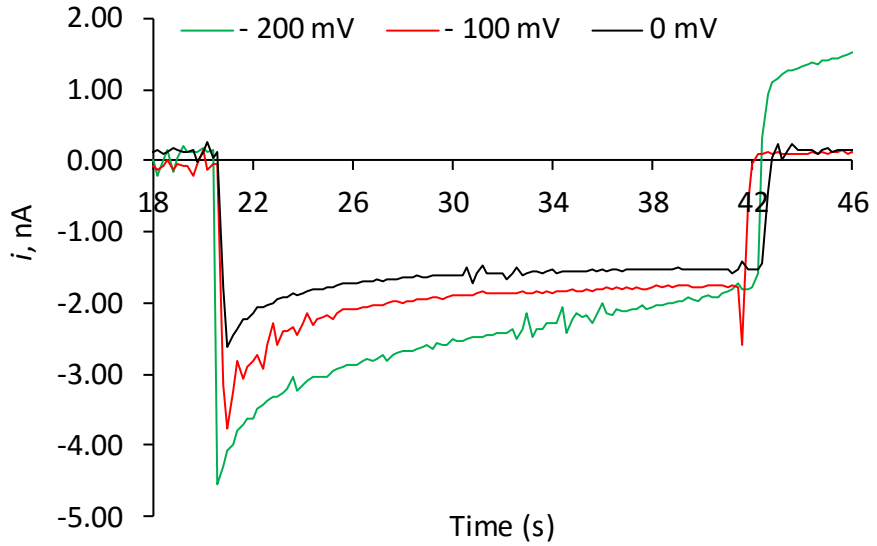


**Figure 20.** Current *vs.* time profiles for a Au electrode at which a SAM of AB-14-172-OEG-Fc$(CH_2)_{11}$SH had been deposited. All profiles were measured in 0.1 M $Na_2SO_4$ (aq.) containing 5 mM $MV^{2+}$ as an electron acceptor. The electrode was kept at either 0 mV (**Black**), – 100 mV (**Red**) or – 200 mV (**Blue**) and illuminated with light of wavelength 430 ± 5 nm. Electrochemical Cell Setup: *Working Electrode*: PEG-AB-14-172-Fc$(CH_2)_{11}$SH. *Reference Electrode*: Ag / AgCl. *Auxiliary Electrode*: Pt Wire. *Electrolytic Solution*: 0.1 M $Na_2SO_4$ + 5 mM $MV^{2+}$. *Solvent*: $H_2O$. *Bias Potential*: Variable. The differences in current (dark ('OFF') and light ('ON')) observed (**Table 9**) were used to quantify the photoelectrochemical outputs.

| | Photocurrent, nA | | |
|---|---|---|---|
| | 'OFF' | 'ON' | Difference |
| -200 mV | 0.149 | -4.541 | 4.690 |
| -100 mV | -0.120 | -3.770 | 3.650 |
| 200 mV | 0.136 | -2.633 | 2.769 |

**Table 9.** Gating the magnitude of the photoelectrochemical response observed upon illuminating a SAM of AB-14-172-OEG-Fc$(CH_2)_{11}$SH by varying the bias potential of the working electrode. The difference, in conjunction with the concentration of porphyrin present at the interface, as obtained by cyclic voltammetry (**Appendix, 8.1.3**), was used to normalise each photoelectrochemical response. An increase in negative bias resulted in greater cathodic photocurrent densities being generated.

## 8.4 – Comparison of the Photocurrent Densities Acquired at Monophasic and Biphasic, Porphyrin-Appended SAMs

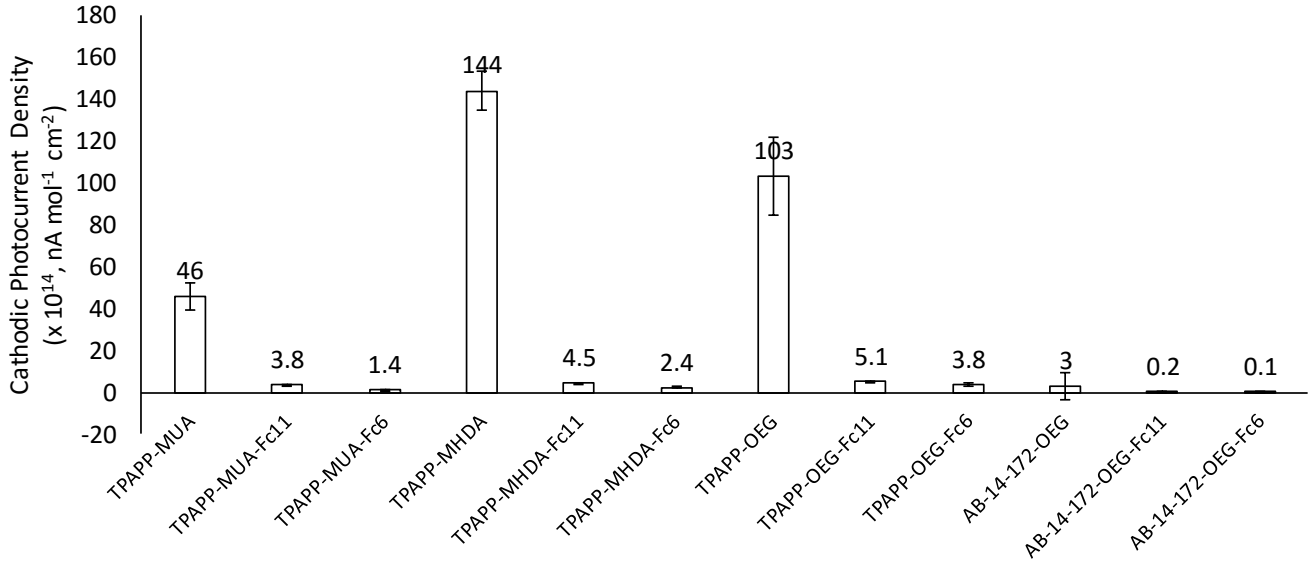

| | Cathodic Photocurrent Density, $x10^{14}$ nA $mol^{-1}$ $cm^{-2}$ | Associated Error, 3SD |
|---|---|---|
| TPAPP-MUA | 46 | 6.3 |
| TPAPP-MUA-Fc11 | 3.8 | 0.2 |
| TPAPP-MUA-Fc6 | 1.4 | 0.3 |
| TPAPP-MHDA | 144 | 9.3 |
| TPAPP-MHDA-Fc11 | 4.5 | 0.3 |
| TPAPP-MHDA-Fc6 | 2.4 | 0.2 |
| TPAPP-OEG | 103 | 18.6 |
| TPAPP-OEG-Fc11 | 5.1 | 0.3 |
| TPAPP-OEG-Fc6 | 3.8 | 0.5 |
| AB-14-172-OEG | 3 | 6.6 |
| AB-14-172-OEG-Fc11 | 0.2 | 0.0 |
| AB-14-172-OEG-Fc6 | 0.1 | 0.1 |

**Figure 21.** Cathodic photocurrent densities acquired at monophasic and biphasic porphyrin-appended SAMs deposited at Au. All cathodic photocurrents were measured in 0.1 M $Na_2SO_4$ (aq.) containing 5 mM $MV^{2+}$ as an electron acceptor. Fc11: $Fc(CH_2)_{11}SH$. Fc6: $Fc(CH_2)_6SH$. The electrodes were kept at – 100 mV (*vs*. Ag / AgCl), illuminated with light of wavelength 430 ± 5 nm and the photocurrents normalised for the concentration of porphyrin present at each interface, as determined by cyclic voltammetry (**Appendix, 8.1.2 and 8.1.3**). Each error bar is equivalent to 3SD and calculated from the data acquired across three (biphasic) or four (monophasic) separately prepared electrodes.

## 8.5 – Characterisation of Rotaxanated Interfaces by XPS

### 8.5.1 – AB-14-172–OEG

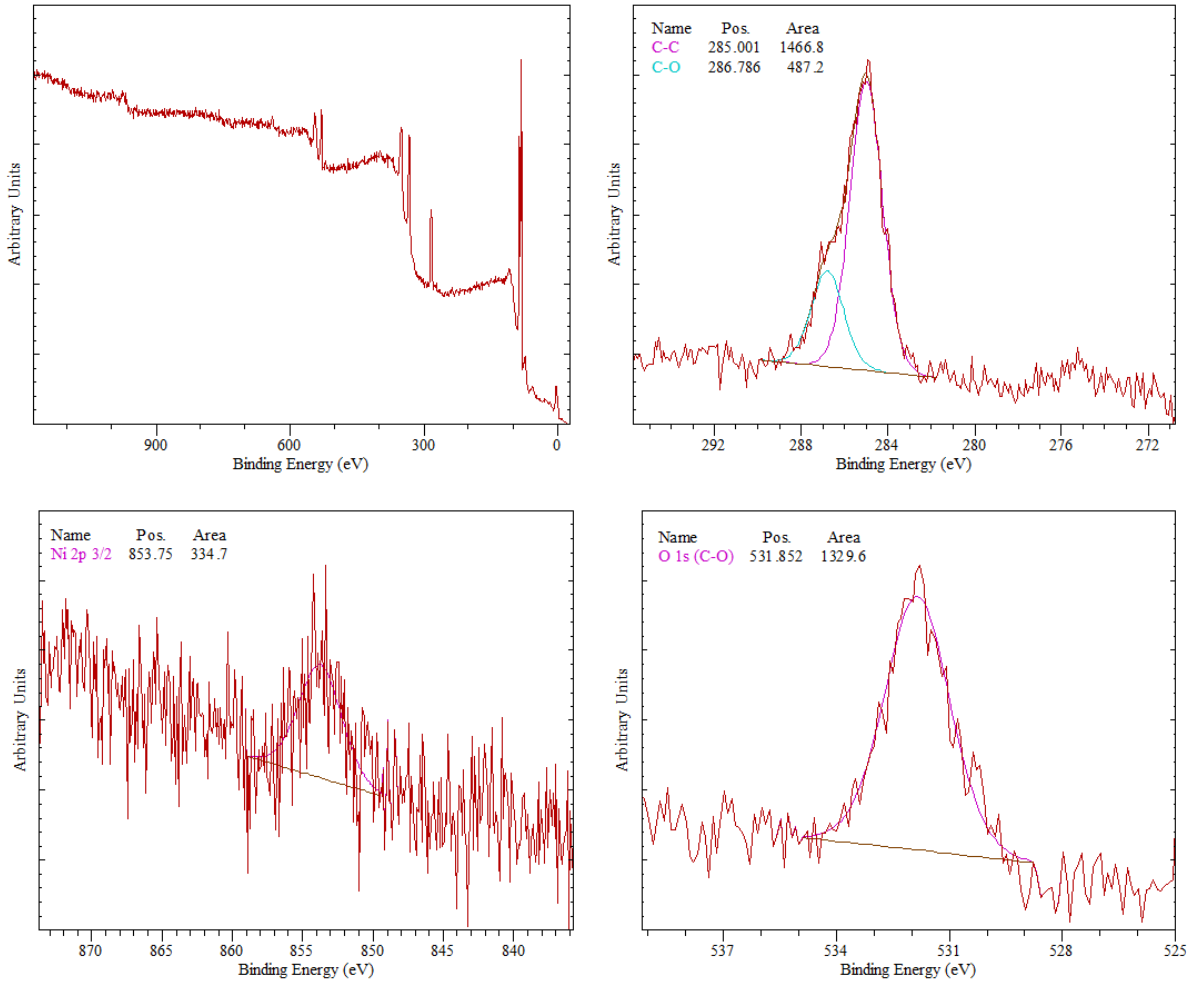


**Figure 22.** XPS spectrum (**Top Left**) of the SAM obtained upon covalent attachment of AB-14-172 to OEG deposited at Au. Narrow scan spectra were recorded in the C 1s (**Top Right**), Ni 2p (**Bottom Left**) and O 1s (**Bottom Right**) regions, and the relative % of each element present at the surface calculated (**Table 10**).

| Element | Normalised Peak Area | Relative % |
|---|---|---|
| **O** | 453.8 | 18.7 |
| **C** | 1954.0 | 80.4 |
| **Ni** | 22.9 | 0.9 |
| Total | 2430.7 | 100.0 |
| **No Fe Present** | | |

**Table 10.** The relative % of C, Ni and O observed at a SAM of AB-14-172–OEG.

## 8.5.2 – (AB-14-172-JL241)–OEG

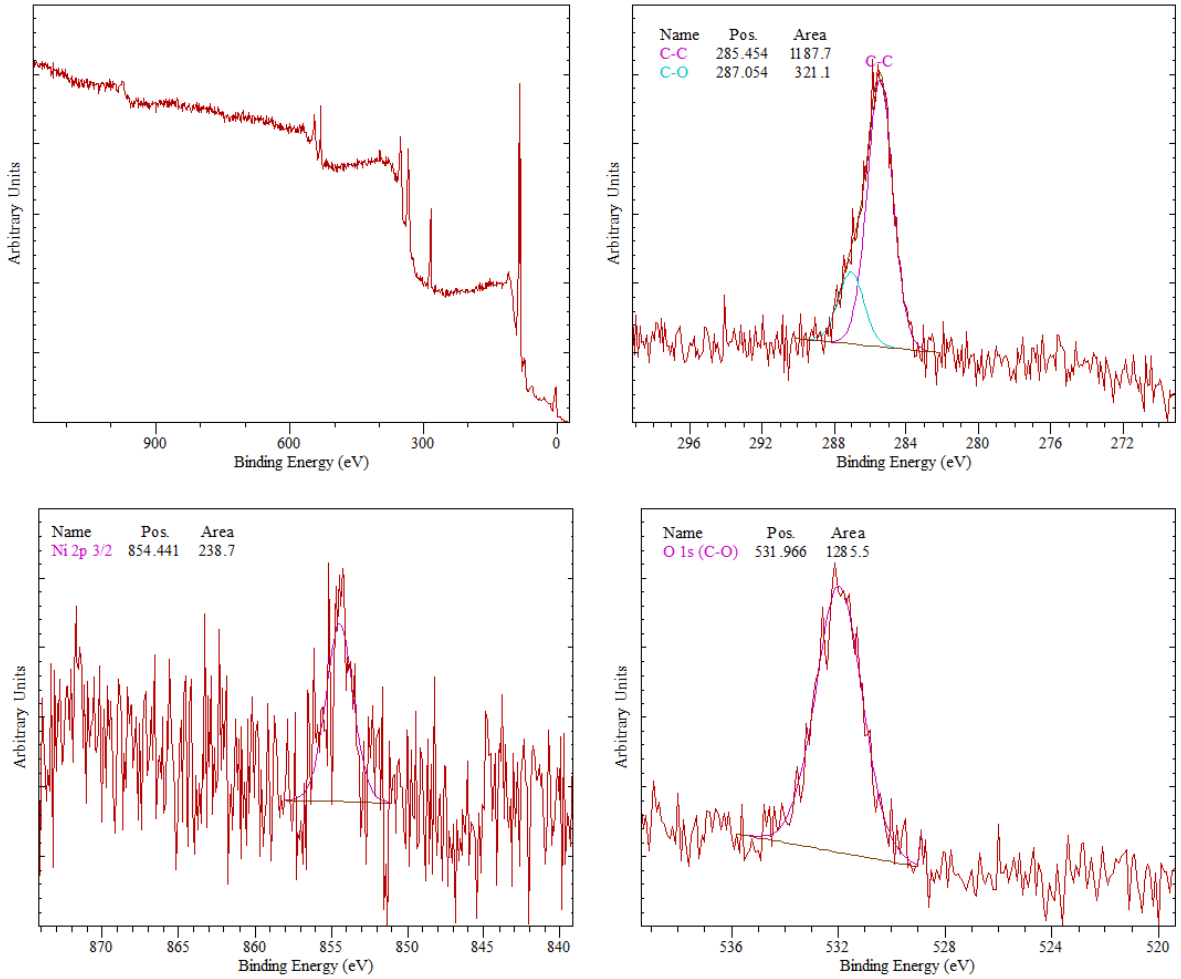


**Figure 23.** XPS spectrum (**Top Left**) of the SAM obtained upon the attempted covalent attachment of (AB-14-172-JL241) to OEG deposited at Au. Narrow scan spectra were recorded in the C 1s (**Top Right**), Ni 2p (**Bottom Left**) and O 1s (**Bottom Right**) regions, and the relative % of each element present at the surface calculated (**Table 11**). A narrow scan spectrum in the N 1s region (392 – 404 eV) was not obtained.

| Element | Normalised Peak Area | Relative % |
|---|---|---|
| **O** | 438.7 | 22.3 |
| **C** | 1508.8 | 76.8 |
| **Ni** | 16.3 | 0.8 |
| Total | 1963.8 | 100.0 |
| No Fe Present | | |

**Table 11.** The relative % of C, Ni and O observed at a SAM of (AB-14-172-JL241)–OEG. No Fe (from JL241) was apparent in the survey spectrum (**Figure 23**, **Top Left**).

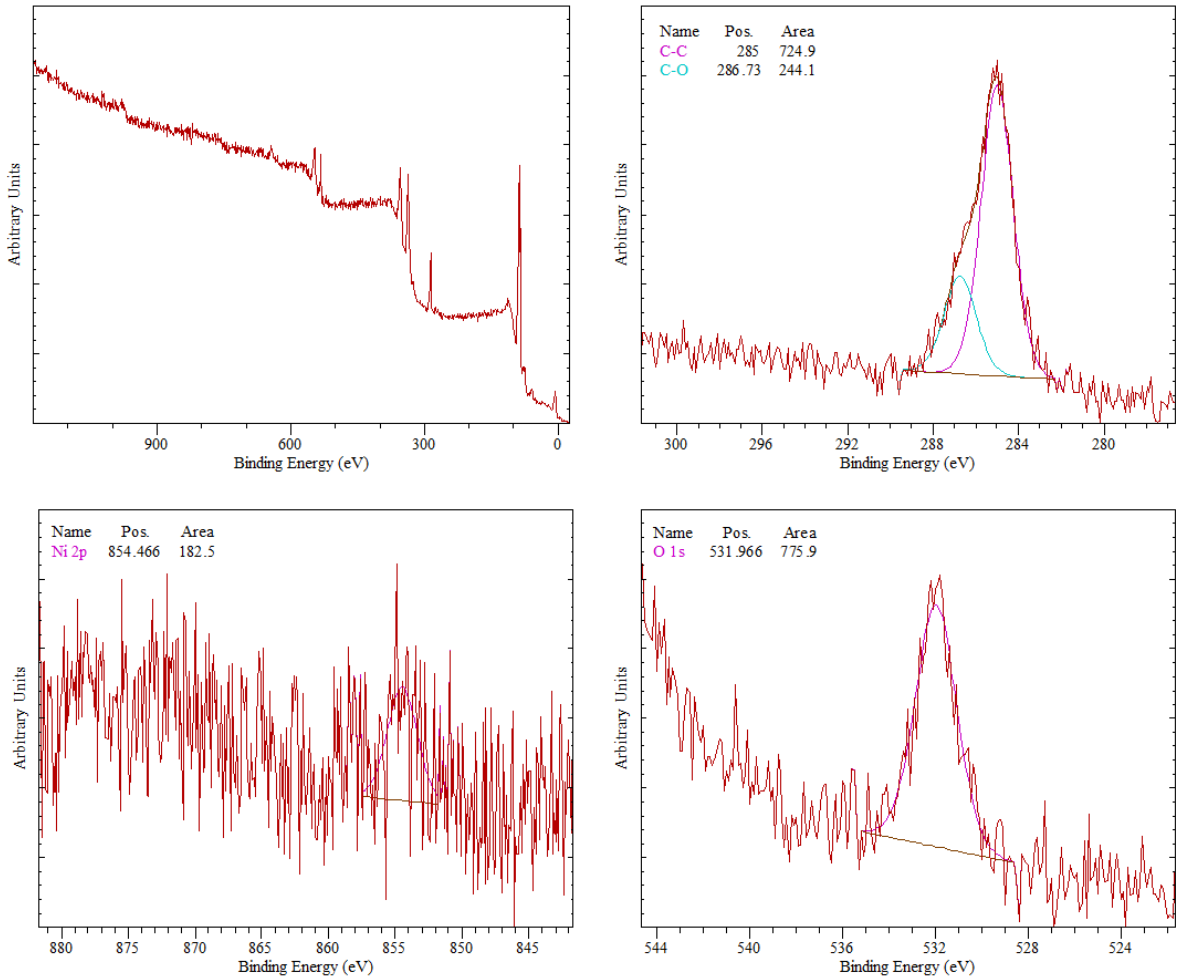


**Figure 24.** XPS spectrum (**Top Left**) of the SAM obtained upon the attempted covalent attachment of (AB-14-172-JL241) to OEG deposited at Au. Narrow scan spectra were recorded in the C 1s (**Top Right**), Ni 2p (**Bottom Left**) and O 1s (**Bottom Right**) regions, and the relative % of each element present at the surface calculated (**Table 12**). A narrow scan spectrum in the N 1s region (392 – 404 eV) was not obtained.

| Element | Normalised Peak Area | Relative % |
|---|---|---|
| **O** | 264.8 | 21.2 |
| **C** | 969.0 | 77.8 |
| **Ni** | 12.5 | 1.0 |
| Total | 1246.3 | 100.0 |

**Table 12.** The relative % of C, Ni and O observed at a SAM of (AB-14-172-JL241)–OEG. No Fe (from JL241) was apparent in the survey spectrum (**Figure 24**, **Top Left**).

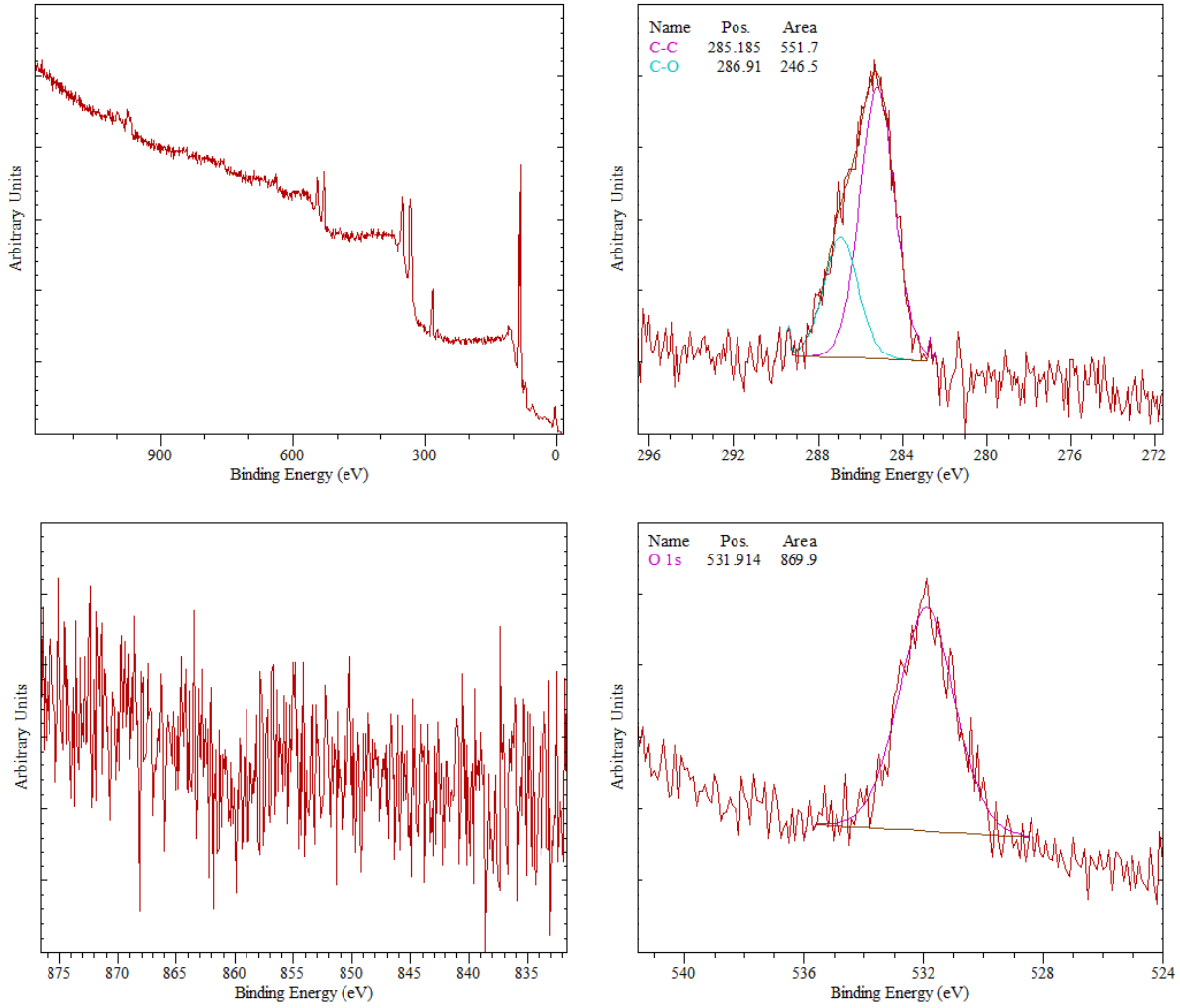


**Figure 25.** XPS spectrum (**Top Left**) of the SAM obtained upon the attempted covalent attachment of (AB-14-172-JL241) to an unactivated (No EDC / NHS was used) SAM of OEG deposited at Au. Narrow scan spectra were recorded in the C 1s (**Top Right**), Ni 2p (**Bottom Left**) and O 1s (**Bottom Right**) regions, and the relative % of each element present at the surface calculated (**Table 13**). A narrow scan spectrum in the N 1s region (392 – 404 eV) was not obtained.

| Element | Normalised Peak Area | Relative % |
|---|---|---|
| **O** | 296.9 | 27.1 |
| **C** | 798.2 | 72.9 |
| **Ni** | 0.0 | 0.0 |
| Total | 1095.1 | 100.0 |
| No Ni Present | | |

**Table 13.** The relative % of C, Ni and O observed at a SAM of OEG following exposure to (AB-14-172-JL241) in the absence of EDC / NHS. Fe (from JL241) and Ni were not apparent in the survey spectrum (**Figure 25**, **Top Left**), as expected in the absence of the coupling reagents.

## 8.5.3 – AB-19-144

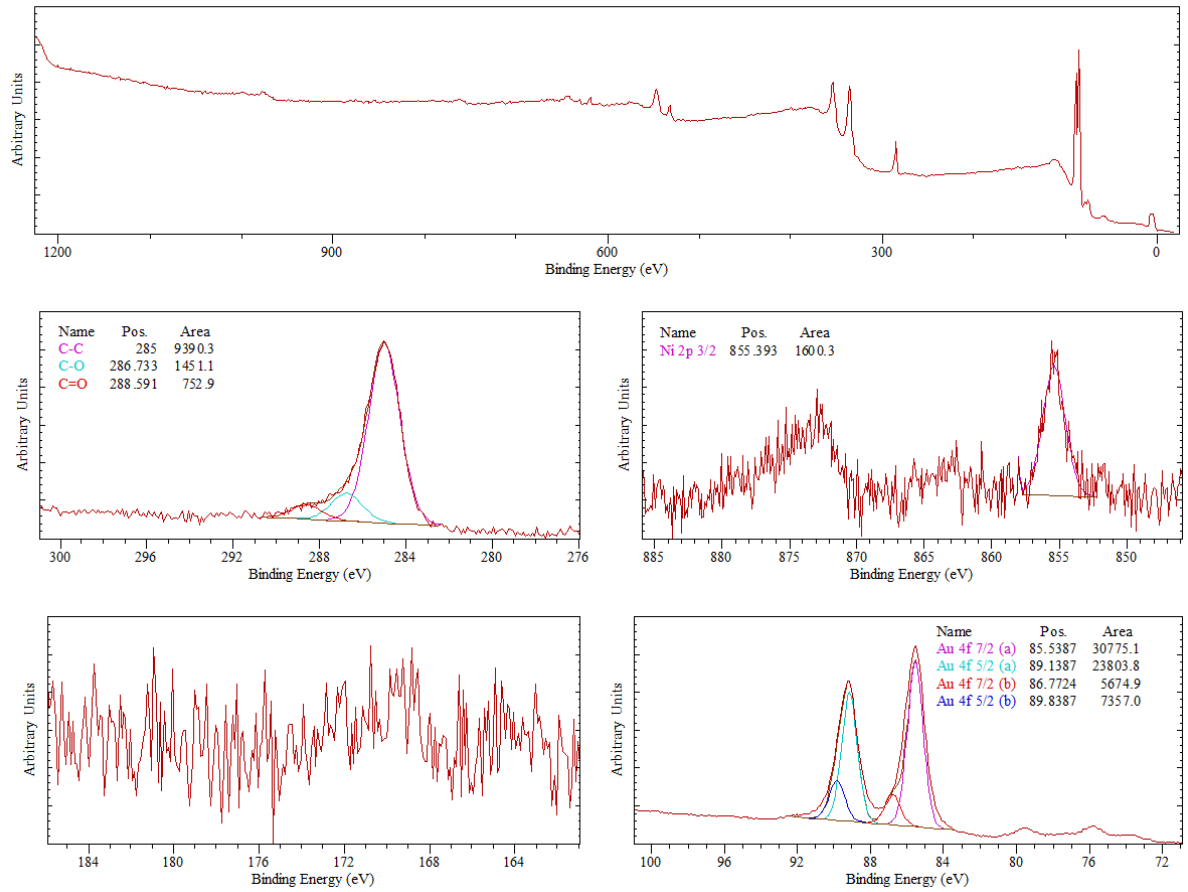


**Figure 26.** XPS spectrum (**Top**) of the SAM obtained upon the deposition of AB-19-144 at Au. Narrow scan spectra were recorded in the C 1s (**Middle Left**), Ni 2p (**Middle Right**), S 2p (**Bottom Left**) and Au 4f (**Bottom Right**) regions. A narrow scan spectrum in the N 1s region (392 – 404 eV) was not obtained. The relative % of each element present at the surface was calculated (**Table 14**).

| Element | Normalised Peak Area | Relative % |
|---|---|---|
| **Au** | 3953.8 | 25.3 |
| **C** | 11594.3 | 74.0 |
| **Ni** | 109.6 | 0.7 |
| Total | 15657.7 | 100.0 |

**Table 14.** The relative % of C, Ni and Au observed upon the deposition of AB-19-144 at Au. The S 2p peak (s) (160 – 172 eV) could not be quantified.

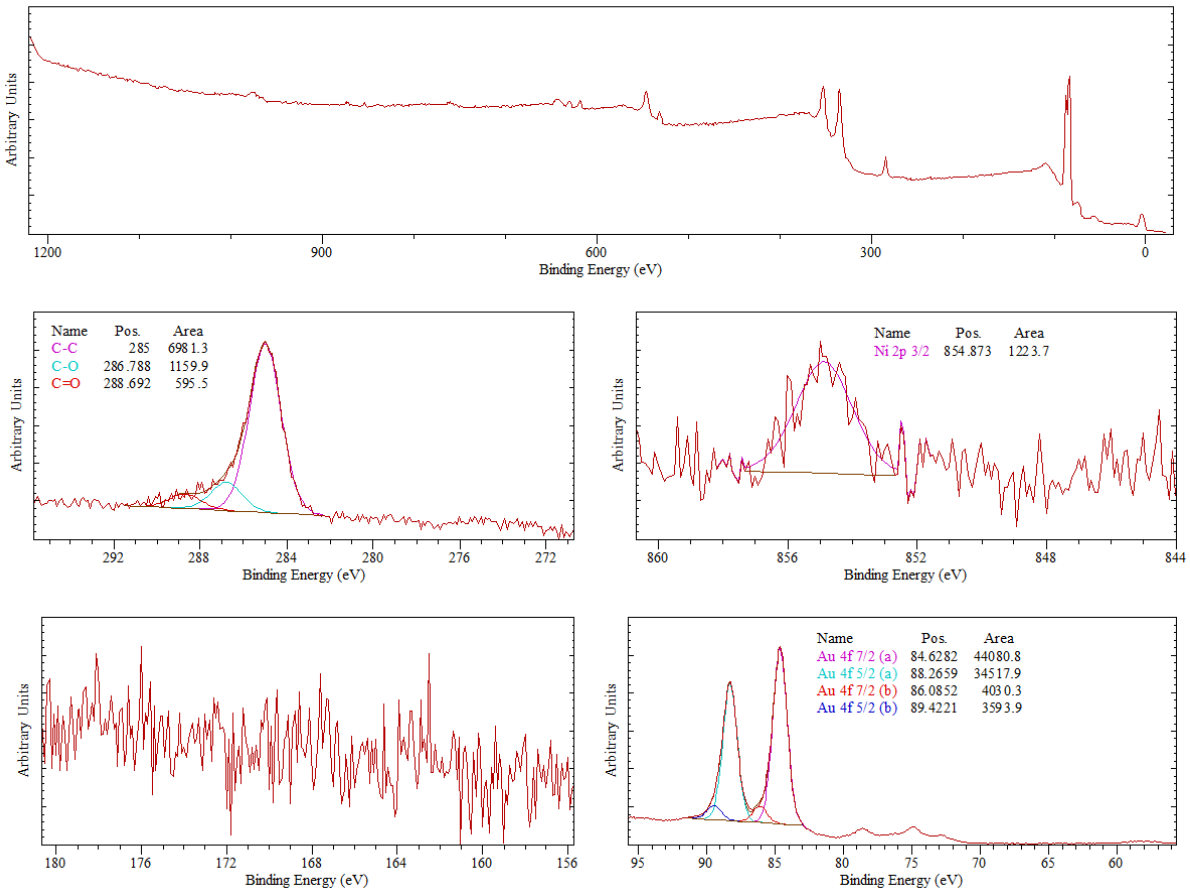


**Figure 27.** XPS spectrum (**Top**) of the SAM obtained upon the deposition of AB-19-144 at Au. Narrow scan spectra were recorded in the C 1s (**Middle Left**), Ni 2p (**Middle Right**), S 2p (**Bottom Left**) and Au 4f (**Bottom Right**) regions. A narrow scan spectrum in the N 1s region (392 – 404 eV) was not obtained. The relative % of each element present at the surface was calculated (**Table 15**).

| Element | Normalised Peak Area | Relative % |
|---|---|---|
| **Au** | 5042.3 | 36.4 |
| **C** | 8736.7 | 63.0 |
| **Ni** | 83.8 | 0.6 |
| Total | 13862.8 | 100.0 |

**Table 15.** The relative % of C, Ni and Au observed upon the deposition of AB-19-144 at Au. The S 2p peak (s) (160 – 172 eV) could not be quantified.

## 8.6 – Cathodic Photocurrent Density Measurements at Rotaxanated Interfaces

### 8.6.1 – AB-14-172–OEG, AB-14-172–OEG–Fc11, (AB-14-172-JL241)–OEG

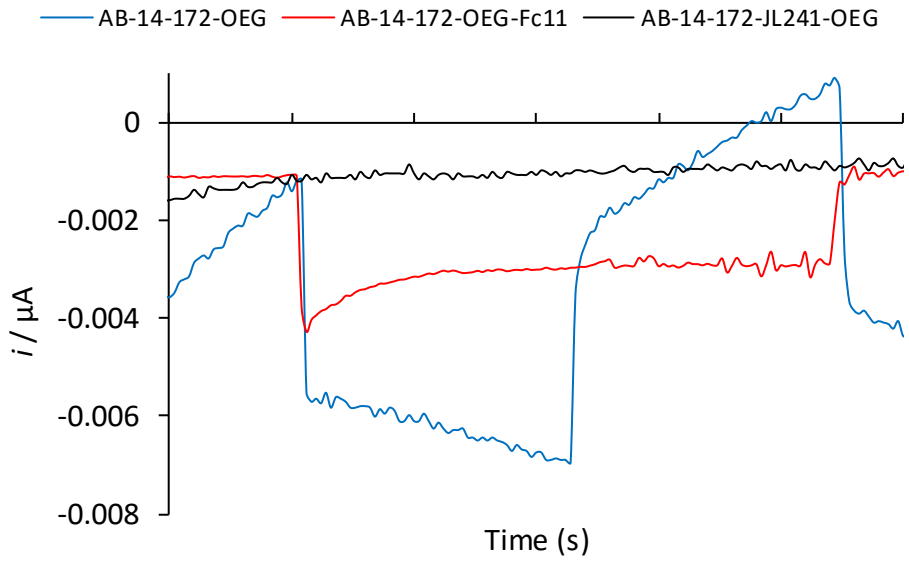


**Figure 28.** Current *vs.* time profiles for gold electrodes modified with SAMs of AB-14-172–OEG (**Blue**), AB-14-172–OEG–Fc11 (**Red**) and (AB-14-172-JL241)–OEG (**Black**). Fc11: $Fc(CH_2)_{11}SH$. All profiles were measured in 0.1 M $Na_2SO_4$ (aq.) containing 5 mM $MV^{2+}$ as an electron acceptor. The electrodes were kept at – 100 mV (*vs.* Ag / AgCl) and illuminated with light of wavelength 425 – 435 nm. The differences in current (dark ('OFF') and light ('ON')) observed (**Table 16**) were used to quantify the photoelectrochemical outputs.

| | Photocurrent, µA | | |
|---|---|---|---|
| | OFF' | ON' | Difference |
| AB-14-172-OEG | -0.0012 | -0.007 | 0.006 |
| AB-14-172-OEG-Fc11 | -0.0011 | -0.0043 | 0.003 |
| AB-14-172-JL241-OEG | N / A | | |

**Table 16.** The difference in current observed at SAMs of AB-14-172–OEG, AB-14-172–OEG–Fc11 and (AB-14-172-JL241)–OEG. Fc11: $Fc(CH_2)_{11}SH$. The difference, in conjunction with the concentration of porphyrin present at the interface, as obtained by cyclic voltammetry (**Chapter 3, Figure 6** and **Appendix, 8.1.3**), was used to normalise each photoelectrochemical response.

## 8.6.2 – AB-18-088, AB-18-088–Fc11

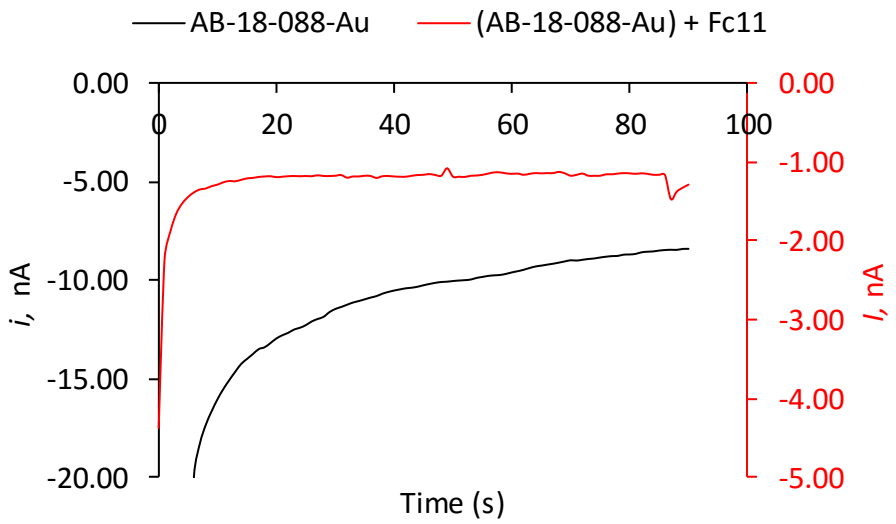


**Figure 29.** Current *vs.* time profiles for gold electrodes exposed to μM solutions (anhydrous $CH_2Cl_2$) of AB-18-088 (**Black**) and AB-18-088–Fc11 (**Red**). Fc11: $Fc(CH_2)_{11}SH$. Both profiles were measured in 0.1 M $Na_2SO_4$ (aq.) containing 5 mM $MV^{2+}$ as an electron acceptor. The electrodes were kept at – 100 mV (*vs.* Ag / AgCl) and illuminated with light of wavelength 425 – 435 nm.

## 8.6.3 – AB-19-144, AB-19-144 + 1 mM FcMeOH

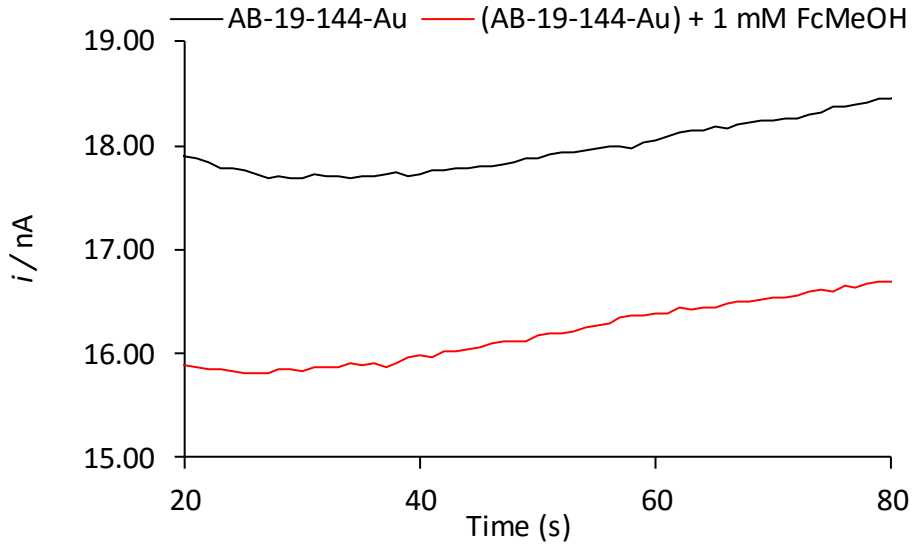


**Figure 30.** Current *vs.* time profiles for a gold electrode at which AB-19-144 had been deposited, prior to (**Black**) and following the addition of 1mM FcMeOH (**Red**) into solution. Both profiles were measured in 0.1 M $Na_2SO_4$ (aq.) containing 5 mM $MV^{2+}$ as an electron acceptor. The electrode was kept at – 100 mV (*vs.* Ag / AgCl) and illuminated with light of wavelength 425 - 435 nm.

## 8.7 – Absorption Spectra of Free Base and Metal-Containing Porphyrin Derivatives

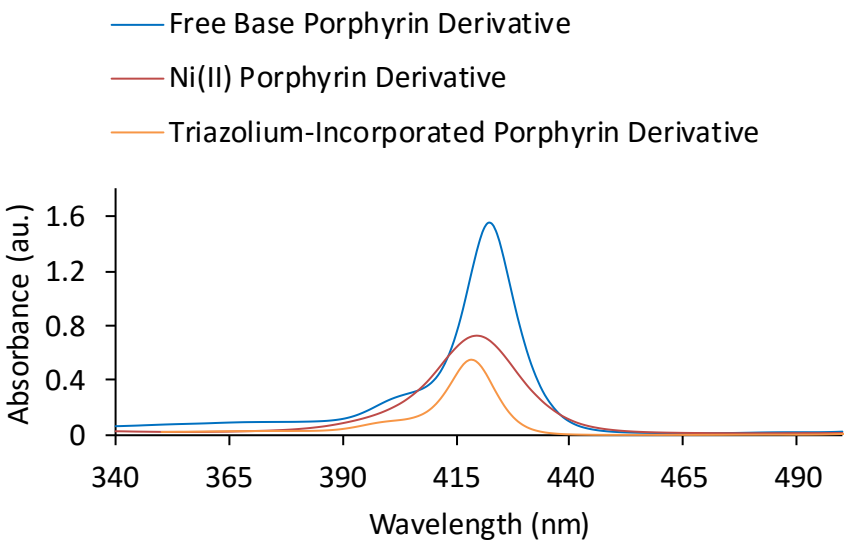


**Figure 31.** Absorption spectra of 5 µM solutions (anhydrous $CH_2Cl_2$) of free base (**Blue**), Ni(II)-coordinated (**Burgundy**), and triazolium-incorporated (**Orange**) porphyrin derivatives.

## 8.8 – Spectroscopic Characterisation of EuNap, ($MV^{2+}$, EuNap) and ($MV^{2+}$, EuNap)-CB[8]

### 8.8.1 – EuNap

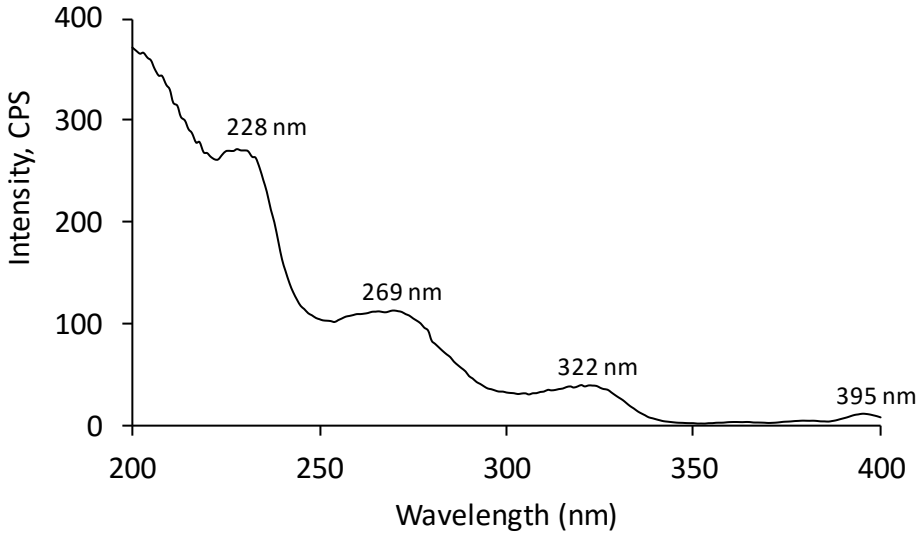


**Figure 32.** Phosphorescent excitation spectrum of a 0.5 mM solution (aqueous, 298 K) of EuNap. Experimental Parameters: $\lambda_{em}$ = 616 nm, excitation slit width = 5 nm, emission slit width = 14 nm, PMT Voltage (V) = 500, CAT 10.

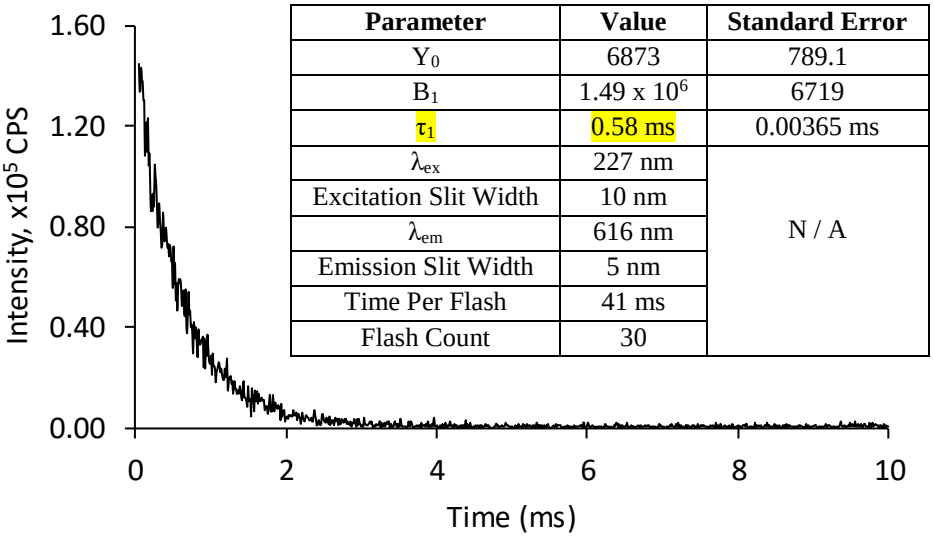


| Parameter | Value | Standard Error |
|---|---|---|
| $Y_0$ | 6873 | 789.1 |
| $B_1$ | 1.49 x $10^6$ | 6719 |
| $\tau_1$ | 0.58 ms | 0.00365 ms |
| $\lambda_{ex}$ | 227 nm | N / A |
| Excitation Slit Width | 10 nm | |
| $\lambda_{em}$ | 616 nm | |
| Emission Slit Width | 5 nm | |
| Time Per Flash | 41 ms | |
| Flash Count | 30 | |

**Figure 33.** Luminescence decay of a 0.5 mM solution (aqueous, 298 K) of EuNap. **Inset.** Experimental parameters.

## 8.8.2 – ($MV^{2+}$, EuNap)

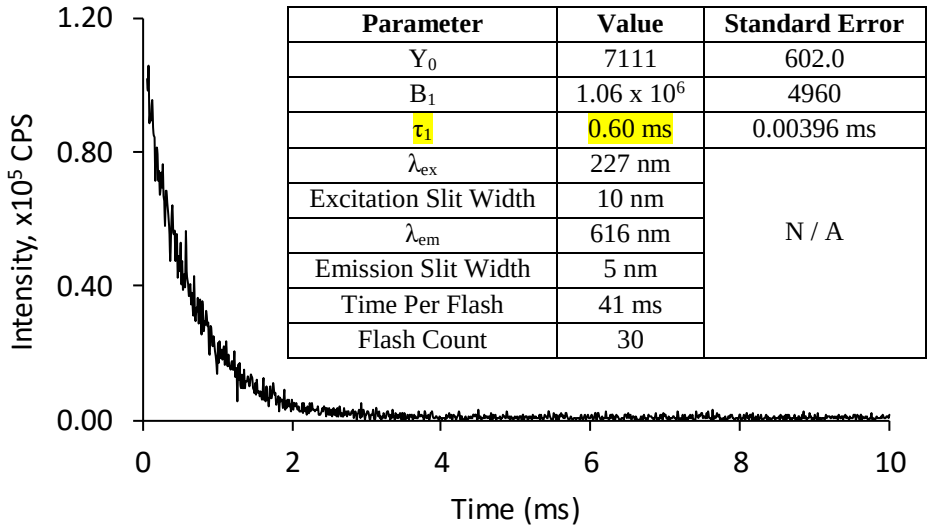


| Parameter | Value | Standard Error |
|---|---|---|
| $Y_0$ | 7111 | 602.0 |
| $B_1$ | 1.06 x $10^6$ | 4960 |
| $\tau_1$ | 0.60 ms | 0.00396 ms |
| $\lambda_{ex}$ | 227 nm | N / A |
| Excitation Slit Width | 10 nm | |
| $\lambda_{em}$ | 616 nm | |
| Emission Slit Width | 5 nm | |
| Time Per Flash | 41 ms | |
| Flash Count | 30 | |

**Figure 34.** Luminescence decay of a 0.5 mM solution (aqueous, 298 K) of EuNap following the addition of 1 equivalent of $MV^{2+}$. **Inset.** Experimental parameters.

## 8.8.3 – ($MV^{2+}$, EuNap)-CB[8]

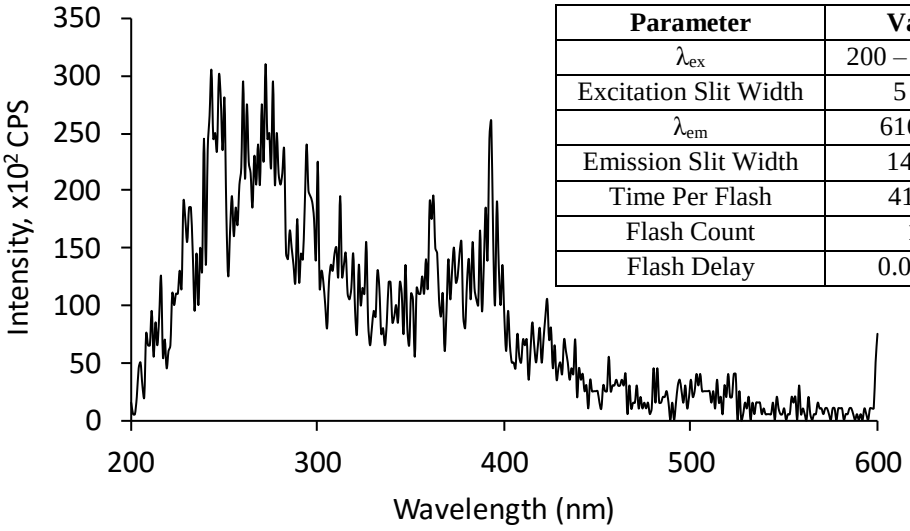


| Parameter | Value |
|---|---|
| $\lambda_{ex}$ | 200 – 600 nm |
| Excitation Slit Width | 5 nm |
| $\lambda_{em}$ | 616 nm |
| Emission Slit Width | 14 nm |
| Time Per Flash | 41 ms |
| Flash Count | 10 |
| Flash Delay | 0.01 ms |

**Figure 35.** Phosphorescent excitation spectrum of a 0.5 mM solution (aqueous, 298 K) of ($MV^{2+}$, EuNap)-CB[8]. **Inset.** Experimental parameters.

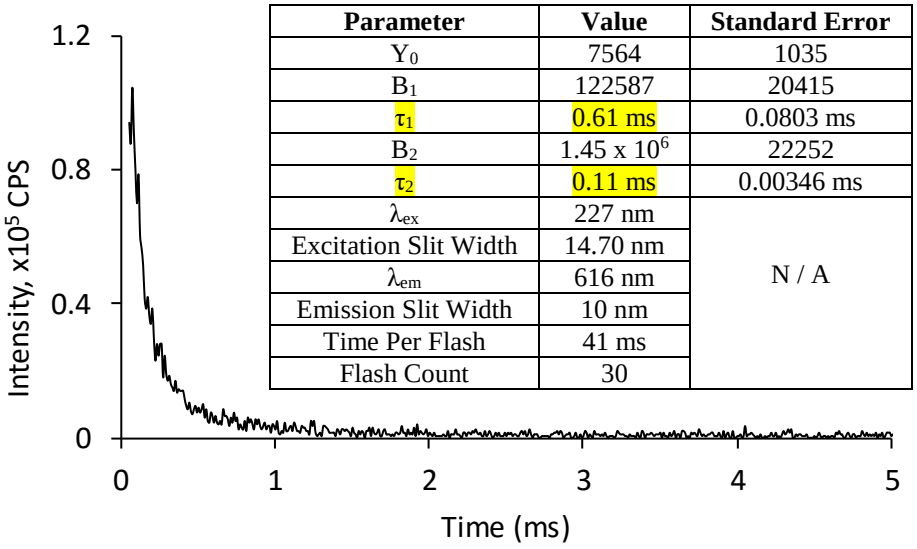


| Parameter | Value | Standard Error |
|---|---|---|
| $Y_0$ | 7564 | 1035 |
| $B_1$ | 122587 | 20415 |
| $\tau_1$ | 0.61 ms | 0.0803 ms |
| $B_2$ | 1.45 x $10^6$ | 22252 |
| $\tau_2$ | 0.11 ms | 0.00346 ms |
| $\lambda_{ex}$ | 227 nm | N / A |
| Excitation Slit Width | 14.70 nm | |
| $\lambda_{em}$ | 616 nm | |
| Emission Slit Width | 10 nm | |
| Time Per Flash | 41 ms | |
| Flash Count | 30 | |

**Figure 36.** Luminescence decay of a 0.5 mM solution (aqueous, 298 K) of ($MV^{2+}$, EuNap)-CB[8]. Decay monitored at $\lambda_{em}$ 616 nm under $\lambda_{ex}$ 227 nm. **Inset.** Experimental parameters.

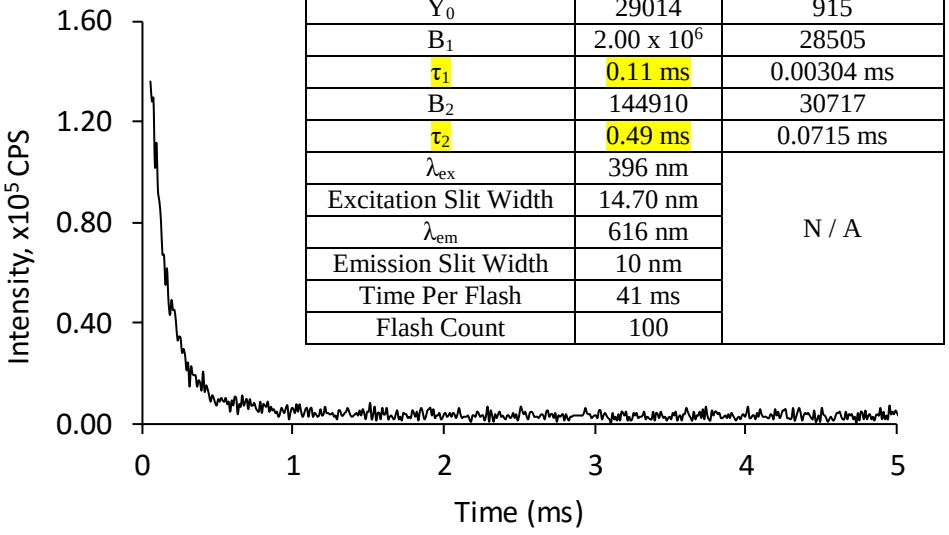


| Parameter | Value | Standard Error |
|---|---|---|
| $Y_0$ | 29014 | 915 |
| $B_1$ | 2.00 x $10^6$ | 28505 |
| $\tau_1$ | 0.11 ms | 0.00304 ms |
| $B_2$ | 144910 | 30717 |
| $\tau_2$ | 0.49 ms | 0.0715 ms |
| $\lambda_{ex}$ | 396 nm | N / A |
| Excitation Slit Width | 14.70 nm | |
| $\lambda_{em}$ | 616 nm | |
| Emission Slit Width | 10 nm | |
| Time Per Flash | 41 ms | |
| Flash Count | 100 | |

**Figure 37.** Luminescence decay of a 0.5 mM solution (aqueous, 298 K) of ($MV^{2+}$, EuNap)-CB[8]. Decay monitored at $\lambda_{em}$ 616 nm under $\lambda_{ex}$ 396 nm. **Inset.** Experimental parameters.

## 8.9 – Monitoring the Formation of $(MV^{+\cdot})_2$-CB[8] Upon Addition of $Na_2S_2O_4$ to a Solution of $(MV^{2+}$, EuNap)-CB[8]

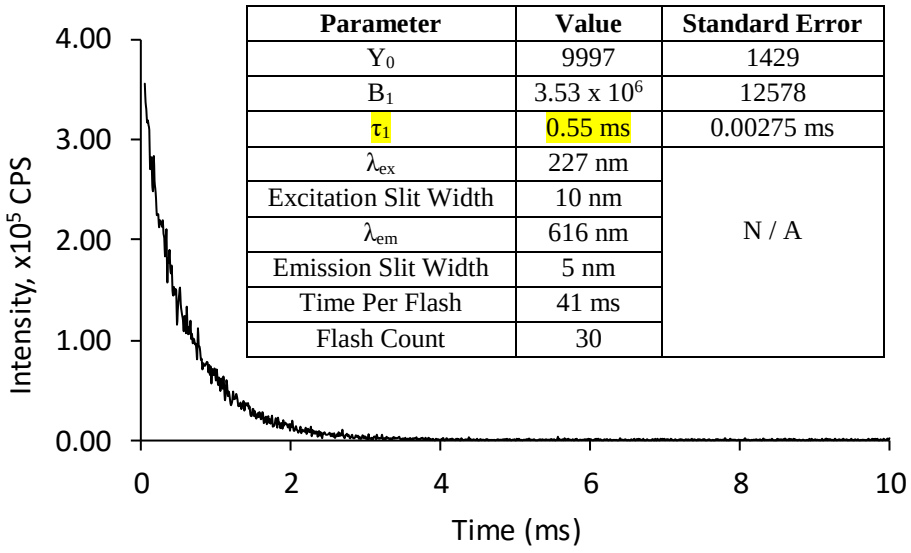


| Parameter | Value | Standard Error |
|---|---|---|
| $Y_0$ | 9997 | 1429 |
| $B_1$ | 3.53 x $10^6$ | 12578 |
| $\tau_1$ | 0.55 ms | 0.00275 ms |
| $\lambda_{ex}$ | 227 nm | N / A |
| Excitation Slit Width | 10 nm | |
| $\lambda_{em}$ | 616 nm | |
| Emission Slit Width | 5 nm | |
| Time Per Flash | 41 ms | |
| Flash Count | 30 | |

**Figure 38.** Luminescence decay of a 0.5 mM solution (aqueous, 298 K) of EuNap. **Inset.** Experimental parameters.

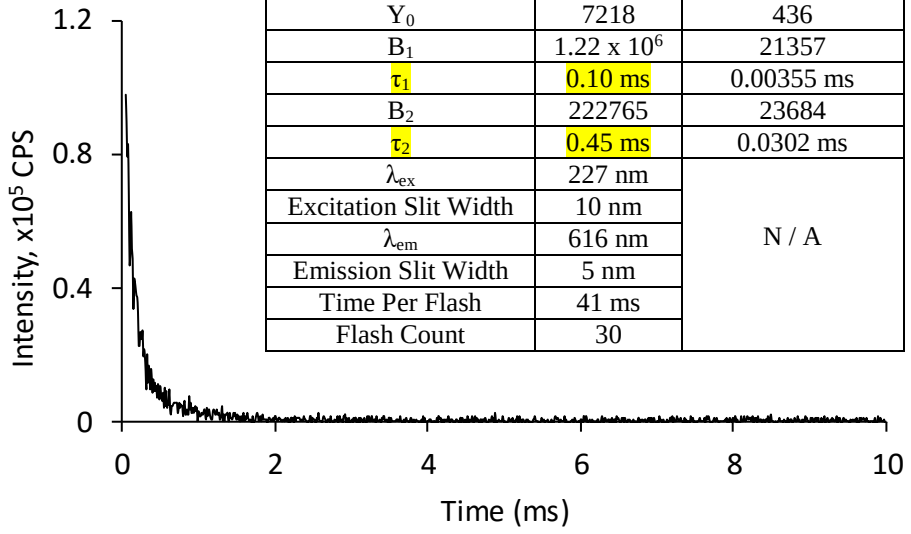


| Parameter | Value | Standard Error |
|---|---|---|
| $Y_0$ | 7218 | 436 |
| $B_1$ | 1.22 x $10^6$ | 21357 |
| $\tau_1$ | 0.10 ms | 0.00355 ms |
| $B_2$ | 222765 | 23684 |
| $\tau_2$ | 0.45 ms | 0.0302 ms |
| $\lambda_{ex}$ | 227 nm | N / A |
| Excitation Slit Width | 10 nm | |
| $\lambda_{em}$ | 616 nm | |
| Emission Slit Width | 5 nm | |
| Time Per Flash | 41 ms | |
| Flash Count | 30 | |

**Figure 39.** Luminescence decay of a 0.5 mM solution (aqueous, 298 K) of $(MV^{2+}$, EuNap)-CB[8]. Decay monitored at $\lambda_{em}$ 616 nm under $\lambda_{ex}$ 227 nm. **Inset.** Experimental parameters.

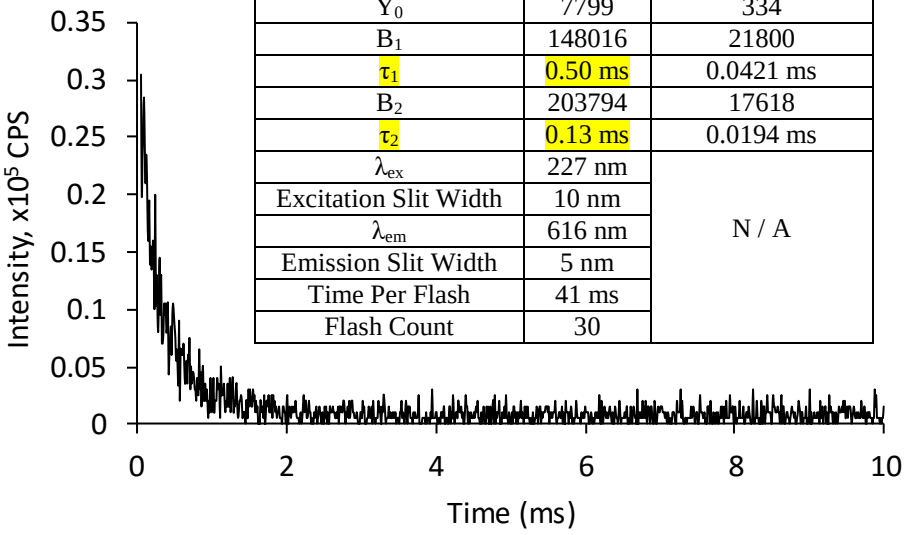


| Parameter | Value | Standard Error |
|---|---|---|
| $Y_0$ | 7799 | 334 |
| $B_1$ | 148016 | 21800 |
| $\tau_1$ | 0.50 ms | 0.0421 ms |
| $B_2$ | 203794 | 17618 |
| $\tau_2$ | 0.13 ms | 0.0194 ms |
| $\lambda_{ex}$ | 227 nm | N / A |
| Excitation Slit Width | 10 nm | |
| $\lambda_{em}$ | 616 nm | |
| Emission Slit Width | 5 nm | |
| Time Per Flash | 41 ms | |
| Flash Count | 30 | |

**Figure 40.** Luminescence decay of a 0.5 mM solution (aqueous, 298 K) of ($MV^{2+}$, EuNap)-CB[8]. Decay monitored at $\lambda_{em}$ 616 nm under $\lambda_{ex}$ 227 nm following the addition of 1equivalent of $Na_2S_2O_4$. **Inset.** Experimental parameters.

## 8.10 – Estimating the Efficacy of Generating $(MV^{+\bullet})_2$-CB[8] in Solution

**Calculating the Percentage of EuNap Confined Within the Cavity of CB[8]:** The percentage of EuNap confined within the cavity of CB[8] prior to and following the addition of excess sodium thiosulfate ($Na_2S_2O_4$), or the formation of the homoternary complex ($(MV^{+\bullet})_2$-CB[8]), was calculated upon measuring the phosphorescence lifetime at $\lambda_{em}$ 616 nm on a Horiba Fluorolog 3 at 298 K. Each experimental emission decay curve was obtained *via* the decay by delay setting in phosphorimeter mode, and the resultant curve fitted to either a monoexponential (**Equation 1**) or biexponential (**Equation 2**) decay function.

$F(t) = A + B_1 e^{\frac{-t}{\tau_1}}$ (**Equation 1**) and $F(t) = A + B_1 e^{\frac{-t}{\tau_1}} + B_2 e^{\frac{-t}{\tau_2}}$ (**Equation 2**), where t = time, A = empirical background noise factor, $B_1$, $B_2$ = empirical amplitude scaling factor for the emissive species 1 and / or 2, and $\tau_1$, $\tau_2$ = luminescence lifetime(s) of species 1 and / or 2.

The percentage of EuNap confined within the cavity of CB[8], prior to and following the addition of $Na_2S_2O_4$, was estimated by comparing the relative concentrations of each component present (EuNap [1], ($MV^{2+}$, EuNap)-CB[8] [2]) and assuming that each component possesses the same quantum yield (QY, normally dependent upon both concentration and brightness).[2]

Prior to Addition of $Na_2S_2O_4$:

$$\left[\frac{B_1}{B_2}\right] = \frac{QY_1[1]}{QY_2[2]}$$

$B_1$: 222765 CPS, $\tau_{Eu}$ (EuNap): 0.45 ms, $B_2$: 1.22 x $10^6$ CPS, $\tau_{Eu}$ ($MV^{2+}$, EuNap)-CB[8]: 0.10 ms, $B_1$ + $B_2$: 1.442765 x $10^6$ CPS.

**Relative % of EuNap Present in Solution:** (222765 / 1.442765 x $10^6$) x 100 = **15.4 %**

**Relative % of EuNap Confined within Apolar Cavity of CB[8]:** (1.22 x $10^6$ / 1.442765 x $10^6$) x 100 = **84.6 %**

Following Addition of $Na_2S_2O_4$:

$$\left[\frac{B_1}{B_2}\right]' = \frac{QY_1}{QY_2} \cdot \frac{[1]'}{[2]'}$$

$B_1$: 148016 CPS, $\tau_{Eu}$ (EuNap): 0.50 ms, $B_2$: 203794 CPS, $\tau_{Eu}$ ($MV^{2+}$, EuNap)-CB[8]: 0.13 ms, $B_1$ + $B_2$: 351810 CPS.

**Relative % of EuNap Present in Solution:** (148016 / 351810) x 100 = **42.1 %**

**Relative % of EuNap Confined within Apolar Cavity of CB[8]:** (203794 / 351810) x 100 = **57.9 %**

## 8.11 – Characterisation of Heteroternary Complexes Formed from the Non-Aromatic Derivatives Acquired *via* Hydrogenation

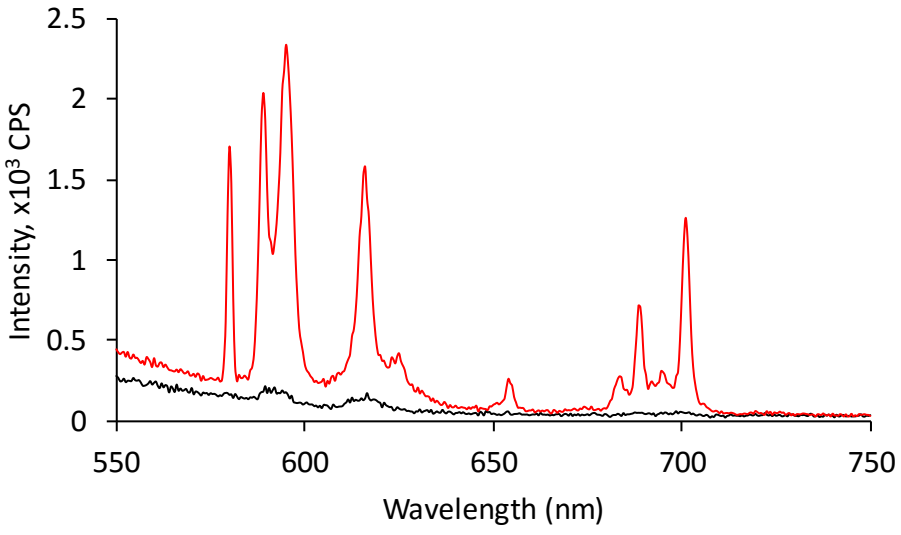


**Figure 41.** Phosphorescent emission spectra of 0.5 mM solutions ($D_2O$, 298 K) of ($MV^{2+}$, EuNap)-CB[8] (**Black**) and (NAMV, EuNap)-CB[8] (**Red**). Experimental Parameters: $\lambda_{ex}$ = 397 nm, excitation slit width = 5 nm, emission slit width = 1 nm, PMT Voltage (V) = 500, CAT 10.

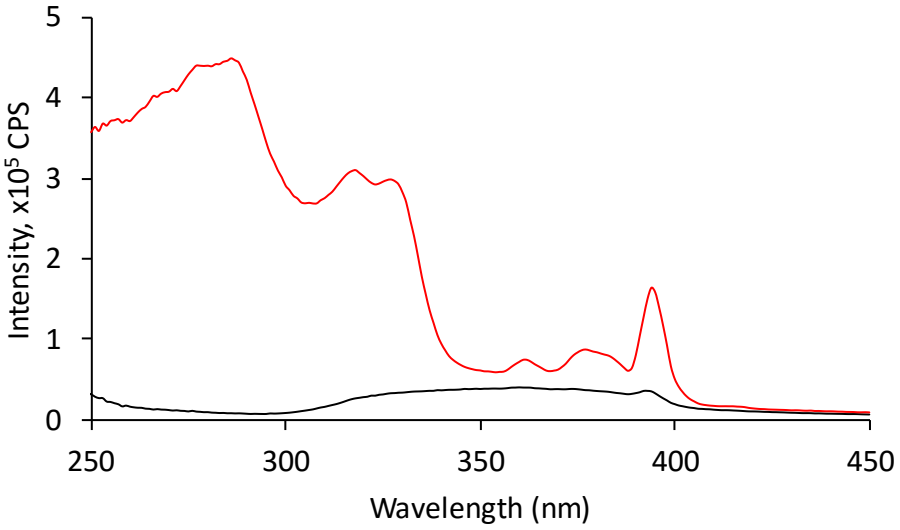


**Figure 42.** Phosphorescent excitation spectra of 0.5 mM solutions ($D_2O$, 298 K) of ($MV^{2+}$, EuNap)-CB[8] (**Black**) and (NAMV, EuNap)-CB[8] (**Red**). Experimental Parameters: $\lambda_{em}$ = 616 nm, excitation slit width = 5 nm, emission slit width = 14 nm, PMT Voltage (V) = 500, CAT 10.

| Parameter | Value | Standard Error |
|---|---|---|
| $Y_0$ | 6098 | 275.2 |
| $B_1$ | 104961 | 2772 |
| $\tau_1$ | 0.58 ms | 0.0197 ms |
| $\lambda_{ex}$ | 397 nm | N / A |
| Excitation Slit Width | 14 nm | |
| $\lambda_{em}$ | 616 nm | |
| Emission Slit Width | 5 nm | |
| Time Per Flash | 41 ms | |
| Flash Count | 10 | |

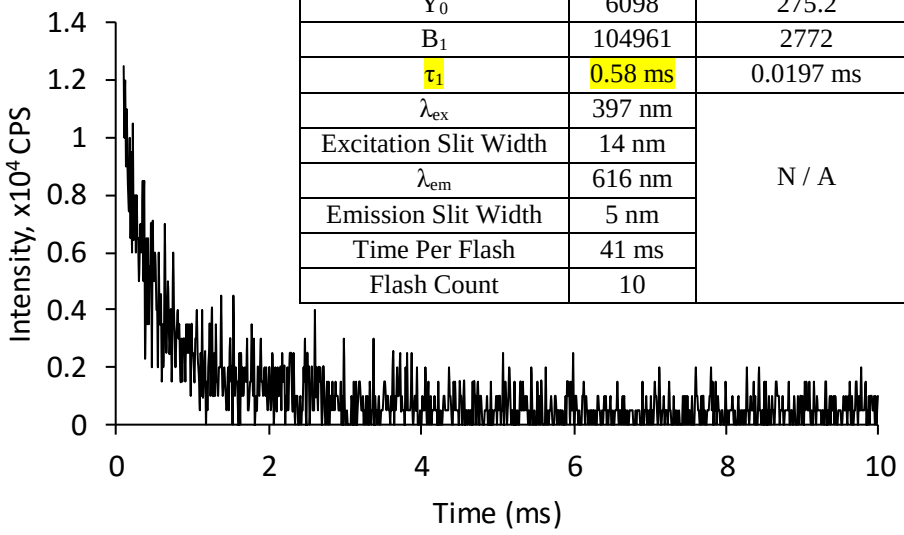


**Figure 43.** Luminescence decay of a 0.5 mM solution ($D_2O$, 298 K) of ($MV^{2+}$, EuNap)-CB[8]. **Inset.** Experimental parameters.

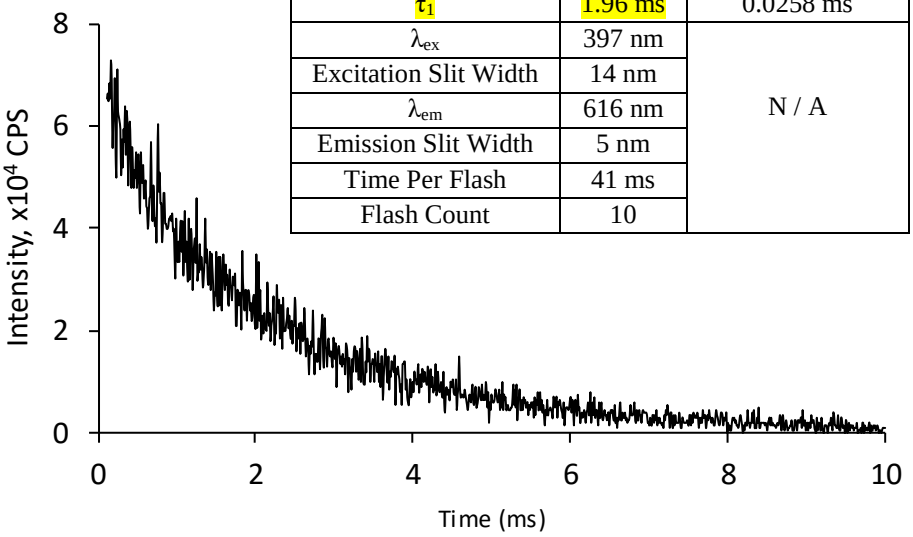


| Parameter | Value | Standard Error |
|---|---|---|
| $Y_0$ | 13004 | 1626 |
| $B_1$ | 645231 | 4166 |
| $\tau_1$ | 1.96 ms | 0.0258 ms |
| $\lambda_{ex}$ | 397 nm | N / A |
| Excitation Slit Width | 14 nm | |
| $\lambda_{em}$ | 616 nm | |
| Emission Slit Width | 5 nm | |
| Time Per Flash | 41 ms | |
| Flash Count | 10 | |

**Figure 44.** Luminescence decay of a 0.5 mM solution ($D_2O$, 298 K) of (NAMV, EuNap)-CB[8]. **Inset.** Experimental parameters.

## 8.12 – Investigating the Quenching Effect of Incorporating Yd and Nd into the Hydrophobic Cavity of CB[8]

### 8.12.1 – ($MV^{2+}$, YdNap)-CB[8]

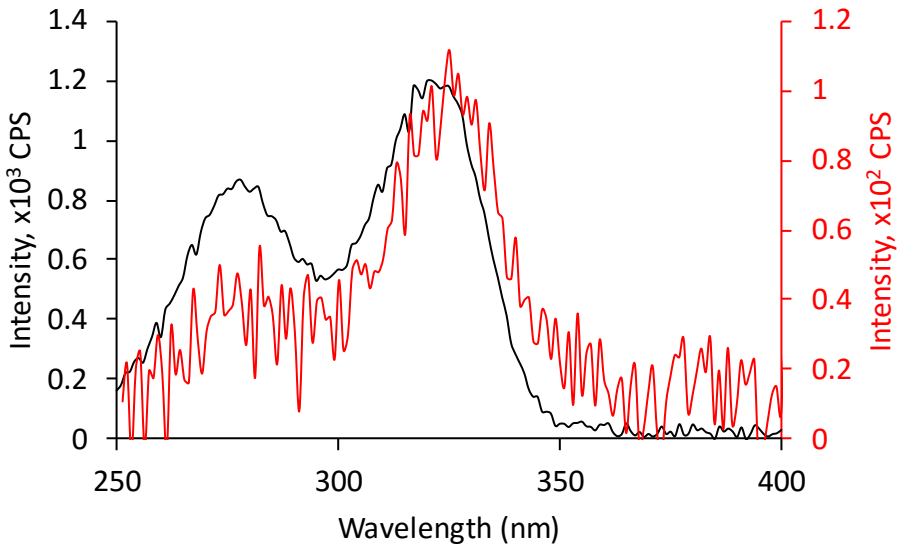


**Figure 45.** Phosphorescent excitation spectra of 0.5 mM solutions ($D_2O$, 298 K) of YbNap (**Black**) and ($MV^{2+}$, YbNap)-CB[8] (**Red**).
Experimental Parameters: $\lambda_{em}$ = 1040 nm, excitation slit width = 5 nm, emission slit width = 5 nm, PMT Voltage (V) = 500, CAT 10.

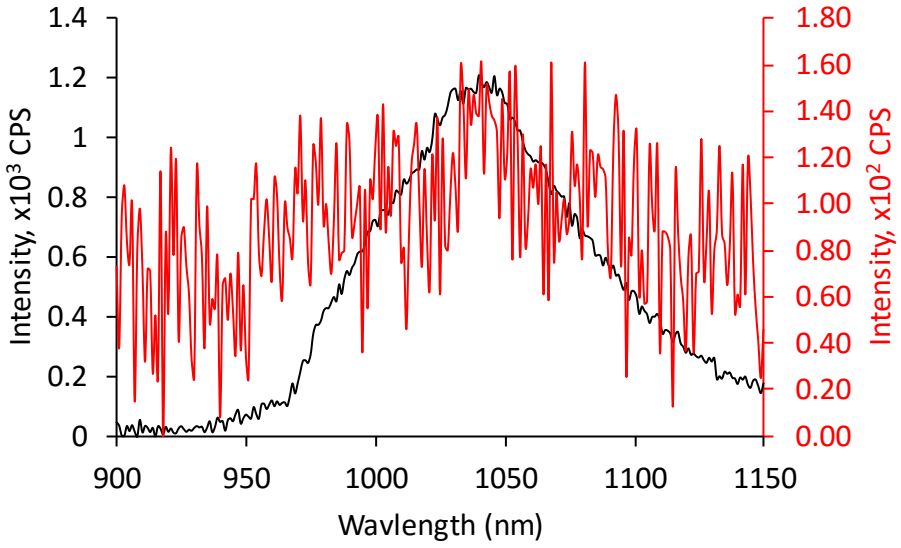


**Figure 46.** Phosphorescent emission spectra of 0.5 mM solutions ($D_2O$, 298 K) of YbNap (**Black**) and ($MV^{2+}$, YbNap)-CB[8] (**Red**). Experimental Parameters: $\lambda_{ex}$= 320 and 325 nm, excitation slit width = 5 nm, emission slit width = 5 nm, PMT Voltage (V) = 500, CAT 10.

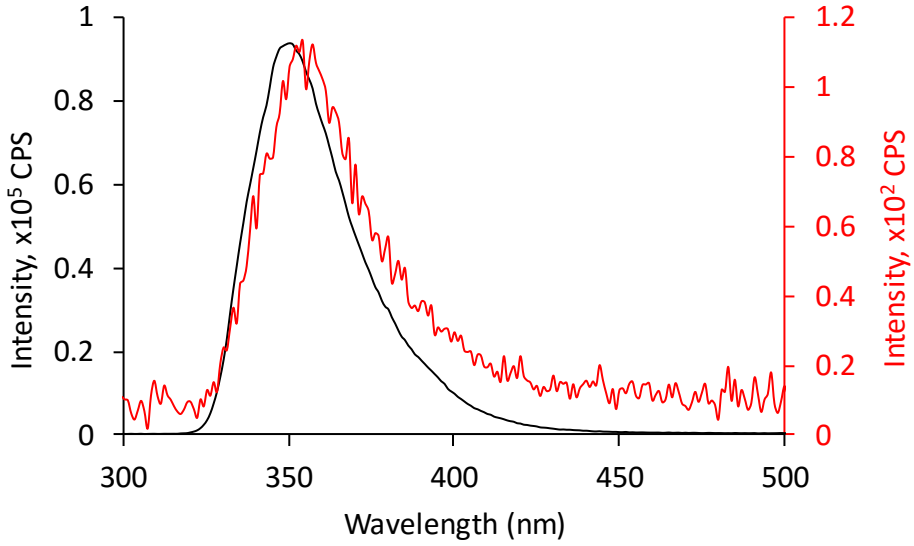


**Figure 47.** Fluorescent emission spectra of 0.5 mM solutions ($D_2O$, 298 K) of YbNap (**Black**) and ($MV^{2+}$, YbNap)-CB[8] (**Red**). Experimental Parameters: $\lambda_{ex}$= 270 nm, excitation slit width = 10 nm, emission slit width = 5 nm, PMT Voltage (V) = 500, CAT 10.

## 8.12.2 – ($MV^{2+}$, NdNap)-CB[8]

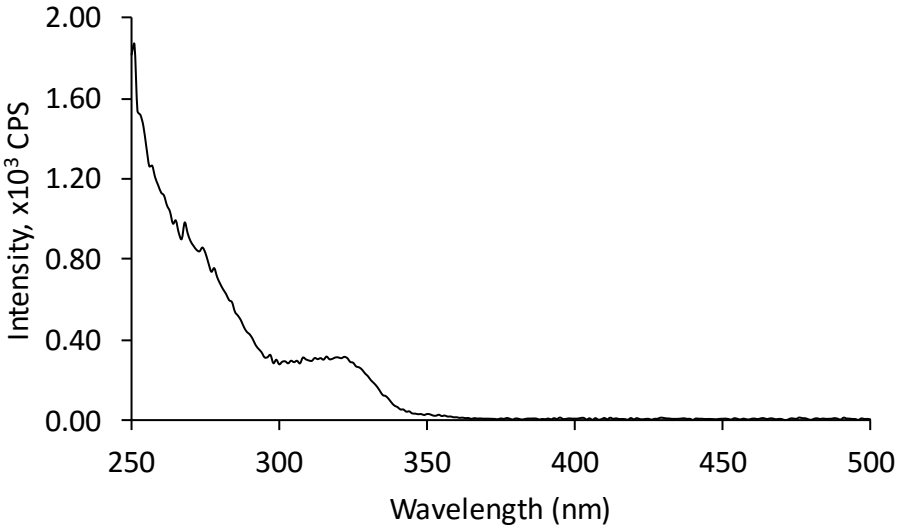


**Figure 48.** Phosphorescent excitation spectrum of a 0.5 mM solution ($D_2O$, 298 K) of NdNap. Experimental Parameters: $\lambda_{em}$ = 1060 nm, excitation slit width = 5 nm, emission slit width = 5 nm, PMT Voltage (V) = 500, CAT 10.

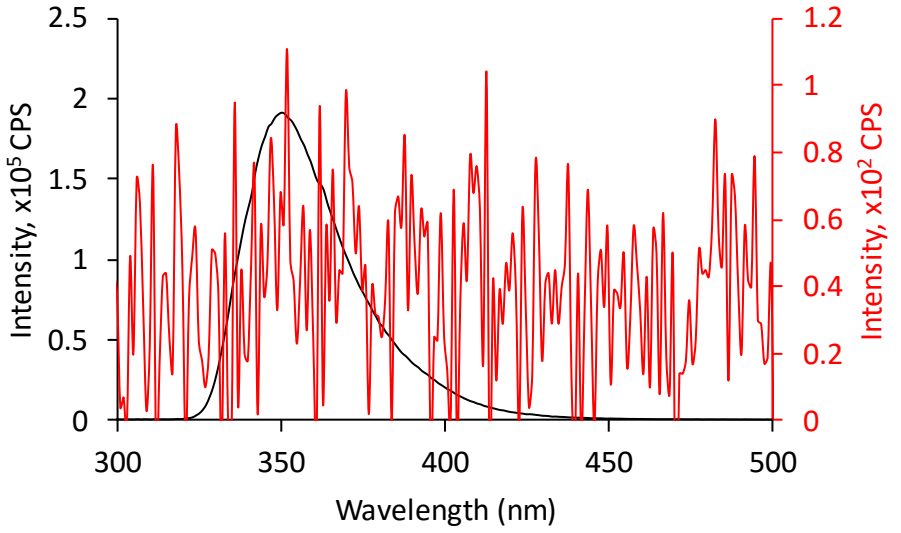


**Figure 49.** Fluorescent emission spectra of 0.5 mM solutions ($D_2O$, 298 K) of NdNap (**Black**) and ($MV^{2+}$, NdNap)-CB[8] (**Red**). Experimental Parameters: $\lambda_{ex}$= 270 nm, excitation slit width = 10 nm, emission slit width = 5 nm, PMT Voltage (V) = 500, CAT 10.

## 8.13 – Investigating the Effect of Chromophore Confinement and the Presence of Oxygen on the Emissive Output from NdNap

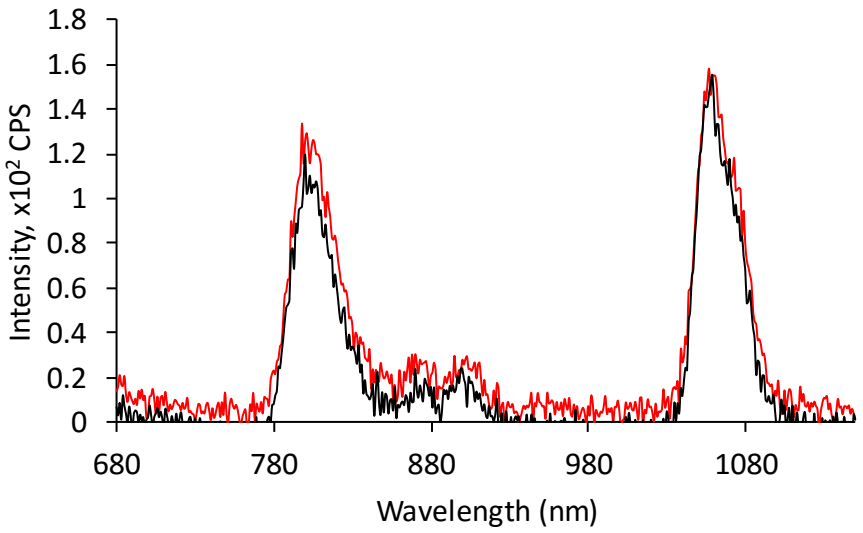


**Figure 50.** Phosphorescent emission spectra of a 0.5 mM solution ($D_2O$, 298 K) of ($MV^{2+}$, NdNap)-CB[8] following the **removal** (10 min., $N_2$ (g)) and subsequent **addition** of oxygen ($O_2$ (g), 60 min. exposure to air) to the solution. Experimental Parameters: $\lambda_{ex}$= 323 nm, excitation slit width = 5 nm, emission slit width = 5 nm, PMT Voltage (V) = 500, CAT 10.

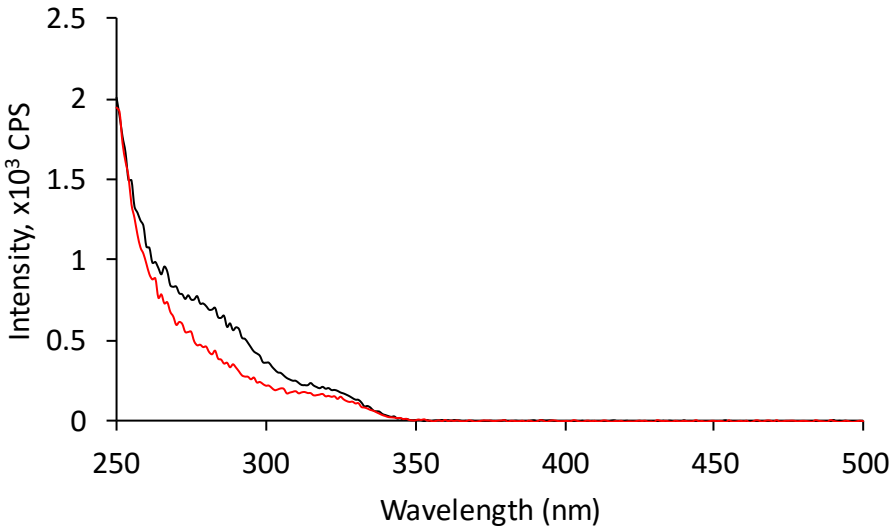


**Figure 51.** Phosphorescent excitation spectra of a 0.5 mM solution ($D_2O$, 298 K) of NdNap-CB[7] following the **removal** (10 min., $N_2$ (g)) and subsequent **addition** of oxygen ($O_2$ (g), 60 min. exposure to air) to the solution. Experimental Parameters: $\lambda_{em}$ = 1060 nm, excitation slit width = 5 nm, emission slit width = 5 nm, PMT Voltage (V) = 500, CAT 10.

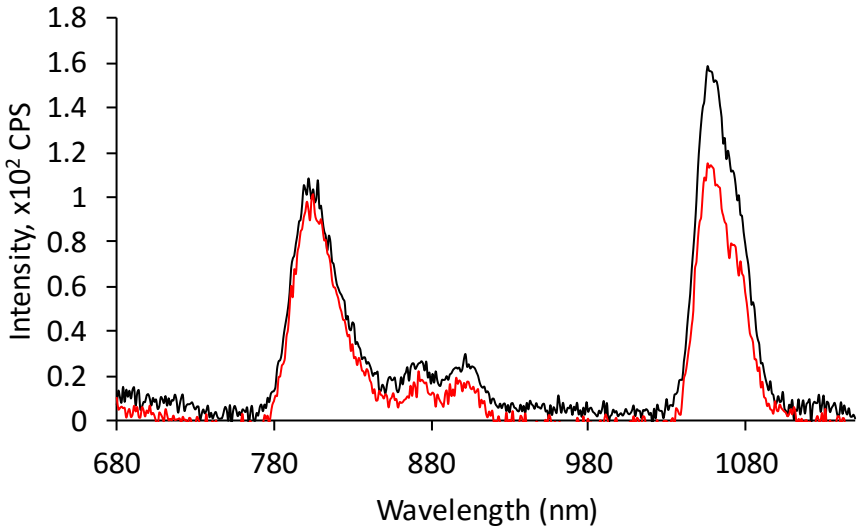


**Figure 52.** Phosphorescent emission spectra of a 0.5 mM solution ($D_2O$, 298 K) of NdNap-CB[7] following the **removal** (10 min., $N_2$ (g)) and subsequent **addition** of oxygen ($O_2$ (g), 60 min. exposure to air) to the solution. Experimental Parameters: $\lambda_{ex}$= 323 nm, excitation slit width = 5 nm, emission slit width = 5 nm, PMT Voltage (V) = 500, CAT 10.

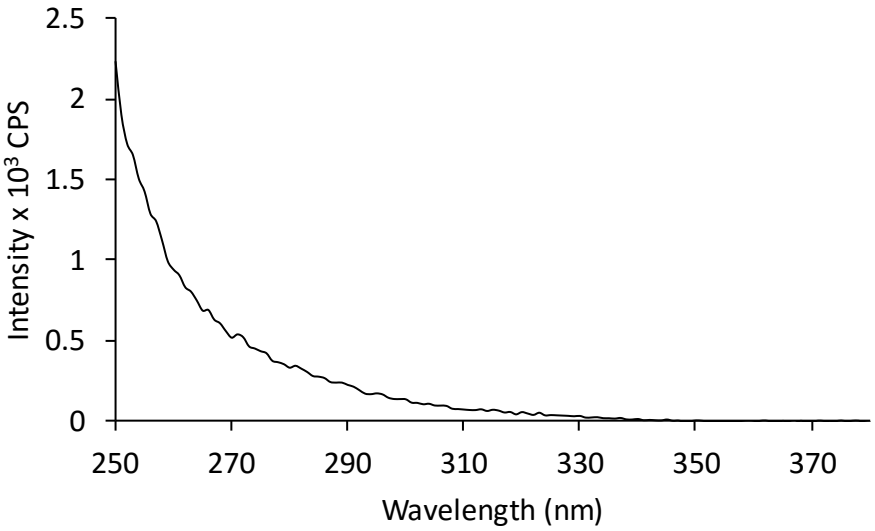


**Figure 53.** Phosphorescent excitation spectrum of a 0.5 mM solution ($D_2O$, 298 K) of NdNap-CB[7] following the removal of $O_2$ (g) (10 min., $N_2$ (g)) and the addition of 1 equivalent of $MV^{2+}$ to the solution. Experimental Parameters: $\lambda_{em}$ = 1060 nm, excitation slit width = 5 nm, emission slit width = 5 nm, PMT Voltage (V) = 500, CAT 10.

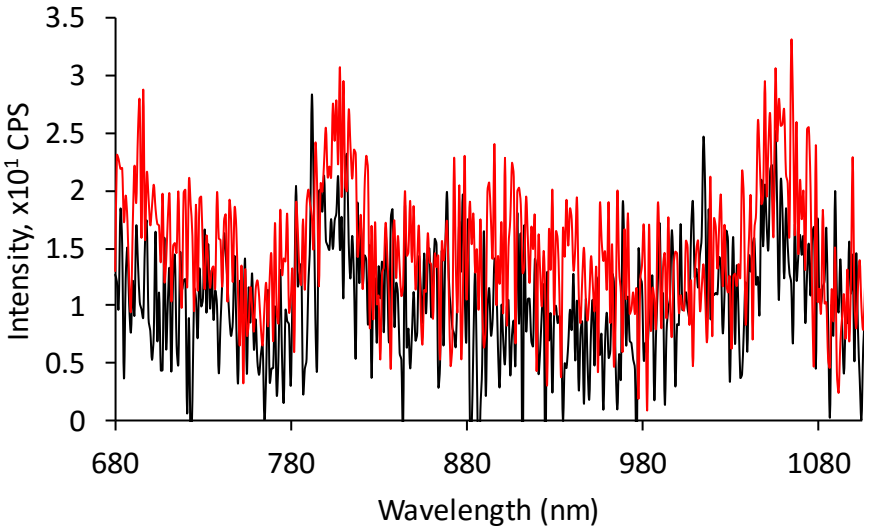


**Figure 54.** Phosphorescent emission spectra of a 0.5 mM solution ($D_2O$, 298 K) of ((NdNap-CB[7]) + $MV^{2+}$) following the **removal** (10 min., $N_2$ (g)) and subsequent **addition** of oxygen ($O_2$ (g), 60 min. exposure to air) to the solution. Experimental Parameters: $\lambda_{ex}$= 323 nm, excitation slit width = 5 nm, emission slit width = 5 nm, PMT Voltage (V) = 500, CAT 10.

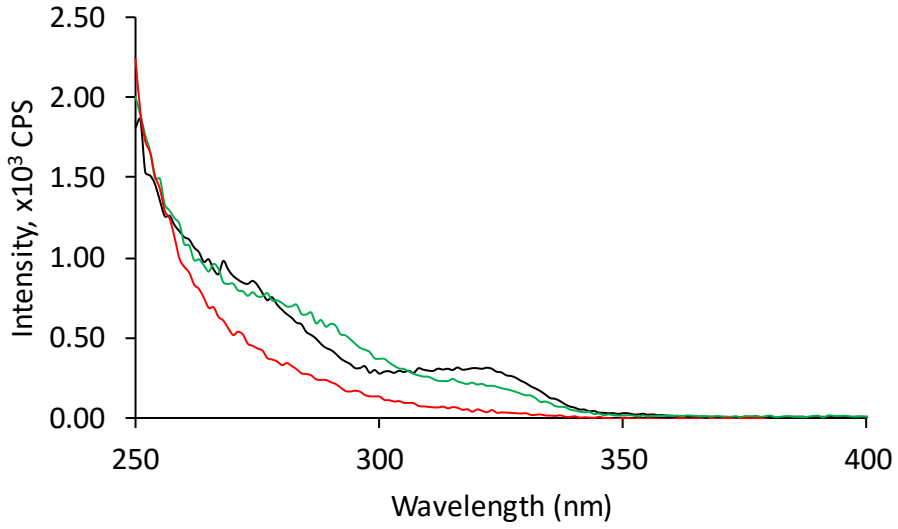


**Figure 55.** Phosphorescent excitation spectra of 0.5 mM solutions ($D_2O$, 298 K) of NdNap (**Black**), NdNap-CB[7] (**Green**), and ((NdNap-CB[7]) + $MV^{2+}$) (**Red**). Experimental Parameters: $\lambda_{em}$ = 1060 nm, excitation slit width = 5 nm, emission slit width = 5 nm, PMT Voltage (V) = 500, CAT 10.

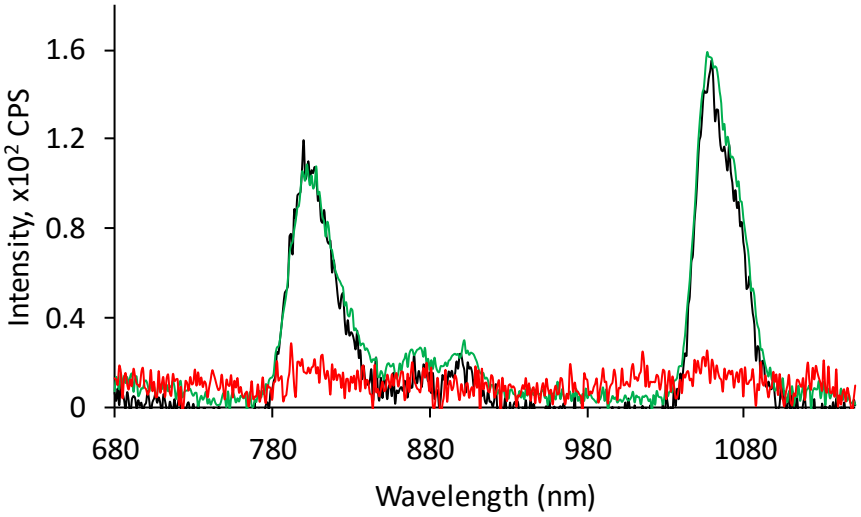


**Figure 56.** Phosphorescent emission spectra of 0.5 mM solutions ($D_2O$, 298 K) of NdNap (**Black**), NdNap-CB[7] (**Green**), and ((NdNap-CB[7]) + $MV^{2+}$) (**Red**). Experimental Parameters: $\lambda_{ex}$= 323 nm, excitation slit width = 5 nm, emission slit width = 5 nm, PMT Voltage (V) = 500, CAT 10.

## 8.14 – Characterisation of Heteroternary Charge Transfer Complexes by UV-Vis Spectroscopy

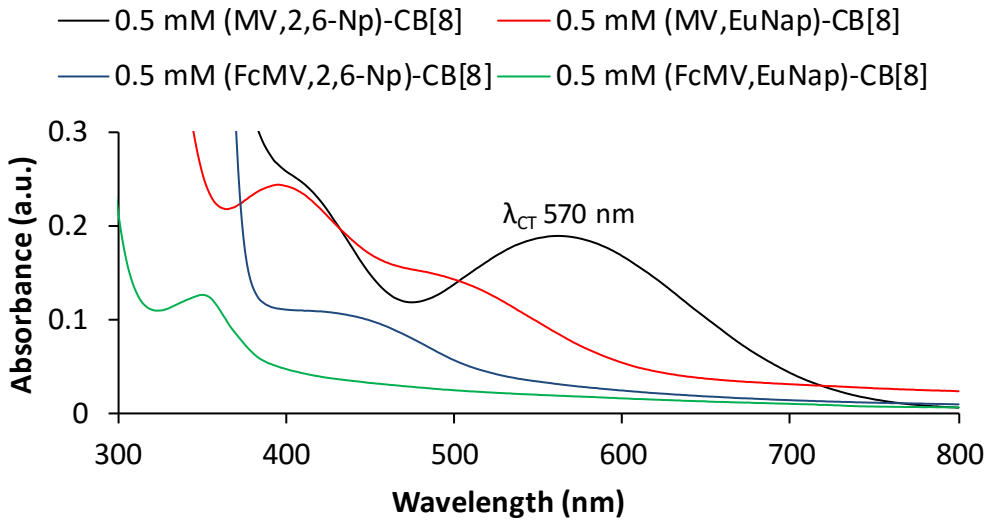


**Figure 57.** Absorption spectra of 0.5 mM solutions (aqueous, 298 K) of ($MV^{2+}$, 2,6-Np)-CB[8] (**Black**), ($MV^{2+}$, EuNap)-CB[8] (**Red**), (FcMV, 2,6-Np)-CB[8] (**Blue**) and (FcMV, EuNap)-CB[8] (**Green**).

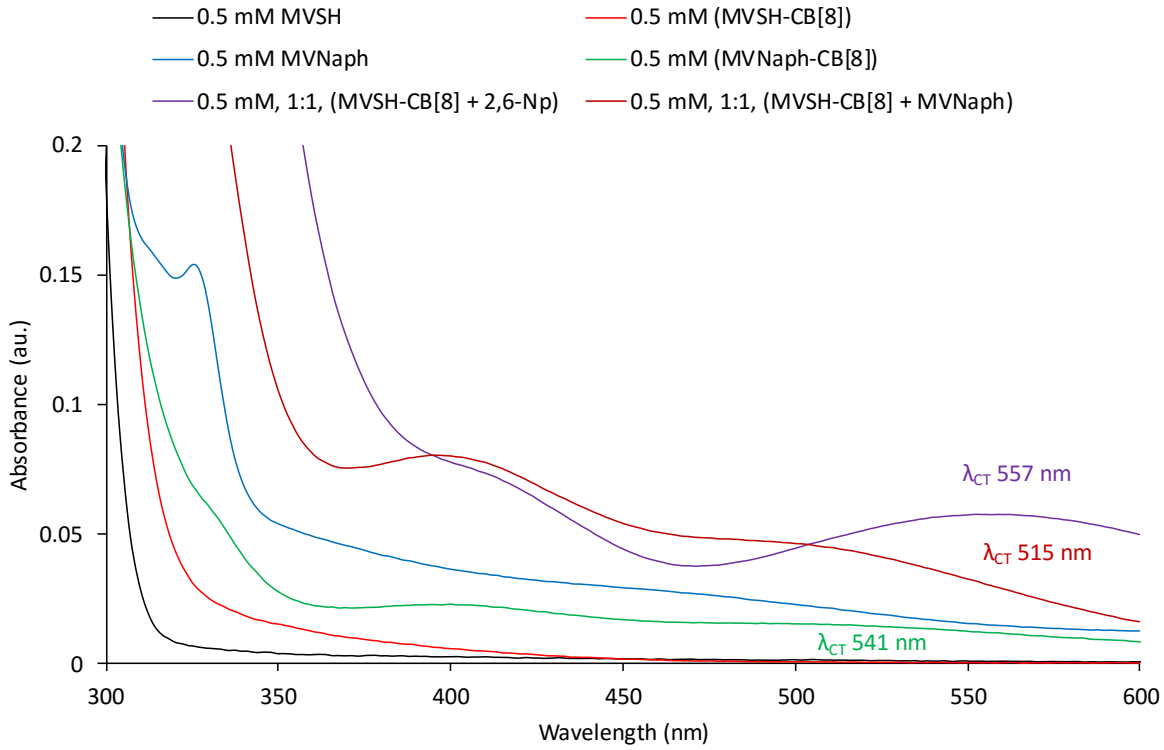


**Figure 58.** Absorption spectra of 0.5 mM solutions (aqueous, 298 K) containing 1-(10-mercaptodecyl)-1'-methyl-[4,4'-bipyridine]-diium bromide or 1-methyl-1'-(10-(naphthalen-2-yloxy)decyl)-[4,4'-bipyridine]-1,1'-diium bromide iodide.

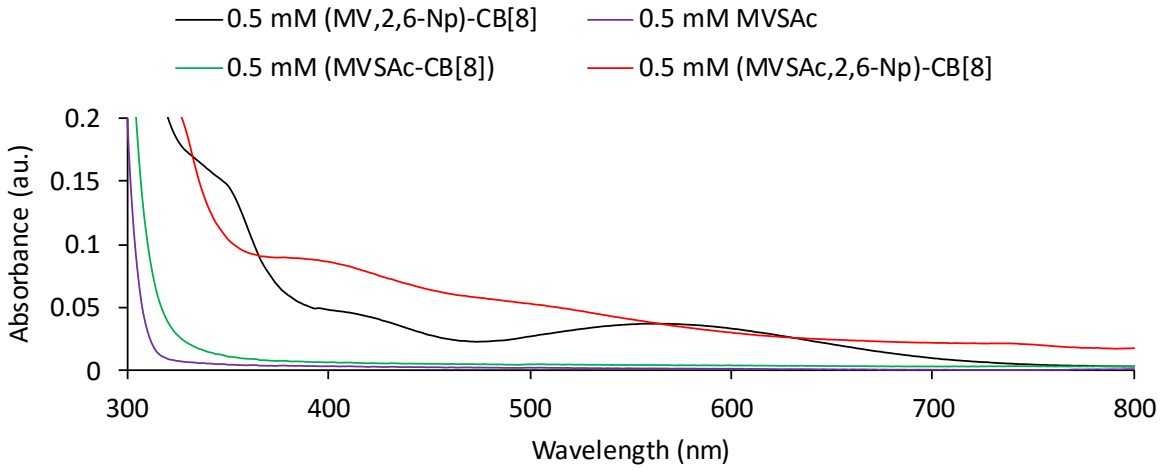


**Figure 59.** Absorption spectra of 0.5 mM solutions (aqueous, 298 K) of ($MV^{2+}$, 2,6-Np)-CB[8] (**Black**), MVSAc (**Purple**), (MVSAc-CB[8]) (**Green**) and (MVSAc, 2,6-Np)-CB[8] (**Red**).

## 8.15 – Characterisation of (FcMV, EuNap)-CB[8]

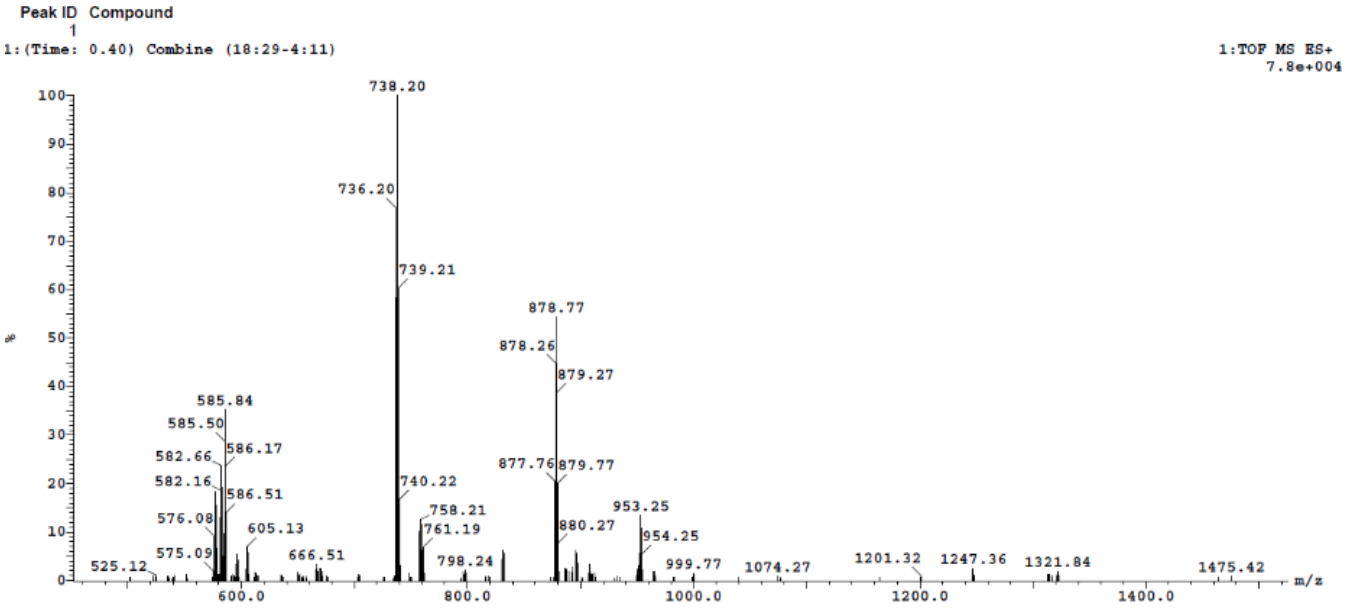


**Figure 60.** MS spectrum of a solution (2 mM, aq., 298 K) of (FcMV, EuNap)-CB[8].

## 8.16 – Recruitment of Fc-Appended Derivatives at CB[7]-Modified Au Electrodes

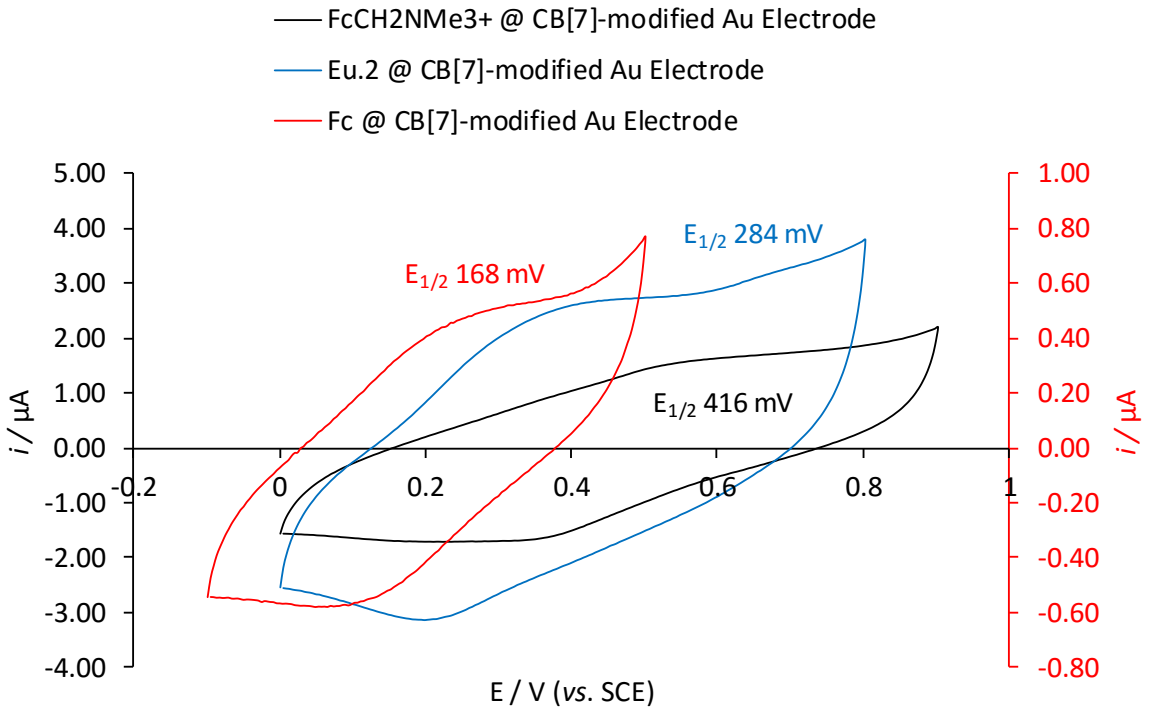


**Figure 61.** Cyclic voltammograms following the recruitment of $FcCH_2NMe_3^+$ (**Black**), Eu.2 (**Blue**) and Fc (**Red**) at CB[7]-functionalised Au electrodes. Electrochemical Setup: *Working Electrode*: CB[7]-functionalised Au . *Reference Electrode*: SCE. *Auxiliary Electrode*: Pt wire. *Electrolytic Solution*: 0.1 M $NaClO_4$ (aqueous, 298 K). *Scan Rate:* 100 mV / s.

## 8.17 – Quantifying the Level of Non-Specific Adsorption of Eu.2 and $FcCH_2NH_2$ at Bare Au

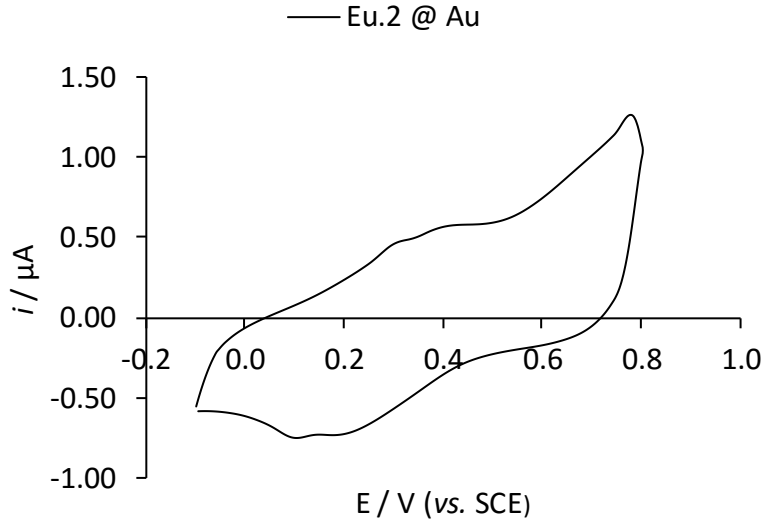


**Figure 62.** Cyclic voltammogram of a bare Au surface following exposure to a 1 mM solution (aqueous, 298 K) of Eu.2. Electrochemical Setup: *Working Electrode*: Au. *Reference Electrode*: SCE. *Auxiliary Electrode*: Pt wire. *Electrolytic Solution*: 0.1 M $NaClO_4$ (aqueous, 298 K). *Scan Rate:* 100 mV / s.

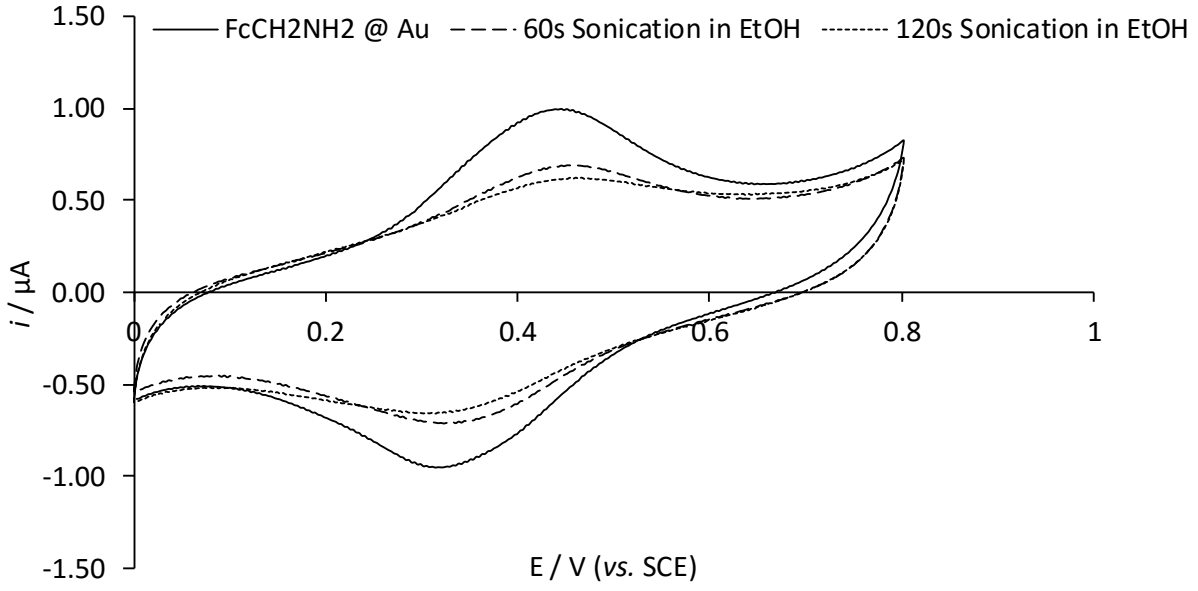


**Figure 63.** Cyclic voltammogram of a bare Au surface following exposure to a 1 mM solution (EtOH, 298 K, 12 h) of $FcCH_2NH_2$, prior to (solid) and following sonication in EtOH for 60 (- - -) and 120 s (---). Electrochemical Setup: *Working Electrode*: Bare Au. *Reference Electrode*: SCE. *Auxiliary Electrode*: Pt wire. *Electrolytic Solution*: 0.1 M $NaClO_4$ (aqueous, 298 K). *Scan Rate:* 100 mV / s.

## **8.18** – Spectroscopic Characterisation of Eu.2

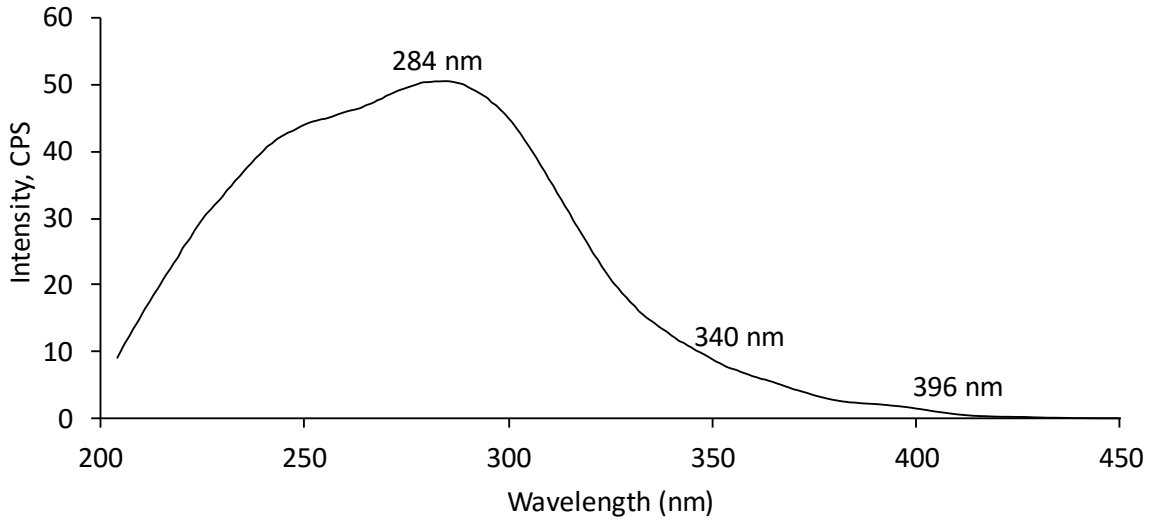


**Figure 64.** Phosphorescent excitation spectrum of a 1 mM solution (aqueous, 298 K) of Eu.2. Experimental Parameters: $\lambda_{em}$ = 616 nm, excitation slit width = 20 nm, emission slit width = 20 nm, PMT Voltage (V) = 1000, CAT 30, number of flashes = 1, total decay time = 0.020 ms, delay time = 0.2 ms, gate time = 1 ms.

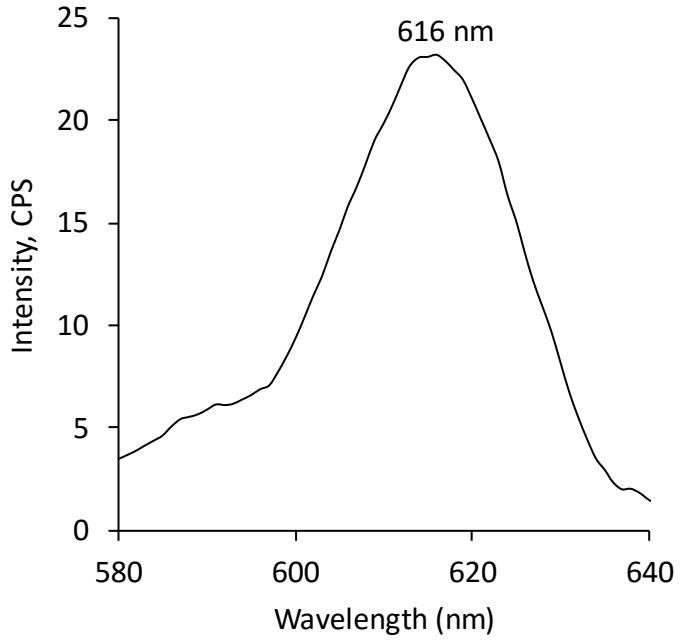


**Figure 65.** Phosphorescent emission spectrum of a 1 mM solution (aqueous, 298 K) of Eu.2. Experimental Parameters: $\lambda_{ex}$ = 340 nm, excitation slit width = 20 nm, emission slit width = 20 nm, PMT Voltage (V) = 1000, CAT 30, number of flashes = 1, total decay time = 0.020 ms, delay time = 0.1 ms, gate time = 1 ms.

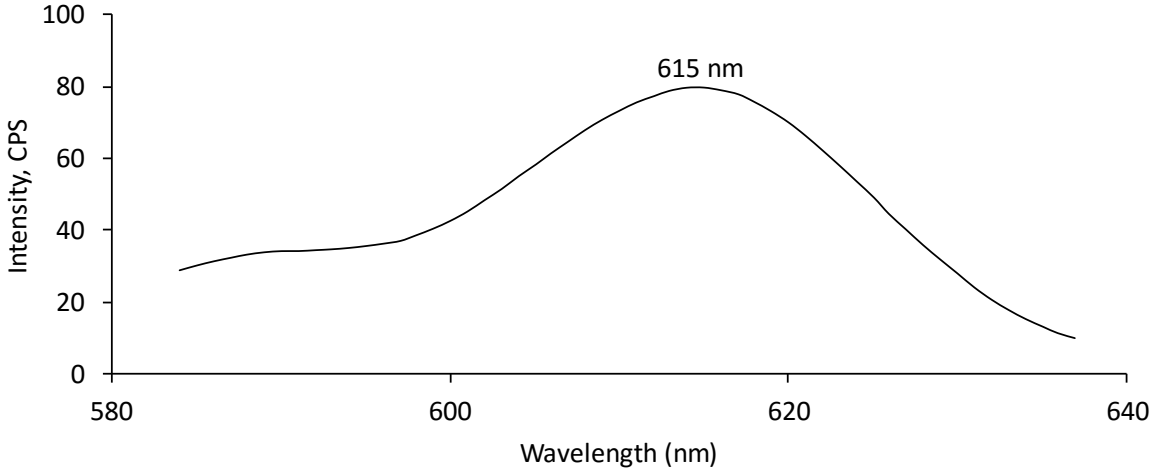


**Figure 66.** Phosphorescent emission spectrum of a 1 mM solution (aqueous, 298 K) of Eu.2. Experimental Parameters: $\lambda_{ex}$ = 280 nm, excitation slit width = 20 nm, emission slit width = 20 nm, PMT Voltage (V) = 1000, CAT 30, number of flashes = 1, total decay time = 0.020 ms, delay time = 0.1 ms, gate time = 0.5 ms.

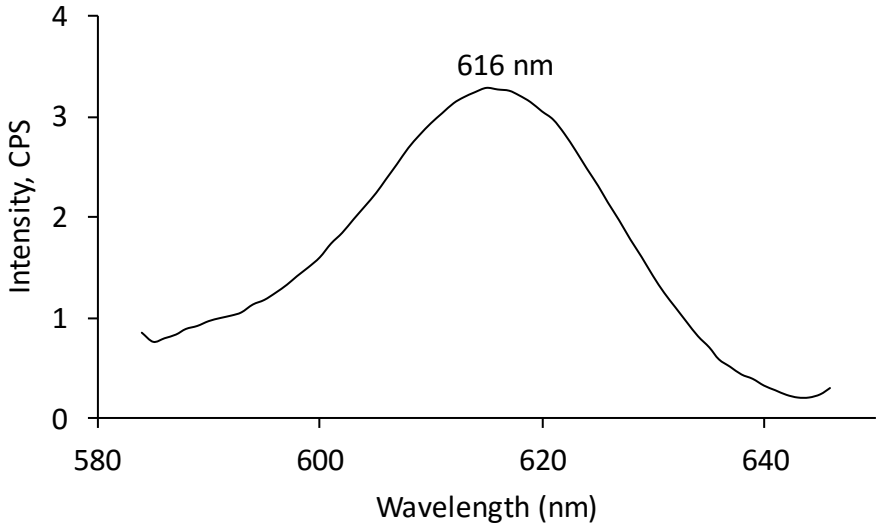


**Figure 67.** Phosphorescent emission spectrum of a 1 mM solution (aqueous, 298 K) of Eu.2. Experimental Parameters: $\lambda_{ex}$ = 397 nm, excitation slit width = 20 nm, emission slit width = 20 nm, PMT Voltage (V) = 1000, CAT 30, number of flashes = 1, total decay time = 0.020 ms, delay time = 0.1 ms, gate time = 1.0 ms.

## **8.19** – Spectroscopic Characterisation of Eu.2-CB[7] at Au

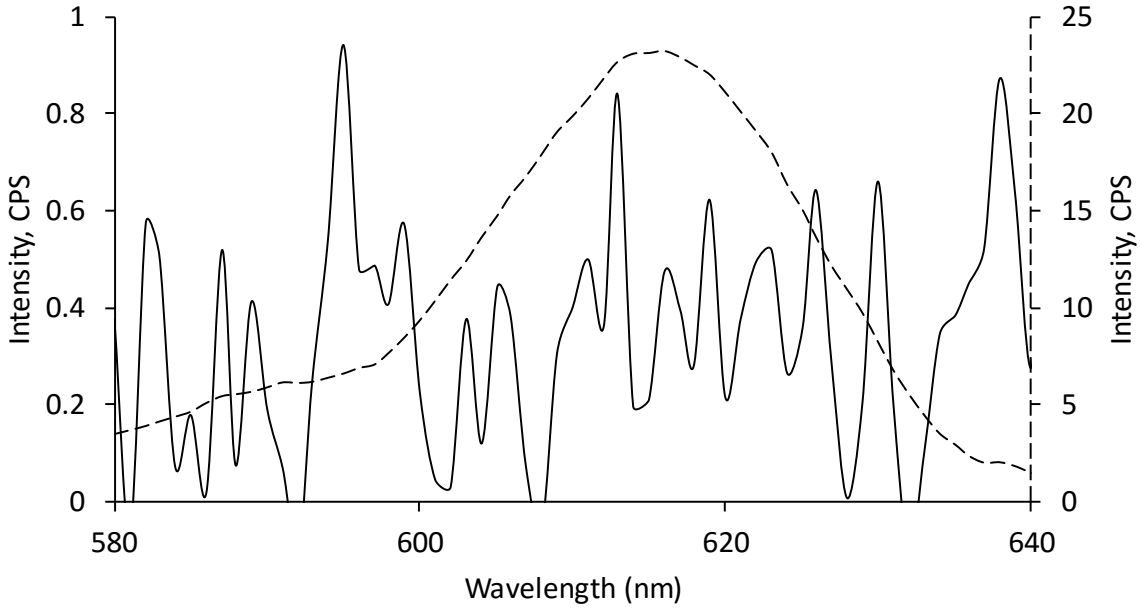


**Figure 68.** Phosphorescent emission spectrum following the recruitment of Eu.2 at a CB[7]-functionalised Au surface. The analogous solution phase spectrum (---, **Section 8.17**, **Figure 64**) is overlaid for comparison and to highlight the lack of sensitised emission at the interface. Experimental Parameters: $\lambda_{ex}$ = 340 nm, excitation slit width = 20 nm, emission slit width = 10 nm, PMT Voltage (V) = 1000, CAT 30, number of flashes = 1, total decay time = 0.020 ms, delay time = 0.2 ms, gate time = 5.0 ms.

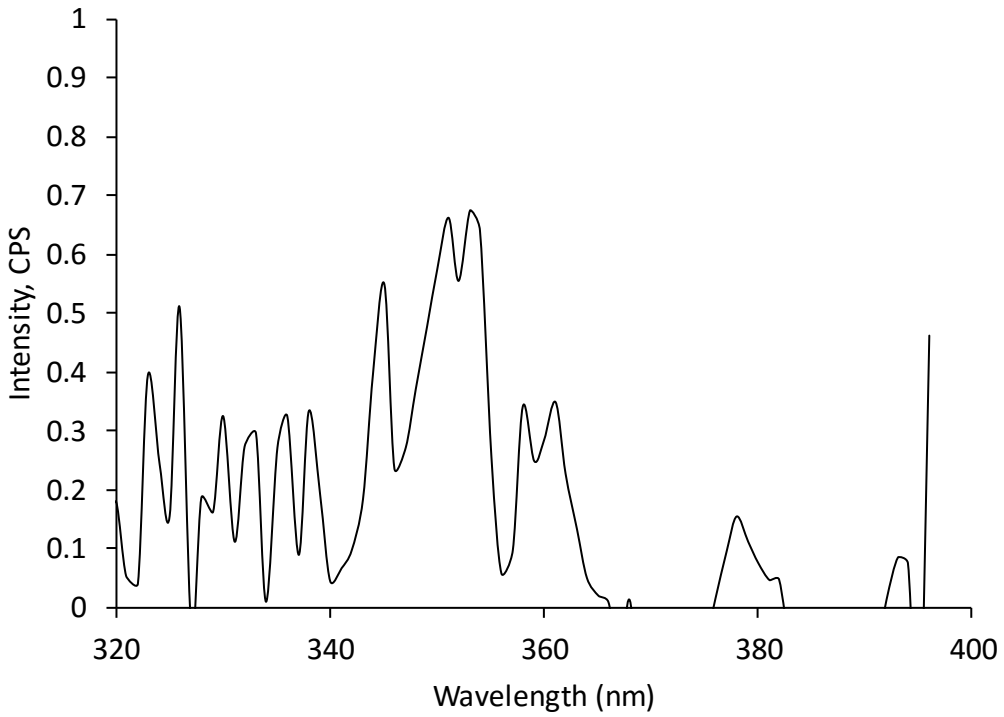


**Figure 69.** Phosphorescent excitation spectrum following the recruitment of Eu.2 at a CB[7]-functionalised Au surface. Experimental Parameters: $\lambda_{em}$ = 616 nm, excitation slit width = 10 nm, emission slit width = 20 nm, PMT Voltage (V) = 1000, CAT 30, number of flashes = 1, total decay time = 0.020 ms, delay time = 0.2 ms, gate time = 5.0 ms.

## List of References

1. R. J. Ward, B. J. Wood, *Surf. Interface Anal.*, **1992**, 18, 679–684.
2. Michael J. Blackman, John E. T. Corrie, John C. Croney, Geoff Kelly, John F. Eccleston, David M. Jameson, *Biochemistry*, **2002**, 41, 12244–12252.

## List of Figures

**Figure 1.** Cyclic voltammogram of a 5 µM solution (anhydrous, deoxygenated ($N_2$ (g), 10 min.) $CH_2Cl_2$) of AB-14-172. Electrochemical Setup: *Working Electrode*: Glassy Carbon. *Reference Electrode*: Ag / $AgNO_3$. *Auxiliary Electrode*: Pt wire. *Electrolytic Solution*: 0.1 M $TBAPF_6$ (298 K). *Scan Rate:* 100 mV / s.

**Figure 2.** Cyclic voltammogram of a 5 µM solution (anhydrous, deoxygenated ($N_2$ (g), 10 min.) $CH_2Cl_2$) of AB-14-172. Electrochemical Setup: *Working Electrode*: Bare Au. *Reference Electrode*: Ag / $AgNO_3$. *Auxiliary Electrode*: Pt wire. *Electrolytic Solution*: 0.1 M $TBAPF_6$ (298 K). *Scan Rate:* 100 mV / s.

**Figure 3.** Cyclic voltammograms of SAMs of TPAPP-MUA (**Black**), TPAPP-MHDA (**Red**), TPAPP-OEG (**Blue**) and AB-14-172 (**Green**) deposited at Au. Electrochemical Setup: *Working Electrode*: SAM. *Reference Electrode*: Ag / AgCl. *Auxiliary Electrode*: Pt wire. *Electrolytic Solution*: 0.1 M $TBAPF_6$ (anhydrous, deoxygenated ($N_2$ (g), 10 min.) $CH_2Cl_2$, 298 K). *Scan Rate:* 1000 mV / s.

**Figure 4.** Cyclic voltammograms of SAMs of Fc6 (**Black**) and Fc11 (**Red**) deposited at Au. Fc11: $Fc(CH_2)_{11}SH$. Fc6: $Fc(CH_2)_6SH$. Electrochemical Setup: *Working Electrode*: SAM. *Reference Electrode*: Ag Wire. *Auxiliary Electrode*: Pt wire. *Electrolytic Solution*: 0.1 M $TBAPF_6$ (anhydrous, deoxygenated ($N_2$ (g), 10 min.) $CH_2Cl_2$, 298 K). *Scan Rate:* 1000 mV / s.

**Figure 5.** Cyclic voltammograms of SAMs of TPAPP-MUA-Fc6 (**Black**) and TPAPP-MUA-Fc11 (**Red**) deposited at Au. Fc11: $Fc(CH_2)_{11}SH$. Fc6: $Fc(CH_2)_6SH$. Electrochemical Setup: *Working Electrode*: SAM. *Reference Electrode*: Ag Wire. *Auxiliary Electrode*: Pt wire. *Electrolytic Solution*: 0.1 M $TBAPF_6$ (anhydrous, deoxygenated ($N_2$ (g), 10 min.) $CH_2Cl_2$, 298 K). *Scan Rate:* 1000 mV / s.

**Figure 6.** Cyclic voltammograms of SAMs of TPAPP-MHDA-Fc6 (**Black**) and TPAPP-MHDA-Fc11 (**Red**) deposited at Au. Fc11: $Fc(CH_2)_{11}SH$. Fc6: $Fc(CH_2)_6SH$. Electrochemical Setup: *Working Electrode*: SAM. *Reference Electrode*: Ag Wire. *Auxiliary Electrode*: Pt wire. *Electrolytic Solution*: 0.1 M $TBAPF_6$ (anhydrous, deoxygenated ($N_2$ (g), 10 min.) $CH_2Cl_2$, 298 K). *Scan Rate:* 1000 mV / s.

**Figure 7.** Cyclic voltammograms of SAMs of TPAPP-OEG-Fc6 (**Black**) and TPAPP-OEG-Fc11 (**Red**) deposited at Au. Fc11: $Fc(CH_2)_{11}SH$. Fc6: $Fc(CH_2)_6SH$. Electrochemical Setup: *Working Electrode*: SAM. *Reference Electrode*: Ag Wire. *Auxiliary Electrode*: Pt wire. *Electrolytic Solution*: 0.1 M $TBAPF_6$ (anhydrous, deoxygenated ($N_2$ (g), 10 min.) $CH_2Cl_2$, 298 K). *Scan Rate:* 1000 mV / s.

**Figure 8.** Cyclic voltammograms of SAMs of AB-14-172-OEG-Fc6 (**Black**) and AB-14-172-OEG-Fc11 (**Red**) deposited at Au. Fc11: $Fc(CH_2)_{11}SH$. Fc6: $Fc(CH_2)_6SH$. Electrochemical Setup: *Working Electrode*: SAM. *Reference Electrode*: Ag Wire. *Auxiliary Electrode*: Pt wire. *Electrolytic Solution*: 0.1 M $TBAPF_6$ (anhydrous, deoxygenated ($N_2$ (g), 10 min.) $CH_2Cl_2$, 298 K). *Scan Rate:* 1000 mV / s.

**Figure 9.** XPS spectrum (**Top Left**) of a SAM of MUA deposited at Au. Narrow scan spectra were recorded in the Au 4f (**Top Right**), O 1s (**Middle Left**), C 1s (**Middle Right**), S 2p (**Bottom Left**) and N 1s (**Bottom Right**) regions, and the relative % of each element present at the surface calculated (**Table 3**).

**Figure 10.** XPS spectrum (**Top Left**) of the SAM obtained upon covalent attachment of TPAPP to MUA deposited at Au. Narrow scan spectra were recorded in the Au 4f (**Top Right**), O 1s (**Middle Left**), C 1s (**Middle Right**), S 2p (**Bottom Left**) and N 1s (**Bottom Right**) regions, and the relative % of each element present at the surface calculated (**Table 4**).

**Figure 11.** XPS spectrum (**Top Left**) of the SAM obtained upon covalent attachment of AB-14-172 to OEG deposited at Au. Narrow scan spectra were recorded in the Au 4f (**Top Right**), C 1s (**Middle Left**), N 1s (**Middle Right**), O 1s (**Bottom Left**) and Ni 2p (**Bottom Right**) regions, and the relative % of each element present at the surface calculated (**Table 5**).

**Figure 12.** XPS spectrum (**Top Left**) of the SAM obtained upon covalent attachment of AB-14-172 to OEG deposited at Au. Narrow scan spectra were recorded in the Au 4f (**Top Right**), C 1s (**Middle Left**), N 1s (**Middle Right**), O 1s (**Bottom Left**) and Ni 2p (**Bottom Right**) regions, and the relative % of each element present at the surface calculated (**Table 6**).

**Figure 13.** XPS spectrum (**Top Left**) of the SAM obtained upon the attempted covalent attachment of AB-14-172 to an unactivated (No EDC / NHS was used) SAM of OEG deposited at Au. Narrow scan spectra were recorded in the Au 4f (**Top Right**), C 1s (**Middle Left**), N 1s (**Middle Right**), O 1s (**Bottom Left**) and Ni 2p (**Bottom Right**) regions, and the relative % of each element present at the surface calculated (**Table 7**).

**Figure 14.** Cathodic photocurrent densities acquired at monophasic, porphyrin-appended SAMs generated at Au. All cathodic photocurrents were measured in 0.1 M $Na_2SO_4$ (aq.) containing 5 mM $MV^{2+}$ as an electron acceptor. The electrodes were kept at – 100 mV (*vs.* Ag / AgCl), illuminated with light of wavelength 425 – 435 nm and the photocurrents normalised for the concentration of porphyrin present at each interface, as determined by cyclic voltammetry. Each error bar is equivalent to 3SD and calculated from the data acquired across four separately prepared electrodes.

**Figure 15.** Cathodic photocurrent densities acquired at a SAM of TPAPP-MUA deposited at Au, prior to and following the additions of 5 mM $MV^{2+}$ and 1 mM FcD ($FcCH_2NMe_3^+$) to the electrolytic solution. All cathodic photocurrents were measured in 0.1 M $Na_2SO_4$ (aq.) whilst the electrodes were kept at – 100 mV (*vs.* Ag / AgCl), illuminated with light of wavelength 430 ± 5 nm and the photocurrents normalised for the concentration of porphyrin present at the interface, as determined by cyclic voltammetry (**Appendix, 8.1.2**). Each error bar is equivalent to 3SD and calculated from the data acquired across four separately prepared electrodes. Electrochemical Cell Setup: *Working Electrode*: TPAPP-MUA. *Reference Electrode*: Ag / AgCl. *Auxiliary Electrode*: Pt Wire. *Electrolytic Solution*: 0.1 M $Na_2SO_4$, (+ 5 mM $MV^{2+}$, + 1 mM FcD ($FcCH_2NMe_3^+$)). *Solvent*: $H_2O$. *Bias Potential*: - 100 mV. $\lambda_{irr}$: 430 ± 5 nm.

**Figure 16.** Manipulating the cathodic photocurrent density acquired at a SAM of TPAPP-MUA deposited at Au by varying the bias potential of the working electrode. All cathodic photocurrents were measured in 0.1 M $Na_2SO_4$ (aq.) containing 5 mM $MV^{2+}$ as an electron acceptor. The electrodes were illuminated with light of wavelength 430 ± 5 nm and the photocurrents normalised for the concentration of porphyrin present at the interface, as determined by cyclic voltammetry (**Appendix, 8.1.2**). Each error bar is equivalent to 3SD and calculated from the data acquired across four separately prepared electrodes. Electrochemical Cell Setup: *Working Electrode*: TPAPP-MHDA. *Reference Electrode*: Ag / AgCl. *Auxiliary Electrode*: Pt Wire. *Electrolytic Solution*: 0.1 M $Na_2SO_4$, + 5 mM $MV^{2+}$, + 1 mM $FcCH_2NMe_3^+$. *Solvent*: $H_2O$. *Bias Potential*: Variable. $\lambda_{irr}$: 430 ± 5 nm.

**Figure 17.** Current *vs.* time profiles for a gold electrode at which a SAM of TPAPP-MUA had been generated. All profiles were measured in 0.1 M $Na_2SO_4$ (aq.) containing 5 mM $MV^{2+}$ as an electron acceptor. The electrode was kept at either + 200 mV (**Blue**), – 100 mV (**Red**) or – 200 mV (**Black**) (*vs.* Ag / AgCl) and illuminated with light of wavelength 425 - 435 nm. The differences in current (dark ('OFF') and light ('ON')) observed (**Table 8**) were used to quantify the photoelectrochemical outputs.

**Figure 18.** Cathodic photocurrent densities acquired at biphasic, porphyrin-appended SAMs deposited at Au. All cathodic photocurrents were measured in 0.1 M $Na_2SO_4$ (aq.) containing 5 mM $MV^{2+}$ as an electron acceptor. Fc11: $Fc(CH_2)_{11}SH$. Fc6: $Fc(CH_2)_6SH$. The electrodes were kept at – 100 mV (*vs.* Ag / AgCl), illuminated with light of wavelength 430 ± 5 nm and the photocurrents normalised for the concentration of porphyrin present at each interface, as determined by cyclic voltammetry (**Appendix, 8.1.3**). Each error bar is equivalent to 3SD and calculated from the data acquired across three separately prepared electrodes.

**Figure 19.** Manipulating the cathodic photocurrent density acquired at a SAM of AB-14-172-OEG-$Fc(CH_2)_{11}SH$ deposited at Au by varying the bias potential of the working electrode. All cathodic photocurrents were measured in 0.1 M $Na_2SO_4$ (aq.) containing 5 mM $MV^{2+}$ as an electron acceptor. The electrodes were illuminated with light of wavelength 430 ± 5 nm and the photocurrents normalised for the concentration of porphyrin present at the interface, as determined by cyclic voltammetry (**Appendix, 8.1.3**). Each error bar is equivalent to 3SD and calculated from the data acquired across three separately prepared electrodes.

**Figure 20.** Current *vs.* time profiles for a Au electrode at which a SAM of AB-14-172-OEG-$Fc(CH_2)_{11}SH$ had been deposited. All profiles were measured in 0.1 M $Na_2SO_4$ (aq.) containing 5 mM $MV^{2+}$ as an electron acceptor. The electrode was kept at either 0 mV (**Black**), – 100 mV (**Red**) or – 200 mV (**Blue**) and illuminated with light of wavelength 430 ± 5 nm. Electrochemical Cell Setup: *Working Electrode*: PEG-AB-14-172-$Fc(CH_2)_{11}SH$. *Reference Electrode*: Ag / AgCl. *Auxiliary Electrode*: Pt Wire. *Electrolytic Solution*: 0.1 M $Na_2SO_4$ + 5 mM $MV^{2+}$. *Solvent*: $H_2O$. *Bias Potential*: Variable. The differences in current (dark ('OFF') and light ('ON')) observed (**Table 9**) were used to quantify the photoelectrochemical outputs.

**Figure 21.** Cathodic photocurrent densities acquired at monophasic and biphasic porphyrin-appended SAMs deposited at Au. All cathodic photocurrents were measured in 0.1 M $Na_2SO_4$ (aq.) containing 5 mM $MV^{2+}$ as an electron acceptor. Fc11: $Fc(CH_2)_{11}SH$. Fc6: $Fc(CH_2)_6SH$. The electrodes were kept at – 100 mV (*vs.* Ag / AgCl), illuminated with light of wavelength 430 ± 5 nm and the photocurrents normalised for

the concentration of porphyrin present at each interface, as determined by cyclic voltammetry (**Appendix, 8.1.2 and 8.1.3**). Each error bar is equivalent to 3SD and calculated from the data acquired across three (biphasic) or four (monophasic) separately prepared electrodes.

**Figure 22.** XPS spectrum (**Top Left**) of the SAM obtained upon covalent attachment of AB-14-172 to OEG deposited at Au. Narrow scan spectra were recorded in the C 1s (**Top Right**), Ni 2p (**Bottom Left**) and O 1s (**Bottom Right**) regions, and the relative % of each element present at the surface calculated (**Table 10**).

**Figure 23.** XPS spectrum (**Top Left**) of the SAM obtained upon the attempted covalent attachment of (AB-14-172-JL241) to OEG deposited at Au. Narrow scan spectra were recorded in the C 1s (**Top Right**), Ni 2p (**Bottom Left**) and O 1s (**Bottom Right**) regions, and the relative % of each element present at the surface calculated (**Table 11**). A narrow scan spectrum in the N 1s region (392 – 404 eV) was not obtained.

**Figure 24.** XPS spectrum (**Top Left**) of the SAM obtained upon the attempted covalent attachment of (AB-14-172-JL241) to OEG deposited at Au. Narrow scan spectra were recorded in the C 1s (**Top Right**), Ni 2p (**Bottom Left**) and O 1s (**Bottom Right**) regions, and the relative % of each element present at the surface calculated (**Table 12**). A narrow scan spectrum in the N 1s region (392 – 404 eV) was not obtained.

**Figure 25.** XPS spectrum (**Top Left**) of the SAM obtained upon the attempted covalent attachment of (AB-14-172-JL241) to an unactivated (No EDC / NHS was used) SAM of OEG deposited at Au. Narrow scan spectra were recorded in the C 1s (**Top Right**), Ni 2p (**Bottom Left**) and O 1s (**Bottom Right**) regions, and the relative % of each element present at the surface calculated (**Table 13**). A narrow scan spectrum in the N 1s region (392 – 404 eV) was not obtained.

**Figure 26.** XPS spectrum (**Top Left**) of the SAM obtained upon the deposition of AB-19-144 at Au. Narrow scan spectra were recorded in the C 1s (**Middle Left**), Ni 2p (**Middle Right**), S 2p (**Bottom Left**) and Au 4f (**Bottom Right**) regions. A narrow scan spectrum in the N 1s region (392 – 404 eV) was not obtained. The relative % of each element present at the surface was calculated (**Table 14**).

**Figure 27.** XPS spectrum (**Top Left**) of the SAM obtained upon the deposition of AB-19-144 at Au. Narrow scan spectra were recorded in the C 1s (**Middle Left**), Ni 2p (**Middle Right**), S 2p (**Bottom Left**) and Au 4f (**Bottom Right**) regions. A narrow scan spectrum in the N 1s region (392 – 404 eV) was not obtained. The relative % of each element present at the surface was calculated (**Table 15**).

**Figure 28.** Current *vs.* time profiles for gold electrodes modified with SAMs of AB-14-172–OEG (**Blue**), AB-14-172–OEG–Fc11 (**Red**) and (AB-14-172-JL241)–OEG (**Black**). All profiles were measured in 0.1 M $Na_2SO_4$ (aq.) containing 5 mM $MV^{2+}$ as an electron acceptor. The electrodes were kept at – 100 mV (*vs.* Ag / AgCl) and illuminated with light of wavelength 425 – 435 nm. The differences in current (dark ('OFF') and light ('ON')) observed (**Table 16**) were used to quantify the photoelectrochemical outputs.

**Figure 29.** Current *vs.* time profiles for gold electrodes exposed to µM solutions (anhydrous $CH_2Cl_2$) of AB-18-088 (**Black**) and AB-18-088–Fc11 (**Red**). Both profiles were measured in 0.1 M $Na_2SO_4$ (aq.) containing 5 mM $MV^{2+}$ as an electron acceptor. The electrodes were kept at – 100 mV (*vs.* Ag / AgCl) and illuminated with light of wavelength 425 – 435 nm.

**Figure 30.** Current *vs.* time profiles for a gold electrode at which AB-19-144 had been deposited, prior to (**Black**) and following the addition of 1mM FcMeOH (**Red**) into solution. Both profiles were measured in 0.1 M $Na_2SO_4$ (aq.) containing 5 mM $MV^{2+}$ as an electron acceptor. The electrode was kept at – 100 mV (*vs.* Ag / AgCl) and illuminated with light of wavelength 425 - 435 nm.

**Figure 31.** Absorption spectra of 5 µM solutions (anhydrous $CH_2Cl_2$) of free base (**Blue**), Ni(II)-coordinated (**Burgundy**), and triazolium-incorporated (**Orange**) porphyrin derivatives.

**Figure 32.** Phosphorescent excitation spectrum of a 0.5 mM solution (aqueous, 298 K) of EuNap. Experimental Parameters: $\lambda_{em}$ = 616 nm, excitation slit width = 5 nm, emission slit width = 14 nm, PMT Voltage (V) = 500, CAT 10.

**Figure 33.** Luminescence decay of a 0.5 mM solution (aqueous, 298 K) of EuNap. **Inset.** Experimental parameters.

**Figure 34.** Luminescence decay of a 0.5 mM solution (aqueous, 298 K) of EuNap following the addition of 1 equivalent of $MV^{2+}$. **Inset.** Experimental parameters.

**Figure 35.** Phosphorescent excitation spectrum of a 0.5 mM solution (aqueous, 298 K) of ($MV^{2+}$, EuNap)-CB[8]. **Inset.** Experimental parameters.

**Figure 36.** Luminescence decay of a 0.5 mM solution (aqueous, 298 K) of ($MV^{2+}$, EuNap)-CB[8]. Decay monitored at $\lambda_{em}$ 616 nm under $\lambda_{ex}$ 227 nm. **Inset.** Experimental parameters.

**Figure 37.** Luminescence decay of a 0.5 mM solution (aqueous, 298 K) of ($MV^{2+}$, EuNap)-CB[8]. Decay monitored at $\lambda_{em}$ 616 nm under $\lambda_{ex}$ 396 nm. **Inset.** Experimental parameters.

**Figure 38.** Luminescence decay of a 0.5 mM solution (aqueous, 298 K) of EuNap. **Inset.** Experimental parameters.

**Figure 39.** Luminescence decay of a 0.5 mM solution (aqueous, 298 K) of ($MV^{2+}$, EuNap)-CB[8]. Decay monitored at $\lambda_{em}$ 616 nm under $\lambda_{ex}$ 227 nm. **Inset.** Experimental parameters.

**Figure 40.** Luminescence decay of a 0.5 mM solution (aqueous, 298 K) of ($MV^{2+}$, EuNap)-CB[8]. Decay monitored at $\lambda_{em}$ 616 nm under $\lambda_{ex}$ 227 nm following the addition of 1equivalent of $Na_2S_2O_4$. **Inset.** Experimental parameters.

**Figure 41.** Phosphorescent emission spectra of 0.5 mM solutions ($D_2O$, 298 K) of ($MV^{2+}$, EuNap)-CB[8] (**Black**) and (NAMV, EuNap)-CB[8] (**Red**). Experimental Parameters: $\lambda_{ex}$ = 397 nm, excitation slit width = 5 nm, emission slit width = 1 nm, PMT Voltage (V) = 500, CAT 10.

**Figure 42.** Phosphorescent excitation spectra of 0.5 mM solutions ($D_2O$, 298 K) of ($MV^{2+}$, EuNap)-CB[8] (**Black**) and (NAMV, EuNap)-CB[8] (**Red**). Experimental Parameters: $\lambda_{em}$ = 616 nm, excitation slit width = 5 nm, emission slit width = 14 nm, PMT Voltage (V) = 500, CAT 10.

**Figure 43.** Luminescence decay of a 0.5 mM solution ($D_2O$, 298 K) of ($MV^{2+}$, EuNap)-CB[8]. **Inset.** Experimental parameters.

**Figure 44.** Luminescence decay of a 0.5 mM solution ($D_2O$, 298 K) of (NAMV, EuNap)-CB[8]. **Inset.** Experimental parameters.

**Figure 45.** Phosphorescent excitation spectra of 0.5 mM solutions ($D_2O$, 298 K) of YbNap (**Black**) and ($MV^{2+}$, YbNap)-CB[8] (**Red**). Experimental Parameters: $\lambda_{em}$ = 1040 nm, excitation slit width = 5 nm, emission slit width = 5 nm, PMT Voltage (V) = 500, CAT 10.

**Figure 46.** Phosphorescent emission spectra of 0.5 mM solutions ($D_2O$, 298 K) of YbNap (**Black**) and ($MV^{2+}$, YbNap)-CB[8] (**Red**). Experimental Parameters: $\lambda_{ex}$= 320 and 325 nm, excitation slit width = 5 nm, emission slit width = 5 nm, PMT Voltage (V) = 500, CAT 10.

**Figure 47.** Fluorescent emission spectra of 0.5 mM solutions ($D_2O$, 298 K) of YbNap (**Black**) and ($MV^{2+}$, YbNap)-CB[8] (**Red**). Experimental Parameters: $\lambda_{ex}$= 270 nm, excitation slit width = 10 nm, emission slit width = 5 nm, PMT Voltage (V) = 500, CAT 10.

**Figure 48.** Phosphorescent excitation spectrum of a 0.5 mM solution ($D_2O$, 298 K) of NdNap. Experimental Parameters: $\lambda_{em}$ = 1060 nm, excitation slit width = 5 nm, emission slit width = 5 nm, PMT Voltage (V) = 500, CAT 10.

**Figure 49.** Fluorescent emission spectra of 0.5 mM solutions ($D_2O$, 298 K) of NdNap (**Black**) and ($MV^{2+}$, NdNap)-CB[8] (**Red**). Experimental Parameters: $\lambda_{ex}$= 270 nm, excitation slit width = 10 nm, emission slit width = 5 nm, PMT Voltage (V) = 500, CAT 10.

**Figure 50.** Phosphorescent emission spectra of a 0.5 mM solution ($D_2O$, 298 K) of ($MV^{2+}$, NdNap)-CB[8] following the **removal** (10 min., $N_2$ (g)) and subsequent **addition** of oxygen ($O_2$ (g), 60 min. exposure to air) to the solution. Experimental Parameters: $\lambda_{ex}$= 323 nm, excitation slit width = 5 nm, emission slit width = 5 nm, PMT Voltage (V) = 500, CAT 10.

**Figure 51.** Phosphorescent excitation spectra of a 0.5 mM solution ($D_2O$, 298 K) of NdNap-CB[7] following the **removal** (10 min., $N_2$ (g)) and subsequent **addition** of oxygen ($O_2$ (g), 60 min. exposure to air) to the solution. Experimental Parameters: $\lambda_{em}$ = 1060 nm, excitation slit width = 5 nm, emission slit width = 5 nm, PMT Voltage (V) = 500, CAT 10.

**Figure 52.** Phosphorescent emission spectra of a 0.5 mM solution ($D_2O$, 298 K) of NdNap-CB[7] following the **removal** (10 min., $N_2$ (g)) and subsequent **addition** of oxygen ($O_2$ (g), 60 min. exposure to air) to the solution. Experimental Parameters: $\lambda_{ex}$= 323 nm, excitation slit width = 5 nm, emission slit width = 5 nm, PMT Voltage (V) = 500, CAT 10.

**Figure 53.** Phosphorescent excitation spectrum of a 0.5 mM solution ($D_2O$, 298 K) of NdNap-CB[7] following the removal of $O_2$ (g) (10 min., $N_2$ (g)) and the addition of 1 equivalent of $MV^{2+}$ to the solution. Experimental Parameters: $\lambda_{em}$ = 1060 nm, excitation slit width = 5 nm, emission slit width = 5 nm, PMT Voltage (V) = 500, CAT 10.

**Figure 54.** Phosphorescent emission spectra of a 0.5 mM solution ($D_2O$, 298 K) of ((NdNap-CB[7]) + $MV^{2+}$) following the **removal** (10 min., $N_2$ (g)) and subsequent **addition** of oxygen ($O_2$ (g), 60 min. exposure to air) to the solution. Experimental Parameters: $\lambda_{ex}$= 323 nm, excitation slit width = 5 nm, emission slit width = 5 nm, PMT Voltage (V) = 500, CAT 10.

**Figure 55.** Phosphorescent excitation spectra of 0.5 mM solutions ($D_2O$, 298 K) of NdNap (**Black**), NdNap-CB[7] (**Green**), and ((NdNap-CB[7]) + $MV^{2+}$) (**Red**). Experimental Parameters: $\lambda_{em}$ = 1060 nm, excitation slit width = 5 nm, emission slit width = 5 nm, PMT Voltage (V) = 500, CAT 10.

**Figure 56.** Phosphorescent emission spectra of 0.5 mM solutions ($D_2O$, 298 K) of NdNap (**Black**), NdNap-CB[7] (**Green**), and ((NdNap-CB[7]) + $MV^{2+}$) (**Red**). Experimental Parameters: $\lambda_{ex}$= 323 nm, excitation slit width = 5 nm, emission slit width = 5 nm, PMT Voltage (V) = 500, CAT 10.

**Figure 57.** Absorption spectra of 0.5 mM solutions (aqueous, 298 K) of ($MV^{2+}$, 2,6-Np)-CB[8] (**Black**), ($MV^{2+}$, EuNap)-CB[8] (**Red**), (FcMV, 2,6-Np)-CB[8] (**Blue**) and (FcMV, EuNap)-CB[8] (**Green**).

**Figure 58.** Absorption spectra of 0.5 mM solutions (aqueous, 298 K) containing 1-(10-mercaptodecyl)-1'-methyl-[4,4'-bipyridine]-diium bromide or 1-methyl-1'-(10-(naphthalen-2-yloxy)decyl)-[4,4'-bipyridine]-1,1'-diium bromide iodide.

**Figure 59.** Absorption spectra of 0.5 mM solutions (aqueous, 298 K) of ($MV^{2+}$, 2,6-Np)-CB[8] (**Black**), MVSAc (**Purple**), (MVSAc-CB[8]) (**Green**) and (MVSAc, 2,6-Np)-CB[8] (**Red**).

**Figure 60.** MS spectrum of a solution (2 mM, aq., 298 K) of (FcMV, EuNap)-CB[8].

**Figure 61.** Cyclic voltammograms following the recruitment of $FcCH_2NMe_3^+$ (**Black**), Eu.2 (**Blue**) and Fc (**Red**) at CB[7]-functionalised Au electrodes. Electrochemical Setup: *Working Electrode*: CB[7]-functionalised Au . *Reference Electrode*: SCE. *Auxiliary Electrode*: Pt wire. *Electrolytic Solution*: 0.1 M $NaClO_4$ (aqueous, 298 K). *Scan Rate:* 100 mV / s.

**Figure 62.** Cyclic voltammogram of a bare Au surface following exposure to a 1 mM solution (aqueous, 298 K) of Eu.2. Electrochemical Setup: *Working Electrode*: Au. *Reference Electrode*: SCE. *Auxiliary Electrode*: Pt wire. *Electrolytic Solution*: 0.1 M $NaClO_4$ (aqueous, 298 K). *Scan Rate:* 100 mV / s.

**Figure 63.** Cyclic voltammogram of a bare Au surface following exposure to a 1 mM solution (EtOH, 298 K, 12 h) of $FcCH_2NH_2$, prior to (solid) and following sonication in EtOH for 60 (- - -) and 120 s (---). Electrochemical Setup: *Working Electrode*: Bare Au. *Reference Electrode*: SCE. *Auxiliary Electrode*: Pt wire. *Electrolytic Solution*: 0.1 M $NaClO_4$ (aqueous, 298 K). *Scan Rate:* 100 mV / s.

**Figure 64.** Phosphorescent excitation spectrum of a 1 mM solution (aqueous, 298 K) of Eu.2. Experimental Parameters: $\lambda_{em}$ = 616 nm, excitation slit width = 20 nm, emission slit width = 20 nm, PMT Voltage (V) = 1000, CAT 30, number of flashes = 1, total decay time = 0.020 ms, delay time = 0.2 ms, gate time = 1 ms.

**Figure 65.** Phosphorescent emission spectrum of a 1 mM solution (aqueous, 298 K) of Eu.2. Experimental Parameters: $\lambda_{ex}$ = 340 nm, excitation slit width = 20 nm, emission slit width = 20 nm, PMT Voltage (V) = 1000, CAT 30, number of flashes = 1, total decay time = 0.020 ms, delay time = 0.1 ms, gate time = 1 ms.

**Figure 66.** Phosphorescent emission spectrum of a 1 mM solution (aqueous, 298 K) of Eu.2. Experimental Parameters: $\lambda_{ex}$ = 280 nm, excitation slit width = 20 nm, emission slit width = 20 nm, PMT Voltage (V) = 1000, CAT 30, number of flashes = 1, total decay time = 0.020 ms, delay time = 0.1 ms, gate time = 0.5 ms.

**Figure 67.** Phosphorescent emission spectrum of a 1 mM solution (aqueous, 298 K) of Eu.2. Experimental Parameters: $\lambda_{ex}$ = 397 nm, excitation slit width = 20 nm, emission slit width = 20 nm, PMT Voltage (V) = 1000, CAT 30, number of flashes = 1, total decay time = 0.020 ms, delay time = 0.1 ms, gate time = 1.0 ms.

**Figure 68.** Phosphorescent emission spectrum following the recruitment of Eu.2 at a CB[7]-functionalised Au surface. The analogous solution phase spectrum (---, **Section 8.17**, **Figure 64**) is overlaid for comparison and to highlight the lack of sensitised emission at the interface. Experimental Parameters: $\lambda_{ex}$ = 340 nm, excitation slit width = 20 nm, emission slit width = 10 nm, PMT Voltage (V) = 1000, CAT 30, number of flashes = 1, total decay time = 0.020 ms, delay time = 0.2 ms, gate time = 5.0 ms.

**Figure 69.** Phosphorescent excitation spectrum following the recruitment of Eu.2 at a CB[7]-functionalised Au surface. Experimental Parameters: $\lambda_{em}$ = 616 nm, excitation slit width = 10 nm, emission slit width = 20 nm, PMT Voltage (V) = 1000, CAT 30, number of flashes = 1, total decay time = 0.020 ms, delay time = 0.2 ms, gate time = 5.0 ms.

## List of Tables

**Table 1.** Concentration of Fc / $Fc^{+}$ and $P^{0}$ / $P^{+1}$ at biphasic, porphyrin-appended monolayers deposited at Au. All concentrations determined by cyclic voltammetry, and each error bar is equivalent to 3SD and calculated from the data acquired across five separately prepared electrodes. Electrochemical Setup: *Working Electrode*: Respective SAM. *Reference Electrode*: Ag / AgCl. *Auxiliary Electrode*: Pt wire. *Electrolytic Solution*: 0.1 M $TBAPF_6$ (anhydrous, deoxygenated ($N_2$ (g), 10 min.) $CH_2Cl_2$, 298 K). *Scan Rate:* 1000 mV / s.

**Table 2.** XPS atomic sensitivity factors[1].

**Table 3.** The relative % of Au, O, C, S, and N observed at a SAM of MUA deposited at Au. No N was observed in either the survey (**Figure 9, Top Left**) or narrow scan (**Figure 9, Bottom Right**) spectra, as was expected in the absence of either TPAPP or AB-14-172.

**Table 4.** The relative % of Au, O, C, S, and N observed at a SAM of TPAPP-MUA.

**Table 5.** The relative % of Au, C, N, O, and Ni observed at a SAM of AB-14-172-OEG.

**Table 6.** The relative % of Au, C, N, O, and Ni observed at a SAM of AB-14-172-OEG.

**Table 7.** The relative % of Au, C, N, O, and Ni observed at a SAM of OEG following exposure to AB-14-172 in the absence of EDC / NHS. No N or Ni was observed in either the survey (**Figure 13, Top Left**) or narrow scan (**Figure 13, Middle and Bottom Right)** spectra, as was expected in the absence of the coupling reagents.

**Table 8.** Gating the magnitude of the photoelectrochemical response observed upon illuminating a SAM of TPAPP-MUA by varying the bias potential of the working electrode. The difference, in conjunction with the concentration of porphyrin present at the interface, as obtained by cyclic voltammetry, was used to normalise each photoelectrochemical response. An increase in negative bias resulted in greater cathodic photocurrent densities being generated.

**Table 9.** Gating the magnitude of the photoelectrochemical response observed upon illuminating a SAM of AB-14-172-OEG-$Fc(CH_2)_{11}SH$ by varying the bias potential of the working electrode. The difference, in conjunction with the concentration of porphyrin present at the interface, as obtained by cyclic voltammetry (**Appendix, 8.1.3**), was used to normalise each photoelectrochemical response. An increase in negative bias resulted in greater cathodic photocurrent densities being generated.

**Table 10.** The relative % of C, Ni and O observed at a SAM of AB-14-172–OEG.

**Table 11.** The relative % of C, Ni and O observed at a SAM of (AB-14-172-JL241)–OEG. No Fe (from JL241) was apparent in the survey spectrum (**Figure 23**, **Top Left**).

**Table 12.** The relative % of C, Ni and O observed at a SAM of (AB-14-172-JL241)–OEG. No Fe (from JL241) was apparent in the survey spectrum (**Figure 24**, **Top Left**).

**Table 13.** The relative % of C, Ni and O observed at a SAM of OEG following exposure to (AB-14-172-JL241) in the absence of EDC / NHS. Fe (from JL241) and Ni were not apparent in the survey spectrum (**Figure 25**, **Top Left**), as expected in the absence of the coupling reagents.

**Table 14.** The relative % of C, Ni and Au observed upon the deposition of AB-19-144 at Au. The S 2p peak (s) (160 – 172 eV) could not be quantified.

**Table 15.** The relative % of C, Ni and Au observed upon the deposition of AB-19-144 at Au. The S 2p peak (s) (160 – 172 eV) could not be quantified.

**Table 16.** The difference in current observed at SAMs of AB-14-172–OEG, AB-14-172–OEG–Fc11 and (AB-14-172-JL241)–OEG. The difference, in conjunction with the concentration of porphyrin present at the interface, as obtained by cyclic voltammetry, was used to norm